Transactions of the ASME

Journal of Fluids Engineering

Published Quarterly by The American Society of Mechanical Engineers

VOLUME 113 • NUMBER 1 • MARCH 1991

(Contents continued on page 30)

Transactions of the ASME, Journal of Fluids Engineering (ISSN 0098-2202) is published quarterly (Mar., June, Sept., Dec.) for $110.00 per year by The American Society of Mechanical Engineers, 345 East 47th Street, New York, NY 10017. Second class postage paid at New York, NY and additional mailing offices. POSTMASTER: Send address changes to Transactions of the ASME, Journal of Fluids Engineering, c/o THE AMERICAN SOCIETY OF MECHANICAL ENGINEERS, 22 Law Drive, Box 2300, Fairfield, NJ 07007-2300.
CHANGES OF ADDRESS must be received at Society headquarters seven weeks before they are to be effective. Please send old label and new address.
PRICES: To members, $36.00, annually: to nonmembers, $110.00. Add $20.00 for postage to countries outside the United States and Canada.
STATEMENT from By-Laws. The Society shall not be responsible for statements or opinions advanced in papers or . . . printed in its publications (B7.1, Par. 3).

INDEXED by Applied Mechanics Reviews and Engineering Information, Inc.

Contents (continued)

(Contents continued on page 30)

Journal of Fluids Engineering

Editorial

In the past few years, there have been many changes in the structure and the operations of the ASME Fluids Engineering Division, and its archival publication, the *Journal of Fluids Engineering*. The procedures and practices of the Editorial Board of the Journal have evolved naturally over the years. In view of the new ideas and goals for the Division, and for the benefit of the new authors and readers of the Journal, we felt that some information on our current operation should be provided.

The Review Process

Papers are submitted to the Technical Editor's (TE) office. A preliminary screening is done at this level. Papers are then logged, checked for length, quality of figures and conformity with the Journal's standard on experimental uncertainty, numerical accuracy, method of referencing, etc. A paper is then assigned to a technical associate editor (TAE). The TE is continuously informed on the reviewing process but a paper is handled by a TAE until a final recommendation is made to the TE. Authors are encouraged to contact the TE or TAE at any time with questions about the review process.

The TAE arranges for two or three reviews of the submitted paper. After all the reviews are in his/her hands, the TAE provides the authors with a critical evaluation of both the paper and the reviews. At this point, the TAE may recommend to the TE and inform accordingly the authors that the paper (i) be accepted, (ii) be rejected, or (iii) be revised and resubmitted. We try hard to complete this process in two to three months after a paper is received. If, however, for some reason the TAE cannot secure enough reviews by this time, he writes to the authors providing a report on the progress of the reviewing process, as well as whatever information is available at that time.

In case a revision of the paper is recommended, the authors are asked to submit the new version of their paper directly to the TAE, sending a copy to the TE's office. A revised paper should be accompanied by a copy on which the authors should clearly mark changes. It helps greatly if the authors provide a detailed response to the points raised by the reviewers and the TAE. With this material in his/her hands, the TAE may turn again to some or all of his/her reviewers or decide to work on the paper on his/her own. The TAE then makes a final recommendation to the TE and the TE informs the authors of the final decision.

This Editorial Board respects the fact that a paper is the intellectual product of the authors. The purpose of the review process is first to provide constructive criticism on an author's effort and second, to decide whether a paper offers significant information, within the domain of interests of the Journal's readership. On the other hand, the Board actively seeks and publishes discussions of papers. This is pursued by the TE and TAEs during the review process, but readers are encouraged to offer their opinion after reading a published paper. The authors are also invited to prepare a response to a discussion on their paper and both are published in the same issue of the Journal.

Guidelines for the Authors

The basic guidelines on the format of submitted papers appear on the inside of the back cover of each issue. Moreover, authors are asked to conform with some simple guidelines on numerical accuracy and experimental uncertainty set by the Division and the Editorial board. The policy of this Journal is "not to accept for publication any paper reporting the numerical solution of a fluids engineering problem that fails to address the task of systematic truncation error evaluation and accuracy estimation." This has been in practice by this Journal for quite some time and was described clearly in the editorial that appeared in the March 1986 issue.

Authors should abide by the Division's guidelines on reporting experimental uncertainty. A description of these guidelines is available upon request from the TE's office. A more detailed set of guidelines has been formulated by the Division's Coordinating Group on flow measurements and will appear in the next issue.

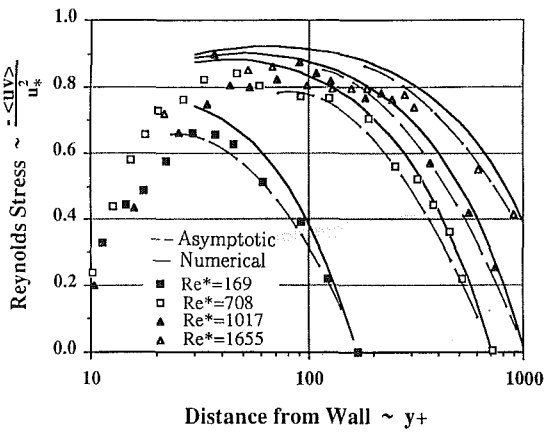

Fig. 1 Reynolds stress in channel flow. Present asymptotic and numerical results compared to the experimental data of Wei and Willmarth (1985) for $l/d = 5$ and $T/T_\infty = 3$.

All papers published in this Journal must now list references alphabetically. A description of the citation format is described in the Editorial of the March 1985 issue.

Finally, we would like to standardize the format of information presented in figures. Authors are urged to try to follow these guidelines. Figures should have well-defined scales so that a reader could obtain the actual numerical dependence of one variable on another. Dependent and independent variables and parameters should be marked on the figure by the same symbols referred to in the text. Quite often, different types of curves, say dashed, or dotted, etc. or different types of symbols, say circles, squares, etc. are employed to denote properties corresponding to values of different parameters. A legend defining this correspondence should be included in the frame of the figure and not in the caption. On the other hand, values of parameters which hold for all the information presented in the figure must be included in the figure caption, beneath the figure. An example is shown in Fig. 1.

The Technical Editor

Journal of Fluids Engineering

Progress Report

Collaborative Testing of Turbulence Models

P.Bradshaw,[1] B. E. Launder,[2] and John L. Lumley[3]

This is a short introduction to an international project, financially supported by U.S. agencies, in which prediction methods for turbulent flow are being compared with the best available experimental data. The project is expected to end in December 1991, with a final report to be available early in 1992.

Most of the readers of this Journal are concerned with predicting turbulent flows (or avoiding them). The exact equations of fluid motion—the Navier-Stokes equations for u,v,w, and p in x,y,z, and t—still require tens or hundreds of hours of supercomputer time to solve for turbulent flows, even in very simple geometries at very low Reynolds numbers. Therefore any engineering prediction method must be formulated in terms of (time)-averaged quantities. This leaves the apparent turbulent stresses (the Reynolds stresses, which are time-averaged products of velocity fluctuations) as unknowns.

Turbulence modeling is the process of deriving semi-empirical equations for the unknown turbulent stresses. Its importance was succinctly stated in 1986 by the late J.N. (Jack) Nielsen, Chief Scientist of NASA Ames Research Center: "Turbulence modeling is the pacing item for the NAS" (the National Aerospace Simulator computer complex at NASA Ames). A recent conference proceedings (Lumley, 1990) gives an introduction to the present state of turbulence research, and a view of its impressively interdisciplinary nature.

Expressions for the Reynolds stresses fall into two classes: correlations between the turbulent stresses and the mean velocity gradients at the same points, in the form of so-called "eddy-viscosity" relations; and term-by-term models of the exact transport equations for Reynolds stresses. The latter equations make it clear that the Reynolds stresses at a given point depend on the whole history of the flow and not on the mean velocity gradients at the same point.

Some explanation is needed for the use, and relative success, of "eddy-viscosity" models, and their close relatives the mixing length models, which also assume a direct, local, relation between (turbulent) stresses and (time-average) rates of strain. Briefly, the effect of history on the local behavior of a turbulent flow is small if the mean flow changes only slowly with distance downstream. Here "slowly" means that the time scale of streamwise change, following the mean motion of the fluid, is large compared to the eddy time scale. "Simple" shear layers, such as attached boundary layers, wakes far behind the body that produces them, and jets far from their origin, are typical examples of slowly-changing flows. However, many real-life turbulent flows change rapidly in the streamwise direction. Examples include boundary layers in the region of separation or of interaction with a shock wave, wakes just downstream of a body, or jets deflected by an oncoming stream or a solid surface. In such "complex" flows, eddy-viscosity models can give misleading results, because the turbulent stresses change much less rapidly than the mean flow. This conclusion applies both to models in which the eddy viscosity is algebraically related to mean-flow scales and those like the "k,ϵ" model in which partial differential equations are solved to yield the eddy viscosity.

Models based directly on the Reynolds-stress transport equations are claimed by their originators, to do much better, and one of the main objects of the "Collaborative Testing ..." project is to test this claim. Whatever the result, the unfinished business of turbulence modeling is the development of prediction methods that give acceptable engineering accuracy, at acceptable cost, for a worthwhile range of "complex" flows.

The project is funded by four U.S. agencies—Air Force Office of Scientific Research, Army Research Office, NASA, and Office of Naval Research, all of which have strong interests in turbulence modeling.

The present project is the natural successor to the meetings of turbulent-flow predictors held at Stanford in 1968 on simple two-dimensional boundary layers (Kline et al., 1968) and in 1980–81 on "complex" flows (Kline et al., 1982). At the 1968 meeting it was shown that many different turbulence models could produce good predictions for attached 2-D boundary layers: it was gradually realized that almost any method which invoked the universal law of the wall would produce good predictions in such cases, almost irrespective of the plausibility of the model used for the outer layer of the boundary layer. At the 1980–81 meeting, data from more complex flows were analyzed and discussed (1980) and compared with predictions of various turbulence models (1981). The conclusion of the 1980–81 meeting, much assailed for its negativity, was that none of the current turbulence models could produce predictions to good engineering accuracy over the whole range of turbulent flows. This conclusion applied both to models using eddy-viscosity concepts and to those based on term-by-term modeling of the Reynolds stress transport equations. When turbulence modeling became a hot topic in the early 1970s, there was a strong feeling that such a "universal" turbulence model could, in principle, exist. Logic, of course, suggested that any simplification of the Navier-Stokes equations (clearly the exact description of any flow of a simple viscous fluid) would be restricted in accuracy or range of applicability, on the standard principle that "you may get what you pay for, but you don't get what you don't pay for."

In the early stages, we planned a conference on the lines of the 1981 meeting, but, in informal discussions at the Cornell

[1]Mechanical Engineering Department, Stanford University, Stanford, CA 94305.
[2]University of Manchester Institute of Science and Technology, Manchester, England M60.
[3]School of Mechanical and Aerospace Engineering, Cornell University, Ithaca, NY 14853.

University "Whither Turbulence" symposium in March 1989, Dr. D. M. Bushnell of NASA Langley Research Center pointed out that a collaborative effort conducted by correspondence (including mailing of tapes and disks plus Fax and electronic mail) would allow better interaction, optimization and discussion than a "sudden death" conference. (A criticism of the 1980/81 conference was that a one-week meeting was too short for thoughtful evaluation of results, and plans for a follow-up meeting fell through.)

In the present "mail order" project, data from experiments on, and simulations of, turbulent flows are distributed on microcomputer disk to developers of (time-averaged) engineering turbulence models. The predictions of each model are returned to the organizers and redistributed to all the modelers, plus some experiments and other experts (total approx. 120), for comment. This is an international effort, with no restrictions except those involving proprietary data: any data or turbulence models resulting from the part of the project supported by U.S. government funds would be freely available. There are participants from the U.S.A., Canada, England, France, The Netherlands, Norway, Sweden, Denmark, Germany, Yugoslavia, Greece, USSR, India, Australia, Japan, and Korea. The "reaction time" of modelers has proved to be much longer than anticipated. One reason for slow progress or complete withdrawal, not clearly foreseen by the organizers or the agencies, is that much funding of turbulence modeling in the 1990s is more closely tied to the sponsor's interests than it was ten years ago, making it difficult to divert effort to a general-interest project. Another reason is that comparisons with data have prompted many modelers to improve their models or numerics. This applies particularly to compressible flows: modelers were asked to predict "flat plate" (constant-pressure) skin friction and heat transfer at Mach numbers up to 8, and it was clear that many models had never been tested at such high Mach numbers. Some codes failed numerically, and some models performed badly at high Mach number (and neither is a disgrace if the code and model were only intended to operate up to transonic Mach numbers). Alas, several codes gave poor heat-transfer results because the modelers had used the wrong definition of Stanton number: the temperature difference in the denominator of St is the difference between external-flow temperature and the adiabatic "recovery" temperature of the surface, and, clearly, the latter must be the value actually calculated by the model. There have been several other examples of minor errors and difficulties which have contaminated the results of models which are in principle capable of giving good performance. A disproportionate amount of time has been taken up in individual communications with modelers to sort out such difficulties.

One remarkable cause of confusion is the wide range of constants in the logarithmic "law of the wall" that are assumed, or predicted, in different methods. According to first-order arguments, which are used implicitly in all the calculation methods, these constants should be universal. The actual range—ignoring a few outlying methods—implies a 10 percent "uncertainty" in skin friction on a flat plate in low-speed flow, the simplest of all test cases. We are trying to achieve a consensus!

The project has been much delayed by the need to "debug" the different calculation methods, but comparisons have been made with some real test cases, including free shear layers, boundary layers in arbitrary pressure gradient, and separated flows. Comparisons with simulation data have proved particularly valuable, especially for testing "low Reynolds number" models for the viscous wall region, which is difficult to resolve in an experiment. Further test cases are now being distributed, and we hope that by the end of the project we shall be able to deliver a useful "state-of-the-art" review to the fluids engineering community—hopefully to the *Journal of Fluids Engineering*.

References

Lumley, J. L. (ed.), 1990, *Whither Turbulence? Turbulence at the Crossroads*, Springer, Berlin.

Kline, S. J., Morkovin, M. V., Sovran, G., and Cockrell, D. J. (eds.), 1968, "Computation of Turbulent Boundary Layers," Thermosciences Division, Mech. Engg. Dept., Stanford.

Kline, S. J., Cantwell, B. J., and Lilley, G. M. (eds.), 1982, "Complex Turbulent Shear Flows: Comparison of Computation and Experiment," Thermosciences Division, Mech. Engg. Dept., Stanford.

Mohamed Gad-el-Hak
Department of Aerospace & Mechanial Engineering,
University of Notre Dame,
Notre Dame, IN 46556
Mem. ASME

Dennis M. Bushnell
Fluid Mechanics Division,
NASA-Langley Research Center,
Hampton, VA 23665
Mem. ASME

Separation Control: Review

Under certain conditions, wall-bounded flows separate. To improve the performance of natural or man-made flow systems, it may be beneficial to delay or advance this detachment process. The present article reviews the status and outlook of separation control for both steady and unsteady flows. Both passive and active techniques to prevent or to provoke flow detachment are considered and suggestions are made for further research.

1 Introduction

1.1 Flow Separation. Fluid particles in a boundary layer are slowed down by wall friction. If the flow is sufficiently retarded, for example due to the presence of an adverse pressure gradient, the momentum of those particles will be reduced by both the wall shear and the pressure gradient. In terms of energy principles, the kinetic energy gained, at the expense of potential energy, in the favorable-pressure-gradient region is depleted by viscous effects within the boundary layer. In the adverse-pressure-gradient region, the remaining kinetic energy is converted to potential energy but is too small to surmount the *pressure hill* and the motion of near-wall fluid particles is eventually arrested. At some point (or line), the viscous layer departs or breaks away from the bounding surface. The surface streamline nearest to the wall leaves the body at this point and the boundary layer is said to separate (Maskell, 1955). At separation, the rotational flow region next to the wall abruptly thickens, the normal velocity component increases, and the boundary-layer approximations are no longer valid.

Due to the large energy losses associated with boundary-layer separation, the performance of many practical devices is often controlled by the separation location. For example, if separation is postponed, the pressure drag of a bluff body is decreased, the circulation and hence the lift of an airfoil at high angle of attack is enhanced, and the pressure recovery of a diffuser is improved.

Great strides have been made in the past few decades in establishing a firm analytical foundation for steady, two-dimensional separation. On the other hand, theoretical or numerical analysis of three-dimensional or unsteady separation is considerably less developed and progress to date in these areas has depended crucially on experimental work. From a practical point of view, the local separation over, say, a lifting surface has a very strong effect on the global aerodynamic properties, and a thorough, fundamental understanding of the phenomenon is obviously needed. Separation on such a surface occurs just prior to or at maximum loading, thus greatly influencing the device's optimum performance.

The breakthrough in unsteady separation research was achieved by Moore, Rott, and Sears during the 1950's. Prior to their work, it was believed that steady and unsteady separations have the same characteristics; namely, the point of vanishing wall shear, the termination of the boundary layer, and the beginning of the wake or bubble of separated fluid. Rott (1956), in analyzing the unsteady flow in the vicinity of a stagnation point, noted that the point of vanishing wall shear does not coincide with the point of boundary-layer detachment. In the same year, Sears made the assumption that the unsteady separation point is characterized by the simultaneous vanishing of the shear and the velocity at a point within the boundary layer as seen by an observer in a coordinate convected with the separation velocity. Two years later, Moore (1958), while investigating a steady flow over a moving wall, arrived at the analogous model to that for unsteady separation. He stated that "for a slowly moving wall separation occurs when, at some point in the boundary layer, the profile velocity and shear simultaneously vanish."

1.2 Control of Separation. As defined by Flatt (1961), the term boundary layer control includes any mechanism or process through which the boundary layer is caused to behave differently than it normally would, were the flow developing naturally along a smooth straight surface. Examples include reduction/delay or enhancement/triggering of transition, separation, skin-friction or pressure drag, heat transfer, lift, and acoustics. Prandtl (1904) pioneered the modern use of flow control in his epoch-making presentation to the Third International Congress of Mathematicians held at Heidelberg, Germany. In just 8 pages (as required for acceptance by the Congress) of a paper entitled "On the Motion of a Fluid with Very Small Viscosity," Prandtl introduced the boundary layer theory and the idea of self similarity, explained the mechanics of steady, two-dimensional separation, opened the way for understanding the motion of real fluids, and described several experiments in which the boundary layer was controlled.

Of all the various types of shear flow control now extant, control of flow separation, historically referred to as

Contributed by the Fluids Engineering Division for publication in the JOURNAL OF FLUIDS ENGINEERING. Manuscript received by the Fluids Engineering Division July 25, 1990.

boundary-layer control or BLC, is probably the oldest and most economically important. Separation control is of immense importance to the performance of air, land or sea vehicles, turbomachines, diffusers, and a variety of other technologically important systems involving fluid flow. Generally it is desired to postpone separation so that form drag is reduced, stall is delayed, lift is enhanced, and pressure recovery is improved. However, in some instances it may be beneficial to provoke separation. For example, to improve the subsonic high-lift performance of an airfoil optimized for high-speed flight, a flap may be used to initiate leading-edge separation followed by reattachment.

Flow separation causes significant deviations from inviscid pressure distributions. Such deviations can be either favorable, as in the vortex lift associated with lee surface separation on swept leading-edges and the use of *spoilers* to obviate ground-effect-lift during landing; or, more commonly, detrimental, resulting, for example, in high form drag and reduced diffuser efficiency. Typical applications and benefits of flow separation control include: effective low-Reynolds-number airfoils for remotely piloted vehicles (RPVs), propellers, windmills, helicopters, etc.; efficient inlets and diffusers; improved axial flow compressors; increased $C_{L\max}$ for increased payload, reduced engine power or noise at takeoff, shorter runways and reduced approach speed; supermaneuverability or *bird-like flight*; efficient and effective stall or spin control; reduced drag on missiles, automobiles, ships and helicopters; as well as a myraid of applications in industrial areo- and hydrodynamics. As examples of estimated benefits, a 5 percent improvement in landing $C_{L\max}$ would allow a 25 percent payload increase (Butter, 1984); mitigation of military stall/spin accidents which from 1977-1986 involved over 150 aircraft; application of flow separation control to tractor-trailer truck drag reduction which could save in excess of 50 million barrels of oil per year (Muirhead and Saltzman, 1979); and diffuser suction in supersonic closed-circuit wind tunnels which would result in an estimated 30–50 percent power reduction on a device which can draw in excess of 20 MW (Bushnell and Trimpi, 1986).

1.3 Methods of Control. Flow separation control is currently employed, for example, via vortex generators on the wings of most Boeing aircraft; via blown flaps on older generation supersonic fighters or leading-edge extensions and strakes on newer generations; and via passive bleed in the inlets of supersonic engines on, for example, the SR-71 and Concorde. Future *possibilities* for aeronautical applications of flow separation control include providing structurally efficient alternatives to flaps or slats; cruise application on conventional takeoff and landing aircraft, CTOL, including BLC on thick spanloader wings (Smith and Thelander, 1973); as well as cruise application on high-speed civil transports, HSCT, for favorable interference wave drag reduction, increased leading-edge thrust, and enhanced fuselage and upper surface lift (Bushnell, 1990). In fact, much of the remaining gains to be made in aerodynamics appear to involve various types of flow control, including separated flow control (e.g., Hazen, 1984; Chambers, 1986).

Typical, in some cases, serious problems associated with flow separation control include parasitic device drag or energy consumption; system weight, volume, complexity, reliability or cost; performance sensitivity to body attitude or orientation; and, especially in the case of the automobile, styling (Poisson-Quinton, 1950; Silhanek, 1969; Decken, 1971; Sovran et al., 1978). The status of flow separation control is still typified by a comment made in 1954 by Darby: "The Germans were experimenting with BLC in the wind tunnel in the 1920's—NACA began wind-tunnel tests in the late 1920's. It was not until 1949 that American agencies became interested—the skepticism seems to be breaking down at long last, but any branch of technology which has gone so long without bearing fruit certainly requires a close scrutiny." "There are an almost bewildering number of systems, at least for separation control, which work."

Nomenclature

C_D = drag coefficient ($\equiv 2D/\rho U_\infty^2 c$)
C_f = local skin-friction coefficient ($\equiv 2\tau_w/\rho U_\infty^2$)
C_L = lift coefficient ($\equiv 2L/\rho U_\infty^2 c$)
$C_{L\max}$ = maximum lift coefficient
C_q = suction coefficient ($\equiv |v_w|/U_0$)
c = airfoil's chord
D = drag force per unit span
L = lift force per unit span
L/D = lift-to-drag ratio
P = instantaneous hydrostatic pressure
P_0 = pressure outside boundary layer
$\bar{P}$ = mean pressure
R = wall's radius of curvature
R_c = Reynolds number based on chord and freestream velocity ($\equiv U_\infty c/\nu$)
$\mathrm{R}_{\delta*}$ = displacement thickness Reynolds number ($\equiv U_0\delta^*/\nu$)
R_θ = momentum thickness Reynolds number ($\equiv U_0\delta_\theta/\nu$)
R_κ = Reynolds number based on height of a roughness element and the velocity in the undisturbed boundary layer at the height of the element ($\equiv U(\kappa)\kappa/\nu$)
Re = Reynolds number
T = instantaneous temperature
t = time
$\bar{T}$ = mean temperature
U_i = instantaneous velocity component
$\overline{U_i}$ = mean velocity component
U_0 = velocity outside the boundary layer
U_∞ = freestream velocity
$U(\kappa)$ = velocity in the undisturbed boundary layer at the height of a roughness element
u_i = fluctuating velocity component
u^* = friction velocity ($\equiv\sqrt{\tau_w/\rho}$)
v_w = normal velocity of fluid injected or withdrawn through the wall
x_i = Cartesian coordinates
x = streamwise distance from leading edge
y = normal distance from the wall
y^+ = normal distance in wall units ($\equiv y\,u^*/\nu$)
z = spanwise coordinate
α = angle of attack
$\dot{\alpha}$ = time rate of change of attack angle
δ = boundary-layer thickness
δ_θ = momentum thickness
δ^* = displacement thickness
κ = height of a discrete roughness element
Λ = shape factor ($\equiv (\delta^2/\nu)(dU_0/dx)$)
μ = dynamic coefficient of viscosity
ν = kinematic viscosity
ν/u^* = viscous length scale (wall unit)
ρ = density
$-\rho\,\overline{uv}$ = tangential Reynolds stress
$\mathfrak{I}$ = period of oscillation of a forcing signal
τ_w = shear stress at the wall ($=\rho\,u^{*2}$)
$[\Omega_z]_0$ = instantaneous spanwise vorticity at the wall ($\equiv -[\partial U/\partial y]_0$)
$[\bar{\Omega}_z]_0$ = mean spanwise vorticity at the wall ($\equiv -[\partial \bar{U}/\partial y]_0$)

In general, the field of flow separation control is far richer than the conventional view which usually considers only suction, injection and vortex generators. Many decades of research have proven that separation control, in most of its guises, will work. The task of researchers and designers now is to improve reliability where necessary and increase net gains through innovation. This richness of existing approaches for flow separation control is mirrored in the extensive literature, partially available for low-speed flows in the publications by Lachmann (1961); Colin and Williams (1971); Chang (1976); Adkins (1977); Gad-el-Hak (1989a), (1989b), (1990a); Lin et al. (1990a); and references therein as well as herein. For high-speed flows, excellent recent reviews for separation control in shock-boundary-layer interactions are provided by Delery (1985) and Viswanath (1988).

Given an imposed pressure field, the kernel problem in separation control is to add momentum to the very near-wall region of the flow by either transferring momentum from flow regions farther from the wall, which are still *momentum rich*, or by direct addition of power drawn from the propulsive system. Probably the most popular flow separation control technique has been to add momentum to the near-wall region either actively, e.g., tangential blowing or wall jets, or passively, for example, boundary-layer tripping, turbulence enhancement or vortex generators of various scales.

1.4 Outline of Present Article. The purpose of the present work is to briefly summarize the status and outlook for flow separation control with an emphasis upon more recent developments such as optimized vortex generators, various methods of turbulence control including dynamic inputs, and wall heat transfer. Direct comparisons between the various approaches on common test problems will be made. The recent advances in computational fluid dynamics are allowing the transformation of much of BLC from an empirical art to a predictive science, and this subject will be briefly revisited near the end of the present article. Due to space limitations, the presentation does not include large-scale-provoked separation or control of vortices (e.g., Williams and Amato, 1989; Bushnell and Donaldson, 1990; Panton, 1990; Williams and Papazian, 1990), nor the related problem of asymmetric nose/body vortex control on missiles, etc., at high angles of attack (Vakili, 1990). However, control *by* vortices is included in this paper. Separation control is addressed for both nominally two-dimensional and three-dimensional flows, although the knowledge base concerning the latter is noticeably deficient. Typically three-dimensional separation occurs sooner but is less catastrophic than the quasi-two-dimensional case (Driver, 1989).

In the present article, we review methods to control separation for both steady and unsteady boundary layers. Both passive and active techniques to prevent or to provoke flow detachment are considered. For historical reasons, most of the separation control methods discussed in here were developed for aircraft wings. The results, however, pertain to fundamental properties of fluid flow and could readily be extended to a variety of systems such as diffusers, steam turbine blades, wind turbine rotors, pump impellers, and off-shore structure components.

To set the appropriate mechanistic framework for discussing the variety of control tools available, differences between steady and unsteady separations are first considered in the following section. The governing equations needed to examine the local and the instantaneous effects of the different control techniques are recalled in Section 3. Available methods to affect the shape of the velocity profile and thus to delay or advance separation are discussed in Section 4. In the following section, tools for controlling moving-wall and time-dependent separations are established. Section 6 addresses the three-dimensional separation problem. Turbulators to promote laminar-to-turbulent transition, thus increasing the boundary layer ability to resist separation, are reviewed in Section 7. Separation control by active or passive near-wall-momentum addition is considered in the following section. In Section 9, a very brief discussion of separation provocation is presented. Finally, general discussion and concluding remarks are given in Section 10.

2 Steady and Unsteady Separation

2.1 Steady Separation. Separation of a steady, two-dimensional boundary layer was explained first by Prandtl (1904) in his milestone presentation *"Über Flüssigkeitsbewegung bei sehr kleiner Reibung,"* in which he introduced the Boundary-Layer Theory. Fluid particles near the surface are retarded by the friction of the wall and by any adverse pressure gradient present in the freestream. If the near-wall fluid has insufficient momentum for it to continue its motion, it will be brought to rest at the separation point (line). Further downstream, the adverse pressure forces will cause reverse flow. Since the velocity at the wall is always zero, the gradient $[\partial U/\partial y]_{y=0}$ must be positive upstream of separation, zero at the point of separation, and negative in the reverse flow region. For an axially symmetric flow, the line of separation becomes a circle, and the point of vanishing shear still coincides with the point of separation.

In Prandtl's view, the separation point is entirely determined by external conditions. Boundary-layer separation is accompanied by a thickening of the rotational flow region and ejection of vorticity. Downstream of the separation point the shear layer either passes over the region of recirculating fluid and reattaches to the body surface or forms a wake and never reattaches to the body. The characteristic dimension of the recirculating region is quite large in the latter case and is of the order of the body height.

Analytically, the solution of the steady, two-dimensional, laminar boundary-layer equations with a prescribed external-pressure (or external-velocity) distribution breaks down at the point of separation, and this is commonly known as the Goldstein's singularity, in honor of Sydney Goldstein who first noted the singular behavior of the solution near a point of zero skin friction (Goldstein, 1948).[1] The singularity of the boundary-layer equations at separation is obviously not a physical property of the flow and can be overcome by prescribing either the displacement thickness or the wall shear distribution instead of the external pressure. This kind of analysis is termed inverse calculation.

2.2 Unsteady Separation. For two-dimensional flow over moving walls, two-dimensional unsteady flows, and three-dimensional steady and unsteady flows, the point (line) of vanishing wall shear does not necessarily coincide with separation, and this greatly complicates the problem. This was first observed by Rott (1956) while analyzing the unsteady flow in the vicinity of a stagnation point. He observed that, while the wall shear vanished with an accompanying reverse flow, there was no singularity or breakdown of the boundary-layer assumptions. In seeking a generalized model for separation, Sears (1956) postulated that the unsteady separation point is characterized by the simultaneous vanishing of the shear and the velocity at a point within the boundary later as seen by an observer moving with the velocity of the separation point.

Moore (1958), while investigating a steady flow over a moving wall, arrived at the same model for unsteady separation. Based on an intuitive relationship between steady flow over a moving wall and unsteady flow over a fixed wall, Moore was able to sketch the expected velocity profiles for both cases as

[1] For a review of other singularities occurring in the equations for three-dimensional and/or unsteady boundary-layer flows, see the article by Williams (1985).

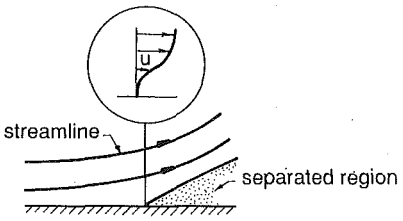

Fig. 1(*a*) Fixed wall

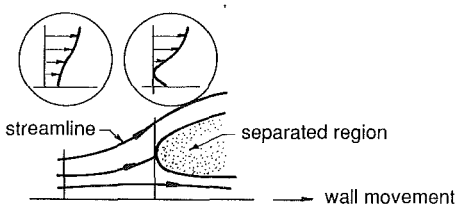

Fig. 1(*b*) Wall moving downstream

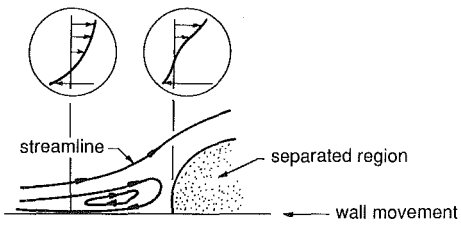

Fig. 1(c) Wall moving upstream

Fig. 1 Streamlines and velocity profiles when a boundary layer over a fixed or moving wall separates.

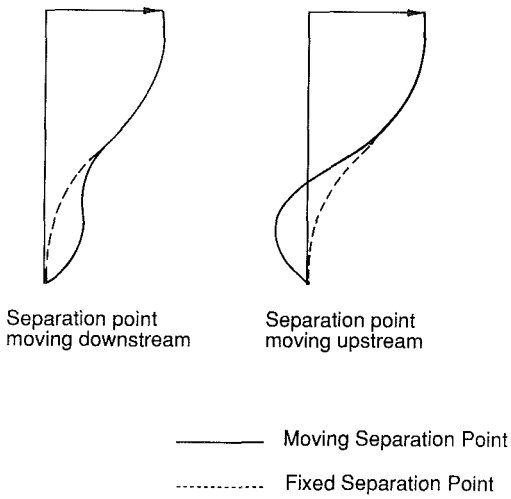

Fig. 2 Moore's (1958) postulated velocity profiles for unsteady separation on a fixed wall.

seen in Figs. 1 and 2. He considered the possibility that a Goldstein type singularity occurs at the location where the velocity profile has simultaneously zero velocity and shear at a point above the moving wall. Equivalently, for unsteady separation on a fixed wall, the separation point is the location at which both the shear and velocity vanish in a singular fashion in a frame of reference moving with the separation point. The main drawback of this Moore-Rott-Sears (MRS) model in the fixed wall case is that the speed of the separation point is not known *a priori*, making it difficult to locate this point and forcing researchers to rely on more qualitative measures for unsteady separation. Sears and Telionis (1972a, 1975) were the first to prove that the boundary-layer separation singularity accompanies detachment of unsteady flows. They suggested that the existence of such singularity could serve as a criterion for unsteady separation when integrating numerically the boundary-layer equations.

Because of the above difficulty, early attempts to verify this important Moore-Rott-Sears model of unsteady separation considered the more tractable problem of steady separation over moving walls. Both Vidal (1959) and Ludwig (1964) investigated experimentally a shrouded rotating cylinder in steady flow. As expected, separation was delayed (moved downstream) when the wall moved in the freestream direction and was advanced when the wall moved opposite the main flow. The measured velocity profiles corresponded to those hypothesized by Moore (1958). Telionis and Werle (1973) presented an analytical verification of the separation model for the case of a downstream moving wall.

Until the work of Williams and Johnson (1974a, 1974b), the relationship between unsteady boundary-layer separation over fixed walls and steady separation over moving walls has been an intuitive one. By considering the rather general class of unsteady, two-dimensional boundary-layer problems which could be treated by the method of semisimilar solutions, Williams and Johnson (1974a) were able to transform an unsteady problem in three independent variables into an equivalent problem in two independent variables. This transformation made it then possible to use conventional numerical techniques for solving steady, nonsimilar boundary-layer problems, and allowed the authors to investigate some time-dependent flows where separation occurs in a coordinate system for which unsteady separation is most easily identified and analyzed. As a practical example, Williams and Johnson (1974a) verified the MRS model for unsteady separation for a particular time-dependent retarded flow the steady flow equivalent of which is the classical linearly retarded flow studied by Howarth (1938).

In a subsequent paper, Williams and Johnson (1974b) established a rigorous analytical link between unsteady separation over a fixed wall and steady separation over a moving wall for the special case in which the external velocity distribution in the fixed coordinate system is a function only of a linear combination of the streamwise coordinate and time and where the wall moves downstream with the (constant) speed of the unstady separation joint. Once more, Williams and Johnson were able to transform a given unsteady flow into a steady flow over a wall moving with the speed of the separation point and then to relate this back to the unsteady flow.

2.2.1 Archetypes of Unsteady Separation. There are two distinctly different kinds of unsteady separation. On a body oscillating in pitch, the pressure gradient may vary both in magnitude and form. On the other hand, if the freestream velocity changes periodically with time, the impressed (mean) pressure gradient over a fixed surface varies in magnitude but not in form during the oscillation. Detailed velocity measurements in the first kind are scarce because of the obvious difficulties involved in instrumenting a moving body. Accordingly, the exact nature of unsteady separation for this case remains unclear, despite the abundance of qualitative flow visualization data (Gad-el-Hak, 1987).

Consider first the case of an airfoil oscillating in pitch. Sudden changes in lift, drag and pitching moment occur near the onset of separation. The *dynamic stall* is characterized by two distinctly different flow phenomena (Ericsson, 1971, 1988; Ericsson and Reding, 1971, 1987). The first is quasi-steady in nature and is due to time lag and boundary layer improvement effects. The second phenomena is transient in nature and concerns the effects of the forward movement of the separation point. As the airfoil leading edge moves upward, the boundary layer between the stagnation and separation points experiences a *moving wall/wall jet* effect very similar to that observed on a rotating cylinder (Ericsson and Reding, 1984, 1986, 1987; Ericsson, 1988). Thus, the boundary layer has a fuller velocity

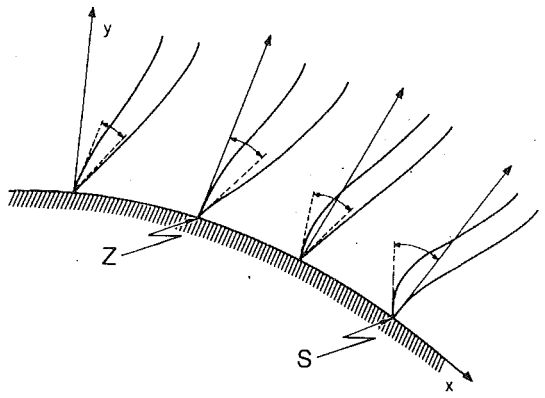

Fig. 3 Envelopes of velocity profiles for periodic oscillations. The dashed lines and the arrows indicate the extreme positions of the tangents to the profiles at the wall. Schematic representation of Despard and Miller's (1971) data.

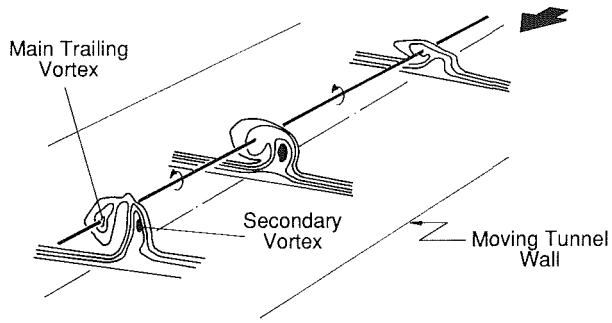

Fig. 4 Surveys of total head. (From Harvey and Perry, 1971.)

profile as compared to the steady case and is therefore more resistant to separation. On the downstroke the effect is the opposite, promoting separation. At stall, a vortex is shed from the leading edge and is convected downstream over the chord. For high reduced frequency, this *spilled vortex* remains over the airfoil a significant portion of the cycle and extra lift is produced.

The relatively simpler second kind of unsteady separation was investigated by Despard and Miller (1971) who performed a series of experiments to measure the instantaneous velocity profiles in oscillating boundary-layers subject to adverse pressure gradients. An array of 10 hot-wire probes was used to measure the normal profiles of streamwise velocity at several points along the rear portion of an airfoil-like body placed in a low-speed wind tunnel. The freestream velocity was varied periodically by a set of rotating shutter valves located downstream of the test section. The resulting envelopes of the velocity profiles throughout the entire cycle of oscillation are shown schematically in Fig. 3 for four different stations along the body. Within half a boundary layer thickness of the beginning of the region of wake formation, the point S in the figure exhibits reverse flow or zero velocity gradient at the wall for the entire cycle of profiles. This led Despard and Miller to propose a practical definition of unsteady separation as the farthest upstream point at which there is zero velocity or reverse flow at some point in the velocity profile throughout the entire oscillation cycle. This approach avoids the difficulty of determining the speed of the separation point as required by the Moore-Rott-Sears model. Point Z in Fig. 3 is the farthest upstream point at which the wall shear stress passes through zero during a complete cycle of oscillation. Therefore, the point of vanishing shear oscillates between S and Z, but the outer flow remains attached until S. Thus, Despard and Miller's results provided the first experimental evidence that a thin layer of reversed flow can be embedded at the bottom of an otherwise attached boundary layer, as postulated by Moore (1958). Despard and Miller further concluded that the presence of an oscillating velocity component and a time-dependent adverse pressure gradient cause the separation point to be displaced upstream of its steady flow position. The distance between the two points diminishes as the frequency of oscillation increases but is rather insensitive to variations in the amplitude of the outer flow oscillations.

Shortly after this important experiment, Sears and Telionis (1975) provided a review of the numerical evidence of the validity of the Moore-Rott-Sears model. Numerical integrations of unsteady laminar and turbulent boundary layers showed no evidence of the Goldstein's singularity, even in a region of partially reversed flow and through the point of zero skin friction. The singularity did appear, however, at the point of unsteady separation as defined by the MRS criterion.

Some controversy still exists over the precise definition of unsteady separation. Telionis (1979) reiterated that separation means the location on the solid boundary where the flow stops creeping over the skin of the body and breaks away from the wall, thus generating a turbulent wake. Sears and Telionis (1972a, 1972b) argued that abrupt changes of boundary-layer properties in the first-order boundary-layer equations may signal the approach of the point of separation, or of the Goldstein singularity. Despard and Miller (1971), on the other hand, defined separation as the farthest upstream station at which the shear fluctuates between zero and some negative value throughout an entire cycle of freestream oscillation. Tsahalis and Telionis (1974) numerically studied the unsteady separation in an oscillating flow and found that Despard and Miller's criterion could be verified under certain but not all situations.

2.2.2 Turbulent Boundary Layers. The carefully executed, well-documented experiments of Simpson and his colleagues (Shiloh et al., 1981; Simpson et al., 1981a, 1981b, 1983; Simpson and Shivaprasad, 1983) are very useful in understanding some of the basics of steady and unsteady separation in turbulent flows. Simpson et al. investigated the structure separating, nominally two-dimensional, turbulent boundary layers in a steady freestream (Shiloh et al., 1981; Simpson et al., 1981a, 1981b) as well as in a sinusoidally oscillating freestream (Simpson et al., 1983; Simpson and Shivaprasad, 1983). Their experiments illustrate both the similarities and differences between steady and unsteady separations. Upstream of where intermittent backflow begins, the flow behaves in a quasisteady manner. Downstream, there are nonquasisteady effects on the ensemble-averaged flow structure. Also, the hysteresis effects in the ensemble-averaged velocity profiles are more pronounced for higher-reduced-frequency freestream oscillations.

2.3 Vortex-Induced Separation. Separation can be triggered experimentally with concentrated vortices moving close to a wall. Harvey and Perry (1971) placed a half-span rectangular wing in a wind tunnel and observed the evolution of the resulting single tip vortex as it passes over a downstream moving floor (Fig. 4). Total-head surveys in planes across the flow were conducted to observe separation and the formation of a secondary vortex of opposite sense to the main one. The secondary vortex causes a rebounding of the trailing vortex, as sketched in Fig. 5. Similar effects are present when a ring vortex approaches a wall normal to its propagation direction (Magarvey and McLatchy, 1964; Schneider, 1980). In the latter case, a downstream-moving unsteady separation is produced.

Ho (1986) attributes the sparseness of a positive experimental proof (or disproof) of the Moore-Rott-Sears criterion for unsteady separation to the difficulty of measuring the separated velocity near the wall. The temporal variation of the resulting three-dimensional velocity field necessitates the use

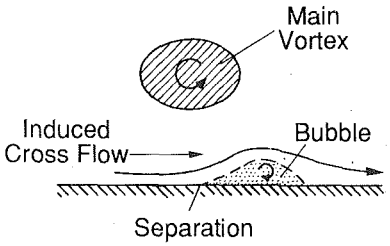

Fig. 5(*a*) A section downstream of the initial separation

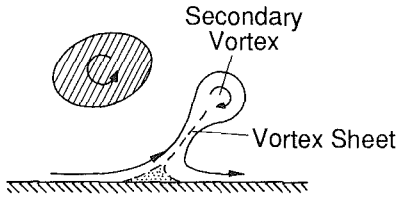

Fig. 5(*b*) Subsequent development of the secondary vortex

Fig. 5 Suggested interpretation of the total-head surveys. (From Harvey and Perry, 1971.)

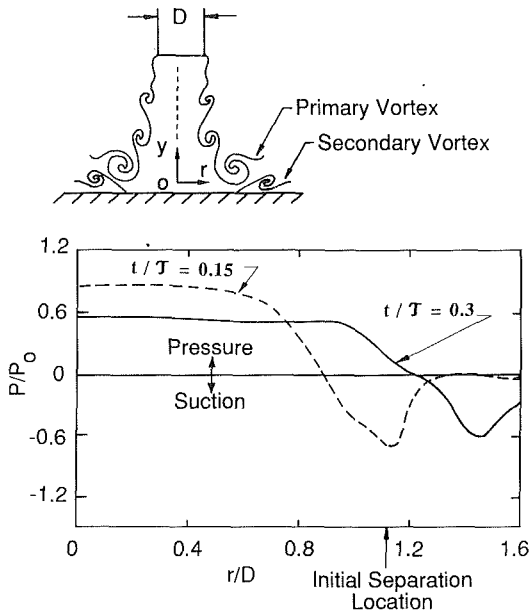

Fig. 6 Forced axisymmetric jet impinging normally onto a flat plate. Phase averaged pressure traces at the instant of separation ($t/\mathfrak{T} = 0.15$) and after a short time interval ($t/\mathfrak{T} = 0.3$). (From Didden and Ho, 1985.)

of a large number of small, fast-response probes and a colossal data acquisition and storage system. This problem is particularly acute for an upstream moving separation, where flow reversal occurs leading to additional measuring difficulties. No flow reversal occurs in a downstream moving separation, and hot-wire probes can then be used to survey the flow field in the vicinity of the wall.

Detailed measurements of the downstream-moving separation caused by periodic ring vortices impinging normally onto a flat plate were conducted by Didden and Ho (1985). They forced an axisymmetric jet to produce a train of primary ring vortices in the air-jet shear layer sketched at the top of Figure 6. The phase-locked flow visualization pictures obtained by Didden and Ho using smoke clearly show that the wall-jet boundary layer evolves into a secondary vortex, counter-rotating with respect to the primary vortex, and periodically separates. The unsteady separation is induced by the primary vortex and moves downstream in the radial mean-flow direction, thus allowing detailed measurements with hot-wire probes. The phase-averaged measurements of normal and radial velocity components provide data for locating the onset of separation in space and time.

Like all other cases discussed thus far, the unsteady separation phenomenon observed in the impinging jet flow involves a strong viscous-inviscid interaction. The detailed data obtained by Didden and Ho (1985) reval the following sequence of events. The primary ring vortex in the inviscid region produces a fast moving stream while it approaches the wall. The resulting accelerating flow causes a negative wall pressure in the low-pressure region downstream from the jet axis. Further downstream, pressure recovery results in an unsteady adverse pressure gradient which retards the flow in the viscous layer. Hence, a strong shear layer is generated at the viscous-inviscid interface. The instability of this shear layer leads to the rollup of the vortex sheet and the formation of a secondary vortex. The ejection of this secondary vortex, believed to be associated with the onset of unsteady separation, leads to an abrupt increase in the momentum thickness and the formation of a bulge that convects downstream at the same speed as the zero-shear-stress point of the radial velocity profile. In other words, the unsteady separation is originated from a local shear layer, which is initiated in the viscous region by the unsteady adverse pressure gradient produced by the primary vortex.

At the instant of apparent separation, a sharp, high-amplitude suction peak occurs in the surface pressure signature of the secondary vortex, as shown with the broken line in Fig. 6 representing the (normalized) phase-averaged surface pressure trace at $t/\mathfrak{T} = 0.15$, where t is time and $\mathfrak{T}$ is the period of the forcing signal. After the passing of both the primary and secondary vortices, the boundary layer reattaches and a high-level pressure is found in the wake of separation, as shown with the solid line in Fig. 6, a short time after separation ($t/\mathfrak{T} = 0.3$).

Because of the appearance of a sharp, negative peak pressure at about the same time as the secondary vortex and the fact that the relatively more gentle negative pressure induced by the primary vortex as it passes very nearly parallel to the wall was not expected to change, Didden and Ho (1985) conjectured that the observed high-amplitude pressure fluctuations are caused by the unsteady separation rather than by the primary vortex. They reiterated that, while viscosity does not play an important role in the stability of the spatially developing local shear layer, viscous effects are essential for producing the shear layer before the onset of the unsteady separation.

Since a local shear layer has been observed in many other separated flows, Ho (1986) contends that such a shear layer is a generic flow module to all separated flows. This interesting idea of associating unsteady separation with a spatially developing local shear layer allows researchers in the subject area to borrow from the extensive knowledge available in free shear layer studies (Ho and Huang, 1982; Ho and Huerre, 1984). Many examples of this association are provided in the review paper by Gad-el-Hak (1987).

The qualitative criteria of separation, namely, the thickening of the boundary layer, the ejection of vorticity, and the vanishing of the wall shear, do not appear at the same time nor convect at the same speed in the unsteady case. The Moore-Rott-Sears criterion for unsteady separation is a quantitative one. However, as mentioned earlier, the convection speed of the separation point is not known *a priori*, and this greatly increases the difficulty of the problem. By choosing an appropriate frame of reference based on a well-documented flow field, Didden and Ho (1985) were able to provide positive proof of the Moore-Rott-Sears criterion for a downstream-moving separation. Moreover, at the separation position and in a frame moving at the local velocity of the point of zero shear stress (or the convection speed of the boundary-layer's bulge), the phase-averaged streamlines were found to form a

closed recirculating region, in qualitative agreement with the calculations reported by Walker (1978) for a line vortex near a wall.

3 Governing Equations

To examine the local and instantaneous effects of many of the separation control tools to be described in this paper, consider a rigid wall such that $U = W = 0$ every where along it. At the wall, $y = 0$, the Navier-Stokes equations for an incompressible fluid read:

$$v_w\left[\frac{\partial U}{\partial y}\right]_0 + \frac{1}{\rho}\left[\frac{\partial P}{\partial x}\right]_0 - \left[\frac{\partial \nu}{\partial y}\right]_0\left[\frac{\partial U}{\partial y}\right]_0 = \left[\nu\frac{\partial^2 U}{\partial y^2}\right]_0, \quad (1)$$

$$0 + \frac{1}{\rho}\left[\frac{\partial P}{\partial y}\right]_0 - 0 = \left[\nu\frac{\partial^2 V}{\partial y^2}\right]_0, \quad (2)$$

$$v_w\left[\frac{\partial W}{\partial y}\right]_0 + \frac{1}{\rho}\left[\frac{\partial P}{\partial z}\right]_0 - \left[\frac{\partial \nu}{\partial y}\right]_0\left[\frac{\partial W}{\partial y}\right]_0 = \left[\nu\frac{\partial^2 W}{\partial y^2}\right]_0, \quad (3)$$

where the subscript $[\,]_0$ indicates flow quantities computed at the wall, U, V, and W are the instantaneous velocity components in the streamwise, normal and spanwise (x, y, and z) directions, respectively, v_w is the normal velocity at the wall (positive for injection and negative for suction), P is the instantaneous pressure, and ν is the kinematic viscosity which in general varies with space and time as a result of surface heating/cooling, film boiling, cavitation, sublimation, chemical reaction, wall injection of higher/lower viscosity fluid, or the presence of shear thinning/thickening additive.

The above equations indicate that the instantaneous flux of spanwise vorticity ($\partial U/\partial y$) and streamwise ($\partial W/\partial y$) at the wall[2] can be affected by suction/injection, streamwise or spanwise pressure gradient, or change of viscosity in the normal direction. Analogies between these stimuli are often made based on equations (1)–(3) or the corresponding equation for the mean streamwise momentum:

$$v_w\left[\frac{\partial \bar{U}}{\partial y}\right]_0 + \frac{1}{\rho}\frac{dP_0}{dx} - \frac{d\nu}{d\bar{T}}\left[\frac{\partial \bar{T}}{\partial y}\frac{\partial \bar{U}}{\partial y}\right]_0 + \left[\frac{\partial\,\overline{uv}}{\partial\, y}\right]_0 = \left[\nu\frac{\partial^2 \bar{U}}{\partial y^2}\right]_0, \quad (4)$$

where $\bar{T}$ is the mean temperature field and $\bar{U}$ is the time-averaged streamwise velocity. In this equation, viscosity is assumed to change as a result of surface heat transfer. The right-hand side of (4) is the flux of mean spanwise vorticity, $\bar{\Omega}_z = -\partial \bar{U}/\partial y$, at the surface. In the absence of suction/injection, pressure gradient, and surface heating/cooling, the first three terms on the left-hand side of (4) vanish.

For a laminar boundary layer, the Reynolds stress term in (4) vanishes. For the turbulent case, the fourth term on the left-hand side is the slope of the normal profile of $\overline{uv}$ at $y = 0$. This term could be asymptotically estimated as the wall is approached. Consider a Taylor's series expansion in powers of y in the neighborhood of the point $y = 0$. As a result of the no-slip condition, the streamwise velocity fluctuations u varies linearly with y. To conserve mass, the normal velocity fluctuations must vary as y^2. It follows then that very near the wall (within the viscous sublayer), the tangential Reynolds stress $\overline{uv}$ varies at least as y^3 and that $\partial\overline{uv}/\partial y$ varies as y^2. At the wall itself, $y = 0$ and $[\partial\overline{uv}/\partial y]_0 = 0$, although close to the wall the slope of the tangential Reynolds stress profile is quite large.

It can be deduced from equation (4) that the mean streamwise velocity profile for the canonical turbulent boundary layer (two-dimensional, incompressible, isothermal, zero pressure gradient, over an impervious, rigid surface) will have a zero curvature at the wall. Notwithstanding this common characteristic with the Blasius boundary layer (Fig. 7(*b*)), the turbulent boundary layer is quite different from the laminar one. As pointed out by Lighthill (1963), turbulent mixing concentrates most of the mean vorticity much closer to the wall as compared to the laminar case. The mean vorticity at the wall, $[\partial \bar{U}/\partial y]_0$, is typically an order of magnitude larger than that in the laminar case. This explains the higher skin-friction drag associated with a turbulent flow. Turbulent mixing also causes the mean vorticity to migrate away from the wall and about 5 percent of the total is found much farther from the surface. The flux of mean spanwise vorticity is zero at the wall itself but very large close to it, reaching a maximum at about the same location where the root-mean-square vorticity fluctuations peak (near the edge of the viscous sublayer). This trait is responsible for the turbulent boundary layer's resistance to separation.

For a steady, incompressible flow around a two-dimensional or axisymmetric surface of small curvature, the time-averaged continuity and streamwise momentum equations can be integrated in the normal direction to yield the von Karman integral equation:

$$C_f = 2\frac{d\delta_\theta}{dx} + 2\delta_\theta\left[\left(2 + \frac{\delta^*}{\delta_\theta}\right)\frac{1}{U_0}\frac{dU_0}{dx} + \frac{1}{R}\frac{dR}{dx}\right] - 2\frac{v_w}{U_0}, \quad (5)$$

where C_f is the local skin-friction coefficient, δ^* and δ_θ are the displacement and momentum thicknesses, respectively, U_0 is the velocity outside the boundary layer, R is the radius of curvature of the wall, and v_w is the normal velocity of fluid injected through the surface. Equation (5) is valid for both laminar and turbulent boundary layers.

In the next five sections, available and contemplated flow control methods to delay or to provoke separation will be discussed. The equations developed in this section for laminar and turbulent boundary layers will help in presenting a unified view of the different control techniques.

4 Velocity Profile Modifiers

As mentioned in Section 2.1, Prandtl (1904) was the first to explain the mechanics of separation. He provided a precise criterion for its onset for the case of a steady, two-dimensional boundary layer developing over a fixed wall. If such a flow is retarded, the near-wall fluid may have insufficient momentum to continue its motion and will be brought to rest at the point of separation. Fluid particles behind this point move in a direction opposite to the external stream and the original boundary-layer fluid passes over a region of recirculating flow. Since the velocity at the wall is always zero, the gradient $[\partial U/\partial y]_0$ will be positive upstream of separation, zero at the point of separation, and negative in the reverse flow region. The velocity profile at separation must then have a positive curvature at the wall. However, $[\partial^2 U/\partial y^2]$ is negative at a large distance from the wall, which means the velocity profile at separation must have a point of inflection somewhere above the wall as shown in Fig. 7(*d*). Since $[\partial^2 U/\partial y^2]_0 > 0$ is a necessary condition for a steady, two-dimensional boundary layer to separate, the opposite, i.e., a negative curvature of the velocity profile at the wall, must be a sufficient condition for the boundary-layer flow to remain attached.

The above arguments naturally lead to several possible

[2] Assuming spatially uniform v_w, $\partial V/\partial x$ and $\partial V/\partial z$ are both zero at the wall. Moreover, normal vorticity must vanish at $y = 0$ due to the no-slip condition.

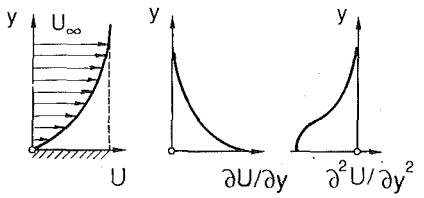

Fig. 7(a) Full profile

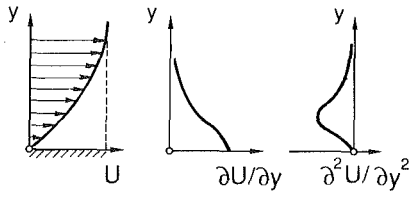

Fig. 7(b) Blasius profile

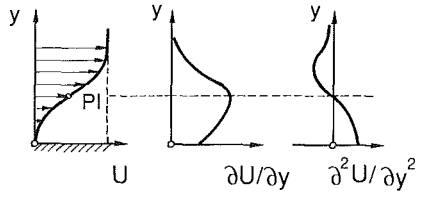

Fig. 7(c) Inflectional profile

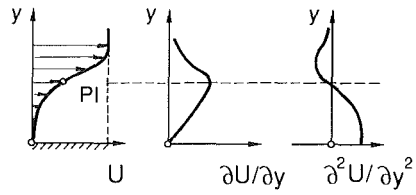

Fig. 7(d) Profile at the point of steady, two-dimensional separation

Fig. 7 Normal velocity profile in a boundary layer.

methods of control to delay (or advance) steady, two-dimensional separation that rely on modifying the shape of the velocity profile near the wall. Namely, the object is to keep $[\partial^2 U/\partial y^2]_0$ as negative as possible, or in other words to make the velocity profile as full as possible (Fig. 7(*a*)). In this case, the magnitude of the spanwise vorticity decreases monotonically away from the wall and the surface vorticity flux is in the positive y direction. Not surprisingly, then, methods of control to postpone separation that rely on changing the velocity profile are similar to those used to delay laminar-to-turbulent transition (Gad-el-Hak, 1989b).

Inspection of the momentum equations, (1)–(3), indicates that separation control methods may include the use of wall suction ($v_w < 0$), favorable pressure gradient ($dP/dx < 0$), surface cooling in gases ($d\mu/dT > 0$; $[\partial T/\partial y]_0 > 0$), or surface heating in liquids ($d\mu/dT < 0$; $[\partial T/\partial y]_0 < 0$). Obviously any one or a combination of these methods may be used in a particular situation. For example, beyond the point of minimum pressure on a streamlined body the pressure gradient is adverse and the boundary layer will separate if the pressure rise is sufficiently steep; however, enough suction may be applied there to overcome the retarding effects of the adverse pressure gradient and to prevent separation. Each of these velocity profile modifiers is covered in more details in the following.

4.1 Shaping. For any two-dimensional, subsonic flow over a closed-surface body, adverse pressure gradient always occurs somewhere in the aft region. Streamlining can greatly reduce the steepness of the pressure rise, leading to the prevention or postponement of separation. Numerous biological species are endowed with body shapes that avoid separation and allow for minimum fluid resistance to their motion in air or water. Archaic Homo sapiens discovered, through scores of trials and errors, the value of streamlining spears, sickle-shaped boomerangs, and fin-stabilized arrows (Williams, 1987). In supersonic flows, pressure always rises across a shock wave and a boundary layer may separate as a result of the wave interaction with the viscous flow (Young, 1953; Lange, 1954).

Laminar boundary layers can only support very small adverse pressure gradients without separation. In fact, if the ambient incompressible fluid decelerates in the streamwise direction faster than $U_0 \sim x^{-0.09}$, the flow separates (Schlichting, 1979). On the other hand, a turbulent boundary layer, being an excellent momentum *conductor*, is capable of overcoming much larger adverse pressure gradients without separation. In this case, separation is avoided for external flow deceleration up to $U_0 \sim x^{-0.23}$ (Schlichting, 1979). The efficient momentum transport that characterizes turbulent flows provides the mechanism for mixing the slower fluid near the wall with the faster fluid particles further out. The forward movement of the boundary-layer fluid against pressure and viscous forces is facilitated and separation is, thus, postponed. According to the experimental results of Schubauer and Spangenberg (1960), a larger total pressure increase with separation is possible in the turbulent case by having larger adverse pressure gradient in the beginning and continuing at a progressively reduced rate of increase.

To expand the attached flow *operational envelope* to off-design conditions using the concept of pressure gradient mitigation generally requires some form of variable geometry such as vanes, slats, or flaps. These can be combined with other separation control techniques such as active or passive blowing, rotating cylinder at the flap *knee*, or use of an injection-stabilized *trapped vortex*. For low-speed flows, bodies can now be designed for incipiently separated flow over large surface areas using the so-called Stratford closure discussed in Section 4.1.1 (Smith, 1977; Smith et al., 1981). While minimizing skin friction drag, this approach exacerbates the attached-flow, viscous-induced form or pressure drag, and the minimum drag body is actually a less extreme design. Also, such bodies tend to generate large separated flow regions off-design, and therefore some form of standby flow separation control would probably be required to ensure reasonable off-design performance.

4.1.1 Skin Friction. The skin friction downstream of the separation line is negative. However, the increase in pressure drag that results from flow detachment is far greater than the saving in skin-friction drag. The papers by Stratford (1959a, 1959b) provide useful discussion on the prediction of turbulent-boundary-layer separation and the concept of flow with continuously zero skin-friction throughout its region of pressure rise. By specifying that the turbulent boundary layer be just at the condition of separation, without actually separating, at all positions in the pressure rise region, Stratford (1959b) experimentally verified that such flows achieve a specified pressure rise in the shortest possible distance and with the least possible dissipation of energy. A lifting surface which could utilize the Statford's distribution immediately after transition from laminar to turbulent flow would be expected to have very low skin-friction as well as pressure drag.

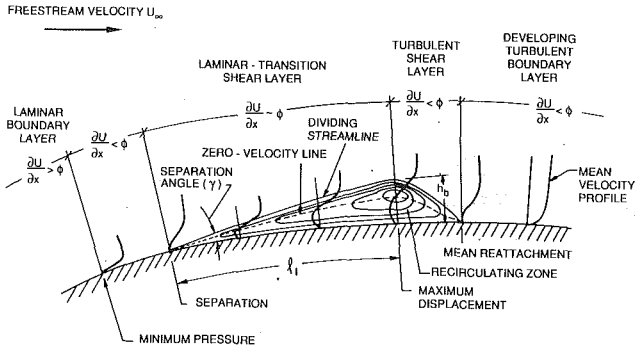

Fig. 8 Sketch of a laminar separation bubble.

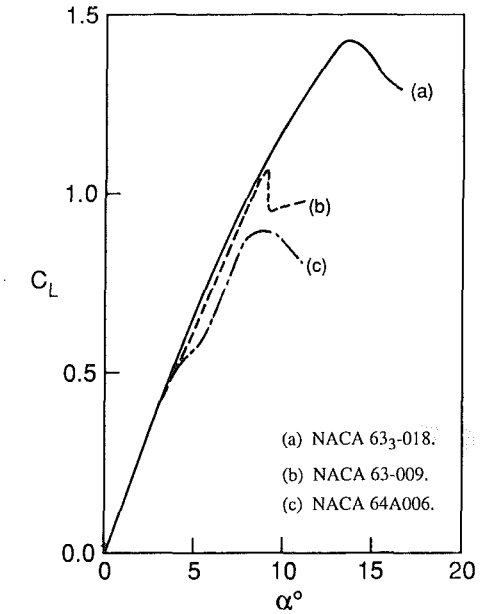

Fig. 9 Lift curves for three airfoils at $R_c = 5.8 \times 10^6$. (Adapted from McCullough and Gault, 1951.)

Liebeck (1978) successfully followed this strategy using a highly polished wing to achieve the best lift-to-drag ratio (over 200) of any airfoil tested in the low-Reynolds-number range of $5\times10^5 - 2\times10^6$. He argued that the entire pressure-recovery region of an airfoil's upper surface would be operating at its maximum capacity if the adverse pressure distribution was uniformly critically close to separation. By assuming an incipient-separation turbulent profile, Liebeck calculated the pressure field required then used an inverse calculation procedure to derive the airfoil shape from the given critical-velocity distribution.

When attempting to reduce skin-friction drag by driving the boundary layer towards separation, a major concern is the flow behavior at off-design conditions as discussed in Section 4.1. A slight increase in angle of attack for example can lead to separation and consequent large drag increase as well as loss of lift. High performance airfoils with lift-to-drag ratio of over 100 utilize carefully controlled adverse pressure gradient to retard the near-wall fluid, but their performance deteriorates rapidly outside a narrow envelope (Carmichael, 1974).

4.1.2 Separation Bubbles. Laminar-to-turbulent transition on the upper surface of a lifting surface typically occurs at the first onset of adverse pressure gradient if the Reynolds number exceeds 10^6. The separation-resistant turbulent boundary layer that evolves in the pressure recovery region results in higher maximum lift and a relatively larger angle of stall. At lower Reynolds numbers and depending on the severity of the initial adverse gradient (hence on the airfoil shape), laminar separation may take place prior to transition. For sufficiently low Re, the separated flow will not reattach to the surface. However, in the intermediate Reynolds number range of typically $10^4 - 10^6$, transition to turbulence takes place in the free-shear layer due to its increased susceptibility (Gad-el-Hak, 1990b). Subsequent turbulent entertainment of high-speed fluid causes the flow to return to the surface, thus forming what is known as a laminar separation bubble, as sketched in Fig. 8. Regardless of whether or not the flow subsequently reattaches, the laminar separation leads to higher form drag and lower maximum lift. Delicate contouring of the airfoil near the minimum pressure point to lessen the severity of the adverse pressure gradient may be used to accomplish separation-free transition (Pfenninger and Vemuru, 1990).

As an example of the effects of the lifting surface's shape on its performance, consider the lift curves for the three airfoil sections NACA 63_3-0.18, NACA 63-009, and NACA 64A006. These airfoils have maximum thicknesses of 0.18c, 0.09c, and 0.06c, respectively, where c is the chord. The respective leading edge radii are 0.021c, 0.006c, and 0.003c. Figure 9, adapted from the measurements by McCullough and Gault (1951), depicts C_L vs. α curves for the three sections at chord Reynolds number of 5.8×10^6. For the thick section, NACA 63_3-018, transition takes place near the minimum pressure point (Fitzgerald and Mueller, 1990). Stalling in this case is of the trailing edge type and is preceded by a gradual movement of the separation point of the turbulent boundary layer forward from the trailing edge as α increases. A laminar separation bubble is formed on the other two sections at small incidence. However, the NACA 63-009 section experiences a sudden leading edge stall when the bubble bursts with no subsequent reattachment, while the NACA 64A006 section experiences a more gradual thin-airfoil stall (McCullough, 1955; Crabtree, 1957). In the latter case, the short bubble breaks down into a longer bubble at an angle of attack of 5 deg causing a slight discontinuity in the lift curve. Subsequent increase in α leads to a movement of the reattachment point towards the trailing edge. The maximum lift in this case is about 40% lower than that for the thick airfoil. The stall angle is also lower.

A second example is provided for an airfoil specifically designed for the low-Reynolds-number regime. The Eppler 61 has a maximum thickness of 0.056c and is highly cambered. Mueller and Burns (1982) reported lift, drag, and smoke visualization data for this airfoil section in the range of Reynolds numbers of $3\times10^4 - 2\times10^5$. A sample of their lift and drag curves at three different speeds is depicted in Figure 10. At a negative angle of attack of about -3 deg, the flow around the cambered airfoil separates at the leading edge on the lower surface, without further reattachment. Zero lift is measured at this angle and is correlated with the appearance of smooth smokelines above and below the airfoil to form an uncambered, symmetrical shape, as shown in the photographs in Fig. 11. This explains the deviation of the zero lift angle as well as the shape of the lift curve from those predicted by thin airfoil theory. Strong Reynolds number effects are evident in both the lift and drag curves. At increasing angles of attack, the Eppler 61's performance is similar to that of the other thin airfoil depicted in Fig. 9(*c*), although the maximum lift coefficient is higher in the former case.

4.2 Transpiration. The second method to avert separation by changing the curvature of the velocity profile at the wall involves withdrawing the near-wall fluid through slots or porous surfaces. Prandtl (1904) applied suction through a spanwise slit on one side of a circular cylinder. His flow visualizatoin photographs convincingly showed that the boundary layer adhered to the suction side of the cylinder over a considerably

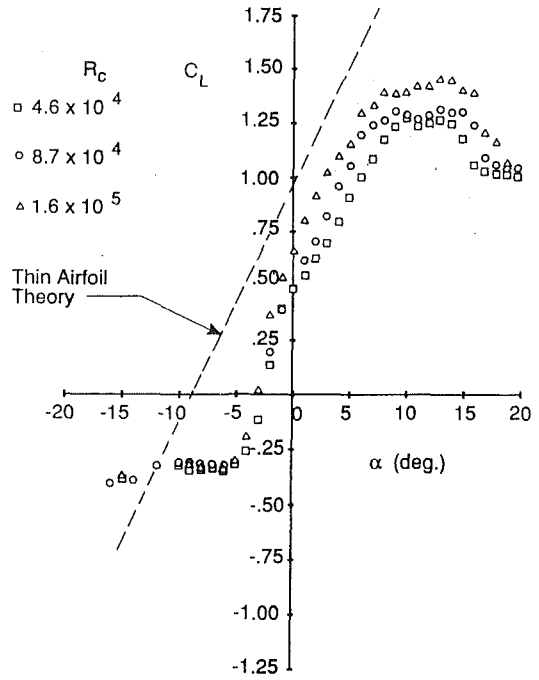

Fig. 10(*a*) Lift curves

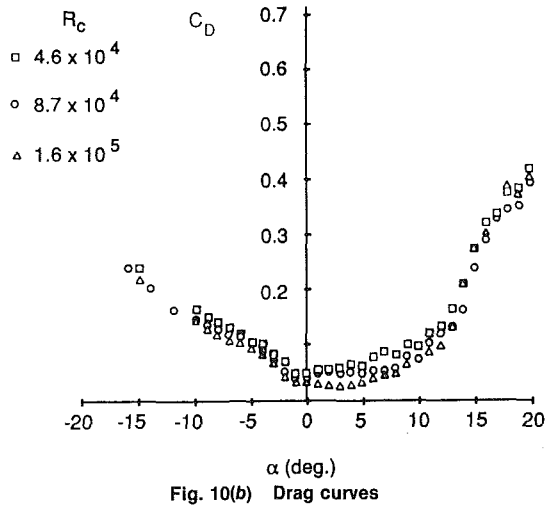

Fig. 10(*b*) Drag curves

Fig. 10 Reynolds number effects on lift and drag of the Eppler 61 airfoil. (Adapted from Mueller and Burns, 1982.)

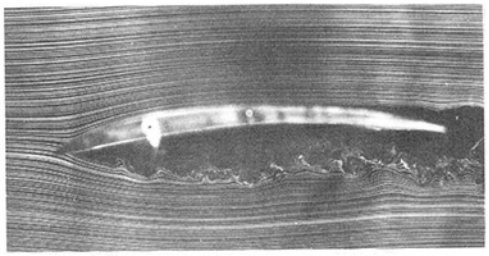

Fig. 11(*a*) $\alpha = -3$ deg

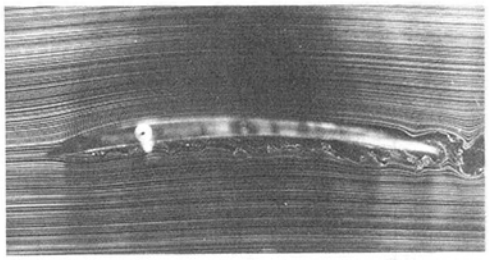

Fig. 11(*b*) $\alpha = 0$ deg

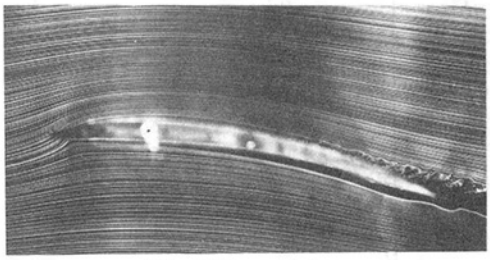

Fig. 11(*c*) $\alpha = 8$ deg

Fig. 11 Smoke-wire flow visualization at $R_c = 8.7 \times 10^4$. (From Mueller and Burns, 1982.)

larger portion of its surface. By removing the decelerated fluid particles in the near-wall region, the velocity gradient at the wall is increased, the curvature of the velocity profile near the surface becomes more negative, and separation is avoided. In the following, an approximate method to compute the amount of suction needed to prevent laminar separation is briefly recalled (Prandtl, 1935).

For a laminar boundary layer, the ratio of pressure forces to viscous forces is proportional to the shape factor, Λ:

$$\Lambda = \frac{\delta^2}{\nu}\frac{dU_0}{dx} = -\frac{dP_0}{dx}\frac{\delta^2}{\mu U_0}, \tag{6}$$

where δ is the boundary layer thickness, U_0 is the velocity outside the boundary layer, ν is the kinematic viscosity, μ is the dynamic viscosity, and dP_0/dx is the pressure gradient in the streamwise direction. At separation, $[\partial U/\partial y]_0 = 0$ and equation (4) reads:

$$\frac{dP_0}{dx} = \mu\left[\frac{\partial^2 U}{\partial y^2}\right]_0. \tag{7}$$

The shape factor at the point of separation of a laminar boundary layer is $\Lambda = -12$, and from equations (6) and (7) the expressions for the curvature of the velocity profile at the wall and the boundary-layer thickness become, respectively:

$$\left[\frac{\partial^2 U}{\partial y^2}\right]_0 = \frac{12\,U_0}{\delta^2}, \tag{8}$$

$$\delta = \sqrt{\frac{-12\,\nu}{dU_0/dx}}. \tag{9}$$

The velocity distribution, dU_0/dx, is determined from the potential flow solution. As an example, suppose we wish to compute the suction coefficient, $C_q \equiv |v_w|/U_0$, which is just sufficient to prevent laminar separation from the surface of a cylinder. By assuming that the velocity profiles in the vicinity of separation are identical with that at the point of separation and computing dU_0/dx at the downstream stagnation point, Prandtl (1935) used the momentum integral equation, (5), and the above results to make a simple estimate of the required suction:

$$C_q = 4.36\ \mathrm{Re}^{-0.5}, \tag{10}$$

where Re is the Reynolds number based on the cylinder diameter and the freestream velocity.

Several researchers have used similar approximate methods to calculate the laminar boundary layer on a body of arbitrary shape with arbitrary suction distribution (see, e.g., Schlichting and Pechau, 1959; Chang, 1970). A particularly simple calculation is due to Truckenbrodt (1956). He reduces the

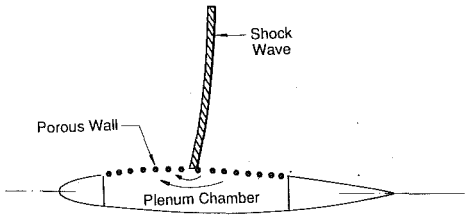

Fig. 12 Schematic of porous airfoil.

problem to solving a first-order ordinary differential equation. As an example, for a symmetrical Zhukovskii airfoil with uniform suction, Truckenbrodt predicts a suction coefficient just sufficient to prevent separation of:

$$C_q = 1.12\ \mathrm{Re}^{-0.5}, \tag{11}$$

where Re is the Reynolds number based on the airfoil chord and the freestream velocity.

For turbulent boundary-layers, semi-empirical methods of calculation are inevitably used due to the well-known closure problem. Suction coefficients in the range of $C_q = 0.002 - 0.004$ are sufficient to prevent separation on a typical airfoil (Schlichting, 1959; Schlichting and Pechau, 1959). Optimally, the suction should be concentrated on the low-pressure side of the airfoil just a short distance behind the nose where, at large angles of attack, the largest local adverse pressure gradient occurs.

4.2.1 Passive Suction. For the high-speed, shock-boundary-layer interaction case, a passive porous surface can be used to mitigate the local pressure gradients and obviate separation as well as reduce wave drag/shock losses (Bahi et al., 1983; Savu and Trifu, 1984; Nagamatsu et al., 1985, 1987; Raghunathan, 1985; Stanewsky and Krogmann, 1985; Barnwell et al., 1987; Koval'nogov et al., 1987) in both transonic and supersonic flows (Bauer and Hernandez, 1988). The basic device, sketched in Fig. 12, is an empty subsurface plenum covered by a porous surface and located underneath the shock-boundary-layer interaction region. Such a passive porous surface allows mass to self-bleed from downstream of the shock to upstream, resulting in a more gradual viscous-inviscid interaction, a series of weaker shock waves and reduced pressure gradients. Flow separation is then delayed and wave drag is minimized. Suction implemented via passive bleed is employed as an integral part of the technologically important case of high-speed inlet design (Delery, 1985; Viswanath, 1988).

4.2.2 Suction Optimization. Flow separation control by suction is the other conventional technique which, along with blowing, is within the capacity of contemporary CFD for design and optimization via tailored and perhaps distributed flow profiles and is well reviewed in readily available literature. Suction can be instituted via active or passive systems, with the boundary-layer diverter constituting the *reductio ad absurdum*. The parameter space for separation control by suction (or injection) includes: distribution of mass transfer location vis-a-vis adverse pressure gradient regions; spatial distribution (discrete, continuous); exit orientation; tailoring of orifice velocity profiles; active or passive source/sink; and distribution of suction/injection both chordwise and spanwise.

In summary, studies of suction control at high speeds indicate that suction holes should probably be inclined in the upstream direction (Purohit, 1987); that upstream control is less effective than direct control of the separated flow region; and that optimum distributed suction requires several independent plenum chambers to avoid local *backflows* and consequent loss of suction control. An additional possibility for high-speed flows is to utilize the embedded near-wall spanwise vortex structure associated with swept shocks to remove the inner portion of the incident boundary layer (S. M. Bogdonoff; private communication). This may require provision of an additional *control* shock upstream of the interaction.

The increased interest in, and favorable flight experience with, hybrid laminar flow control (where suction is employed in the leading-edge region ahead of wing box) has revived interest in suction control for the subsonic case. Preliminary studies indicate that the LFC suction system for cruise application is not incompatible with leading-edge region suction separation control or high-lift requirements for both CTOL and SST (supersonic transport) applications. Flight experiments of leading-edge suction systems for high lift (e.g., Hunter and Johnson, 1954) and LFC (Hefner and Sabo, 1987) do not indicate any *stoppers*. A combined approach has considerable promise, using the same suction surface and system for both LFC at cruise and leading-edge-region high lift for takeoff and landing. For LFC, there is the added benefit of eliminating the joints, etc., associated with conventional leading-edge, variable-geometry devices.

4.3 Wall Heat Transfer. The third term in equation (1) points to yet another method to delay boundary-layer separation. By transferring heat from the wall to the fluid in liquids or from the fluid to the wall in gases, this term adds a negative contribution to the curvature of the velocity profile at the wall and, hence, causes the separation point to move farther aft. If the surface of a body in a compressible gas is cooled, the near-wall fluid will have larger density and smaller viscosity than that in the case with no heat transfer. The smaller viscosity results in a fuller velocity profile and higher speeds near the wall. Combined with the larger density, this yields a higher momentum for the near-wall fluid particles and, hence, the boundary layer becomes more resistant to separation. Although this method of control has been successfully applied to delay transition in both water and air flows (see the review article by Gad-el-Hak, 1989b), its use to prevent separation has been demonstrated only for high-speed gaseous flows. These effects are confirmed via the analytical results of Libby (1954), Illingworth (1954), and Morduchow and Grape (1955). Experimental verification is provided by the work of Gadd et al. (1958), Bernard and Siestrunck (1959), and Lankford (1960; 1961). Excellent summaries of the problem of heat transfer effects on the separation of a compressible boundary layer are available in Gadd (1960) and Chang (1970, 1976).

Active separation control by wall cooling in air is straightforward. The technique might be particularly appropriate for high-altitude, long-endurance vehicles (HALE) having thick, low-Reynolds-number wings and cryogenic fuel to provide the requisite heat sink (e.g., Baullinger and Page, 1989). Unfortunately the method is mainly restricted to cryogenically-fueled aircraft. This makes it particularly appropriate for hypersonic applications such as shock-boundary-layer interactions on hydrogen-fueled vehicles. Cooling in air *works* according to both experiment and theory for low (Macha et al., 1972; Lin and Ash, 1986) as well as high (Spaid, 1972; Ogorodnikov et al., 1972) speeds.

In liquids, surface heating lowers the near-wall viscosity but the density remains essentially unchanged. Using simple asymptotic analysis of the coupled energy and momentum equations, Aroesty and Berger (1975) compared the effectiveness of wall heating to suction as a means of delaying separation for a prescribed adverse pressure gradient in a water boundary layer. They concluded that surface heating can be used in water to delay separation somewhat. However, it seems that this analytical result has not been confirmed experimentally.

In addition to surface heating/cooling, several other methods are available to establish a viscosity gradient in a

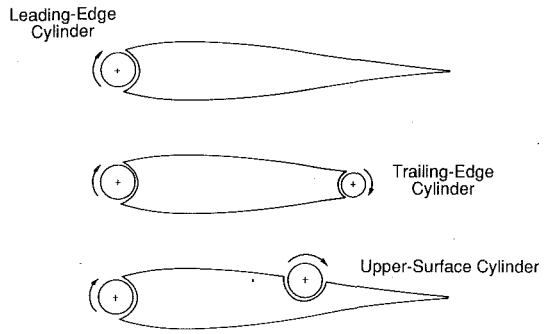

Fig. 13 Various rotating cylinder configurations used to increase lift and delay stall of an airfoil.

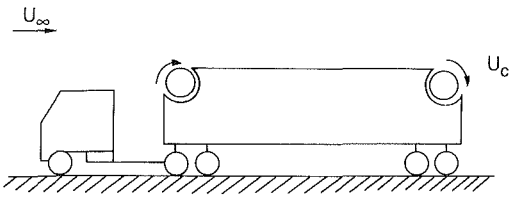

Fig. 14 Tractor-trailer truck with rotating cylinders.

wall-bounded flow and thus to affect the location of separation. These include, film boiling, cavitation, sublimation, chemical reaction, wall injection of a secondary fluid having lower/higher viscosity, and the introduction into the boundary layer of shear-thinning/shear-thickening additive.

5 Moving-Wall and Time-Dependent Separations

5.1 Moving Walls. The moving-wall effects can be exploited to postpone separation. For a surface moving downstream, the relative motion between the wall and the freestream is minimized and thus the growth of the boundary layer is inhibited. Furthermore, the surface motion *injects* additional momentum into the near-wall flow. Prandtl (1925) demonstrated the effects of rotating a cylinder placed in a uniform stream at right angles to its axis. Separation is completely eliminated on the side of the cylinder where the wall and the freestream move in the same direction. On the other side of the cylinder separation is developed only incompletely. In fact, for high enough values of circulation, the entire flow field can be approximated by the potential flow theory. The asymmetry causes a force on the cylinder at right angle to the mean flow direction. This important phenomenon, known as the Magnus effect (Magnus, 1852; Swanson, 1961), is exploited in several sport balls (Mehta, 1985a) and even in an experimental device used for propelling ships, known as the Flettner's (1924) rotor.

From a practical point of view, wall motion for body shapes other than circular cylinders or spheres is prohibitively complicated, although it is feasible to replace a small portion of the surface of, say, an airfoil by a rotating cylinder thus energizing the boundary-layer and avoiding separation (Alvarez-Calderon, 1964). Rotating cylinders have been successfully employed to delay separation at the leading and trailing edges of airfoils and control surfaces (Johnson et al., 1975; Mokhtarian and Modi, 1988; Mokhtarian et al., 1988a, 1988b; Modi et al., 1989) at flap junctures (Alvarez-Calderon, 1964; Lee, 1974; Tennant et al., 1975; Modi et al., 1980), and in diffusers (Tennant, 1973). Critical parameters include rotational speed and cylinder-to-fixed surface gap.

Flight tests were conducted on an YOV-10A STOL-type aircraft having flaps with rotating cylinders at their leading edges (Cichy et al., 1972; Weiberg et al., 1973; Cook et al., 1974). With the flaps in lowered position, the cylinders were rotated at high speed and lift coefficients as high as 4.3 were recorded at a modest flying speed of 30 m/s along approaches up to -8 deg. Modi and his colleagues (Modi et al., 1981; Mokhtarian and Modi, 1988) carried out a comprehensive wind tunnel test program involving a family of airfoils each having one or more rotating cylinders located at the leading edge, the trailing edge or the upper surface, as sketched in Fig. 13. Under optimum conditions, the lift coefficient increased by as much as 200 percent and the stall angle was delayed to 48 deg.

Quite recently, Modi et al. (1990) extended the concept of moving surface boundary-layer control to reduce the drag of land vehicles. On a scale-model of a typical tractor-trailer truck configuration having a splined rotating cylinder at the top leading edge of the trailer (Fig. 14), drag was lowered by as much as 27 percent when the cylinder surface velocity was 3.7 times the freestream speed. Modi et al. maintain that this separation control concept is essentially semi-passive in character requiring negligible amount of power for its implementation.

Creating a wall-slip layer biases the mean flow such that a larger pressure gradient can be tolerated before separation occurs. There are essentially two techniques for establishing a slip layer on the wall to mitigate separation. The first of these is to actually translate the wall itself, e.g., moving belts or embedded rotating cylinders as discussed above. The other approach is the establishment of stabilized cavity vortex flows. Either small-scale (Migay, 1960a, 1960b, 1961, 1962a, 1962b, 1962c; Stull and Velkoff, 1975; Howard and Goodman, 1985) or large-scale (Ringleb, 1961; Adkins, 1975; Adkins et al., 1980; Burd, 1981; Chow et al., 1985; Krall and Haight, 1972; Haight et al., 1974) vortex stabilization is necessary, otherwise the *trapped* vortex will generally periodically shed downstream causing disrupted operation and higher drag and losses. Stabilization techniques include injection (Krall and Haight, 1972; Haight et al., 1974); suction (Adkins, 1975; Adkins et al., 1980; Burd, 1981; Chow et al., 1985); and/or viscous forces via low-cavity-Reynolds number (e.g., Howard and Goodman, 1985). The *vortex flap* is the latest version of such a device. These slip-layer separation control techniques *work* for moderately separated flows, but in extreme cases reverse flow can still occur away from the surface (Zhuk and Ryzhov, 1980).

5.2 Time-Dependent Separation. For time-dependent flows, the separation point is no longer stationary but rather moves along the surface of the body. The Moore-Rott-Sears (MRS) criterion states that unsteady separation occurs when the shear and velocity vanish simultaneously and in a singular fashion at a point within the boundary layer as seen by an observer moving with the separation point (Rott, 1956; Sears, 1956; Moore, 1958). Steady separation is clearly included in this model as a special case. The main drawback of the MRS criterion is that the speed of the separation point is not known a priori, making it difficult to locate this point and forcing researchers to rely on more qualitative measures for unsteady separation.

In analogy to the moving wall case, unsteady separation is (temporally) postponed when the separation point moves upstream as is the case on the suction side of airfoil undergoing a pitching motion from small to large angles of attack. Conversely, when an airfoil is pitched from large to small attack angle, the separation point on the suction side moves downstream and separation is advanced, much the same as the case of a wall moving upstream.

An airfoil oscillating sinusoidally through high angles of attack can produce very high lift coefficients and maintain flow attachment well beyond static stall attack angles (McCroskey, 1977; 1982). During the upstroke, the separation point moves upstream and reverse flow exists in an attached and mathematically well-behaved boundary layer. The global aerodynamic properties of a pitching airfoil are strongly in-

fluenced by the local unsteady separation. Sudden changes of lift, drag, and pitching moment occur near the onset of separation and the *spillage* of a leading edge vortex. These effects are particularly significant at high frequencies and large amplitudes. Moment stall is observed when the reverse-flow region extends over most of the airfoil and a large-scale vortex is formed near the leading edge. A discontinuous increase in circulation is associated with the spilled vortex. During this phase of the cycle, lift continues to increase. Lift stall follows moment stall and occurs when the separation vortex reaches the latter half of the airfoil and a double-peaked pressure distribution results on the suction side. In other words, the suction on the upper surface of the airfoil continues to increase at the initial stages of separation, and a sudden decrease in suction does not occur until the leading edge is in the wake of separation.

Similar phenomena are observed on three-dimensional lifting surfaces undergoing pitching motion (Gad-el-Hak, 1986, 1988a, 1988b; Gad-el-Hak and Ho, 1986a). For highly swept wings, both steady as well as unsteady flows are vortex dominated. The latter flow is characterized by the existence of unsteady large- and small-scale vortices that go through a growth-decay cycle with hysteresis during each period (Gad-el-Hak and Ho, 1985, 1986b; Kandil and Chuang, 1990a, 1990b; Atta and Rockwell, 1990; Huyer et al., 1990).

According to Ericsson (1967; 1988), the forces on an airfoil oscillating in pitch will deviate from the static forces realized at the instantaneous angle of attack due to the superposition of two effects. First, the frequency-induced normal velocity distribution over the airfoil. This so-called q effect can be visualized as a frequency-induced camber. Secondly, the effect of attack angle rate of change, the so-called $\dot{\alpha}$ effect. This can be visualized as a frequency-induced change of the *mean* velocity vector or plunging. During the upstroke, a pitching airfoil will appear as having a positive camber and as plunging. According to the unsteady Bernoulli's equation, the local pressure gradient is less adverse in the dynamic case. Thus, the boundary layer at a particular α during the upstroke has a more favorable upstream time history as compared to the static case. The opposite effects take place during the downstroke.

Insects, most of whom mate and eat while airborne, exploit unsteady separation effects to achieve remarkable aerodynamic characteristics. The dragonfly, in existence for approximately 250 million years, presumably survived innumerable life and death aerodynamic struggles (Luttges et al., 1984; Luttges, 1989). The enviably large lift coefficients generated by the chalcid wasp during hovering suggest the existence of an efficient unsteady lift generation mechanism (Weis-Fogh, 1973; Lighthill, 1973; Maxworthy, 1979; 1981).

6 Three-Dimensional Separation

Three-dimensional boundary layers are more common in practical flow situations than two-dimensional ones. Bodies of revolution at some angle of attack, flow near wing tips, turbine blades, pump impellers, and low-aspect-ratio wings are examples of flow fields in which three-dimensional effects dominate. As mentioned earlier, the point of boundary-layer separation from a three-dimensional body does not necessarily coincide with the point of vanishing wall shear. Instead, the shear stress at the wall is equal to zero only at a limited number of points along the separation line. The number and type of these critical or singular points must satisfy certain topological laws (Lighthill, 1963; Tobak and Peake, 1982). The projection of the limiting streamlines as the distance from the wall goes to zero coincides with the skin-friction lines on the surface of the body. Oil-streak techniques and the like are usually used to obtain separation and attachment patterns for steady, three-dimensional flows (Maltby, 1962). A necessary condition for the occurrence of flow separation is the convergence of skin-friction lines onto a particular line. Because of the three-dimensionality of the flow, the near-wall fluid may move in a direction in which the pressure gradient is more favorable and not against the adverse pressure in the direction of the main flow as is the case for two-dimensional flows. Consequently, three-dimensional boundary-layers are in general more capable of overcoming an adverse pressure gradient without separation.

Three-dimensional relief of the streamwise adverse pressure gradient may be exploited to delay separation. Properly designed corrugated trailing edges can provide sufficient easement to postpone the separation at higher angles of attack. In nature, three-dimensional serrated geometry is to be found in the trailing edges of the fins and wings of many aquatic animals and birds (Norman and Fraser, 1937; Lighthill, 1975). For man-made lifting surfaces, the same concept was tested in the low-Reynolds-number regime by Vijgen et al. (1989). They reported a modest 5 percent increase in the maximum lift-to-drag ratio when triangular serrations were added to the trailing edge of a natural-laminar-flow airfoil (Gad-el-Hak, 1990b).

7 Turbulators

A turbulent boundary layer is more resistant to separation than a laminar one and mostly for that reason transition advancement may be desired in some situations. In low-Reynolds-number terminology, the transition promoting devices are called *turbulators*. For a zero-pressure-gradient boundary layer, transition typically occurs at a Reynolds number based on distance from leading edge of the order of 10^6. The critical Re below which perturbations of all wave numbers decay is about 6×10^4. To advance the transition Reynolds number, one may attempt to lower the critical Re, increase the growth rate of Tollmien-Schlichting waves, or introduce large disturbances that can cause *bypass* transition. The first two routes involve altering the shape of the velocity profile using wall motion, injection, adverse pressure gradient, or surface heating in gases or cooling in liquids. The third route, exposing the boundary layer to large disturbances, is much simpler to implement though more difficult to analyze (Smith and Kaups, 1968; Cebeci and Chang, 1978; Nayfeh et al., 1986; Cebeci and Egan, 1989).

Morkovin (1984) broadly classifies the large disturbances that can cause bypass transition into steady or unsteady ones originating into the freestream or at the body surface. The most common example is single, multiple or distributed roughness elements placed on the wall. The mechanical roughness elements, in the form of serrations, strips, bumps or ridges, are typically placed near the airfoil's leading edge. If the roughness characteristic-length is large enough, the disturbance introduced is nonlinear and bypass transition takes place. For a discrete three-dimensional roughness element of height-to-width ratio of one, Tani (1969) reports a transition Reynolds number of $R_\delta^*\simeq300$ for a roughness Reynolds number of $R_\kappa\simeq10^3$. In here, R_δ^* is based on the velocity outside the boundary layer and the displacement thickness ($R_\delta^*\equiv U_0\delta^*/\nu$), and R_κ is based on the height of the roughness element and the velocity in the undisturbed boundary layer at the height of the element ($R_\kappa\equiv U(\kappa)\kappa/\nu$). Note that the transition Reynolds number, R_δ^*, indicated above is below the critical $R_\delta^*=420$ predicted from the linear stability theory. For a roughness Reynolds number of about 600, transition occurs at $R_\delta^*\simeq10^3$. For a smooth surface, transition typically takes place at $R_\delta^*\simeq2.6\times10^3$. An important consideration when designing a turbulator is to produce turbulence and suppress laminar separation without causing the boundary layer to become unnecessarily thick. A thick turbulent wall-bounded flow suffers more drag and is more susceptible to separation

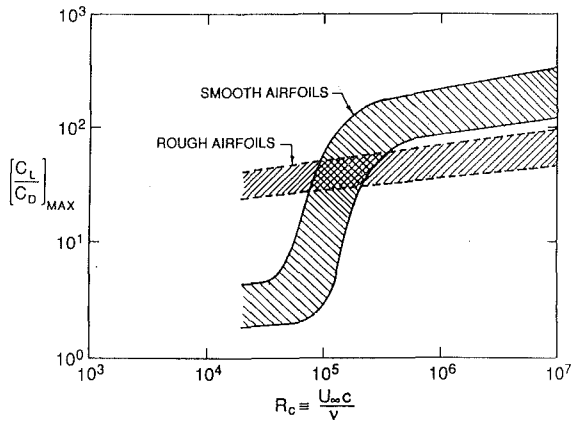

Fig. 15 Airfoil performance as a function of chord Reynolds number. (From McMasters and Henderson, 1980.)

than a thin one. Consistent with this observation, available data (Fig. 15) indicates that a rough airfoil has higher lift-to-drag ratio than a smooth one for $R_c < 10^5$, but that this trait is reversed at higher Reynolds numbers.

For low-Reynolds-number airfoils, performance may be improved by reducing the size of the laminar separation bubble through the use of *transition ramps* (Eppler and Somers, 1985), boundary layer trips (Davidson, 1985; Van Ingen and Boermans, 1986), or even pneumatic turbulators (Pfenninger and Vemuru, 1990). Donovan and Selig (1989) provide extensive data using both methods for 40 airfoils in the Reynolds number range of $6\times10^4 - 3\times10^5$. A long region of roughly constant adverse pressure gradient on the upper surface of a lifting surface (termed a bubble ramp) achieves a lower drag than the more conventional laminar-type velocity distribution in which initially the pressure remains approximately constant and then quickly recovers. Trips were also used to shorten the separation bubble. A simple two-dimensional trip performed as well or better than zig-zag tape, hemisphere bumps, and normal blowing. Donovan and Selig concluded that an airfoil which performs poorly at low Reynolds numbers can be improved through the use of turbulators. Trips were less effective, however, at improving airfoils which normally had low drag.

Other large disturbances that could lead to early transition include high turbulence levels in the freestream, external acoustic excitations, particulate contamination, and surface vibration. These are often termed environmental tripping. Transition could also be effected by detecting naturally occurring T-S waves and artificially introducing in-phase waves. Transition could be considerably advanced, on demand, using this wave superposition principle.

Early transition could also be achieved by exploiting other routes to turbulence such as Taylor-Görtler or cross-flow vortices (Taylor, 1923; Görtler, 1955; Gregory et al., 1955; Reed and Saric, 1987; Saric and Reed, 1989). For example, a very mild negative curvature of $(0.003/\delta^*)$ results in the generation of strong streamwise vortices. In this case, transition Reynolds number is lowered from $R_\delta^* \simeq 2600$ for the flat-plate case to $R_\delta^* \simeq 700$ for the curved surface (Tani, 1969). For high Mach number flows, the general decay in spatial amplification rate of T-S waves makes conventional tripping more difficult as the Mach number increases (Reshotko, 1976). For these flows, trips that generate oblique vorticity waves of appropriate wavelength may be most effective to advance the transition location.

The last issue to be considered in this section is augmentation of the turbulence for a shear flow that has already undergone transition. Notwithstanding that the turbulence levels and the Reynolds stresses are highest immediately following transition (Harvey et al., 1969), the newly developed turbulent flow is in general less capable of resisting separation than a corresponding flow at higher speeds (Lissaman, 1983). Turbulence augmentation in the low-Reynolds-number case is then a useful control goal to energize the flow and to enhance its ability to resist separation at higher angles of attack. Roughness will enhance the turbulence, but its associated drag must be carefully considered. Other devices to enhance the turbulent mixing include vane-type vortex generators, which draw energy from the external flow, or wheeler-type or Kuethe-type generators, which are fully submerged within the boundary layer and presumably have less associated drag penalty (Rao and Kariya, 1988). These and other devices will be detailed in the next section.

8 Momentum Addition to Near-Wall Flow

8.1 Introductory Remarks. Near-wall momentum addition is the usual *approach of choice* for control of residual flow separation remaining after mitigation of the causative pressure field or for off-design conditions. Common to all these control methods is the supply of additional energy to the near-wall fluid particles which are being retarded in the boundary layer. The additional longitudinal momentum is provided either from an external source or through local redirection into the wall region. Passive techniques do not require auxiliary power, but do have an assoicated drag penalty, and include intentional tripping of transition from laminar to turbulent flow upstream of what would be a laminar separation point (Mangalam et al., 1986; Harvey, 1986), boundary-layer fences to prevent separation at the tips of swept-back wings, placing an array of vortex generators on the body to raise the turbulence level and enhance the momentum and energy in the neighborhood of the wall (Mehta, 1985b; Rao and Kariya, 1988), rippled trailing edge (Werle et al., 1987), streamwise corrugations (Mabey, 1988), stepped afterbodies to form a system of captive vortices in the base of a blunt body (Kentfield, 1985a, 1985b; Kidd et al., 1990), or using a screen to divert the flow and increase the velocity gradient at the wall.

Active methods to postpone separation require energy expenditure. Obviously, the energy gained by the effective control of separation must exceed that required by the device. In addition to suction or heat transfer reviewed in Sections 4.2 and 4.3, fluid may be injected parallel to the wall to augment the shear-layer momentum or normal to the wall to enhance the mixing rate (Horstmann and Quast, 1981). Either a blower is used or the pressure difference that exists on the aerodynamic body itself is utilized to discharge the fluid into the retarded region of the boundary layer. The latter method is found in nature in the thumb pinion of a pheasant, the split-tail of a falcon, or the layered wing feathers of some birds.

In man-made devices, passive blowing through leading-edge slots and trailing-edge flaps is commonly used on aircraft wings, as sketched in Fig. 16. Although in this case direct energy expenditure is not required, the blowing intensity is limited by the pressure differentials obtainable on the body itself. Nevertheless, the effect of passive blowing on lift and drag could be dramatic. This is shown convincingly in Figure 17 for the NACA 23012 airfoil section with no flap, with a single trailing-edge flap and with a double-slotted flap. Compared to the clean (no flap) case, when a single trailing-edge flap is used the maximum lift is increased by about 175 percent while the section drag at $C_{L\max}$ is increased by more than 180 percent. The corresponding numbers when a double-slotted flap is used are respectively, 230 and 500 percent. The induced drag, which must be considered in addition to the section drag, is proportional to C_L^2, and the total drag, therefore, rises sharply at low aircraft speeds.

Many of the control methods discussed in this section could be used for external as well as internal flows. For example,

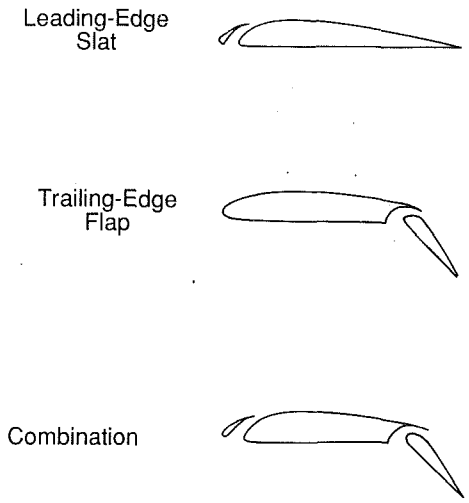

Fig. 16 Passive blowing through leading-edge slats and trailing-edge flaps.

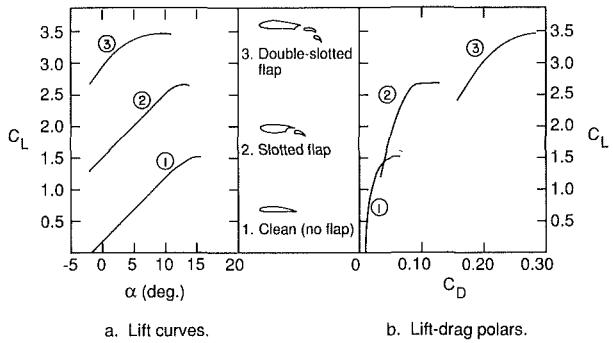

Fig. 17 Effects of trailing-edge flaps on lift and section drag. NACA 23012 airfoil section. (Adapted from data by Abbott and von Doenhoff, 1959.)

Viets (1980) used an asymmetrical rotating cam embedded in the wall to produce large eddies in a turbulent boundary layer with zero- and adverse-pressure gradients. By using this device in a wide-angle diffuser, Viets et al. (1981a) were able to postpone the natural separation and dramatically improve the diffuser's performance.

8.2 Passive Vortex Generation. Passive momentum addition is most commonly carried out via one of two general approaches, either macro overturning of the mean flow using embedded streamwise vortices generated by fixed lifting surfaces, or Reynolds stress amplification which leads to increased cross-stream momentum transfer. Conventional passive vortex generators (VGs) date from the 1940's (Taylor, 1948a) and are simple, effective and generally the first tried as a *fix* to an existing flow separation problem. Passive VGs have been applied, for example, to compressor blades (Staniforth, 1958), diffusers (Henry et al., 1956; Feir, 1965; Brown et al., 1968), airfoils (Pearcey, 1961; Nickerson, 1986; Bragg and Gregorek, 1987), and the afterbody of aircraft fuselages (Calarese et al., 1985; Wortmann, 1987). What these embedded vortices do is cause *overturning* of the near-wall flow via *macro motions*. Fluid particles with high streamwise momentum are swept along helical paths toward the surface to mix with and, to a certain extent, to replace the retarded near-wall flow. The vortex influence upon the turbulence can actually be debilitating due to streamline curvature-induced stabilization.

Essentially small-aspect-ratio airfoils mounted normal to the surface, the vortex generators' individual parametrization include planform shape, section profile and camber, yaw angle, aspect ratio, and height with respect to the boundary-layer thickness. The spatial relationship of the devices is also critical, e.g., co-rotating versus contra-rotating biplane and wing, use of downstream *reinforcers*, and spacing. Counter-rotating vortices force large regions of vorticity to rise above the surface and hence are often not as efficient as corotating devices. However, corotating vortices with too close a spacing undergo mutual vorticity cancellation, therefore spacing is critical in this case.

Nominal guidelines for conventional VGs are given in the papers by Taylor (1948b); Henry et al. (1956); and Pearcey (1961): aspect ratio of 0.5-1; rectangular or triangular planform with either simple flat plate or low-Reynolds-number airfoil cross-section; yaw angle less than 15 deg; and individual height on the order of the boundary-layer thickness. For co-rotating devices, the spanwise spacing should be greater than 3 times the device height to avoid interactive cancellation or annihilation of the vortical structures. The recommended nominal spanwise spacing for contra-rotating vortex production devices is on the order of 4–5 device heights. These conventional vortex generating devices produce sizable parasitic drag. When employed to handle off-design problems, the VGs cause a reduction in cruise performance, unless the devices are retracted when not needed. The papers by Schubauer and Spangenberg (1960); Gadetskii et al. (1972); Liandrat et al. (1986); Cutler and Bradshaw (1986; 1989); Inger and Siebersma (1988); Mehta (1988); and Briedenthal and Russell (1988) provide generic studies of vortex generator physics and operation. Application to supersonic flows is summarized by Gartling (1970).

Several approaches are now available to optimize the performance of passive vortex generators. The first of these is the use of downstream reinforcers; which are vortex generators of the same sense located in the path of the upstream-generated vortex to maintain the strength of the *overturning* motion (Kuethe, 1973; Wheeler, 1984; Lin and Howard, 1989; Rao and Kariya, 1988). A second optimizatoin approach is surprisingly recent and consists of simply reducing the device height from the order δ to $0[\delta/5]$ or less (Rao and Kariya, 1988; Lin and Howard, 1989; Lin et al., 1990a). This size reduction significantly diminishes the parasitic drag and is enabled by the extreme fullness of the mean velocity profile in a turbulent boundary layer. In other words, with sizable longitudinal momentum levels readily available quite close to the surface, it is not necessary to have $0[\delta]$ devices. Such *sub-δ* devices must be placed closer to the nominal separation location and therefore may be less suitable than larger devices for situations where the separation region is not relatively localized.

Alternative approaches for separation control by streamwise vortices are the V-shaped cutouts of the NACA's flush inlet, leading-edge serrations (Harris and Bartlett, 1972; Soderman, 1972; Barker, 1986) and use of large-scale (flow field versus boundary-layer scale) vortical motions to control separation on highly swept wings. Such motions can be generated by either auxiliary lifting devices, e.g., canards, or by simple abrupt planform variations such as wing leading-edge extensions (LEXs). Such large-scale vortical motions alter both the near-wall momentum and the basic pressure field, generating increased lift. Problems with such an approach include vortex bursting, usually caused primarily by adverse pressure gradients. Control of bursting is actually control *of* vortices and is a subsidiary problem of separation control *by* vortices (Vakili, 1990).

8.3 Passive Turbulence Amplification. The fundamental flow separation control approach associated with turbulence amplification is augmentation of the cross-stream momentum via Reynolds stresses in as much as the overall pressure rise for incipient separation is directly proportional to the square root of the skin-friction coefficient of the undisturbed boundary

layer (Hayakawa and Squire, 1982). The zeroth order consideration for most separation control is to ensure a turbulent rather than laminar boundary-layer state. For Reynolds numbers less than $0[10^7]$, this may necessitate use of various boundary-layer *tripping* devices such as roughness and waviness, passive or active mass transfer, acoustic fields, body vibration, or even elevated freestream disturbance levels.

Once a turbulent boundary-layer flow is established, large-scale dynamic transverse vortical entities can be generated to augment the innate turbulent Reynolds stress field beyond the usual amplification concomitant with the adverse pressure gradients usually associated with separation. Applicable devices include transverse cylinders or *flow control rails* mounted just above, or in the outer part of, the boundary layer (Sajben et al., 1976). Airfoils with chord the $0[\delta]$ mounted parallel to the body in the outer part of the boundary layer and set at angle of attack also generate large transverse dynamic vortical motions (Corke et al., 1980), as can embedded cavity (Helmholtz) resonator surfaces. Dynamic three-dimensional *horseshoe* or hairpin eddies can be generated in the tip flow of three-dimensional stubs mounted normal to the surface. Except for the flow control rail, which works quite well, these passive devices have received only limited attention and development for flow separation control.

Howard and Goodman (1985; 1987) recently investigated the effectiveness of two passive techniques to reduce flow separation, transverse rectangular grooves and longitudinal V-grooves placed in the aft shoulder region of a bluff body. Both types of grooves were beneficial in reducing the form drag on a body at zero and moderate angles of yaw. Basically, the grooves work by redirecting the outer-flow momentum to the near-wall region through the *three-dimensionalization* of a two-dimensional flow. This is an example of locally mitigating the adverse pressure gradient through partial *boattailing*. Lin et al. (1990b) extended the longitudinal groove approach to the low-speed, two-dimensional rearward-facing ramp. Their closely packed grooves resulted in a reduction of the reattachment distance by up to 66 percent. Selby and Miandoab (1990) reported that the base pressure of a blunt trailing-edge airfoil with surface grooves increased with increasing groove depth and angle. They speculated that *minimally* attached flow in the grooves is the mechanism by which fluid of higher momentum is redirected to the base flow region to effect an increase in the pressure.

Additional turbulence amplification ploys include destabilizing longitudinal surface curvature in order to increase wall shear, concave for boundary layers and convex for wall jets (coanda effect). For high speeds, use of upstream shock-wave-interaction, which can amplify turbulence significantly (Anyiwo and Bushnell, 1982; Zang et al., 1984), also delays separation (Schofield, 1985; Gol'd Fel'd and Zatoloka, 1979). The use and/or generation of freestream turbulence/disturbance fields with intermediate scale motions also amplifies turbulence in the boundary layer and delays separation (Hoffmann, 1981; Sasaki and Kiya, 1985; Hoffmann et al., 1988; Isomoto and Honami, 1989).

8.4 Active Wall-Region Momentum Addition. Active momentum addition techniques include streamwise vortex generation via discrete blowing or injection, turbulence/Reynolds stress amplification through use of dynamically activated or driven devices, and direct tangential injection of high-velocity fluid. The two passive techniques discussed in Sections 8.2 and 8.3, vortex generation and turbulence amplification, can also be employed via active systems. Of particular interest is the use of discrete jet injection for streamwise vortex generation. This concept arose in the 1950's (Wallis and Stuart, 1958; Pearcey, 1961; Kukainis, 1969; Wimpenny, 1970) and is the subject of current research (Zhang and Sheng, 1987; Reynolds et al., 1988; Johnston and Nishi, 1989; 1990; Compton and Johnston, 1991). What is particularly appealing is the ability to deploy or retract the *vortex generators* as required, which eliminates parasitic drag in the *retracted* nonblowing condition. The associated fluid supply lines operate at high pressure and are thus relatively small. They might even be utilizable as structural reinforcement elements. The status of research in this area is such that, while it is clear that discrete jets will generate vortices and delay separation, the approach has not yet been optimized. Research is required to determine optimal injection orientation, spacing, individual hole geometry and size, velocity, pressure, and finally location vis-a-vis the adverse pressure gradient regions. Papell (1984) addresses vortex generation within the injection jet itself. Another use of injection for vortex generation is spanwise injection along the leading edges of swept wings for upper surface separation control (e.g., Bradley and Wray, 1974). Employing spanwise arrays of small, skewed, pitched jets from holes in the surface, Johnston and Nishi (1990) have shown that the jets can produce longitudinal vortices strong enough to substantially reduce and nearly eliminate a large stalled region of a turbulent separated flow.

A relatively recent development in flow separation control is active turbulence amplification in the bounding shear layer for flows already separated. The fundamental concept is excitation and, through phasing, enhanced interaction of large transverse eddy structures near and downstream of the separation point, thereby amplifying the mixing in the shear layer bounding the separated flow region. This increases entrainment and generally reduces the extent of separation. For initially laminar flows, the zeroth order influence of dynamic forcing is to both trip transition and enhance the eddy dynamics of the low-Reynolds-number shear-layer (e.g., Collins, 1979; 1981; Mullin et al., 1980; Sigurdson and Roshko, 1985; DeMeis, 1986; Durbin and McKinzie, 1987; Huang et al., 1987; Neuburger and Wygnanski, 1988; Zaman and McKinzie, 1989; Bar-Sever, 1989).

Various dynamic devices have been tried for the initially turbulent flow case including acoustic drivers (Bhattacharjee et al., 1985), oscillating embedded plates, spoilers and flaps (Reisenthel et al., 1985; Roos and Kegelman, 1986; Miau et al., 1988; Chen and Shi Ying, 1989; Katz et al., 1989a; 1989b), both chordwise and spanwise dynamic blowing (Oyler and Palmer, 1972; Ely and Berrier, 1975; Vakili et al., 1988; Vakili, 1990), rotating cams (Viets et al., 1979, 1981a, 1981b, 1981c, 1984), and even dynamic motions of the entire body. One of the few large-scale dynamic experiments thus far is also one of the earliest (Oyler and Palmer, 1972). The same incremental increase in lift was achieved with only 50 percent of the blowing mass flow required for the steady-state case. What is obvious from the initially turbulent, dynamic-input separation control research thus far is that, once again, the method works. What is not so obvious is how well it would work in engineering applications and the nature and operating range of the optimal dynamic devices.

8.4.1 Wall Jets. Direct tangential injection, wall jet, was and still is the preferred and straightforward flow separation control technique which has been applied to military fighters and STOL transports. High-pressure air can be used enabling relatively small interior lines as opposed to suction control which, while generally more energy efficient than blowing at both low and high speeds, usually requires larger interior ducting (Gratzer, 1971). In some applications, a lighter gas is introduced to reduce the rate at which heat is exchanged between the wall and the external stream and, thus, to provide thermal protection at high supersonic velocities.

High-pressure bleed air was readily available from the early jet engines but less so for modern high-bypass-ratio turbofans. CFD can now be used to design the system and optimize the

injection velocity profile for a given mass flow for optimal separation delay (see Saripalli and Simpson, 1980). Performance can be further enhanced by convex longitudinal curvature (coanda effect). Tangential blowing is also used to stabilize a *trapped vortex*, particularly in the knee region of wing flaps. The literature for the steady blowing case is both extensive and readily available, with most information dating from the 1950's. Separation control by blowing at high speeds is covered in the reviews by Delery (1985) and Viswanath (1988). Of possible interest for separation control via direct tangentional injection is the application of turbulence control techniques to *reduce* the mixing between the injected and incident flows and thereby preserve the high near-wall momentum for a larger extent downstream (McInville et al., 1985).

Tangential jet blowing over the upper surface of a rounded trailing-edge airfoil sets an effective Kutta condition by fixing the location of separation. This circulation control concept was initially described by Cheeseman and Seed (1967), and a substantial data base has been gathered since then for the purpose of performance evaluation (Kind, 1967; Wood and Nielsen, 1985; Novak, 1987). More recently, McLachlan (1989) conducted an experimental study of the flow past a two-dimensional circulation control airfoil under steady leading/trailing-edge blowing. In the range of chord Reynolds numbers of $1.2\times10^5-3.9\times10^5$, McLachlan observed a dramatic increase in the lift coefficient when trailing-edge blowing was used to control the location of the rear separation points. He reported a gain in the lift coefficient of the order of 80 times the injected momentum coefficient. When leading-edge blowing was employed simultaneously, a slight decrease in lift was observed.

Although not directly related to separation control, jets in the form of thin sheets exiting in the spanwise direction from the tips of a straight wing can be used to enhance the lift through an effective enlargement of the wing span (Wu et al., 1983; 1984; Tavella et al., 1988; Lee et al., 1989; Vakili, 1990). This application was first reported in 1956 by Ayers and Wild, and suggests the possibility of using such an arrangement in place of conventional ailerons or flaps to alter the aerodynamic forces acting on an aircraft (Tavella et al., 1986b). Either a single long slot (Lee et al., 1986; Tavella et al., 1986a) or several short ones (Wu et al., 1983; 1984) are used along the entire chord at the wing tips. The enlargement of the aspect ratio associated with the lateral displacement of the tip vortices via blowing leads also to a reduction of the induced drag as well as to a beneficial effect on stall.

8.4.2 Additional Active Control Methods. Other active methods for controlling boundary layer separation and reattachment include the use of acoustic excitations (Collins and Zelenevitz, 1975; Ahuja et al., 1983; Ahuja and Burrin, 1984, Zaman et al., 1987; Huang et al., 1987), periodic forcing of the velocity field via an oscillating flap or wire (Koga et al. 1984; Sigurdson and Roshko, 1985; Reisenthel et al., 1985; Roos et al., 1986; Katz et al., 1989a; 1989b; Bar-Sever, 1989), and oscillatory surface heating (Maestrello et al., 1988).

As early as 1948, Schubaur and Skramstad observed that sound at particular frequencies and intensities could enhance the momentum exchange within a boundary layer and could, therefore, advance the transition location. Collins and Zelenevitz (1975) and Collins (1979; 1981) introduced the external acoustic excitation technique to enhance the lift of an airfoil. In this case, sound is radiated onto the wall from a source outside the boundary layer. Using the same technique at chord Reynolds number up to 1×10^6, Ahuja et al. (1983) and Ahuja and Burrin (1984) successfully demonstrated that sound at a preferential frequency and sufficient amplitude can postpone turbulent separation on an airfoil in both pre- and post-stall regimes. The optimum frequency was found to be $4U_\infty/c$ (Strouhal number = 4), where U_∞ is the freestream velocity and c is the airfoil chord. Goldstein (1984) speculates that the delay in separation in Ahuja et al.'s (1983) experiment resulted from enhanced entrainment promoted by instability waves that were triggered on the separated shear layer by the acoustic excitation.

Zaman et al. (1987) conducted further study of the beneficial interaction between external acoustic excitation and the separated flow around an airfoil at high angle of attack. They found that the most effective separation control is achieved at frequencies at which the acoustic standing waves in their wind tunnel induce transverse velocity fluctuations in the vicinity of the lifting surface. The loudspeakers used by Zaman et al. (1987) as well as by Ahuja et al. (1983) essentially excited the resonant modes in their respective wind tunnels and one of these modes forced the shear layers separating from their respective airfoils. Extremely high level of excitation was required, however, to maintain these wind tunnel resonance modes, making the external acoustic excitation technique impractical for actual applications. Zaman et al. (1987) speculated that a more effective separation control can be obtained by direct introduction of velocity disturbances.

Huang et al. (1987) introduced the *internal acoustic excitation technique*, in which sound is emanated from a hole or a slot on the surface of a lifting surface. The loudspeaker in this case is essentially used as a piston to produce localized vorticity perturbations at the leading edge of the airfoil. Very recently, Hsiao et al. (1990) reported improved aerodynamic performance of a two-dimensional airfoil using sound emitted from three narrow wall slots located near the leading edge. The sound pressure levels used in their experiment was substantially lower than that used externally by other researchers. Additionally, a correct Strouhal number scaling was achieved. Hsiao et al. (1990) concluded that the enhancement of momentum transport resulting from the sound excitation produce a suction peak at the leading edge, an increase of lift and a narrower wake, as long as the excitation frequency is locked-in to the most unstable frequency of the separated shear layer.

To directly disturb the velocity field, Koga et al. (1984) used a computer-controlled spoiler-like flap in a flat-plate turbulent boundary layer with and without modelled upstream separation. They were able to manipulate the separated flow region and its reattachment length characteristics by varying the frequency, amplitude and waveform of the oscillating flap. Reynolds and Car (1985) offer a plausible explanation, from the viewpoint of a vorticity framework, for the experimental observations of Koga et al. It seems that the large-scale vortical structures produced by forcing play a major role in enhancing mixing and entrainment, thus leading to reattachment. The active flap controls the size of the separated region by providing an additional mechanism for removing vorticity from this zone, namely, large-scale vortex convection. Recent experiments by Nelson et al. (1987; 1990) seem to confirm that the dominant mechanism of vorticity transport behind an oscillating spoiler is convective.

Periodic forcing of the velocity field has been shown to reduce reattachment length in both laminar and turbulent flows on a number of other basic geometrical configurations (Sigurdson and Roshko, 1985; Roos et al., 1986; Katz et al., 1989a, 1989b; Bar-Sever, 1989). At a chord Reynolds number in the range of $1\times10^5-3\times10^5$, Bar-Sever (1989) used an oscillating wire to introduce transverse velocity fluctuations into a separated shear layer on an airfoil at high incidence. The effectiveness of this separation control technique is depicted in Fig. 18, showing the variation of unforced and forced lift coefficients as a function of angle of attack. For each angle, the forced case represents the best lift achieved at any combination of forcing frequency and amplitude. At $\alpha=20$ deg, the controlled forcing moved the separation from the leading edge to about 0.8c. A wide band of forcing re-

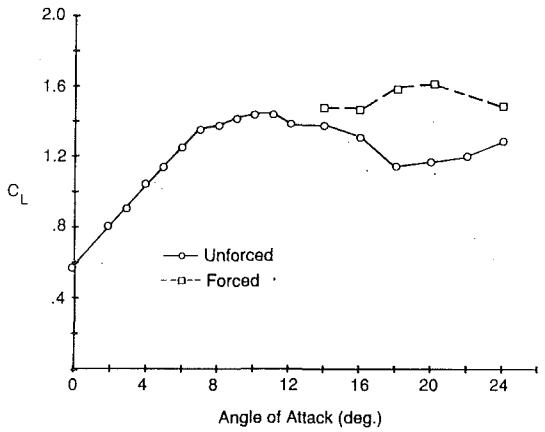

Fig. 18 Lift coefficient variation with angle of attack for unforced and best forced case; $R_c = 1.5 \times 10^5$. (From Bar-Sever, 1989.)

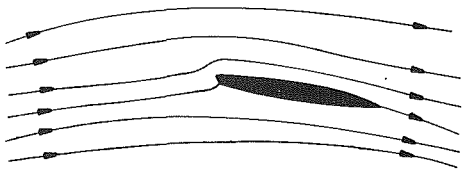

Fig. 19(*a*) During supersonic flight

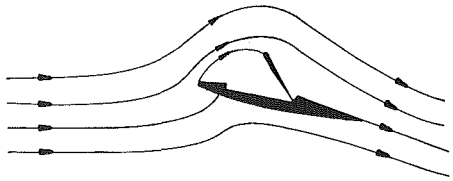

Fig. 19(*b*) During takeoff and landing

Fig. 19 Freestream flap.

duced frequencies (0.7 – 2.7) was found to be effective, with diminishing influence at lower frequencies.

9 Separation Provocation

Although most of the control methods reviewed thus far are designed to prevent separation, under certain circumstances the designer may wish to provoke separation. Controlled separation is associated with the formation of jets, throttling action in household faucets, and noisy as well as musical acoustic effects generated by flow. During takeoff and landing of a supersonic aircraft, a freestream flap may be used to provoke leading-edge separation followed by reattachment at the leading edge of the flap, thus forming a thicker pseudo-body with the desired aerodynamic shape as shown in Fig. 19 adapted from Hurley (1961). The airfoil has then a relatively high lift coefficient, although its lift-to-drag ratio is quite low.

The detached bow shock forming upstream of a blunt body in supersonic flight may be changed into a weaker, attached oblique shock by placing a spike in front of the body. The pressure rise and the presence of a solid surface on which a boundary layer forms causes the flow to separate downstream of the spike tip. A properly designed spike may result in lower drag, higher lift, and corresponding change in pitching moment (Wood, 1961).

Periodic separation may also be provoked by changes in the wall geometry. Francis et al. (1979) initiated separation on an airfoil by periodically inserting and removing a spoiler at the wall. Viets et al. (1984) studied separation inducement and control by use of a cam-shaped rotor mounted on an airfoil. The cam, either driven or free-wheeling, periodically extended out into the flow causing the boundary layer to separate. Large-scale coherent spanwise structures were periodically generated and were responsible for the flow detachment as explained by Reynolds and Carr (1985).

9.1 Delta Wings. On a sharp-leading-edge delta wing, the separation position is fixed and a strong shear layer is formed along the entire edge (Lee and Ho, 1989; 1990). The shear layer is wrapped up in a spiral fashion, which results in a large-bound vortex on each side of the wing. The two vortices appear on the suction surface of the wind in the form of an expanding helix when viewed from the apex. The low pressure assoicated with the vortices produces additional lift on the wing, often called nonlinear or vortex lift, which is particularly important at large angles of attack. The recent experiments of Gad-el-Hak and Blackwelder (1985) have indicated that small discrete vortices are shed parallel to the leading edge at a repeatable frequency, determined by the angle of attack and Reynolds number. Repeated vortex pairings result in the formation of progressively larger vortices. This process can be modulated by weak, periodic suction/injection through a leading edge slot. In particular, when the perturbation frequency is a subharmonic of the natural shedding frequency, the evolution of the bounded shear layer is dramatically altered (Gad-el-Hak and Blackwelder, 1987; Blackwelder et al., 1987).

Wood and Roberts (1986; 1988) examined the feasibility of vortex control by tangential mass injection at the leading edge of a 60 deg delta wing. Their initial experimental results indicate that modest continuous blowing was capable of extending the regime of stable, controlled vortical flow over the upper surface of the wing by approximately 30 deg angle of attack. Increases in maximum normal force of 30 percent were achieved and significant rolling moments were produced at attack angles of 35–60 deg. On a delta wing with rounded leading edges, the blowing seems to control the location of the crossflow separation points and hence the trajectories of the ensuing vortices. Wood and Roberts (1988) propose that this blowing scheme may be a practical solution for changing the normal force without changing attitude, for the production of both steady and transient control moments at extremely high angles of attack, and for increasing the lift-to-drag ratio of very slender bodies at modest attack angles. In a recent experiment, Wood et al. (1990) have shown that the effects of asymmetric leading-edge blowing are uncoupled at prestall angles of attack. In this case, the overall forces and moments for symmetric blowing can be simply deduced by superposition of asymmetric blowing situations. On the other hand, the response of the vortical flowfield is strongly coupled for asymmetric blowing at poststall conditions. Wood et al.'s results imply that tangential leading-edge blowing may result in substantial rolling moments at conditions where other control devices cease to be effective.

Controllable leading-edge flaps provide an active method of influencing the large vortices on a delta wing (Rao, 1979; Marchman et al., 1980). These devices appear to be capable of improving L/D ratio of a given wing, primarily through drag reduction. Unlike the control by blowing discussed above, the use of flabs results in only a modest improvement in the angle-of-attack envelope.

10 Discussion and Conclusions

10.1 Computational Fluid Dynamics. The tremendous increases in CFD capability which have occurred as a direct result of increases in computer storage capacity and speed are

transforming flow separation control from an empirical art to a predictive science. Control techniques such as mitigation of imposed pressure gradients, blowing and suction are all readily parameterized via viscous CFD. Current inaccuracies in turbulence modeling can severely degrade CFD predictions once separation has occurred, however the essence of separation control is the calculation of attached flows, estimation of separation location, and indeed whether or not separation will occur. These tasks can in fact be performed reasonably well via CFD within the uncertainties of the transition location estimation (e.g., Smith, 1974). This latter uncertainty has been significantly reduced for low-disturbance freestreams and smooth surfaces using CFD along with the e^n method (Bushnell et al., 1989). Therefore it is now possible, at least to first order, to design bodies over which the flow will not separate (Cooke and Brebner, 1961; Pinebrook and Dalton, 1983; Yang et al., 1984; Dillner et al., 1984; Waggoner and Allison, 1987; Szodruch and Shneider, 1989), and this is generally done, for aircraft, for the cruise condition. This is not currently done, for example, for helicopters and automobiles.

The cab-top fairings on tractor trailer trucks (Kirsch, 1974) and fairings at afterbody junctures (Howard et al., 1981) are useful experimental attempts at reducing the causative adverse pressure fields. An exploratory study documented by Whitehead and Bertram (1971) indicates that continuous-curvature surface geometry can, presumably via minimization of pressure gradients, profoundly reduce three-dimensional separation. Current CFD capability allows the design of intersection regions which are properly filleted to obviate formation of the usual organized horseshoe vortices found in 3-D separated flows (e.g., Lakshmanan et al., 1988).

10.2 Applications and Comparisons. It should be evident from the discussion thus far that there are a large number of techniques which can control/mitigate flow separation. The choice of which technique to employ is a function of the particular flow situation and purpose for the control. Considerations include system aspects such as volume, weight, complexity, cost, reliability, overall energy and drag budgets, and any requirements for dynamic response and styling. Aside from design for separation minimization, thus far significant applications have been relatively limited though important. Examples of successful separation control systems include active injection on several 1950's and 1960's era fighters, STOL transports, the ubiquitous vortex generators, passive bleed for supersonic inlets, leading edge extensions for the 1970's and 1980's fighters, cab top fairing for tractor trailer trucks, and various types of blown flaps on transport airplanes.

Particularly intriguing in the future are possible applications at cruise, especially at high speeds, as well as *standby techniques* for *off-design* situations, thereby allowing extremely tight designs. In addition, increased knowledge of the control innovations for vortical flows should allow solutions to the problems of high-angle-of-attack maneuvering and stall/spin prevention or recovery. Alternate techniques should also be sought for either supplementation or replacement of conventional high-lift flap systems. Candidate approaches include use of the LFC leading-edge suction system along with air jet vortex generators and perhaps either rotating wings or airport *ski jumps*. Also, there exists tremendous energy saving potential in further separation control or form drag reduction for vehicles which have notoriously high drag—automobiles, helicopters, and tractor-trailer trucks.

Various comparisons have been made between candidate separation control techniques on common test beds. Vakili et al. (1985) report that vortex generators perform better than a *flow control rail* for a diffusing S-duct. For a swept wing, experiments indicate that slot blowing is more effective than either vane or air jet vortex generators (Kukainis, 1969). For CTOL wings, improvements in the design of mechanical high-lift systems have tended to keep pace with the trend toward higher wing loading so that benefits from BLC techniques have not appeared sufficiently attractive (Gratzer, 1971). Butter (1984) and Dillner et al. (1984) provide excellent analyses and discussions of current CTOL high-lift design practice, problems, and performance. As a suggestion for further work a technique which has not yet been researched sufficiently is the three-dimensionalization of a nominally two-dimensional problem which, from the work of Ball (1971), McLean and Herring (1974), and Lin and Howard (1989), tends to reduce the extent of separation.

10.3 Summary. The performance of many practical devices is often controlled by the separation location. For a steady, two-dimensional boundary layer, the streamwise velocity and its normal gradient vanish at the point (or line) of separation. For three-dimensional or unsteady flows, the point of vanishing shear does not necessarily coincide with separation. Under some circumstances, a thin layer of reverse flow can be embedded at the bottom of an otherwise attached and mathematically well-behaved boundary layer.

Advancing or delaying boundary layer detachment is of immense importance to the performance of biological or man-made systems involving fluid flow. Postponing separation may lead to pressure-drag reduction, lift enhancement, stall delay, and pressure-recovery improvement. Provoking flow detachment, on the other hand, may improve the subsonic performance during takeoff and landing of a thin airfoil optimized for supersonic cruising.

Methods of separation control that rely on modifying the shape of the velocity profile near the wall include shaping, transpiration, and establishing a normal viscosity gradient through surface heating/cooling, film boiling, cavitation, sublimation, chemical reaction, wall injection of a secondary fluid having lower/higher viscosity, and the introduction into the boundary layer of shear-thinning/shear-thickening additive. To delay separation, anyone or a combination of the above techniques is configured to make the velocity profile as full as possible. The wall in this case is a source of spanwise vorticity. To advance separation, the reverse technique is employed to make the wall a sink of vorticity.

For a moving wall, separation is delayed when the motion of the surface is in the same direction as that of the freestream. This phenomenon is exploited in sport balls, Flettner's rotor, and some experimental STOL-type aircraft. In analogy to the moving wall case, unsteady separation is postponed when the separation point moves upstream and is advanced when the point of detachment moves downstream. Airfoils oscillating through high angles of attack can produce very high lift and maintain flow attachment well beyond their static stall angles. Insects exploit these unsteady separation effects to achieve remarkable aerodynamic characteristics.

In three-dimensional flows, the near-wall fluid may move in a direction in which the pressure gradient is more favorable and not against the adverse pressure in the direction of the main flow as is the case for two-dimensional flows. Consequently, three-dimensional boundary-layers are in general more capable of overcoming an adverse pressure gradient without extensive/catastrophic separation.

A turbulent boundary layer is more resistant to separation than a laminar one and mostly for that reason transition advancement may be desired in some situations. In low-Reynolds-number terminology, the transition promoting devices are called *turbulators* and are in the form of single, multiple or distributed roughness elements placed on the wall. The mechanical roughness elements, in the form of serrations, strips, bumps or ridges, are typically placed near the airfoil's leading edge.

Many other passive and active methods to postpone separa-

tion for low- and high-speed flows are available. Common to all these control methods is an attempt to supplying additional energy to the near-wall fluid particles which are being retarded in the boundary layer. Passive techniques include intentional tripping of transition from laminar-to-turbulent flow upstream of what would be a laminar separation point, boundary-layer fences to prevent separation at the tips of swept-back wings, placing an array of vortex generators on the body to enhance the momentum and energy in the neighborhood of the wall, rippled trailing edge, streamwise corrugations, and using a screen to divert the flow and increase the velocity gradient at the wall. Active methods to postpone separation include fluid injection parallel to the wall to augment the shear-layer momentum or normal to the wall to enhance the mixing rate, the use of acoustic excitations, periodic forcing of the velocity field via an oscillating flap or wire, and oscillatory surface heating.

10.4 Recommendations for Future Work. Flow separation control will be of increasing importance in the future as declining petroleum reserves, concern over the greenhouse effect, economic development of the third world, continued population growth, and increasing economic competition force stringent energy conservation and efficiency improvements. Much of the remaining gains in aerodynamics involve some form of viscous flow control, including flow separation control. Particularly intriguing is the possibility of replacing or at least augmenting conventional high-lift devices, i.e., flaps and slats. In the limit, this may require wing rotation as some increase in wing angle of attack would probably be required.

With the exception of vortex generators, the rapid development of CFD has transformed much of conventional flow separation control from art to science, including the capability to mitigate the causative pressure fields and optimize several control approaches. However, the effects of combinations of separation control approaches require considerable further research.

The use of flow separation control at cruise for high-speed, supersonic civil transports may allow significant increases in lift-to-drag ratio, via increased leading-edge thrust, upper surface and fuselage lift contribution, and effective favorable interference wave drag reduction from shock-boundary-layer interaction separation control. The art and science of flow separation control is far richer than the conventional view of blowing/suction and vortex generators. The recent research regarding miniaturized and jet injection vortex generators allows reduction of parasitic cruise drag for such devices and is particularly intriguing for several applications including replacement or supplementation of conventional high-lift systems.

Suggested future research directions include further work on: optimization of air jet vortex generators including pulsed injection; three-dimensionalization of nominally two-dimensional surfaces; use of weak *upstream* shocks for turbulence amplification and swept shocks for spanwise removal of the near-wall low-momentum region; downstream vortex reinforcers and miniaturized near-wall vortex generators; and techniques to force momentum toward wall, for example downwash from embedded lifting surfaces.

Acknowledgment

Portions of this article were presented as invited talks at the ASME *International Symposium on Non-Steady Fluid Dynamics*, 4–7 June 1990, Toronto, Canada (Gad-el-Hak, 1990a), and the *AIAA 29th Aerospace Sciences Meeting*, 7–10 January 1991, Reno, Nevada (Gad-el-Hak and Bushnell, 1991). The authors would like to acknowledge the encouragement and help of the Technical Editor of this journal, Professor Demetri P. Telionis, who carefully read the manuscript and provided us with many valuable suggestions for improvement.

References

Abbott, I. H., and von Doenhoff, A. E., 1959, *Theory of Wing Sections*, Dover, New York.

Adkins, R. C., 1975, "A Short Diffuser with Low Pressure Loss," ASME JOURNAL OF FLUIDS ENGINEERING, Vol. 97, pp. 297–302.

Adkins, R. C., 1977, "Diffusers and Their Performance Improvement by Means of Boundary Layer Control," *AGARD Special Course on Concepts for Drag Reduction*, AGARD-R-654, Paper No. 6, Rhode-Saint-Génèse, Belgium.

Adkins, R. C., Mathaus, D. S., and Yost, J. O., 1980, "The Hybrid Diffuser," ASME Paper No. 80-GT-136, New York.

Ahuja, K. K., and Burrin, R. H., 1984, "Control of Flow Separation by Sound," AIAA Paper No. 84-2298, New York.

Ahuja, K. K., Whipkey, R. R., and Jones, G. S., 1983, "Control of Turbulent Boundary Layer Flows by Sound," AIAA Paper No. 83-0726, New York.

Alvarez-Calderon, A., 1964, "Rotating Cylinder Flaps of V/STOL Aircraft," *Aircraft Eng.*, Vol. 36, pp. 304–309.

Anyiwo, J. C., and Bushnell, D. M., 1982, "Turbulence Amplification in Shock Wave-Boundary Layer Interaction," *AIAA J.*, Vol. 20, pp. 893–899.

Aroesty, J., and Berger, S. A., 1975, "Controlling the Separation of Laminar Boundary Layers in Water: Heating and Suction," RAND Corporation Report No. R-1789-ARPA, Santa Monica, CA. (Also available from U.S. NTIS; Document Number AD-AO20026.)

Atta, R., and Rockwell, D., 1990, "Leading-Edge Vortices Due to Low Reynolds Number Flow Past a Pitching Delta Wing," *AIAA J.*, Vol. 28, pp. 995–1004.

Ayers, R. F., and Wilde, M. R., 1956, "An Experimental Investigation of the Aerodynamic Characteristics of a Low Aspect Ratio Swept Wing with Blowing in a Spanwise Direction from the Tips," College of Aeronautics, Note No. 57, Cranfield, England.

Bahi, L., Ross, J. M., and Nagamatsu, H. T., 1983, "Passive Shock Wave/Boundary Layer Control for Transonic Airfoil Drag Reduction," AIAA Paper No. 83-0137, New York.

Ball, K. O., 1971, "Flap Span Effects on Boundary Layer Separation," *AIAA J.*, Vol. 9, pp. 2080–2081.

Bar-Sever, A., 1989, "Separation Control on an Airfoil by Periodic Forcing," *AIAA J.*, Vol. 27, pp. 820–821.

Barker, R. A., 1986, "The Aerodynamic Effects of a Serrated Strip Near the Leading Edge of an Airfoil," M. S. thesis, Royal Air Force College, Report No. ETN-87-99480, Cranwell, England.

Barnwell, R., Bushnell, D. M., Nagamatsu, H. T., Bahi, L., and Ross, J., 1985, "Passive Drag Control of Airfoils at Transonic Speeds," U.S. Patent No. 4,522,360.

Bauer, S. X. S., and Hernandez, G., 1988, "Reduction of Cross-Flow Shock-Induced Separation with a Porous Cavity at Supersonic Speeds," AIAA Paper No. 88-2567, New York.

Baullinger, N., and Page, V., 1989, "High Altitude Long Endurance (HALE) RPV," AIAA Paper No. 89-2014, New York.

Bernard, J. J., and Siestrunck, R., 1959, "Échanges de Chaleur dans les Écoulements Présentant des Décollements," *Proc. First Int. Congr. Aero. Sci.*, Madrid, Spain, *Adv. in Aero. Sci.*, Vol. 1, eds. Th. von Karman et al., Pergamon Press, London, England, pp. 314–332.

Bhattacharjee, S., Scheelke, B., and Troutt, T. R., 1985, "Modification of Vortex Interactions in a Reattaching Separated Flow," AIAA Paper No. 85-0555, New York.

Blackwelder, R. F., Gad-el-Hak, M., and Srnsky, R. A., 1987, "Method and Apparatus for Controlling Bound Vortices in the Vicinity of Lifting Surfaces, U.S. Patent No. 4,697,769.

Bradley, R. G., and Wray, W. O., 1974, "A Conceputal Study of Leading-Edge-Vortex Enhancement by Blowing," *J. Aircraft*, Vol. 11, pp. 33–38.

Bragg, M. B., and Gregorek, G. M., 1987, "Experimental Study of Airfoil Performance with Vortex Generators," *J. Aircraft*, Vol. 24, pp. 305–309.

Briedenthal, R. E., Jr., and Russell, D. A., 1988, "Aerodynamics of Vortex Generators," NASA CR-182511, Washington, D.C.

Brown, A. C., Nawrocki, H. F., and Paley, P. N., 1968, "Subsonic Diffusers Designed Integrally with Vortex Generators," *J. Aircraft*, Vol. 5, pp. 221–229.

Burd, J. E., 1981, "Flow Control for a High Energy Laser Turret Using Trapped Vortices Stabilized by Suction," M.Sc. thesis, Naval Postgraduate School, Monterey, CA. (Also available from U.S. NTIS; Document Number AD-A115263.)

Bushnell, D. M., 1990, "Supersonic Aircraft Drag Reduction," AIAA Paper No. 90-1596, New York.

Bushnell, D. M., and Donaldson, C. D., 1990, "Control of Submersible Vortex Flows," NASA Tech. Memo. 102693, Washington, D.C.

Bushnell, D. M., and Trimpi, R. L., 1986, "Optimum Supersonic Wind Tunnel," AIAA Paper No. 86-0773, New York.

Bushnell, D. M., Malik, M. R., and Harvey, W. D., 1989, "Transition Prediction in External Flows via Linear Stability Theory," *IUTAM Symposium Transsonicum III*, eds. J. Zierep and H. Oertel, Springer-Verlag, Berlin, pp. 225–242.

Butter, D. J., 1984, "Recent Progress on Development and Understanding of High Lift Systems," in *AGARD Conference on Improvement of Aerodynamic Performance through Boundary Layer Control and High Lift Systems*, AGARD-CP-365, pp. 1-1 to 1-26, Brussels, Belgium.

Calarese, W., Crisler, W. P., and Gustafson, G. L., 1985, "Afterbody Drag Reduction by Vortex Generators," AIAA Paper No. 85-0354, New York.

Carmichael, B. H., 1974, "Application of Sailplane and Low-Drag Underwater Vehicle Technology to the Long-Endurance Drone Problem," AIAA Paper No. 74-1036, New York.

Cebeci, T., and Chang, K. C., 1978, "Calculation of Incompressible Rough-Wall Boundary-Layer Flows," *AIAA J.*, Vol. 16, pp. 730-735.

Cebeci, T., and Egan, D. A., 1989, "Prediction of Transition due to Isolated Roughness," *AIAA J.*, Vol. 27, pp. 870-875.

Chambers, J. R., 1986, "High-Angle-Of-Attack Aerodynamics: Lessons Learned," AIAA Paper No. 86-1774-CP, New York.

Chang, P. K., 1970, *Separation of Flow*, Pergamon Press, Oxford, England.

Chang, P. K., 1976, *Control of Flow Separation*, Hemisphere, Washington, D.C.

Cheeseman, I. C., and Seed, A. R., 1967, "The Application of Circulation Control by Blowing to Helicopter Rotors," *J. Royal Aeronautical Society*, Vol. 71, pp. 451-467.

Chen, D., and Shi Ying, Z., 1989, "Control of Separation in Diffusers Using Forced Unsteadiness," AIAA Paper No. 89-1015, New York.

Chow, C. Y., Chen, C. L., and Huang, M. K., 1985, "Trapping of Free Vortex by Airfoils with Surface Suction," AIAA Paper No. 85-0446, New York.

Cichy, D. R., Harris, J. W., and MacKay, J. K., 1972, "Flight Tests of a Rotating Cylinder Flap on a North American Rockwell YOV-10A Aircraft," NASA CR-2135, Washington, D.C.

Colin, P. E., and Williams, J., 1971, "Assessment of Lift Augmentation Devices," AGARD-LS-43-71, Rhode-Saint-Génèse, Belgium.

Collins, F. G., 1979, "Boundary Layer Control on Wings Using Sound and Leading Edge Serrations," AIAA Paper No. 79-1875, New York.

Collins, F. G., 1981, "Boundary Layer Control on Wings Using Sound and Leading-Edge Serrations," *AIAA J.*, Vol. 19, pp. 129-130.

Collins, F. G., and Zelenevitz, J., 1975, "Influence of Sound upon Separated Flow Over Wings," *AIAA J.*, Vol. 13, pp. 408-410.

Compton, D. A., and Johnston, J. P., 1991, "Streamwise Vortex Development by Pitched and Skewed Jets in a Turbulent Boundary Layer," AIAA Paper No. 91-0038, New York.

Cook, W. L., Mickey, D. M., and Quigley, H. G., 1974, "Aerodynamics of Jet Flap and Rotating Cylinder Flap STOL Concepts," AGARD Fluid Dynamics Panel on V/STOL Aerodynamics, Paper No. 10, Delft, Netherlands.

Cooke, J. C., and Brebner, G. G., 1961, "The Nature of Separation and Its Prevention by Geometric Design in a Wholly Subsonic Flow," *Boundary Layer and Flow Control*, Vol. 1, ed. G. V. Lachmann, pp. 144-185, Pergamon Press, Oxford, England.

Corke, T. C., Guezennec, Y., and Nagib, H. M., 1980, "Modification in Drag of Turbulent Boundary Layers Resulting from Manipulation of Large-Scale Structures," *Viscous Flow Drag Reduction*, ed. G. R. Hough, AIAA *Prog. in Astro. & Aero.*, Vol. 72, pp. 128-143, New York.

Crabtree, L. F., 1957, "Effects of Leading-Edge Separation on Thin Wings in Two-Dimensional Incompressible Flow," *J. Aeronaut. Sci.*, Vol. 24, pp. 597-604.

Cutler, A., and Bradshaw, P., 1986, "The Interaction Between a Strong Longitudinal Vortex and a Turbulent Boundary Layer," AIAA Paper No. 86-1071, New York.

Cutler, A., and Bradshaw, P., 1989, "Vortex/Boundary-Layer Interactions," AIAA Paper No. 89-0083, New York.

Darby, R. A., 1954, "An Aircraft Manufacturer Loks at Boundary Layer Control," Fairchild Aircraft Division, Fairchild Engine and Airplane Corp., Report No. RR-1, Hagerstown, MD.

Davidson, C. J., 1985, "The Experimental Investigation of the Effects of Roughness upon Aerofoil Characteristic at Low Reynolds Numbers," M.Sc. thesis, Cranfield Institute of Technology, Cranfield, England.

Decken, J. V., 1971, "Aerodynamics of Pneumatic High-Lift Devices," *AGARD Conference on Assessment of Lift Augmentation Devices*, eds. P. E. Colin and J. Williams, AGARD-LS-43-71, Paper No. 2, Rhode-Saint-Génèse, Belgium.

Delery, J. M., 1985, "Shock Wave/Turbulent Boundary Layer Interaction and Its Control," *Prog. Aerospace Sci.*, Vol. 22, pp. 209-280.

DeMeis, R., 1986, "Sounding a Happy Note for Lift," *Aerospace America*, Vol. 24, pp. 10-11.

Despard, R. A., and Miller, J. A., 1971, "Separation in Oscillating Laminar Boundary-Layer Flows," *J. Fluid. Mech.*, Vol. 47, pp. 21-31.

Didden, N., and Ho, C-M., 1985, "Unsteady Separation in a Boundary Layer Produced by an Impinging Jet," *J. Fluid Mech.*, Vol. 160, pp. 235-256.

Dillner, B., May, F., and McMasters, J. H., 1984, "Aerodynamic Issues in the Design of High-Lift Systems for Transport Aircraft," *AGARD Conference on Improvement of Aerodynamic Performance through Boundary Layer Control and High Lift Systems*, AGARD-CP-365, Paper No. 9, Brussels, Belgium.

Donovan, J. F., and Selig, M. S., 1989, "Low Reynolds Number Airfoil Design and Wind Tunnel Testing at Princeton University," *Low Reynolds Number Aerodynamics*, ed. T. J. Mueller, Springer-Verlag, *Lecture Notes in Engineering*, Vol. 54, pp. 39-57, Berlin.

Driver, D. M., 1989, "Experimental Study of a Three-Dimensional Shear-Driven Turbulent Boundary Layer with Streamwise Adverse Pressure Gradient," Ph.D. thesis, Stanford University, Stanford, CA.

Durbin, P. A., and McKinzie, D. J., 1987, "Corona Anemometry for Qualitative Measurement of Reversing Surface Flow with Application to Separation Control by External Excitation," *Proc. Forum on Unsteady Flow Separation*, Cincinnati, OH, ed. K. N. Ghia, ASME, New York, pp. 15-18.

Ely, W. L., and Berrier, F. C., 1975, "Performance of Steady and Intermittent Blowing Jet Flaps and Spanwise Upper Surface Slots," Air Force Flight Dynamics Laboratory, AFFDL-TR-75-128, Wright-Patterson Air Force Base, OH.

Eppler, R., and Somers, D. M., 1985, "Airfoil Design for Reynolds Numbers between 50,000 and 500,000," *Proc. Conf. on Low Reynolds Number Airfoil Aerodynamics*, ed. T. J. Mueller, pp. 1-14, University of Notre Dame, Notre Dame, IN.

Ericsson, L E., 1967, "Comment on Unsteady Airfoil Stall," *J. Aircraft*, Vol. 4, pp. 478-480.

Ericsson, L. E., 1971, "Unsteady Airfoil Stall and Stall Flutter," NASA CR-111906, Washington, D.C.

Ericsson, L. E., 1988, "Moving Wall Effects in Unsteady Flow," *J. Aircraft*, Vol. 25, pp. 977-990.

Ericsson, L. E., and Reding, J. P., 1971, "Unsteady Airfoil Stall, Review and Extension," *J. Aircraft*, Vol. 8, pp. 609-616.

Ericsson, L. E., and Reding, J. P., 1984, "Unsteady Flow Concepts for Dynamic Stall Analysis," *J. Aircraft*, Vol. 21, pp. 601-606.

Ericsson, L. E., and Reding, J. P., 1986, "Fluid Dynamics of Unsteady Separated Flow. Part I. Bodies of Revolution," *Prog. Aerospace Sci.*, Vol. 23, pp. 1-84.

Ericsson, L. E., and Reding, J. P., 1987, "Fluid Dynamics of Unsteady Separated Flow. Part II. Lifting Surfaces," *Prog. Aerospace Sci.*, Vol. 24, pp. 249-356.

Feir, J. B., 1965, "The Effects of an Arrangement of Vortex Generators Installed to Eliminate Wind Tunnel Diffuser Separation," Institute for Aerospace Studies, University of Toronto, UTIAS Technical Note No. 87, Toronto, Canada.

Fitzgerald, E. J., and Mueller, T. J., 1990, "Measurements in a Separation Bubble on an Airfoil Using Laser Velocimetry," *AIAA J.*, Vol. 28, pp. 584-592.

Flatt, J., 1961, "The History of Boundary Layer Control Research in the United States of America," *Boundary Layer and Flow Control*, Vol. 1, ed. G. V. Lachmann, Pergamon Press, Oxford, England, pp. 122-143.

Flettner, A., 1924, "Die Anwendung der Erkenntnisse der Aerodynamik zum Windantrieb von Schiffen," *Jb. Schiffbautech. Ges.*, Vol. 25, pp. 222-251.

Francis, M. S., Keesee, J. E., Lang, J. D., Sparks, G. W., and Sisson, G. E., 1979, "Aerodynamic Characteristics of an Unsteady Separated Flow," *AIAA J.*, Vol. 17, pp. 1332-1339.

Gad-el-Hak, M., 1986, "The Use of the Dye-Layer Technique for Unsteady Flow Visualization," ASME JOUNAL OF FLUIDS ENGINEERING, Vol. 108, pp. 34-38.

Gad-el-Hak, M., 1987, "Unsteady Separation on Lifting Surfaces," *Appl. Mech. Rev.*, Vol. 40, pp. 441-453.

Gad-el-Hak, M., 1988a, "Review of Flow Visualization Techniques for Unsteady Flows," *Flow Visualization*, Vol. IV, ed. C. Véret, pp. 1-12, Hemisphere, Washington, D.C.

Gad-el-Hak, M., 1988b, "Visualization Techniques for Unsteady Flows: An Overview," ASME JOURNAL OF FLUIDS ENGINEERING, Vol. 110, pp. 231-243.

Gad-el-Hak, M., 1989a, "The Art and Science of Flow Control," *Frontiers in Experimental Fluid Mechanics*, ed. M. Gad-el-Hak, Springer-Verlag, *Lecture Notes in Engineering*, Vol. 46, Berlin, pp. 365-428.

Gad-el-Hak, M., 1989b, "Flow Control," *Appl. Mech. Rev.*, Vol. 42, pp. 261-293.

Gad-el-Hak, M., 1990a, "Separation Control For Steady and Unsteady Flows," *Proc. Int. Symp. on Non-Steady Fluid Dynamics*, eds. J. A. Miller and D. P. Telionis, FED-Vol. 92, ASME, New York, pp. 261-275.

Gad-el-Hak, M., 1990b, "Control of Low-Speed Airfoil Aerodynamics," *AIAA J.*, Vol. 28, pp. 1537-1552.

Gad-el-Hak, M., and Blackwelder, R. F., 1985, "The Discrete Vortices from a Delta Wing," *AIAA J.*, Vol. 23, pp. 961-962.

Gad-el-Hak, M., and Blackwelder, R. F., 1987, "Control of the Discrete Vortices from a Delta Wing," *AIAA J.*, Vol. 25, pp. 1042-1049.

Gad-el-Hak, M., and Bushnell, D. M., 1991, "Status and Outlook of Flow Separation Control," AIAA Paper No. 91-0037, New York.

Gad-el-Hak, M., and Ho, C.-M., 1985, "The Pitching Delta Wing," *AIAA J.*, Vol. 23, pp. 1660-1665.

Gad-el-Hak, M., and Ho, C.-M., 1986a, "Unsteady Vortical Flow Around Three-Dimensional Lifting Surfaces," *AIAA J.*, Vol. 24, pp. 713-721.

Gad-el-Hak, M., and Ho, C.-M., 1986b, "Unsteady Flow Around An Ogive-Cylinder," *J. Aircraft*, Vol. 23, pp. 520-528.

Gadd, G. E., 1960, "Boundary Layer Separation in the Presence of Heat Transfer," NATO Advisory Group for Aerospace Research and Development, AGARD Report No. 280.

Gadd, G. E., Cope, W. F., and Attridge, J. L., 1958, "Heat-Transfer and Skin-Friction Measurements at a Mach Number of 2.44 for a Turbulent Boundary Layer on a Flat Surface and in Regions of Separated Flow," Aeronautical Research Council R&M No. 3148, London, England.

Gadetskii, V. M., Serebriiskii, I. A. M., and Fomin, V. M., 1972, "Investigation of the Influence of Vortex Generators on Turbulent Boundary Layer Separation," *Uchenye Zapiski TSAGI*, Vol. 3, pp. 22-28.

Gartling, D. K., 1970, "Tests of Vortex Generators to Prevent Separation of Supersonic Flow in a Compression Corner," Applied Research Laboratory, University of Texas, Report No. ARL-TR-70-44, Austin, TX. (Also available from U.S. NTIS; Document Number AD-734154.)

Gol'd Fel'd, M. A., and Zatoloka, V. V., 1979, "On the Improvement of Separating Properties of a Turbulent Boundary Layer as a Result of the Effect of a Shock Wave," *Izvestiya Sibirskogo Otdeleniya, Akademii Nank*, Vol. 3, pp. 40–47.

Goldstein, M. E., 1984, "Generation of Instability Waves in Flows Separating from Smooth Surfaces," *J. Fluid Mech.*, Vol. 145, pp. 71–94.

Goldstein, S., 1948, "On Laminar Boundary Layer Flow Near a Position of Separation," *Q. J. Mech. Appl. Math.*, Vol. 1, pp. 43–69.

Görtler, H., 1955, "Dreidimensionales zur Stabilitätstheorie laminarer Grenzschichten," *ZAMM*, Vol. 35, pp. 362–363.

Gratzer, L. B., 1971, "Analysis of Transport Applications for High Lift Schemes," *AGARD Course on Assessment of Lift Augmentation Devices*, eds. P. E. Colin and J. Williams, AGARD-LS-43-71, Paper No. 7, Rhode-Saint-Génèse, Belgium.

Gregory, N., Stuart, J. T., and Walker, W. S., 1955, "On the Stability of Three-Dimensional Boundary Layers with Applications to the Flow due to a Rotating Disk," *Phil. Trans. R. Soc. London A*, Vol. 248, pp. 155–199.

Haight, C. H., Reed, T. D., and Morland, B. T., 1974, "Design Studies of Transonic and STOL Airfoils with Active Diffusion Control," Advanced Technology Center Report No. ATC-B-94300/4CR-24, Dallas, TX. (Also available from U.S. NTIS; Document Number AD-A011928/9.)

Harris, C. D., and Bartlett, D. W., 1972, "Wind-Tunnel Investigation of Effects of Underwing Leading Edge Vortex Generators on a Supercritical-Wing Research Airplane Configuration," NASA TMX-2471, Washington, D.C.

Harvey, J. K., and Perry, F. J., 1971, "Flowfield Produced by Trailing Vortices in the Vicinity of the Ground," *AIAA J.*, Vol. 9, pp. 1659–1660.

Harvey, W. D., 1986, "Low-Reynolds Number Aerodynamics Research at NASA Langley Research Center," *Proc. Int. Conf. on Aerodynamics at Low Reynolds Numbers*, Vol. II, Royal Aeronautical Society, London, England, pp. 19.1–19.49.

Harvey, W. D., Bushnell, D. M., and Beckwith, I. E., 1969, "On the Fluctuating Properties of Turbulent Boundar Layers for Mach Numbers up to 9.0," NASA TND-5496, Washington, D.C.

Hayakawa, L., and Squire, L. C., 1982, "The Effect of the Upstream Boundary Layer State on the Shock Interaction at a Compression Corner," *J. Fluid Mech.*, Vol. 122, pp. 369–394.

Hazen, D. C., 1984, "Aeronautics Technology Possibilities for 2000: Report of a Workshop," Aeronautics and Space Engineering Board, Commission on Engineering and Technical Systems, U.S. National Research Council, Washington, D.C.

Hefner, J. N., and Sabo, F. E., eds., 1987, *Research in Natural Laminar Flow and Laminar Flow Control, Part 1*, NASA CP-2487, Washington, D.C.

Henry, J. R., Wood, C. C., and Wilbur, S. W., 1956, "Summary of Subsonic Diffuser Data," NACA RML-56F05, Washington, D.C.

Ho, C-M., 1986, "An Alternative Look at the Unsteady Separation Phenomenon," *Recent Advances in Aerodynamics*, eds. A. Krothappalli and C. A. Smith, Springer-Verlag, New York, pp. 165–178.

Ho, C-M., and Huang, L-S., 1982, "Subharmonics and Vortex Merging in Mixing Layers," *J. Fluid Mech.*, Vol. 119, pp. 443–473.

Ho, C-M., and Huerre, P., 1984, "Perturbed Free Shear Layers," *Ann. Rev. Fluid Mech.*, Vol. 16, pp. 365–424.

Hoffmann, J. A., 1981, "Effects of Free Stream Turbulence on Diffuser Performance," ASME JOURNAL OF FLUIDS ENGINEERING, Vol. 103, pp. 385–390.

Hoffmann, J. A., Kassir, S. M., and Larwood, S. M., 1988, "The Influence of Free Stream Turbulence on Turbulent Boundary Layers with Mild Adverse Pressure Gradients," NASA CR-184677, Washington, D.C.

Horstmann, K.-H., and Quast, A., 1981, "Widerstandsverminderung durch Blasturbulatoren," DFVLR Report No. FB-81-33, Braunschweig, West Germany.

Howard, F. G., and Goodman, W. L., 1985, "Axisymmetric Bluff-Body Drag Reduction Through Geometrical Modification," *J. Aircraft*, Vol. 22, pp. 516–522.

Howard, F. G., and Goodman, W. L., 1987, "Drag Reduction on a Bluff Body at Yaw Angles to 30 Degrees," *J. Spacecraft & Rockets*, Vol. 24, pp. 179–181.

Howard, F. G., Quass, B. F., Weinstein, L. M., and Bushnell, D. M., 1981, "Longitudinal Afterbody Grooves and Shoulder Radiusing for Low Speed Bluff Body Drag Reduction," ASME Paper No. 81-WA/FE-5, New York.

Howarth, L., 1938, "On the Solution of the Laminar Boundary Layer Equations," *Proc. R. Soc. Lond. Ser. A*, Vol. 164, pp. 547–579.

Hsiao, F.-B., Liu, C.-F., and Shyu, J.-Y., 1990, "Control of Wall-Separated Flow by Internal Acoustic Excitation," *AIAA J.*, Vol. 28, pp. 1440–1446.

Huang, L. S., Maestrello, L., and Bryant, T. D., 1987, "Separation Control Over an Airfoil at High Angles of Attack by Sound Emanating from the Surface," AIAA Paper No. 87-1261, New York.

Hunter, P. A., and Johnson, H. I., 1954, "A Flight Investigation of the Practical Problems Associated with Porous Leading-Edge Suction," NACA TN-3062, Washington, D.C.

Hurley, D. G., 1961, "The Use of Boundary Layer Control to Establish Free Streamline Flows," *Boundary Layer and Flow Control*, Vol. 1, ed. G. V. Lachmann, Pergamon Press, Oxford, England, pp. 295–341.

Huyer, S. A., Robinson, M. C., and Luttges, M. W., 1990, "Unsteady Aerodynamic Loading Produced by a Sinusoidally Oscillating Delta Wing," AIAA Paper No. 90-1536, New York.

Illingworth, C. R., 1954, "The Effect of Heat Transfer on the Separation of a Compressible Laminar Boundary Layer," *Quart. J. Mech. Appl. Math.*, Vol. 7, pp. 8–34.

Inger, G. R., and Siebersma, T., 1988, "Computational Simulation of Vortex Generator Effects on Transonic Shock/Boundary Layer Interaction," AIAA Paper No. 88-2590, New York.

Isomoto, K., and Honami, S., 1989, "The Effect of Inlet Turbulence Intensity on the Reattachment Process Over a Backward-Facing Step," ASME JORUNAL OF FLUIDS ENGINEERING, Vol. 111, pp. 87–92.

Johnson, W. S., Tennant, J. S., and Stamps, R. E., 1975, "Leading-Edge Rotating Cylinder for Boundary Layer Control on Lifting Surfaces," *J. Hydronautics*, Vol. 9, pp. 76–78.

Johnston, J., and Nishi, M., 1989, "Vortex Generator Jets—A Means for Passive and Active Control of Boundary Layer Separation," AIAA Paper No. 89-0564, New York.

Johnston, J., and Nishi, M., 1990, "Vortex Generator Jets—Means for Flow Separation Control," *AIAA J.*, Vol. 28, pp. 989–994.

Katz, Y., Nishri, B., and Wygnanski, I., 1989a, "The Delay of Turbulent Boundary Layer Separation by Oscillatory Active Control," AIAA Paper No. 89-0975, New York.

Katz, Y., Nishri, B., and Wygnanski, I., 1989b, "The Delay of Turbulent Boundary Layer Separation by Oscillatory Active Control," *Phys. of Fluids*, Vol. 1, pp. 179–181.

Kentfield, J. A. C., 1985a, "Drag Reduction of Controlled Separated Flows," AIAA Paper No. 85-1800, New York.

Kentfield, J. A. C., 1985b, "Short, Multi-Step, Afterbody Fairings," *J. Aircraft*, Vol. 21, pp. 351–352.

Kidd, J. A., Wikoff, D., and Cottrell, C. J., 1990, "Drag Reduction by Controlling Flow Separation Using Stepped Afterbodies," *J. Aircraft*, Vol. 27, pp. 564–566.

Kind, R. J., 1967, "A Proposed Method of Circulation Control," Ph.D. dissertation, Cambridge University, Cambridge, England.

Kirsch, J. W., 1974, "Drag Reduction of Trucks with S^3 Air Vane," *Second Symp. on Aerodynamics of Sports and Competition Automobiles*, AIAA Lecture Series, Vol. 16, New York, pp. 251–263.

Koga, D. J., Reisenthel, P., and Nagib, H. M., 1984, "Control of Separated Flowfields Using Forced Unsteadiness," Illinois Institute of Technology, Fluids & Heat Transfer Report No. R84-1, Chicago, IL.

Koval'nogov, S. A., Fomin, V. M., and Shapovalov, G. K., 1987, "Experimental Study of the Possibility of Passive Control of Shock-Boundary Layer Interactions," *Uchemye kZapiski TSAGI*, Vol. 18, pp. 112–116.

Krall, K. M., and Haight, C. H., 1972, "Wind Tunnel Tests of a Trapped Vortex-High Lift Airfoil," Advanced Technology Center Report No. ATC-B-94300/3TR-10, Dallas, TX. (Also available from U.S. NTIS; Document Number AD-762 077).

Kuethe, A. M., 1973, "Boundary Layer Control of Flow Separation and Heat Exchange," U.S. Patent No. 3,741,285.

Kukainis, J., 1969, "Effects of Three-Dimensional Boundary Layer Control Devices on a Quasi-Two-Dimensional Swept Wing at High Subsonic Speeds," Arnold Engineering Development Center, AEDC-TR-69-251, Arnold Air Force Base, TN.

Lachmann, G. V., 1961, *Boundary Layer and Flow Control*, Vols. 1 and 2, Pergamon Press, Oxford, England.

Lakshmanan, B., Tiwari, S. N., and Hussaini, M. Y., 1988, "Control of Supersonic Interaction Flow Fields Through Filleting and Sweep," AIAA Paper No. 88-3534, New York.

Lange, R. H., 1954, "Present Status of Information Relative to the Prediction of Shock-Induced Boundary Layer Separation," NACA TN-3065, Washington, D.C.

Lankford, J. L., 1960, "Investigation of the Flow Over an Axisymmetric Compression Surface at High Mach Numbers," U.S. Naval Ordnance Laboratory, Report No. 6866, Corona, CA.

Lankford, J. L., 1961, "The Effect of Heat Transfer on the Separation of Laminar Flow Over Axisymmetric Compression Surfaces. Preliminary Results at Mach No. 6.78," U.S. Naval Ordnance Laboratory, Report No. 7402, Corona, CA.

Lee, D. G., 1974, "Subsonic Force Characteristics of a Low Aspect Ratio Wing Incorporating a Spinning Cylinder," DTNSRDC Report No. ASED-329, Bethesda, MD. (Also available from U.S. NTIS; Document Number AD-AOO11135.)

Lee, M., and Ho, C.-M., 1989, "Vortex Dynamics of Delta Wings," *Frontiers in Experimental Fluid Mechanics*, ed. M. Gad-el-Hak, Springer-Verlag, *Lecture Notes in Engineering*, Vol. 46, Berlin, pp. 365–428.

Lee, M., and Ho, C.-M., 1990, "Lift Force of Delta Wings," *Appl. Mech. Rev.*, Vol. 43, pp. 209–221.

Lee, C. S., Tavella, D. A., Wood, N. J., and Roberts, L., 1986, "Flow Structure of Lateral Wing-Tip Blowing," AIAA Paper No. 86-1810, New York.

Lee, C. S., Tavella, D. A., Wood, N. J., and Roberts, L., 1989, "Flow Structure and Scaling Laws in Lateral Wing-Tip Blowing," *AIAA J.*, Vol. 27, pp. 1002–1007.

Liandrat, J., Aupoix, B., and Cousteix, T., 1986, "Calculation of Longitudinal Vortices Embedded in a Turbulent Boundary Layer," *Fifth Symposium on Turbulent Shear Flows*, Cornell University, Ithaca, NY, eds. F. Durst, B. E. Launder, F. W. Schmidt and J. H. Whitelaw, Springer-Verlag, NY, pp. 7.17–7.22.

Libby, P. A., 1954, "Method for Calculation of Compressible Laminar Boundary Layer with Axial Pressure Gradient and Heat Transfer," NACA TN-3157, Washington, D.C.

Liebeck, R. H., 1978, "Design of Subsonic Airfoils for High Lift," *J. Aircraft*, Vol. 15, pp. 547–561.

Lighthill, M. J., 1963, "Introduction—Boundary Layer Theory," *Laminar Boundary Layers*, ed. L. Rosenhead, Clarendon Press, Oxford, England, pp. 46–113.

Lighthill, M. J., 1973, "On the Weis-Fogh Mechanism of Lift Generation," *J. Fluid Mech.*, Vol. 60, pp. 1–17.

Lighthill, M. J., 1975, "Aerodynamic Aspects of Animal Flight," *Swimming and Flying in Nature*, Vol. 2, eds. T. Y. Wu, C. J. Brokaw and C. Brennen, Plenum, New York, pp. 423–491.

Lin, J. C., and Ash, R. L., 1986, "Wall Temperature Control of Low-Speed Body Drag," *J. Aircraft*, Vol. 23, pp. 93–94.

Lin, J. C., and Howard, F. G., 1989, "Turbulent Flow Separation Control Through Passive Techniques," AIAA Paper No. 89-0976, New York.

Lin, J. C., Howard, F. G., Bushnell, D. M., and Selby, G. V., 1990a, "Investigation of Several Passive and Active Methods for Turbulent Flow Separation Control," AIAA Paper No. 90-1598, New York.

Lin, J. C., Howard, F. G., and Selby, G. V., 1990b, "Control of Turbulent Separated Flow Over a Rearward-Facing Ramp Using Longitudinal Grooves," *J. Aircraft*, Vol. 27, pp. 283–285.

Lissaman, P. B. S., 1983, "Low-Reynolds-Number Airfoils," *Ann. Rev. Fluid Mech.*, Vol. 15, pp. 223–239.

Ludwig, G. R., 1964, "An Experimental Investigation of Laminar Separation from a Moving Wall," AIAA Paper No. 64-6, New York.

Luttges, M. W., 1989, "Accomplished Insect Fliers," in *Frontiers in Experimental Fluid Mechanics*, ed. M. Gad-el-Hak, Springer-Verlag: *Lecture Notes in Engineering*, Vol. 46, Berlin, pp. 429–456.

Luttges, M. W., Somps, C., Kliss, M., and Robinson, M., 1984, "Unsteady Separated Flows: Generation and Use by Insects," *Unsteady Separated Flows*, eds. M. S. Francis and M. W. Luttges, U.S. Air Force Academy, Colorado Springs, CO.

Mabey, D. G., 1988, "Design Features Which Influence Flow Separations on Aircraft," *Aero. J.*, Vol. 92, pp. 409–415.

Macha, J. M., Norton, D. J., and Young, J. C., 1972, "Surface Temperature Effect on Subsonic Stall," AIAA Paper No. 72-960, New York.

Maestrello, L., Badavi, F. F., and Noonan, K. W., 1988, "Control of the Boundary Layer Separation about an Airfoil by Active Surface Heating," AIAA Paper No. 88-3545-CP, New York.

Magarvey, R. H., and McLatchy, C. S., 1964, "The Disintegration of Vortex Rings," *Can. J. Phys.*, Vol. 42, pp. 684–689.

Magnus, G., 1852, "On the Deflection of a Projectile," *Abhandlung der Akademie der Wissenschaften*, Berlin, Germany.

Maltby, R. L., 1962, "Flow Visualization in Wind Tunnels Using Indicators," NATO Advisory Group for Aerospace Research and Development, AGARDograph No. 70.

Mangalam, S. M., Bar-Sever, A., Zaman, K. B. M. Q., and Harvey, W. D., 1986, "Transition and Separation Control on a Low-Reynolds Number Airfoil," *Proc. Int. Conf. on Aerodynamics at Low Reynolds Numbers*, Vol. I, Royal Aeronautical Society, London, England, pp. 10.1–10.19.

Marchman, J. F., Manor, D., and Plentovich, E. B., 1980, "Performance Improvement of Delta Wings at Subsonic Speeds Due to Vortex Flaps," AIAA Paper No. 80-1802, New York.

Maskell, E. C., 1955, "Flow Separation in Three Dimensions," Royal Aircraft Establishment RAE Report No. Aero.-2565, Farnborough, England.

Maxworthy, T., 1979, "Experiments on the Weis-Fogh Mechanism of Lift Generation by Insects in Hovering Flight. Part 1. Dynamics of the 'Fling'," *J. Fluid Mech.*, Vol. 93, pp. 47–63.

Maxworthy, T., 1981, "The Fluid Dynamics of Insect Flight," *Ann. Rev. Fluid Mech.*, Vol. 13, pp. 329–350.

McCroskey, W. J., 1977, "Some Current Research in Unsteady Fluid Dynamics," ASME JOURNAL OF FLUIDS ENGINEERING, Vol. 99, pp. 8–39.

McCroskey, W. J., 1982, "Unsteady Airfoils," *Ann. Rev. Fluid Mech.*, Vol. 14, pp. 285–311.

McCullough, G. B., 1955, "The Effect of Reynolds Number on the Stalling Characteristics and Pressure Distributions of Four Moderately Thin Airfoil Sections," NACA TN-3524, Washington, D.C.

McCullough, G. B., and Gault, D. E., 1951, "Examples of Three Representative Types of Airfoil-Section Stall at Low Speed," NACA TN-2502, Washington, D.C.

McInville, R. M., Hassan, H. A., and Goodman, W. L., 1985, "Mixing Layer Control for Tangential Slot Injection in Turbulent Flows," AIAA Paper No. 85-0541, New York.

McLachlan, B. G., 1989, "Study of a Circulation Control Airfoil with Leading/Trailing-Edge Blowing," *J. Aircraft*, Vol. 26, pp. 817–821.

McLean, J. D., and Herring, H. J., 1974, "Use of Multiple Discrete Wall Jets for Delaying Boundary Layer Separation," NASA CR-2389, Washington, D.C.

Mehta, R. D., 1985a, "Aerodynamics of Sports Balls," *Ann. Rev. Fluid Mech.*, Vol. 17, pp. 151–189.

Mehta, R. D., 1985b, "Effect of a Longitudinal Vortex on a Separated Turbulent Boundary Layer," AIAA Paper No. 85-0530, New York.

Mehta, R. D., 1988, "Vortex/Separated Boundary-Layer Interactions at Transonic Mach Numbers," *AIAA J.*, Vol. 26, pp. 15–26.

Miau, J. J., Chen, M. H., and Chow, J. H., 1988, "Flow Structures of a Vertically Oscillating Plate Immersed in a Flat-Plate Turbulent Boundary Layer," *Proc. Eleventh Symposium on Turbulence*, Paper No. A28, University of Missouri, Rolla, MO.

Migay, V. K., 1960a, "Diffuser with Transverse Fins (English translation from Russian)," *Energomashinostroenie*, No. 4, p. 31.

Migay, V. K., 1960b, "On Improving the Effectiveness of Diffuser Flows with Separation (English translation from Russian," *Mekhanika i Mashinostroyeniye*, No. 4, pp. 171–173.

Migay, V. K., 1961, "Increasing the Efficiency of Diffusers by Fitting Transverse Fins (English translation from Russian)," *Teploenergetika*, No. 4, pp. 41–43.

Migay, V. K., 1962a, "The Efficiency of a Cross-Ribbed Curvilinear Diffuser (English translation from Russian)," *Energomashinostroenie*, No. 1, pp. 45–46.

Migay, V. K., 1962b, "The Aerodynamic Effectiveness of a Discontinous Surface (English translation from Russian)," *Inzhenerno-Fizicheskiy Zhurnal*, Vol. 5, pp. 20–24.

Migay, V. K., 1962c, "Investigating Finned Diffusers: Effects of Geometry on Effectiveness of Finned Body Diffusers (English translation from Russian)," *Teploenergetika*, No. 10, pp. 55–59.

Modi, V. J., Fernando, M., and Yokomizo, T., 1990, "Drag Reduction of Bluff Bodies Through Moving Surface Boundary Layer Control," AIAA Paper No. 90-0298, New York.

Modi, V. J., Mokhtarian, F., Fernando, M., and Yokomizo, T., 1989, "Moving Surface Boundary Layer Control as Applied to 2-D Airfoils," AIAA Paper No. 89-0296, New York.

Modi, V. J., Sun, J. L. C., Akutsu, T., Lake, P., McMillan, K., Swinton, P. G., and Mullins, D., 1980, "Moving Surface Boundary Layer Control for Aircraft Operations at High Incidence," AIAA Paper No. 80-1621, New York.

Modi, V. J., Sun, J. L. C., Akutsu, T., Lake, P., McMillian, K., Swinton, P. G., and Mullins, D., 1981, "Moving Surface Boundary Layer Control for Aircraft Operation at High Incidence," *J. Aircraft*, Vol. 18, pp. 963–968.

Mokhtarian, F., and Modi, V. J., 1988, "Fluid Dynamics of Airfoils with Moving Surface Boundary Layer Control," *J. Aircraft*, Vol. 25, pp. 163–169.

Mokhtarian, F., Modi, V. J., and Yokomizo, T., 1988a, "Effect of Moving Surfaces on the Airfoil Boundary Layer Control," AIAA Paper No. 88-4337-CP, New York.

Mokhtarian, F., Modi, V. J., and Yokomizo, T., 1988b, "Rotating Air Scopp as Airfoil Boundary Layer Control," *J. Aircraft*, Vol. 25, pp. 973–975.

Moore, F. K., 1958, "On the Separation of the Unsteady Laminar Boundary Layer," *Boundary-Layer Research*, ed. H. Görtler, Springer-Verlag, Berlin, pp. 296–310.

Morduchow, M., and Grape, R. G., 1955, "Separation, Stability, and Other Properties of Compressible Laminar Boundary Layer with Pressure Gradient and Heat Transfer," NACA TN-3296, Washington, D.C.

Morkovin, M. V., 1984, "Bypass Transition to Turbulence and Research Desiderata," *Transition in Turbines Symposium*, NASA CP-2386, Washington, D.C.

Mueller, T. J., and Burns, T. F., 1982, "Experimental Studies of the Eppler 61 Airfoil at Low Reynolds Numbers," AIAA Paper No. 82-0345, New York.

Muirhead, V. U., and Saltzman, E. G., 1979, "Reduction of Aerodynamic Drag and Fuel Consumption for Tractor-Trailer Vehicles," *J. Energy*, Vol. 3, pp. 279–284.

Mullin, T., Greated, C. A., and Grant, I., 1980, "Pulsating Flow Over a Step," *Phys. of Fluids*, Vol. 23, pp. 669–674.

Nagamatsu, H. T., Dyer, R., and Ficarra, R. V., 1985, "Supercritical Airfoil Drag Reduction by Passive Shock Wave/Boundary Layer Control in the Mach Number Range .75 to .9," AIAA Paper No. 85-0207, New York.

Nagamatsu, H. T., Trilling, T. W., and Bossard, J. A., 1987, "Passive Drag Reduction on a Complete NACA 0012 Airfoil at Transonic Mach Numbers," AIAA Paper No. 87-1263, New York.

Nayfeh, A. H., Ragab, S. A., and Al-Maaitah, A., 1986, "Effects of Roughness on the Stability of Boundary Layers," AIAA Paper No. 86-1044, New York.

Nelson, C. F., Koga, D. J., and Eaton, J. K., 1987, "Control of the Unsteady Separated Flow Behind an Oscillating Two-Dimensional Flap," AIAA Paper No. 89-1027, New York.

Nelson, C. F., Koga, D. J., and Eaton, J. K., 1990, "Unsteady, Separated Flow Behind an Oscillating, Two-Dimensional Spoiler," *AIAA J.*, Vol. 28, pp. 845–852.

Neuburger, D., and Wygnanski, I., 1988, "The Use of a Vibrating Ribbon to Delay Separation on Two-Dimensional Airfoils: Some Preliminary Observations," *Proc. Workshop II on Unsteady Separated Flow*, ed. J. M. Walker, pp. 333–341, Frank J. Seiler Research Laboratory, U.S. Air Force Systems Command FJSRL-TR-88-0004, Colorado Springs, CO.

Nickerson, J. D., 1986, "A Study of Vortex Generators at Low Reynolds Numbers," AIAA Paper No. 86-0155, New York.

Norman, J. R., and Fraser, F. C., 1937, *Giant Fishes, Whales and Dolphins*, Putnam, London, England.

Novak, C. J., and Cornelius, K. C., and Roads, R. K., 1987, "Experimental Investigations of the Circular Wall Jet on a Circulation Control Airfoil," AIAA Paper No. 87-0155, New York.

Ogorodnikov, D. A., Grin, V. T., and Zakharov, N. N., 1972, "Boundary Layer Control of Hypersonic Air Inlets," NASA TTF-13927, Washington, D.C.

Oyler, T. E., and Palmer, W. E., 1972, "Exploratory Investigation of Pulse Blowing for Boundary Layer Control," Columbus Aircraft Division, North American Rockwell Corp., Report No. NR 72H-12, Columbus, OH. (Also available from U.S. NTIS; Document Number AD-742 085.)

Panton, R. L., 1990, "Effects of a Contoured Apex on Vortex Breakdown," *J. Aircraft*, Vol. 27, pp. 285–288.

Papell, S. S., 1984, "Vortex Generating Flow Passage Design for Increased Film-Cooling Effectiveness and Surface Coverage," NASA TM-83617, Washington, D.C.

Pearcey, H. H., 1961, "Shock Induced Separation and Its Prevention by Design and Boundary Layer Control," *Boundary Layer and Flow Control, Its Principle and Applications*, Vol. 2, ed. G. V. Lachmann, Pergamon Press, Oxford, England, pp. 1166–1344.

Pfenninger, W., and Vemuru, C. S., 1990, "Design of Low Reynolds Number Airfoils," *J. Aircraft*, Vol. 27, pp. 204–210.

Pinebrook, W. E., and Dalton, C., 1983, "Drag Minimization on a Body of Revolution Through Evolution," *Computer Methods in Appl. Mech. and Engineering*, Vol. 39, pp. 179–197.

Poisson-Quinton, Ph., 1950, "On the Mechanism and the Application of the Control of the Boundary Layer of Airplanes," *International Colloquium on Mechanics*, Vol. II, Poitiers, France.

Prandtl, L., 1904, "Über Flüssigkeitsbewegung bei sehr kleiner Reibung," *Proc. Third Int. Math. Congr.*, Heidelberg, Germany, pp. 484–491.

Prandtl, L., 1925, "Magnuseffeckt und Windkraftschiff," *Naturwissenschaften*, Vol. 13, pp. 93–108.

Prandtl, L., 1935, "The Mechanics of Viscous Fluids," *Aerodynamic Theory*, Vol. III, ed. W. F. Durand, Springer, Berlin, pp. 34–208.

Purohit, S. C., 1987, "Effect of Vectored Suction on a Shock-Induced Separation," *AIAA J.*, Vol. 25, pp. 759–760.

Raghunathan, S., 1985, "Passive Control of Shock-Boundary Layer Interaction," *Prog. Aerospace Sci.*, Vol. 25, pp. 271–296.

Rao, D. M., 1979, "Leading-Edge Vortex Flap Experiments on a 74-Deg. Delta Wing," NASA CR-159161, Washington, D.C.

Rao, D. M., and Kariya, T. T., 1988, "Boundary-Layer Submerged Vortex Generators for Separation Control—An Exploratory Study," AIAA Paper No. 88-3546-CP, New York.

Reed, H. L., and Saric, W. S., 1987, "Stability and Transition of Three-Dimensional Flows," *Proc. 10th U.S. Nat. Cong. Applied Mech.*, ed. J. P. Lamb, ASME, New York, pp. 457–468.

Reisenthel, P. H., Nagib, H. M., and Koga, D. J., 1985, "Control of Separated Flows Using Forced Unsteadiness," AIAA Paper No. 85-0556, New York.

Reshotko, E., 1976, "Boundary-Layer Stability and Transition," *Ann. Rev. Fluid Mech.*, Vol. 8, pp. 311–349.

Reynolds, W. C., and Carr, L. W., 1985, "Review of Unsteady, Driven, Separated Flows," AIAA Paper No. 85-0527, New York.

Reynolds, W. C., Eaton, J. K., Johnston, J. P., Hesselink, L., Powell, D. J., Roberts, L., and Kroo, E., 1988, "Flow Control for Unsteady and Separated Flows and Turbulent Mixing," AFOSR-TR-89-0232, Washington, D.C. (Also available from U.S. NTIS; Document Number AD-A205989.)

Ringleb, E. O., 1961, "Separation Control by Trapped Vortices," *Boundary Layer and Flow Control*, Vol. 1, ed. G. V. Lachmann, Pergamon Press, Oxford, England, pp. 265–294.

Roos, F. W., and Kegelman, J. T., 1986, "Control of Coherent Structures in Reattaching Laminar and Turbulent Shear Layers," *AIAA J.*, Vol. 24, pp. 1956–1963.

Rott, N., 1956, "Unsteady Viscous Flow in the Vicinity of a Stagnation Point," *Q. Appl. Math.*, Vol. 13, pp. 444–451.

Sajben, M., Chen, C. P., and Kroutil, J. C., 1976, "A New, Passive Boundary Layer Control Device," AIAA Paper No. 76-700, New York.

Saric, W. S., and Reed, H. L., 1989, "Stability of Three-Dimensional Boundary Layers," *Ann. Rev. Fluid Mech.*, Vol. 21, pp. 235–284.

Saripalli, K. R., and Simpson, R. L., 1980, "Investigation of Blown Boundary Layers with an Improved Wall Jet System," NASA CR-3340, Washington, D.C.

Sasaki, K., and Kiya, M., 1985, "Effect of Free-Stream Turbulence on Turbulent Properties of a Separation-Reattachment Flow," *Bulletin of JSME*, Vol. 28, pp. 610–616.

Savu, G., and Trifu, O., 1984, "Porous Airfoils in Transonic Flow," *AIAA J.*, Vol. 22, pp. 989–991.

Schlichting, H., 1959, "Einige neuere Ergebnisse über Grenzschichtbeein flussung," *Proc. First Int. Congr. Aero. Sci.*, Madrid, Spain, *Adv. in Aero. Sci.*, Vol. 2, eds. Th. von Karman et al., Pergamon Press, London, England, pp. 563–586.

Schlichting, H., 1979, *Boundary-Layer Theory*, Seventh Edition, McGraw-Hill, New York.

Schlichting, H., and Pechau, W., 1959, "Auftriebserhöhung von Tragflügeln durch kontinuierlich verteilte Absaugung," *ZFW*, Vol. 7, pp. 113–119.

Schneider, P. E. M., 1980, "Sekundärwirbelbildung bei Ringwirbeln und in Freistrahlen," *Z. Flugwiss.*, Vol. 4, pp. 307–318.

Schofield, W. H., 1985, "Turbulent Boundary Layer Development in an Adverse Pressure Gradient After an Interaction with a Normal Shock Wave," *J. Fluid Mech.*, Vol. 154, pp. 43–62.

Schubauer, G. B., and Skramstad, H. K., 1948, "Laminar Boundary-Layer Oscillations and Transition on a Flat Plate," NACA Report No. 909, Washington, D.C.

Schubauer, G. B., and Spangenberg, W. G., 1960, "Forced Mixing in Boundary Layers," *J. Fluid Mech.*, Vol. 8, pp. 10–32.

Sears, W. R., 1956, "Some Recent Developments in Airfoil Theory," *J. Aeronaut. Sci.*, Vol. 23, pp. 490–499.

Sears, W. R., and Telionis, D. P., 1972a, "Unsteady Boundary-Layer Separation," *Recent Research on Unsteady Boundary Layers*, ed. E. A. Eichelbrenner, Vol. 1, Presses de l'Universite Laval, Quebec, Canada, pp. 404–442.

Sears, W. R., and Telionis, D. P., 1972b, "Two Dimensional Laminar Boundary Layer Separation for Unsteady Flow or Flow Past Moving Walls, Considering Singularity due to Bifurcating Wake Bubble," *Recent Research on Unsteady Boundary Layers*, ed. E. A. Eichelbrenner, Vol. 1, Presses de l'Universite Laval, Quebec, Canada, pp. 443–447.

Sears, W. R., and Telionis, D. P., 1975, "Boundary-Layer Separation in Unsteady Flow," *J. Appl. Math.*, Vol. 28, pp. 215–235.

Selby, G. V., and Miandoab, F. H., 1990, "Effect of Surface Grooves on Base Pressure for a Blunt Trailing-Edge Airfoil," *AIAA J.*, Vol. 28, pp. 1133–1135.

Shiloh, K., Shivaprasad, B. G., and Simpson, R. L., 1981, "The Structure of a Separating Turbulent Boundary Layer. Part 3: Transverse Velocity Measurements," *J. Fluid Mech.*, Vol. 113, pp. 75–90.

Sigurdson, L. W., and Roshko, A., 1985, "Controlled Unsteady Excitation of a Reattaching Flow," AIAA Paper No. 85-0552, New York.

Silhanek, V., 1969, "On Aircraft Longitudinal Motion after Boundary Layer Control System Failure During Take-off and Landing," Aeronautical Research and Test Institute, Summary Report No. Z-13, Prague, Czechoslovakia.

Simpson, R. L., and Shivaprasad, B. G., 1983, "The Structure of a Separating Turbulent Boundary Layer. Part 5: Frequency Effects on Periodic Unsteady Freestream Flows," *J. Fluid Mech.*, Vol. 131, pp. 319–339.

Simpson, R. L., Chew, Y.-T., and Shivaprasad, B. G., 1981a, "The Structure of a Separating Turbulent Boundary Layer. Part 1: Mean Flow and Reynolds Stresses," *J. Fluid Mech.*, Vol. 113, pp. 23–51.

Simpson, R. L., and Chew, Y.-T., and Shivaprasad, B. G., 1981b, "The Structure of a Separating Turbulent Boundary Layer. Part 2: Higher-Order Turbulent Results," *J. Fluid Mech.*, Vol. 113, pp. 53–73.

Simpson, R. L., Shivaprasad, B. G., and Chew, Y.-T., 1983, "The Structure of a Separating Turbulent Boundary Layer. Part 4: Effects of Periodic Freestream Unsteadiness," *J. Fluid Mech.*, Vol. 127, pp. 219–261.

Smith, A. M. O., 1974, "High Lift Aerodynamics, AIAA Paper No. 74-939, New York.

Smith, A. M. O., 1977, "Stratford's Turbulent Separation Criterion for Axially-Symmetric Flows," *J. Applied Math. and Physics*, Vol. 28, pp. 929–939.

Smith, A. M. O., and Kaups, K., 1968, Aerodynamics of Surface Roughness and Imperfections," Society of Automotive Engineers Paper No. SAE-680198, New York.

Smith, A. M. O., and Thelander, J. A., 1973, "The Power Profile—A New Type of Airfoil," McDonnell Douglas Corporation, Report No. MDC-J6236, Long Beach, CA. (Also available from U.S. NTIS; Document Number AD-773 655/6.)

Smith, A. M. O., Stokes, T. R., Jr., and Lee, R. S., 1981, "Optimum Tail Shapes for Bodies of Revolution," *J. Hydronautics*, Vol. 15, pp. 67–73.

Soderman, P. T., 1972, "Aerodynamic Effects of Leading Edge Separation on a Two-Dimensional Airfoil," NASA TMX-2643, Washington, D.C.

Sovran, G., Morel, T., and Mason, W. T., Jr., 1978, *Aerodynamic Drag Mechanisms of Bluff Bodies and Road Vehicles*, Plenum Press, New York.

Spaid, F. W., 1972, "Cooled Supersonic Turbulent Boundary Layer Separated by a Forward Facing Step," *AIAA J.*, Vol. 19, pp. 1117–1119.

Stanewsky, E., and Krogmann, P., 1985, "Transonic Drag Rise and Drag Reduction by Active/Passive Boundary Layer Control," *Aircraft Drag Prediction and Reduction*, AGARD R-723, pp. 11-1 to 11-41, Rhode-Saint-Génèse, Belgium.

Staniforth, R., 1958, "Some Tests on Cascades of Compressor Blades Fitted with Vortex Generators," National Gas Turbines Establishment, NGTE Memorandum No. M.314, Farnborough, England. (Also Aeronautical Research Council, CP-487, London, England.)

Stratford, B. S., 1959a, "The Prediction of Separation of the Turbulent Boundary Layer," *J. Fluid Mech.*, Vol. 5, pp. 1–16.

Stratford, B. S., 1959b, "An Experimental Flow with Zero Skin Friction Throughout its Region of Pressure Rise," *J. Fluid Mech.*, Vol. 5, pp. 17–35.

Stull, F. D., and Velkoff, H. R., 1975, "Flow Regimes in Two-Dimensional Ribbed Diffusers," ASME JOURNAL OF FLUIDS ENGINEERING, Vol. 97, pp. 87–96.

Swanson, W. M., 1961, "The Magnus Effect: A Summary of Investigations to Date," ASME *Journal of Basic Engineering*, Vol. 83, pp. 461–470.

Szodruch, J., and Schneider, H., 1989, "High Lift Aerodynamics for Transport Aircraft by Interactive Experimental and Theoretical Tool Development," AIAA Paper No. 89-0267, New York.

Tani, I., 1969, "Boundary-Layer Transition," *Ann. Rev. Fluid Mech.*, Vol. 1, pp. 169–196.

Tavella, D. A., Lee, C. S., and Wood, N. J., 1986a, "Influence of Wing Tip Configuration on Lateral Blowing Efficiency," AIAA Paper No. 86-0475, New York.

Tavella, D. A., Wood, N. J., Lee, C. S., and Roberts, L., 1986b, "Two Blowing Concepts for Roll and Lateral Control of Aircraft," Department of Aeronautics and Astronautics, Stanford University, Report No. TR-75, Stanford, CA.

Tavella, D. A., Wood, N. J., Lee, C. S., and Roberts, L., 1988, "Lift Modulation with Lateral Wing-Tip Blowing," *J. Aircraft*, Vol. 25, pp. 311–316.

Taylor, G. I., 1923, "Stability of a Viscous Liquid Contained Between Two Rotating Cylinders," *Phil. Trans. R. Soc. London A*, Vol. 223, pp. 289–343.

Taylor, H. D., 1948a, "Application of Vortex Generator Mixing Principles to Diffusers," Research Department, United Aircraft Corporation, Concluding Report No. R-15064-5, East Hartford, CN.

Taylor, H. D., 1948b, "Design Criteria for and Applications of the Vortex Generator Mixing Principle," Research Department, United Aircraft Corporation, Report No. M-15038-1, East Hartford, CN.

Telionis, D. P., 1979, "Review—Unsteady Boundary Layers, Separated and Attached, ASME JOURNAL OF FLUIDS ENGINEERING, Vol. 101, pp. 29–43.

Telionis, D. P., and Werle, M. J., 1973, "Boundary-Layer Separation from Downstream Moving Boundaries," ASME *Journal of Applied Mechanics*, Vol. 40, pp. 369–374.

Tennant, J. S., 1973, "A Subsonic Diffuser with Moving Walls for Boundary Layer Control," *AIAA J.*, Vol. 11, pp. 240–242.

Tennant, J. S., Johnson, W. S., Keanton, D. D., and Krothapalli, A., 1975, "The Application of Moving Wall Boundary Layer Control to Submarine Control Surfaces," University of Tennessee, Report No. MAE-75-01210-1, Knoxville, TN. (Also available from U.S. NTIS; Document Number AD-AO23536.)

Tobak, M., and Peake, D. J., 1982, "Topology of Three-Dimensional Separated Flows," *Ann. Rev. Fluid Mech.*, Vol. 14, pp. 61–85.

Truckenbrodt, E., 1956, "Ein einfaches Näherungsverfahren zum Berechnen der laminaren Reibungsschicht mit Absaugung," *Forschg. Ing.-Wes.*, Vol. 22, pp. 147–157.

Tsahalis, D. Th., and Telionis, D. P., 1974, "Oscillating Laminar Boundary Layers and Unsteady Separation," *AIAA J.*, Vol. 12, pp. 1469–1476.

Vakili, A. D., 1990, "Review of Vortical Flow Utilization," AIAA Paper No. 90-1429, New York.

Vakili, A. D., Wu, J. M., Bhat, M. K., 1988, "High Angle of Attack Aerodynamics of Excitation of the Locked Leeside Vortex," Society of Automotive Engineers Paper No. SAE-88-1424, New York.

Vakili, A. D., Wu, J. M., Liver, P., and Bhat, M. K., 1985, "Flow Control in a Diffusing S-Duct," AIAA Paper No. 85-0524, New York.

Van Ingen, J. L., and Boermans, L. M. M., 1986, "Aerodynamics at Low Reynolds Numbers: A Review of Theoretical and Experimental Research at Delft University of Technology," *Proc. Int. Conf. on Aerodynamics at Low Reynolds Numbers*, Vol. I, Royal Aeronautical Society, London, England, pp. 1.1-1.40.

Vidal, R. J., 1959, "Research on Rotating Stall in Axial-Flow Compressors: Part III—Experiments on Laminar Separation from a Moving Wall," Wright Air Development Center Technical Report No. 59-75, Wright-Patterson Air Force Base, OH.

Viets, H., 1980, "Coherent Structures in Time Dependent Shear Flows," in *Turbulent Boundary Layers*, AGARD/NATO CPP-271, Paper No. 5, Nevilly Sur Seine, France.

Viets, H., Ball, M., and Bougine, D., 1981a, "Performance of Forced Unsteady Diffusers," AIAA Paper No. 81-0154, New York.

Viets, H., Palmer, G. M., and Bethke, R. J., 1984, "Potential Applications of Forced Unsteady Flows," *Unsteady Separated Flows*, eds. M. S. Francis and M. W. Luttges, U.S. Air Force Academy, Colorado Springs, CO, pp. 21–27.

Viets, H., Piatt, M., and Ball, M., 1979, "Unsteady Wing Boundary Layer Energization," AIAA Paper No. 79-1631, New York.

Viets, H., Piatt, M., and Ball, M., 1981b, "Forced Vortex Near a Wall," AIAA Paper No. 81-0256, New York.

Viets, H., Piatt, M., and Ball, M., 1981c, "Boundary Layer Control by Unsteady Vortex Generation," *J. Wind Eng. & Industrial Aerodynamics*, Vol. 7, pp. 135–144.

Vijgen, P. M. H. W., van Dam, C. P., Holmes, B. J., and Howard, F. G., 1989, "Wind-Tunnel Investigations of Wings with Serrated Sharp Trailing Edges," *Low Reynolds Number Aerodynamics*, ed. T. J. Mueller, Springer-Verlag: Lecture Notes in Engineering, Vol. 54, Berlin, pp. 295–313.

Viswanath, P. R., 1988, "Shockwave-Turbulent Boundary Layer Interaction and Its Control: A Survey of Recent Developments," *Sādhanā*, Vol. 12, pp. 45–104.

Waggoner, E. G., and Allison, D. O., 1987, "EA-6B High Lift Wing Modifications," AIAA Paper No. 87-2360-CP, New York.

Walker, J. D. A., 1978, "The Boundary Layer due to Rectilinear Vortex," *Proc. R. Soc. Lond. Ser. A*, Vol. 359, pp. 167–188.

Wallis, R. A., Stuart, C. M., 1958, "On the Control of Shock Induced Boundary Layer Separation with Discrete Jets," Aeronautical Research Council, Current Paper No. 494, London, England.

Weiberg, J. A., Giulianettij, D., Gambucci, B., and Innis, R. C., 1973, "Takeoff and Landing Performance and Noise Characteristics of a Deflected STOL Airplane with Interconnected Propellers and Rotating Cylinder Flaps," NASA TM X-62,320, Washington, D.C.

Weis-Fogh, T., 1973, "Quick Estimates of Flight Fitness in Hovering Animals, Including Novel Mechanisms for Lift Production," *J. Exp. Biol.*, Vol. 59, pp. 169–230.

Werle, M. J., Paterson, R. W., and Presz, W. M., Jr., 1987, "Trailing-Edge Separation/Stall Alleviation, *AIAA J.*, Vol. 25, pp. 624–626.

Wheeler, G. O., 1984, "Means for Maintaining Attached Flow of a Flow Medium," U.S. Patent No. 4,455,045.

Whitehead, A. H., and Bertram, M. H., 1971, "Alleviation of Vortex-Induced Heating to the Lee Side of Slender Wings in Hypersonic Flow," *AIAA J.*, Vol. 9, pp. 1870–1872.

Williams, D. R., and Amato, C. W., 1989, "Unsteady Pulsing of Cylinder Wakes," *Frontiers in Experimental Fluid Mechanics*, ed. M. Gad-el-Hak, Springer-Verlag, *Lecture Notes in Engineering*, Vol. 46, New York, pp. 337–364.

Williams, D. R., and Papazian, H., 1990, "Control of Asymmetric Vortices Around a Cone-Cylinder Geometry with Unsteady Based Bleed," submitted to *AIAA J.*

Williams, J. C., 1985, "Singularities in Solutions of the Three-Dimensional Laminar-Boundary-Layer Equations," *J. Fluid Mech.*, Vol. 160, pp. 257–279.

Williams, J. C., III, and Johnson, W. D., 1974a, "Semisimilar Solutions to Unsteady Boundary-Layer Flows Including Separation," *AIAA J.*, Vol. 12, pp. 1388–1393.

Williams, J. C., III, and Johnson, W. D., 1974b, "Note on Unsteady Boundary-Layer Separation," *AIAA J.*, Vol. 12, pp. 1427–1429.

Williams, T. I., 1987, *The History of Invention*, Facts on File Publications, New York.

Wimpenny, J. C., 1970, "Vortex Generators," U.S. Patent No. 3,525486.

Wood, C. J., 1961, "A Study of Hypersonic Separated Flow," Ph.D. thesis, University of London, England.

Wood, N. J., and Nielsen, J. N., 1985, "Circulation Control Airfoils—Past, Present, Future," AIAA Paper No. 85-0204, New York.

Wood, N. J., and Roberts, L., 1986, "Experimental Results of the Control of a Vortical Flow by Tangential Blowing," Stanford University Report No. JIAA TR-71, Stanford, CA.

Wood, N. J., and Roberts, L., 1988, "Control of Vortical Lift on Delta Wings by Tangential Leading-Edge Blowing," *J. Aircraft*, Vol. 25, pp. 236–243.

Wood, N. J., Roberts, L., and Celik, Z., 1990, "Control of Asymmetric Vortical Flows Over Delta Wings at High Angles of Attack," *J. Aircraft*, Vol. 27, pp. 429–435.

Wortmann, A., 1987, "Alleviation of Fuselage from Drag Using Vortex Flows," Department of Energy Report No. DOE/CE/15277-T1, Washington, D.C.

Wu, J. M., Vakili, A. D., and Chen, Z. L., 1983, "Investigation on the Effects of Discrete Wingtip Jets," AIAA Paper No. 83-0546, New York.

Wu, J. M., Vakili, A. D., and Gilliam, F. T., 1984, "Aerodynamic Interactions of Wingtip Flow with Discrete Wingtip Jets," AIAA Paper No. 84-2206, New York.

Yang, T., Ntone, F., Jiang, T., and Pitts, D. R., 1984, "An Investigation of High Performance, Short Thrust Augmenting Ejectors," ASME Paper No. 84-WA/FE-10, New York.

Young, A. D., 1953, "Boundary Layers," *Modern Developments in Fluid Dynamics: High Speed Flow*, Vol. 1, ed. L. Howarth, Clarendon Press, Oxford, England, pp. 375–475.

Zaman, K. B. M. Q., and McKinzie, D. J., 1989, "Control of 'Laminar Separation' Over Airfoils by Acoustic Excitation," NASA TM-101379, Washington, D.C. (Also AIAA Paper No. 89-0565, New York.)

Zaman, K. B. M. Q., Bar-Sever, A., and Mangalam, S. M., 1987, "Effect of Acoustic Excitation on the Flow Over a Low-Re Airfoil," *J. Fluid Mech.*, Vol. 182, pp. 127–148.

Zang, T. A., Hussaini, M. Y., and Bushnell, D. M., 1984, "Numerical Computations of Turbulence Amplification in Shock Wave Interactions," *AIAA J.*, Vol. 22, pp. 13–22.

Zhang, F., and Sheng, C., 1987, "A Prediction Method for Optimum Velocity Ratio of Air Jet Vortex Generator," *J. Aerospace Power*, Vol. 2, pp. 55–60, 92, 93.

Zhuk, V. I., and Ryzhov, O. S., 1980, "Formation of Recirculation Zones in the Boundary Layer on a Moving Surface," *Fluid Dynamics*, Vol. 15, pp. 637–644.

About the Authors

Mohamed Gad-el-Hak received his B.Sc. (summa cum laude) in mechanical engineering from Ain Shams University in 1966 and his Ph.D. in fluid mechanics from the Johns Hopkins University in 1973. He has since taught and conducted research at the University of Virginia and the University of Southern California and has lectured extensively at seminars in the United States and overseas. Dr. Gad-el-Hak is currently Professor of Aerospace and Mechanical Engineering at the University of Notre Dame. Prior to that, he was a Senior Research Scientist and Program Manager at Flow Research Company in Seattle, Washington, where he has managed a variety of aerodynamic and hydrodynamic research projects. Dr. Gad-el-Hak has published over 150 articles in the basic and applied research areas of isotropic turbulence, boundary layer flows, stratified flows, compliant coatings, unsteady aerodynamics, biological flows, non-Newtonian fluids, and flow control. He is the editor of

two volumes in Springer-Verlag's *Lecture Notes in Engineering* entitled *Frontiers in Experimental Fluid Mechanics*, and *Advances in Fluid Mechanics Measurements*. Professor Gad-el-Hak is a member of the American Chemical Society, an associate fellow of the American Institute of Aeronautics and Astronautics, a life member of the American Physical Society, and a member of The American Society of Mechanical Engineers. He is currently serving as associate editor for both the *AIAA Journal* and the *Applied Mechanics Reviews*, as well as a contributing editor for Springer-Verlag's *Lecture Notes in Engineering*.

Dennis M. Bushnell received his B.Sc. in mechanical engineering (with highest honors, Distinction, University Scholar) from the University of Connecticut in 1963 and an M.S. in mechanical engineering from the University of Virginia in 1967. Since 1963, he has conducted and managed viscous flow research at the Langley Research Center of the National Aeronautics and Space Administration, holding the positions of Aerospace Engineer, Section Head, Branch Head and, currently, Associate Chief of the Fluid Mechanics Division. Mr. Bushnell has published and presented over 150 papers in the areas of hypersonic two-phase flows, interference heat transfer, turbulence modeling, transition, laminar flow control, turbulent drag reduction and turbulence control, scramjet mixing enhancement, and vortex and separation control. Mr. Bushnell has served on over 25 technical committees and has presented over 80 invited lectures in national and international meetings. He is the editor of *Viscous Drag Reduction in Boundary Layers*, in the AIAA's *Progress in Astronautics and Aeronautics* series and is currently serving as an associate technical editor for the ASME *Journal of Fluids Engineering*. Mr. Bushnell is a fellow of the American Institute of Aeronautics and Astronautics and a member of THE AMERICAN SOCIETY OF MECHANICAL ENGINEERS. He is the recipient of the AIAA's Lawrence Sperry Award and the NASA's Medal for Outstanding Scientific Achievement.

Fine Structure of Vortex Sheet Rollup by Viscous and Inviscid Simulation

G. Tryggvason
Department of Mechanical Engineering and Applied Mechanics.

W. J. A. Dahm
Department of Aerospace Engineering.

K. Sbeih
Department of Mechanical Engineering and Applied Mechanics.

The University of Michigan, Ann Arbor, MI 48109-2125

Numerical simulations of the large amplitude stage of the Kelvin-Helmholtz instability of a relatively thin vorticity layer are discussed. At high Reynolds number, the effect of viscosity is commonly neglected and the thin layer is modeled as a vortex sheet separating one potential flow region from another. Since such vortex sheets are susceptible to a short wavelength instability, as well as singularity formation, it is necessary to provide an artificial "regularization" for long time calculations. We examine the effect of this regularization by comparing vortex sheet calculations with fully viscous finite difference calculations of the Navier-Stokes equations. In particular, we compare the limiting behavior of the viscous simulations for high Reynolds numbers and small initial layer thickness with the limiting solution for the roll-up of an inviscid vortex sheet. Results show that the inviscid regularization effectively reproduces many of the features associated with the thickness of viscous vorticity layers with increasing Reynolds number, though the simplified dynamics of the inviscid model allows it to accurately simulate only the large scale features of the vorticity field. Our results also show that the limiting solution of zero regularization for the inviscid model and high Reynolds number and zero initial thickness for the viscous simulations appear to be the same.

Introduction

In several classes of fluid dynamics problems, it is natural to focus on the motion of relatively sharp interfaces separating different flow domains. Examples of such interfaces include the boundaries between fluids of differing densities or viscosities (e.g., fingering instabilities in Hele-Shaw cells, Homsy, 1987; two-fluid Stokes problems, Pozrikidis, 1990; the Rayleigh-Taylor instability, Sharp, 1984; various free surface and interface problems, e.g., Dahm, Scheil, and Tryggvason, 1989) and vorticity layers separating regions of relatively uniform velocity (e.g., Patnaik, Sherman, and Corcos, 1976; Corcos and Sherman, 1976; Corcos and Sherman, 1984). Often, such layers at high Reynolds number are modeled as inviscid vortex sheets evolving in an otherwise irrotational fluid. Although inviscid modeling simplifies the formulation of this evolution considerably, and allows for a more efficient computational procedure than if the full Navier-Stokes equations are used, the complete neglect of viscosity, and the zero thickness of the interface, generally makes the problem ill-posed and susceptible to short wave instability and singularity formation. "Regularized" inviscid models provide a remedy for some of these difficulties, but the relation of these models to real viscous problems (as well as to the non-regularized inviscid problem) remains somewhat controversial.

The Kelvin-Helmholtz instability, where a thin vorticity layer is unstable to waves longer than the thickness of the layer and evolves into large vortical structures, occurs naturally in many situations and is easily generated in the laboratory. Although we will not review the literature in detail here, we note that numerous experimental, analytical and numerical studies of this classic problem have been reported. These include investigations of "the real thing" (viscous flows) as well as models in which the layer is treated as an inviscid vortex sheet. Such inviscid models were, of course, proposed and studied early on. A stability analysis of vortex sheets was reported by Kelvin (1871) and Rosenhead (1931), in a remarkably modern study, approximated the vortex sheet as a row of point vortices and numerically followed their motion to form large vortical structures. Rosenhead's study, too cumbersome to be elaborated upon in the thirties, was re-examined when computers became more widely available. These later studies, pioneered by Birkhoff (1962), showed that the point vortex model generally does not produce a smooth and well behaved solution at long times. Instead, evidence suggests that the sheet forms a singularity after a finite critical time (Moore, 1979; Meiron, Baker, and Orszag, 1982; Krasny, 1986a). Chorin and Bernard (1973) showed that a "regularization" of the point vortex model, using vortex blobs instead of point vortices, improved the results considerably. Krasny (1986b) showed, by careful numerical studies, that any finite regularization leads to well-behaved solutions for sufficiently accurate numerical calculations. He further concluded that as the regularization scale is reduced, most of the solution becomes independent of the

Contributed by the Fluids Engineering Division for publication in the JOURNAL OF FLUIDS ENGINEERING. Manuscript received by the Fluids Engineering Division May 23, 1990.

precise value of the regularization parameter. Although Krasny's study has stimulated considerable work in the area of vortex sheet modeling, the fundamental question of what these inviscid, regularized models are telling us about the physical problem of finite thickness viscous vorticity layers remains unanswered.

In this paper, we study the large amplitude evolution of the Kelvin-Helmholtz instability, with particular attention being paid to the relation between the viscous problem and the inviscid, regularized models. Specifically, we compare results of full Navier-Stokes simulations of the vorticity layer evolution with those obtained from inviscid vortex sheet modeling. Most of the results are for two-dimensional flows, but we also examine briefly the three-dimensional aspects of the problem. We hope to answer two questions by comparing results from these viscous simulations with the inviscid model. First, are the limits of high Reynolds number and small initial thickness in the viscous problem the same as the limit of zero regularization scale in the inviscid vortex sheet model? Second, does a finite regularization scale in the vortex sheet model correspond in any useful way to a "real" (finite thickness and viscous) vorticity layer?

Numerical Formulations

The large amplitude evolution of the fundamental mode of the Kelvin-Helmholtz instability is followed numerically by solving the full Navier-Stokes equations for the viscous problem and then compared with solutions obtained using the Biot-Savart integral for the inviscid vortex sheet model. The numerical formulation of each is described briefly below. Note that all variables have been made non-dimensional by normalization with the wave-length λ of the fundamental mode and the circulation density γ of the vorticity layer as

$$x_i \equiv \tilde{x}_i/\lambda \quad t \equiv \tilde{t}/(\lambda/\gamma) \quad u_i \equiv \tilde{u}_i/\gamma \quad \omega \equiv \tilde{\omega}/(\gamma/\lambda)$$

where the tildes denote the dimensional variables.

Full Navier-Stokes Simulations. The two-dimensional Navier-Stokes equations in vorticity form are

$$\frac{\partial \omega}{\partial t} + J(\psi, \omega) = \frac{1}{\mathrm{Re}} \nabla^2 \omega; \quad \nabla^2 \psi = -\omega \tag{1}$$

where $J(\psi,\omega) \equiv (\partial\psi/\partial y)(\partial\omega/\partial x) - (\partial\psi/\partial x)(\partial\omega/\partial y)$. We solve these equations with a finite difference method, second order both in space and time. The spatial differencing uses centered differences with Arakawa's differencing of the Jacobian, and a predictor-corrector time integration. The computational domain is square and periodic in the horizontal direction with stress-free no flow-through top and bottom boundaries. In addition to following the evolution of the vorticity field, we also track the rollup of the material surface that initially marks the points of maximum vorticity in the layer. Note that this viscous evolution is governed entirely by the Reynolds number

$$\mathrm{Re} \equiv (\lambda\gamma/\nu)$$

and the initial geometry of the vorticity distribution. For these full viscous simulations, this initial vorticity distribution was specified using equations (2) and (4) so as to be identical to the initial condition used in the inviscid vortex sheet model. We should also note that, while the vortex sheet calculations are done for an unbounded fluid domain (top and bottom boundaries are at infinity), these viscous calculations are done in a finite size domain. To check that this difference does not affect the conclusions presented here, we have repeated some of the viscous calculations in a domain where the top and bottom boundaries are further away, and found that the results are only minimally affected (less than one percent). Most of these simulations have also been checked for convergence by repeating the calculations with increasingly finer resolution.

Inviscid Vortex Sheet Modeling. For the inviscid model, we treat the vorticity layer as a periodic array of N individual vortex blobs with initial positions given by

$$x_i = \frac{i}{N} + 0.05 \sin\frac{2\pi}{N} i; \quad y_i = -0.05 \sin\frac{2\pi}{N} i, \tag{2}$$

corresponding to a 5 percent perturbation of an otherwise planar vortex sheet. Each of these vortex blobs has a dimensionless circulation $\Gamma_i = 1/N$ and regularization length scale δ. Following Krasny (1986), we find the velocity of vortex j by an algebraic regularization of the Biot-Savart law as

$$u_j = \frac{-1}{2} \sum_{i=1}^{N} \Gamma_i \frac{\sinh 2\pi(y_j - y_i)}{\cosh 2\pi(y_j - y_i) - \cos 2\pi(x_j - x_i) + \delta^2} \tag{3a}$$

$$v_j = \frac{1}{2} \sum_{i=1}^{N} \Gamma_i \frac{\sin 2\pi(x_j - x_i)}{\cosh 2\pi(y_j - y_i) - \cos 2\pi(x_j - x_i) + \delta^2} \tag{3b}$$

The vortex positions are advanced in time by integrating $d(x_j, y_j)/dt = (u_j, v_j)$ with a fourth order predictor-corrector scheme.

For a nonzero δ, the velocity field resulting from equations (3a, b) is not irrotational away from the vortex sheet. Indeed, it is easy to show that the vorticity field is given by

$$\omega(x, y) = \pi\delta^2 \sum_{i=1}^{N} \Gamma_i \frac{\cosh 2\pi(y - y_i) + \cos 2\pi(x - x_i)}{(\cosh 2\pi(y - y_i) - \cos 2\pi(x - x_i) + \delta^2)^2} \tag{4}$$

which is strongly peaked at the sheet itself when δ is small. In this sense, the regularization scale δ effectively assigns a thickness to the initial vorticity layer. It is important to point out that equation (4) is an exact solution to the inviscid form of equation (1) only for $\delta = 0$, corresponding to a set of point vortex singularities. Note that for $\delta \neq 0$, although the vorticity due to each point on the interface is not zero away from the interface, it is attached to the interface points and is constrained to move with these points.

Results

We begin by examining the limiting behavior of the viscous Navier-Stokes simulations as $\delta \to 0$ and $\mathrm{Re} \to \infty$. In Fig. 1 we show the vorticity field $\omega(x, y)$ at $t = 2$, corresponding to a relatively large amplitude stage in the evolution of the vortex layer rollup, for several different Reynolds numbers and different initial layer thicknesses. The Reynolds number increases in going from top to bottom; $\mathrm{Re} = 10^3$ in the top row, 10^4 in the middle row, and $2 \cdot 10^4$ in the bottom row. Similarly, the initial thickness δ decreases in going from left to right; $\delta = 0.316$ in the left column, 0.158 in the middle, and 0.079 in the right column.

From results such as those in Fig. 1, we can identify some of the principal physical characteristics of the viscous evolution as Re increases and δ decreases. First, we note that at the lowest Reynolds number shown, the vorticity field consists of one big blob with essentially no fine structure. There is a prominent peak at its center, and this peak increases as the initial thickness δ is decreased (and hence the maximum initial vorticity is increased). Second, as the Reynolds number is increased, a distinct fine structure develops in the vorticity field. In particular, a pair of spiral "arms" evolve that can be seen to wind their way inward from the braid at the edges of the periodic domain to the core at the center. Notice that at any fixed Re, as δ is decreased the vorticity layers comprising the outer windings of this spiral structure appear to reach a nearly asymptotic shape. This can be seen, for example, by comparing the results shown for the two smaller δ's. Both the thickness and position of these outer windings become nearly independent of δ. The former suggests that the thickness of these outer layers is instead largely a result of a local equilibrium between the straining of the layer, which tends to thin the

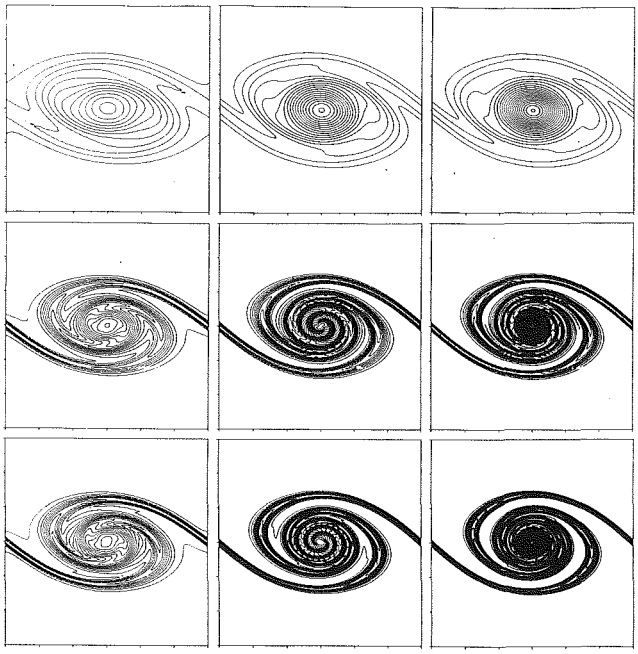

Fig. 1 Vorticity contours at $t = 2.0$ calculated by finite difference simulations of the full viscous two-dimensional Navier-Stokes equations for differing initial layer thicknesses δ and Reynolds numbers. The lowest contour level, as well as the contour interval, is the same for all cases shown. From top to bottom: Re = 1,000; 10,000; 20,000. From left to right: δ = 0.316; 0.158; 0.079.

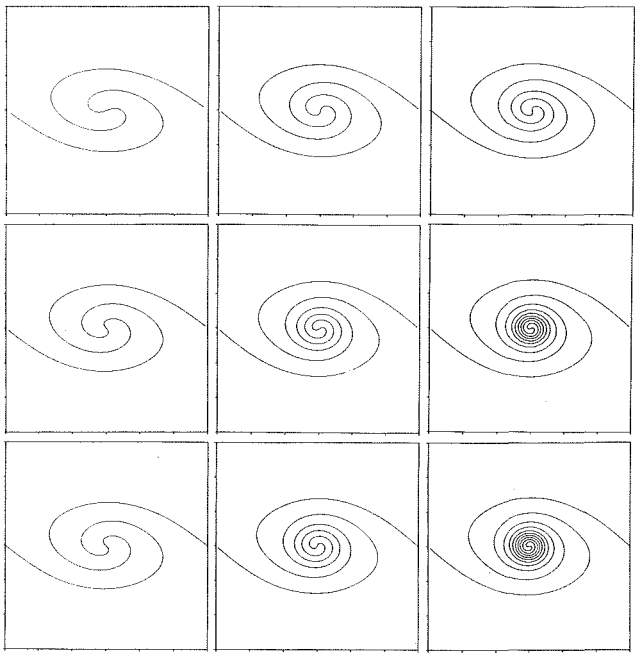

Fig. 2 Computed roll-up of the material interface for each of the cases shown in figure 1.

vorticity, and the diffusion of vorticity, which tends to thicken the layer. This local strain-diffusion balance is of course very similar to the classical Burgers solution for a steady axisymmetric strain rate field (Burgers, 1948). For an unsteady strain rate field, the strain-diffusion competition for both the planar and axisymmetric cases is given by Carrier et al. (1975). This balance between strain and diffusion for the large amplitude rollup of the Kelvin-Helmholtz instability is discussed in some detail by Corcos and Sherman (1984). In Fig. 1, the thinning of the vorticity layers in regions of extensional strain between the vortices, and the thickening in compressive regions, can

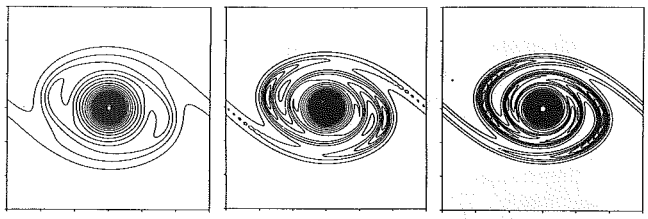

Fig. 3 Vorticity contours at $t = 2.0$ calculated by the inviscid vortex sheet model for the same initial layer thicknesses as for the cases shown in figure 1. The lowest contour level and the contour interval are the same as in figure 1. From left to right: δ = 0.316; 0.158; 0.112.

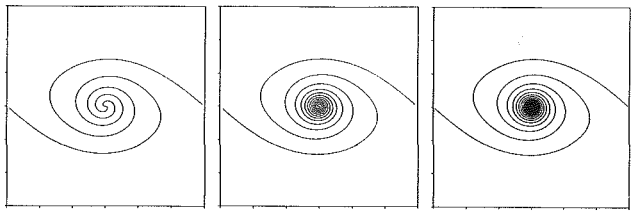

Fig. 4 Computed roll-up of the vortex sheet for each of the cases shown in figure 3.

be clearly seen. Indeed, if the strain rate experienced by these layers scales with the total circulation of the vortex, then the resulting equilibrium strain-limited vorticity diffusion layer thickness should be expected to scale like $l_\nu \sim \mathrm{Re}^{-1/2}$. Note that this is in at least qualitative agreement with the results shown. For the purposes of our discussion here of the limiting behavior, we note that this would suggest that the thickness l_ν of these layers will tend to zero as $\mathrm{Re} \to \infty$ regardless of the initial thickness δ.

Figure 2 shows the position at $t = 2$ of the material line initially marking the points of the maximum vorticity for each of the cases shown in Fig. 1. For the lowest Reynolds number and the largest δ (top left frame), relatively little roll-up has taken place, but increasing Re or reducing δ causes this interface to stretch more and wrap up more around the vortex center. The largest number of windings corresponds to the smallest initial layer thickness and the largest Reynolds number (lower right frame). Comparing Figs. 1 and 2 shows that, for the lowest Re, it is not possible to identify the position of this material interface from the vorticity distribution at this relatively large amplitude stage of the layer evolution. However, for the higher Reynolds numbers, the vorticity distribution more clearly corresponds to the material interface for at least the outermost windings of the vortex. Indeed, since at these higher Re's the strain-diffusion balance produces a comparatively small vorticity layer thickness around this interface, the layers corresponding to the outer few windings remain relatively well separated from adjacent ones.

In Figs. 3 and 4 we show results from calculations of the roll-up process using the regularized inviscid vortex sheet model. The interface itself is shown in Fig. 4 and the vorticity, as constructed by equation (4), is shown in Fig. 3. In these inviscid calculations, the regularization scale δ is the only parameter to vary. These results show that, as this regularization scale is reduced, similar development as seen in Figs. 1 and 2 is observed. Smaller regularization leads to increased roll-up in the core, but the shape of the interface away from the core is relatively independent of δ.

While there are considerable similarities between the results from these viscous and inviscid calculations, it is clear that for a given value of δ there is much more roll-up for the vortex sheet model than for the full viscous calculation with the same initial layer thickness and vorticity distribution. A comparison of the vorticity distributions in Figs. 1 and 3 amplifies these differences. In particular, for the vortex sheet calculations

there is in all cases a large circular peak in the vorticity distribution at the center of the vortex. Although in the viscous simulations the vorticity also has its maximum at the center of the vortex, its value is considerably lower. In fact, the vorticity peak resulting from the inviscid model is much higher than the initial vorticity at the center point. This is a result of the somewhat unrealistic vorticity dynamics of the regularized inviscid model. The fundamental constraint of inviscid, two-dimensional, vortical flow—that the vorticity of a material particle remains the same—requires compressed regions of a vortex layer of finite thickness to "bulge out." The vortex sheet model does not allow this to happen. The sheet has, by definition, no thickness, and compression will increase the local vortex sheet strength but not its thickness. When the vortex sheet is regularized by introducing a smoothing kernel, the vorticity field is no longer confined to an infinitely thin sheet, but spread around the original interface. However, it still moves with the points on the interface. In regions of compressive strain, as in the core of the vortex, the vorticity therefore becomes much higher than its initial value since the vortex sheet strength has increased but its thickness is still the same. The resulting large vorticity peak in the regularized inviscid calculations generally accelerates the rollup of the interfacial points considerably. Overall, we can conclude that a decrease in the regularization scale δ in Fig. 3 effectively mimics many of the features associated with the thinning of the vorticity layers with increasing Re in Fig. 1. However, the absence of the proper strain-diffusion competition in the vorticity dynamics of such a fixed δ regularization limits it to accurately simulating only the relatively large scale features of the vorticity field. This also suggests the possibility of accurately simulating the detailed fine scale structure of the vorticity field with a variable δ regularization incorporating the essential strain-diffusion dynamics.

After identifying these similarities and differences in the evolution calculated from the regularized inviscid model and the full viscous simulations, we next want to examine how the evolution of the inviscid calculations as $\delta \to 0$ compares with the limiting behavior of the viscous simulations as $\mathrm{Re} \to \infty$ and $\delta \to 0$. First, we note that while the detailed structure of the core (e.g., the number of windings) is clearly not the same, the shape of the outermost windings is very similar. To put this observation on a more quantitative ground, we plot in Fig. 5 the vertical coordinate of the two outermost windings of the interface as they cross the vertical line through the core at $t = 2$, for both the viscous and inviscid calculations for various values of δ. The symbols at the top of each set are the regularized vortex sheet results, and the remaining symbols denote the viscous simulation results for differing Reynolds numbers. Obviously, the differences are quite large for large δ, but the results suggest that as $\delta \to 0$ at least the outermost windings of the interface seem to converge to the inviscid result as $\mathrm{Re} \to \infty$.

A more detailed comparison is presented in Fig. 6, which examines not just the outermost windings of the vortex but the limiting behavior of the entire interfacial roll-up. In particular, we plot $r(s)$, the distance of the interface from the vortex center, as a function of the arc length s measured along the interface from the braid, for the viscous Navier-Stokes simulations and the regularized inviscid model calculations. In Fig. 6(*a*), we first examine the approach of the inviscid calculations to the $\delta = 0$ case by successively reducing the regularization scale δ. As the results show, the outermost parts of the interface are very similar, particularly for the smaller values of δ. However, as we move along the interface toward the core, the results obtained for the larger values of δ begin to diverge, at first slowly but then more rapidly. Each curve eventually intersects the horizontal axis as we arrive at the vortex center, and this happens at a different total arc length for the various values of δ. Of particular importance for our

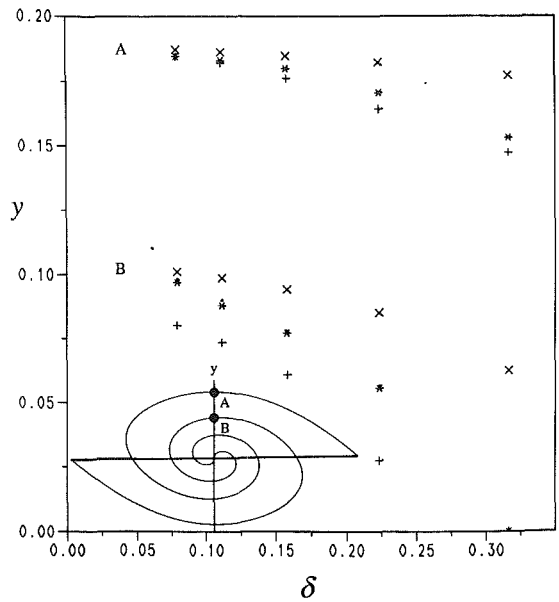

Fig. 5 Convergence of the outer arms for the full viscous simulations and the regularized inviscid vortex model calculations in the limits Re $\to \infty$ and $\delta \to 0$. Shown are the vertical coordinates of the two outermost windings of the interface as it crosses the y-axis at $t = 1.0$. Finite difference simulations: + Re = 1,000; * Re = 10,000; • Re = 20,000. × Vortex sheet calculations.

purposes here, note that the major effect of decreasing δ is to increase the distance along the spiral arms over which the computed roll-up agrees with the next smaller value of δ. In other words, as δ is reduced the convergence to the limiting solution for $\delta = 0$ appears to work its way inward from the outer arms of the spiral to the vortex core. As a result, from the succession of cases shown, we can infer that for $\delta = 0$, the limiting solution will be essentially the same as that given for the smallest value of δ in Fig. 6(a) except very near the core.

We now examine in a similar manner how the viscous simulations approach this limiting solution as $\mathrm{Re} \to \infty$ and the initial layer thickness $\delta \to 0$. In Fig. 6(*b*), we show the effect of increasing Re for the smallest initial vorticity layer thickness ($\delta = 0.079$). From the results shown we can draw at least two conclusions regarding the $\mathrm{Re} \to \infty$ limiting process. First, we can see that with increasing Re the viscous solutions do appear to tend closer to the inviscid solution, though the convergence with increasing Reynolds number appears to become quite slow. Second, however, we can also see that increasing Re alone does not appear to be sufficient to reach this limiting solution. In particular, note that even in the outer few windings, the solutions for Re = 10,000 and 20,000 do not appear to differ very much at all, and still show significant differences from the inviscid solution. This suggests that in addition to increasing Re, we must also decrease the initial layer thickness δ in order to reach the limiting inviscid solution. The results obtained by decreasing δ for the highest Reynolds number (Re = 20,000) are shown in Fig. 6(*c*). Notice that this reduction in δ appears to drive the viscous solution closer to the inviscid result even in the outer arms of the spiral. As a consequence, even though these calculations can span only a limited parameter range, the results appear to support the conjecture that the limiting solution of the regularized inviscid calculation is the same as the limit of the viscous full Navier-Stokes simulations as $\mathrm{Re} \to \infty$ and the initial layer thickness $\delta \to 0$.

Strictly speaking, of course, these results and in particular the apparent limiting convergence of the viscous and inviscid calculations are specific to the "algebraic" blob regularization in equation (4). To investigate the effects of different blob structures on these results, we have made a number of cal-

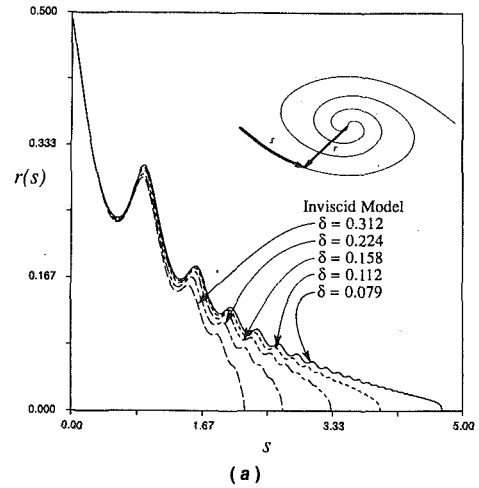

(a)

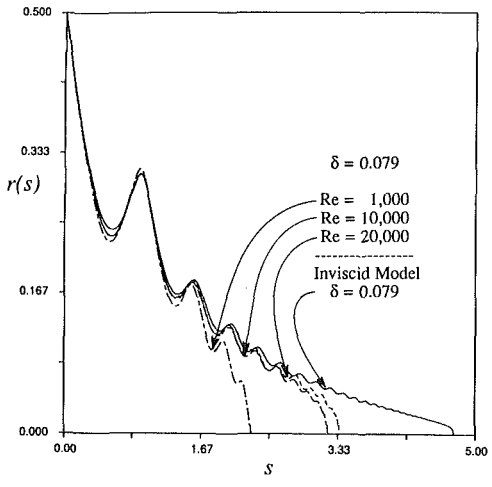

(b)

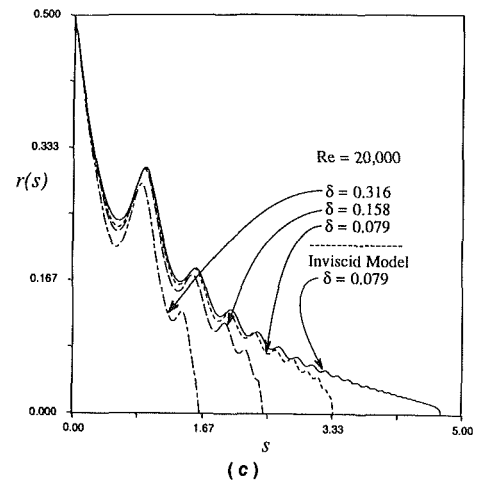

(c)

Fig. 6 Convergence of the whole interface, showing the distance *r(s)* from the center of the vortex versus the arclength *s* measured from the braid at $t = 2.0$. (*a*) Convergence of the inviscid model as $\delta \to 0$. (*b*) Convergence of the viscous simulations with increasing Re for $\delta = 0.079$ to the $\delta \to 0$ inviscid result. (*c*) Convergence of the viscous simulations with decreasing δ for Re = 20,000 to the $\delta \to 0$ inviscid result.

culations with an "exponential" blob, where instead of modifying the kernel in equations (3*a*,*b*) by introducing a nonzero δ, the kernel is instead multiplied by $(1 - \exp(r^2/4\pi^2\delta^2))$. The results obtained are in all major aspects identical to those obtained above with the algebraic blob. The only difference is that the outer windings are now better converged for the same δ. This suggests that a more compact regularization generally may be more efficient, a conclusion also reached by Tryggvason (1989) who compared the algebraic regularization with calculations using a vortex-in-cell method. However, we note that the exponential blob is computationally more expensive, and not as convenient for periodic domains as the algebraic regularization in equations (3*a*,*b*).

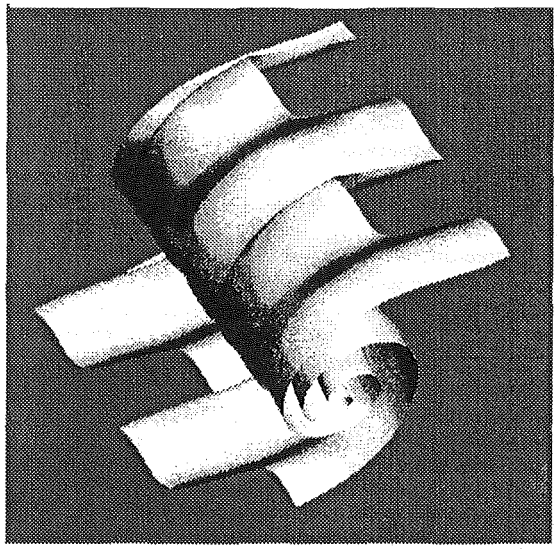

(a)

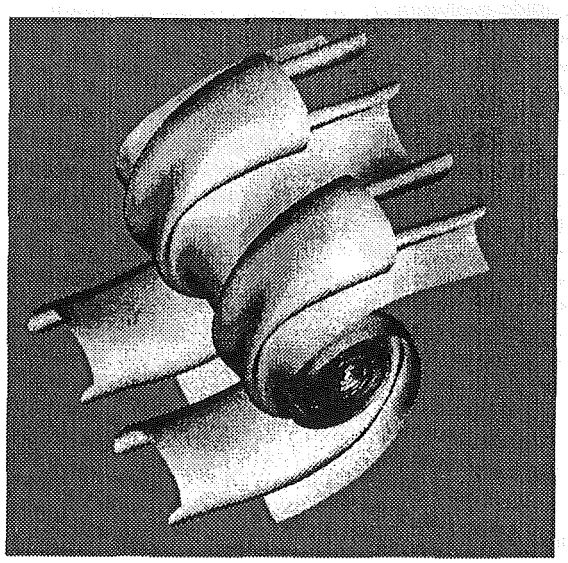

(b)

Fig. 7 The large amplitude stage in the evolution of a three-dimensional vortex sheet perturbed by both streamwise and spanwise disturbances for two different regularization scales. Note that the effects of regularization scale are similar as in two dimensions. (*a*) Large regularization. (*b*) Smaller regularization.

Lastly, to address three-dimensional aspects of the vortex sheet evolution we are currently using a three-dimensional vortex-in-cell (VIC) method to compute the nonlinear evolution. In the VIC method the vorticity associated with each point on the vortex sheet is spread out onto a grid for the purpose of calculating the velocities. This has the same effect as assigning a finite area core to the vortices but the reduction in computational time is substantial (see Tryggvason, 1989). Figure 7 shows results obtained for the large amplitude evolution from a calculation where the vortex sheet has been given perturbations in both the streamwise and spanwise directions. The result in Fig. 7(*a*) is for a 16^3 grid, and in Fig. 7(*b*) is for a 32^3

grid. Note that as the sheet rolls up into a predominantly two-dimensional vortex, the spanwise perturbations grow to form streaks in the flow direction that consist of pairs of vortices with alternating sense of circulation. The finer grid corresponds to a smaller regularization parameter, and hence achieves more roll-up, as was observed above for the two-dimensional calculations. We note that Corcos and Lin (1984) and Lin and Corcos (1984) present numerical results for the initial development and subsequent evolution of such streamwise vortices, and full three-dimensional simulations by Metcalfe et al. (1987) also examine these secondary Kelvin-Helmholtz instabilities of a vorticity layer. However, we have not yet performed detailed comparisons of our inviscid model results with full viscous three-dimensional Navier-Stokes calculations, as those described above for the two-dimensional evolution, and include these results only to suggest that the basic conclusions reached here will likely carry over to three dimensions as well.

Conclusions

Our comparison between an inviscid, regularized vortex sheet model and a full viscous Navier-Stokes solution for the large amplitude evolution of the Kelvin-Helmholtz instability of a relatively thin vorticity layer suggests that the limit of zero regularization scale for the inviscid model and the limit of high Reynolds number and small initial thickness for the viscous calculations appear to be the same. While the limits for zero thickness and high Reynolds number may be the same, it is clear that there are important differences in the results obtained for vortex sheets with large regularization and viscous layers with finite initial thickness. In particular, although our results show that the outer parts of the roll-up are very similar, the results do not correlate well with each other as far as the detailed core structure goes. It may therefore not be possible to identify a physically meaningful role for finite values of a fixed regularization parameter. Whether it is possible to modify these regularized vortex sheet models in such a way as to retain their desirable computational properties, but to better mimic the detailed fine structure of real viscous vorticity layers, remains an open question.

Acknowledgments

This work was supported by NSF grant No. MSM87-07646 and by the Gas Research Institute (GRI) under contract No. 5088-260-1692. We gratefully acknowledge interactions with R. Krasny in the Applied Mathematics group at Michigan, and C. Churchill of the University of Michigan Visualization Laboratory for help with the three-dimensional graphics. Some of the calculations were done on the computers at the San Diego Supercomputer Center, which is sponsored by the NSF.

References

Birkhoff, G., 1962, "Helmholtz and Taylor Instability," *Proceedings, 13th Symp. Appl. Math.*, Amer. Math. Soc., Providence, R.I., p. 55.

Burgers, J. M., 1948, "A Mathematical Model Illustrating the Theory of Turbulence," *Adv. Appl. Mech.*, Vol. 1, pp. 171–199.

Carrier, G. F., Fendell, F. E., and Marble, F. E., 1975, "The Effect of Strain Rate on Diffusion Flames," *SIAM J. Appl. Math.*, Vol. 28, pp. 463–500.

Chorin, A. J., and Bernard, P. S., 1973, "Discretization of Vortex Sheets with an Example of Roll-Up," *J. Comput. Phys.*, Vol. 13, pp. 292–313.

Corcos, G. M., and Lin, S. J., 1984, "The Mixing Layer: Deterministic Models of Turbulent Flow. Part 2. The Origin of the Three-Dimensional Motion," *J. Fluid Mech.*, Vol. 139, pp. 67–95.

Corcos, G. M., and Sherman, F. S., 1976, "Vorticity Concentrations and the Dynamics of Unstable Free Shear Layers," *J. Fluid Mech.*, Vol. 73, pp. 241–264.

Corcos, G. M., and Sherman, F. S., 1984, "The Mixing Layer: Deterministic Models of Turbulent Flow. Part 1. Introduction and the Two-Dimensional Flow," *J. Fluid Mech.*, Vol. 139, pp. 29–65.

Dahm, W. J. A., Scheil, C. M., and Tryggvason, G., 1989, "Dynamics of Vortex Interaction with a Density Interface," *J. Fluid Mech.*, Vol. 205, pp. 1–43.

Homsy, G. M., 1987, "Viscous Fingering in Porous Media," *Ann. Rev. Fluid Mech.*, Vol. 19, pp. 271–311.

Krasny, R., 1986a, "A Study of Singularity Formation in a Vortex Sheet by the Point-Vortex Approximation," *J. Fluid Mech.*, Vol. 167, pp. 65–93.

Krasny, R., 1986b, "Desingularization of Periodic Vortex Sheet Roll-Up" *J. Comput. Phys.*, Vol. 65, pp. 292–313.

Lin, S. J., and Corcos, G. M., 1984, "The Mixing Layer: Deterministic Models of Turbulent Flow. Part 3. The Effect of Plane Strain on the Dynamics of Streamwise Vortices," *J. Fluid Mech.*, Vol. 141, pp. 139–178.

Lord Kelvin, 1871, "Hydrokinetic Solutions and Observations," *Phil. Mag.*, Vol. 42, p. 362.

Meiron, D. I., Baker, G. R., and Orszag, S. A., 1982, "Analytical Structure of Vortex Sheet Dynamics. I. Kelvin-Helmholtz Instability," *J. Fluid Mech.*, Vol. 114, pp. 283–298.

Metcalfe, R. W., Orszag, S. A., Brachet, M. E., Menon, S., and Riley, J. J., 1987, "Secondary Instability of a Temporally Growing Mixing Layer," *J. Fluid Mech.*, Vol. 184, pp. 207–243.

Moore, D. W., 1979, "The Spontaneous Appearance of a Singularity in the Shape of Evolving Vortex Sheet," *Proc. R. Soc. Lond.*, Series A 365, pp. 105–119.

Patnaik, P. C., Sherman, F. S., and Corcos, G. M., 1976, "A Numerical Simulation of Kelvin-Helmholtz Waves of Finite Amplitude," *J. Fluid Mech.*, Vol. 73, pp. 215–240.

Pozrikidis, C., 1990, "The Instability of a Moving Viscous Drop," *J. Fluid Mech.*, Vol. 210, pp. 1–21.

Rosenhead, L., 1931, "The Formation of Vortices from a Surface of Discontinuity," *Proc. Roy. Soc. Lond. A*, Vol. 134, p. 170.

Sharp, D. H., 1984, "An Overview of the Rayleigh-Taylor Instability," *Physica*, Vol. 12D, pp. 3–18.

Tryggvason, G., 1989, "Simulations of Vortex Sheet Roll-Up by Vortex Methods," *J. Comput. Phys.*, Vol. 80, pp. 1–16.

Effect of Freestream Velocity on the Three-Dimensional Separated Flow Region in Front of a Cylinder

W. A. Eckerle
Fluids Metrology,
Cummins Engine Co., Inc.,
Columbus, IN 47202

J. K. Awad
Clarkson University,
Mechanical and Aeronautical Engineering
Department,
Potsdam, N.Y. 13699

Details of the horseshoe vortex formation around a cylinder were studied to determine the flow parameters that affect the flow separation in front of the cylinder. An experimental setup consisting of a circular cylinder vertically mounted on the floor of the wind tunnel test section was assembled. The approaching turbulent boundary layer was four centimeters thick. Pressures were measured on the cylinder surface and the tunnel floor with surface static pressure taps. Surface flow visualizations were accomplished to locate singular points and the size of separation region on the endwall surface. Interior mean and fluctuating velocity data and Reynolds stresses in front of the cylinder were nonintrusively measured with a two-component Laser Doppler Anemometer system. Freestream stagnation at the endwall/cylinder surface occurred in all cases, but two types of separation were identified in this investigation. The flow pattern in the separation region depends on the freestream momentum and the boundary layer displacement thickness. A large-scale fully developed vortex was formed in the plane of symmetry for low approaching freestream velocities. A fully developed vortex was not present at higher approach velocities. Maximum production of turbulent kinetic energy was measured around the core of the vortex when fully formed.

Introduction

The three-dimensional separation of a turbulent boundary layer approaching an obstacle mounted on a wall is an important problem in many applications. Specifically, in gas turbine engines, the horseshoe vortex system that forms upstream of a turbine blade cascade brings hot flow from the combustor in contact with the engine casing and blade hub and tip. Since higher engine efficiencies are being sought by increasing the combustor exit temperature, proper cooling of the separation region is becoming more important in the new high technology engines. However, in order to design efficient cooling schemes, the flow field and the parameters affecting the flow field in the separation region must be understood. The emphasis of this paper is to define the role of approaching freestream momentum and boundary-layer thickness on the flow field that forms in the separation region upstream of obstacles. The symmetrical separation of a turbulent boundary layer flow normal to a single cylinder is perhaps the simplest of geometries that demonstrates the horseshoe vortex formation on the endwall of a cascade of turbine airfoils (Eckerle, 1985). As a two-dimensional turbulent boundary-layer flow approaches the cylinder, the boundary-layer flow experiences the adverse pressure gradient created by the cylinder and separates. The three-dimensional separation that develops in front of the cylinder includes a reverse flow in the plane of symmetry leading to the formation of a large scale vortex around the cylinder. Viewed from the top, the vortex formation has a horseshoe-like shape, and is defined in the literature as a horseshoe vortex. Understanding the flow in this simple geometry is a first step leading to the explanation and prediction of the behavior of three-dimensional flows that exist in complex geometries such as in turbomachinery applications.

Baker (1978) studied the separation of turbulent boundary layers caused by the obstruction of cylinders with different diameters mounted on a flat plate in a wind tunnel test section. The presence of multiple vortices in the plane of symmetry was inferred from the photographs of smoke injected into the wind tunnel. Two saddle points and two separation points were deduced from surface flow visualizations. A "four vortex" model was developed to correlate these observations. This inferred interpretation of the flow is similar to the well-documented separation of a laminar boundary layer where multiple vortices form. Other researchers such as Moore and Forlini (1984) and Blair (1985) have also applied this model to their flow separations based on similar interpretations of measured floor data. However, none of these researchers acquired any interior measurements to document this model. Furthermore, a close examination of Baker's published results shows that the photograph of the smoke pattern indicating multiple vortices in the plane of symmetry was acquired at a very low velocity. The shape factor of the approaching boundary layer was 1.75 indicating that the boundary layer was not fully turbulent. Evidently the four-vortex model was based on smoke flow visualizations obtained for a transitioning boundary layer rather than a fully turbulent boundary layer.

The separation in front of a cylinder was also examined by Eckerle and Langston (1987). Surface flow visualization and static pressure data at the floor and the cylinder were obtained

Contributed by the Fluids Engineering Division for publication in the JOURNAL OF FLUIDS ENGINEERING. Manuscript received by the Fluids Engineering Division November 13, 1989.

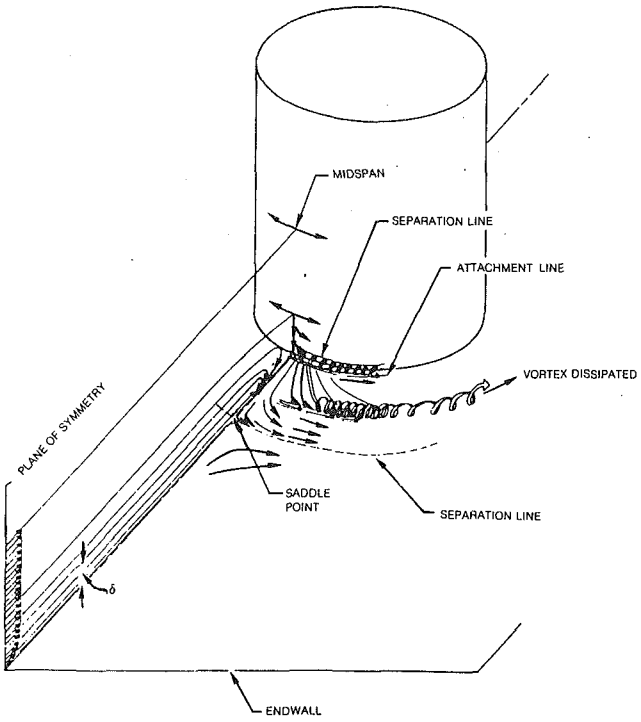

Fig. 1 Eckerle and Langston's endwall separation

in the separation region. Interior pressure and velocity data were acquired with a five-hole probe. Figure 1 illustrates the flow pattern measured by Eckerle and Langston. Only one saddle point and corresponding separation line were determined from the endwall flow visualizations. The steep flow separation leading to the formation of multiple vortices in the plane of symmetry was not measured. Rather the main vortex was a single vortex that developed away from the plane of symmetry as the separated flow moved around the cylinder. A small vortex in the endwall/cylinder junction was also inferred.

Pierce et al. (1987) studied the flow around a streamlined (teardrop shaped) cylinder placed normal to a flat surface in a relatively thick boundary layer. The conditions of Pierce et al. are quite similar to one of the conditions set by Baker. Pierce et al.'s detailed endwall and five-hole probe measurements upstream of the cylinder indicate a flow pattern similar to the measurements of Eckerle and Langston, except the rudiments of a vortex are more apparent in the plane of symmetry.

The results of Eckerle and Langston and Pierce et al. demonstrate that the complicated four-vortex model is not appropriate for turbulent boundary layers. Turbulence, evidently, generates large enough wall shear stresses to prevent the formation of multiple vortices as has been documented in a separated laminar boundary layer. Recent computational studies by Chima and Yokota (1988), Lai and Makomaski (1988), and Wagner (1989) also predict flow patterns similar to the measured pattern of Eckerle and Pierce. The interior measurements of Merati et al. (1988), Kubendran et al. (1986), and Oguz (1980) tend to indicate a single vortex, but the measurements do not show enough detail in the vortex formation region to make a distinct determination of the vortex structure.

A question remains, however, regarding the conditions associated with a vortex forming in the plane of symmetry, as indicated by Pierce et al.'s data, or a vortex forming away from the plane of symmetry as measured by Eckerle. Defining parameters that determine these different types of separation is important since this flow separation brings hot combustion gases adjacent to the engine casing in a gas turbine engine. The performance of a coolant film, and the associated heat transfer coefficients, would be different in the two separated flow regimes.

Both Eckerle and Baker have indicated the importance on the separation process of the boundary-layer thickness and the Reynolds number based on the approaching freestream velocity and the cylinder diameter. For example, Eckerle found that the freestream momentum relative to the blockage of the boundary layer (represented by the boundary-layer displacement thickness) was an important aspect of the separation process. For that work, the boundary layer was relatively thin resulting in the freestream flow stagnating at the endwall/cylinder junction before reversing and flowing toward the separation line. In that study, the basis for freestream stagnation was the pressure measured with a pressure tap located at the endwall/cylinder junction being equal (or very close) to the freestream stagnation pressure. For this case, the reverse flow near the plane of symmetry had too much momentum to roll up into a vortex. Instead, the flow tended to proceed out to the separation line and around the cylinder as shown in Fig. 1. If the boundary layer had been thicker or the freestream momentum lower in that test, the momentum of the reverse flow would also have been reduced, possibly allowing the reverse flow to roll up into a vortex in the plane of symmetry.

With the exception of Eckerle and Pierce, detailed interior measurements in the vortex formation region that document the details of the separated flow in the plane of symmetry are not available in the literature. However, endwall pressure data, which can be used to determine whether freestream stagnation occurred at the junction of the obstacle and the endwall for a particular configuration, have been measured for a wide range of freestream velocities and approaching boundary-layer thicknesses. Since the flow conditions associated with freestream stagnation (high freestream momentum and a thin boundary layer) also are associated with a vortex not forming in the plane of symmetry, a correlation of these results might be extended to correlate the two flow regimes. For example, freestream stagnation occurred in Eckerle's experiment where a vortex was not present, and freestream stagnation did not occur in Pierce's experiment where a vortex was formed in the plane of symmetry.

The boundary-layer parameter $(\mathrm{Re}_D)^{1/3}$ (D/δ^*) was devel-

Nomenclature

C_{ps} = static pressure coefficient
D = cylinder diameter
h = test section height, 45.7 cm
H = boundary layer shape factor, δ^*/Θ
P_s = local static pressure
P_{s0} = reference static pressure near test-section entrance
P_{t0} = reference total pressure near test-section entrance
Re_D = Reynolds number based on the cylinder diameter
u = velocity in X-direction
u' = axial rms velocity in X-direction
$\overline{-\hat{u}'\hat{v}'}$ = turbulence shear stresses
U_0 = reference velocity near test-section entrance
v = velocity in Y-direction
v' = vertical RMS velocity
X, Y, Z = Cartesian coordinate system originated at cylinder/endwall junction
δ = boundary-layer thickness
δ^* = boundary-layer displacement thickness
Θ = boundary-layer momentum thickness

oped through regression analysis to correlate freestream stagnation with freestream conditions and boundary-layer blockage. This parameter nondimensionally incorporates the ratio of freestream velocity to the approaching boundary-layer displacement thickness. The cylinder diameter was used to nondimensionalize this factor because the cylinder diameter controls the size of the separation. The exponent 1/3 shows the relative importance of the freestream velocity and displacement thickness. A summary of the correlation is shown in Table 1. All previous investigations whose tests correspond to a parameter value above 1040 (Baker, Ram (1963), Eckerle and Langston) measured freestream stagnation pressures at the junction. Previous configurations where the measured pressure at the junction was less than the freestream stagnation pressure (Baker, Moore and Forlini; Pierce et al.) correspond to a parameter value less than 673.

The above correlation shows the importance of these parameters on the separation process. A similar correlation might then be expected for vortex formation in the plane of symmetry. Since not enough flow measurements in the literature are available to develop a correlation for vortex formation, an experiment was conducted where flow measurements in the separation region were acquired over a range of $(\mathrm{Re}_D)^{1/3}(D/\delta^*)$. In this particular test, the parameter value was varied by changing the freestream velocity for a fixed cylinder diameter and nearly constant boundary-layer thickness.

Experimental Setup

Wind Tunnel. Tests were conducted in a suction-type subsonic wind tunnel located at Clarkson University. A schematic of the test setup is shown in Fig. 2. After entering the 1.8 m by 2.1 m inlet, the flow was conditioned by honeycomb sandwiched between two fine mesh screens to create a uniform flow with low turbulence entering the three-dimensional contraction section. The test section had a cross section of 0.61 m by 0.45 m and was placed to create a test-section entrance boundary-layer thickness of approximately 3.8 cm. The velocity in the test section was controlled by a valve located just upstream of a centrifugal blower powered by a 30 horsepower motor. The blower could provide velocities up to 22 m/s in the tunnel test section. Leakage past the valve resulted in a lower limit on velocity of 3.5 m/s through the test section.

Test Section. The experimental setup consisted of a cylinder mounted vertically inside the test section. Because of the simplicity of the cylinder geometry, the approaching boundary layer separated symmetrically on each endwall. Therefore, it was adequate to document the data in only the one quadrant shown in Fig. 2 to get a full understanding of the separated flow upstream of the cylinder. The coordinate system is illustrated in Fig. 2.

The test section was made of 12.7 mm thick plexiglass. Pressure taps were installed in the floor in the plane of symmetry, 10, 25, 45, 60, and 90-degree planes. The cylinder was machined from 60/61 aluminum pipe to final dimensions of 14 cm I.D., 15.2 cm O.D., and 45.7 cm length (which was the test section height). Pressure taps were installed in the cylinder in the same six planes as the floor pressure taps.

Instrumentation. Pressure measurements were acquired with a computer controlled data acquisition system. Pressure taps and reference probes were connected to ±1.2 kPa pressure transducers. The transducers were calibrated with an inclined water manometer.

Interior velocity measurements were acquired with a two-component commercially available Laser Doppler Anemometer (LDA) system. The system was used in the backscatter mode with a water-cooled 4-watt Argon-Ion laser. The laser beam was transmitted through modular optics and split into three beams with different colors: cyan, green and blue. The three beams were then transmitted to the test section via mirror units and a 600 mm focal lens placed on an automated 3-D traversing system. The probe volume created at the intersection of the three beams was of an ellipsoid shape with a minor axis of 0.124 mm and a major axis of 2.68 mm. Since it was important to document the velocity close to the floor, the laser beams were oriented so that the plane formed by the green and blue beams, which contained the beam intersection point,

Table 1 Correlation of freestream stagnation

Freestream stagnation did not occur

Investigator	U_0 (m/s)	H	D/δ^*	$(\mathrm{Re}_D)^{1/3}(D/\delta^*)$
Baker	1.18	1.60	4.70	77
Baker	1.40	1.72	7.60	132
Moore and Forlini	23.30	1.42	4.80	187
Baker	11.65	1.42	6.40	225
Baker	19.22	1.37	6.80	283
Baker	16.00	1.40	9.60	375
Baker	21.70	1.35	9.80	424
Ram	40.00	1.35	7.70	544
Pierce et al.	23.15	1.30	12.09	673

Freestream stagnation did occur

Investigator	U_0 (m/s)	H	D/δ^*	$(\mathrm{Re}_D)^{1/3}(D/\delta^*)$
Baker	12.00	1.47	29.40	1044
Baker	18.40	1.47	30.90	1264
Baker	25.40	1.47	32.10	1463
Ram	40.00	1.56	33.33	2354
Eckerle and Langston	30.50	1.35	65.00	5311

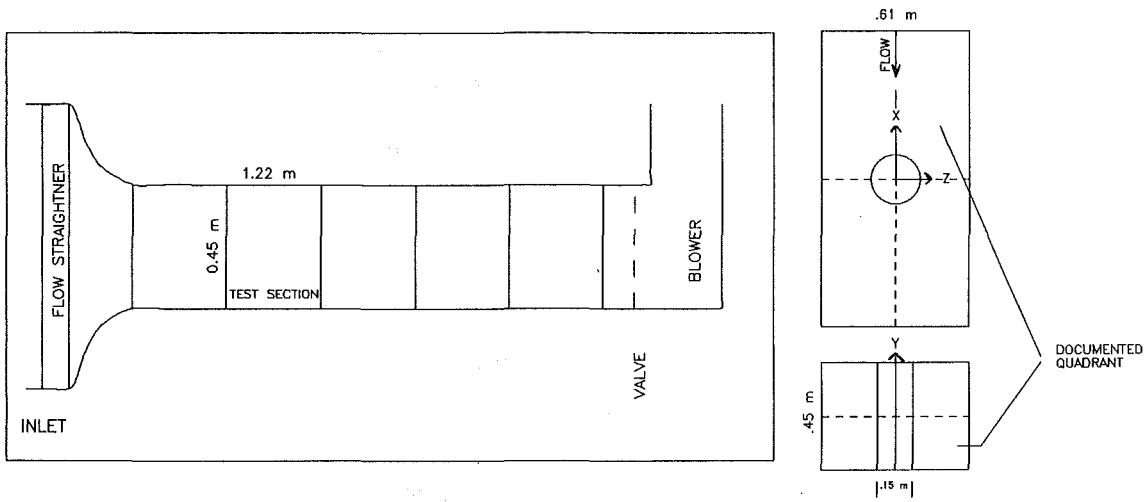

Fig. 2 Wind tunnel schematic and coordinate system

was parallel to the test section floor. By using this configuration and slightly tilting the optical bench toward the direction of beam propagation, measurements were acquired to within 0.25 mm of the test section floor without the floor clipping the incoming converging beams.

Data were acquired with counter-type processors. Acquisition was controlled with software provided by the LDA manufacturer. The coincidence window was set at its minimum level to gather data from both channels as simultaneously as possible for the Reynolds stress calculations. Data are presented for ensemble sizes of 500–1000.

The wind-tunnel inlet flow was seeded with fine oil droplets (the majority of the droplets were less than one micron) created by a commercially available fogger. The seed particles were injected into a box located on the floor upstream of the tunnel inlet. The box distributed the seed across the inlet through a staggered arrangement of holes in its sides.

The accuracy of the probe measurement data was calculated using the uncertainty analysis of Kline and McClintock (1953), with the uncertainty intervals being calculated based on 20 to 1 odds. The probable errors in mean velocities and fluctuating velocities of the LDA measurements were calculated at a 95 percent confidence level based on the uncertainty analysis method of Patrick (1985).

Results

Inlet Conditions. The flow field entering the test section was documented with a pitot-static probe at several approach velocities without the cylinder mounted in the test section. The probe was vertically traversed in the plane of symmetry and 11 cm on each side of the plane of symmetry 22.9 cm downstream of the test section inlet. In order to correct for the slight variations of the flow condition during a test, another pitot-static probe was placed in the freestream flow just upstream of the test section to measure reference conditions. The pressure data from the traverses were normalized by the reference conditions.

The pressure profiles documented that both the horizontal and vertical symmetry planes were present and that the freestream flow was nearly uniform across the test section inlet. Floor boundary-layer parameters in the plane of symmetry are presented in Table 2 for the range of velocities tested. To calculate the boundary-layer displacement and momentum thicknesses, the measured velocity profile was extended to the floor using the correlation developed by Burton (1965) before performing the integrations. The shape factor was approximately 1.3, indicating that the boundary layer in the test section was turbulent (White, 1974).

Surface Flow Visualization. Surface flow visualizations were accomplished to identify the size of the separation region and the singular points upstream of the cylinder. An ink dot technique developed by Langston and Boyle (1982) was used. Streakline patterns are shown in Fig. 3 for freestream velocities of 22 and 3.5 m/s. As will be shown, these velocities correspond to the two different flow regimes discussed previously. Only one quadrant is shown for each velocity since the flow was symmetric about the plane of symmetry. The row of dots on each side of the white line corresponds with the plane of symmetry. The separation line is more apparent near the plane of symmetry where a saddle point of separation can be seen. The normalized radial distance from the cylinder leading edge to the saddle point, X/D, was approximately 0.92 for both velocities. The incoming flow and the reverse flow from the cylinder converged at the saddle point and then passed tangentially around the cylinder. Unlike the four-vortex model reported by Baker, only one saddle point can be identified in the plane of symmetry. The attachment line located near the cylinder was difficult to determine from the ink traces. The streaklines for both velocities are similar except near the plane of symmetry in the separation region. At 3.5 m/s, the streaklines show that reverse flow proceeding away from the cylinder turned out of the plane of symmetry closer to the cylinder than at the higher velocity. This result indicates that, at the lower velocity, the reverse flow did not contain enough momentum to overcome wall shear stresses and proceed closer to the separation line before turning to go around the cylinder. The implication here is that the lower momentum reverse flow can also turn away from the endwall and roll up into a vortex in the plane of symmetry region.

Table 2 Boundary-layer parameters in the plane of symmetry. (Uncertainty in $U_0 = \pm 0.176$ m/s, $\delta^*/h = \pm 0.00007$, $\delta^*/\Theta = \pm 0.0299$, $(Re_D)^{1/3}\, D/\delta^* = \pm 18.8$ at 20:1 odds.)

U_0 (m/s)	δ^*/h	δ^*/Θ	$(Re_D)^{1/3}(D/\delta^*)$
22	0.0097	1.34	2050
15	0.0110	1.36	1470
10	0.0115	1.36	1360
6	0.0117	1.39	1150
3.5	0.0112	1.42	960

Endwall Static Pressure Measurements. Local static pressures measured at the floor were converted to static pressure coefficients, C_{Ps}, using the reference conditions measured at the test section inlet to normalize the local static pressures:

$$C_{P_s} = \frac{P_s - P_{so}}{P_{to} - P_{so}}$$

Pressures were measured at all of the floor tap locations at freestream velocities of 22, 15, 10, 6, and 3.5 m/s. Only pressure data in the plane symmetry will be presented in this paper. The trends shown by the pressure data in the documented quadrant are similar to the results of Eckerle and Langston.

The measured static pressure coefficients and the corresponding potential flow distribution in the plane of symmetry are plotted versus the nondimensional distance from the leading edge of the cylinder in Fig. 4. At $U_0 = 22$ m/s, the static pressure coefficient is highest ($C_{Ps} = 0.97$) next to the cylinder leading edge ($X/D = 0.5$). This high value indicates that freestream flow from outside approaching boundary layer stagnated at the endwall surface. As X/D increases from the cylinder, the coefficient drops rapidly to a local minimum ($C_{Ps} = 0.39$) between the cylinder leading edge and the saddle point at an X/D of 0.75. This sudden decrease in the pressure is associated with the reverse flow accelerating away from the cylinder leading edge towards the saddle point as shown in the surface flow visualization streaklines. As the reverse flow approaches the saddle point, the static pressure coefficient rises slowly and reaches a local peak at an X/D of 0.87. As the

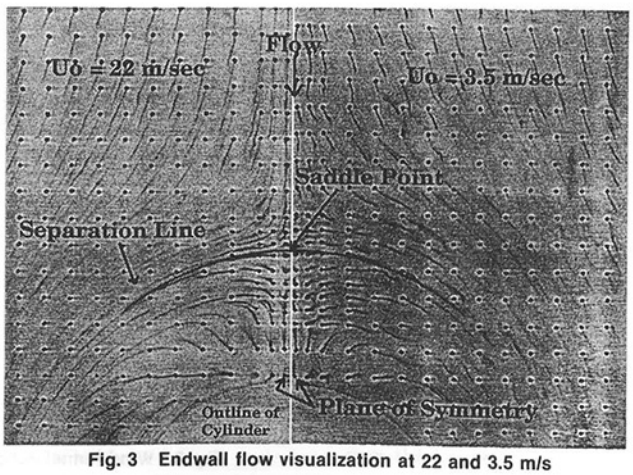

Fig. 3 Endwall flow visualization at 22 and 3.5 m/s

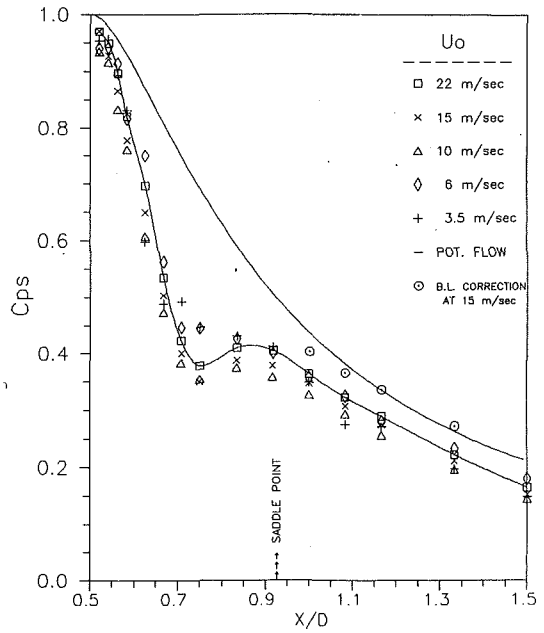

Fig. 4 Endwall pressure distribution in the plane of symmetry.

(Uncertainty in C_{ps} = ± 0.0096, in X/D = ± 0.0052.)

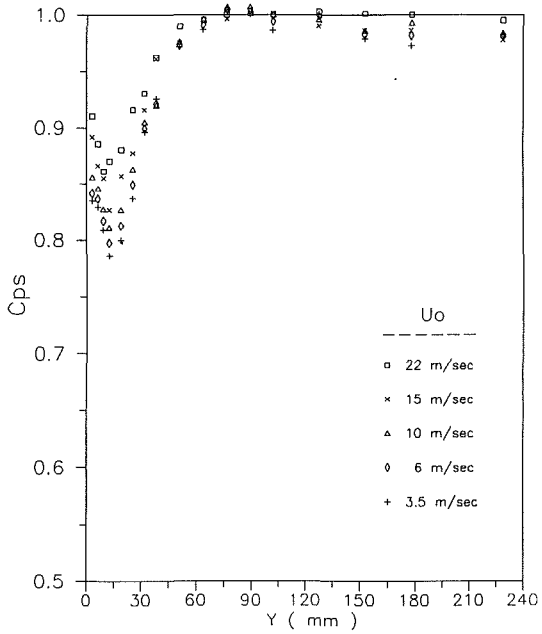

Fig. 5 Cylinder lateral surface pressure distribution in the plane of symmetry.

(Uncertainty in C_{ps} = ± 0.0096, in Y = ± 0.10 mm.)

incoming flow approaches the saddle point, the measured adverse pressure gradient is similar to the gradient predicted by the potential flow theory for flow around a single cylinder.

The static pressure coefficient curves at freestream velocities of 15 and 10 m/s are similar to the data measured at a freestream velocity of 22 m/s. Both curves show a local minimum pressure coefficient at an X/D of 0.75. However, the distribution is shifted downward with decreasing velocity. The decrease in static pressure coefficient with velocity is small (less than 1.5 percent) compared to the freestream velocity reduction (~ 54 percent).

There is a significant difference between the static pressure coefficient curves measured at freestream velocities of 6 and 3.5 m/s and those measured at higher velocities. These curves do not show the local minimum present in the other curves. Rather, the curves show a slight pressure rise near an X/D of 0.75 before increasing sharply near the cylinder.

Comparing these curves in the region upstream of the saddle point with the one obtained using potential flow theory, the experimental values of the static pressure coefficients are slightly lower in magnitude. The boundary layers developing on the four sides of the test section increase the freestream velocity in the test section relative to the reference position resulting in lower static pressures. The pressure coefficients upstream of the separation line have been corrected in Fig. 4 using the local boundary-layer displacement thickness determined from LDA measurements for U_0 = 15 m/s.

The pressure measured at the endwall/cylinder junction was near the freestream stagnation pressure. The parameter $(\mathrm{Re}_D)^{1/3}$ (D/δ^*) was varied from 2050 (U_0 = 22 m/s) to 960 (U_0 = 3.5 m/s). These values are consistent with the correlation presented previously, though the lower value is between the limits of the two regimes shown in Table 1.

Cylinder Surface Static Pressure. Cylinder surface static pressures measured in the plane of symmetry are shown in Fig. 5 for the six velocities tested. Since freestream flow stagnated at the endwall/cylinder junction for all conditions, the entire leading edge of the cylinder was covered with freestream flow. Consequently, the pressure distributions are nearly constant except for a decrease near the wall at approximately y = 15 mm. The local minimum pressure is associated with the presence of a small vortex at the junction between the cylinder and the endwall. Note that at the lower velocities, the local minimum is more significant indicative of a relatively stronger corner vortex. The pressure distributions on the cylinder at the other angular locations display trends similar to the results of Eckerle and Langston.

Velocity Measurements. Velocity components in the plane of symmetry are shown from X/D = 1.2 (100 mm upstream of the cylinder) to the cylinder leading edge between y = 0.25 and 59 mm. Data are presented in the form of velocity vector arrows with the arrow base located at the measurement point.

Figure 6 shows the velocity vectors measured at U_0 = 15 m/s. The trends displayed by these data are similar to the trends measured at U_0 = 22 and 10 m/s. Upstream of the saddle point, the velocity vector profiles look like those of a two-dimensional boundary layer. The velocity vectors indicate the presence of a horizontal reverse flow starting near the cylinder leading edge and vanishing near the saddle point. The reverse flow is confined to the lower 15 percent of the boundary layer. In the upper region of the viscous layer, the flow is horizontal and is in the same direction as the freestream flow. A fully developed vortex was not present between the forward and reverse flows. The velocity vectors along the cylinder leading edge show that freestream flow moved vertically downward toward a small vortex at the endwall/cylinder junction. This small vortex created the dip in the cylinder leading edge pressure profiles shown in Fig. 5. This flow pattern is also consistent with the high static pressure coefficient measured on the endwall close to the cylinder which is indicative of freestream stagnation.

The velocity vectors near the endwall are combined with the plane of symmetry pressure distribution and flow visualization in Fig. 7 for comparison. This combined plot indicates that the reverse flow accelerated away from the cylinder in the region with the high pressure gradient. Contrary to the assumption of some previous investigators, the location of the local minimum pressure does not correspond to the center of flow rotation. Rather, the local minimum is associated with the meeting of the incoming and reverse flows near the endwall.

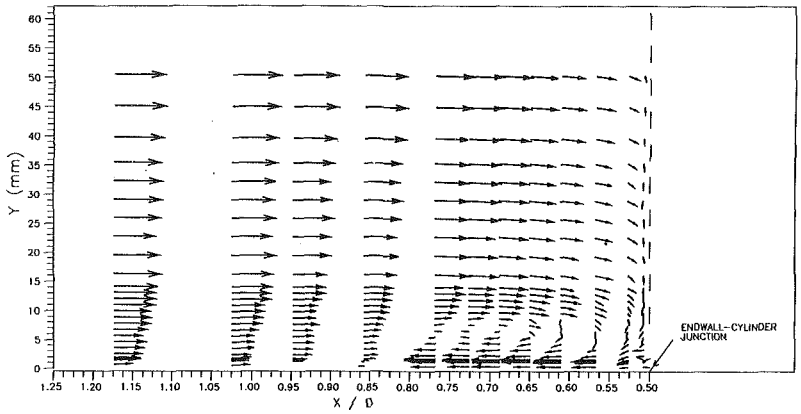

Fig. 6 Velocity vector plot at U_0 = 15 m/s

(Uncertainty in Y = ± 0.1 mm, in X/D = ± 0.0052. Uncertainty for mean velocity is 1.97 percent)

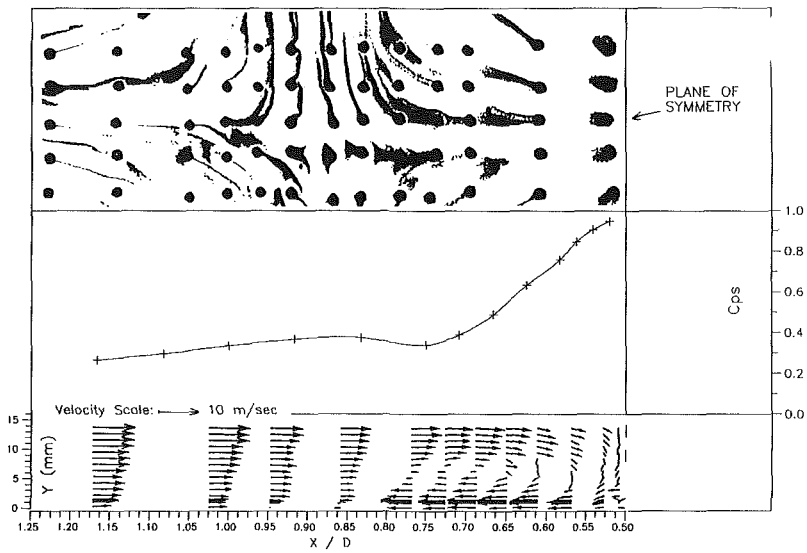

Fig. 7 Endwall streakline pattern, static pressure distribution, and velocity vectors near the endwall at U_0 = 15 m/s

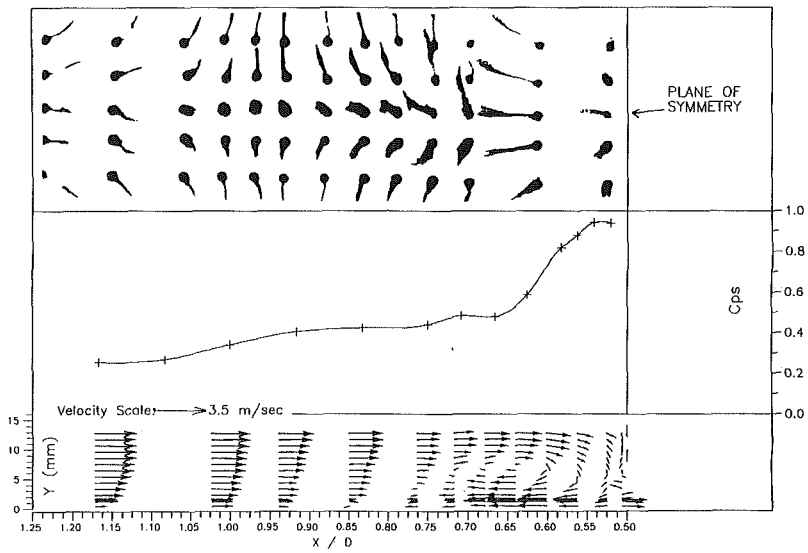

Fig. 8 Endwall streakline pattern, static pressure distribution, and velocity vectors near the endwall at U_0 = 3.5 m/s

The separation line between the forward and reverse flow is very shallow near the saddle point. Consequently, the reverse flow is eventually blocked by the incoming flow, creating an adverse pressure gradient to the reverse flow. The local minimum occurs because of the two opposing pressure gradients. The flow visualization indicates that the reverse flow started to turn tangentially and flow around the cylinder near this location.

The velocity vector plot for a freestream velocity of 6 m/s indicate a flow pattern similar to the pattern at the higher freestream velocities except for the region containing the circulating flow. The rudiments of a vortex are more apparent in the region between $Y=3$ and 8 mm. The velocity vectors near the center of the vortex were staggered, indicating that the vortex may have been unstable.

Figure 8 shows the combined plot at $U_0 = 3.5$ m/s. At this velocity, a fully developed vortex can be more clearly identified. The vortex center corresponds with the location of the center of the recirculating flow measured at the higher velocities. The axial location of the vortex center is slightly closer to the cylinder relative to the location where the endwall static pressure distribution starts to level out in the reverse flow region. This again indicates that the pressure field at the endwall reflects the local flow near the endwall and cannot be used to infer the internal flow field. Since some of the reverse flow rolled up into the vortex, the local minimum in the endwall pressure distribution created by the interaction of the incoming and reverse flows at the higher velocities is not present. The velocity magnitudes within the small vortex at the endwall/cylinder junction were larger at $U_0 = 3.5$ m/s than at the other freestream velocities.

The relative strength of the recirculating flow at each approach velocity was quantified by calculating the circulation, Γ, in the region bounded by $0.566 \leq X/D \leq 0.743$ and 2 mm $\leq Y \leq 8$ mm. The calculated circulation, normalized by the nominal approaching boundary layer thicknesses of 3.8 cm and U_0, is shown in Table 3 for each of the approach velocities. These results show that the normalized circulation is stronger at the lower velocities, which is consistent with the flow pattern where a fully formed vortex was only measured at the lower velocities.

The vector plots indicate that two different flow regimes were established over the velocity range tested. The parameter $(\mathrm{Re}_D)^{1/3}$ (D/δ^*) can be used to correlate the flow regimes. Referring to Table 2, a fully formed vortex was not measured in the plane of symmetry for $(\mathrm{Re}_D)^{1/3}$ $(D/\delta^*) > 1360$ ($U_0 >$ 10 m/s). At $(\mathrm{Re}_D)^{1/3}(D/\delta^*) = 1150$ ($U_0 = 6$ m/s), the rudiments of a vortex were measured. At $(\mathrm{Re}_D)^{1/3}(D/\delta^*) = 960$ ($U_0 = 3.5$ m/s), a fully formed vortex was measured. These data are consistent with the work of Eckerle and Langston ($(\mathrm{Re}_D)^{1/3}(D/\delta^*) = 5311$ and no vortex formed) and Pierce et al. ($(\mathrm{Re}_D)^{1/3}(D/\delta^*) = 673$ and a fully formed vortex present in the plane of symmetry). These results indicate, then, that a value of $(\mathrm{Re}_D)^{1/3}(D/\delta^*) = 1000$ approximately represents a critical value between the two-flow regimes.

The physical mechanism determining whether a vortex forms in the plane of symmetry is the momentum of the reverse flow. The flow in the separation region is dominated by viscous forces. At a low approach velocity, the resultant reverse flow momentum is reduced enough by the relatively higher viscous forces to allow a vortex to form in the plane of symmetry. At the higher freestream velocities, viscous dissipation in the reverse flow is not large enough to allow a vortex to be formed. The high momentum of the reverse flow carries it toward the separation line and away from the plane of symmetry instead of allowing the reverse flow to roll up into a vortex.

While the same mechanisms determine whether freestream stagnation occurs as demonstrated by the previous correlation, freestream stagnation does not correlate vortex formation in the plane of symmetry. Freestream stagnation was measured in all cases, while a vortex was formed in the plane of symmetry at the low velocity condition. This is further evidence of the difficulty associated with inferring interior flow conditions in the separation region from surface measurements.

Table 3 Circulation analysis results. (Uncertainty in $U_0 = \pm 0.176$ m/s, in $\Gamma/U_0\delta = \pm 0.000372$.)

U_0 (m/s)	$\Gamma/U_0\delta$
3.5	0.0278
6	0.0217
10	0.0172
15	0.0089

Turbulence Intensities. Axial and vertical rms velocities and Reynolds stresses were measured in the plane of symmetry boundary layer upstream of the separation region at $X/D = 1.22$ as a reference for data measured in the separation region. The distributions are typical for a two-dimensional boundary layer formed from a freestream with low turbulence. The axial turbulence intensities are larger and match the measurements of Klebanoff (1955).

A detailed description of the turbulence measurements in the separation region is presented by Awad (1989). A portion of the data that indicates the main conclusions is presented here. Vertical turbulence intensities for a freestream velocity of 3.5 m/s are presented in Fig. 9. Data are shown starting at 1 mm from the endwall. The vertical fluctuating velocities peaked at $X/D = 0.64$ for all of the approach velocities. When a vortex was formed at $U_0 = 3.5$ m/s, v'/U_0 peaked in the vortex core. Only a small peak was measured at the higher velocities with no vortex present. Along the face of the cylinder ($X/D = 0.5002$) where the mean direction of the flow was vertically down along the cylinder leading edge, the values of v' are higher than u'. A large vertical turbulence intensity was measured at $Y = 2$ mm near the cylinder due to the vortex at the endwall/cylinder junction. This peak was not measured at the higher velocities where the small vortex was relatively less intense.

Reynolds shear stresses are shown in Fig. 10 for $U_0 = 3.5$ m/s. The stress distribution shows two sharp peaks around the vortex core at $X/D = 0.64$ which are not present at the higher velocities. Significant variations in the stress values were measured upstream of the vortex at $X/D = 0.74$ where the incoming and reverse flow interacted. The shear stress distribution fluctuations from positive to negative values in the separation region existed for all velocities. This indicates that the Boussinesq approximation of eddy viscosity for a shear flow, which states that the cross moments are proportional to the rate of change of the velocity with respect to Y, is not applicable to this region.

Summary and Conclusions

A horseshoe vortex system was generated by blocking an endwall turbulent boundary layer with a cylinder. The separation in front of cylinder depended on the momentum of the reverse flow in the separation region. This momentum is related to the approaching freestream velocity and boundary-layer thickness. Two types of separation were identified, for the nearly constant boundary layer thickness of this experiment. At high incoming freestream velocities, a vortex was not formed in the plane of symmetry. The high momentum of the reverse flow near the plane of symmetry carried it toward the saddle point and then around the cylinder. Peak turbulence was measured where the reverse flow and the incoming flow interacted. At relatively low incoming freestream velocities, the reverse flow did roll up into a vortex in the plane of symmetry. Peak turbulence was measured in the vicinity of the vortex center. The small vortex at the endwall/cylinder junction was stronger for this flow regime. The nondimensional parameter,

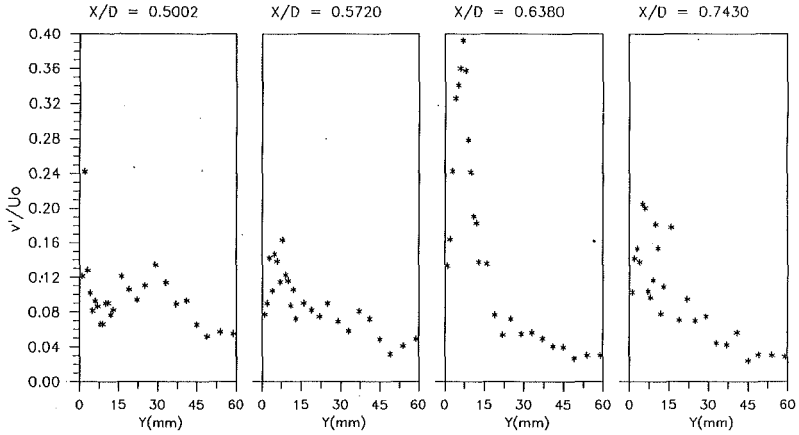

Fig. 9 Vertical turbulence intensities at U_0 = 3.5 m/s

(Uncertainty in v'/U_0 is 5 percent, in Y = ± 0.1 mm)

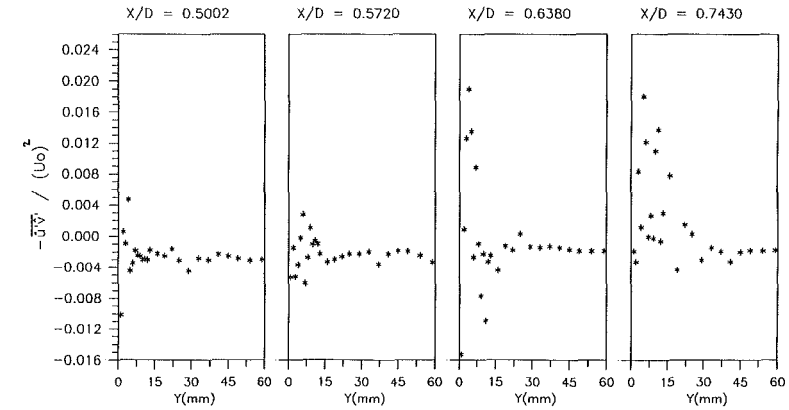

Fig. 10 Turbulence shear stresses at U_0 = 3.5 m/s

(Uncertainty in $(\overline{u'v'}/U_0^2)$ is 13.2 percent, in Y = ± 0.1 mm.)

$(\mathrm{Re}_D)^{1/3}(D/\delta^*)$, correlates the results of this experiment and two other cases in the literature. A vortex was not created in the plane of symmetry for values of this parameter greater than approximately 1000. A fully formed vortex was measured in the plane of symmetry in tests corresponding to lower values of this parameter. These different flow regimes are expected to have different effects on the heat transfer and effectiveness of a coolant film in this region.

Acknowledgments

The authors gratefully acknowledge the National Science Foundation for funding this research. We would also like to thank Prof. G. Ahmadi for his assistance.

References

Awad, J. K., 1989, "Cooling of the Endwall Region Upstream of a Cylinder," Ph.D. thesis, Clarkson University, Potsdam, NY.

Baker, C. J., 1978, "Vortex Flow Around the Bases of Obstacles," Ph.D. thesis, University of Cambridge, Cambridge, England.

Blair, M. F., 1985, "Heat Transfer in the Vicinity of a Large-Scale Obstruction in a Turbulent Boundary," *AIAA Journal of Propulsion and Power*, Vol. 1, No. 2, pp. 158–160.

Burton, R. A., 1965, "A Simple Universal Velocity Profile Equation," Tech. Note, *AIAA Journal*, Vol. 3, No. 4, pp. 784–785.

Chima, R. V., and Yokota, J. W., 1988, "Numerical Analysis of Three-Dimensional Viscous Internal Flows," *First National Fluid Dynamics Congress*, Cincinnati, Ohio.

Eckerle, W. A., 1985, *Horseshoe Vortex Formation Around a Cylinder*, Ph.D. thesis, University of Connecticut, Storrs, CT.

Eckerle, W. A., and Langston, L. S., 1987, "Horseshoe Vortex Formation Around a Cylinder," ASME *Journal of Turbomachinery*, Vol. 109, pp. 278–285.

Klebanoff, P. S., 1955, "Characteristics of Turbulence in a Boundary Layer with Zero Pressure Gradient," NACA Rep. 1247.

Kline, S. J., and McClintock, F. A., 1953, "Describing Uncertainties in Single-Sample Experiments," *Mechanical Engineering*, pp. 3.

Kubendran, L. R., McMahon, H. M., and Hubbart, J. E., 1986, "Turbulent Flow Around a Wing/Fuselage-Type Juncture," *AIAA Journal*, Vol. 24, No. 9, pp. 1447–1452.

Lai, K. Y. M., and Makomaski, A. H., 1988, "Three-Dimensional Flow Pattern Upstream of a Surface-Mounted Rectangular Obstruction," ASME Gas Turbine and Aeroengine Congress and Exposition, Amsterdam, The Netherlands, No. 88-Gt-291.

Langston, L. S., and Boyle, M. T., 1982, "A New Surface-Streamline Flow-Visualization Technique," *Journal of Fluid Mechanics*, Vol. 125, pp. 53–57.

Merati, P., McMahon, H. H., and Yoo, K. M., 1988, "Experimental Modeling of a Turbulent Flow in the Junction and Wake of an Appendage Flat Plate," AIAA/ASME/SIAM/APS 1st National Fluid Dynamics Congress, Cincinnati, OH, Paper No. 88-3756-CP.

Moore, J., and Forlini, T. J., 1984, "A Horseshoe Vortex in a Duct," ASME *Journal of Engineering for Gas Turbines and Power*, Vol. 106, pp. 668–676.

Oguz, E. O., 1980, "An Experimental Investigation of the Turbulent Flow in the Junction of a Flat Plate and a Body of Constant Thickness," Ph.D. thesis, Georgia Institute of Technology, Atlanta, GA.

Patrick, W., 1985, "Error Analysis for Benchmark Fluid Dynamic Experiments, Part I: Error Analysis Methodology and the Quantification of Laser Velocimeter Error Sources," UTRC Report, R85-151772.

Pierce, F. J., Kim, C. M., and Harsh, M. D., 1987, "The Mean Flow Structure of a Turbulent Junction Vortex," *Virginia Polytechnic Institute and State University*, Rept. VPI-E-87-6, Blacksburg, Va.

Ram, V. V., 1963, "Untersuchungen uber die Eckengrenzschicht an einem Kreiszlyinder mit Seitenwand," Institute of Fluid Mechanics, Technische Hochschule, Republic of Germany, Report 63/46.

Wagner, C., 1989, "Computations of a Horseshoe Vortex Around an Endwall Mounted Cylinder," Ph.D. thesis, University of Connecticut, Storrs, CT.

White, F. M., 1974, *Fluid Mechanics*, McGraw-Hill, New York, pp. 400–403.

Wake Characteristics of Two Circular Cylinders Arranged Perpendicular to Each Other

T. A. Fox
Department of Civil Engineering,
University of Queensland,
St. Lucia, 4072
Australia

The turbulent fluid motion established in the wake of two long, smooth circular cylinders arranged perpendicular to each other has been investigated in a steady, low-turbulence, uniform flow at Reynolds numbers of 2×10^4 and 2×10^3 (based on cylinder diameter and freestream velocity). A complex three-dimensional regime was found at the center of the configuration, the precise nature of which is dependent upon the spacing of the cylinders. If the distance between the axis of each cylinder is less than three diameters, the fluid motion in the central near wake is dominated by secondary flows associated with trailing vortices and horseshoe vortices, whereas at spacings beyond this critical value there is a considerable reduction in the influence of secondary flow. The paper examines these spacing related regimes in detail and considers the extent of the associated interference effects.

1 Introduction

When a uniform flow is forced to pass around an obstruction composed of circular cylinders arranged perpendicular to each other, a turbulent three-dimensional flow field is created, the characteristics of which are of interest over a wide range of engineering applications. For example, such a configuration is often found in the grids used for turbulence control in wind tunnel studies, or in lattice frameworks exposed to a wind or marine environment, and may be utilised in thermal cooling devices and heat exchangers. However, despite the common occurrence of this geometry, the associated flow regimes have only received attention in a small number of recent studies.

Among these are investigations undertaken to examine the fluid motion induced by two circular cylinders which intersect in a single plane and form a cross geometry. In this case, Osaka et al. (1983a, b) have studied the structure of the turbulent wake and Zdravkovich (1985) has examined the corresponding surface flow patterns. Both of these authors found that the overall flow field created by a cross can be divided into two characteristic regions. These are: an outer region of flow conditions typical of a single cylinder, and an inner region of highly three-dimensional flow close to the center of the geometry. In the latter region the fluid motion is dominated by strong secondary flows which are present as a result of eight trailing vortices arranged symmetrically in the wake, that is, two in each quadrant of the configuration.

In addition, Zdravkovich (1983) has determined details of the airflow around two circular cylinders placed one behind the other to form a perpendicular geometry with a point of contact and Tomita et al. (1987) have considered the acoustic characteristics of such an arrangement. Although in this case the overall flow field can again be divided into an inner and outer region dependent upon the level of disturbance, Zdravkovich (1983) found the regime in the highly three-dimensional inner region to be somewhat different to that produced by the cross geometry. In this respect the fluid motion at the center of the configuration is dominated by a pair of horseshoe vortices, which are generated near the point of contact, in addition to four trailing vortices formed at the rear of the upstream cylinder.

This paper considers the effect upon the wake of the introduction of a gap at the center of the configuration for the case of perpendicular cylinders with axis spacings up to ten diameters. It reports the results of experiments carried out in a wind tunnel at a Reynolds number of 2×10^4, which involved extensive measurements of mean surface pressure and mean velocity components for the calculation of flow vorticity and turbulence intensity, and presents observations from a complementary flow visualization study performed in a water tunnel facility at a Reynolds number of 2×10^3.

2 Experimental Details

The experimental measurements were made in a low-speed, blow-down, open-circuit wind tunnel in the Department of Civil Engineering at the University of Surrey, United Kingdom. This has a working section of 1.067m width × 1.372m height × 9.0m length and produces a steady, uniform airflow with a freestream turbulence intensity less than 0.2 percent at the model testing station. Further details can be found in Savory and Toy (1984) and Fox and Toy (1988).

Two long, smooth, polished aluminum cylinders of 30 mm diameter formed the model and these completely spanned the working section in the vertical and horizontal directions. This arrangement ensured that large aspect ratios were achieved between the fixed ends of each cylinder (45 and 35 for the ver-

Contributed by the Fluids Engineering Division of THE AMERICAN SOCIETY OF MECHANICAL ENGINEERS for presentation at the Joint ASME-JSME Fluids Engineering Conference, Portland, Oregon, June 24-26, 1991. Manuscript received by the Fluids Engineering Division March 17, 1990.

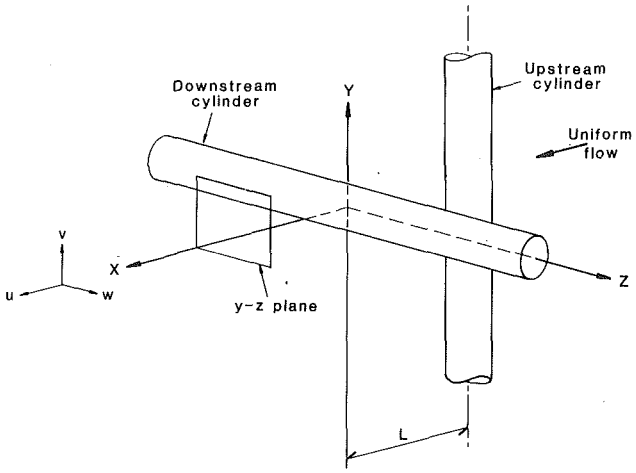

Fig. 1 Geometry of the perpendicular cylinders and the coordinate system

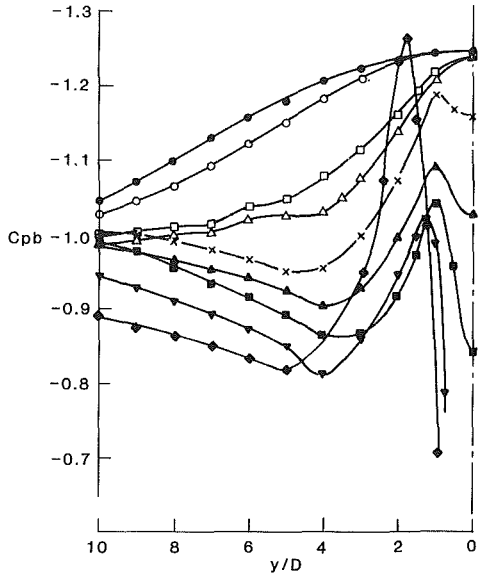

Fig. 2 Mean base pressure distributions measured on the upstream cylinder at a Reynolds number Re = 2 × 10⁴; ◆ L = 1D, ▼ L = 1.5D, ■ L = 2D, ▲ L = 2.5D, × L = 3D, △ L = 4D, □ L = 5D, ○ L = 10D, ● single cylinder. (Uncertainty in Cp = 1.5 percent and in y/D = ±0.017.)

tical and horizontal respectively), with low area blockage (2.8 and 2.2 percent), and it was therefore considered unnecessary to apply a correction factor to the experimental data. The vertical cylinder could be displaced to establish a gap at the center of the configuration, as shown in Fig. 1. The latter also gives the coordinate system based on the geometry and defines the spacing between the axis of each cylinder as L.

Mean surface pressure distributions were measured by the use of 0.5 mm (±0.02mm) diameter tappings connected to a low-pressure transducer via a Scanivalve switch mechanism. The latter was controlled by a microcomputer, which also performed data acquisition and on-line analysis as described by Savory and Toy (1984). The freestream reference pressure was obtained from a pitot-static tube positioned in the uniform flow. Values of the coefficient of mean pressure, C_p, with an uncertainty of 1.5 percent, were calculated from 30,000 samples at each location in accordance with the expression:

$$C_p = \frac{P_L - P_0}{0.5\,\rho U_0^2}$$

where P_L is the mean local surface pressure, P_0 is the freestream static pressure, and $0.5\rho U_0^2$ is the dynamic pressure of the freestream.

Velocity measurements were made with a pulsed-wire anemometer of the type described by Bradbury and Castro (1971), this being an appropriate instrument for use in highly turbulent flows. Data collection over the near wake were achieved by mounting the probe on a three-dimensional traversing system, which has a positional accuracy of ±0.02mm. On-line data acquisition and analysis was performed by the microcomputer, values of the normalised mean velocity components and turbulence intensities being calculated from 10,000 velocity samples taken at each measurement position. The uncertainty associated with the measurement of mean velocity was 1.0 percent.

In order to calculate the distribution of X-direction vorticity, ω_x, over related plans in the wake, it was necessary to obtain normalised mean velocity components; $\bar{u}/U_0$, $\bar{v}/U_0$, and $\bar{w}/U_0$. To achieve this, each two-dimensional traverse over the measurements plane was repeated five times with the probe at yaw angles of 0 and ±45 deg, and the data were reduced by the method of Cheun (1981). From these results an approximate differentiation of the mean velocity profiles was undertaken to give the X-direction vorticity:

$$\omega_x = \frac{\partial \bar{w}}{\partial y} - \frac{\partial \bar{v}}{\partial z}$$

Flow visualization was performed in a low-speed closed-circuit water tunnel in the Department of Civil Engineering at The University of Queensland, Australia. This is driven by a variable-speed axial flow impeller and has a 1.63m long working section of 331.5mm diameter. The velocity profile is uniform at the model testing station with a turbulence intensity less than 1 percent.

Nomenclature

C_p = mean pressure coefficient = $\frac{P_L - P_0}{0.5\,\rho U_0^2}$

C_{pb} = mean pressure coefficient measured on the base ($\theta = 180$ deg)

D = diameter of cylinder

L = distance between central axis of each cylinder

P_L = mean local pressure on cylinder's surface

P_0 = static pressure

Re = Reynolds number = DU_0/ν

U_0 = mean freestream velocity in the X-direction

u, v, w = instantaneous velocity components in the X, Y, and Z directions, respectively

$\bar{u}, \bar{v}, \bar{w}$ = mean velocity components in the X, Y, and Z directions, respectively

u', v', w' = velocity fluctuations in the X, Y, and Z directions, respectively

X = Cartesian coordinate in the longitudinal direction

Y = Cartesian coordinate in direction perpendicular to the wind tunnel floor

Z = Cartesian coordinate in lateral direction

θ = Azimuth angle from stagnation point

μ = dynamic viscosity of fluid

ν = kinematic viscosity of fluid

ρ = density of fluid

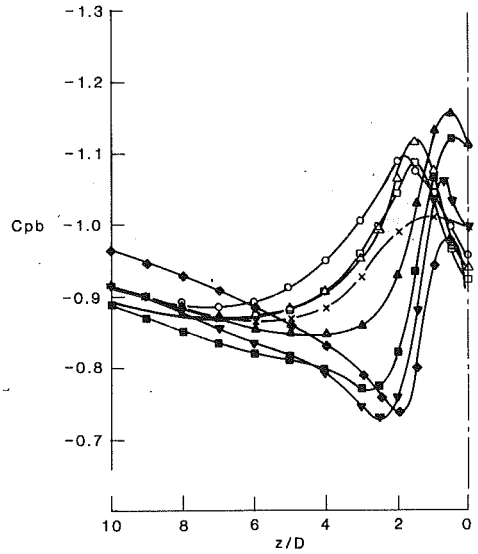

Fig. 3 Mean base pressure distributions measured on the downstream cylinder at a Reynolds number Re = 2 x 10^4; ♦ L = 1D, ▼ L = 1.5D, ■ L = 2D, ▲ L = 2.5D, × L = 3D, △ L = 4D, □ L = 5D, ○ L = 10D. (Uncertainty in Cp = 1.5 percent and in z/D = ±0.017.)

A pair of smooth, polished brass cylinders of 16mm diameter formed the model geometry used in the visualization experiments and these completely spanned the working section in the vertical and horizontal directions. The vertical cylinder could be displaced to give a maximum distance between the axis of each cylinder of five diameters. Flow visualization was achieved by the injection of dye through 1.0mm diameter holes drilled in a fixed configuration on the model's surface. A permanent record of visual observations was obtained by photography using 500 Watt studio lighting and 400ASA Kodak Tri-X pan black and white print film.

3 Discussion of Results

3.1 Surface Pressure Measurements. Surface pressure measurements were made in the wind tunnel for a range of cylinder spacings from the point of contact case, $L = 1$D, to a distance between cylinder axes of ten diameters, $L = 10$D, at a Reynolds number of 2×10^4. The latter, which is in the upper subcritical range associated with a single circular cylinder, was chosen for its practical significance and compatibility with previous work in this field.

The distributions of mean pressure measured on the base ($\theta = 180$ deg) of the upstream cylinder over half of the span (symmetry about the mid-span is assumed) are presented in Fig. 2 in terms of the mean base pressure coefficient, *Cpb*. These can be divided into two spacing related groups of $L \leq 3$D and $L > 3$D, with the $L = 1$D distribution as a unique case. The latter exhibits an inner region of interference effects characterised by a strong peak in suction located adjacent to the center of the span, at $y = 1.75$D, and associated pressure gradients which are indicative of strong secondary flows at the rear surface of the cylinder. Indeed, such flows were identified in oil film visualization experiments performed by Zdravkovich (1983) on the surface of two similar cylinders forming the point of contact geometry ($L = 1$D) and were found to be associated with the existence of intense trailing vortices on either side of the base line.

A distinct peak in suction indicative of the presence of similar trailing vortices is evident in the group of distributions recorded for axis spacings in the range: $L \leq 3$D, Fig. 2. However, in this case the pressure gradients are weaker than those recorded when $L = 1$D and the suction peak is located closer to the center of the span, at $y = 1$D. This suggests a

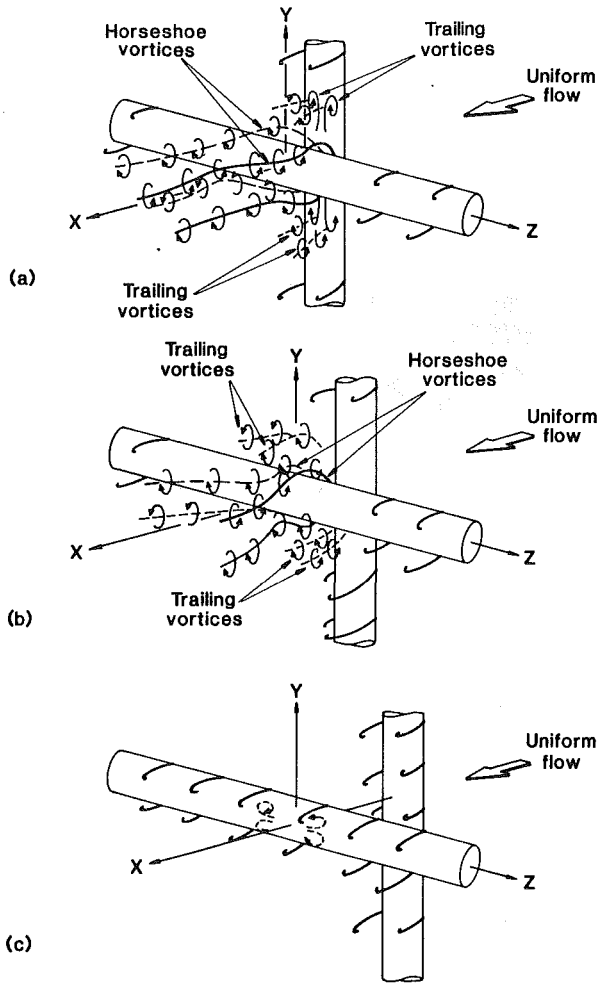

Fig. 4 Sketch of the flow regime in the near wake of the perpendicular cylinders; (*a*) with a point of contact at the center of the geometry L = 1D, (*b*) with axes spacings in the range 1D < L < 3D, (*c*) with axes spacings in the range L > 3D.

change in the mechanism of trailing vortex generation and a reduction in the spanwise extent of the associated interference region. Indeed, Fig. 2 shows that when $L \leq 3$D the inner region of highly disturbed flow generally extends to within four diameters of the center of the configuration, $y < 4D$, compared with five diameters in the case of $L = 1D$, and that beyond this the value of *Cpb* tends toward that measured at an equivalent location on a single cylinder.

As the distance separating the axis of each cylinder is increased towards the critical value of three diameters, $L = 3$D, the pressure gradients indicate a reduction in secondary flow in the disturbed inner region, until eventually, when $L > 3$D, the peak suction associated with the trailing vortices is no longer evident. With increased spacing in this second range the pressure distributions tend towards that recorded on the single cylinder (it should, however, be noted that the latter exhibits some degree of spanwise non-uniformity due to the fact that the cylinders were not fitted with end plates).

Strong secondary flows associated with a highly disturbed inner region are also evident in the spanwise distributions of base pressure recorded on the surface of the downstream cylinder, Fig. 3, and these can again be divided into two main groups. At spacings in the range $L < 3$D, the distributions exhibit a peak in suction adjacent to the center of the geometry which appears to be similar to that recorded on the upstream cylinder at corresponding spacings. However, in this case the position of the peak is much closer to the center of the span

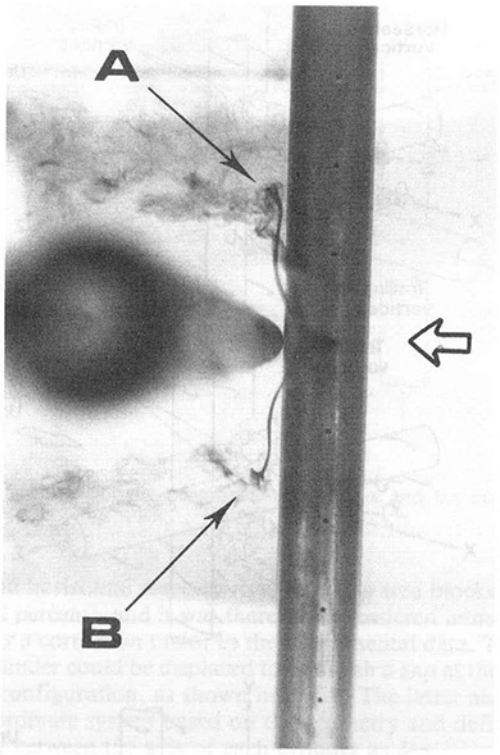

Fig. 5 Two of the trailing vortices generated in the wake of the upstream cylinder at the center of the configuration when the cylinders form a point of contact, L = 1D, Re = 2 x 10^3

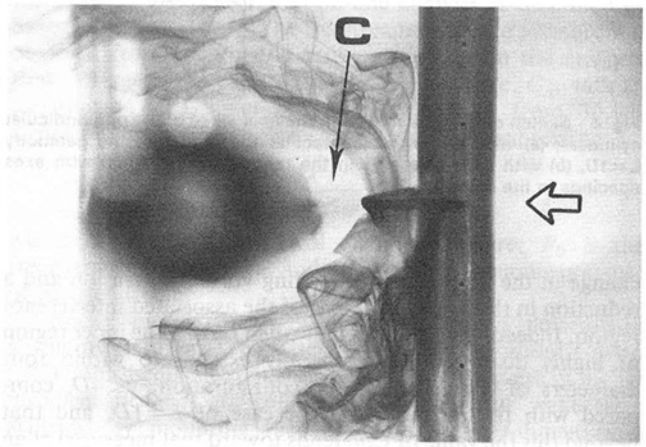

Fig. 6 The generation of vorticity from the center of the configuration when the cylinder axes are two diameters apart, L = 2D, Re = 2 x 10^3

and, therefore, the inner region of highly disturbed conditions is reduced in spanwise extent to approximately $z < 3D$.

Zdravkovich (1983) also found the inner region of gross interference to the flow conditions around the downstream member of the cylinders in contact configuration ($L = 1D$) to be restricted to a shorter portion of the span. In the latter case, oil film visualization of the surface flow patterns revealed this apparent reduction in the extent of the interference effects to be due to the presence of secondary circulations which are somewhat different to those found at the surface of the upstream cylinder. In this respect two horseshoe vortices are generated, one from each side of the point of contact, and these converge in the immediate wake of the downstream cylinder. The pressure distributions presented in Fig. 3 suggest that such a mechanism continues for axis spacings up to a critical value of three diameters.

When the distance between the axes is in excess of three

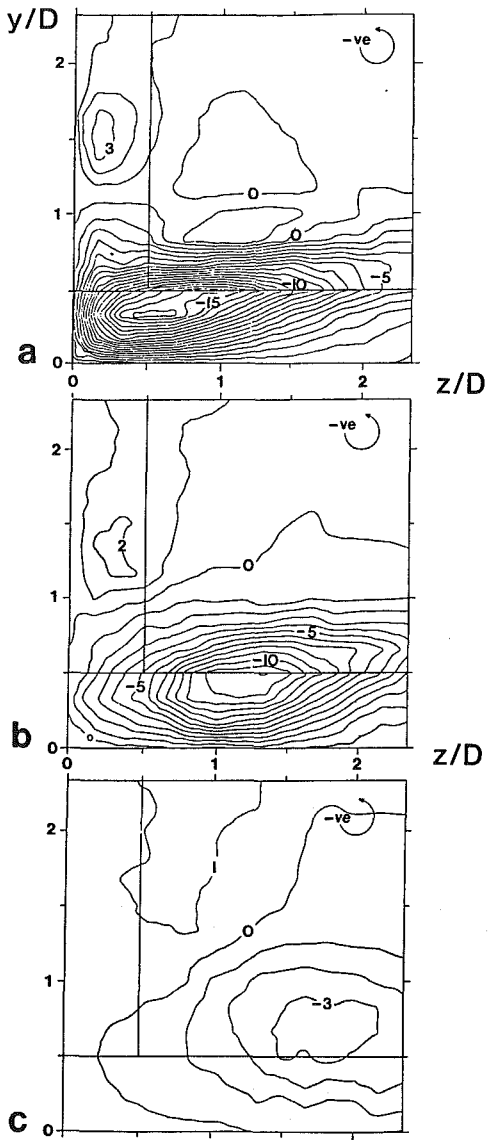

Fig. 7 Distribution of X-direction vorticity in the central near wake of the perpendicular cylinders when L = 2D, Re = 2 x 10^4; (a)x = 1D, (b)x = 2D, (c)x = 4D (Contours = $10D\omega_x/U_0$ with an uncertainty of 10 percent. Uncertainty in y/D and z/D = ±0.0007.)

diameters, $L > 3D$, the distributions in Fig. 3 exhibit a suction peak which is further from the center of the span. In this respect these distributions resemble that recorded on the upstream cylinder when $L = 1D$ and are, as such, indicative of secondary flows feeding a trailing vortex mechanism at $z = 2D$. Figure 3 shows that this regime gives rise to an inner region of interference effects extending as far as $z = 7D$, which persists over the range of cylinder spacings examined (up to ten diameters).

3.2 Flow Visualization. The spacing related secondary flows identified in the surface pressure measurements of Section 3.1 were investigated further through visualization experiments performed in the water tunnel at a comparable Reynolds number of 2×10^3. Figure 4 presents the principal observations in sketch form. When the configuration composed of two cylinders in contact ($L = 1D$) was examined, Fig. 4(*a*), the central near wake was seen to be dominated by four trailing vortices generated at the surface of the upstream cylinder, one in each quadrant of the geometry, and a pair of horseshoe vortices which develop around the center of the downstream cylinder. Periodic vortex shedding, similar to that

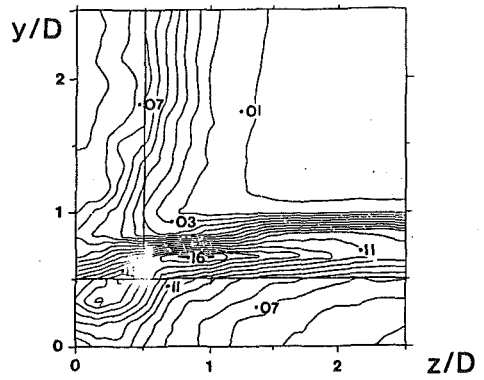

Fig. 8 Distribution of turbulence intensity at $x = 1D$ in the central near wake of the perpendicular cylinders when $L = 2D$, $Re = 2 \times 10^4$ (Contours = $\overline{u'^2}/U_0^2$ with an uncertainty of 1 percent. Uncertainty in other parameters the same as for Fig. 7.)

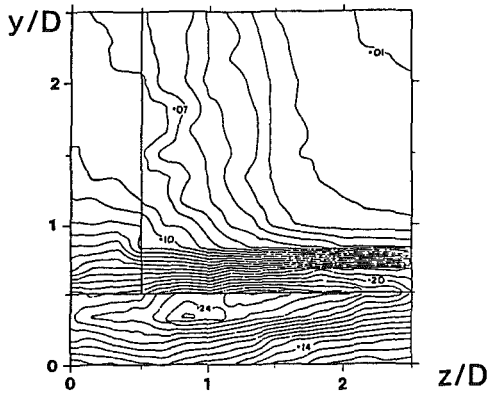

Fig. 9 Distribution of turbulence intensity at $x = 1D$ in the central near wake of the perpendicular cylinders when $L = 3D$, $Re = 2 \times 10^4$. (Uncertainty in all parameters the same as for Fig. 8.)

associated with a single cylinder, was observed in the wake of both the upstream and downstream cylinders at spanwise locations in the outer region away from the center of the geometry. This is consistent with the surface pressure measurements described in Section 3.1 and the results of hot-wire anemometer measurements made by Zdravkovich (1983) in the near wake of a similar configuration. In the latter work, a strong output signal associated with periodic vortex shedding was recorded at all spanwise locations in the wake of the upstream cylinder, except in close proximity to the trailing vortices. Similarly, a traverse in the wake of the downstream cylinder revealed that periodic vortex shedding dominates the fluid motion at spanwise locations away from the horseshoe vortices.

Two of the trailing vortices sketched in Fig. 4(*a*) are shown in Fig. 5. The vortices are marked by arrows A and B, respectively, and are located at a spanwise position approximately centered on $|y| = 1.75D$, which is consistent with the suction peak recorded in the associated pressure distribution of Fig. 2. This implies that changes of Reynolds number in the subcritical regime have little effect on the position of this secondary flow structure. Further, Fig. 5 clearly shows that the trailing vortices are sustained by a ventilation of fluid away from the mid-span of the upstream cylinder, which is in agreement with the pressure gradient recorded on the surface (Fig. 2) and, as such, corroborates the mechanism identified in the oil film visualization experiments performed by Zdravkovich (1983).

Figure 4(*b*) summarizes the flow regime observed in the wake of configurations with axis spacings below the critical value of three diameters ($1D < L < 3D$). In this range the central near wake is again dominated by four trailing vortices and a pair of horseshoe vortices, with periodic vortex shedding in an outer region. However, the mechanism of trailing vortex generation is, as suggested in Section 3.1, somewhat different to that associated with the cylinders in contact case. In this respect observation of the vortices revealed them to be the result of a movement of circulating fluid away from the gap between the cylinders at the center of the configuration.

Fox (1990) and Fox and Toy (1988) have clearly shown that the flow regime in the gap is dominated by two recirculation 'cells' which form in the x-z plane when the spacing is below the critical value of three diameters. It was observed that the vorticity associated with each of these cells moves away from the center of the configuration in the Y-direction, as shown by the dye movement in Fig. 6, is forced over the downstream cylinder by the primary flow in the direction of the freestream, and results in the trailing vortices sketched in Fig. 4(*b*). This mechanism is consistent with the suction peaks and pressure gradients recorded in the associated pressure distributions of Fig. 2.

The horseshoe vortex regime which forms around the downstream cylinder is also evident in Fig. 6 as a dye-free area marked by arrow C. This is in sharp contrast to the intense dye concentration associated with the trailing vortices and therefore shows that the horseshoe vortex structures are sustained by fluid from outside of the recirculation cells formed at the center of the configuration.

When the spacing between the axis of each cylinder is three diameters, the flow regime in the wake of the configuration was observed to change significantly, Fig. 4(*c*). The horseshoe vortices are replaced by weak secondary flows, which no longer dominate the central near wake, and the conditions around the upstream cylinder become similar to those associated with the single cylinder. Indeed, Fox (1990) has clearly shown that periodic vortex shedding dominates the wake at the mid-span of both cylinders when $L > 3D$ and that the weak secondary circulations are confined within the vortex formation region of the downstream cylinder.

3.3 Wake Measurements. In Section 3.2 it was shown that complex, spacing related secondary flows occur in the central near wake of two circular cylinders arranged perpendicular to each other. Further investigation of these flows was undertaken in the wind tunnel. Measurements were made of the distribution of vorticity and u-component turbulence intensity over y-z planes (see Fig. 1) covering one quadrant of the geometry and defined within the limits; $y \leq 2.5D$, $z \leq 2.5D$, symmetry being assumed in the wake.

The distribution of secondary vorticity in the near wake of the configuration with an axis spacing of two diameters, $L = 2D$, is presented in Fig. 7. The result shows that in the immediate wake, at $x = 1D$, Fig. 7(*a*), two dominant areas of vorticity are present which correspond to the principal features identified in the flow visualization experiments (as illustrated in Fig. 4(*b*)). In this respect, the intense circulation with its center at $z/D \approx 0.5$, $y/D \approx 0.25$ is associated with an arm of one of the horseshoe vortices, and the weaker circulation centered on $z/D \approx 0.25$, $y/D \approx 1.5$ corresponds to a trailing vortex. The latter decays rapidly in the streamwise direction, as shown by Figs. 7(*b*) and (*c*), the vorticity of this feature being negligible by four diameters downstream of the geometry. This suggests that the vortices are much weaker than those associated with intersecting perpendicular cylinders which Osaka et al. (1983a) have shown to be detectable in the far wake at $x = 30.5D$.

In the case of the significantly stronger horseshoe vortex, the location of the center of vorticity in the y-z plane at $x = 1D$, Fig. 7(*a*), coincides with the position of the suction peak recorded at $z/D = 0.5$ on the base centerline of the

downstream cylinder, Fig. 3, and the direction of the circulation is compatible with the associated pressure gradients. However, Figs. 7(*b*) and (*c*) show that this center of maximum vorticity moves laterally away from the center of the configuration in the near wake, it being located at $z/D \approx 1.75$, $y/D \approx 0.7$ by $x = 4D$. In addition the vortex is seen to decay rapidly during this migration, the maximum vorticity recorded at $x = 4D$ being only 20 percent of that found in the immediate wake at $x = 1D$, and it is therefore suggested that the horseshoe vortex structure does not persist into the far wake.

The effect of this secondary flow regime upon the distribution of longitudinal turbulence intensity, $\overline{u'^2}/U_0^2$, in the near wake of the cylinders can be assessed through Fig. 8. The general contour pattern in the quadrant is influenced to a large degree by the perpendicular arrangement of the cylinders and, in respect of this, the result is similar to that found by Osaka et al. (1983, b) in the wake of intersecting cylinders forming a cross. Indeed, the latter investigation revealed a cross pattern in the turbulence intensities measured in the wake at $x = 30.5D$, with a maximum intensity at the center of the distribution.

In the case of the $L = 2D$ configuration, Fig. 8 shows the peak intensity recorded to be located close to the center of the configuration and, as such, coincident with the position of the horseshoe vortex. However, the contours in the region $z/D > 1$ are parallel to the axis of the downstream cylinder and are indicative of the mean position of the free shear layer separated from that member. This confirms visual observation that a vortex shedding process dominates the wake in this region despite the presence of secondary flow. Indeed, Zdravkovich (1983) recorded a Strouhal number compatible with periodic vortex shedding at a similar location in the near wake of the downstream member of two cylinders forming the point of contact geometry ($L = 1D$). In the latter work, evidence of periodic vortex shedding was found at all spanwise locations except in close proximity to the center of the configuration, where the horseshoe vortex regime suppresses the process.

It was shown in Section 3.2 that at an axis spacing of $L = 3D$ a reduction in the influence of the secondary flow field upon the streamwise conditions in the near wake allows periodic vortex shedding to occur at the center of the downstream span. This change in the flow regime is particularly evident in the distribution of longitudinal turbulence intensity presented in Fig. 9. In this respect, the influence of the perpendicular geometry on the turbulence field is considerably reduced and, instead, the effect of the downstream cylinder dominates the contour pattern. Indeed, the secondary circulation has little effect on the behavior of the free shear layer in the immediate wake and the intensities recorded in the region $y < 0.5D$ are of an order to be expected in a vortex formation region.

4 Conclusions

The results of an extensive experimental investigation have provided details of the near wake characteristics associated with two long, smooth circular cylinders arranged perpendicular to each other in a uniform, low-turbulence flow. It was found that at a Reynolds number in the subcritical range two fundamental spacing related flow regimes are possible.

If the distance between the axis of each cylinder is less than three diameters, the central near wake of the configuration is dominated by four trailing vortices, one in each quadrant of the geometry, and a pair of horseshoe vortices generated around the downstream cylinder. Although these secondary circulations decay rapidly in the direction of the mainstream, they have a considerable influence on the motion of fluid immediately behind the cylinders and are responsible for a suppression of periodic vortex shedding at the mid-span. By contrast, at spanwise locations away from this inner region of highly three-dimensional flow, the wake is dominated by conditions typical of a single cylinder in uniform flow.

If the axis spacing is three diameters or above, there is a significant reduction in the influence of secondary flow in the wake of the configuration. In this respect the four trailing vortices are no longer generated and the horseshoe vortex regime is replaced by weak circulations which are not strong enough to dominate the wake. Indeed, over the range of spacings examined (up to 10 diameters), the wake structure of each cylinder is dominated by periodic vortex shedding and tends towards single cylinder conditions with increased distance between the axes.

Acknowledgment

The author is a Postdoctoral Research Fellow funded by The University of Queensland, and is grateful for this support. The supervision of Dr. N. Toy of the University of Surrey is acknowledged with regard to the wind tunnel investigation which was supported through an S.E.R.C. Studentship.

References

Bradbury, L. J. S., and Castro, I. P., 1971, "A Pulsed Wire Technique for Velocity Measurements in Highly Turbulent Flows," *Journal of Fluid Mechanics*, Vol. 49, pp. 657–691.

Cheun, B. S., 1981, "Separated Shear Layers Behind Two-Dimensional Square-Edged Bodies," Ph.D. thesis, University of Surrey.

Fox, T. A., 1990, "Flow Visualization at the Center of a Cross Composed of Tubes," *International Journal of Heat and Fluid Flow*, Vol. 11, pp. 160–162.

Fox, T. A., and Toy, N., 1988, "Fluid Flow at the Center of a Cross Composed of Tubes," *International Journal of Heat and Fluid Flow*, Vol. 9, pp. 53–61.

Osaka, H., Nakamura, I., Yamada, H., Kuwata, Y., and Kageyama, Y., 1983a, "The Structure of a Turbulent Wake Behind a Cruciform Circular Cylinder, 1st Report: the Mean Velocity Field," *Bulletin of the Japanese Society of Mechanical Engineers*, Vol. 26, pp. 356–363.

Osaka, H., Yamada, H., Nakamura, I., Kuwata, Y., and Kageyama, Y., 1983b, "The Structure of a Turbulent Wake Behind a Cruciform Circular Cylinder, 2nd Report: the Streamwise Development of Turbulent Flow Fields," *Bulletin of the Japanese Society of Mechanical Engineers*, Vol. 26, pp. 521–528.

Savory, E., and Toy, N., 1984, "Microcomputer Control of Wind Tunnel Instrumentation with On-Line Data Acquisition and Analysis," *Software and Microsystems*, Vol. 3, pp. 93–97.

Tomita, Y., Inagaki, S., Suzuki, S., and Muramatsu, H., 1987, "Acoustic Characteristics of Two Circular Cylinders Forming a Cross in Uniform Flow," *J.S.M.E. International Journal*, Vol. 30, pp. 1069–1079.

Zdravkovich, M. M., 1983, "Interference Between Two Circular Cylinders Forming a Cross," *Journal of Fluid Mechanics*, Vol. 128, pp. 231–246.

Zdravkovich, M. M., 1985, "Flow Around Two Intersecting Circular Cylinders," ASME JOURNAL OF FLUIDS ENGINEERING, Vol. 107, pp. 507–511.

Turbulent Flow Around a Bluff Rectangular Plate. Part I: Experimental Investigation

N. Djilali

Assistant Professor,
Department of Mechanical Engineering,
University of Victoria,
Victoria, Canada V8W 3P6

I. S. Gartshore

Professor,
Department of Mechanical Engineering,
University of British Columbia,
Vancouver, Canada V6T1W5

Measurements are reported for the separated reattaching flow around a long rectangular plate placed at zero incidence in a low-turbulence stream. This laboratory configuration, chosen for its geometric simplicity, exhibits all of the important features of two-dimensional flow separation with reattachment. Conventional hot-wire anemometry, pulsed-wire anemometry and pulsed-wire surface shear stress probes were used to measure the mean and fluctuating flow field at a Reynolds number, based on plate thickness, of 5×10^4. *The separated shear layer appears to behave like a conventional mixing layer over the first half of the separation bubble, where it exhibits an approximately constant growth rate and a linear variation of characteristic frequencies and integral timescales. The characteristics of the shear layer in the second half of the bubble are radically altered by the unsteady reattachment process. Much higher turbulent intensities and lower growth rates are encountered there, and, in agreement with other reattaching flow studies, a low frequency motion can be detected.*

1 Introduction

Separated-reattaching flows, typical of flows around bluff bodies, occur in a large variety of environmental and engineering situations. The recirculating flow regions—known as separation bubbles—encountered in these flows have a significant impact on the performance of, for example, airfoils at higher angles of attack, turbine blades, diffusers, heat exchangers and combustors. Separated flows determine, to a large extent, the drag of road vehicles and are the dominant feature of atmospheric flows over buildings, fences and hills. They are also a critical factor in the design of structures, such as bridges, which are susceptible to potentially disastrous wind induced oscillations.

In the last decade, experimental research in separated-reattaching flows has been greatly stimulated by the development of instruments suitable for measurements in recirculating flows, especially the laser-Doppler and pulsed-wire anemometers. General reviews of the literature have been undertaken by Bradshaw and Wong (1972) for earlier experimental work, and by Westphal et al. (1984) and Simpson (1981; 1985) for more recent developments. The last reference is a comprehensive survey of measurement techniques, experimental studies, as well as calculation methods.

In an effort to isolate those flow features of fundamental importance, a number of laboratory geometries have been devised to generate two-dimensional separated reattaching flows. Some of these geometries are shown in Figure 1. The flow around the blunt rectangular section (Fig. 1) is one of the simplest two-dimensional recirculating flows, yet it exhibits all the salient features of separated reattaching flows. It also combines several of the advantages of the other geometries: fixed separation point, single primary recirculation zone and, due to the strong favorable pressure gradient on the front face, an extremely thin separating shear layer compared with the overall scale of the separation bubble. Further, the typical bluff body shape and the simple upstream boundary conditions make this flow an "ideal" test case for numerical methods.

One of the earliest studies of the flow past a blunt rectangular section is due to Roshko and Lau (1965), who also considered, in the same paper, the flow around various forebody shapes with splitter plates. The main focus of their study was the pressure recovery process in reattaching flows. An important finding of Roshko and Lau was that, for all cases considered, the pressure distributions collapsed to a single curve when the pressure was normalized by the pressure at separation and the streamwise distance was normalized by the reattachment length. This suggested that some features of separated-reattaching flows are universal, and that the reattachment length is an important characteristic length scale of these flows.

Ota and co-workers (Ota and Kon, 1974; Ota and Itasaka, 1976; Ota and Narita, 1978; Ota and Motegi, 1983) performed extensive measurements on the bluff plate geometry. While these measurements give a good description of the gross features of the flow, their accuracy is dubious because the mean and fluctuating velocities were measured using a Pitot tube and a hot-wire anemometer respectively. Both techniques are known to be unreliable in this kind of flow. Additionally, important three-dimensional effects are likely to have been present as a result of the low aspect ratio (tunnel width/plate thickness $AR = 5$).

Contributed by the Fluids Engineering Division of THE AMERICAN SOCIETY OF MECHANICAL ENGINEERS and presented at the Fluids Engineering Conference, Toronto, Canada, June 1990. Manuscript received by the Fluids Engineering Division August 8, 1989. Paper No. 90-FE-4.

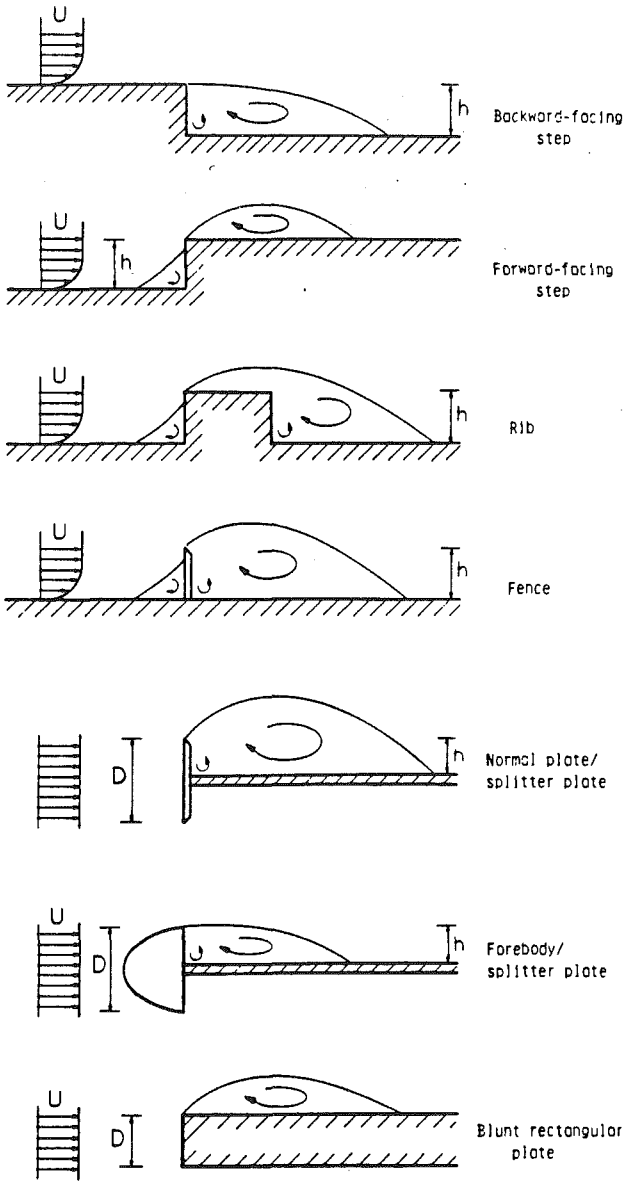

Fig. 1(*a-g*) Configurations which exhibit two-dimensional flow separation with reattachment

Extending an earlier study (Kiya et al., 1982) where conventional hot-wire anemometry was used, Kiya and Sasaki (1983a) reported on a comprehensive set of measurements in which directionally sensitive split-film sensors were used in conjunction with hot-wire anemometry. Mean and fluctuating velocities and forward flow fraction data were presented. Important aspects of the unsteady nature of the flow were also reported in this paper and are reviewed later.

The effect of Reynolds number was investigated by Ota et al. (1981) who also considered the effect of separation angle. Using flow visualization (with aluminium powder), they observed three flow régimes: (i) the laminar separation-laminar reattachment régime in which, in agreement with the observations of Lane and Loehrke (1980), the reattachment length increases with Reynolds number; (ii) the laminar separation-turbulent reattachment régime characterized by the appearance of instabilities in the shear layer near separation and transition to turbulence before reattachment; (iii) the turbulent separation-turbulent reattachment régime ($Re \gtrsim 2 \times 10^4$) where the separated shear layer becomes turbulent very soon after separation. The Reynolds number was found to have no effect on the reattachment length in this last flow régime.

The Reynolds-number-independent régime was also observed by Hillier and Cherry (1981a). They noted that the flow is essentially Reynolds number independent in the range $3.4 \times 10^4 < Re < 8.0 \times 10^4$, with a weak elongation appearing only when $Re \geq 8.0 \times 10^4$. In the same paper, Hillier and Cherry showed that the flow is very sensitive to grid-generated freestream-turbulence levels. For example, a shortening of the bubble from 4.88D to 2.72D was reported when the freestream turbulence intensity was increased from about 1.0 percent to 6.5 percent. The effect of freestream turbulence was also investigated by Kiya and Sasaki (1983b). They used a rod upstream of the plate to generate the turbulence and obtained results similar to those of Hillier and Cherry. Dziomba (1985) used wires on the front face of the plate to tip the boundary layer just before separation. He found this to have the same qualitative effect as an increase in free stream turbulence. He argued, however, that the shortening of the bubble was mostly due to an effective change in the angle of separation.

The unsteady structure of the separation bubble has been the subject of a series of thorough studies by Hillier and Cherry (1981b), Cherry et al. (1983; 1984), and Kiya and Sasaki (1983a). These studies, using a combination of flow visualization, measurements of fluctuating surface pressures and a judicious use of pressure-velocity correlations, clearly demonstrated that, near separation, the shear layer exhibits a low-frequency flapping motion. The mechanisms for this low frequency unsteadiness are not clearly understood. It was also found that large scale vortices are shed from the separation bubble in pseudoperiodic bursts. In a further study, Kiya and Sasaki (1985a,b) used conditional sampling of the velocity field to deduce the structure of the large scale vortices. They concluded that these vortices have a hairpin structure.

The unsteadiness of the reattachment process seems to be an inherent feature of separation bubbles in all two dimensional geometries. For example, it has been observed in the backward facing step flow (Eaton and Johnston, 1982) and in the flow

Nomenclature

AR = Aspect ratio ($= S/D$)
BR = Solid blockage ratio ($= D/H$)
C_f = Wall shear stress coefficient ($= \tau_w/\frac{1}{2}\rho U^2_\infty$)
C_p = Pressure coefficient ($= (p - p_\infty)/\frac{1}{2}\rho U^2_\infty$
D = plate thickness
F_τ = flatness factor of τ
f = frequency
H = Wind-tunnel/channel height
$P(\tau)$ = Probability density function of τ
p = static pressure
Re = Reynolds number ($= U_\infty D/\nu$)
R_{uu} = Autocorrelation of u
S = Span of wind-tunnel model
S_τ = Skewness factor of τ
T_u = Integral timescale
U, u = Mean and r.m.s. value of x-component of velocity
x, y = Cartesian coordinates
x_r = Time-mean reattachment length
γ = Forward flow fraction
ν = Kinematic viscosity
τ = Shear stress; also time lag
Ψ = nondimensional stream function $\left(= \int_0^{y/D} (U/U_\infty) d(y/D)\right)$

Subscripts/Superscripts

∞ = free stream value
$( )'$ = R.m.s. value of fluctuating quantity
$\overline{( )}$ = time-averaged value

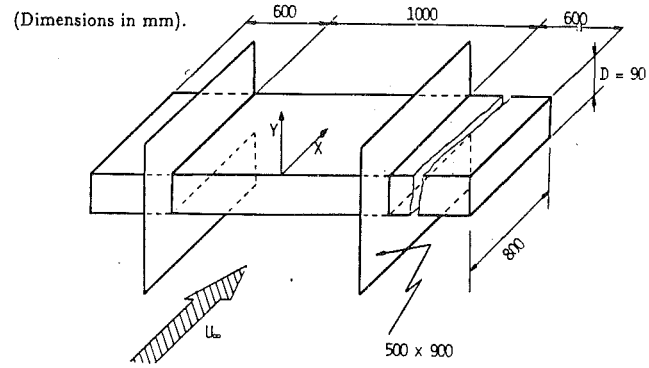

Fig. 2 Model of blunt rectangular plate used in wind tunnel experiments (dimensions in mm)

around the flat plate/splitter plate combination (Gartshore and Savill, 1982). Cherry et al. (1984) suggested that it is the large-scale shedding of vorticity that causes the maximum shear layer turbulent stresses and pressure fluctuations to occur in the vicinity of reattachment.

This paper summarizes a detailed experimental investigation of the two-dimensional flow around a long rectangular section placed at zero incidence in a uniform low-turbulence stream. The results of flowfield and surface measurements made in the highly turbulent and unsteady separated-reattaching flow region are presented. The measurements were made using conventional hot-wire anemometry, directionally sensitive pulsed-wire anemometers and surface shear stress probes. Further information about the structure of the separated shear layer are deduced from velocity spectra and autocorrelations.

2 Apparatus and Experimental Procedures

The experiments were conducted in the U.B.C. low speed, blower type boundary layer wind tunnel. This tunnel has a 2.4m wide, 1.6m high, 24.5m long test section, and a maximum design wind speed of 25 m/s. In the velocity range used for the present experiments (4–15 m/s), the velocity distribution in the empty test section was uniform within 1 percent, with turbulent intensities in the range 0.25–0.4 percent. The model consisted of a rectangular base section with endplates and side extensions. This configuration, shown in Fig. 2, was selected after a careful series of tests, (Dziomba, 1985) indicated that the use of endplates was crucial to the two-dimensionality of the flow.

The rectangular section had a chord of 800 mm, a thickness D of 89.9 mm (3½in.)—corresponding to a solid blockage ratio, *BR*, of 5.6 percent— and a span between end plates of 1000 mm, giving an aspect ratio, *AR*, of 11.1. With the side extensions mounted, the model spanned 2.2 m across the wind tunnel. In addition, a tapered tail was attached to the trailing edge of the model to suppress any periodic vortex shedding which might otherwise have "contaminated" the flow in the separation bubble. The model was mounted at zero incidence, and was fastened to the roof and floor of the wind tunnel by eight steel wires.

Two-dimensionality and symmetry (spanwise and top-to-bottom) were investigated by surface flow visualization and mean pressure measurements. The present configuration resulted in a nominally two-dimensional separation region extending over the central 2/3 portion of the plate, or about $\pm 3.5D$ either side of the midspan. Pressures at corresponding symmetric locations were equal to each other within 1 percent of the dynamic head.

The static pressure distribution on the surface of the bluff plate was measured using a Barocel differential pressure transducer and a 48-port Scanivalve system. The Scanivalve was mounted inside the model and connected to the 0.5 mm diameter pressure taps on the surface of the model by short lengths of Tygon tubing. Reference static and dynamic pressures were measured with a Pitot-static probe located at a distance 10D upstream of the front face of the bluff body. Integration times of 10 seconds were used for the mean pressure measurements. The estimated measurement uncertainties are given in Table 1.

Table 1 Measurement uncertainties

Measured quantity	*Uncertainty estimate*
C_p (Pressure transducer)	± 0.007
U/U_∞ (Hot-wire)	$\pm 2\%$ (for $u/U < 0.3$)
U/U_∞ (Pulsed-wire)	± 2 to 5%
u/U_∞ (Hot- wire)	$\pm 4\%$ (for $u/U < 0.3$)
u/U_∞ (Pulsed-wire)	± 2 to 5% (for $u/U > 0.05$)
γ (Wall probe)	± 0.02
C_f (Wall probe)	$\pm 25\%$
$\sqrt{C_f'^2}$ (Wall probe)	$\pm 30\%$
x_r	$\pm 0.1D$
x	$\pm 0.015D$
y	$\pm 0.001D$

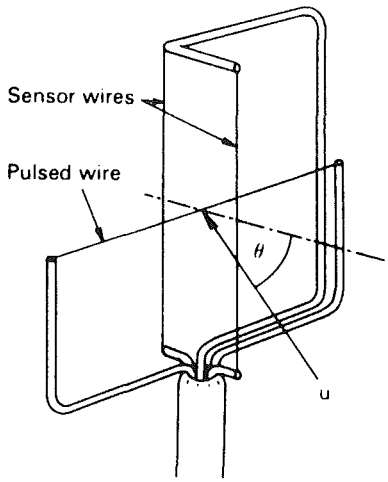

Fig. 3 Pulsed-wire anemometer probe

The velocity field measurements were made by traversing hot-wire and pulsed-wire probes using an automated traverse. This consisted of a lead screw mechanism driven by a microcomputer controlled stepper motor. The bulk of the mechanism was placed under the floor of the wind tunnel. The only parts protruding into the flowfield were the probe and its support. Their interference with the flow was minimal: changes in pressure distribution were less than 0.01 in C_p, and the reattachment length was unaffected by the presence of the probe and its support. The rigidity of the mechanism was also checked, and no flow induced vibrations were detected.

The traverse measurements were made at 10 streamwise stations; each traverse consisted of 20 to 34 points. The repeatability of the measurements was usually within 1 percent for the mean velocities and within 2.5 percent for the fluctuating velocities. A CBM SuperPET microcomputer was used for the calibration of the probes and measurement of the velocity and shear stress data, as well as for the control of the traverse mechanism.

Outside the recirculating flow region, hot-wire probes were used to measure stream-wise mean and fluctuating velocities, correlations, and frequency spectra. Standard DISA single wire probes, with 5 μm diameter, 1.25 mm length platinum-coated tungsten wires were operated using a constant temperature anemometer bridge. The probes were calibrated in a low tur-

bulence flow against a Pitot-static probe and the calibration was checked after each profile measurement. A digital sampling rate of 4 KHz and an integration time of 10 sec. were used.

A pulsed-wire anemometer system (see, for example, Bradbury and Castro, 1971) manufactured by PELA Flow Instruments, was used for the flowfield measurements in the recirculating flow region. The pulsed-wire probe consists of an array of three wires as shown in Fig. 3. The central "transmitting" wire is heated periodically by short voltage pulses; the time taken by the heated tracer to travel to either of the two "receiving" wires is a measure of the instantaneous velocity. The response of the instrument is not linear due to thermal diffusion and viscous wake effects. This is taken into account by using, as recommended by Bradbury and Castro (1971), an empirical calibration fit of the form

$$U=\frac{A}{T}+\frac{B}{T^3} \tag{1}$$

where U is the flow velocity, A and B are calibration constants, and T is the time of flight of the heat tracer. The pulsed-wire measurements were made at a sampling rate of 50 Hz, with 5000 samples taken in the outer region and 7500 in the shear-layer/recirculating flow region.

The accuracy of the pulsed-wire anemometer has been assessed (Bradbury, 1976; Castro and Cheun, 1982; Westphal et al., 1984), and its performance was found to be comparable to the hot-wire anemometer in regions where both instruments are applicable. Due to electronic noise, there is a lower limit of 2 percent to the turbulent intensities that can be measured with the instrument (Bradbury, 1976). The possible influence of small scale turbulence on the probe response (Bradbury and Castro, 1971) was minimized in the present experiments by the relatively large scale of the experimental facility. The estimated uncertainties quoted in Table 1 are those given by Westphal et al. (1984).

The distribution of the mean and fluctuating wall shear stresses, and of the forward-flow-fraction at the wall were obtained with a pulsed wall-probe which was mounted on a supporting block. The block fitted flush with the surface of the model, and could slide along a groove which was cut out along the centerline of the model. The groove was 600 mm long and allowed positioning of the probe anywhere between x/D = 1.0 to 8.5. The pulsed wall-probe is an instrument which has evolved from the PWA. The probe (see Westphal et al., 1981; Castro and Dianat, 1983, 1985) consists of an array of three fine parallel wires mounted about 50 μm above the surface of a circular plug. The wall probe was operated using the same electronics as the PWA and a calibration function of the same form as equation (1). The measurement procedure assumes that the velocity profiles remain similar very close to the wall and scale on the wall shear stress (Westphal et al., 1981).

Because of the nonlinearity of the calibration function, calibration of the probe in a turbulent boundary layer leads to a nonlinear averaging error, even for moderate turbulent intensities. Although it is possible to compensate for this error (Westphal et al., 1981), calibrating the probe in a laminar flow eliminates the averaging error altogether. This procedure was adopted by Castro and Dianat (1983) and Westphal et al. (1984) who had high aspect ratio laminar channel facilities. Since no such facility was available, the calibration for the present measurements was carried out in a two-dimensional laminar boundary layer generated on a flat plate. The near wall velocity profiles were measured using a hot-wire anemometer, and the wall shear stress was deduced from the resulting gradient $\partial U/\partial y$ at the wall. This calibration procedure became increasingly uncertain with higher wall shear stress because of the decreasing thickness of the boundary layer at the highest velocities. Consequently, there is a relatively large uncertainty in the shear stress measurements ($\pm$25 percent in τ and $\pm$ 30 percent in τ'). In retrospect, a smaller measurement uncertainty could have been obtained by calibrating the probe in a turbulent boundary layer and correcting for the non-linear averaging error.

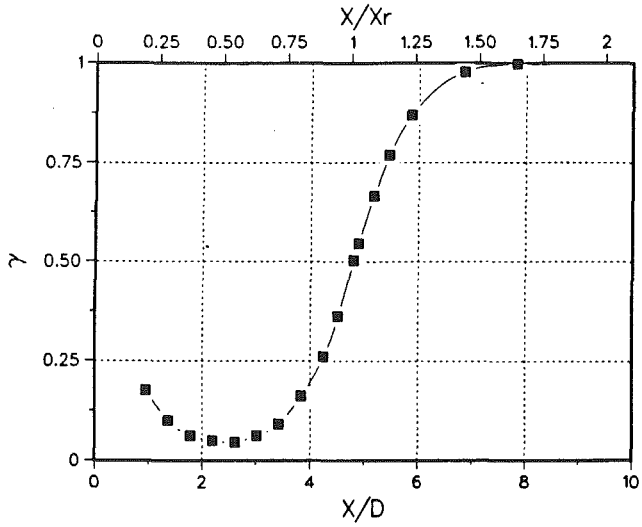

Fig. 4 Distribution of surface forward flow fraction

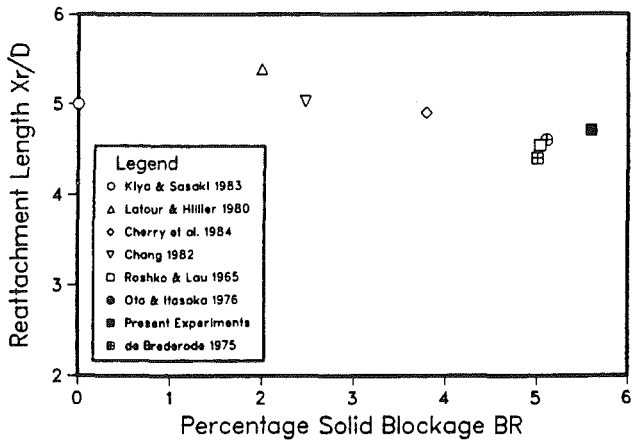

Fig. 5 Reattachment lengths found for various solid blockage ratios (data compiled by Cherry et al., 1984)

The PWA and the shear-stress probe were also used to measure the forward-flow-fraction γ. This is the fraction of the time the flow moves in the downstream direction; it is equal to the ratio of the number of positive samples to the sum of all samples, and is defined by

$$\gamma=\int_0^{+\infty} P(\tau_w)\,d\tau_w \tag{2}$$

where $P(\tau_w)$ is the probability density of τ_w.

3 Results

Structure of the Separation Bubble. Preliminary experiments indicated that both the reattachment length and pressure distribution remained unchanged over the Reynolds number range 2.5×10^4 to 9.0×10^4 confirming the observation of Hillier and Cherry (1981a) that the flow is essentially Reynolds number independent for Re $\gtrsim 2.7 \times 10^4$. All present experiments were conducted at a Reynolds number of $5.0 \times 10^4 \pm 0.1 \times 10^4$.

The simplest characteristic scale for the separation region is the reattachment length. This is measured from the line of separation (the sharp leading edge in this case) to the time-averaged reattachment line which is defined as the location where the time-averaged wall shear stress $\overline{\tau_w}$ vanishes. Westphal

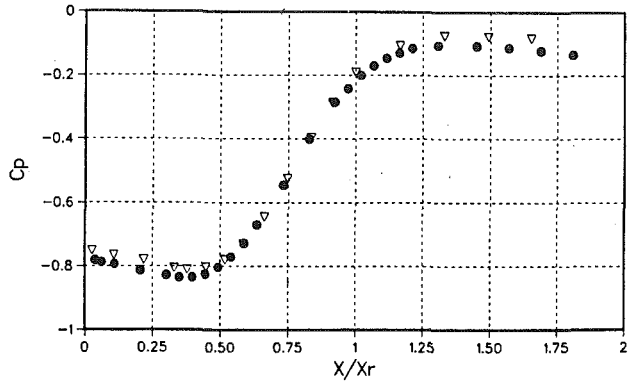

Fig. 6 Distribution of surface pressure coefficient: •, present measurements; ▽, measurements of Cherry et al., (1984)

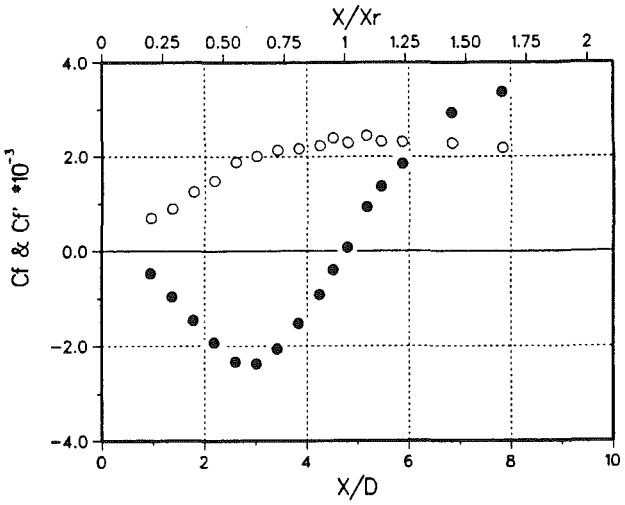

Fig. 7 Distribution of wall shear stress coefficients: •, mean; ○, r.m.s

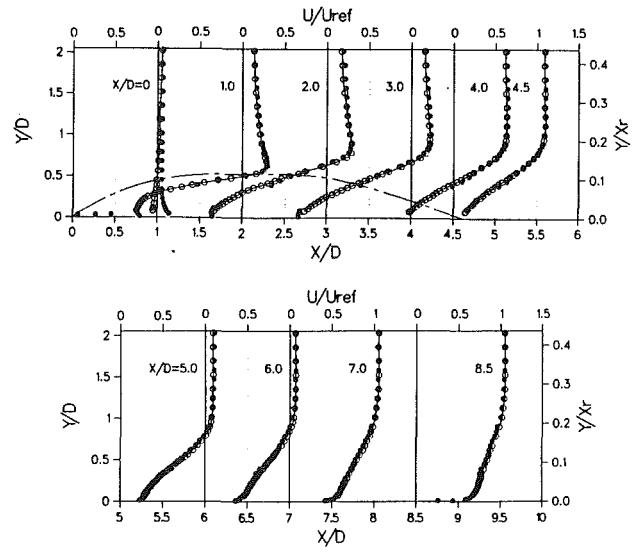

Fig. 8(*a,b*) Mean longitudinal velocity profiles: ○, pulsed-wire data; •, hot-wire data; ——— · ——— , separation streamline ($\Psi = 0$)

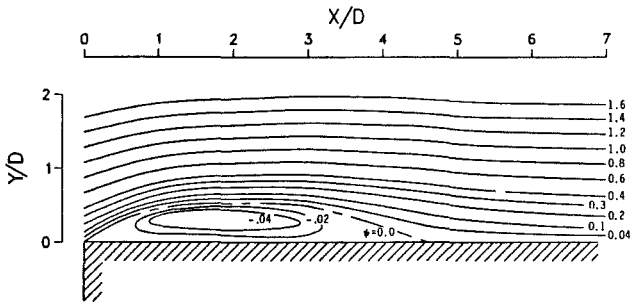

Fig. 9 Mean streamlines deduced from pulsed-wire measurements

et al. (1981) showed that the reattachment line also corresponds to the location where the surface forward-flow-fraction γ is equal to 0.5. The distribution of γ is shown Fig. 4. The reattachment length deduced from these measurements, x_r/D = 4.7, is in very good agreement with the value deduced from surface flow visualization. It is interesting to note that γ is never equal to zero; that is the flow is never fully reversed even in the middle of the separation bubble. Furthermore there is a broad region, extending about 2.5*D* downstream of the mean reattachment point, where the near-wall flow can be moving instantaneously in either downstream or upstream direction. This suggests that the *instantaneous* location of zero wall stress wanders up and downstream in a region surrounding the time-averaged reattachment point; this view is consistent with the large scale unsteadiness of the flow observed by Kiya and Sasaki (1983) (hereafter, KS) and Cherry et al. (1984) (hereafter, CHL). If the reattachment zone is defined, somewhat arbitrarily, as a region where $0.1 \leq \gamma \leq 0.9$, its width is then about 2.4D or $0.5x_r$.

A comparison of the reattachment length obtained in the present experiments and various other studies is shown in Fig. 5; only data obtained in low freestream turbulence is included. The reattachment length is seen to decrease with increasing solid blockage, with the exception of the value reported by KS which is low compared to the trend of the remainder of the data. This may be attributed to slight differences in free stream turbulence, but it should also be noted that the nominal 0 percent blockage of KS was obtained by fitting false boundaries to the wind tunnel. This might not have eliminated all blockage effects.

The mean pressure coefficient distribution, shown in Fig. 6, is found to compare well with the C_p values reported by CHL. Both distributions are uncorrected for blockage; this accounts for the small differences between the present measurements where BR = 5.6 percent and those of CHL where *BR* = 3.8 percent. After a small initial dip of about 0.05 in C_p the pressure remains approximately constant up to about $x = 0.5x_r$; a rapid recovery takes place thereafter. This recovery continues beyond the reattachment point up to $x \simeq 1.4x_r$.

Figure 7 shows the distribution of the mean and fluctuating shear stress coefficients. The position at which the mean shear stress is equal to zero corresponds to the position where γ = 0.5 as anticipated.[2] C_f attains a minimum value of -2.4×10^{-3} at $x = 0.63x_r$ and rises rapidly thereafter. The r.m.s. value of the shear stress coefficient increases steadily throughout the reversed flow region and attains a plateau ($C_f \simeq 2.4 \times 10^{-3}$) in the reattachment zone. The magnitudes of both mean and fluctuating shear stress coefficients are higher by a factor of (about) two than those encountered in the backward facing step geometry (see, e.g., Westphal et al., 1984).

The mean velocity profiles are presented in Figs. 8(*a*) and (*b*) for the reversed and reattached flow regions respectively. Hot-wire data are presented only in regions where $\gamma > 0.9$ or $\gamma < 0.1$. All velocity data are normalized by the free stream velocity U_∞ (measured ahead of the bluff body), and the origin for y is the plate surface. The mean separation streamline, calculated from the velocity profiles, is also plotted for reference. Backflow velocities as large as $0.3U_\infty$ are encountered in the reversed flow region. This value is about 50 percent larger than that in the backward facing step geometry (West-

[2]The equivalence of $\tau_w = 0$ and $\gamma = 0.5$ is not always true. Examination of the data of Ruderich and Fernholz (1986) for the flat plate/splitter plate geometry reveals that the forward-flow-fraction is equal to about 0.7 at the zero shear stress location associated with a secondary reseparation.

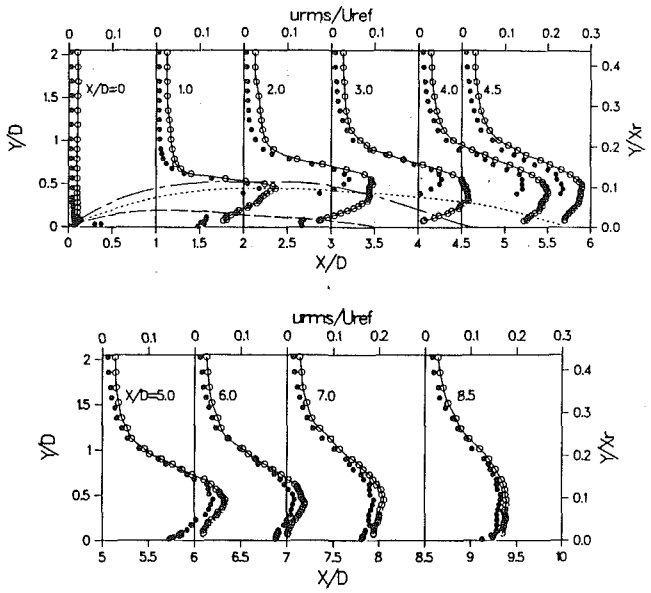

Fig. 10(*a,b*) Fluctuating (r.m.s.) longitudinal velocity profiles: ○, pulsed-wire data; •, hot-wire data; ——— - ———, separation streamline ($\Psi = 0$); ----- $\gamma = 0.9$; —— ——, $\gamma = 0.1$

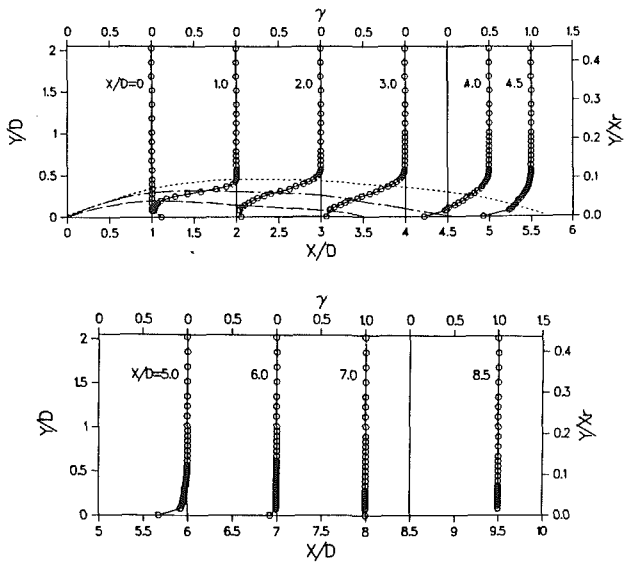

Fig. 11(*a,b*) Forward flow fraction profiles: ----, $\gamma = 0.9$; —— - ——, $\gamma = 0.5$; —— —— ——, $\gamma = 0.1$

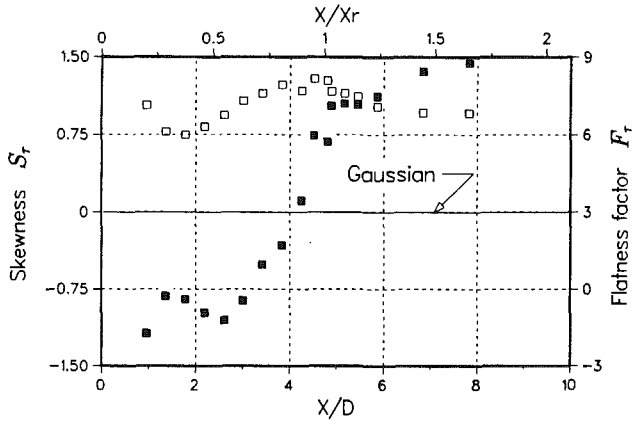

Fig. 12 Skewness and flatness distributions of fluctuating wall shear stress: ■, S_τ; □, F_τ

phal et al., 1984) which accounts partly for the correspondingly higher wall shear stresses. The backflow velocities remain relatively high in the near-wall region, and local maxima in the velocity profiles are apparent in the first half of the bubble. The velocities further away from the wall remain higher than the free stream as a result of blockage effects.

The recovery region profiles show an inflexion point as a result of the merging of a new boundary layer with the reattaching shear layer, and there is a rapid increase of the near-wall velocities with downstream distance. The mean streamline pattern obtained by integration of the velocity profiles is shown in Fig. 9. The time-averaged streamlines are somewhat deceptive in that they disguise the highly unsteady nature of the reattachment process, illustrated earlier by the forward-flow-fraction distribution.

Figure 10 shows the r.m.s. longitudinal velocity profiles. The consistently higher values of the PWA data are due to electronic noise which makes the instrument unsuitable for measurements of turbulent intensities smaller than about 2 percent (Bradbury, 1976). The HWA data on the other hand appear reasonable only when the forward-flow-fraction γ is outside the range $0.1 \leq \gamma \leq 0.9$ *and* when the *local* intensity is below 20 percent. The results show the same overall trends as the split-film sensor results of KS, with the notable exception that their turbulent intensities are generally lower by 15 to 20 percent. This discrepancy is probably due to their use of split film sensors which can result in fluctuating quantity measurements that are up to 30 percent too low (c.f. Young, quoted by Simpson, 1985).

The peak turbulence intensity u/U_∞ is observed to occur upstream of reattachment, probably as a result of the higher velocity difference across the shear layer. After a gradual decrease within the reattachment region, the maximum turbulent intensities fall rapidly in the recovery region. The turbulence intensities decay fairly rapidly in the outer region of the shear layer, but remain high next to the wall. These near-wall intensities decrease more slowly with streamwise distance than the maximum intensities. The peak turbulence intensity of about 30 percent found in the separated shear-layer is substantially higher than the value of about 18 percent found in the plane mixing layer (PML) (Wygnansky and Fiedler, 1970). A more appropriate comparison, however, can be made by using the velocity difference across the shear layer to normalize the present data. The maximum value of $u/(U_{max} - U_{min})$ varies from about 22 percent at $x/D = 3$ to about 25 percent at $x/D = 5$. This is still higher by 20 to 40 percent than the PML value. These higher values, also observed in the case of the flat plate/splitter plate geometry (Ruderich and Fernholz, 1986; Castro and Haque, 1987) indicate that the turbulence structure of the reattaching shear layer, at least over its second half, is very different from that of a PML.

The forward-flow-fraction profiles are shown in Fig. 11 together with the loci of $\gamma = 0.1$, 0.5 and 0.9. The data points at $y/D = 0$ are from the surface probe measurements. Similarly to the wall data, the position of $\gamma = 0.5$ is found to correspond to $U = 0$. At $x/D = 1$ and 2, γ reaches a minimum slightly away from the wall, but further downstream the minimum is reached at the wall; this is consistent with the location of the maximum backflow velocities in Fig. 8. In fact the shapes of the mean velocity and forward-flow-fraction profiles are strikingly similar.

Further insight into the structure of the separation bubble can be gained by examining the skewness, S_τ, and the flatness factor, F_τ, of the wall shear stress. These are the normalized third and fourth moments of the probability density, P_τ, and are defined by

$$S_\tau = \frac{\overline{\tau'^3}}{(\overline{\tau'^2})^{3/2}} = \frac{1}{(\overline{\tau'^2})^{3/2}} \int_{-\infty}^{\infty} \tau'^3 P(\tau) d\tau \tag{3}$$

$$F_\tau = \frac{\overline{\tau'^4}}{(\overline{\tau'^2})^2} = \frac{1}{(\overline{\tau'^2})^2} \int_{-\infty}^{\infty} \tau'^4 P(\tau) d\tau \tag{4}$$

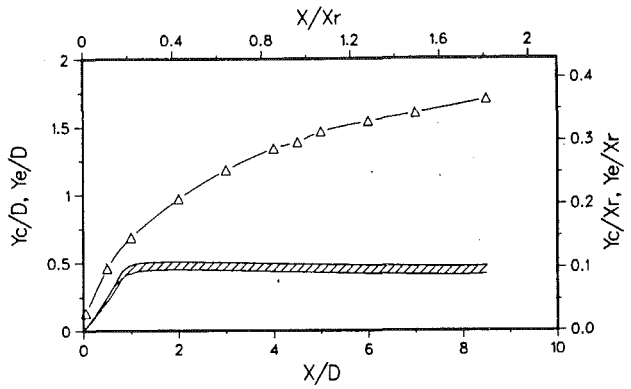

Fig. 13 Representative shear layer positions: Δ, y_e (location of u/U = 2.5 percent; ZZZZ, y_c (location of $(u/U_\infty)_{max}$)

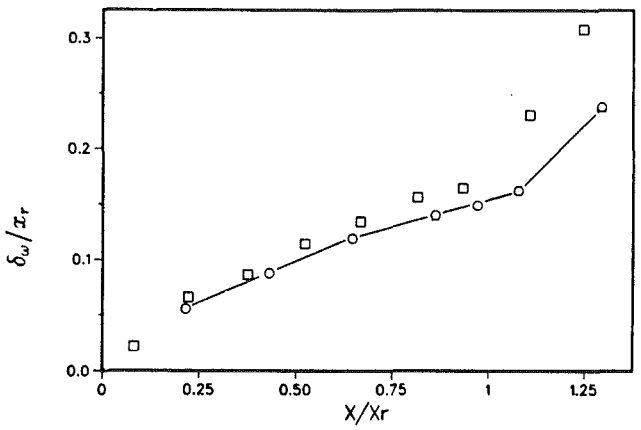

Fig. 14 Growth of the shear layer. Vorticity thickness δ_ω: ○, present; □, Ruderich and Fernholz (1986)

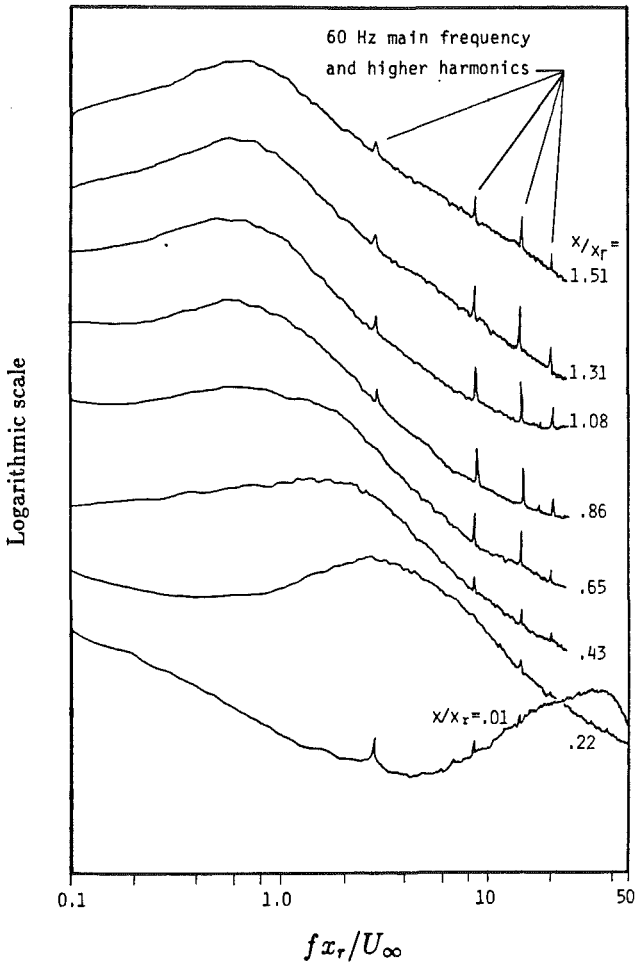

Fig. 15 Frequency spectra of velocity fluctuations along shear layer edge y_e

The skewness and flatness factor distributions, shown in Fig. 12, exhibit the same trends as reported by Ruderich and Fernholz (1986) for the flat plate/splitter plate geometry. Both skewness and flatness factors, are found to depart markedly from their respective Gaussian values of 0 and 3. High values of the flatness factor are usually indicative of a burst-type or large amplitude intermittent signal (Townsend, 1976). Such behavior of the fluctuating shear stress and near-wall velocity could be associated with the large scale, low frequency, unsteadiness and bubble bursting phenomena reported by both KS and CHL. The incursions of high velocity fluid resulting from these phenomena would cause large amplitude fluctuations leading to probability distributions having a higher flatness factor. The observed increase of F_τ in the reattachment region is compatible with this explanation, since the activity associated with the large scale unsteadiness is most vigorous there. The skewness is negative in most of the reversed flow region, presumably because of the burst-like occurrences of flow reversals caused by the low frequency unsteadiness. After a local minimum in the middle of the separation bubble, the skewness rises steadily, and takes a value of zero close to the mean reattachment point where the intense mixing inhibits intermittent large amplitude negative and positive fluctuations. After reattachment, the skewness continues to rise due to increasing occurrences of large amplitude positive fluctuations.

Structure of the Shear Layer. The position y_c where the r.m.s. velocity u attains a maximum can be interpreted as representing the center of the shear layer bounding the separation bubble since it corresponds closely to the position where the velocity profiles have an inflexion point. Figure 13 shows that the position of y_c changes very little with x even in the reattachment region (the shaded plot reflects the uncertainty in locating u_{max} due to scatter in the data). Figure 13 also shows the streamwise variation of an edge of the shear layer y_e defined as the position of 2.5 percent local turbulent intensity. This corresponds closely to the position where turbulence first appears in an otherwise irrotational flow.

The growth of the shear layer is commonly deduced from the vorticity thickness δ_ω, defined by

$$\delta_\omega = \frac{U_{max} - U_{min}}{(\partial U/\partial y)_{max}} \tag{5}$$

The streamwise variation of δ_ω, plotted in Fig. 14, indicates that, over the first half of the separation bubble, the shear layer grows in an approximately linear fashion. From the limited number of velocity profiles available in this region, the growth rate $d\delta_\omega/dx$ is found to be equal to 0.147; this is essentially identical to the value of 0.148 reported by Ruderich and Fernholz for the normal-plate/splitter-plate geometry, and is within the range of values (0.145-0.22) reported by Brown and Roshko (1974) for the conventional single stream PML. In the second half of the separated shear layer, the growth rate decreases sharply, taking a value of about 0.1 at $x/x_r \simeq 0.65$. The sharp change in the slope after $x/x_r \simeq 1.1$ is due to the smaller $(\partial U/\partial y)_{max}$ gradients. The separated flat plate boundary layer data of Dianat and Castro (1989) and the flat plate/splitter plate measurements of Castro and Haque (1987) show similar trends. In the latter case however, the initial growth rate of the shear layer for $x/x_r \lesssim 0.2$ is substantially higher than the PML value, and their data indicate a slowly decreasing growth rate up to reattachment, instead of a linear increase in δ_ω.

Frequency spectra and autocorrelation functions of the longitudinal fluctuating velocity were evaluated along y_e. At this

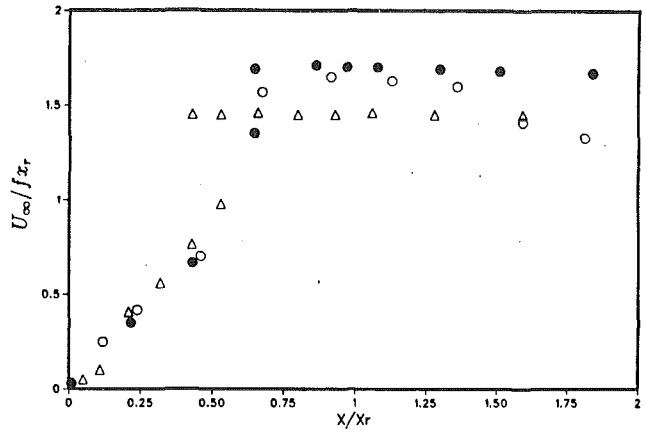

Fig. 16 Dominant frequencies of velocity spectra: •, present measurements; ○, Dziomba (1985); △, Cherry et al. (1984)

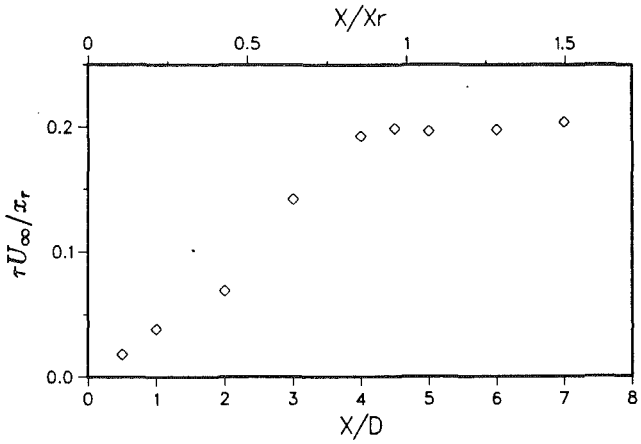

Fig. 18 Integral time scales deduced from autocorrelation measurements

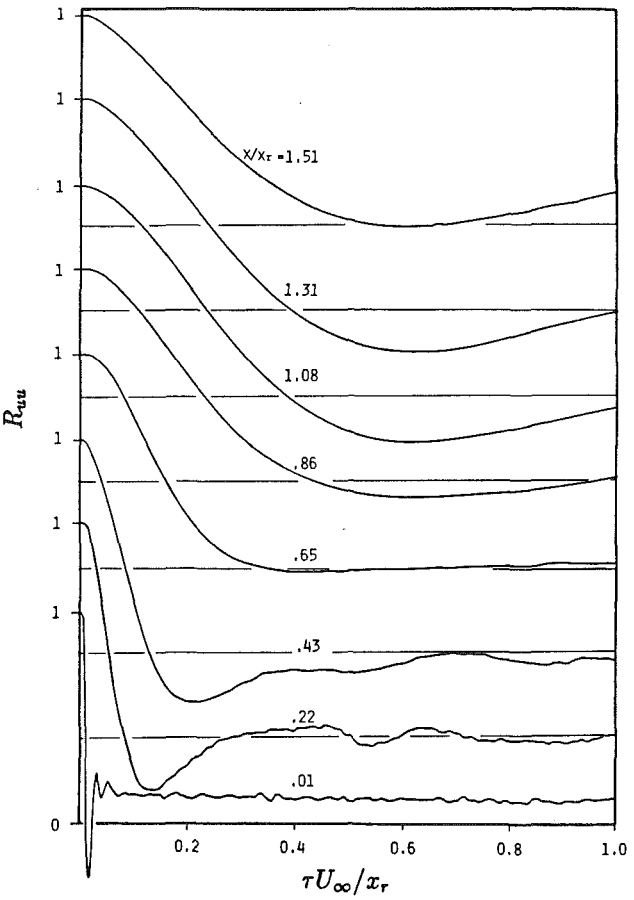

Fig. 17 Autocorrelation of velocity fluctuations along shear layer edge y_e

position, the velocity fluctuations are irrotational most of the time; with high-frequency bursts occurring very occasionally. Most of the information contained in these fluctuations is therefore related to the large scale structure of the shear layer.

The spectra at various streamwise positions along y_e, presented in Fig. 15, show the same features as the measurements of CHL. At $x/x_r = 0.01$ there is a distinct high frequency contribution with a peak at a reduced frequency fx_r/U_∞ of about 34. As we progress further downstream from separation, a progressive fall in the dominant frequency takes place. This fall ceases at $x/x_r = 0.64$, where the spectra become dominated by a broader band contribution centered around $fx_r/U_\infty \simeq 0.6$. This streamwise variation is illustrated in Fig. 16 which also shows the measurements of Dziomba (1985) and CHL. All measurements show the same trends, and two regions can be observed. In the first region, extending from separation to about 60 percent of the separation bubble length, the frequency decreases linearly with x, indicating that the large scale structures grow linearly just as in a conventional free shear layer. In the second region, overlapping the first and starting at $x/x_r \simeq 0.6$, the characteristic frequency remains essentially constant (decreasing values shown by the data of Dziomba for $x > 1.2$ are due to the contamination from the trailing edge of the model which was not equipped with a tail). This characteristic frequency is associated with the pseudo-periodic shedding of vorticity from the bubble, a phenomenon observed by KS and CHL among others.

Figure 17 shows the autocorrelation R_{uu} plotted as a function of the non-dimensional time lag $\tau U_\infty/x_r$. Close to separation, at $x/x_r = 0.01$, the autocorrelation exhibits a long tail. A similar observation was made by KS who attributed this tail to the flapping of the shear layer caused by the large scale unsteadiness of the bubble. This tail could also be due to disturbances in a not fully turbulent shear layer. The higher frequency waviness of the tail is due to the contributions from the large scale structures of the shear layer. This waviness can still be detected, with correspondingly lower frequencies, at $x/x_r = 0.22$ and 0.43. At $x/x_r = 0.86$, the negative correlations reappear and become even larger around reattachment. The streamwise distribution of the integral timescales T_u, obtained by integrating the corresponding autocorrelation to the first zero crossing, are shown in Fig. 18. Consistent with earlier observations, the timescales increase in a linear fashion with x up to $x/x_r \simeq 0.85$ and stabilize thereafter at a value of $T_u U_\infty/x_r \simeq 0.2$.

Castro and Haque (1987) argue convincingly, based on detailed comparisons of the turbulent structures, that there is no reason why the separated shear layer should grow linearly or behave like a PML. From the foregoing observations, it appears, nevertheless, that the structure of the separated shear layer is not as radically different in the first half of the bubble as it is in the second half from the structure of the PML.

Concluding Remarks

Experimentally, it is difficult to establish an accurately two-dimensional mean flow field in a separated reattaching flow region. Considerable effort has been expended in this study to approximate these ideal conditions over the central part of the bluff rectangular plate. A mean reattachment length of $4.7D$ is obtained from both wall shear stress measurements and surface streamline visualization.

Within the separation bubble, the mean wall shear stress is found to be of the same order of magnitude as in the reattached flow, and backflow velocities of the order of 30 percent of the

free stream velocity are encountered. Over the first 60 percent or so of the bubble, the separated shear-layer bounding the reversed flow region has a mean flow growth rate similar to that of a plane mixing layer. The growth of the shear-layer is approximately linear, and both characteristic frequencies and integral scales vary linearly with streamwise distance.

At about $x \simeq 0.6x_r$, the shear-layer undergoes a fairly abrupt change in structure: the shear-layer growth rate becomes significantly lower and the maximum turbulence intensities become substantially higher than the corresponding plane mixing-layer values, probably as a result of the large scale unsteadiness of the reattachment process. In this reattachment region, the linear variation of the characteristic frequencies and integral scales ceases. Consistent with the observations of Kiya and Sasaki (1983a) and Cherry et al. (1984), the shear layer is characterized by a low-frequency unsteadiness. This unsteadiness of the reattachment process is further illustrated by the forward-flow-fraction measurements which suggest that the *instantaneous* reattachment point, or point at which $\tau_\omega = 0$, moves around the time-averaged reattachment point over a distance of about $0.5x_r$.

In addition to the carefully established two-dimensionality of the flow, a number of precautions have been taken to ensure the reliability of the present data and its suitability as a test case for numerical predictions, the subject of Part II of this paper. The measurements have been made in a large scale facility, and probe interference effects have been assessed and minimized. Flowfield measurements have been made using both pulsed-wire and hot-wire anemometry in flow regions where both techniques are applicable. It appears, from the present measurements and those made in other reattaching flow geometries, that the characteristics of the separated shear layer over the first half or so of the bubble are not radically different from those of a plane mixing layer, whereas the characteristics of the second half of the shear layer depart markedly from it and are dictated mainly by the reattachment process. The unsteady nature of this reattachment process points to the need for further studies involving unsteady measurements.

Acknowledgment

This work was supported by an operating grant from the Natural Sciences and Engineering Research Council of Canada.

References

Bradbury, L. J. S., 1976, "Measurements With a Pulsed-Wire and a Hot-Wire Anemometer in the Highly Turbulent Wake of a Normal Flat Plate," *J. Fluid Mech.*, Vol. 77, pp. 473–497.

Bradbury, L. J. S., and Castro, I. P., 1971, "A Pulsed-Wire Technique for velocity Measurements in Highly Turbulent Flows," *J. Fluid Mech.*, Vol. 49, pp. 657–691.

Bradshaw, P. B., and Wong, F. Y. F., 1972, "The Reattachment and Relaxation of a Turbulent Shear Flow," *J. Fluid Mech.*, Vol. 52, pp. 113–135.

Brederode, V. A. S. L. De, 1975, "Three-Dimensional Effects in Nominally Two-Dimensional Flows," Ph.D. thesis, Univ. London.

Brown, G. L., and Roshko, A., 1974, "On Density Effects and Large Structures in Turbulent Mixing Layers," *J. Fluid Mech.*, Vol. 64, pp. 775–816.

Castro, I. P., and Cheun, B. S., 1982, "The Measurement of Reynolds Stresses With a Pulsed-Wire Anemometer," *J. Fluids Mech.*, Vol. 118, pp. 41–58.

Castro, I. P., and Dianat, M., 1983, "Surface Flow Patterns on Rectangular Bodies in Thick Boundary Layers," *J. Wind Engng & Ind. Aero.*, Vol. 11, pp. 107–119.

Castro, I. P., and Dianat, M., 1985, "The Pulsed-Wire Skin-Friction Measurement Technique," "*Proc. 5th Symp. on Turbulent Shear Flows,* Cornell Univ., Ithaca, 11.19–11.24.

Castro, I. P., and Haque, A., 1987, "The Structure of a Turbulent Shear Layer Bounding a Separation Region," *J. Fluid Mech.*, Vol. 179, pp. 439–468.

Cherry, N. J., Hillier, R., and Latour, M. E. M. P., 1983, "The Unsteady Structure of Two-Dimensional Separated and Reattaching Flows," *J. Wind Engng & Ind. Aero.*, Vol. 11, pp. 95–105.

Cherry, N. J., Hillier, R., and Latour, M. E. M. P., 1984, "Unsteady Measurements in a Separated and Reattaching Flow," *J. Fluid Mech.*, Vol. 144, pp. 13–46.

Dianat, M., and Castro, I. P., 1989, "Measurements in Separating Boundary Layers," *AIAA J.*, Vol. 27, pp. 719–724.

Dziomba, B., 1985, "Experimental Investigation of Bluff Body Separation Regions," Presented at CASI Aerodynamics Symposium, Montréal.

Eaton, J. K., and Johnston, J. P., 1982, "Low Frequency Unsteadiness of a Reattaching Turbulent Shear Layer," *Turbulent Shear Flows 3*, ed., L. J. S., Bradbury, F. Durst, B. E. Launder, F. W. Schmidt and J. H. Whitelaw, Springer-Verlag, Berlin, pp. 162–170.

Gartshore, I. S., and Savill, M., 1982, "Some Effects of Free Stream Turbulence on the Flow Around Bluff Bodies," Presented at Euromech 160: Periodic Flow and Wake Phenomena, Berlin.

Hillier, R., and Cherry, N. J., 1981a, "The Effect of Stream Turbulence on Separation Bubbles," *J. Wind Engng & Ind. Aero.*, Vol. 8, pp. 49–58.

Hillier, R., and Cherry, N. J., 1981b, "Pressure Fluctuations Under a Turbulent Shear Layer," *Proc. 3rd Symp. on Turbulent Shear Flows*, Univ. California, Davis, pp. 16.23–16.29.

Hillier, R. and Dulai, B. S., 1985, "Pressure Fluctuations in a Turbulent Separated Flow," *Proc. 5th Symp. on Turbulent Shear Flows, Cornell Univ.*, Ithaca, pp. 5.15–5.18.

Kiya, M., Sasaski, K., and Arie, M., 1982, "Discrete-Vortex Simulation of a Turbulent Separation Bubble," *J. Fluid Mech.*, Vol. 120, pp. 219–244.

Kiya, M., and Sasaki, K., 1983a, "Structure of a Turbulent Separation Bubble," *J. Fluid Mech.*. Vol. 137, pp. 83–113.

Kiya, M., and Sasaki, K., 1983b, "Free-stream Turbulence Effects on a Separation Bubble," *J. Wind Engng & Ind. Aero.*, Vol. 14, pp. 375–386.

Kiya, M., and Sasaki, K., 1985a, "Structure of Large-Scale Vortices and Unsteady Reverse Flow in the Reattaching Zone of a Turbulent Separation Bubble," *J. Fluid Mech.*, Vol. 154, pp. 463–491.

Kiya, M., and Sasaki, K., 1985b, "Turbulence Structure and Unsteadiness in a Separation Reattachment Flow," *Proc. 5th Symp. on Turbulent Shear Flows*, Cornell Univ., Ithaca, pp. 5.7–5.12.

Lane J. C., and Loehrke, R. I., 1980, "Leading Edge Separation From a Blunt Plate at Low Reynolds Number," ASME J. FLUIDS ENGNG., Vol. 102, pp. 494–496.

Ota, T., Asano, Y., and Okawa, J., 1981, "Reattachment Length and Transition of the Separated Flow Over Blunt Flat Plates," *Bull. JSME*, Vol. 24 (192), pp. 941–947.

Ota, T., and Itasaka, M., 1976, "A Separated and Reattached Flow on a Blunt Flat Plate," *J. Fluids Engng.*, Vol. 98, pp. 79–84.

Ota, T., and Kon, N., 1974, "Heat Transfer in the Separated and Reattached Flow on a Blunt Flat Plate," ASME *Journal of Heat Transfer*, Vol. 96, pp. 459–462.

Ota, T., and Motegi, H., 1983, "Measurements of Spatial Correlations and Autocorrelations in a Separated and Reattached Flow Over a Blunt Plate," *J. Wind Engng & Ind. Aero.* Vol. 12, pp. 291–312.

Ota, T., and Narita, M., 1978, "Turbulence Measurements in Separated and Reattached Flow Over a Blunt Flat Plate," ASME JOURNAL FLUIDS ENGINEERING, Vol. 100, pp. 224–228.

Roshko, A., and Lau, J. C., 1965, "Some Observations on Transition and Reattachment of a Free Shear Layer in Incompressible Flow," *Proc. Heat Transfer & Fluid Mech. Inst.*, Vol. 18, ed. A. F. Charwatt, Stanford University Press, pp. 157–167.

Ruderich, R., and Fernholz, H. H., 1986, "An Experimental Investigation of a Turbulent Shear Flow with Separation, Reverse Flow, and Reattachment," *J. Fluid Mech.*, Vol. 163, pp. 283–332.

Simpson, R. L., 1981, "A Review of Some Phenomena in Turbulent Flow Separation," ASME JOURNAL FLUIDS ENGINEERING, Vol. 103, pp. 520–532.

Simpson, R. L., 1985, "Two-Dimensional Turbulent Separated Flow," AGARDograph No. 287.

Townsend, A. A., 1976, *The Structure of Turbulent Shear Flow*, 2nd edition, Cambridge University Press.

Westphal, R. V., Eaton, J. K., and Johnston, J. P., 1981, "A New Probe for Measurement of Velocity and Wall Shear Stress in Unsteady Reversing Flow," ASME JOURNAL FLUIDS ENGINEERING, Vol. 103, pp. 478–482.

Westphal, R. V., Johnston, J. P., and Eaton, J. K., 1984, "Experimental Study of Flow Reattachment in a Single Sided Sudden Expansion," NASA Contractor Report 3765.

Wygnanski, I. and Fiedler, H. E., 1970, "The Two-Dimensional Mixing Layer," *J. Fluid Mech.*, Vol. 41, pp. 327–361.

N. Djilali
Assistant Professor,
Department of Mechanical Engineering,
University of Victoria,
Victoria, Canada V8W 3P6

I. S. Gartshore
Professor.

M. Salcudean
Professor and Head.

Department of Mechanical Engineering,
University of British Columbia,
Vancouver, Canada V6T 1W5

Turbulent Flow Around a Bluff Rectangular Plate. Part II: Numerical Predictions

This paper presents calculations of the time-averaged separated-reattaching flow around a bluff rectangular plate, using a finite difference procedure and the k-ϵ turbulence model. Two discretization methods are used: the hybrid differencing scheme, and the bounded skew hybrid differencing scheme. The latter, although superior to the former for all grid distributions, results in a reattachment length about 30 percent shorter than the measured value. When a modification which takes into account streamline curvature is incorporated into the k-ϵ model, a marked improvement in the predictions is obtained. A reattachment length of 4.3 plate thicknesses (D), compared to an experimental value of 4.7D, is obtained, and the predicted mean flow field, turbulent kinetic energy and pressure distributions within the separation bubble are found to be in good agreement with experiments.

1 Introduction

The theoretical analysis of separated-reattaching flows poses many difficulties as a result of shear layer curvature, strong pressure gradients, flow recirculation, complex turbulence structure, and large scale unsteadiness. In recent years, prediction methods for recirculating flows have increasingly relied on numerical analyses based mostly on finite difference solutions of the Navier-Stokes equations (in their time-averaged form in the case of turbulent flows). Due to a combination of numerical errors and turbulence model inadequacies, varying degrees of success have been obtained.

Detailed laminar flow predictions for the blunt plate geometry (Fig. 1) are reported by Djilali (1987). A finite volume method was used in conjunction with two discretization schemes: the hybrid-upwind differencing (HD) scheme, and the bounded-skew-hybrid differencing (BSHD) scheme. A systematic grid refinement study was conducted, and the results, summarized in Figs. 2 and 3, highlight the importance of the discretization scheme. Figure 2 shows that there is a significant difference between the reattachment lengths predicted with the two discretization schemes. Whereas the BSHD solutions become grid independent for a sufficiently fine grid, the HD solutions remain sensitive to grid refinement even for the finest grids and tend asymptotically—from below—toward the grid independent BSHD solution. As a result of false diffusion errors, which appears to be particularly severe for this flow configuration, the HD predictions give reattachment lengths which are up to 35 percent shorter than experimental values.

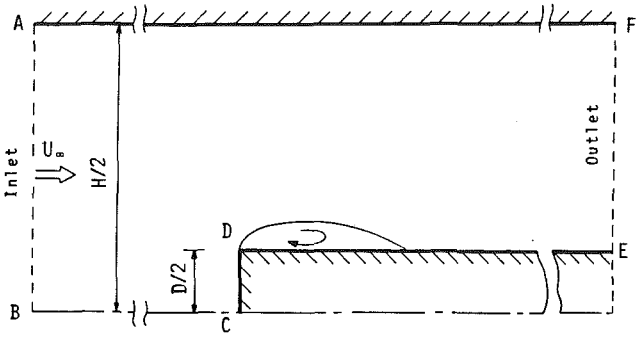

Fig. 1 Flow domain

The BSHD predictions, on the other hand, are in excellent agreement with the experimental measurements of Lane and Loehrke (1980), as shown in Fig. 3.

An inviscid simulation of the turbulent flow on a blunt flat plate was carried out by Kiya et al. (1982) using the discrete vortex method. The simulation consisted of tracking elemental vortices which were shed downstream from the separation corner. In order to represent the viscous/turbulent dissipation of vorticity, the circulation of elemental vortices was reduced as a function of their age. The model required some empirical input (pressure at separation and mean reattachment length) to determine some free parameters. In general, the predictions of the mean velocity and surface pressure were only fair and deteriorated in the reattachment region, but the gross features of the flow, such as the unsteadiness, were reasonably well reproduced. Furthermore, the fluctuating component of the surface pressure, a quantity which cannot be obtained at all using a steady state approach, was in tolerable agreement with experiments.

Contributed by the Fluids Engineering Division of The American Society of Mechanical Engineers and presented at the Fluids Engineering Conference, Toronto, Canada, June 1990. Manuscript received by the Fluids Engineering Division August 8, 1989. Paper No. 90-FE-5.

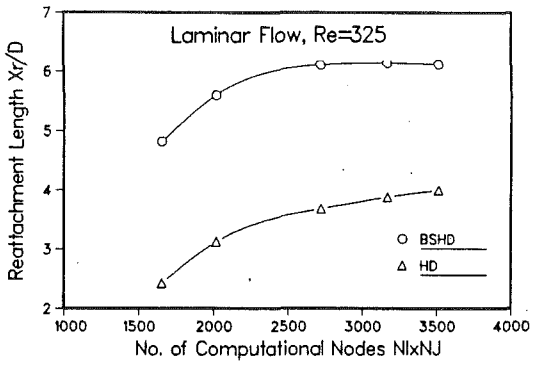

Fig. 2 Effect of grid refinement on laminar flow reattachment length

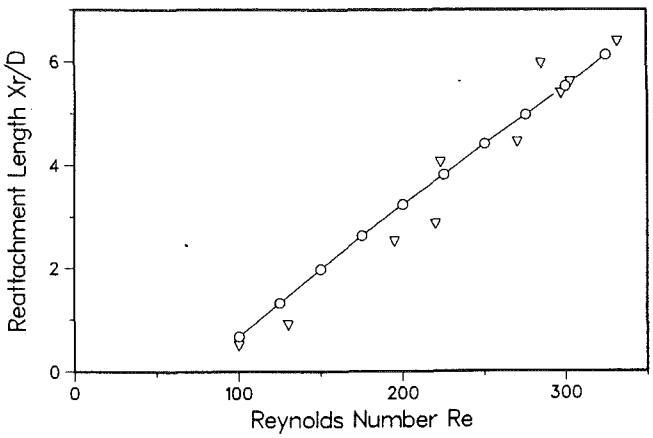

Fig. 3 Variation of laminar flow reattachment length with Reynolds number: ○, BSHD computations; ▽, measurements of Lane and Loehrke (1980)

No finite difference predictions of the turbulent flow around a flat plate are reported in the literature. Many such predictions have, however, been attempted for other reattaching flow geometries, a favorite being the downward facing step. A comprehensive and critical survey of many of these predictions, all based on the solution of the time-averaged Navier-Stokes equations in conjunction with a turbulence closure model, can be found in the review article of Nallassamy (1987). In the context of this study, it is of special interest to note that in most computations the equations were discretized using some form of upstream differencing. The gross features of the recirculation zone were in general underpredicted, and discrepancies of up to 30 percent in the reattachment length were reported. This was partly due to false diffusion, which is inherent to first order accurate upstream differencing. Many early authors, however, attributed the discrepancies to inadequate turbulence modeling. Because modeling and numerical errors cannot usually be dissociated, turbulence model deficiencies can only be determined by reducing false diffusion to negligible levels. This can be achieved—as an alternative to the often impractical approach of grid refinement—by using one of the "higher order" differencing schemes such as the "skew-upwind differencing" of Raithby (1976) or the "quadratic upstream interpolation" of Leonard (1977). The application of these schemes to turbulent recirculating flows has, in general, improved turbulent flow predictions (e.g., Leschziner and Rodi, 1981).

This paper reports numerical predictions, presented in preliminary form in Djilali et al. (1987), of the two-dimensional flow around a long rectangular section placed at zero incidence in a uniform stream. The finite difference solutions were obtained using a modified version of the TEACH code. Two discretization schemes were used: hybrid (HD) and bounded-skew hybrid differencing (BSHD). The performances of the standard k-ϵ turbulence model and a variant which incorporates a curvature correction are assessed with respect to the experimental data presented in a companion paper (Djilali and Gartshore, 1991).

2 Computational Procedure

Mathematical Model. For statistically steady two-dimensional turbulent flow, the governing equations are:

continuity equation:

$$\frac{\partial U}{\partial x}+\frac{\partial V}{\partial y}=0 \tag{1}$$

x-momentum equation:

$$\rho\frac{\partial}{\partial x}(UU)+\rho\frac{\partial}{\partial y}(VU)=-\frac{\partial p}{\partial x}+2\frac{\partial}{\partial x}\left\{\mu_{\text{eff}}\frac{\partial U}{\partial x}\right\}+\frac{\partial}{\partial y}\left\{\mu_{\text{eff}}\left(\frac{\partial U}{\partial y}+\frac{\partial V}{\partial x}\right)\right\} \tag{2}$$

y-momentum equation:

$$\rho\frac{\partial}{\partial x}(UV)+\rho\frac{\partial}{\partial y}(VV)=-\frac{\partial p}{\partial y}+\frac{\partial}{\partial x}\left\{\mu_{\text{eff}}\left(\frac{\partial V}{\partial x}+\frac{\partial U}{\partial y}\right)\right\}+2\frac{\partial}{\partial y}\left\{\mu_{\text{eff}}\frac{\partial V}{\partial y}\right\} \tag{3}$$

Nomenclature

BR = solid blockage ratio ($=D/H$)
C = convective flux coefficient
C_f = wall shear stress coefficient ($=\tau w/\frac{1}{2}\rho U_\infty^2$)
C_p = pressure coefficient ($=(p-p_\infty)/\frac{1}{2}\rho U_\infty^2$)
D = plate thickness; also diffusive flux coefficient
E = integration constant in logarithmic law of the wall
E_x,E_y = grid expansion ratio
G = generation of turbulent kinetic energy
H = wind-tunnel/channel height
k = turbulent kinetic energy
L_u,L_d = distance from recirculation zone to upstream and downstream boundaries
p = static pressure
Re = Reynolds number ($=U_\infty D/\nu$)
U,V = mean velocity in x and y directions
U_τ = friction velocity ($=\sqrt{\tau/\rho}$)
u,v = R.m.s value of fluctuating velocity ($=\sqrt{\overline{u^2}}, \sqrt{\overline{v^2}}$)
x,y = Cartesian coordinates
x_r = time-mean reattachment length
y^+ = wall coordinate ($=yU_\tau/\nu$)
$\Delta x,\Delta y$ = cells near plate corner
ϵ = dissipation rate of turbulent kinetic energy
κ = von Karman constant
μ = dynamic viscosity
ν = kinematic viscosity
τ = shear stress
Ψ = nondimensional stream function ($=\int_0^{y/D}(U/U_\infty)\,d(y/D)$)
ρ = fluid density

Here the effective viscosity concept has been used to represent the combined molecular and turbulent (Reynolds) stresses. Within the framework of the k-ϵ turbulence model (Launder and Spalding, 1974), the effective eddy viscosity is determined from the two auxiliary equations

$$\mu_{\text{eff}} = \mu + \mu_t \tag{4}$$

$$\mu_t = C_\mu \rho \frac{k^2}{\epsilon} \tag{5}$$

and the turbulent kinetic energy k and its dissipation rate ϵ are determined from modeled transport equations which can be written as:

k-transport equation:

$$\rho \frac{\partial}{\partial x}(Uk) + \rho \frac{\partial}{\partial y}(Vk) = \frac{\partial}{\partial x}\left(\frac{\mu_{\text{eff}}}{\sigma_k}\frac{\partial k}{\partial x}\right) + \frac{\partial}{\partial y}\left(\frac{\mu_{\text{eff}}}{\sigma_k}\frac{\partial k}{\partial y}\right) + G - \rho\epsilon \tag{6}$$

ϵ-transport equation:

$$\rho \frac{\partial}{\partial x}(U\epsilon) + \rho \frac{\partial}{\partial y}(V\epsilon) = \frac{\partial}{\partial x}\left(\frac{\mu_{\text{eff}}}{\sigma_\epsilon}\frac{\partial \epsilon}{\partial x}\right) + \frac{\partial}{\partial y}\left(\frac{\mu_{\text{eff}}}{\sigma_\epsilon}\frac{\partial \epsilon}{\partial y}\right) + C_1 \frac{\epsilon}{k} G - C_2 \rho \frac{\epsilon^2}{k} \tag{7}$$

where G represents the generation of turbulent kinetic energy and is given by

$$G = \mu_t \left\{ 2\left[\left(\frac{\partial U}{\partial x}\right)^2 + \left(\frac{\partial V}{\partial y}\right)^2 \right] + \left(\frac{\partial U}{\partial y} + \frac{\partial V}{\partial x}\right)^2 \right\} \tag{8}$$

The values of the empirical constants appearing in equations (5–7) are the standard values recommended in Launder and Spalding (1974).

The modification to the k-ϵ model used here was originally proposed by Hanjalić and Launder (1979) to account for the preferential influence of normal stresses (over shear stresses) in promoting the transfer of turbulent energy from large to small eddies and thereby increasing the rate of dissipation. The modification, in the form given by Leschziner and Rodi (1981) for recirculating flow, replaces the term representing "production of dissipation" in the ϵ transport equation, $P_\epsilon = C_1 \frac{\epsilon}{k} G$, by

$$P'_\epsilon = \frac{\epsilon}{k}\left[C'_1 G - C''_1 \mu_t S_{ns}^2\right] \tag{9}$$

where $C'_1 = 2.24$ and $C''_1 = 0.8$ (giving, consistently with the standard k-ϵ model, $C'_1 - C''_1 = C_1$). The shear strain in the direction of the streamline, S_{ns}, is calculated as in Leschziner and Rodi (1981).

Boundary Conditions. The computational domain boundaries for the blunt rectangular plate geometry are shown in Fig. 1. The upper boundary (AF) corresponds to the wind tunnel wall, and all dimensions correspond to the experimental test conditions described in Djilali and Gartshore (1991).

At the inlet boundary (AB), uniform flow conditions are imposed for all variables using experimental inlet conditions: $U = U_\infty$, $V = 0$, $k_\infty = 9.375 \times 10^{-6} U_\infty^2$. The inlet dissipation rate ϵ_∞ is estimated as follows:

$$\epsilon_\infty = k_\infty^{3/2}/(\lambda H)$$

A value of $\lambda = 0.09$ is chosen to ensure that the turbulent kinetic energy is maintained at its free stream level at $x/D \simeq -4$ as is observed experimentally. the choice of λ is otherwise not critical, and changing λ by a factor of five has virtually no effect on the computed results (less than 0.2 percent change in x_r).

A zero streamwise gradient condition, $\frac{\partial(\,)}{\partial x} = 0$, is applied across the outflow boundary (EF). Although this boundary condition is strictly valid only when the flow is fully developed, its use in other flow conditions is also permissible for computational convenience provided the outlet boundary is located (1) in a region where the flow is in the downstream direction, and (2) sufficiently far downstream from the region of interest. Along the symmetry axis (BC), a zero cross-stream gradient condition, $\frac{\partial(\,)}{\partial y} = 0$, is specified with $V = 0$. No-slip boundary conditions are imposed along solid boundaries (AF, CD, and DE). The near wall values of the parallel velocity component, the turbulent kinetic energy k, and its dissipation rate ϵ are determined from the standard log-law based wall functions (Launder and Spalding, 1974).

Solution Method. A finite volume formulation is used to derive algebraic approximations to the differential equations. Two discretization schemes are used: hybrid (HD) and bounded skew hybrid differencing (BSHD). The BSHD scheme (Lai and Gossman, 1982; Benodekar et al., 1985) takes into account the local direction of the flow, thereby greatly reducing the "skewness error" which, in two-dimensional flows, is often the largest contribution to false diffusion. This scheme also uses a flux-blending technique to eliminate the non-physical overshoots and undershoots typical of higher order schemes.

A staggered nonuniform grid arrangement, with velocity nodes offset from scalar nodes, is used in the present computations. The set of difference equations are solved iteratively using a modified version of the TEACH-II code (Benodekar et al., 1983) which incorporates the PISO (Pressure Implicit Split Operator) solution algorithm. The code uses a line by line solution method in conjunction with a tridiagonal matrix solver. The iteration cycle is terminated and the solution considered converged, when the overall mass and momentum residuals (normalized using inlet conditions) reach a value of less than 0.2 percent.

It is important to note that, as a result of the staggered grid arrangement, the corner cells of the bluff plate (Fig. 4) require a special treatment. These cells have only a half-face in contact with the wall, and to evaluate the convective fluxes across the half-faces correctly one needs to: (i) assume a normal velocity across these half faces equal to that at the outer edge of the half cell (i.e., V_S is used for the normal velocity across the half-face of the U-cell and vice-versa), and (ii) take an effective area for the flux calculations equal to $\Delta y/2 \times 1$ and $\Delta x/2 \times 1$ for U and V, respectively. This treatment of the corner cells was found to have a drastic effect on the solution: HD turbulent flow calculations without this special treatment result in a 40 percent shorter reattachment length (for a 80×40 grid).

Preliminary Computations. Several computations were carried out to determine the effect of the inlet and outlet boundaries on the solutions. The location of this boundary was found to have no noticeable effect on the flow in the recirculation region, provided that $Lu > 9D$. For $Lu < 9D$ a small increase (typically about 0.3 percent for $Lu = 7.5D$) in the separation bubble was observed. The effect of the location of the downstream boundary was noted for $L_d = 15D$ to $8D$. The effect was negligible for $L_d \gtrsim 11D$. Computations with smaller L_d resulted in gradually longer bubbles (typically about 1.0 percent for $L_d = 8D$). All subsequent computations were therefore performed with $L_u \simeq 10D$ and $L_d \simeq 12D$.

To minimize the truncation errors associated with nonuniform grid distributions, the effect of the grid expansion factors $E_x = \Delta x_i/\Delta x_{i-1}$ and $E_y = \Delta y_j/\Delta y_{j-1}$ was investigated. It was found that an economy in computational cells (compared to a uniform distribution) can be obtained with no noticeable

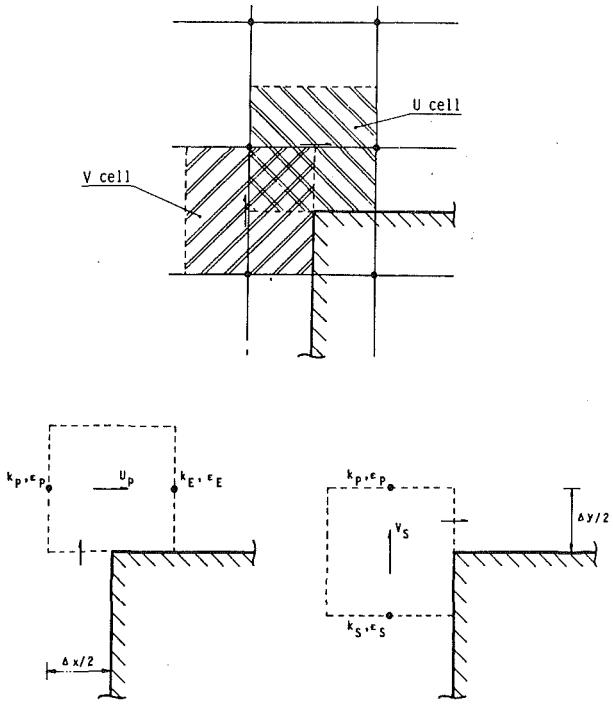

Fig. 4 Computational cells near plate corner

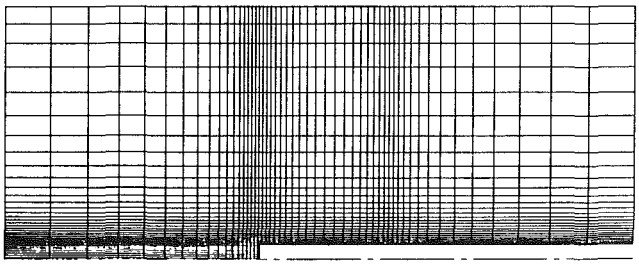

Fig. 5 Typical grid distribution

loss in accuracy, provided that the expansion factors are kept within the following ranges:

$$0.8 < E_x, E_y < 1.2 \text{ for } \begin{cases} x < -D \text{ and } x > x_r \\ y > D \end{cases}$$

$$0.9 < E_x, E_y < 1.1 \text{ for } \begin{cases} -D \le x \le x_r \\ -0.5D \le y \le D \end{cases}$$

All subsequent computations were performed with expansion factors within these ranges.

A number of different grid distributions were investigated. A proper resolution of the region immediately upstream of and around the sharp corner was found to be particularly critical to the accuracy of the solutions. Consequently, a cluster of fine equally spaced grids was located there. It was also found that optimum array sizes are obtained when the mesh at the corner has a ratio $\Delta x = \Delta y \simeq 2.5$. The grid spacings were expanded on either side of this sharp corner, in both x and y-directions, as shown in Fig. 5. In addition, the x-direction grid was refined locally around the reattachment region. This local refinement was not critical to the computation, but allowed a more precise location of the reattachment lengths, which were determined by linear interpolation from the computed wall shear stress distributions.

In the course of preliminary computations using the BSHD scheme, the stagnation flow in the region immediately upstream of the bluff plate was found to be inaccurately predicted, with stagnation pressure coefficients reaching a maximum of about 0.92 instead of 1.0. This type of problem has also been observed by Lai (1983) who showed that the performance of skewed based schemes deteriorates in the presence of strong pressure gradients. A similar problem was reported by Castro et al. (1981) when using a vector differencing scheme for the flow over a normal flat plate. For the present calculations this deficiency of the BSHD scheme was "rectified" by using the BSHD scheme in the region downstream of the plate leading edge and the HD scheme upstream of it. This split, though it may seem arbitrary, is in fact based on Lai's conclusions that, in situations of strong pressure gradients, the hybrid differencing scheme performs better than the skewed differencing scheme because numerical diffusion is less significant under these circumstances. The use of a split domain produced differences of less than 7 percent in computed values of x_r, the split domain resulting in the longest separation bubble and a stagnation pressure coefficient of essentially unity. This technique was used in all subsequent BSHD calculations.

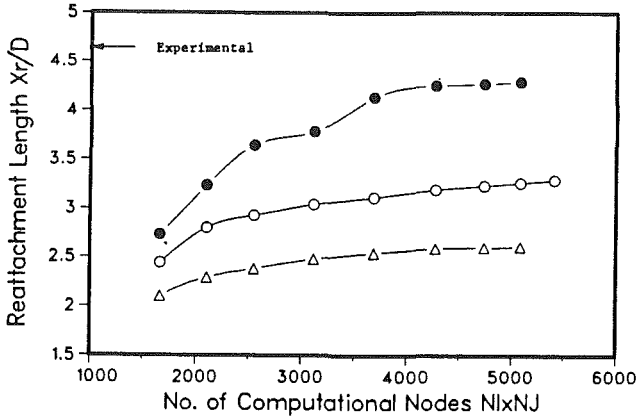

Fig. 6 Effect of grid refinement on computed reattachment length: Δ, HD scheme with k-ϵ model; ○, BSHD scheme with k-ϵ model; ●, BSHD scheme with PDM

3 Numerical Results

Effect of Grid Refinement. The turbulent flow calculations were carried out at a Reynolds number of 5×10^4 for a blockage ratio of 5.6 percent; these conditions correspond to the measurements described in Part I.

The results of the grid refinement studies are shown in Fig. 6 for three cases: HD scheme with standard k-ϵ model, BSHD with standard k-ϵ model, and BSHD with standard k-ϵ model and preferential dissipation modification. These will simply be referred to as HD, BSHD, and PDM, respectively. The grid distributions used range from 49×34 ($\Delta x_{min}/D = 20$ percent, $\Delta y_{min}/D = 5.6$ percent) to 82×66 ($\Delta x_{min}/D = 3.6$ percent, $\Delta y_{min}/D = 0.9$ percent).

Based on laminar flow results shown earlier, the HD scheme was expected to yield a shorter reattachment length than the experimentally observed value of $x_r/D = 4.7$, and while this is borne out by the results, the magnitude of the discrepancy (44 percent with a fine 82×62 grid) was somewhat surprising. The discrepancies reported in the literature for various other geometries are much smaller even though less computational nodes were used. For example, Durst and Rastogi (1977) reported a 30 percent underprediction of x_r for the flow around a surface mounted block using used a 50×27 grid. For the backward facing step flow, Hackman (1982) reported a 12 percent underprediction with a 50×50 grid.

The BSHD scheme produces a substantially longer reattachment length as shown in Fig. 6, but the discrepancy with the experimental value is still large at 30 percent. In view of

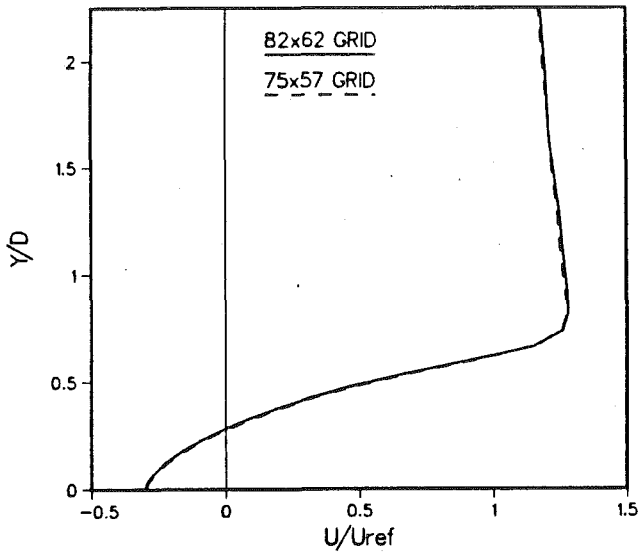

Fig. 7 Effect of grid refinement on computed velocity profile at $x/D = 2$ (PDM computation)

the good agreement found between laminar flow BSHD predictions and experiments, these rather poor predictions can, with confidence, be attributed to turbulence model deficiencies. The use of the modified turbulence model, which was in fact prompted by these results, leads to an encouraging improvement of the predictions. The PDM solutions appear to be independent of grid refinement for a 75×57 grid, and a reattachment length of $4.3D$ is produced—this is within 10 percent of the experimentally observed value of $4.7D$. As a further check of grid independence, Fig. 7 shows streamwise velocity profiles at $x/D = 2$ predicted by the PDM using two different grid distributions. These profiles are to all intents and purposes identical.

However, a disturbing feature of the computations is that the grid independence, demonstrated both in terms of the reattachment length and in the flowfield, does not extend to the computed wall shear stresses which were found to change by as much as 10 percent when refining the grid from 75×57 to 82×62 nodes. The reason for this lies in the inordinately fine grid spacing required to properly resolve the flow around the sharp corner ($\Delta y_{\min}/D \simeq 1$ percent). This results in near-wall computational nodes which are within the viscous sublayer (i.e., $y^+ < 11.63$). The standard wall-function treatment is not entirely rigorous in these circumstances, and although the present computations suggest that the flow field is not sensitive to the details of the near-wall flow—and this is substantiated by the results of Hackman (1982) who found different wall function treatments to have little impact on the backward facing step flow—this matter clearly deserves further investigation. A more detailed discussion on the wall function treatment is given by Djilali et al. (1989) in the context of convective heat transfer predictions where the near-wall treatment is of critical importance.

Predictions and Comparison With Experimental Data. Examination of Fig. 8 shows that the BSHD computations underpredict not only the reattachment length, but also the height of the separation bubble and the maximum backflow velocity. The PDM predictions (Fig. 9) are, on the other hand, in very good agreement with the experimental data in the recirculating flow region. A reattachment length of $4.3D$, compared to the experimental value of $4.7D$, is predicted; this small difference (< 9 percent) may be due, in part, to a slight departure in the experiments from ideal two-dimensional conditions. The PDM predictions start to deteriorate after reattachment as a result of a slower rate of recovery of the reattached boundary layer.

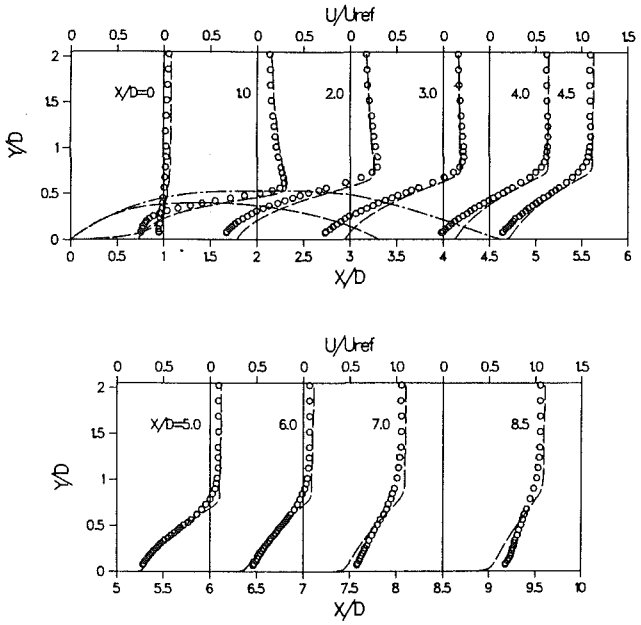

Fig. 8(*a,b*) Mean longitudinal velocity profiles: — —, BSHD computation; ○, PWA measurements. Separation streamlines: — — —, computed; ——·——, experimental

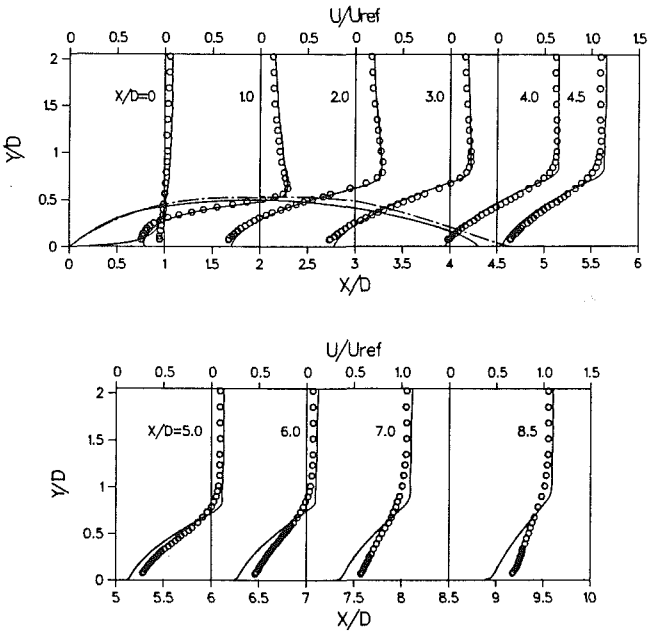

Fig. 9(*a,b*) Mean longitudinal velocity profiles: ———, PDM computation; ○, PWA measurements. Separation streamlines: ———, computed; ——·——, experimental

The deterioration of the predicted velocity profiles in the recovery region is a common feature of many reattaching flow calculations (see Nallasamy, 1987) and is perhaps not surprising in view of the complex and unsteady nature of the reattachment process.

Figure 10 shows the effective viscosity contours. The use of the PDM affects most significantly the eddy viscosity levels immediately upstream and downstream of separation, and along a region corresponding roughly to the center of the shear-layer. In the first part of the separated shear-layer, it is expected that the strong stabilizing curvature would reduce turbulent stresses and hence the eddy viscosity. The PDM appears to reproduce, at least in part, these effects. In their experimental study of the normal-plate/splitter-plate geometry, Castro and Haque (1987) argue that curvature effects may not be impor-

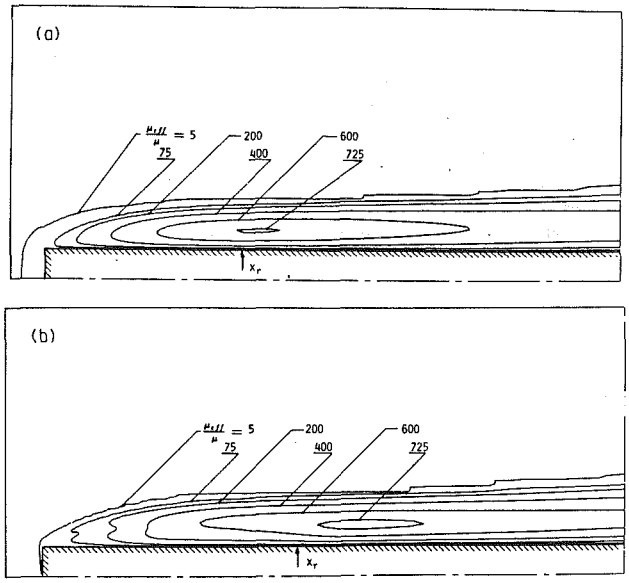

Fig. 10(*a,b*) Contours of constant effective viscosity: (*a*) BSHD computation; (*b*) PDM computation

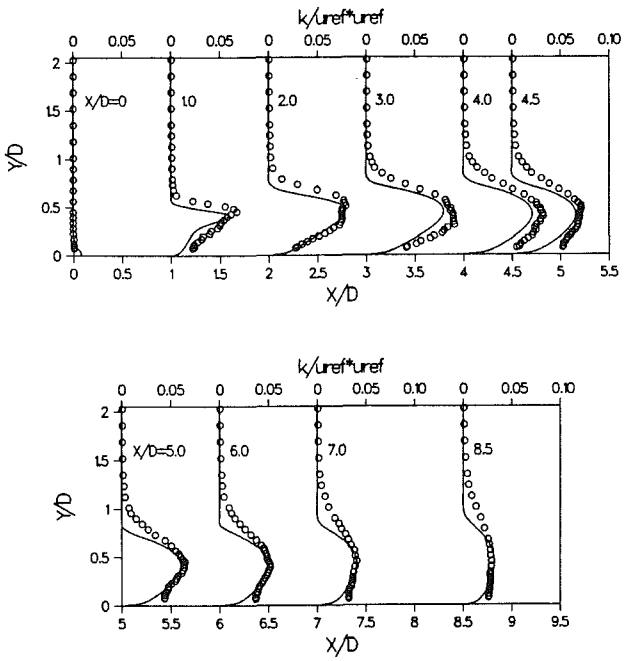

Fig. 11(*a,b*) Turbulent kinetic energy profiles: ——— , computed (PDM); ○, estimated from PWA measurements

tant in the separating shear layer. This conclusion was based on measurements for $x/x_r \geq 0.35$ and is not necessarily in contradiction with the present computations, where the PDM affects most significantly the eddy viscosity in the vicinity of separation. The improved velocity field predictions result from the reduced eddy viscosities which contribute to a slower growth rate of the separated shear layer and hence a longer separation bubble. The highest eddy viscosities occur in both cases slightly downstream of the reattachment point.

The predicted turbulent kinetic energy profiles are presented in Fig. 11. Since no experimental measurements of k were available, this was estimated from the measured longitudinal r.m.s. velocity using the relation $k = u^2/\alpha$, where α is a measure of the degree of anisotropy of the flow. An average value of $\alpha = 1.1$ was estimated from the flat plate/splitter plate data of Ruderich and Fernholz (1986). The profiles show a remarkable similarity with the estimated values both in recirculating flow

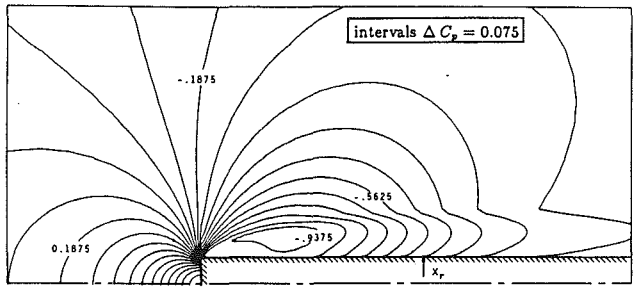

Fig. 12 Contours of pressure (PDM computation)

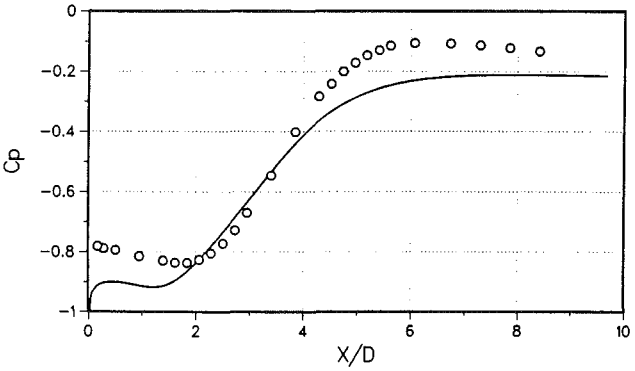

Fig. 13 Comparison of computed and experimental pressure distributions on top surface of the plate: ——— , computed (PDM); ○, measured

and recovery regions. In particular the highest k is predicted to occur at the same streamwise location as the estimated value ($x/D = 3$). A comparison of these results with the standard k-ϵ model predictions shows that the PDM, by increasing ϵ in the high streamline curvature region close to separation, results in more realistic values of k. An important feature of the estimated profiles which is not well reproduced is the spread of k into the outer region. This feature, also present in the standard k-ϵ predictions, indicates a possible inadequacy of the modeled diffusion term of the k-equation.

The predicted pressure field shown in Fig. 12 sheds light on some interesting points. The pressure remains fairly uniform within the first half of the separation bubble. Large cross-stream gradients are present along a region corresponding roughly to the outer part of the shear layer. These gradients are more pronounced near separation, probably as a result of the higher streamline curvature. The corresponding pressure distribution along the surface of the plate is shown in Fig. 13. This pressure distribution reproduces fairly well the trends of the experimental data, and the broad region of relatively constant pressure with a small dip preceding recovery. The minimum pressure coefficient, excluding the separation value, is underpredicted by about 10 percent, probably as a result of the shorter bubble. The unrealistically low pressure coefficient predicted at separation is due to the singularity associated with the sharp corner. In the actual flow, this corner is slightly rounded, since in practice it is not possible to manufacture a model with a perfectly sharp corner. Figure 14 shows the wall shear stress distribution. Again the experimental trends are well reproduced and the maxima and minima compare well bearing in mind the large uncertainty in the measured values (±25 percent).

The predicted effect of blockage ratio on the reattachment length is shown on Fig. 15 together with measured values reported in the literature. The experimental trends are well reproduced and the computed values are within 10 percent of the measured ones. Varying departures from strict two-dimensionality in the measured case could account, in part, for the generally higher experimental values of x_r. It should also

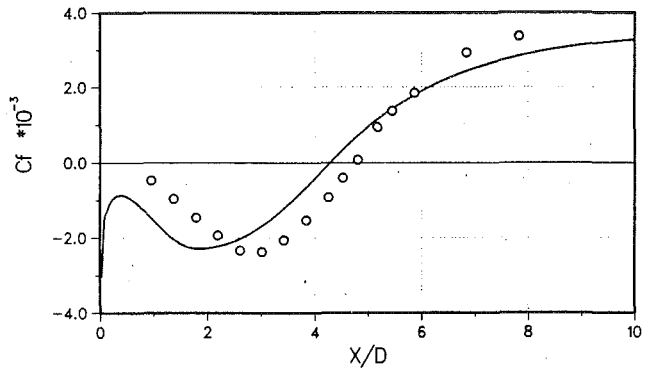

Fig. 14 Comparison of computed and experimental wall shear stress distributions: ———, computed (PDM); ○, measured

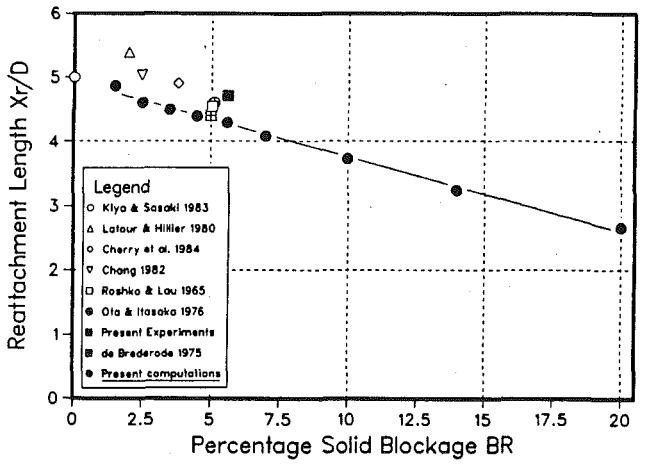

Fig. 15 Effect of blockage on reattachment lengths (experimental data compiled by Cherry et al., 1984)

be noted that all calculations were carried out assuming the boundary layers originated at the inlet of the computational domain, and initial profiles for k and ϵ were kept unchanged. These assumptions do not necessarily correspond to the actual experimental conditions, but the resulting errors are expected to be small—at least for small blockage and low free-stream turbulence conditions.

Computational Costs. Most of the present computations were performed on a VAX 11/750 computer. The computations required from 45 minutes of CPU time and 83 iterations, for a 49×34 grid, to 545 minutes and 329 iterations, for a 82×62 grid. The PDM computations required, for a given grid, about 20 percent more CPU time than the BSHD computations as a result of the slower convergence of the modified turbulence model.

4 Concluding Discussion

Numerical predictions for the turbulent separated-reattaching flow over a bluff rectangular section have been presented. The finite difference method investigated here shows that significant errors can occur through false diffusion when predicting this flow using the standard hybrid differencing scheme, even with very fine grid spacings. The use of skewed-hybrid differencing results in a substantial improvement, but gives rise to some errors near the stagnation region where the discretized equations are source dominated. In the present computations, this deficiency was "corrected" by reverting to hybrid differencing in the stagnation region.

The results of the BSHD computations show that the standard k-ϵ model fails to represent accurately the effects of turbulence in the region around separation. The use of the preferential dissipation modification (PDM) leads to significantly improved predictions, and results in a reattachment length within 10 percent of the experimental value. The small difference may be due to a slight departure in the experiments from two-dimensionality. Detailed comparison of the present predictions within the separated flow region give a much more satisfactory agreement with measurements than is obtained with the discrete vortex method (Kiya et al., 1982). Agreement gradually deteriorates as the wall boundary layer redevelops downstream of reattachment. As noted elsewhere (e.g., Bradshaw and Wong, 1972), the turbulence structures in this region are unlike those typical of more "normal" turbulent boundary layers. In particular, the turbulent length scales are roughly independent of y, and the law of the wall formulation is inapplicable within the redeveloping flow region. Modifications of the usual k-ϵ and near-wall models are obviously required for accurate calculations in this region. Possibly, only Reynolds stress models—which do not suffer from the physical drawback of the eddy viscosity concept—could account properly for the complicated turbulence structure around reattachment.

In the present computations, there is some uncertainty in the initial conditions for the boundary layers developing on the wind tunnel walls. The errors arising from this uncertainty are expected to be small for the low blockage ratios considered in this study. Otherwise, the boundary conditions for the flow around the bluff rectangular plate are clearly defined. The present results show that this flow constitutes a severe test for discretization schemes as well as turbulence models. In both, inadequacies appear to be magnified as a result of streamline curvatures, large gradients, and the stagnation flow region. These features, as well as the simple uniform flow inlet boundary conditions—an important factor in numerical solutions (Nallasamy, 1987)—make this representative bluff-body configuration a good benchmark test for numerical methods and turbulence models.

In light of the unsteadiness of the flow and the complexity of the turbulence structure in the reattachment region, the present predictions are quite remarkable. A logical extension of this work would be a time dependent solution that takes into account the experimentally observed large scale unsteadiness.

Acknowledgment

This work was supported by an operating grant from the Natural Sciences and Engineering Research Council of Canada.

References

Benodekar, R. W., Gosman, A. D., and Issa, R. I., 1983, "The TEACH-II Code for the Detailed Analysis of Two-Dimensional Turbulent Recirculating Flow," Dept. Mech Engng, Imperial College, Rept. FS/83/3.

Benodekar, R. W., Goddard, A. J. H., Gosman, A. D., and Issa, R. I., 1985, "Numerical Prediction of Turbulent Flow Over Surface-Mounted Ribs," *AIAA J.*, Vol. 23, pp. 359–366.

Bradshaw, P. B., and Wong, F. Y. F., 1972, "The Reattachment and Relaxation of a Turbulent Shear Flow," *J. Fluid Mech.*, Vol. 52, pp. 113–135.

Castro, I. P., Cliffe, K. A., and Norgett, M. J., 1981, "Prediction of the Low Reynolds Number Laminar Flow Over a Normal Flat Plate, and Its Application to Turbulent Flow Calculations," *Proc. 3rd Symp. on Turbulent Shear Flows*, Univ. California, Davis, 18.7–18.14.

Castro, I. P., and Haque, A., 1987, "The Structure of a Turbulent Shear Layer Bounding a Separation Region," *J. Fluid Mech.*, Vol. 179, pp. 439–468.

Cherry, N. J., Hillier, R., and Latour, M. E. M. P., 1984, "Unsteady Measurements in a Separated and Reattaching Flow," *J. Fluid Mech.*, Vol. 144, pp. 13–46.

Djilali, N., 1987, "An Investigation of Two-Dimensional Flow Separation With Reattachment," Ph.D. thesis, Univ. of British Columbia, Vancouver.

Djilali, N., and Gartshore, I. S., 1991, "Turbulent Flow Around a Bluff Rectangular Plate. Part I: Experimental Investigation," ASME JOURNAL OF FLUIDS ENGINEERING, Vol. 113, pp. 51–59.

Djilali, N., Gartshore, I., and Salcudean, M., 1987, "An Experimental and Numerical Study of the Flow Around a Blunt Rectangular Section: A Test Case for Computational Methods?" *Proc. 6th Symp. on Turbulent Shear Flows*, Toulouse, 19.3.1-6.

Djilali, N., Gartshore, I., and Salcudean, M., 1989, "Calculation of Convective Heat Transfer in Recirculating Turbulent Flow Using Various Near-Wall Turbulence Models," *Num. Heat Transfer*, Part A, Vol. 16, pp. 189–212.

Durst, F., and Rastogi, A. K., 1977, "Theoretical and Experimental Investigation of Turbulent Flow With Separation," *Turbulent Shear Flows 1*, eds. F. Durst, B. E. Launder, F. W. Schmidt, and J. H. Whitelaw, Springer-Verlag, Berlin, pp. 208–219.

Hackman, L. P., 1982, "A Numerical Study of the Turbulent Flow Over a Backward Facing Step Using a Two-Equation Turbulence Model," Ph.D. thesis, Univ. Waterloo.

Hanjalić, K., and Launder, B. E., 1979, "Preferential Spectral Transport by Irrotational Straining," in *Turbulent Boundary Layers*, ASME.

Kiya, M., Sasaski, K., and Arie, M., 1982, "Discrete-Vortex Simulation of a Turbulent Separation Bubble," *J. Fluid Mech.*, Vol. 120, pp. 219–244.

Lai, K. Y. M., 1983, "Numerical Analysis of Fluid Transport Phenomena," Ph.D. thesis, Univ. London.

Lai, K. Y. M., and Gosman, A. D., 1982, "Finite Difference and Other Approximations for the Transport and Navier-Stokes Solutions," Dept. Mech Engng, Imperial College, Rept. FS/82/16.

Lane, J. C., and Loehrke, R. I., 1980, "Leading Edge Separation From a Blunt Plate at Low Reynolds Number," ASME JOURNAL OF FLUIDS ENGINEERING, Vol. 102, pp. 494–496.

Launder, B. E., and Spalding, D. B., 1974, "The Numerical Computation of Turbulent Flow," *Comp. Meths. Appl. Mech. Engng*, Vol. 3, pp. 269–289.

Leonard, B. P., 1977, "News Flash: Upstream Parabolic Interpolation," *Proc. 2nd GAMM Conference on Numerical Methods in Fluid Mechanics*, Köln, p. 97.

Leschziner, M. A., and Rodi, W., 1981, "Calculation of Annular and Twin Parallel Jets Using Various Discretization Schemes and Turbulence-Model Variations," ASME JOURNAL OF FLUIDS ENGINEERING, Vol. 103, pp. 352–360.

Nallasamy, M., 1987, "Turbulence Models and Their Applications to the Prediction of Internal Flows: A Review," *Computers and Fluids*, Vol. 15, pp. 151–194.

Raithby, G. D., 1976, "Skew Upwind Differencing Schemes for Problems Involving Fluid Flow," *Comp. Meths Appl. Mech. Engng*, Vol. 9, pp. 153–164.

Ruderich, R., and Fernholz, H. H., 1986, "An Experimental Investigation of a Turbulent Shear Flow With Separation, Reverse Flow, and Reattachment," *J. Fluid Mech.*, Vol. 163, pp. 283–322.

E. Savory
Research Fellow.

N. Toy
Senior Lecturer.

Department of Civil Engineering,
University of Surrey,
Guildford GU2 5XH,
United Kingdom

Real-Time Video Analysis of Twin Jets in a Crossflow

The research presented in this paper is an investigation of the interaction between twin side-by-side circular jets issuing into a crossflow, utilizing a real-time video digitization system to obtain quantitative data from the visualized flow fields. The intermittency field results obtained from experiments with different jet spacings and jet velocity/crossflow velocity ratios are reported.

Introduction

The single circular jet in a crossflow configuration occurs in many branches of aeronautics and, hence, the interaction between the jet and the crossflow has been the subject of considerable research, as reviewed by Ransom and Wood (1974), Bradbury (1981), and Hancock (1987). The main characteristics of the flow field, namely the formation of a pair of counter-rotating vortices, which dominate the deflected jet, and the generation of a turbulent wake, are now well established.

Research into the case of multiple jets in a crossflow is somewhat more limited, Walker and Kors (1973), Kamotani and Greber (1974), Karagozian et al. (1986), with much of the work being motivated by the need to improve the efficiency of dilution zone mixing in gas turbine combustion chambers, such as that of Holdeman and Walker (1977) and Khan et al. (1981). In most instances a row of jets normal to the flow direction has been utilized. The emphasis has been on determining the result of the mixing process in the downstream flow regime in terms of temperature or gas concentrations, rather than examining the actual jet flows themselves. The case of two jets, either in-line (tandem) or side-by-side, has been studied by Ziegler and Wooler (1973), Schwendemann (1973), Makihata and Miyai (1979), Isaac (1982), and Isaac and Jakubowski (1985). The latter authors presented comparisons between hot-wire turbulence data obtained with a single jet and with two jets in tandem. Their results indicated that the tandem jets showed greater vertical penetration than the single jet, for the same jet ratio. In addition, the basic shapes of the velocity and turbulence profiles were similar for both cases, such that the twin jets appeared to merge into one, forming a jet with greater dimensions and higher turbulence intensities than the single jet case.

The present work is an examination of the interaction between twin side-by-side circular jets issuing normally into a crossflow, in order to increase our knowledge of the influence on the jet development of geometrical parameters such as jet nozzle spacing and jet velocity to crossflow velocity ratio. The research utilizes a system for the real-time analysis of video images using a PDP-11/73 minicomputer, Toy and Wisby (1988a,b).

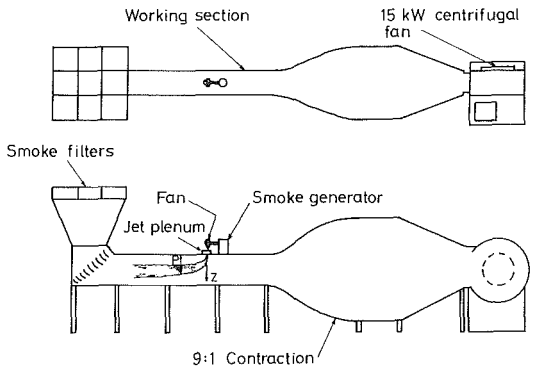

Fig. 1 Smoke tunnel facility

Experimental Details

The experiments were conducted in a purpose built, open-circuit, smoke tunnel facility, shown in Fig. 1, which has working section dimensions of 0.75×0.62m and a turbulence level of 0.2 percent. The tunnel outlet is fitted with high efficiency filters to remove practically all the smoke particles. Smoke was produced by a Concept Genie generator and introduced into the tunnel through two 13.5mm internal diameter copper nozzles inserted into a common plenum chamber. A range of these plenums was constructed, giving jet nozzle spacings of 1, 3, and 5 diameters. The generator and plenums were mounted on the roof of the tunnel in an arrangement which allows variation of orientation of the jets to the crossflow direction. The experiments were conducted with a crossflow velocity of lm/s, representing a Reynolds number of 9.3×10^2 based on nozzle diameter. The approach flow boundary layer was turbulent with a thickness of 60mm, that is 4.44D. Three jet velocity to crossflow velocity ratios were studied, namely 6, 8, and 10. In each case the jet velocity was that measured at the center of the nozzle exit. In the work reported here only the side-by-side configuration was examined, with measurements undertaken in YZ planes at downstream locations of $X/D = 2.5$, 5, 10, 20, and 30, for each jet spacing and velocity ratio.

Contributed by the Fluids Engineering Division for publication in the JOURNAL OF FLUIDS ENGINEERING. Manuscript received by the Fluids Engineering Division May 10, 1990.

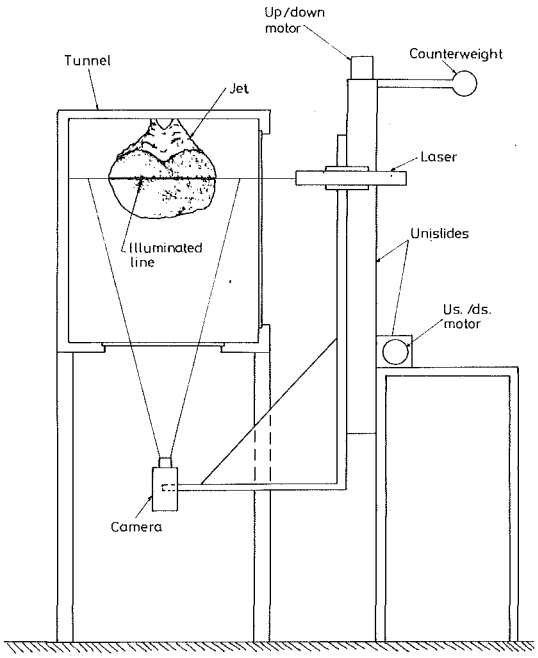

Fig. 2 Laser and camera traversing system

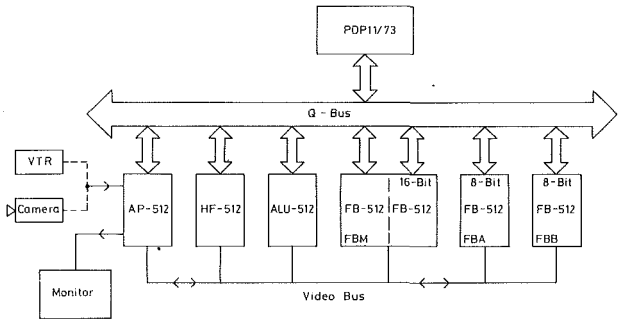

Fig. 3 Block diagram of image processing system

Intermittency contour maps of the jet structures were obtained at each downstream location by illuminating the flow at a series of relative "heights" (spaced 1D apart) using a single 10mW laser beam directed across the flow. The laser was attached to a computer-controlled two-dimensional traversing mechanism along with a monochrome video camera which was used to record the laser-line traces. This setup is illustrated in Fig. 2. Hence, the positions of the laser-line and the camera were fixed relative to each other, with each digitized pixel representing a flow area of approximately 0.67×0.67mm. The traversing mechanism had a positional accuracy of better than ± 0.02mm. The positional error of any measured point in the flow field was ± 0.03D.

The video digitization and analysis were undertaken by a PDP-11/73 minicomputer-based system incorporating Imaging Technology boards for analogue processing (AP-512 board), arithmetic logic operations (ALU-512), histogram computations (HF-512), and frame buffer storage (FB-512). The full monochrome system is illustrated by the block diagram in Fig. 3, although in the present work it was necessary to utilize only the AP board and a single frame buffer. It has been demonstrated in previous work that the video system can be used to obtain quantitative data such as intermittencies, interface statistics, and relative turbulence intensities from smoke visualization, Toy and Wisby (1988b). In the case of intermittency measurements, earlier researchers, such as Fiedler and Head (1966), have shown that smoke can be used as a discriminator between nonturbulent and turbulent flow regions. Indeed, comparisons with the standard hot-wire anemometry approach for measuring intermittency demonstrate that the smoke/no-smoke interface is highly correlated with the turbulent/nonturbulent interface, Falco (1980). In the present experiments the fully turbulent jets were seeded with smoke, while the crossflow, which was nonturbulent (except for within the wall boundary layer approaching the jets), was unseeded. Hence, when the interaction region was viewed by the camera, the "white" portions of each laser-illuminated line (smoke present) represented regions of turbulent flow and the "black" portions represented nonturbulent flow regions. By acquiring 5000 line traces (100 seconds sampling time) at each horizontal location it was possible to compute the intermittency function along that line, defined as

$$I(x, t) = \begin{cases} 1 \text{ if the point } (x,t) \text{ is in a fully turbulent region} \\ 0 \text{ if the point } (x,t) \text{ is in a nonturbulent region.} \end{cases}$$

Comparative experiments showed that the intermittency function measurements were within ± 0.020 of those measured by standard hot-wire anemometry (in those regions where the hot-wire data were valid), with a repeatability of ± 0.003 at any pixel. Six-bit digitization was used to substantially reduced signal noise effects and to produce a reliable discriminator between the turbulent and nonturbulent flow regions. Complete investigation of the largest jet cross sections required approximately 60 minutes of experimental measurement and analysis, highlighting the potential of this technique for rapidly obtaining a significant amount of data when compared to standard techniques.

In addition to the quantitative data acquisition work, some purely qualitative full-field images were obtained. For these experiments the smoke jets were illuminated in planes across the jet paths by a halogen lamp directed through a slit in the tunnel wall. The flows were observed by the video camera, located downstream in the working section, and these images were then processed by the minicomputer. By weighted averaging of successive video images, the shapes and sizes of the jets at each downstream location were determined. Grey

Nomenclature

D = jet nozzle diameter
$I(x, t)$ = intermittency function
P = maximum penetration of the combined jets at any downstream location
S = spacing between jet nozzle centers
t = arbitrary time during flow field measurements
W = maximum width of the combined jets at any downstream location
x = arbitrary point located in the flow field
X = Cartesian coordinate in crossflow direction, with origin at center of nozzle exit
Y = Cartesian coordinate in lateral direction
Z = Cartesian coordinate normal to ground plane
α = jet velocity/crossflow velocity ratio

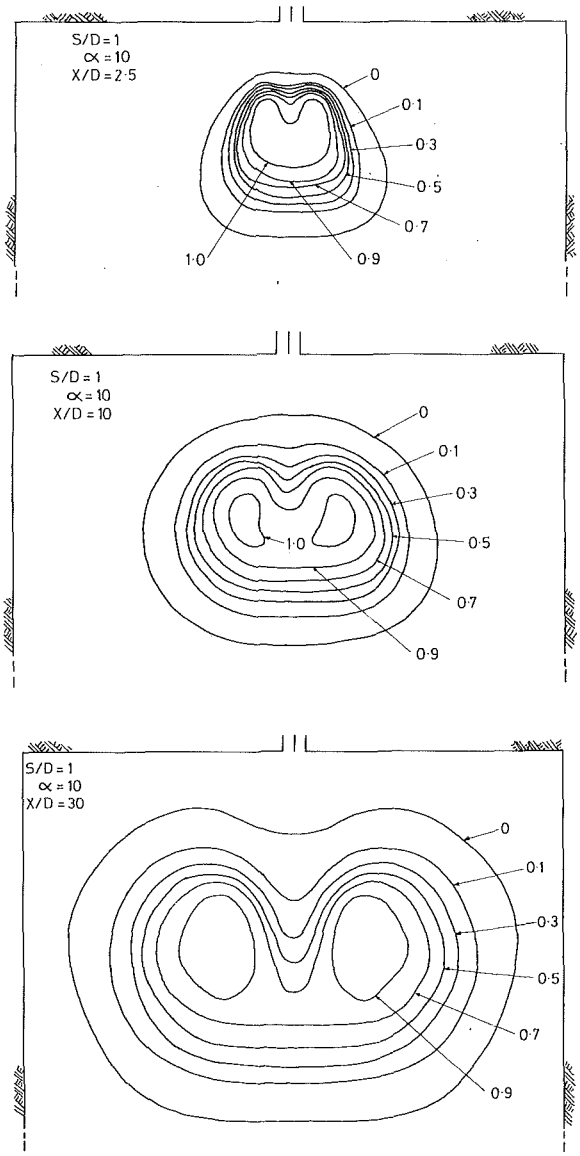

Fig. 4 Intermittency distributions at three locations for $\alpha = 10$ and S/D = 1

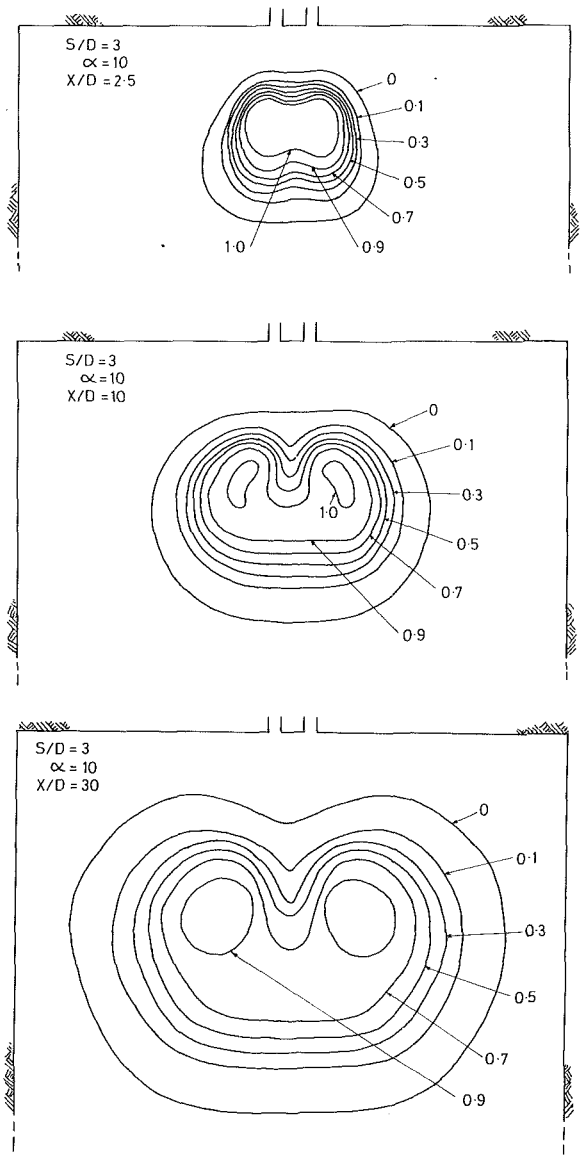

Fig. 5 Intermittency distributions at three locations for $\alpha = 10$ and S/D = 3

level contouring, with additional pseudo-coloring, highlighted the locations of the vortex centers within the jets. These tests provided a rapid indication of the range of laser-lines which were required at each downstream location.

Discussion

Before discussing the development of the twin jets in terms of the intermittency results it is appropriate to mention the most significant finding arising from visual observations and qualitative interpretation of individual video images. Even in the cases where both vortices (of the counter-rotating pair associated with each jet) form in the initial development region, the inner vortices rapidly diminish such that the outer vortices then form a pair similar to that which exists for the single jet case. It is this process which appears to result in the coalescing of the jets noted by Isaac (1982) and Isaac and Jakubowski (1985).

It is only possible to illustrate in this paper a selection of the 45 planes of intermittency data surveyed during the present work. Hence, in order to examine the effect of jet nozzle spacing, Figs. 4, 5, and 6 show the profiles at $X/D = 2.5$, 10, and 30 for $\alpha = 10$ with $S/D = 1$, 3, and 5, respectively. All the data indicate that in the initial region ($X/D = 2.5$) there is a single area of fully turbulent flow ($I = 1$), continuous across both jets and approximately 4D wider than the spacing of the outer edges of the two nozzles. At the smallest nozzle spacings, the indentation of the contours on the ground plane side of the jets illustrate where the dominant outer vortices are beginning to entrain fluid into the combining jets. With increasing spacing this indentation decreases and is not present at $S/D = 5$ (until much further downstream at $X/D = 10$). However, there are indentations on the opposite side of the jet for $S/D = 5$ indicating a reduction in jet turbulence where the crossflow is passing between the jets. This effect diminishes with jet spacing such that at $S/D = 1$ it appears that no crossflow is penetrating between the jets.

As the jets bend and develop in the downstream direction the fully turbulent region becomes confined to two lobes on either side of the plane of symmetry (by $X/D = 10$). These are probably closely associated with the centers of the vortices, although comparative vorticity measurements of the kind undertaken by the present authors for the single jet case, Toy and Savory (1988), would be necessary to confirm this. Further downstream the fully turbulent regions diminish in size, most rapidly for $S/D = 1$, until by $X/D = 30$ they have disap-

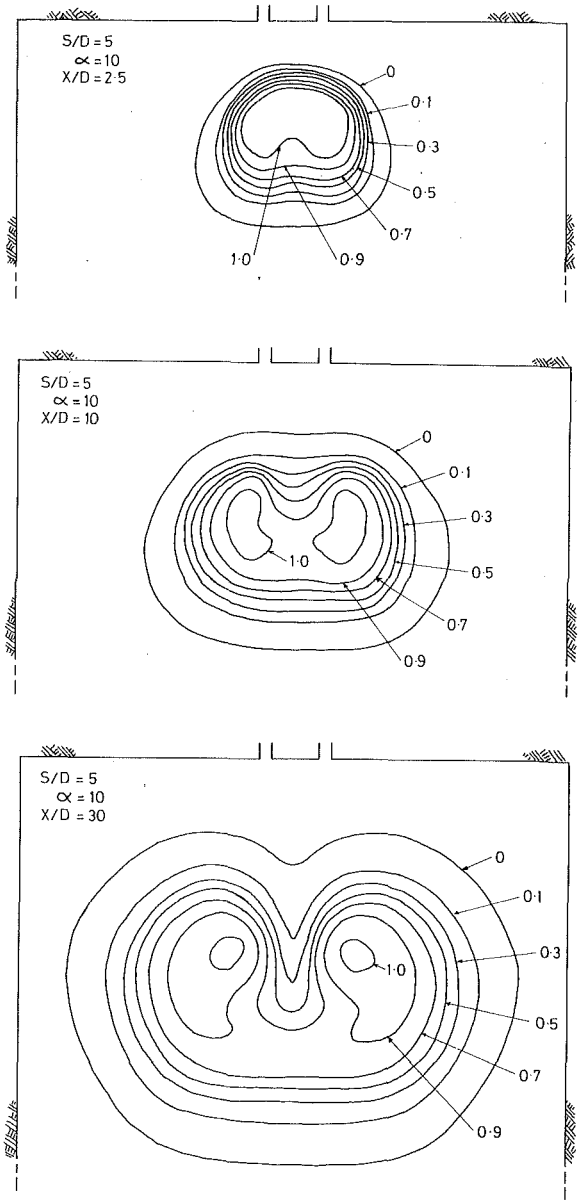

Fig. 6 Intermittency distributions at three locations for $\alpha = 10$ and $S/D = 5$

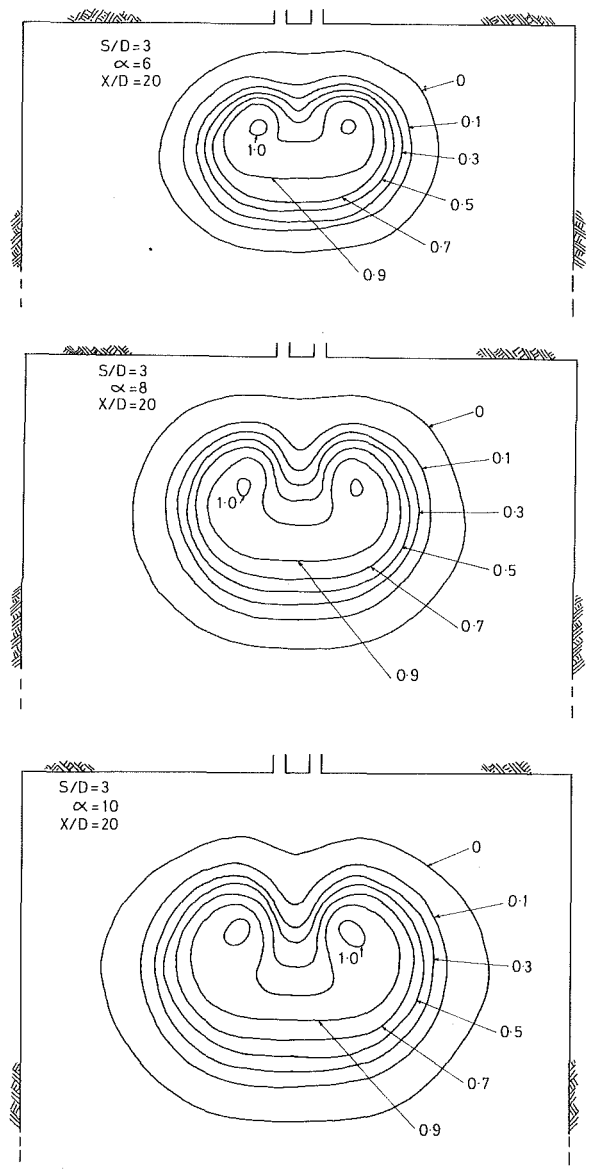

Fig. 7 Intermittency distributions at $X/D = 20$ with $S/D = 3$ for three jet ratios

peared, except for the largest nozzle spacing. In addition, at this downstream location the combined jets are beginning to exhibit the characteristic kidney shape aoociated with a fully developed single jet in a crossflow. This similarity with the shape of a single jet, together with the presence of only the two outer fully turbulent lobes, provides evidence that the inner vortices of each pair either do not form or are very short-lived.

The effect of varying the jet velocity ratio for a given nozzle geometry and downstream location is illustrated in Fig. 7, for $S/D = 3$ at $X/D = 20$. Essentially, α is a scaling parameter for the gross jet characteristics of width, depth and penetration, such that the jet at $\alpha = 10$ is more fully developed than the $\alpha = 6$ case.

Previous work on single jets has shown that the main geometrical characteristics, such as jet penetration and width, are largely functions of α and X/D only. Hence, the maximum jet penetration, P, and the maximum width, W, may be adequately described by the following relationships, Pratte and Baines (1967);

$$\frac{P}{\alpha D} = A\left(\frac{X}{\alpha D}\right)^m \tag{1}$$

$$\frac{W}{\alpha D} = B\left(\frac{X}{\alpha D}\right)^n \tag{2}$$

where A, B, m, and n are constants. Using the present data and taking the $I = 0$ contour as the jet boundary the results for these constants are as tabulated in Table 1.

In the present work the maximum jet penetration is defined as the distance from the wall to the furthest location of the $I = 0$ contour, measured on the plane of symmetry. Similarly, the maximum width is the maximum lateral distance within the $I = 0$ contour. The present data shows some similarity with the single jet studies of Gordier (1959) and Pratte and Baines (1967), who utilized water and smoke jets, respectively. The most notable exception is that the width of the combined twin jets tends to be at least twice that of the single jet. In those studies both sets of workers obtained penetration and width data by estimating the locations of the jet boundaries from photographs. There does not appear to be any data from previous work on twin or multiple jets with which to sensibly compare the present results. This is because the definitions of penetration and width adopted in those studies are different, utilizing the loci of temperature or velocity maxima, or vortex trajectories, for example.

Table 1 Jet penetration and width parameters

Test	Penetration A	Penetration m	Width B	Width n
$S/D=1$	2.56	0.26	2.61	0.39
$S/D=3$	2.38	0.28	2.47	0.37
$S/D=5$	2.51	0.25	2.79	0.35
Pratte and Baines (1967)	2.63	0.28	1.25	0.40
Gordier (1959)	-	-	1.20	0.39

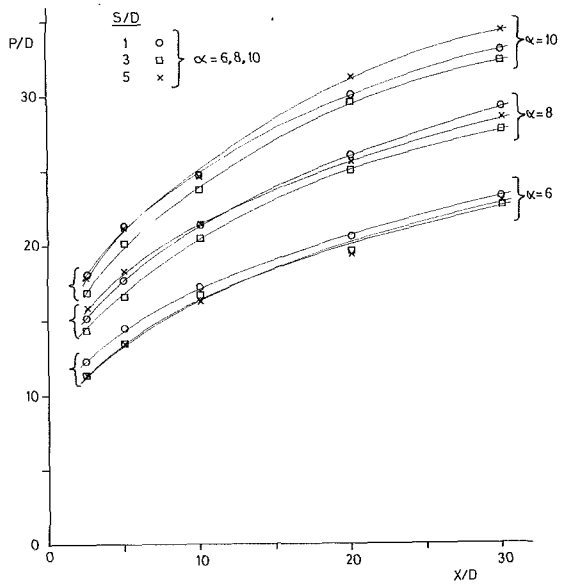

Fig. 8 Variation of twin jet penetration with nozzle spacing and velocity ratio

From the limited number of jet geometries studied in the present work it is apparent that S/D cannot be used as a scaling parameter since the interaction between the crossflow and widely spaced jets is fundamentally different from the closely-spaced-jets case. At very large jet spacings there is little mixing between the two jets and they behave in a similar manner to single jets. With decreasing spacing the jet penetration decreases due to the greater interference between the jets, as noted by Kamotani and Greber (1974) and Holdeman and Walker (1977). However, at very close spacings the crossflow no longer passes between the two jets. In this case the inner vortices of the two counter-rotating pairs do not appear to form, or are extremely weak, with the initial jet vorticity being turned and concentrated in the outer vortices only. The present data for $S/D=1$ shows that this results in an increase in jet penetration, as illustrated by the curves in Fig. 8. The results indicate that the increase in jet penetration is not substantial but that it is consistent for all velocity ratios. This finding agrees with the case of a row of multiple side-by-side jets, studied by Kamotani and Greber (1974), who found that at nozzle spacings below about $S/D=3$ the configuration behaved like a two-dimensional slot jet, with less entrainment, producing a slower decay of the initial jet momentum flux and a resultant increase in penetration.

Concluding Remarks

The present work on side-by-side twin jets issuing into a crossflow has indicated that the scaling parameters of jet velocity ratio and downstream distance, commonly used to predict the gross characteristics of single jets, such as penetration and width, may also be used for the combined twin jets. However, the nozzle spacing is not a suitable scaling parameter since the development of widely spaced jets (where the crossflow passes both sides of each jet) is fundamentally different from that of closely spaced jets (such as $S/D=1$ where there is no crossflow penetration between the jets). The most striking feature of twin jet development, from all the cases studied, is the manner in which the two jets rapidly combine (with the apparent disappearance of the inner vortices of the two counter-rotating paris) to form a large jet with single jet characteristics.

It is intended to undertake further work in order to establish the effect on jet development of staggering the two jets such that the downstream jet is issuing into the static pressure field generated by the upstream jet. In addition, detailed measurements of the velocity vector distributions will be undertaken in order to ascertain the strengths and extents of the vortices.

References

Bradbury, L. J. S., 1981, "Some Aspects of Jet Dynamics and Their Implications for VTOL Research," N.A.T.O. AGARD CP 308.

Falco, R. E., 1980, "Combined Simultaneous Flow Visualization/Hot-Wire Anemometry for the Study of Turbulent Flows," ASME JOURNAL OF FLUIDS ENGINEERING, Vol. 102, pp. 174–182.

Fiedler, H., and Head, M. R., 1966, "Intermittency Measurements in the Turbulent Boundary Layer," *Journal of Fluid Mechanics*, Vol. 24, pp. 719–735.

Gordier, R. L., 1959, "Studies on Fluid Jets Discharging Normally into Moving Liquid," *Technical Paper Number 28, Series B*, St. Anthony Falls Hydraulics Laboratory, University of Minnesota.

Hancock, G. J., 1987, "A Review of the Aerodynamics of a Jet in a Cross Flow," *Aeronautical Journal*, Vol. 91, pp. 201–213.

Holdeman, J. D., and Walker, R. E., 1977, "Mixing of a Row of Jets with a Confined Crossflow," *A.I.A.A. Journal*, Vol. 15, pp. 243–249.

Isaac, K. M., 1982, "Experimental and Analytical Investigation of Multiple Jets in a Cross-Flow," Ph.D. thesis, Virginia Polytechnic Institute and State University, Blacksburg.

Isaac, K. M., and Jakubowski, A. K., 1985, "Experimental Study of the Interaction of Multiple Jets with a Crossflow," *A.I.A.A. Journal*, Vol. 23, pp. 1679–1683.

Kamotani, Y., and Greber, I., 1974, "Experiments on Confined Turbulent Jets in Crossflow," N.A.S.A. CR-2392.

Karagozian, A. R., Nguyen, T. T., and Kim, C. N., 1986, "Vortex Modelling of Single and Multiple Dilution Jet Mixing in a Crossflow," *Journal of Propulsion and Power*, Vol. 2, pp. 354–360.

Khan, Z. A., McGuirk, J. J., and Whitelaw, J. H., 1981, "A Row of Jets in a Crossflow," N.A.T.O. AGARD-CP-308, 10.1–10.11.

Makihata, T., and Miyai, Y., 1979, "Trajectories of Single and Double Jets Injected into a Crossflow of Arbitrary Velocity Distribution," ASME JOURNAL OF FLUIDS ENGINEERING, Vol. 105, pp. 91–97.

Pratte, B. D., and Baines, W. D., 1967, "Profiles of the Round Turbulent Jet in a Crossflow," A.S.C.E. *Journal of the Hydraulics Division*, HY6, Vol. 92, pp. 53–64.

Ransom, E. C. P., and Wood, P. M., 1974, "Jet Interference Literature Survey and Critical Review," Kingston Polytechnic, U.K., Report 75/1/ER.

Schwendemann, M. F., 1973, "A Wind Tunnel Investigation of Stratified Jets and Closely Spaced Jets Exhausting into a Crossflow," Northrop Aircraft Division, Hawthorn, CA, U.S.A., Report NOR 73-98, May.

Toy, N., and Savory, E., 1988, "An Experimental Study of a Jet in a Crossflow," MoD Final Report, Agreement No 2064/088 XR/AERO, U.K., Dec.

Toy, N., and Wisby, C., 1988a, "The Real Time Image Analysis of a Visualised Turbulent Wake," *Proceedings 1st National Fluid Dynamics Congress*, Cincinnati, U.S.A., July, pp. 695–702, A.I.A.A. Paper Number 88-3552-CP.

Toy, N., and Wisby, C., 1988b, "Real-Time Image Analysis of Visualized Turbulent Flows," Proceedings 11th Biennial Symposium on Turbulence, University of Missouri-Rolla, U.S.A., October, pp. A21.1–21.10.

Walker, R. E., and Kors, D. L., 1973, "Multiple Jet Study," N.A.S.A. CR-121217.

Ziegler, H., and Wooler, P. T., 1973, "Analysis of Stratified and Closely Spaced Jets Exhausting into a Crossflow," N.A.S.A. CR-132297.

Experimental Analysis and Flow Visualization of a Thin Liquid Film on a Stationary and Rotating Disk

S. Thomas

A. Faghri

W. Hankey

Department of Mechanical and Materials Engineering, Wright State University, Dayton, OH 45435

The mean thickness of a thin liquid film of deionized water with a free surface on a stationary and rotating horizontal disk has been measured with a nonobtrusive capacitance technique. The measurements were taken when the rotational speed ranged from 0–300 rpm and the flow rate varied from 7.0–15.0 lpm. A flow visualization study of the thin film was also performed to determine the characteristics of the waves on the free surface. When the disk was stationary, a circular hydraulic jump was present on the disk. Upstream from the jump, the film thickness was determined by the inertial and frictional forces on the fluid, and the radial spreading of the film. The surface tension at the edge of the disk affected the film thickness downstream from the jump. For the rotating disk, the film thickness was dependent upon the inertial and frictional forces near the center of the disk and the centrifugal forces near the edge of the disk.

Introduction

The heat transfer from a rotating disk to a thin film has been recognized in the past to be superior to conventional falling films because the centrifugal force tends to thin and accelerate the film, which translates into higher heat transfer coefficients. As a first step in determining the heat transfer to a thin film, the hydrodynamic characteristics of a thin film with a free surface flowing over stationary and rotating disks have been studied experimentally. The major motivation of the present experimental investigation was directed toward the use of a thin film on a rotating disk to promote the absorption of a vapor into the liquid on the disk. Specifically, the absorber unit of a space-based vapor-absorption refrigeration system will use a liquid film thinned by the centrifugal force on a rotating disk to enhance the absorption of the refrigerant vapor into the absorbent because a falling film cannot be produced in a microgravity environment. The vapor-absorption cycle is more appropriate than a vapor-compression cycle for a microgravity application because the vapor compressor is replaced by a liquid pump, which is lighter, requires less maintenance, and is easier to manufacture for space-based applications. The vapor-absorption cycle will use the waste heat which is available in the spacecraft for refrigeration.

Watson (1964) analyzed a free-falling jet which impinges on a horizontal plane. The jet spreads out radially in a thin film and is surrounded by a hydraulic jump, outside of which the thickness of the liquid is much greater. Watson measured the diameter of the hydraulic jump (r_1) with dividers, the depth of the fluid outside the jump (d) with a point gage, and the flow rate (Q) with a measuring jar and stop watch. The experimental data ranged from $25.4 < r_1 < 177.8$ mm, $3.30 < d < 16.5$ mm, and $0.73 < Q < 26.8$ lpm. The jet Reynolds number $\mathrm{Re} = Q/a\nu$ ranged from 7×10^3 to 1.2×10^5, where a is the radius of the jet. The theoretical results of the location of the hydraulic jump and the depth of the liquid outside the jump were compared to experimental results with a satisfactory agreement.

Espig and Hoyle (1965) measured the maximum thickness of a liquid film on a horizontal rotating disk. The maximum thickness is the height of the film to the crest of the waves on the film. Measurements were taken by using a needle probe which completed an electrical circuit when it touched the film surface. The Reynolds number $\mathrm{Re} = (4\dot{Q}/\pi\mu D)$ ranged from 10 to 600, where $\dot{Q}$ is the mass flow rate, μ is the dynamic viscosity, and $D/2$ is the distance from the center of the disk. The flow conditions were also observed visually with a stroboscope which showed rivulets, circumferential waves, and helical waves. The experimental results were in agreement with the experimental results of Kirkbride (1933) and the theoretical results of Nusselt (1916) and Kapitsa (1948).

Butuzov and Rifert (1972) measured the heat transfer of condensing steam onto one side of a rotating copper disk, the opposite side of the disk being cooled with a condenser. The results for the average heat transfer coefficient versus the disk angular speed were presented. The disk speed varied from 95.5 to 2140 rpm and the heat flux ranged from 2×10^4 to 19×10^4 W/m^2. The measured condensate Reynolds number was compared to the theoretical results with an agreement to within 5–10 percent. The Reynolds number was defined as $\mathrm{Re}_{\mathrm{bot}} = \bar{\alpha}\,\Delta T\, R/2\rho\nu r$, where $\bar{\alpha} = \lambda/\bar{\delta}$ is the mean laminar heat transfer coefficient, $\bar{\delta}$ is the mean film thickness, λ is the thermal conductivity, ΔT is the temperature difference between the steam and the disk, R is the disk radius, r is the heat of vaporization,

Contributed by the Fluids Engineering Division for publication in the JOURNAL OF FLUIDS ENGINEERING. Manuscript received by the Fluids Engineering Division January 11, 1990.

ρ is the density, and ν is the kinematic viscosity. The theoretical results were obtained by using a previously derived equation for the thickness of a laminar liquid film on a rotating disk. This was related to the flow rate of the condensate on the disk for steam condensation.

Charwat et al. (1972) studied the effects of varying the viscosity and surface tension of a thin liquid film on a rotating glass plate. The film thickness was determined by the infrared absorption technique, and it was found that the thickness varied from 1–150 μm for flow rates up to 0.78 lpm. Concentric, spiral, and irregular waves were found on the surface of the film, and were strongly affected by varying the kinematic viscosity ($10^{-3}-2.5\times10^{-3}$ N•s/m^2) and surface tension ($20\times10^{-3}-72\times10^{-3}$ N/m).

Matsumoto et al. (1973) compared various theoretical solutions of previous authors with a polynomial approximation for the thickness of a thin liquid film on a rotating disk. The authors also devised an experiment where constant temperature liquid was supplied to the center of a rotating disk by a feed nozzle above the disk. The liquid film height was measured along the radius by a needle attached to two micrometer screws. The kinematic viscosity of the liquid ranged from $9.61\times10^{-6}-58.3\times10^{-6}$ m^2/s, the rotational speed varied from 250 to 1500 rpm, and the flow rate range from 0.3 to 1.87 lpm. It was concluded that a polynomial of fourth degree or higher agreed very well with the experimental results.

Miyasaka (1974) compared the results of an experimental study with those of a theoretical study of the thickness of a thin film on a rotating disk. The liquid film was generated with a jet of liquid falling onto the center of a horizontal rotating disk. The film height was measured by comparing the electrical resistance of the liquid on the disk with that of a standard thickness of the liquid, which resulted in an uncertainty of ±0.02 mm. The jet Reynolds number was varied from 200 to 18,000. The theoretical values were obtained by solving the governing equations of motion with the boundary-layer approximation. The theoretical results include the dimensionless film thickness, $H=h/r_0$, versus the dimensionless radius, $\xi=r/r_0$, where r_0 is the jet radius, when viscosity is and is not present. It was concluded that the theoretical values were in agreement with the experimental results.

Ishigai et al. (1977) measured the liquid film thickness and heat transfer from a thin film generated by an impinging liquid jet onto a perpendicular surface. The film thickness was measured with a needle and micrometer arrangement, and a voltage source applied to the surface of the plate. When the needle touched the surface of the film an electric circuit was completed, which was read by an oscilloscope. The flow rate ranged from 3.0 to 30 lpm. The experimental data of the liquid film height were compared to the analytical equation given by Watson (1964) with satisfactory results.

Labus and DeWitt (1978) examined experimentally the flow patterns of the free surface of an impinging jet of liquid on a disk perpendicular to the jet in zero gravity. This was achieved in a drop facility in which a 2.2 second period of 10^{-5} g's could be sustained. Flow visualization studies revealed that surface tension and inertia were the major forces acting on the liquid.

Craik et al. (1981) studied experimentally the circular hydraulic jump formed by an impinging jet of liquid on a horizontal plate. The liquid film thickness in the region near the hydraulic jump was measured using a light-absorption technique with a laser and a strong dye. The parameters which were varied are as follows: the flow rate, 0.27 to 1.56 lpm; the jet radius, 1.0 to 2.15 mm; the jump radius, 12.0 to 40.0 mm; and the outer depth, 1.8 to 3.5 mm. The experimental data were compared to Watson's (1964) theory with an unsatisfactory agreement. Flow visualization studies were performed, and a recirculation bubble attached to the plate just downstream of the hydraulic jump was found.

Muzhilko et al. (1983) measured the liquid film thickness on a horizontal rotating disk where the liquid is introduced onto the center of the disk by an impinging jet. The film thickness was measured by sensing electrodes embedded into the surface of the disk, whose resistance is a function of the film thickness. The mean film thickness was measured at radii of 30, 60, and 90 mm. The angular velocity ranged from 95 to 1900 rpm, and the flow rate varied from 0.04 to 1.2 lpm. The mean film thickness results were correlated by an empirical equation which predicted the data to within ±15 percent in the wavy-laminar region.

Azuma and Hoshino (1984) examined the laminar-turbulent transition, liquid film thickness, velocity profile, stability, and wall pressure fluctuations of thin liquid films on a stationary horizontal disk in a series of four reports. The liquid was directed onto the glass plate by a circular nozzle which was set very close to the surface of the plate.

For laminar-turbulent transition, Azuma and Hoshino set the nozzle inside diameter to: $D=10$, 15, 20, 25, 30 mm. The gap height was $H=0.5$, 1.0, 2.0, 3.0, 5.0 mm. The volumetric flow rate ranged from $Q=3-39$ lpm. Laminar-turbulent transition was determined as when sandpaper-like waves covered 50 percent of the peripheral direction. The critical Reynolds number was given as $\mathrm{Re}_{t,cr}=7.4\times10^4$, where $\mathrm{Re}=Q/\sqrt{CDH}\nu$, $C=Q/\pi DHU_0$ is the discharge coefficient, $U_0=\sqrt{2P/\rho}$ is the discharge velocity, P is the stagnation pressure, ρ is the density, and ν is the kinematic viscosity. The transition radius was nondimensionalized ($r_r^*=[r_t/\sqrt{CDH}]\mathrm{Re}^{-1/3}$) and plotted against the Reynolds number, so that the dimensional transition radius could be determined for a particular arrangement.

The liquid film thickness across the horizontal disk was measured by Azuma and Hoshino using the point gage method with a needle sensor and micrometer screw. The film thickness on both the bottom and the top of the disk was measured. On top of the disk, the film thickness was measured in the supercritical region. On the bottom of the disk, the film thickness was measured to the radius where the liquid fell off the disk in droplets. Following the analysis given by Watson (1964), the authors analytically derived the liquid film thickness in three regions: the stagnation region (Region I), the region in which the laminar boundary layer reaches the fluid surface (Region II), and after the point of transition to turbulent flow (Region III). The equations for the film thickness were in agreement with the experimental values.

Azuma and Hoshino measured the velocity profile of a thin liquid film on the underside of the glass plate with a laser Doppler velocimeter. Regions (I) and (II) mentioned above were

Nomenclature

E_{rss} = root-sum-square error in the liquid film height measurement, mm
h = gap between capacitance sensor and disk at the innermost radius, mm
Δh = change in h along the radius, mm
h' = amount the probe was raised when the disk was wet, mm
h'' = gap between capacitance sensor and liquid film surface, mm
δ = liquid film height, mm

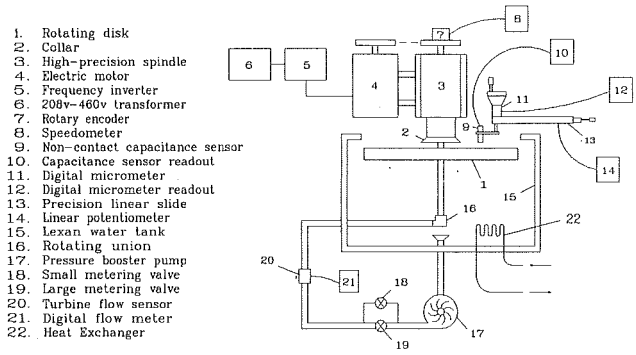

Fig. 1 Experimental setup of the rotating disk unit

again studied to determine whether the velocity profile could be approximated best by the profile given by Watson or by a fourth-order polynomial profile. Watson's profile is given as

$$f(\eta) = \sqrt{3} + 1 - \frac{2\sqrt{3}}{1 + cn\{3^{1/4}K(1-\eta)\}}$$

where $f = u/U$, $\eta = z/\delta$, U is the velocity at $z = \delta$, δ is the boundary layer thickness, cn is Jacobi's elliptic function with modulus sin 75 deg, and $K = 1.402$. The fourth-order profile given by Azuma and Hoshino is $f(\eta) = 2\eta - 2\eta^3 + \eta^4$. The authors found that in Region (I), the velocity profile is best approximated by the fourth-order profile. In Region (II) the profile is closer to Watson's profile.

Azuma and Hoshino investigated analytically the stability of the liquid film by integrating the Orr-Somerfield equation in Regions (I) and (II) using the Blasius and Watson profiles. In Region (I), the stability limit was given by $\mathrm{Re}_{\delta,cr} = U_0\delta/\nu = 1970$ and 707 for the Blasius and Watson profiles, respectively. In Region (II), the stability limit for the Blasius and Watson profiles was $\mathrm{Re}_{\delta,cr} = 1596$ and 450, respectively. The pressure at the wall was measured with semiconductor pressure transducers. The authors found that from the stagnation point, the time-averaged pressure distribution dropped off suddenly, but at a certain downstream radius the pressure had a significant maximum value. This maximum was attributed to the transition from laminar to turbulent flow. The experimental and analytical results for the location of transition were in agreement.

Carper et al. (1986) studied experimentally the heat transfer from one side of a rotating disk with an approximately uniform surface temperature. The liquid was supplied to the center of the disk by a nozzle. The average Nusselt number ($\mathrm{Nu}_D = \bar{h}D/k$) was presented for the following parameters: the rotational Reynolds number ($16{,}000 < \mathrm{Re}_r = \omega D^2/\nu < 545{,}000$), the Prandtl number ($87 < \mathrm{Pr} < 400$), and the impinging jet Reynolds number ($180 < \mathrm{Re}_j = dU_j/\nu < 1300$). D is the disk diameter, ω is the angular velocity of the disk, ν is the kinematic viscosity, d is the jet nozzle diameter, U_j is the average jet velocity, $\bar{h}$ is the average convective heat transfer coefficient over the disk, and k is the thermal conductivity of the fluid. An empirical equation for the average Nusselt number was derived by a multiple linear regression analysis which represented 95 percent of the data to within ± 30 percent.

Most of the previous investigations were concerned with thin liquid films which were generated by an impinging jet onto the center of a rotating or stationary disk. In the present study, the liquid film was generated on a rotating or stationary disk by a circular collar which directed the pressurized liquid onto the center of the disk with a constant initial height and velocity. This arrangement was amenable to accurate numerical simulation because the inlet conditions were more easily modeled than those of an impinging liquid jet. The flow rates for the rotating disk were much larger than most of the previous studies because the problems associated with the splashing of the working fluid onto the measuring device were eliminated with the new collar design.

The effects of two parameters on the thickness of the liquid film were studied: the flow rate (7.0 – 15.0 lpm) and the rotational speed (0 – 300 rpm) at the steady state. The liquid film thickness was measured with a nonobtrusive capacitance probe and digital micrometer arrangement. The characteristics of the waves on the free surface were studied with a video camera at low and high shutter speeds.

Experimental Setup

The purpose of this experiment was to measure the liquid film thickness on a stationary and rotating horizontal disk where the liquid emanates from a pressurized vessel in the center of the disk. The schematic of the experimental setup is shown in Fig. 1. The 406.4 mm diameter rotating disk [1] was mounted onto a high-precision stainless steel spindle [3] which was hollow from the 101.6 mm diameter stainless steel collar [2] to the rotating union [16]. The rotating disk was made of aluminum with a surface finish of 3.8×10^{-4} mm and flatness of 2×10^{-3} mm. The working fluid flowed from the circulating pump [17] through the stationary pipe to the rotating union, which coupled the stationary pipe and the hollow spindle. The liquid then passed up above the rotating disk and through eight 3.17 mm diameter radial holes in the hollow rotating spindle, which were covered by the collar. The collar directed the eight liquid streams down and outwardly so that the fluid flowed onto the top side of the disk with a velocity only in the radial direction. The collar also made sure that the height of the liquid at the collar did not change with respect to the azimuthal direction. The gap height between the bottom face of the collar and the top of the disk (0.267 mm) was set by a stainless-steel shim which separated them. After the fluid flowed over the disk, it was collected by the water tank [15] to be recirculated. The flow rate of the liquid was varied by the large and small metering valves [18 and 19], which provided the gross and fine adjustments. The volumetric flow rate was determined with the turbine flow sensor [20] and the digital flow meter [21]. Since the circulating pump heated the working fluid, a heat exchanger [22] was placed in the water tank to keep the water temperature constant at room temperature (22 °C). The rotational speed was varied by the frequency inverter speed controller [5] which powered the electric motor [4] and was read with the rotary encoder [7] and speedometer [8].

In order to decrease the vibrations in the system, it was mounted onto a machine table. The total mass of the support frame and the machine table was approximately 450 kg. The table was also fitted with four vibration mounts which were made of neoprene and were approximately 25 mm thick × 75 mm in diameter. The system was located in the corner of the building, which aided in decreasing the vibrations seen in the laboratory by being very close to the foundation.

To measure the height of the liquid film, a nonobtrusive measurement technique using a capacitance sensor (for example, Spiers, 1974; and Tharmalingam and Wilkinson, 1978) was devised as shown in Fig. 1. This measurement method has several advantages over other techniques used in the archival literature. Unlike the needle probe method (Espig and Hoyle, 1965), the capacitance technique does not disturb the free surface of the film. The capacitance technique can measure the film thickness all along the radius of the disk, whereas the liquid conductivity method (Miyasaka, 1974) can measure the film thickness at only a few discrete points. The light absorption technique (Charwat et al., 1972) was not chosen due to the necessity of a metallic disk for future heat transfer experiments.

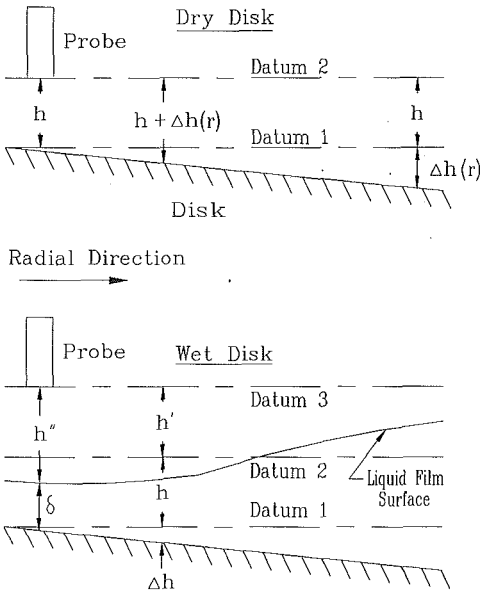

Fig. 2 Liquid film height measurement

A noncontact capacitance sensor [9] was used to locate the surface of the disk and the free surface of the liquid. The capacitance sensor directly related the strength of the electric field to the air gap between the sensor and the target. This relation was linear within the stated range of the probe. The sensor was attached to a digital positioner [11] by which the sensor could be raised or lowered. The probe and digital positioner were both mounted onto a linear slide [13] which moved the sensor along the radius of the disk. The radial location of the capacitance probe was measured by a linear potentiometer [14] attached to the linear slide. The procedure to measure the liquid film height is described below and is shown graphically in Fig. 2. This procedure eliminated the error due to the runout of the disk and the error due to the disk and linear slide not being perfectly parallel.

1. The capacitance probe was calibrated to the digital micrometer at the innermost radius by bringing the probe down until it touched the disk very lightly, which could be seen with a light directed behind the probe. This was the datum 1 line shown in Fig. 2. The capacitance sensor was then zeroed at this point with the offset adjustment. The capacitance probe was raised slightly above the disk, where the digital micrometer was zeroed. The probe was then raised until it read the maximum value of its range. The value read on the capacitance sensor readout [10] was compared to what was shown on the digital micrometer readout [12]. Any discrepancy could be eliminated by a gain adjustment which was supplied on the capacitance sensor readout. This set the slope of the linear curve which related the electric strength to the height of the air gap. It was found that the digital micrometer did have a small amount of backlash (<0.008 mm), but this was eliminated by consistently raising the probe to the desired location instead of lowering it.

2. With the disk dry, the capacitance probe was then moved to the datum 2 line with the digital micrometer, which was set to zero at this location. The height h at the inner radius was an arbitrary value which was within the range of the probe.

3. The probe was moved along the radius to measure the deviation of the disk from the datum 1, which is called the tare data $(h+\Delta h)$.

4. The probe was then raised to datum 3. The liquid flow was started and allowed to reach the steady state. The distance between datum 2 and datum 3 (h') was shown on the digital micrometer readout. The distance from datum 3 to the liquid film surface (h'') was measured by the capacitance probe. The liquid film height δ along the radius of the disk was calculated with the following equation:

$$\delta = h' + (h + \Delta h) - h'' \tag{1}$$

The capacitance sensor readout [10] was equipped with a 10 VDC output, which was proportional to the air gap between the probe and the target. This voltage signal was sampled by a Fluke 2280A Datalogger at a rate of one every two seconds to average the readings and to determine the standard deviation of each reading. This procedure was necessary due to the waves present on the surface of the liquid film. Also, the capacitance probe had a sensing spot which had a diameter of 11.28 mm, so a given reading was assigned to the radial location underneath the center of the sensing spot. When the disk was rotating, the same procedure was followed except that the tare data $(h+\Delta h)$ and the air gap measurements between the probe and the free surface (h'') were averaged in the azimuthal direction as well.

Error Analysis

The errors in the liquid film measurements are described and quantified, which involve two instruments: the digital micrometer and the capacitance sensor. A brief summary of the method to determine the error is discussed. A more detailed description was outlined by Thomas (1989) using the analysis given by Miller (1989).

The liquid film height is given by equation (1). The root-sum-square error of the system is

$$E_{\text{rss}} = \sqrt{(\Delta h')^2 + [\Delta(h+\Delta h)]^2 + (\Delta h'')^2} \tag{2}$$

The first term in equation (2) is the stated uncertainty of the digital micrometer, which was calibrated at the factory with a NBS traceable Mark-Tech Laser Gage Model 7980. The maximum deviation over the range of movement reported on the calibration certificate was 0.001 mm, which was taken as the uncertainty of the instrument.

The second term in equation (2) had different values when the disk was either stationary or rotating. When the disk was stationary, the second term was the uncertainty of the capacitance sensor, which was ± 0.1 percent of the range (2.54 mm) when calibrated to a known standard, which was the digital micrometer. The maximum deviation from linearity of the capacitance probe when compared to the digital micrometer was 0.008 mm. This value was added to the stated uncertainty of the probe. Therefore, the second term when the disk was stationary was 0.01 mm. When the disk was rotating, the error due to the disk not being perfectly flat and the wobble caused by the bearings had to be taken into account. This error was the sum of the standard deviation of the air gap measurement between the probe and the dry disk taken at the outer edge of the disk (where it was maximum) and the error of the capacitance sensor. Multiple populations with an increasing number of samples were taken and the means were compared with a two-tailed z-test to give a sample number which ensured a mean at the 95 percent confidence level. The standard deviation of the dry rotating disk with 50 samples was $\sigma = 0.02$ mm, so the second term in equation (2) was 0.03 mm.

The last term in equation (2) was again the error associated with the capacitance sensor. Since the mean film thickness is reported, further comments concerning the third term in equation (2) are necessary. At all flow rates and rotational speeds, waves were present on the free surface of the liquid film. A test was performed to compare the means of different numbers of samples in the subcritical and supercritical regions to determine a suitable number of data points for a mean

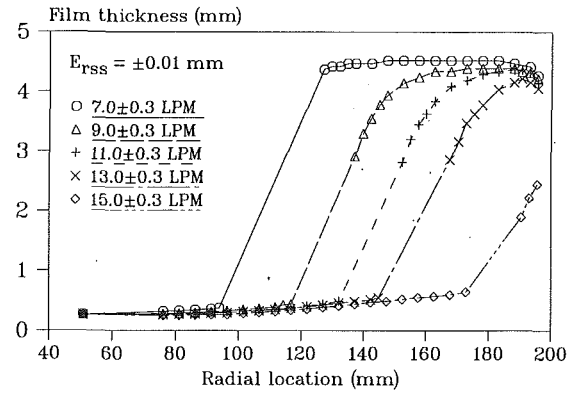

Fig. 3 Film thickness versus radial location for different flow rates (stationary disk)

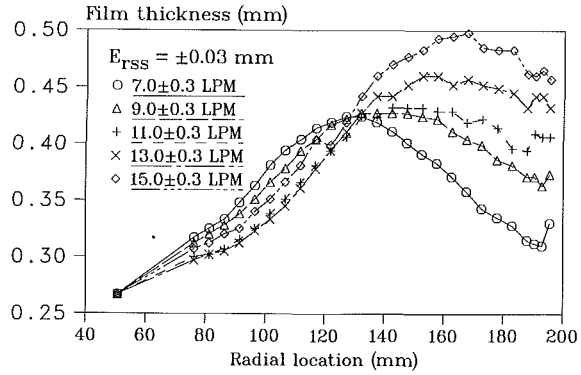

Fig. 6 Film thickness versus radial location for different flow rates (100 ± 2 rpm)

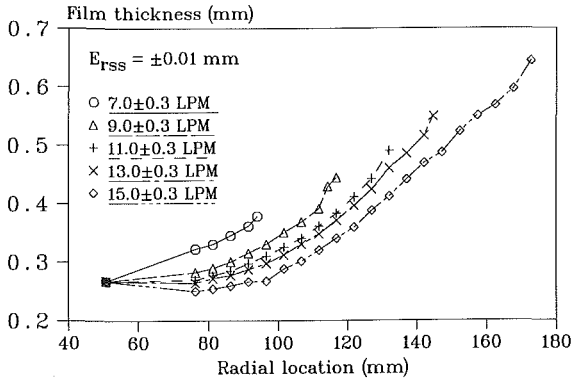

Fig. 4 Film thickness versus radial location in the supercritical region for different flow rates (stationary disk)

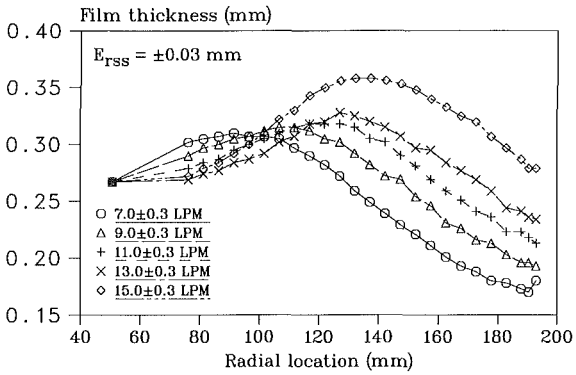

Fig. 7 Film thickness versus radial location for different flow rates (200 ± 2 rpm)

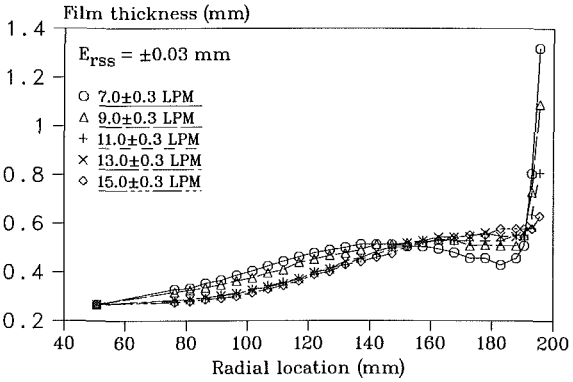

Fig. 5 Film thickness versus radial location for different flow rates (55 ± 2 rpm)

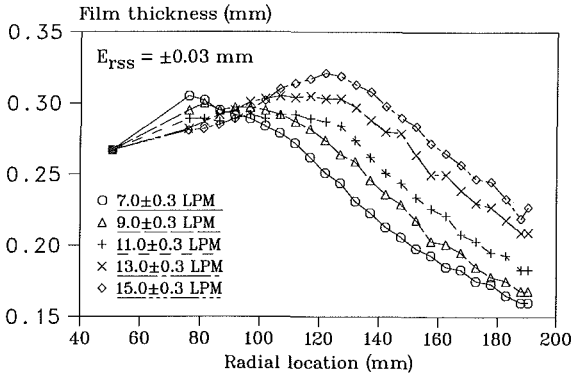

Fig. 8 Film thickness versus radial location for different flow rates (300 ± 2 rpm)

which falls in the 95 percent confidence level. For subcritical flow, a normal z-test was performed. It was found that for 125 and 250 samples, the means were equal at the 95 percent confidence level, so 250 samples were taken for each data point reported. Likewise, for supercritical flow 80 samples were taken in order to achieve the same confidence level. A similar test performed when the disk was rotating showed that 80 samples were needed. The root-sum-square error in the liquid film height measurement is as follows:

$$\text{Stationary disk} - E_{rss} = \pm 0.01 \text{ mm}$$

$$\text{Rotating disk} - E_{rss} = \pm 0.03 \text{ mm}$$

The gap between the collar and the disk was measured with feeler gages and the uncertainty of this data point was ±0.01 mm.

Results and Discussion

1 Liquid Film Thickness Measurements. The mean thickness of a liquid film of deionized water as it flowed across a horizontal disk has been measured experimentally. The flow rate ranged from 7.0–15.0 lpm and the rotational rate varied from 0–300 rpm. The upper limits of these ranges were defined by the limitations of the experimental apparatus. The film thickness when the rotational speed was held constant and the flow rate was varied is presented in Figs. 3–8. The film thickness when the flow rate was held constant and the rotational speed was changed is shown in Fig. 9. In all of the measurements presented in this report, a duplicate measurement was made and the two runs were within 5 percent of each other.

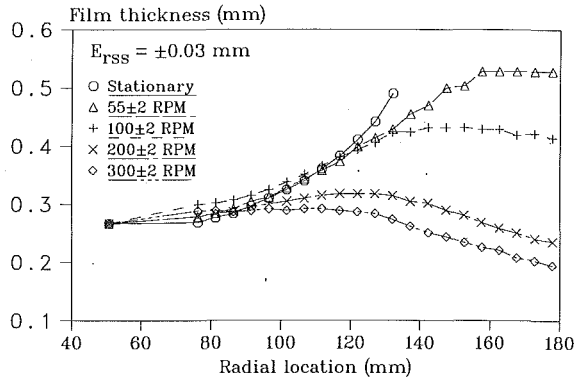

Fig. 9 Film thickness versus radial location for different rotational speeds (11.0 ± 0.3 lpm)

The film thickness when the disk was stationary in both the supercritical and subcritical regions is shown in Fig. 3. The supercritical region is upstream from the hydraulic jump and the subcritical region is downstream from the jump. This terminology should not be confused with distinguishing between the turbulent versus laminar regimes of the bulk flow. As the flow rate increased, the hydraulic jump moved toward the outer edge of the disk. The exact shape of the jump could not be determined with the present measuring instrument because if an attempt were made to measure the film thickness in the supercritical region very near the jump, the free surface of the subcritical region would touch the side of the capacitance sensor and saturate the signal. Therefore, in Fig. 3, the straight line without data points between the supercritical and subcritical regions denotes the region in which the hydraulic jump resided.

The first data point at 50.8 mm is the gap height between the collar and the disk (0.267 mm). The next data point at 76.2 mm is the first point which could be read by the capacitance probe. Therefore, the line connecting these two points is simply a linear interpolation and no conclusions can be drawn concerning this region. Even though the outer radius of the disk is 203.2 mm, measurements are not reported past 195.6 mm because part of the sensing spot of the capacitance sensor was over the edge of the disk.

In Fig. 3, the film was nearly horizontal in part of the subcritical region when the flow rate was 7.0 lpm and then dropped off near the edge of the disk. This decrease in the film thickness at the edge was due to the acceleration of the flow as the liquid exited the disk. The radius of curvature at the edge was nearly constant up to approximately 13.0 lpm and produced significant surface tension effects. This can be noticed in Fig. 3 by the curves showing 7.0–13.0 lpm, which approach the same film thickness near the edge of the disk. For 15.0 lpm, the hydraulic jump was nearly pushed off the edge of the disk, so it did not reach the same height as the curves with lower flow rates. This phenomenon is termed a "partial" hydraulic jump. Figure 3 also shows that the liquid film thickness in the subcritical region was an order of magnitude greater than that in the supercritical region.

As shown in Fig. 4, the film thickness in the supercritical region when the disk was stationary increased along the radius of the disk. In the supercritical region, the major forces on the liquid film were due to inertia and friction. Since the frictional forces tend to slow the liquid, the film thickness increased due to continuity.

It is also shown in Fig. 4 that the film thickness in the supercritical region may increase monotonically or may first decrease and then increase downstream. This decrease in the film thickness was due to the radial spreading of the fluid as it traveled across the disk. This effect was then overtaken by that due to friction, at which point the film thickness increased.

The film thickness for different flow rates when the rotational speed was 55 rpm is shown in Fig. 5. For 7.0 lpm, the flow from the collar to a radius of 120 mm had the same trend as the supercritical flow of the stationary disk: As the flow rate increased, the film thickness decreased due to the effect of the radial spreading of the flow overtaking the effect of friction. Past this region, however, the profile takes on a very different appearance. The film thickness began to flatten out and then decrease past 120 mm. When the disk was rotating, the frictional, inertial, and centrifugal forces determined the thickness of the film. Near the center of the disk, the frictional and inertial forces were prevalent. Closer to the edge of the disk the centrifugal force came into play. Near the edge of the disk one would expect that the film would accelerate because of the centrifugal force and become thinner due to continuity. It can also be seen in Fig. 5 that as the flow rate increased, the point where the curves begin to flatten due to centrifugal force travels downstream. This was because the effect of inertia on the flow was dominant over the effect of the centrifugal force for a longer distance. Near the edge of the disk, the film thickness increased dramatically due to the partial hydraulic jump at the edge of the disk. As the flow rate increased, the height of the partial jump decreased because the liquid was supercritical for a longer distance across the disk. Unfortunately, the rotational speed could not be varied in the range of 0–55 rpm.

The film thickness is presented in Figs. 6, 7, and 8 when the flow rate was varied from 7.0 to 15.0 lpm for rotational speeds of 100, 200, and 300 rpm, respectively. Again, the same trend is evident where the film thickness first increased due to frictional effects and then decreased due to the effect of centrifugal force. In comparing these figures, it can be seen that the radial location where the effect of centrifugal force dominated the flow moved toward the center of the disk as the rotational speed increased. This is shown further in Fig. 9 where the flow rate was held constant at 11.0 lpm and the rotational speed was varied from 55 to 300 rpm. As the rotational speed increased the maximum thickness occurred closer to the center of the disk. Also shown in Fig. 9 is the supercritical region when the disk was stationary. It can be seen that the film thickness in the supercritical region was generally close to the case when the rotational speed was 55 rpm. The exception was near the downstream end of the supercritical region. Since the stationary film was not being acted upon by centrifugal forces, the film thickness continued to increase in this region because of the effect of friction.

2 Flow Visualization. A photographic study was performed to determine the basic phenomena which occur when the disk was stationary and rotating. When the disk was stationary, waves could be seen both in the subcritical and supercritical regions. The waves in the subcritical region had larger amplitudes than those in the supercritical region. At low flow rates, a toroidal "roller" was found at the hydraulic jump when the disk was stationary. At high flow rates, the roller flattened out until it could not be distinguished from the increase in the film thickness at the hydraulic jump. At high spin rates, waves appeared on the disk which ran nearly radially across the disk on top of a thin substrate of fluid.

In Figs. 10(*a*) and 10(*b*), the disk was stationary and the flow rate was set to 7.0 lpm with a shutter speed of 1/1000 second. In all of the photographs presented, the direction of the flow was from right to left and the direction of rotation was clockwise. The waves in the supercritical region are shown in Fig. 10(*a*). Near the collar the amplitudes of the waves were small, but were larger close to the hydraulic jump. The waves in the subcritical region can be seen in Fig. 10(*b*). These waves had a much larger amplitude than those in the supercritical region. This was verified when the liquid film height was

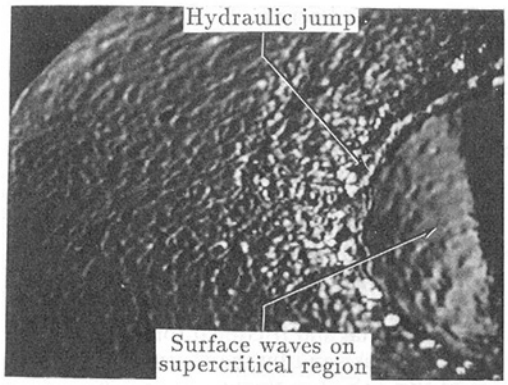

Fig. 10(*a*)

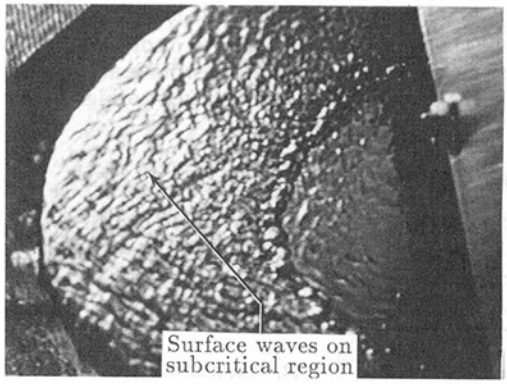

Fig. 10(*b*)

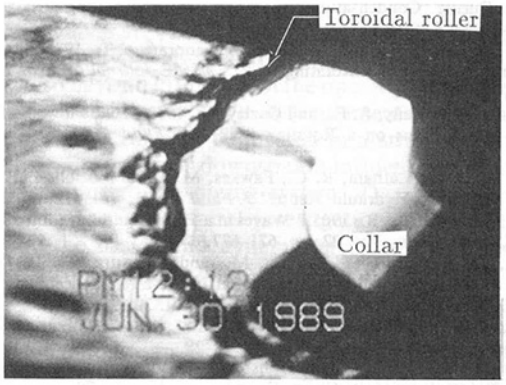

Fig. 10(*c*)

Fig. 10 Stationary disk; (*a*) 7.0 lpm, supercritical region highlighted, (*b*) 7.0 lpm, subcritical region highlighted, (*c*) 4.0 lpm, toroidal roller

measured with the capacitance sensor. Even though the actual height of the waves could not be measured, the standard deviations of the signals from the mean film thickness were much larger in the subcritical region than in the supercritical region.

The hydraulic jump is shown in Fig. 10(*c*) at a flow rate of 4.0 lpm. This photograph was taken with a shutter speed of 1/60 second. The hydraulic jump occurred approximately 30 mm from the collar. A toroidal roller was formed at the hydraulic jump. At this flow rate, the cross section of the roller was nearly circular. At higher flow rates, it was found that the shape of the roller changed significantly. At flow rates between 3.0–6.0 lpm, the roller had a nearly circular cross section as shown in Fig. 11(*a*). At flow rates between 7.0–8.0 lpm, the cross section of the roller was oval in shape as shown in Fig. 11(*b*). At flow rates between 9.0–15.0 lpm, the shape of the roller was no longer distinguishable from the gradual increase in the film height, which is presented in Fig. 11(*c*). The surface of the film at the hydraulic jump at this flow rate

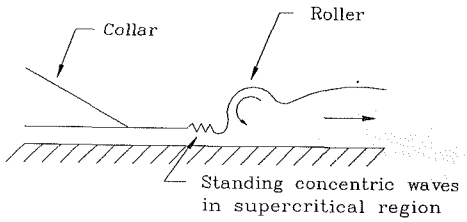

Fig. 11(*a*)

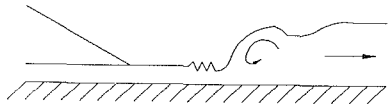

Fig. 11(*b*)

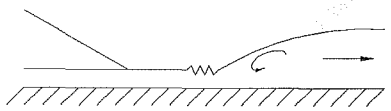

Fig. 11(*c*)

Fig. 11 Toroidal roller, 3.0–15.0 lpm; (*a*) 3.0–6.0 lpm, (*b*) 7.0–8.0 lpm, (*c*) 9.0–15.0 lpm

could clearly be seen to be falling down toward the center of the disk in the direction opposite to the main direction of the flow. At lower flow rates, the velocity of the fluid within the roller and the surface velocity of the liquid film did not have sufficient momentum to overcome the surface tension which held the circular shape of the roller. As the flow rate and the surface velocity of the supercritical liquid film increased, the effect of the momentum of the liquid overcame that of surface tension, which resulted in the change in the shape of the roller. Also shown in Fig. 11 is a series of small concentric waves immediately upstream from the hydraulic jump. These concentric waves were present at flow rates between 4.0–15.0 lpm and had larger amplitudes at higher flow rates.

Photographs of the rotating disk are given in Fig. 12 for a flow rate of 7.0 lpm and rotational speeds of 55, 100, and 200 rpm. The disk rotating with a speed of 55 rpm is shown in Fig. 12(*a*). The waves on the free surface appeared to be similar to the waves found in the subcritical region on the stationary disk with the same flow rate (see Fig. 10(*b*)). Measurements of the standard deviation from the mean film thickness, however, showed that the amplitude of the waves were closer in height to those in the supercritical region.

Two flow regions were found to exist on the rotating disk: wavy-laminar and radial-wave flow. The transition from the wavy-laminar flow to the radial-wave flow was visually examined at 7.0 and 13.0 lpm and is shown for 7.0 lpm in Fig. 12. The wavy-laminar flow was seen at lower rotational speeds and the radial-wave flow occurred at higher rotational speeds. The wavy-laminar flow is shown in Fig. 12(*a*) for 7.0 lpm and 55 rpm. In this regime, no recurring wave patterns were distinguishable except the partial jump at the outer edge of the disk. When the rotational rate was slowly changed from 55 rpm to 100 rpm for 7.0 lpm, the waves on the free surface began to form a pattern which could be easily distinguished, as shown in Fig. 12(*b*). Parts of the free surface broke free from the wavy-laminar regime to form V-shaped waves that ran at a diagonal angle between the radial and circumferential directions opposite to the rotation of the disk. At the lower rotational speeds, these waves were present only at the outer edge of the disk. As the rotational speed increased, the width of the V-shaped waves decreased and the length increased until the waves traversed the radius of the disk as shown in Fig. 12(*c*).

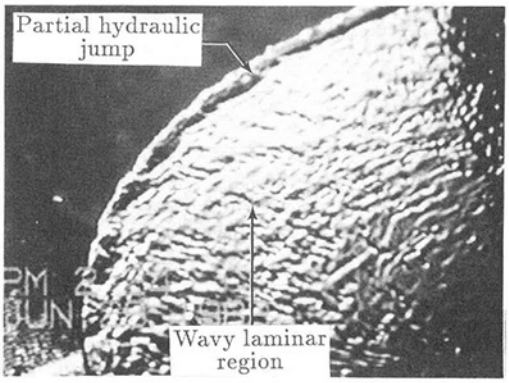

Fig. 12(a)

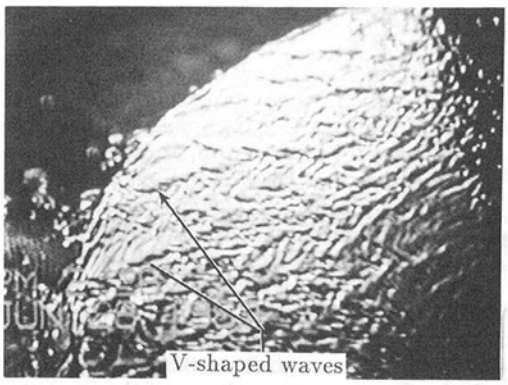

Fig. 12(b)

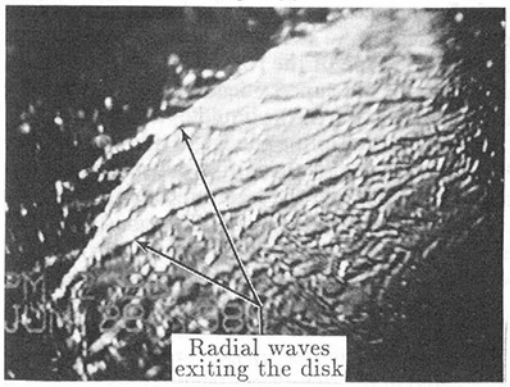

Fig. 12(c)

Fig. 12 Rotating disk, 7.0 lpm; (a) 55 rpm, (b) 100 rpm, (c) 200 rpm

The radial-wave regime is shown in Fig. 12(*c*) at 7.0 lpm and 200 rpm. Several well-defined radial waves can be seen to flow across the disk on top of a thin substrate and carry the bulk of the fluid off of the disk. In Fig. 12(*c*), a radial wave was exiting the disk on the left-hand side in the center. Immediately below this wave, very little fluid was leaving the disk where the thin substrate was present. It can be seen in Fig. 12(*c*) that the spacing between the radial waves increased with the radius because of the increase in the flow area. The transition region for 7.0 lpm was found to be 100–200 rpm. The transition region for 13.0 lpm was approximately 150–200 rpm, which was higher than that of 7.0 lpm.

Conclusions

The characteristics of a thin liquid film with a free surface on a stationary and rotating horizontal disk have been examined experimentally. The film thickness was measured at different flow rates and rotational speeds with a noncontact capacitance technique. Also, the nature of the waves on the free surface was determined photographically. When the horizontal disk was stationary the thin film experienced a hydraulic jump, at which the velocity decreased and the thickness increased at a certain radial distance. In the supercritical region upstream from the jump, the film thickness was governed by the inertial and frictional forces on the fluid, as well as the radial spreading of the fluid. Downstream from the jump in the subcritical region, the film thickness was mainly determined by the frictional forces and the surface tension of the liquid. The liquid film thickness on the rotating disk was affected by the inertial and frictional forces on the fluid near the center of the disk, and by the centrifugal force near the outer edge of the disk. The flow visualization study revealed the presence of a roller at the hydraulic jump on the stationary disk, whose shape changed with the flow rate. Also, the transition between wavy-laminar flow to radial-wave flow was observed on the rotating disk as the rotational speed was increased. The range of transition shifted to higher rotational speeds as the flow rate increased.

Acknowledgment

Funding for this work was provided by the NASA Goddard Space Flight Center, Greenbelt, Maryland, under contract NAG5-956.

References

Azuma, T., and Hoshino, T., 1984, "The Radial Flow of a Thin Liquid Film, 1st–4th Reports," *Bulletin of JSME*, Vol. 27, pp. 2739–2770.

Butuzov, A. I., and Rifert, V. F., 1972, "An Experimental Study of Heat Transfer During Condensation of Steam at a Rotating Disk," *Heat Transfer-Soviet Research*, Vol. 4, pp. 150–153.

Carper, H. J., Jr., Saavedra, J. J., and Suwanprateep, T., 1986, "Liquid Jet Impingement Cooling of a Rotating Disk," ASME *Journal of Heat Transfer*, Vol. 108, pp. 540–546.

Charwat, A. F., Kelly, R. E., and Gazley, C., 1972, "The Flow and Stability of Thin Liquid Films on a Rotating Disk," *J. Fluid Mech.*, Vol. 53, pp. 227–255.

Craik, A. D. D., Latham, R. C., Fawkes, M. J., and Gribbon, P. W. F., 1981, "The Circular Hydraulic Jump," *J. Fluid Mech.*, Vol. 112, pp. 347–362.

Espig, H., and Hoyle, R., 1965, "Waves in a Thin Liquid Layer on a Rotating Disk," *J. Fluid Mech.*, Vol. 22, pp. 671–677.

Ishigai, S., Nakanishi, S., Mizuno, M., and Imamura, T., 1977, "Heat Transfer of the Impinging Round Water Jet in the Interference Zone of Film Flow Along the Wall," *Bulletin of the JSME*, Vol. 20, pp. 85–92.

Kapitsa, P. L., 1948, "Wave Motion of a Thin Layer of a Viscous Liquid," *J. Exp. Theor. Phys.*, U.S.S.R., Vol. 18, pp. 3–28.

Kirkbride, C. G., 1933, "Heat Transfer by Condensing Vapour on Vertical Tubes," *Trans. Amer. Inst. Chem. Engng.*, Vol. 30, pp. 170–193.

Labus, T. L., and DeWitt, K. J., 1978, "Liquid Jet Impingement Normal to a Disk in Zero Gravity," ASME JOURNAL OF FLUIDS ENGINEERING, Vol. 100, pp. 204–209.

Matsumoto, S., Saito, K., and Takashima, Y., 1973, "The Thickness of a Viscous Liquid Film on a Rotating Disk," *J. Chemical Engineering of Japan*, Vol. 6, pp. 503–507.

Miller, R. W., 1989, *Flow Measurement Engineering Handbook*, 2nd ed., McGraw-Hill.

Miyasaka, Y., 1974, "On the Flow of a Viscous Free Boundary Jet on a Rotating Disk," *Bulletin of the JSME*, Vol. 17, pp. 1469–1475.

Muzhilko, A. A., Rifert, V. G., and Barabash, P. A., 1983, "Flow of Liquid Film over the Surface of a Rotating Disk," *Heat Transfer - Soviet Research*, Vol. 15, pp. 1–6.

Nusselt, W. Z., 1916, "Die Oberflachenkondensation des Wasserdampfes," *Z. Ver deut. Ing.*, Vol. 60, pp. 541–546.

Spiers, R. P., 1974, "Free Coating of a Newtonian Liquid onto a Vertical Surface," *Chem. Engn. Sci.*, Vol. 29, pp. 389–396.

Tharmalingam, S., and Wilkinson, W. L., 1978, "The Coating of Newtonian Liquids onto a Rotating Roll," *Chem. Engn. Sci.*, Vol. 33, pp. 1481–1487.

Thomas, S., 1989, "Numerical and Experimental Analysis of a Thin Liquid Film on a Stationary and Rotating Disk," Master's thesis, Department of Mechanical and Materials Engineering, Wright State University, Dayton, OH.

Watson, E. J., 1964, "The Radial Spread of a Liquid Jet over a Horizontal Plane," *J. Fluid Mech.*, Vol. 20, pp. 481–499.

An Experimental Investigation of Butterfly Valve Performance Downstream of an Elbow[1]

M. J. Morris
Scientist,
McDonnell Douglas Research Laboratories,
McDonnell Douglas Corporation,
St. Louis, MO 63166

J. C. Dutton
Associate Professor,
Department of Mechanical
and Industrial Engineering,
University of Illinois at Urbana-Champaign,
Urbana, IL. 61801

The results of an experimental investigation concerning the operating characteristics of a butterfly valve downstream of a mitered elbow are reported. Primary emphasis is given the influences of valve disk angle, valve/elbow spacing, and valve/elbow orientation on the dimensionless pressure drop, mass flow coefficient, and aerodynamic torque coefficient characteristics of the valve. The results show that when the valve is located two pipe diameters downstream of the elbow, the performance characteristics are substantially affected by the relative valve/elbow orientation. However, at a spacing of eight diameters the effect of the elbow on the valve operating characteristics is small.

Introduction

Butterfly valves are found in countless piping configurations for a wide variety of applications. Many of these piping geometries also have an influence on the operating characteristics of the included butterfly valve. A fundamental configuration is for a butterfly valve to be located in a straight section of pipe with no upstream or downstream influences on the valve performance due to the piping system. This basic geometry has been the focus of several investigations and is ideal for identifying the basic fluid dynamic mechanisms influencing butterfly valve operating characteristics. In fact, most investigations of butterfly valve performance have been conducted in a straight section of pipe. A discussion of the findings for these investigations can be found in Morris (1987). Unfortunately, this basic geometry is rarely encountered in actual valve applications; as a result, investigations using specific valve/piping geometries are necessary to better understand valve performance in more practical situations.

A geometry that has received some attention recently is a valve/elbow combination. This geometry has been shown to strongly influence the performance characteristics of butterfly valves under certain conditions. The operating characteristics of several butterfly valve/elbow geometries are reported herein. A cursory view of a valve/elbow combination might indicate a relatively simple experimental plan with few parameters. However, the possible combinations of valve/elbow geometries are extensive. The elbow alone provides many possibilities since the elbow could range from a long radius to a short radius design. A 90 deg mitered elbow is an extreme limit for the short radius design and for this reason was chosen for this investigation. The butterfly valve could also be located either upstream or downstream of the elbow with any relative spacing. Further, the valve could be rotated relative to the elbow with the valve shaft position ranging from being parallel to perpendicular to the plane of the elbow (Fig. 1). Finally, butterfly valves with asymmetric disk geometries might be sensitive to which surface of the disk faces the elbow.

Experimental Parameters

This investigation focuses on the operating characteristics of three butterfly valve models over a range of operating conditions using air as the working fluid and featuring several key geometric parameters. The experiments were conducted over a range of back pressure-to-upstream stagnation pressure ratios, P_2/P_{01}, where compressibility was a factor. The pipe Reynolds numbers for this range of operating conditions were approximately 3×10^4 to 7×10^5. In addition, the valve disk angles were positioned in a range from 0 deg (fully open) to 70 deg (nearly closed). Operating characteristics of interest were: the dimensionless static pressure drop, $(P_1-P_2)/P_1$, the mass flowrate capacity, reported as a flow coefficient defined as the ratio of the actual-to-ideal mass flowrate, $C_f \equiv w_{\text{actual}}/w_{\text{ideal}}$,[2] and the aerodynamic torque, reported as a dimensionless torque coefficient, $C_T \equiv T/D^3(P_1-P_2)$, where T is the aerodynamic torque and D is the nominal valve diameter.

Initially, a set of experiments was conducted to identify the baseline operating characteristics of these valve models in a straight section of pipe. During these experiments, straight sections of pipe twenty diameters long were located upstream and downstream of the valve models. The static and stagnation pressure levels were measured at locations ten diameters upstream and downstream of the valve models using CEC strain gauge pressure transducers. Both the torque and the mass flowrate were measured for a broad range of valve angles and operating pressure ratios.

[1]This work was conducted as unfunded independent research at the University of Illinois at Urbana-Champaign prior to the employment of M. J. Morris at McDonnell Douglas Research Laboratories.

Contributed by the Fluids Engineering Division for publication in the JOURNAL OF FLUIDS ENGINEERING. Manuscript received by the Fluids Engineering Division August 3, 1989.

[2]w_{ideal} is the ideal mass flowrate through a converging nozzle with the same nominal diameter and operating under the same pressure ratio conditions as the test valve.

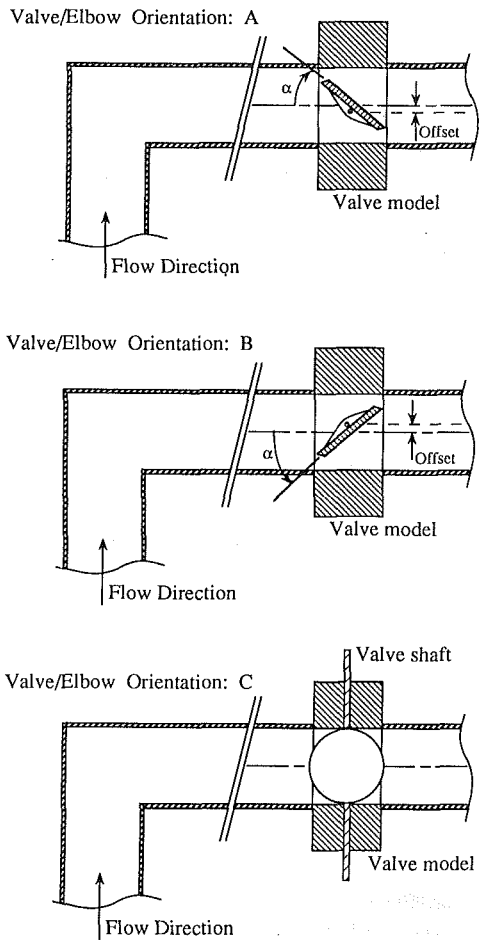

Fig. 1 The three valve orientations relative to the upstream mitered elbow

The baseline experiments were followed by a series of experiments at similar operating conditions that included a mitered elbow/butterfly valve combination. A 90 deg mitered elbow was chosen because it was expected to impose the most severe influence on the operating characteristics of the valves. In all cases of this investigation, the butterfly valves were located downstream of the mitered elbow with the valve shaft located on the upstream side of the valve disk (Fig. 1). The valves and the elbow were spaced at distances of two, four, and eight pipe diameters. For these experiments the elbow was preceded by and the test valve was followed by a long section of straight pipe (>20D). The approach static and stagnation pressure levels were measured ten diameters upstream of the mitered elbow.

In addition to the valve/elbow spacing, these experiments included the additional parameter of valve/elbow orientation. The experiments were conducted for three such orientations (see Fig. 1). In the first (Orientation A), the valve shaft was perpendicular to the plane of the elbow and the valve closed with the leading edge of the valve disk moving towards the outer wall of the elbow. In contrast, the valve shaft was perpendicular to the plane of the elbow and the valve closed with the leading edge of the valve disk moving towards the inner wall of the elbow in the second orientation (Orientation B). Lastly, the valve shaft was parallel to the plane of the elbow for the third orientation (Orientation C).

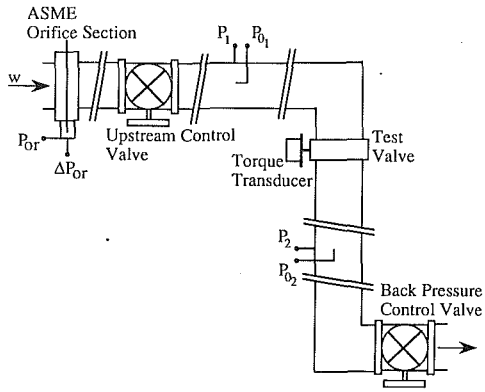

Fig. 2 Schematic of the experimental test section

The three butterfly valve models used during the experiments had flat plate valve disks nominally 76.2 mm in diameter, each with different valve disk thicknesses ($t/D = 0.09$, 0.11, and 0.13). The model with the largest thickness-to-diameter ratio will be the principal focus of this paper with additional references to the other models. A schematic of the experimental setup is shown in Fig. 2. The valve model was equipped with a Lebow torque transducer to measure the aerodynamic torque. In addition, the mass flowrate through the model was measured using an ASME orifice plate in conjunction with strain gauge pressure transducers. A control valve was used to set the upstream stagnation pressure, P_{01}. A second control valve was located downstream of the test valve and was used to adjust the downstream static pressure, P_2. The data were collected using a digital data acquisition system and stored on a computer for reduction and analysis.

Experimental Results

The operating characteristics of a butterfly valve, such as mass flowrate, pressure drop, and aerodynamic torque, are dependent upon the local flowfield through the valve. This flowfield and the operating characteristics of butterfly valves located in straight sections of pipe have been discussed in detail by the authors (Addy et al., 1985; Morris, 1987; Morris and Dutton, 1989a, 1989b; Morris et al., 1986, 1987) as well as others. The flowfield has been shown to be very complex for even this basic application and, in addition, the flowfield and the related operating characteristics have been shown to be strongly influenced by separation and reattachment phenomena. Compressibility effects were also shown to be significant for relatively high operating pressure ratios, P_2/P_{01}. These effects include phenomena associated with supersonic veloci-

Nomenclature

C_f = dimensionless mass flow coefficient
C_T = dimensionless torque coefficient
D = nominal valve disk diameter
P = pressure
P_{or} = pressure at the ASME orifice
t = valve disk thickness
T = aerodynamic torque
w = mass flowrate
α = valve disk angle (0 deg is fully open)
ΔP_{or} = differential pressure across the ASME standard measurement section

Subscripts

0 = stagnation properties of the air supply
01 = stagnation properties upstream of the test section
02 = stagnation properties downstream of the test section
1 = static properties upstream of the test section
2 = static properties downstream of the test section

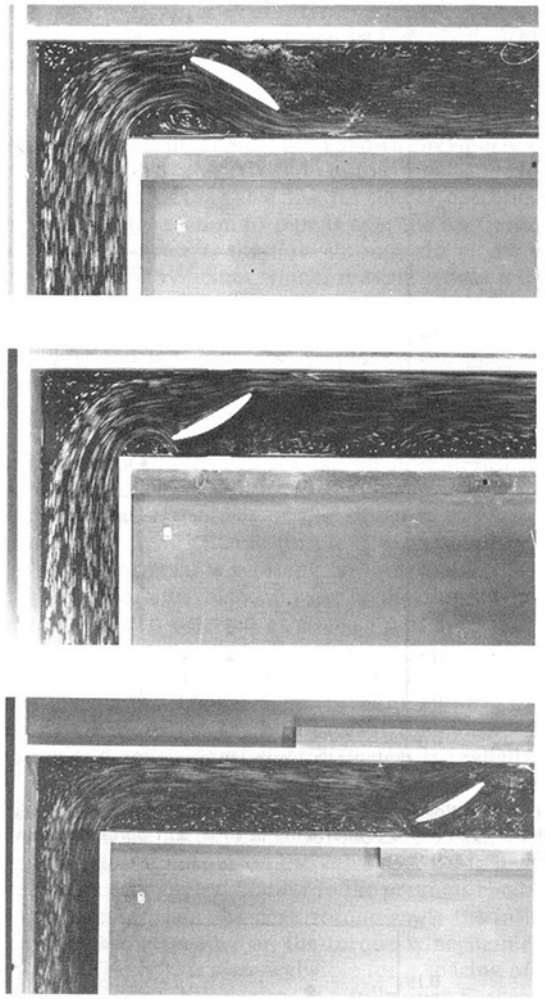

Fig. 3 Typical results from a water table investigation of a butterfly valve/mitered elbow interaction

ties such as choking, both steady and unsteady shock waves, and expansion waves.

The flowfield of a 90 deg mitered elbow/butterfly valve combination is similarly complex and will exhibit similar compressible phenomena. In addition, the influence of the elbow is expected to futher complicate the flowfield and thereby modify the operating characteristics. A water table simulation of a butterfly valve/mitered elbow geometry by Coers (1983) qualitatively characterized the flowfield. The results of this investigation show a separated flow region beginning at the inside radius of the elbow and extending to the valve model. A region of high velocity flow (and high mass flux) also results as the flow accelerates from the separation point towards the outer wall of the channel through an aerodynamic minimum of the flowfield cross section. Typical results from Coers (1983) are shown in Fig. 3 (used with permission); the upper two photos are for two different valve orientations at a valve/elbow spacing of 1.5 diameters while the lower photo is for a spacing of five diameters. The flow direction is from the bottom of each photograph to the right edge. In all cases, the separation region can be seen to extend downstream of the elbow and to consume a large part of the channel cross-section. The actual size and shape of the separated flow region is dependent upon the operating conditions and the specific geometry. For the cases considered in Coers (1983) (valve/elbow spacings up to five diameters), the separated and nonuniform flowfield of the elbow interacts strongly with the butterfly valve disk.

The operating characteristics of the valve models down-

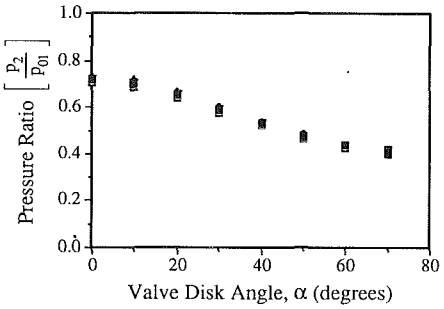

Fig. 4 Operating pressure ratio as a function of valve disk angle for all valve/elbow orientations and spacings and a stagnation pressure of P_{01} = 35 psia (Uncertainty in $P_2/P_{01} = \pm 1$ percent and in $\alpha = \pm 1$ deg)

stream of the elbow have qualitative trends that are similar to those of butterfly valves in a straight section of pipe (Addy et al., 1985; Morris, 1987; Morris and Dutton, 1989a, 1989b; Morris et al., 1987). For a fixed valve/elbow spacing and orientation, the capacity of the valve, as determined by the flow coefficient, decreases monotonically as the valve disk angle approaches a fully closed position. A peak aerodynamic torque coefficient can also be identified at an intermediate valve disk angle and, as the valve disk approaches a fully closed position, the aerodynamic torque is significantly reduced. However, the relative magnitude of these characteristics is dependent upon both the orientation and the spacing between the valve and the elbow. Further, the aerodynamic torque on a butterfly valve at small valve angles is strongly dependent upon the local geometry.

The minimum level of the static pressure downstream of the test section, P_2, was limited by the capacity of the downstream control valve and the adjacent exhaust elbow. This influence caused the operating pressure ratio, P_2/P_{01}, to vary with the valve disk angle. The operating pressure ratio for all of the valve/elbow results that follow are shown in Fig. 4. These conditions are seen to be consistent for all valve orientations and spacings. The results from the base case experiments, a single valve in a straight section of pipe, were chosen to match these operating conditions. As a result, any variation in the operating characteristics of the valve can be attributed to the valve/elbow interaction.

The dimensionless static pressure drop across the valve/elbow combination is shown in Figs. 5(*a*), 5(*b*), and 5(*c*). The pressure drop is primarily a function of the operating pressure ratio and the valve disk angle. The results for each of the orientations and valve/elbow spacings are the same as for the base case results. This finding indicates that the losses associated with the valve dominate the overall static pressure losses of the valve/elbow combination. As expected, the pressure drop is small for the cases with small valve disk angles and is large (a decrease in the static pressure recovery) for large valve disk angles. Decreasing the operating pressure ratio, P_2/P_{01}, resulted in a decrease in the static pressure recovery. Decreasing the valve disk thickness resulted in improved static pressure recovery at small valve disk angles, but similar recovery at large valve disk angles.

As might be expected, the mass flow capacity of the butterfly valve for a valve/elbow combination is less than that for a butterfly valve in a straight section of pipe for corresponding operating conditions due to the additional losses introduced by the elbow. Figures 6(*a*), 6(*b*), and 6(*c*) show the flow coefficient for the thickest disk model, $t/D = 0.13$, positioned in Orientations A, B, and C, respectively. The capacity is reduced approximately 12 percent from the base case experiments for the small (nearly open) valve disk angles and with the valve positioned in Orientation A. As the valve disk angle approaches a closed positioned for this orientation, the mass flow capacity approaches that of the straight pipe case. For Orientation A,

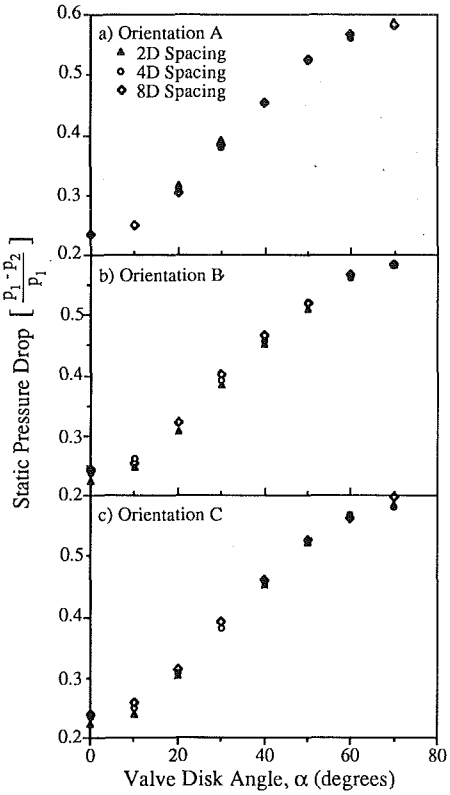

Fig. 5 Dimensionless static pressure drop as a function of valve disk angle for Orientations A, B, and C (Uncertainty in $(P_1 - P_2)/P_1 = \pm 1$ percent and in $\alpha = \pm 1$ deg)

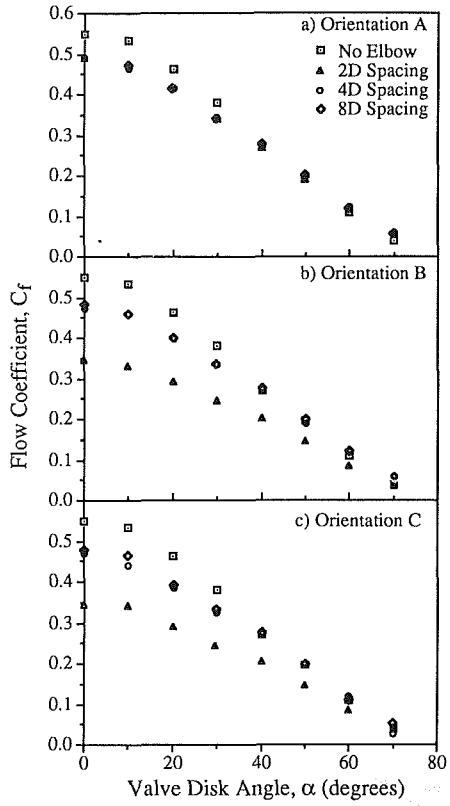

Fig. 6 Mass flow coefficient as a function of valve disk angle for Orientations A, B, and C (Uncertainty in $C_f = \pm 1$ percent and in $\alpha = \pm 1$ deg)

the spacing between the valve and elbow also does not appear to influence the capacity of the valve, since the results for all three spacings collapse on a single curve. However, Orientations B and C exhibit a substantially reduced mass flow capacity (approximately 38 percent) at small valve disk angles for a valve/elbow spacing of two diameters as compared to the baseline straight pipe case. This reduced capacity is likely to result from an increase in blockage in the high velocity field associated with the separated flow region originating at the inner radius of the mitered elbow. This effect can be seen quantitatively in the water table visualizations of Fig. 3. For the larger valve disk angles and at a spacing of two diameters, the flow coefficient results for these orientations approach those of the baseline case. For the experiments with a valve/elbow spacing of four and eight diameters, the flow capacity of the models is essentially independent of both spacing and the relative valve/elbow orientation. Finally, the noted differences in the mass flow characteristics between the orientations is less pronounced for the thinner valve disk models as compared to the thick disk case, $t/D = 0.13$, just discussed.

At small valve disk angles, the aerodynamic torque is strongly influenced by both the valve/elbow spacing and the relative valve orientation. In contrast, at large valve disk angles the aerodynamic torque is insensitive to both. Unfortunately, the definition of the torque coefficient prevents a direct comparison between the baseline straight pipe and elbow experiments. For the valve/elbow experiments, the static pressure measurement upstream of the valve is also upstream of the elbow. As a result, the pressure drop due to the loss mechanisms associated with the elbow is also included in the calculation of the torque coefficient, thereby causing an artificial reduction in the torque coefficient. However, for a valve/elbow spacing of eight diameters, the torque coefficient is virtually independent of the valve orientation, which is an indication that the influence of the upstream elbow has diminished. Based on this argument, the aerodynamic torque results for a valve/elbow

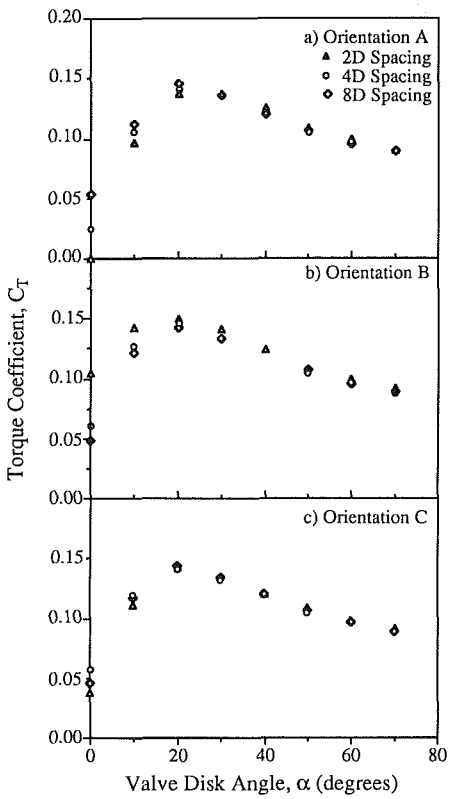

Fig. 7 Torque coefficient as a function of valve disk angle for Orientations A, B, and C (Uncertainty in $C_T = \pm 2$ percent and in $\alpha = \pm 1$ deg)

spacing of eight diameters are used as a basis for relative comparison with the two and four diameter spacings.

The aerodynamic torque coefficient results for valve/elbow orientations A, B, and C are shown in Figs. 7(*a*), 7(*b*), and 7(*c*), respectively, for the thickest disk model, $t/D = 0.13$. At large valve angles (nearing a closed position), the aerodynamic torque on the valve disk is not influenced by the valve/elbow spacing or orientation. As has been shown previously by the authors (Morris, 1987; Morris and Dutton, 1989a, 1989b), the flowfield upstream of the valve disk for similar operating conditions in a straight section of pipe is near the upstream stagnation state. As a result, the flow through the elbow would have relatively low velocities which, in turn, would minimize the losses related to the elbow. Similarly, for a valve/elbow spacing of eight diameters, the torque is not strongly influenced by the elbow and is comparable to that of the straight pipe case. However, for the spacings of two and four diameters and valve angles less than that of the peak torque, the influence of the elbow is significant.

The torque coefficient for orientation A is shown in Fig. 7(*a*). In the fully open position and for a valve/elbow spacing of two diameters, the effect of the elbow is to reverse the direction of the aerodynamic torque (i.e., a small negative value). Torque reversal is typically an undesirable operating condition and is often avoided in valve applications. The effect of the elbow is also detected at a spacing of four diameters near the fully open position. For this condition, the torque coefficient is approximately 50 percent of that for the eight diameter spacing and is positive, i.e., in the direction of closure. Finally, as noted above, the influence of the elbow for this orientation and a spacing of eight diameters is negligible.

For orientation B (Fig. 7(*b*)), the valve opens in a direction opposite to that of orientation A. As a result, the influence of the elbow on the aerodynamic torque is reversed, with the aerodynamic closing torque on the valve disk being increased for small valve disk angles. Similar to the previous results, for disk angles greater than the peak torque angle the influence of the valve/elbow spacing on the torque is negligible. The influence of the elbow is also negligible for a spacing of eight diameters at all valve disk angles. In a fully open position and at a spacing of two diameters, however, the closing torque is increased by 100 percent as compared to that for the eight diameter spacing. In situations where valve closure is essential, this valve/elbow orientation might therefore be desirable.

Unlike orientations A and B, the valve/elbow spacing appears to have little effect on the aerodynamic torque at any disk angle for orientation C. At all valve disk angles, the aerodynamic torque is similar to that of the straight pipe case. For this orientation, the valve shaft is in the plane of the elbow. As a result, the separated flow region originating at the inside radius of the elbow (and also the high velocity flow region near the outer radius) would be exposed to both faces of the valve disk, thereby negating any force imbalance across the disk related to the elbow separation.

For the thinner disk models the variations of the aerodynamic torque coefficient with valve disk angle, valve/elbow spacing, and valve/elbow orientation are qualitatively similar to those for the $t/D = 0.13$ case just presented. One noticeable difference is that much larger negative torques (i.e., opening torques) are measured for the thinner disks near fully open conditions at a two diameter spacing for Orientation A.

Conclusions

Valve/elbow interactions can dramatically change the operating characteristics of a butterfly valve. When the valve is positioned two diameters downstream of the elbow, the performance characteristics are sensitive to the relative valve/elbow orientation. However, with a spacing of eight diameters the influence of the elbow on the valve operating characteristics is small. The mass flow capacity of the valve/elbow combination is in all cases less than that of a valve in a straight section of pipe. This reduction in capacity can be minimized by rotating the valve relative to the elbow, e.g., Orientation A. The aerodynamic torque is particularly sensitive to the influence of an upstream elbow for small valve disk angles and small valve/elbow spacings. The torque is also sensitive to valve/elbow orientation in these cases resulting in an amplification of the closing torque for one orientation (B) and a reversal of the torque for a second orientation (A). By understanding the influences of the local flowfield for a particular valve/elbow geometry, the valve performance characteristics could possibly by optimized for a given application by improving the mass flow capacity and/or by modifying the areodynamic torque on the valve disk.

References

Addy, A. L., Morris, M. J., and Dutton, J. C., 1985, "An Investigation of Compressible Flow Characteristics of Butterfly Valves," ASME JOURNAL OF FLUIDS ENGINEERING, Vol. 107, pp. 512–517.

Coers, B. A., 1983, "A Parametric Study of a Butterfly Valve Utilizing the Hydraulic Analogy," M.S. thesis, Department of Mechanical Engineering, Bradley University, Peoria, IL.

Morris, M. J., 1987, "An Investigation of Compressible Flow Through Butterfly Valves," Ph.D. thesis, Department of Mechanical and Industrial Engineering, University of Illinois at Urbana-Champaign, Urbana, IL.

Morris, M. J., and Dutton, J. C., 1989a, "Aerodynamic Torque Characteristics of Butterfly Valves in Compressible Flow," ASME JOURNAL OF FLUIDS ENGINEERING, Vol. 111, pp. 392–399.

Morris, M. J., and Dutton, J. C., 1989b, "Compressible Flowfield Characteristics of Butterfly Valves," ASME JOURNAL OF FLUIDS ENGINEERING, Vol. 111, pp. 400–407.

Morris, M. J., Dutton, J. C., and Addy, A. L., 1986, "Unsteady Flow Characteristics of Fully Open Butterfly Valves," *Proceedings of the Forum on Unsteady Flow*, ASME FED-Vol. 39, pp. 25–27.

Morris, M. J., Dutton, J. C., and Addy, A. L., 1987, "Peak Torque Characteristics of Butterfly Valves," *Proceedings of the Forum on Industrial Applications of Fluid Mechanics*, ASME FED-Vol. 54, pp. 63–66.

Viscosity Flow Correction for Small Control Valve Trim

H. D. Baumann
H. D. Baumann Assoc., Ltd.,
Portsmouth, NH 03801

A valve sizing method is developed to permit the correct selection of the size of small flow control valve trim handling minute flowing quantities. Most valves such as these operate primarily in laminar or transitional flow regimes, with either gaseous or liquid fluids, due to the geometries involved. The proposed sizing method can be combined with existing turbulent flow equations by the establishment of a valve style modifier F_d which describes the correct relationship between the hydraulic diameter and the equivalent single orifice diameter of a specific valve trim, thereby permitting calculation of the correct Reynolds number for a given flow condition. Finally, a correction factor F_R is used which permits necessary flow corrections when used in connection with the correct valve Reynolds number. This method appears to be reasonably accurate and validated to the extent that the experimental data permit.

Introduction

Control valves that rely on narrow gaps between the closure member and the valve orifice in order to reduce the flow capacity, quite often operate with low Reynolds number and, therefore, in the laminar flow regime. Present Instrument Society of America or International Electrotechnical Commission valve sizing equations have a viscosity correction formula; however, available experimental data indicate that the desired level of accuracy is not adequate. Additionally, these equations cover only the liquid portion of the sizing spectrum, yet many small flow valves with C_v ranges from 0.1 to 1×10^{-6} do quite often operate in the laminar regime with gaseous flow media at moderate pressure drops. Finally, it should be recognized that C_v numbers published by small flow valve manufacturers usually do not fit the traditional definition for a C_v flow coefficient obtained from a turbulent flow test.

This paper attempts to clarify the issue and to establish meaningful sizing rules, including establishment of F_d valve style modifiers for small trim that eliminate the present potential for erroneous valve sizing that can reach errors of up to 5000 percent.

Present Sizing Equations

Control valves are now nearly universally sized with the aid of equations published in the Instrument Society of America Standard S75.01 [1] or the equivalent equations in IEC Standard Publication 534-2 [2].

Since control valves quite often handle viscous liquids, a correction factor F_R is employed to account for the apparent loss in flow capacity of a valve (see equations (9) and (10) of reference [1]). The Reynolds number correction factor, F_R, states the fraction of flow passing a valve with a highly viscous fluid and resultant low Reynolds number over the flow of water at turbulent flow conditions.

The published ISA Correction Curve (Fig. 1 in reference [1]) was based on published test data by G. Stiles [3] and measured with single and double-seated globe valves in sizes 1/2 to 2 in. In a recent paper by J. A. George [4], it was stated that the ISA curves for F_R do not apply for small flow trim (C_v below 0.012). As a matter of fact, the curves missed by a factor of more than 2:1! A similar nonconformity was found by L. Marcadet [5] in France.

There are two possible explanations for this discrepancy:

1) Stiles did not account correctly for the effects of the valve style modifier F_d which the ISA Standard S75.01 simply defines as "valve style modifier," and which I define as the ratio of the hydraulic diameter to the equivalent circular orifice diameter of the total flow area of a given valve trim (for more details see below). Stiles' Reynolds number calculations are based on an F_d factor of 1 (except for a double-seated valve where he used 0.71), when in fact his trims had F_d's[1] of between 0.2 and 0.5.

2) It should be expected that a valve with an orifice diameter equal or close to the valve body bore should have different head losses caused by laminar friction than a small trim valve where the equivalent orifice diameter (D_0) is at least one order of magnitude smaller than the body bore. Here the head losses, caused by body wall friction, become negligible in relationship to those experienced by the trim.

Finally, the ISA sizing equation makes no corrections for laminar flow conditions with gases, a condition practically never encountered with conventional process control valves, but quite often found with small laboratory valves.

Contributed by the Fluids Engineering Division of THE AMERICAN SOCIETY OF MECHANICAL ENGINEERS for presentation at the Joint ASME-JSME Fluids Engineering Conference, Portland, Oregon, June 24-26, 1991. Manuscript received by the Fluids Engineering Division, March 1990.

[1] As defined herein and as calculated by the author.

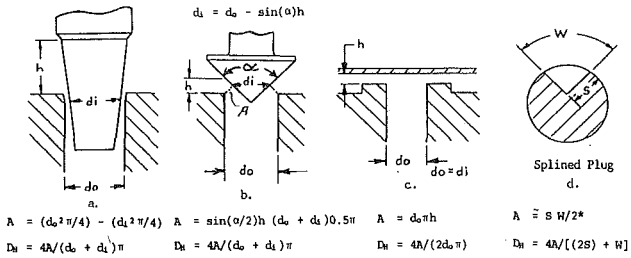

Fig. 1 Various small flow trim configurations with their respective flow area and hydraulic diameter calculations

On the other hand, it would be beneficial if the current ISA equation could be extended to cover low flow trim. Hence, the need for a method to calculate F_d and F_R, and mainly to redefine F_d.

The Valve Style Modifier, F_d

In order to calculate the correct Reynolds number under a given flow condition, the hydraulic diameter of a given valve plug or trim must be used.

As defined herein:

$$F_d = \frac{D_H}{D_0}. \tag{1}$$

Use of the F_d factor now enables the conversion of the more familiar orifice diameter D_0 into the correct hydraulic diameter D_H.

Neglecting the "Velocity of Approach," due to the large body section, the valve Reynolds number (Re_v) can be calculated (from reference [1], equation (11))

$$\mathrm{Re}_v = \frac{76000\, F_d\, q}{\nu F_L^{0.5}\, C_v^{0.5}} \tag{2}$$

based on the familiar relationship,

$$R = \frac{D\, V}{\nu}. \tag{3}$$

The constant 76000 $\mathrm{gpm}^{0.5}/(\mathrm{psi}^{0.25}$ inch), taken from Reference [1], includes a conversion from $C_v^{1/2}$ and $F_L^{1/2}$ to an equivalent circular orifice (D_0) and a unit conversion.

The well-established equation for the hydraulic diameter D_H is:

$$D_H = \frac{4\mathrm{A}\ (\text{Flow Area})}{\text{Wetted Circumference}} \tag{4}$$

Figure 1 shows a number of small flow trim configurations and their corresponding equations for their respective A and D_H calculations.

$$D_0 = \text{The equivalent orifice diameter} = (4\,A/\pi)^{1/2} \tag{5}$$

Having thus found from equation (1) (or obtained from a manufacturer's catalog), the applicable F_d factor, one can now calculate the Reynolds number of the trim for liquids as well as for gases (equation (2)).

The Reynolds Number Factor, F_R

The friction factor, f, in the laminar regime is given [6] as,

$$f = \frac{64}{\mathrm{Re}_v}, \tag{6}$$

and the equivalent L/D factor for a 0.4 in. inside diameter pipe and K of 1 is ≈ 33 from reference [6]. This is the smallest pipe data published, but it may serve as a useful reference point. The velocity head loss coefficient K was chosen as 1.0 since all air flow tests under assumed fully turbulent flow conditions established a pressure recovery factor F_L of essentially 1.0, thus indicating total velocity head loss. This is understandable in view of the fact that the ratio between the flow areas of the body cavities and the flow area of the trim is above 60:1.

Solving for $\mathrm{Re}_v = 64 \times 33 = 2112$ at $K = 1$, i.e., $F_R = 1$ (fully turbulent), which is close to the generally accepted turbulent flow inception at $\mathrm{Re}_v = 2000$. We also know from reference [1] that F_R varies as the square root of Re_v. Thus, we can construct the fully laminar portion of the F_R correction curve as shown in Fig. 2 having its origin at Re_v 2100; hence,

$$F_R = \sqrt{\mathrm{Re}_v/2100}. \quad (F_R \text{ max.} = 1). \tag{7}$$

However, there is no sudden change from turbulent to laminar flow, and instead, we encounter a transition zone following my suggested empirical relationship:

$$F_R = \sqrt[n]{\frac{\mathrm{Re}_v}{1000}} \tag{8}$$

Where: $n = 1 + \log(\mathrm{Re}_v)$.

The transition from equation (7) to equation (8) occurs at $\mathrm{Re}_v = 130$.

The resultant curve shown in Fig. 2 agrees well, within a few percent, with the average test data taken by J. A. George [4] on a number of tapered, cylindrical plugs with turbulent C_v's ranging from 0.0008 to 0.012, and it produces slightly more conservative F_R values.

The F_R factor can now be used to correct laminar or transitional flow by simply dividing the calculated C_v (using the standard turbulent flow ISA equations for gas and liquid) by F_R. This gives the required flow coefficient (C_v) that a valve must have in order to pass the desired flowing quantity.

Experimental Results

Very commendable work has been performed by J. A. George [4], particularly in bringing attention to this sizing problem. However, it was necessary to verify the recommended F_R curve with other than tapered needle type trim styles in order to prove their universal applicability.

To this end, a number of tests with air, nitrogen gas, and water were conducted with commercial valves having trim styles corresponding to types c. and d. in Fig. 1.

The first step was to establish the turbulent C_v or flow coefficient of a given test specimen. This was done with air, or in case of C_v's below 0.005, with high pressure N_2-gas. The criterion for establishing that fully turbulent flow existed, was no increase in flow by more than 5 percent with a constant in-

Nomenclature

- A = assumed flow area
- C_v = turbulent valve flow coefficient, $\mathrm{gpm/psi}^{1/2}$
- D = diameter
- D_H = hydraulic diameter of flow area
- F_d = valve style modifier, D_H/D_0
- D_0 = equivalent orifice diameter of flow area
- d_i = plug diameter
- d_0 = orifice diameter
- F_L = liquid pressure recovery factor, $(P_1 - P_2/P_1 - P_0)^{0.5}$
- F_R = valve Reynolds number factor
- K = velocity head loss coefficient
- q = flow rate in m^3/h
- R = Reynolds number
- Re_v = valve Reynolds number
- V = velocity
- ν = kinematic viscosity (centistokes), $10^{-6}\ \mathrm{m}^2/\mathrm{s}$

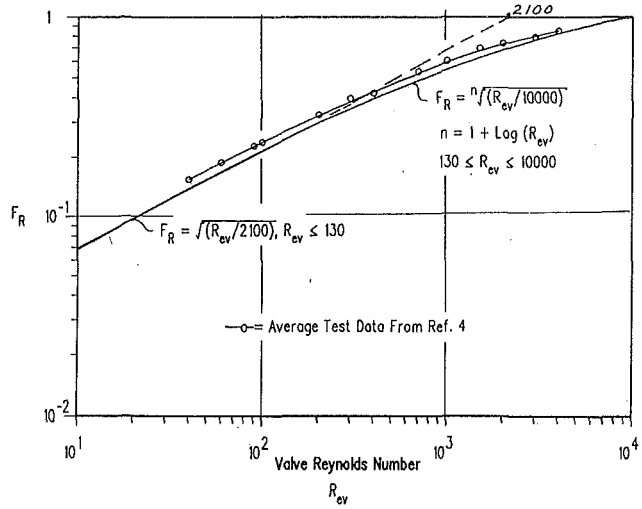

Fig. 2 Valve Reynolds number factors for valve trim having C_v numbers of 0.1 and below

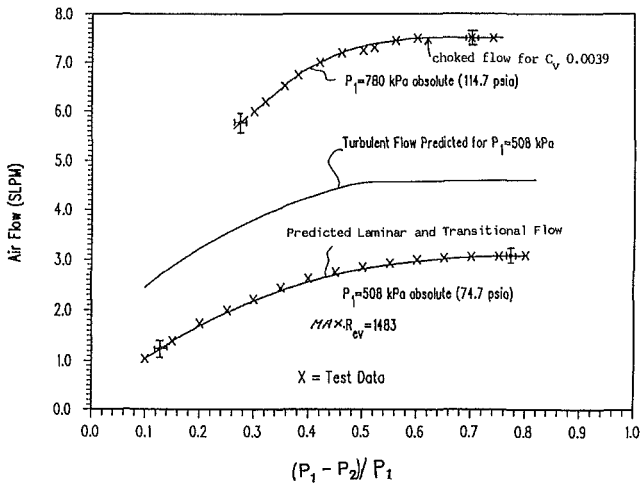

Fig. 3 Comparison of choked versus nonchoked air flow in a valve having a narrow, parallel flow path with a 0.063 in. orifice diameter, $C_v = 0.039$ and $F_d = 0.10$

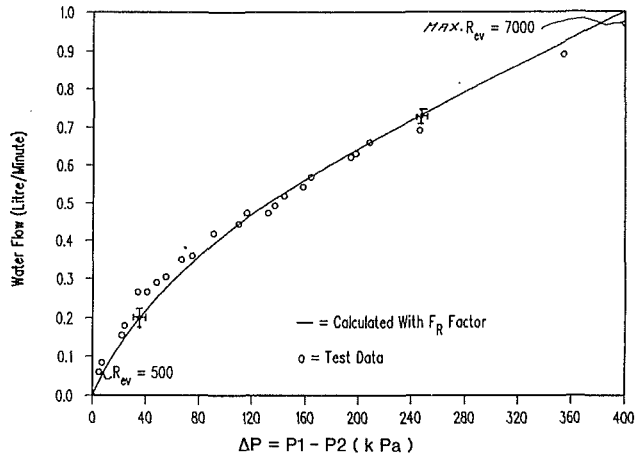

Fig. 4 Comparison between predicted and tested water flow under laminar and transitional flow conditions. Same valve as Fig. 3 at a $C_v = 0.037$, and $F_d = 0.29$.

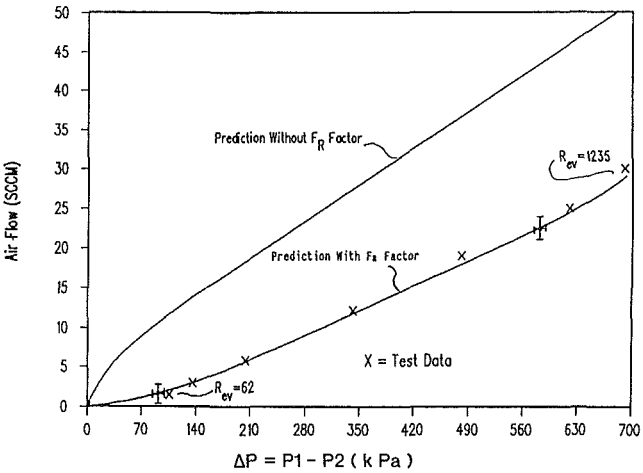

Fig. 5 Air flow of V-notched plug assuming fully turbulent (upper curve) or laminar/transitional flow (lower curve), $C_v = 2.5 \times 10^{-5}$, $F_d = 0.7$

let pressure and measured between a pressure drop ratio $X = \Delta P/P_1$ of 0.5 and 0.8 using criteria in reference [8]. Thus, the onset of choked flow and resultant constant flow rate was taken as evidence of fully turbulent flow. It is important to achieve a Reynolds number Re_v of at least 5000 in order to obtain a reasonably certain turbulent C_v number under choked flow conditions. This will require the use of a sufficiently high air inlet pressure, at 20°C, determined as follows:

$$P_{1\,\text{min.}} = 7/(C_v F_L)^{0.5}\, F_d \ \text{(kPa)}, \qquad (9)$$

but no less than 200 kPa absolute. (The units of the constant "7" are $\text{gpm}^{0.5} \cdot \text{kg}/(\text{psi}^{0.25} \cdot \text{m} \cdot \text{s}^2)$.

The data in Fig. 3 may exemplify the difference between turbulent and finally choked flow (onset of sonic velocity) at pressure ratios exceeding 0.5, which limits further flow increase. Here the test data for $P_1 = 780$ kPa show a flow increase of only 3.4 percent above $X = 0.5$. With lowering inlet pressure and the resultant lower Reynolds number, a different pattern emerges. Here the flow rate is not only substantially below that predicted by the turbulent equations, but also shows no sign of choking. The test data with $P_1 = 508$ kPa still exhibit a flow increase of 11 percent above $X = 0.5$, which indicates laminar or transitional flow.

Having established the turbulent C_v, additional tests were conducted with lower flow rates with both air and water. The corresponding Reynolds numbers were calculated using the measured flow rate, and a comparison was made between the flow from the experiment and the flow predicted using the C_v value established from the choked flow test outlined above and modified by F_R using the F_R values calculated from equations (7) or (8). The data in Fig. 3 show a typical prediction accuracy of within 3 percent using the F_R correction from Fig. 2. However, omitting F_R would have resulted in an undersizing of the valve by about 35 to 55 percent. With the exception of the data shown in Fig. 6, all test data indicated average prediction accuracies of within +/− 5 percent using the F_R curve in Fig. 2.

The prediction accuracy generally tends to improve with increase in valve C_v as exemplified by the test data in Fig. 4. Despite the tendency for a lowering of F_R values with lowering of flow coefficients from reference [7], I believe that the accuracy level is sufficient if one uses a combined F_R curve for all C_v values of 0.1 and below as proposed in Fig. 2.

Another element of inaccuracy may be caused by the difficulties in measuring extremely small flow rates of liquids. For example, while an air test with a V-notch plug in Fig. 5 shows very good agreement between experimental and predicted flow, errors of about 100 percent did show up when the same valve was subjected to a flow test with water (see Fig. 6). However, as one can see from the scattering of test points, the measurement of a flow rate of only a few cubic centimeters

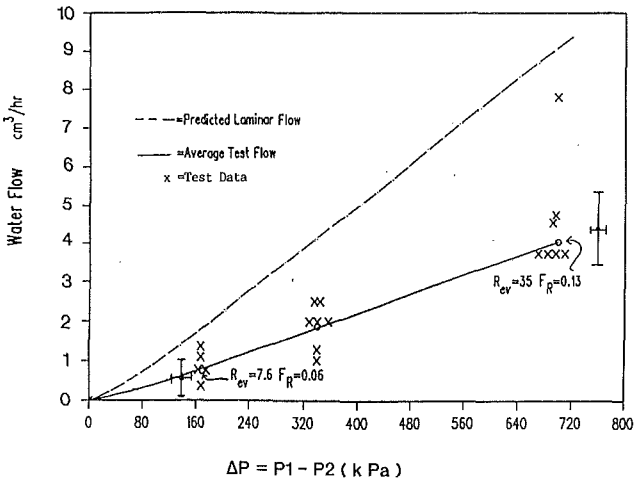

Fig. 6 Water test on plug of Fig. 5 shows significant error in predicted laminar flow rate, possibly due to gas entrainment

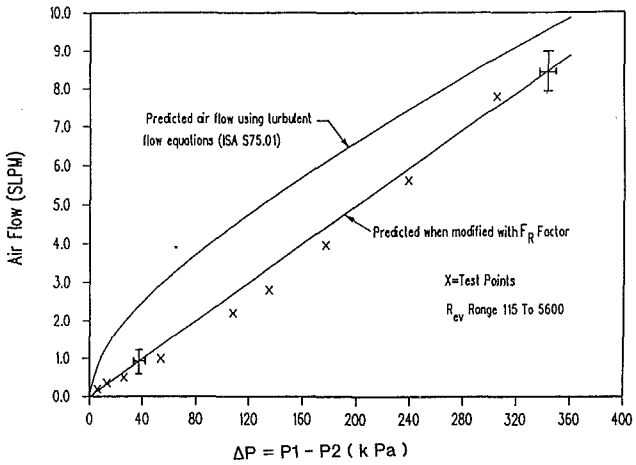

Fig. 7 Comparison of air flow assuming turbulent flow (upper curve) versus laminar and transitional flow (lower curve), $C_v = 0.009$, $F_d = 0.20$

per hour (3 cm^3/hr equals only about 7 US gallons per year!) was difficult, and a portion of the flow may not be accounted for due to evaporation or gas entrainment. Nevertheless, at the low Reynolds number of 7.6, standard sizing equations would have predicted a flow rate about 17 times higher than measured! Or, to put it in other terms, using the present sizing method, a C_v value of 7.5×10^{-7} would have been measured at 200 kPa ΔP instead of the actual 2.5×10^{-5}.

Conclusion

The available test data confirm that it is possible to predict low flow valve capacity with the aid of a single correction factor (F_R), proposed in this paper and calculated with the manufacturers' published F_d, F_L, and C_v factors. This can be done with reasonable accuracy and by using established valve sizing equations published by ISA and others. However, in order to be effective, manufacturers of low flow valves have to redefine the published flow capacity of their valves in strict adherence to C_v measurement in the turbulent regime instead of by the current practice of defining the C_v arbitrarily, at say, 100 psi pressure drop with air. This means that there may be no more valve trims having published C_v's of less than 1×10^{-5}! In addition, the F_d factor of each valve trim has to be established either by test or by calculation as indicated in this paper.

All testing so far has been limited to C_v values below 0.1, and the conclusions presented here may not be applicable for different sizes and types of valve trim.

As this and other data from reference [7] indicate, laminar flow is encountered at much higher pressure differentials than anticipated, even with gaseous fluids, leading to serious sizing errors if not accounted for. However, laminar flow in itself is quite a positive phenomenon. If properly applied in flat seat and diaphragm designs, it can vary the flow rate to the third power of valve travel [9], thereby achieving more than 1000:1 flow rangeability at a constant pressure drop. Additionally, laminar flow cannot create cavitation damage to a valve trim even at high pressure drops. Finally, as the test data show, laminar flow, with the associated high friction losses, enables us to control much smaller flow rates than typical minimum clearances would otherwise allow, due to machining tolerances between the plug and seat ring.

References

1 Instrument Society of America (ISA), Standard ISA S75.01, "Flow Equations for Sizing Control Valves," Instrument Society of America, Research Triangle Park, N.C., 1985.

2 International Electrical Commission (IEC), "Sizing Equations for Incompressible Fluid Flow Under Installed Conditions," Publication 534-2, Part 2, 1978, American National Standards Institute, New York, NY.

3 Stiles, G. F., "Liquid Viscosity Effects on Control Valve Sizing," Technical Manual TM17, Oct. 1967, Fisher Controls International, Marshalltown, IA.

4 George, J. A., "Sizing and Selection of Low Flow Control Valves," INTECH, Nov. 1989, pp. 46-48.

5 Marcadet, L., "Low Flow Valve Sizing and Selection," publication by Masoneilan-Dresser, 107 Avenue Charles de Gaulle, Neuilly-s/Seine, France.

6 Crane, "Technical Paper No. 410," 1969, Crane Co., Chicago, pp. A-31.

7 George, J. A., "Sizing and Application of Low Flow Control Valves for Gas Service," ISA Paper 89-0706, October 1989, pp. 1.560, Fig. 4, Instrument Society of America, Research Triangle Park, N.C.

8 Instrument Society of America, Standard S75.02, "Control Valve Capacity Test Procedure," Instrument Society of America, Research Triangle Park, N.C., 1988.

9 Baumann, H. D., "Control Valve with Laminar Flow Characteristic," ISA Paper C.I. 81-540, Mar. 1981, Instrument Society of America, Research Triangle Park, N.C.

Suction Reverse Flow in an Axial-Flow Pump

K. Alpan
Chief Test Engineer,
Dresser Pump Division,
Dresser Industries, Inc.,
Huntington Park, CA 90255

W. W. Peng
Professor,
Department of Mechanical and
Industrial Engineering,
California State University, Fresno
Fresno, CA 93740

Experiments are carried out to determine the effects of different inlet geometries on the onset of suction recirculation and its associated power consumption in an axial-flow pump. The critical flow rate is determined by both the "string" visual technique and "pressure" method. The results are correlated with the inlet area and flow velocity distribution upstream of the impeller. Four different conical covers matching the impeller leading edge are employed to cover the impeller inlet completely or partially. Covering the inlet area reduces the critical flowrate corresponding to the onset of suction recirculation and eliminates all recirculation at higher flowrates. The power consumption associated with the suction recirculation flow for the uncovered impeller is determined by comparing the shaft powers with and without inlet covers. At the shut-off condition, the power is estimated from a comparison with the shaft power measured with the impeller inlet completely covered. Experimental studies conclude that the power consumption due to suction recirculation is mainly controlled by the impeller inlet area and is insensitive to the inlet pipe configuration. At shut-off condition, the power coefficient correlates well with the parameter based on the hydraulic radius of inlet area. At a finite through flowrate the analytical model recommended by Tuzson (1983) is adequate, except for a proportionality coefficient determined from the test data.

1 Introduction

Flow recirculation is a common phenomenon at suction and discharge regions of the impeller of both axial-flow and centrifugal pumps. Problems associated with suction recirculation in these pumps include:

1) erosion of the vane at the impeller inlet
2) surging in the suction pipe, and
3) premature cavitation at reduced flowrate.

If a pump is operated under the suction recirculation condition, part of the energy produced by the impeller is carried back and dissipated in the suction pipe.

Both Schweiger (1976) and Murakami and Heya (1966) have noticed a decrease in the shaft power consumption, with the elimination of backflow, when they tested the improved pumps with corresponding delayed onset of backflow. A series of studies on flow recirculation in axial-flow pumps have been carried out by Toyokura (1961).

In an axial-flow pump, the recirculation flow can be so severe that excessive power can make the maximum brake horsepower occur at the shut-off condition. In some pump applications, the maximum brake horsepower is a primary design consideration; hence a study on the power consumption due to recirculation in an axial-flow pump is warranted. In this study, the onset of suction recirculation and the associated power consumptions of an axial-flow pump is determined experimentally, and the results are correlated with the appropriate nondimensional parameters.

At the onset of suction recirculation, flow prerotation takes place; hence higher static pressure can be detected at the inlet pipe wall immediately upstream of the impeller. Both a visual observation and the sudden increase of suction pressure can be used to determine the critical flowrate when suction recirculation starts.

2 Experimental Apparatus

A schematic diagram of the test loop is shown in Fig. 1. The test pump is equipped with an axial-flow impeller shown schematically in Fig. 2. It is a special patented-pump (Cooper, 1973), designed originally as an aircraft fuel pump, manufactured by TRW, Inc. The impeller has three blades, with the blade element inclined 45 degrees with respect to the axis at the leading edge, and gradually changing to be perpendicular to the axis at the trailing edge. The specific speed is estimated to be 2.55 in nondimensional quantity (or 7000 rpm $(gpm^{1/2}/(ft)^{3/4}$ in conventional dimensional units). The impeller and the electrical motor are integrated into a single unit. Aboard the aircraft, the whole unit is submerged in the fuel tank and no additional coolant and lubricant are required for the motor. In the laboratory set-up shown in Figs. 1 and 2, a separate cooling/lubricating system is provided since water is used as the test fluid medium.

The pump through flowrate is determined from the pressure drop across an orifice plate. Pump inlet and outlet pressures are monitored with pressure transducers. Two transparent

Contributed by the Fluids Engineering Division for publication in the JOURNAL OF FLUIDS ENGINERING. Manusrcipt received by the Fluids Engineering Division July 27, 1989.

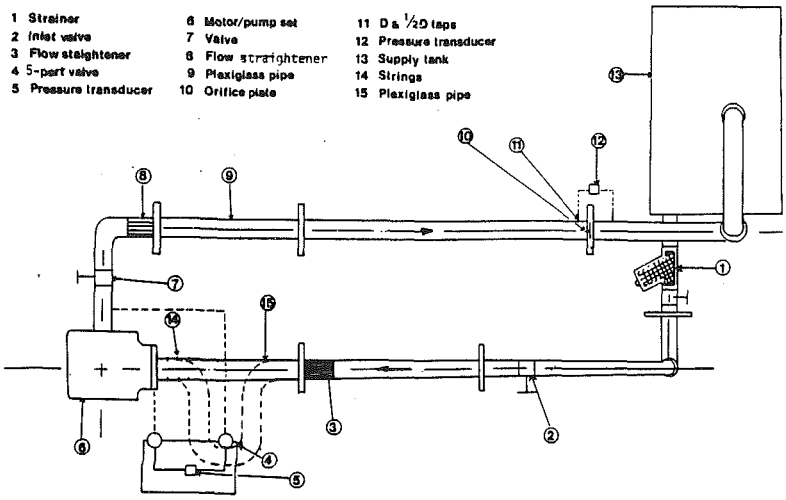

Fig. 1 Experimental apparatus

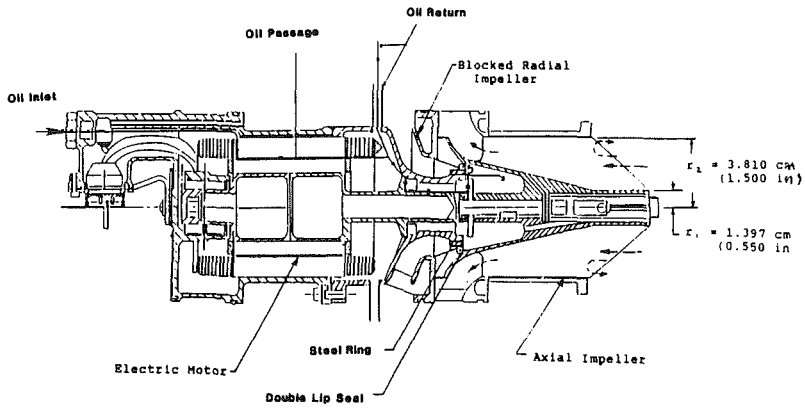

Fig. 2 Test pump with modifications for motor oil lubrication

plexiglass pipes are installed at pump suction and discharge to provide visual observation of the water flow.

The electrical motor is of an induction type; its rotating speed varies with the frequency of the a-c electrical power. An a-c generator with two sets of pulleys, driven at two different speeds, is used to generate the two a-c frequencies needed to drive the test pump at two rotating speeds around 5600 rpm and 3800 rpm (to be identified as high- and low-speed pump operations in the present study).

Since the impeller and the motor are integrated into a single unit, the electrical input power is monitored with wattmeters and then converted to the shaft power through a motor calibration curve which is provided by the manufacturer. The actual speed is also obtained from the motor calibration curve relating the impeller rotational speed and the electrical input power. To obtain consistent data, the motor is cooled and maintained at constant temperature during the tests.

The straight pipe with conical guide vane and the U-pipe shown in Fig. 3 are installed to test their effects on the onset of suction recirculation and the associated power consumption.

3 Experimental Studies

3.1 Critical Flowrate Determination. Flow recirculation

Nomenclature

A = impeller inlet area
d = suction pipe inside diameter
n = exponent
P_{av} = average circumferential pressure on any suction test section
P_f = reference suction pressure
P_r = power consumption due to suction recirculation
Q = pump flowrate
Q_0 = design flowrate
Q_{ri} = sectional critical flowrate
Q_{cr} = pump critical flowrate
Re = Reynolds number
r = radius variable
r_c = characteristic radius
r_h = hydraulic radius of impeller inlet open area
r_1 = inner radius of impeller inlet open area
r_2 = outer radius of impeller inlet open area
S = wetted perimeter of impeller inlet
$\bar{V}$ = average flow velocity
ρ = fluid density
ω = impeller rotating speed
μ = dynamic viscosity of fluid
ϕ = flow coefficient
$\bar{\pi}_{s/0}$ = power coefficient due to suction recirculation at shutoff
π_i = nondimensional parameters relevant to critical flowrate
$\bar{\pi}$ = power coefficient due to suction recirculation at finite through flowrate

has been studied by numerous investigators, but only a few of them have actually determined the critical flowrate, Q_{cr} at which the reverse flow is initiated. Visual observation of string motions, velocity and pressure measurement techniques have been proven to be the effective ways to determine this crucial point.

In the "string" method, a set of nylon strings are installed in the clear plexiglass pipe so that they extend into the flow region. As the flowrate is gradually decreased the strings start to reverse from their normal flow direction, and the point where the reversal occurs is called the "critical flowrate." In the "string" method the strings are placed circumferentially at three different upstream test sections, as shown in Fig. 4, closest to the pump being designated as the "first section." When the flow reversal is observed at this section it is referred to as the "first section critical flowrate," Q_{r1}, and the last (most upstream) one being "the third section critical flowrate," Q_{r3}. This nomenclature is used throughout this study.

In the pressure technique three different test sections are designated again, but in this case the strings are replaced by pressure taps. Each test section has four pressure taps distributed circumferentially 90 degrees apart which enables easy connection via any one of the four. The four circumferential pressure readings taken at each section are averaged and are deducted from the upstream static pressure,

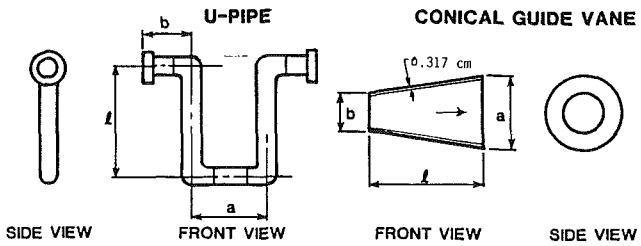

INLET GEOMETRY	ℓ (cm)	a(cm)	b(cm)
U-PIPE	71.12	26.52	14.63
CONICAL GUIDE VANE	10.16	5.59	4.27

Fig. 3 Inlet geometries

which serves as a reference point since it is not affected by recirculation. The pressure-difference $(P_{av} - P_f)$ for each of the three test sections are plotted against the flowrate, from fully open to shutoff. All test results clearly indicate the presence of two pressure trends. Initially, at high flowrates we observe small negative values, but at a certain point the pressure suddenly increases and this increase continues steadily with the gradual decrease of the flowrate. The high and low-pressure-zone data points are each fitted with best-fit straight lines and the discontinuity point where they intersect is designated as the "section critical flowrate." In each graph three of these flowrate are obtained, with the section closest to the pump having the highest value. The case B with the conical inlet guide vane located 2.77 cm away from the impeller plane is provided as a sample for the above mentioned procedure in Fig. 5 for the low speed case.

The three section critical flowrates are then plotted with respect to the corresponding distances from the pump's inlet plane. In all plots the procedure adopted by Sen (1978) is followed; a straight line is fitted to the three section critical flowrate points and the point where this line intersects the vertical axis is taken as the "pump critical flowrate;" *Qcr*, as shown in Fig. 6. Tests with the conical inlet guide vane located up-stream of the impeller with the distance $X_c = 0.97$, 2.77, and 4.615 cm, respectively, as shown in Fig. 4, are called Case A, B and C.

The suction recirculation is initiated from the boundary-layer separation at the leading edge of the impeller. The phenomenon is similar to that on the flow over an airfoil, where the angle of attack is the primary parameter to affect the onset of boundary-layer separation. Reasoning along this line, it is expected that a conical inlet guide vane producing a higher flow velocity at the outer radius, will delay the onset of reverse flow since it is initiated at this region. This velocity distribution has been measured at three sections downstream of the vane with the distances corresponding to the three locations of the vane places upstream of the impeller leading edge. The results expressed in terms of the normalized flow velocity and inside radius of the pipe are shown in Fig. 7.

3.2 Power Associated With Suction Recirculation. The recirculating suction flow pattern is depicted qualitatively in Fig. 2. It extends towards upstream as the through flowrate is reduced, and eventually covers the whole region around the impeller leading edge. The energy associated with the backflow imparted by the impeller is dissipated in the recirculation zone of the suction pipe. Partial reduction of the im-

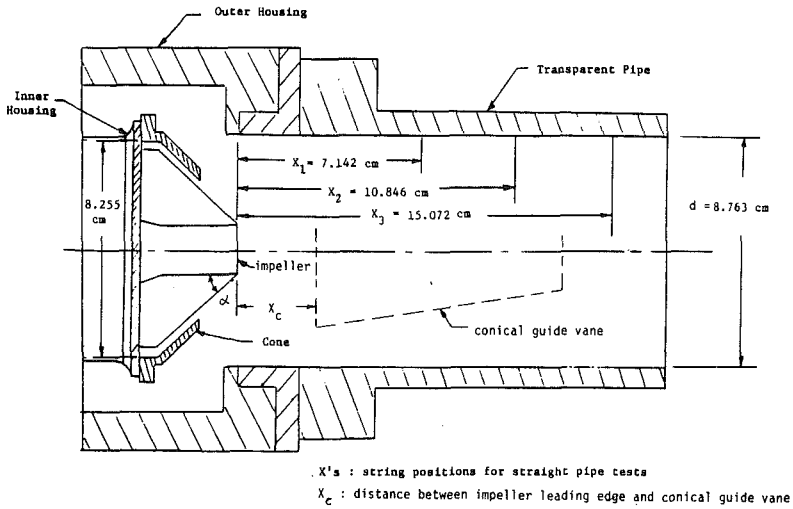

Fig. 4 Test section with sample conical cone and string positions

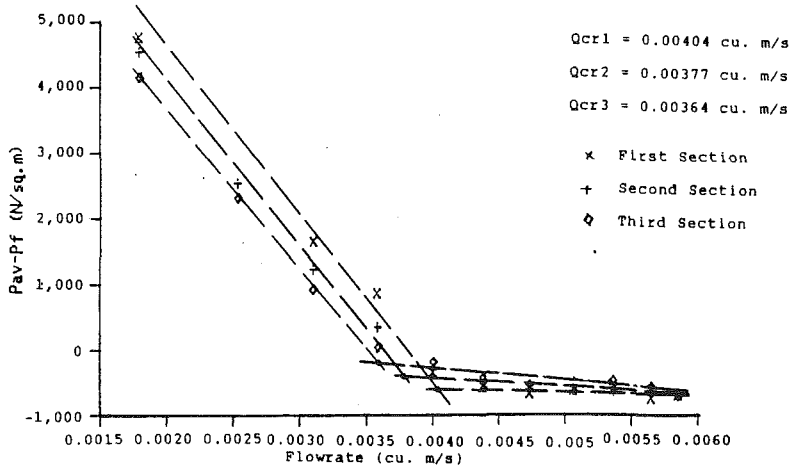

Fig. 5 Section critical flowrate determination for case B of the conical guide vane at low speed

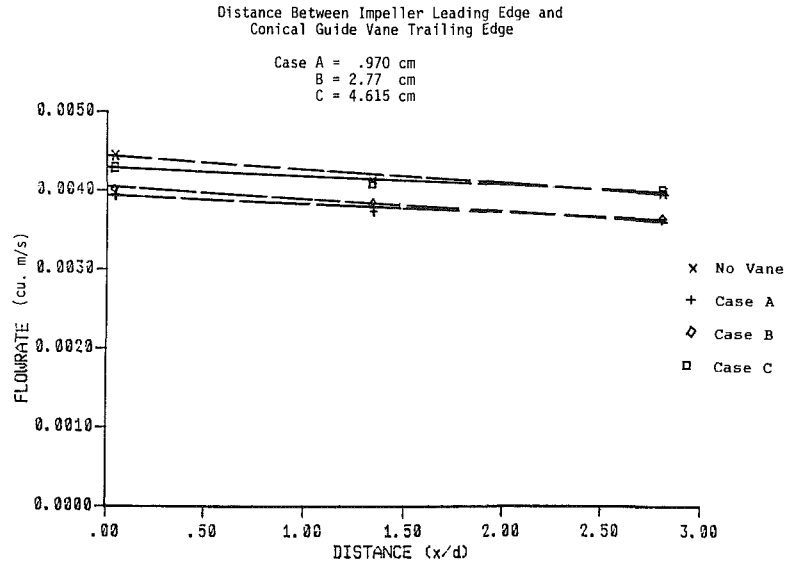

Fig. 6 Pump critical flowrate determination for the straight pipe, with and without guide vane at low speed

peller inlet area can reduce the recirculating flow and its associated power consumption. A complete covering of the inlet area should totally eliminate the recirculation power consumption at the shut-off condition, except for an insignificant amount of power associated with the short-circuit recirculation flow within the impeller.

The power consumption associated with the suction recirculation is determined with four different conical covers matching the impeller leading edge. Their inside dimensions are given in Fig. 8. The cone "0" is a simple ring leaving the impeller inlet fully open, while the fourth cone completely covers the impeller inlet area. A partial cone installed is shown in Fig. 4. The cone is fixed on the inner housing of the pump.

The shaft horsepower versus flowrate was determined for each of the four covers and without cover at both high and low rotating speeds (around 5600 and 3800 rpm, respectively). The results are shown in Figs. 9 and 10. Since the fourth cone completely covers the impeller inlet, the power measurement with this cone excludes suction recirculation power, while measurements with other cones include certain amount of power due to suction recirculation at the low flowrate and shut-off conditions. The power consumption associated with the recirculating flow at shut-off conditions can be obtained by subtracting the power measurements with the fourth cone installed from that with one of the other cones installed. The results are expressed in terms of the nondimensional power coefficient defined as:

$$\bar{\pi}_{s/0} \equiv \frac{P_r}{\rho r_c{}^5 \omega^3} \tag{1}$$

where ω is the angular speed in rad/s, r_c is characteristic radius, and ρ is water density.

3.3 Experimental Uncertainty. The experimental uncertainty of both flowrate and pressure difference should be within 5 percent, while that of the power measurement is estimated to be around 10 percent of the nominal value due to the uncertainty of motor calibration curves.

4 Data Correlations and Analysis

The test results on critical flowrate, Q_{cr} at two rotating speeds with various inlet geometries are tabulated in Table 1. The relevant nondimensional parameters are flow coefficient, angular momentum ratio, the ratio of tip radius over hydraulic radius of the impeller leading edge, and the ratio of the flow velocity at outer radius over the average flow velocity. They can be expressed as follows:

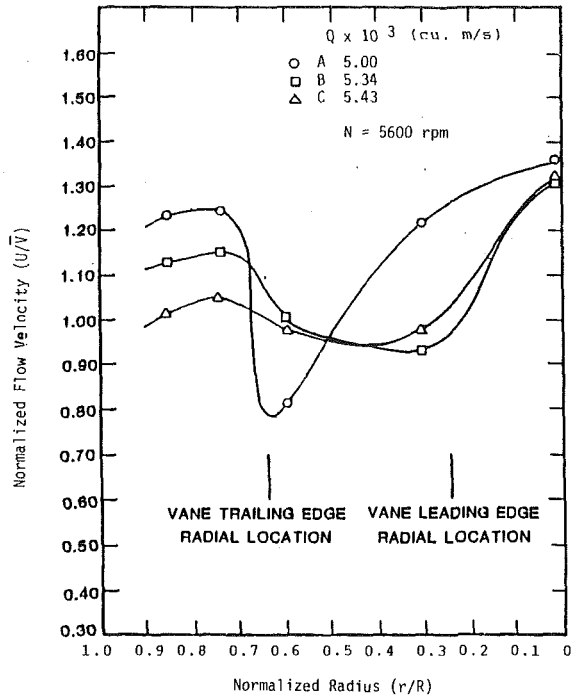

Fig. 7 Velocity profiles at top portion of impeller plane for all three locations of the conical inlet guide vane

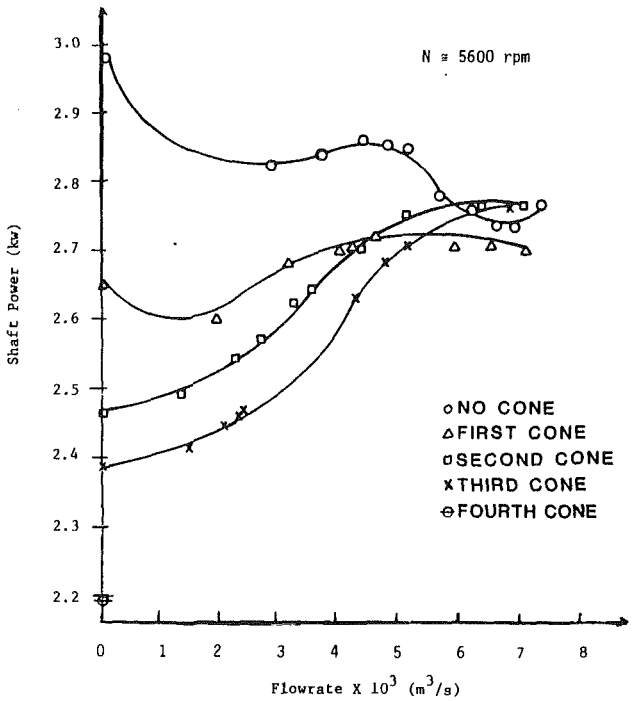

Fig. 9 Shaft power for high speed tests

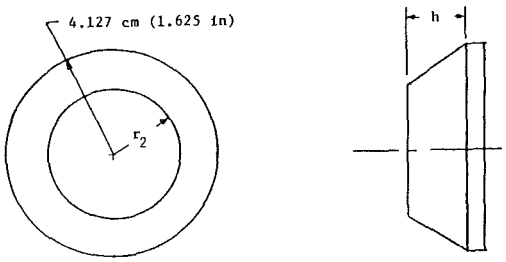

cone	h(cm)	r_2(cm)
0	—	3.81
1	1.206	3.124
2	1.778	2.642
3	2.078	2.387
4	3.254	1.397

Fig. 8 Inside dimensions of conical covers

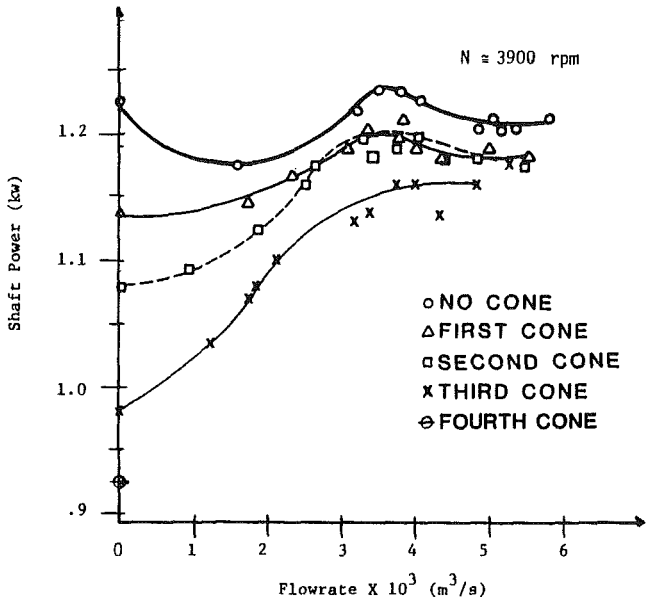

Fig. 10 Shaft power for low speed tests

$$\pi_1 = \frac{Q_{cr}}{\omega\, r_h^{\,3}}, \quad \pi_2 = \frac{\omega\, r_h^{\,2}}{\omega_0 r_0^{\,2}}$$

$$\pi_3 = \frac{r_t}{r_h}, \quad \text{and} \quad \pi_4 = \frac{u}{\bar{v}}.$$

where $r_h = \dfrac{2A}{S} = \dfrac{2\pi(r_2^{\,2} - r_1^{\,2})}{\sin\partial \times 2\pi(r_2 + r_1)} = \dfrac{(r_2 - r_1)}{\sin\partial}$

∂ is the inclination angle of the impeller leading edge with respect to the axis, the $(\omega_0 r_0^{\,2})$ in π_2 is a characteristic quantity, which is set to be the magnitude of μ/ρ in this study (hence π_2 is equivalent to Reynolds number). The hydraulic radius is related to the area while the tip radius is the linear dimension of impeller inlet geoemtry.

These parameters can be related with a functional relationship, $\pi_1 = F(\pi_2, \pi_3, \pi_4)$, where π_2 is a flow dynamic parameter, π_3 is a geometric parameter, while π_4 is a flow kinematic parameter. A fairly good correlation of the data can be achieved by grouping the π's into $\pi_1 \pi_4^{0.5}$ and $\pi_3 \pi_2^{-0.1}$ as also tabulated in Table 1 and plotted in Fig. 11. This correlation imply that the critical flowrate is primarily controlled by the geometric parameter, to a less degree by the flow kinematic parameter, and only slightly by the flow dynamic parameter.

The shut-off power coefficient, $\bar{\pi}_{s/0}$ defined in equation (1) versus π_2 are tabulated in Table 2. The correlation shown in Fig. 12 gives a satisfactory result. Another set of tests with a

Table 1 Critical flowrates and the relevant parameters

cone / vane	Q_{cr} ($\times 10^{-3}$ m3/s)	r_2 (cm)	r_h (cm)	π_4	π_1	$\pi_1\pi_4^{.5}$	π_{2_5} (10^5)	π_3	$\pi_3\pi_2^{-0.1}$
-	4.43	3.81	3.76	0.97	0.20	0.20	5.85	1.01	0.267
1	4.14	3.12	2.67	↓	0.53	0.53	2.94	1.17	0.332
2	3.63	2.64	1.93	↓	1.24	1.22	1.54	1.37	0.415
3	2.28	2.39	1.52	↓	1.57	1.55	0.96	1.56	0.495
A	3.94	3.81	3.76	1.24	0.18	0.20	5.85	1.01	0.267
B	4.05	↓	↓	1.14	0.19	0.20	↓	↓	↓
C	4.30	↓	↓	1.03	0.20	0.20	↓	↓	↓
-	6.76	↓	↓	0.97	0.22	0.21	8.41	↓	0.258
1	5.60	3.12	2.67	↓	0.50	0.50	4.23	1.17	0.320
2	4.83	2.64	1.93	↓	1.15	1.13	2.22	1.37	0.400
3	3.14	2.39	1.52	↓	1.51	1.49	1.38	1.56	0.478
A	5.00	3.81	3.76	1.24	0.16	0.18	8.41	1.01	0.258
B	5.34	↓	↓	1.14	0.17	0.18	↓	↓	↓
C	5.43	↓	↓	1.03	0.17	0.18	↓	↓	↓

Notes:

1. Cones 1, 2 and 3 are the conical cones partially cover the impeller leading edge, depicted in Figure 4.
2. Vanes A, B and C are the conical guide vanes located upstream of the impeller, depicted in Figures 3 and 4.

Table 2 Recirculation power at shut-off condition with relevant parameters

	Cone	r_h (cm)	N(rpm)	Pr(kw)	$\bar{\pi}_{s/0}$(10^-2)	π_2 (10^5)
Low	-	3.76	3918	0.298	5.74	5.80
Speed	1	2.67	3984	0.209	21.2	2.97
↓	2	1.93	4029	0.149	74.08	1.57
↓	3	1.52	4068	0.052	82.9	0.98
High	-	3.76	5545	0.813	5.52	8.21
Speed	1	2.67	5626	0.463	16.68	4.20
↓	2	1.93	5668	0.276	49.29	2.21
↓	3	1.52	5688	0.194	113.10	1.37

(a) Straight Pipe

Low	-	3.76	3819	0.443	9.21	5.65
Speed	1	2.67	3955	0.275	28.5	2.95
↓	2	1.93	4008	0.201	101.5	1.56
↓	3	1.52	4035	0.162	264.6	0.97
High	-	3.76	5495	0.791	5.52	8.13
Speed	1	2.67	5603	0.431	15.7	4.18
↓	2	1.93	5634	0.295	53.6	2.20
↓	3	1.52	5679	0.082	48.0	1.37

(b) U-Pipe

U-pipe replacing the straight suction pipe has also been carried out. The results are included in Table 2 and Fig. 12.

Power consumption due to the suction recirculation at a given through flow can also be determined by comparing the shaft power measurements with and without inlet partial coverings. At a certain flowrate, when the inlet partial cover just eliminates the recirculating flow, which will otherwise exist without the cover, the difference in shaft powers measured with and without the cover can be ascertained to be due to the suction recirculation. Test data expressed in terms of the power coefficient, $\bar{\pi}$ and the flow coefficient, ϕ, defined as the ratio of the measured flowrate over the best efficient flowrate, are tabulated in Table 3 and correlated in Fig. 13 for both high and low-speed conditions. The correlation can be expressed by $\bar{\pi} = \pi_{s/0}(1-\phi)^n$, or in dimensional form,

$$P_r = \rho \bar{\pi}_{s/0} \omega^3 r_h^5 (1 - Q/Q_0)^n$$
$$= \rho \bar{\pi}_{s/0} \omega^3 \left[\frac{(r_2 - r_1)}{\sin \partial}\right]^5 (1 - Q/Q_0)^n \quad (2)$$

where $\bar{\pi}_{s/0}$ is the power coefficient at shut-off condition, discussed in the previous paragraph, and the exponent n can be determined from the slope of the least-square-fitted straight line on log-log scale as shown in Fig. 13. It is estimated to be approximately 3.4 for both high and low-speed cases from the present study.

5 Conclusion

The determination of critical flowrate with a visual technique using thread and with a "pressure" method are comparable, but the latter method is more consistent and reliable.

Although the impeller inlet area should be kept as small as possible to achieve a lower critical flowrate, this parameter is normally fixed by the specified design flowrate. The suction flow velocity distribution has been proved to be an important parameter to affect the critical flowrate and should be properly manipulated in the design and further studied in more detail.

The power consumption associated with the suction recirculation flow is similar but different from that associated with a rotating disk in an enclosed chamber, which has been studied by Daily and Nece (1960) and Mann and Manston (1961). The former is due to dynamic pumping, while the latter is mostly due to viscous shear. And the characteristic length used in these nondimensional parameters are different. In the former

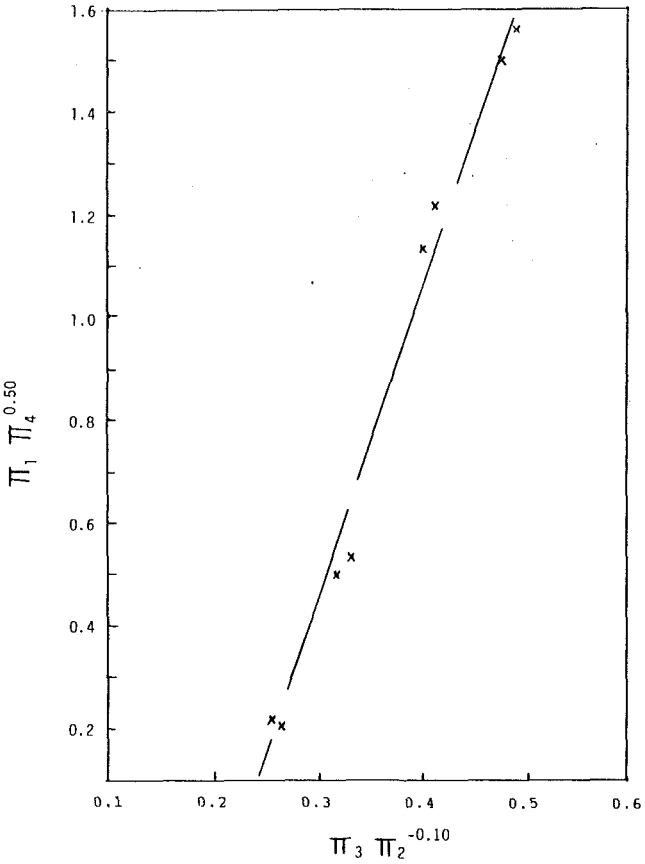

Fig. 11 Correlation of critical flowrates

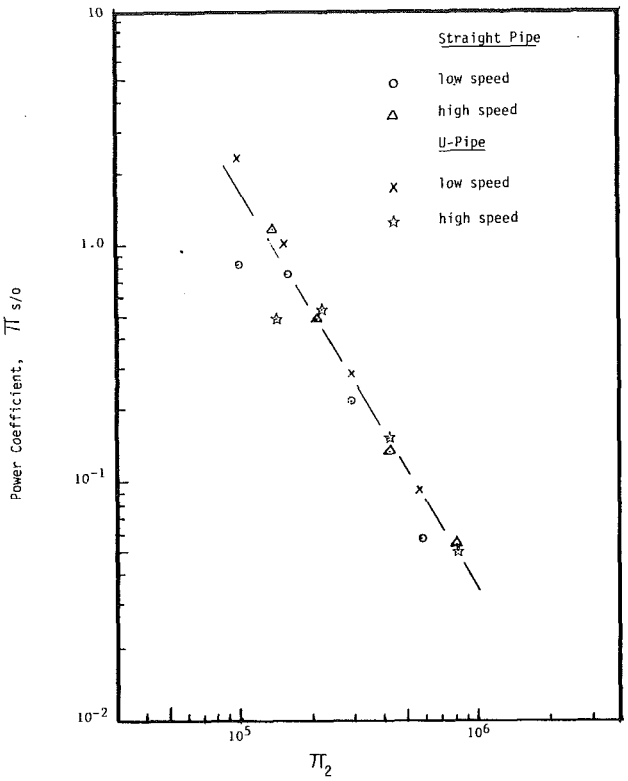

Fig. 12 Correlation of shut-off power coefficients

Table 3 Suction recirculation power versus through flowrate with relevant parameters

	N(rpm)	Q (10^-3 m^3/s)	Pr(kw)	$\overline{\Pi}$ (10^-2)	ϕ	1 - ϕ
Low	3918	0	0.298	5.74	0	1
Speed	4008	2.40	0.071	1.28	0.31	0.69
↓	4022	3.59	0.037	0.66	0.47	0.53
	4024	4.13	0.033	0.58	0.54	0.46
High	5545	0	0.813	5.52	0	1
Speed	5609	3.28	0.321	2.11	0.29	0.71
↓	5633	4.85	0.134	0.87	0.43	0.57
	5636	5.55	0.112	0.72	0.49	0.51

(a) Straight Pipe

Low	3819	0	0.443	9.21	0	1
Speed	3956	2.40	0.100	1.87	0.31	0.69
↓	3963	3.40	0.082	1.53	0.44	0.56
	3974	3.94	0.056	1.03	0.51	0.49
High	5495	0	0.791	5.52	0	1
Speed	5551	3.15	0.362	2.45	0.28	0.72
↓	5579	4.92	0.142	0.95	0.43	0.57
	5591	5.67	0.052	0.34	0.50	0.50

(b) U-Pipe

case, the hydraulic radius of the impeller inlet area should be used; while in the latter case, it is the geometric radius of the disk.

All the test data for both straight and U-shape suction pipes can be correlated well along a single straight line on log-log scale for the shut-off condition. The implication is that the power consumption associated with suction recirculation depends on the impeller inlet geometry and is not sensitive to the suction pipe configuration. It is also concluded that reducing the impeller inlet area is an effective method of reducing the power consumption for high specific speed axial-flow pumps. This can be implemented by installing a variable shutter valve at pump inlet if possible.

In the case of a finite through flow, the empirical formula derived from the present study is similar to that reported by Tuzson (1983) with some minor differences. It is concluded that more tests especially with the other types of impellers are needed to establish a universally applicable formula for the suction recirculation.

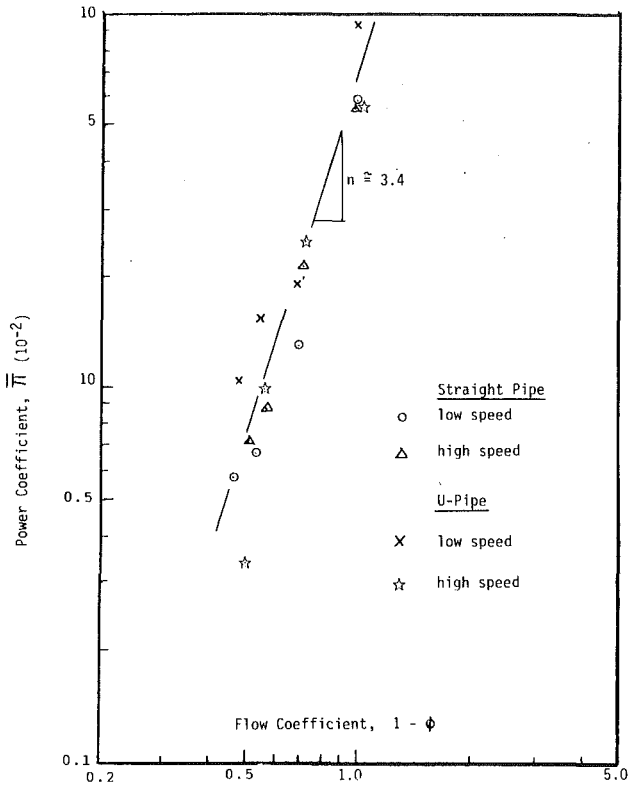

Fig. 13 Correlation of power coefficients with flow coefficients

Acknowledgment

The present work was carried out when the authors were at Texas A&M University. Partial support was provided by TRW, Inc. appreciation is acknowledged.

References

Cooper, P., 1973, "High Flow Pump Impeller for Low Net Positive Suction Head and Method of Designing Same," U.S. Patent 3,737,249, June 5.

Daily, J. W., and Nece, R. E., 1960, "Chamber Dimension Effects on Induced Flow and Frictional Resistance of Enclosed Rotating Disks," *J. Basic Engineering, Trans. ASME*, Vol. 82, pp. 217–232.

Mann, R., and Manston, C. H., 1961, "Friction Drag on Bladed Discs in Housings as a Function of Reynolds Number, Axial and Radial Clearance and Blade Aspect Ratio and Solidity," *J. Basic Engineering, Trans. ASME*, Dec., pp. 719–723.

Murakami, M., and Heya, N., 1966, "Swirling Flow in Suction Pipe of Centrifugal Pumps. First report: Distribution of Velocity and Energy," *Bulletin JSME*, Vol. 9, No. 34.

Schweiger, F., 1976, "Stability of Centrifugal Pump Characteristics at Part Capacity," *International Conference on Pump and Turbine Design and Development*.

Sen, M., 1978, "Off-Design Performance, Prerotation in Centrifugal Pumps," *VKI LS 1978-3*, Mar.

Toyokura, T., 1961, "Studies on the Characteristics of Axial-Flow Pumps," (Parts 1–6), *Bulletin JSME*, Vol. 4, pp. 287–340.

Tuzson, J. J., 1983, "Inlet Recirculation in Centrifugal Pumps," *Symposium on Performance Characteristics of Hydraulic Turbines and Pumps*, ASME Winter Annual Meeting, Nov.

General Correlations and Selection Procedures for Flow in Polyethylene Tubes With Uniformly Spaced Wall Orifices

E. Brundrett
Department of Mechanical Engineering,
University of Waterloo,
Waterloo, Ontario, Canada, N2L 3G1

A previously described experimentally based numerical procedure is used to characterize the flow in thin walled polyethylene tubes with uniformly spaced wall orifices (polytubes). The procedure evaluates the required supply pressure for specified geometry, supply flow, and supply swirl angle; and then predicts the pressure and discharge profiles along the polytube. The predicted values are in good agreement with reported experimental results and are used to develop a data base of the most significant ranges of polytube and supply parameters. Then, explicit design correlations and recommendations are obtained for satisfactory and economical performance.

Introduction

Thin-walled polytubes are used for overhead greenhouse and industrial ventilation and recently for solar heating of several automotive factories (Fig. 1). They may be characterized as thin walled perforated polyethylene pipes with wall thicknesses of 0.05 mm to 0.15 mm. They have total wall orifice areas that are usually one to two times the cross sectional area of the tube. Typically, the ratio of polytube length to diameter is 50 to 150, the tube diameter range is 300 mm to 750 mm or larger, and the orifice diameter range is 25 mm to 130 mm.

In an earlier paper, Brundrett (1991) described an analysis and numerical procedure that provided good agreement with the experimental data of flow in polytubes for four supply swirl angles for two polytube sizes, and also with the data of other investigators. The procedure is extended in this paper to examine the flow characteristics of polytubes, for supply swirl angles of 0 to 35 deg, for tube length to diameter ratios of 25 to 250, and for orifice to tube area ratios of 1.0 to 2.0. The required supply pressure is obtained for each supply flow and polytube geometry. Then, the discharge and pressure profiles along the polytube are computed and examined to determine whether they lie within acceptable design limits.

The computed database is sufficiently extensive to permit rapid prediction of the inlet pressure and discharge profile using explicit dimensionless correlations. Then, based upon power consumption and uniformity of polytube discharge, the correlations are used to place realistic limitations upon polytube geometry and supply flow.

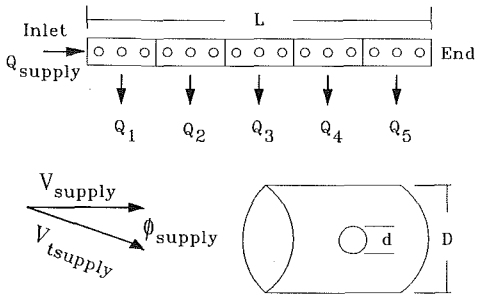

Fig. 1 Polytube geometry and supply parameters

Computational Procedure

The required supply pressure (P_{supply}) is obtained for a specified supply flow (Q_{supply}), supply swirl angle (ϕ_{supply}), and polytube geometry by satisfying the continuity equation and polytube pressure equations by trial and error. The continuity equation requires that the computed discharge from the exit of any end sealed polytube is zero. The computational procedure divides the polytube into five equal length segments, computes the discharge from each segment, and determines the static pressure at the end of each segment (Fig. 1).

Polytube static pressure is controlled by friction loss and by static pressure regain. Following the recommendation of Haaland (1983), the friction factor (f) for polytubes with swirl was experimentally determined by Brundrett and Vermes (1987) to be correlated by:

$$(f)^{-0.5} = 1.86 \log\left(\frac{R_D}{6.9}\right) \quad (1)$$

Contributed by the Fluids Engineering Division for publication in the JOURNAL OF FLUIDS ENGINEERING. Manuscript received by the Fluids Engineering Division, April 10, 1990.

They reported that the friction loss of a segment depended upon the actual near wall flow path expressed as,

$$\Delta P_f = f\left(\frac{L_{\text{swirl}}}{D}\right)\left(\frac{\rho(V)^2_{\text{ave}}}{2}\right) \tag{2}$$

where the average of the square of the inlet and outlet axial velocity components is used to construct $(V)^2_{\text{ave}}$ and,

$$L_{\text{swirl}} = \frac{L_{\text{seg}}}{\cos(\phi_{\text{seg}})} \tag{3}$$

is the actual path length of the fluid at the wall in the tube segment of length L_{seg}. It was defined by the average swirl angle for the segment (ϕ_{seg}), measured 50 mm inwards from the wall by Brundrett and Vermes (1987), who observed a linear reduction of ϕ_{supply} from the polytube inlet to end. Hence, they found that;

$$\phi_{\text{seg}} = \phi_{\text{supply}} \times \left(1 - \frac{X_{\text{seg}}}{L}\right) \tag{3a}$$

Also, the pressure change from polytube supply to end is due in part to static pressure regain as fluid is discharged and the average polytube velocity decreases. This can be expressed as for a diffuser as (Brundrett (1991)),

$$\Delta P_r = C_r\,\rho\left(\frac{V_{\text{in}}^2 - V_{\text{out}}^2}{2}\right) \tag{4}$$

where, C_r the empirically obtained coefficient of static regain was found to be dependent upon the supply swirl angle, i.e.,

$$C_r = 0.565 - 5.28 \times 10^{-6}\phi_{\text{supply}}^3 \tag{5}$$

Fortunately, typical polytube sizes and supply flows are large. Hence, Reynolds numbers of 300,000 or more are encountered at the polytube inlet (Brundrett and Vermes (1987)). Thus, the friction factor and static regain coefficients do not vary significantly from one polytube application to another. A complementary effect is the retardation of boundary layer growth in the polytube by the skimming of near wall flow by the orifices; thereby simulating higher Reynolds number flows in nonperforated tubes of comparable size and flow.

The total area of the orifices of the polytube was found to be quite significant, since it defines the area ratio (AR). However, a wide range of orifice diameters and numbers were satisfactorily modelled without any adjustment for orifice size in the range of 25 mm to 130 mm. Also, the dimensionless polytube discharge profiles were satisfactorily predicted by a five segment model which groups the discharge of orifices of a segment at the segment mid point for computational convenience. Typically, the computed discharge profiles exhibited less than ± 0.2 percent variation over the recommended supply pressure range of 20 Pa to 60 Pa. Hence, 30 Pa was used throughout the analyses, since it is the optimal value and predicts all of the recommended pressure range to within ± 0.15 percent. Finally, the exit pressure of each polytube segment, obtained through the pressure control and continuity equations, is used with the supply pressure to construct the pressure profiles.

Evaluation of Results

The agreement obtained by the computational procedure of Brundrett (1991) with his experimental data was within ± 1.8 Pa for the pressure predictions, was within ± 3.1 percent for the discharge predictions, and was within ± 1.2 percent for the supply pressure and flow predictions. Also, agreement with reported supply pressure and flow data of other investigators were within -0.4 to $+3.3$ percent for significantly extended ranges of L/D and orifice diameter. The computational procedure was used to examine realistic ranges of the polytube parameters; $1.0 \le AR \le 2.0$, $25 \le L/D \le 250$, 300 mm $\le D \le$ 750 mm, and 0 deg $\le \phi_{\text{supply}} \le$ 35 deg; for the supply pressure range of 20 Pa to 60 Pa. Supply pressures lower than 20 Pa may lead to incomplete polytube inflation (Bailey (1975a, b)), whereas pressures above 60 Pa can require the selection of a fan with a higher than normal rating. The large

Nomenclature

ΣA_o = total area of wall orifices, m^2
A_t = polytube flow area, m^2
$AR = \Sigma A_o / A_t$ = polytube orifice to flow area ratio
C_r = static regain coefficient, equation (5)
d = polytube orifice diameter, mm
D = polytube diameter, mm
f = friction coefficient, equation (1)
K_p = supply pressure coefficient, equations (6), (8)
K_q = polytube fan matching coefficient, equation (19)
L = total length of polytube, mm
L_{swirl} = path length of flow in a segment, mm
L/D = length to diameter ratio
N_f = flow-pressure coefficient for fan or blower, equation (15)
N_{tube} = number of polytubes required for an application, equation (21)
P = static pressure at any axial location (50 mm from the wall), Pa
ΔP_f = friction pressure loss, Pa, equation (2)
ΔP_r = static pressure regain, Pa, equation (4)
$\mathbb{P} = P.Q$ = power input to polytube flow, W, equation (9)
$\mathcal{P} = \mathbb{P}/A_t$ = power density, W/m^2, equation (12)
P^* = dimensionless supply pressure $P_{\text{supply}}/P_{\text{max}}$, equation (16)
Q = flow, m^3/s
Q^* = dimensionless supply flow $Q_{\text{supply}}/Q_{\text{max}}$, equation (16)
R_D = Reynolds number based on V_{ave} and D, equation (1)
V_{ave} = average axial velocity of a segment, m/s
$(V)^2_{\text{ave}}$ = segment averaged velocity squared (from segment inlet and exit values)
V_{supply} = axial component of supply velocity, m/s, Fig. 1
$V_{t\text{supply}}$ = total velocity of the supply, m/s, equation (7), Fig. 1
X_{seg} = distance from inlet to mid point of segment, mm
ρ = fluid density, kg/m^3
ϕ = swirl angle at any axial location (50 mm from the wall), degrees

Subscripts

ave = averaged property
demand = required supply flow or pressure for an application
in = property at segment inlet
max = maximum pressure or flow of fan or blower
out = property at segment outlet
seg = property at segment mid point
supply = property of the supplied fluid
1, 2, 3, 4, 5 = polytube segment number (5 in total), Fig. 1

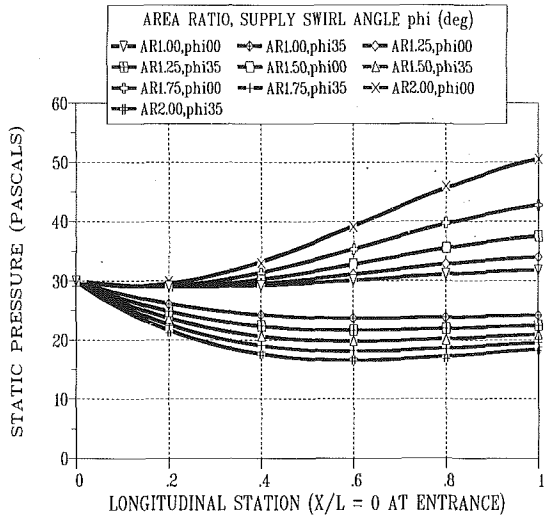

Fig. 2 Pressure profile along polytubes with L/D = 100 for 1.0 ≤ AR ≤ 2.0 and for ϕ_{supply} of 0 or 35 deg, (i.e., AR = 1.0 and ϕ_{supply} = 35 deg expressed as AR1.00,phi35)

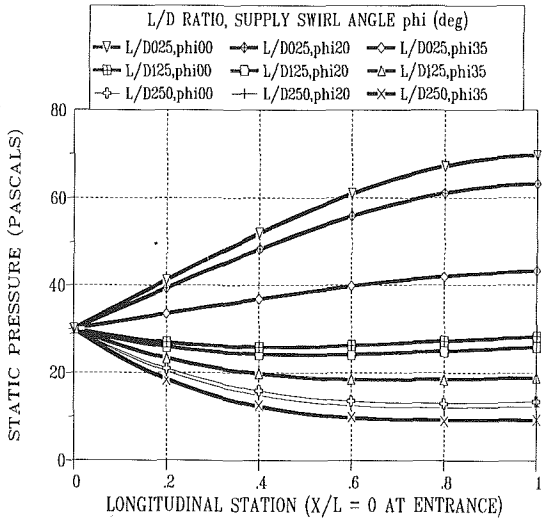

Fig. 4 Pressure profiles along an AR = 1.25 polytube for L/D of 25, 125, and 250, and for ϕ_{supply} of 0, 20, and 35 deg (nomenclature as for Fig. 2)

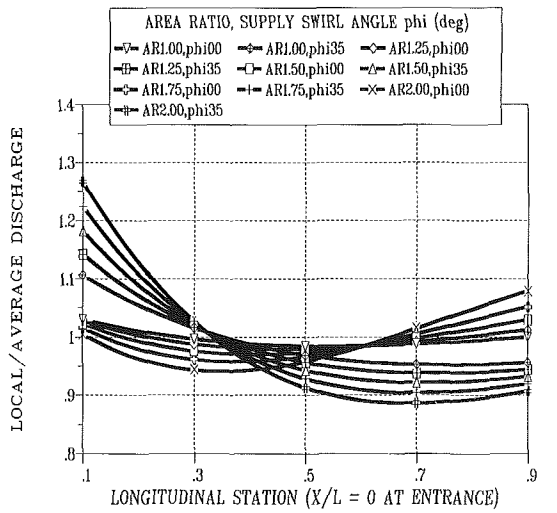

Fig. 3 Discharge profiles along L/D = 100 polytubes for the area ratio and ϕ_{supply} ranges of Fig. 2 (nomenclature as for Fig. 2)

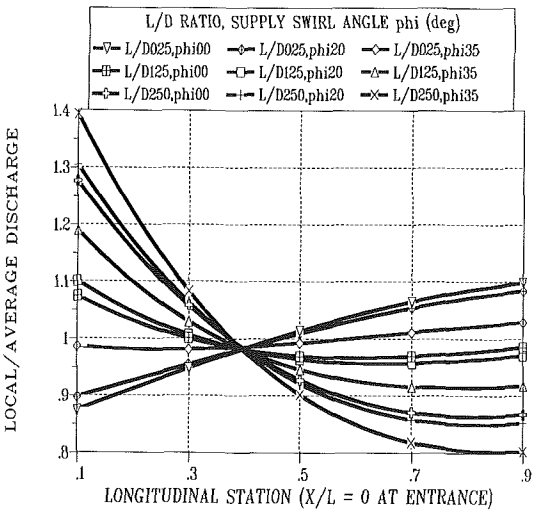

Fig. 5 Discharge profiles along an AR = 1.25 polytube for the parameters of Fig. 4.

range of ϕ_{supply} was chosen because values of up to 38 deg were observed in polytubes directly connected to a propeller fan via a contraction piece (Brundrett and Vermes (1987)).

The database shows progressive trends in the pressure and discharge profiles that were not influenced by D, due to the large Reynolds numbers. Hence, the results can be used for any polytube with a diameter of at least 300 mm for the recommended supply pressure range of 20 Pa to 60 Pa.

The influence of increasing ϕ_{supply} upon static pressure is to significantly increase pressure loss due to friction and to dramatically reduce pressure regain (Fig. 2). As AR is increased, a larger supply flow is required for a specified supply pressure and swirl angle, since the polytube presents a lower resistance to discharge. If static pressure regain dominates, as is the case for small supply swirl angles, then the static pressure increases with distance along the polytube, and increases more dramatically for the higher supply flows associated with larger AR. However, pressure loss dominates for large ϕ_{supply} and even more so for large AR.

The discharge profiles along a polytube are presented as ratios of local segment discharge to the average of the five segments, with data presented at the mid point of each of the equal length segments (Fig. 3). An increase of ϕ_{supply} dramatically affects the profile by increasing discharge from the inlet segment of the polytube. The effect is related to the swirl increased velocity and total pressure of near wall fluid, particularly in the first segment, and to flow skimming by the orifices. The skimming effect was clearly identified by Rogers and Hersh (1976) during their examination of combustor orifice discharge of grazing flows.

The polytube evaluation is continued for AR = 1.25 and for representative values of L/D and ϕ_{supply}. Again, increasing L/D and ϕ_{supply} lead to reduced static pressure regain along the polytube (Fig. 4). This may or may not be desirable, since L/D = 25 and ϕ_{supply} = 35 deg yield a fairly constant discharge profile (Fig. 5). Generally, increases of L/D or of ϕ_{supply} lead to a shifting of the polytube discharge to the inlet end.

Polytube Correlations

Supply Pressure Correlation. The supply pressure P_{supply} was correlated for a particular polytube geometry and supply swirl angle by the experimentally based dimensionless pressure ratio K_p and axial component of the supply velocity as,

$$K_p = \frac{P_{\text{supply}}}{0.5\rho\ V_{\text{supply}}^2} \tag{6}$$

where V_{supply} the axial component of the supply velocity is obtained from the continuity equation and the polytube flow area (A_t). Formally, the value of K_p should be based upon an integration across the inlet plane of the polytube. However, the large Reynolds numbers and negligible boundary layer thicknesses of the flows at the inlet will result in very small variations of K_p, between the values obtained by integration or by using the average velocity. This is because of the momentum-flux and kinetic energy correction factors vary by less than 1.5 percent from unity (White (1986)). Also, the use of the average velocity was supported by the very good results obtained by Brundrett (1991), who used equation (6) to predict flow from wind tunnel contractions, from directly connected fans, and from supply via a fan and contraction piece. Thus, equation (6) is recommended for design purposes, unless it is suspected that there is a distortion of more than 10 percent of the inlet velocity profile or that there is a thick boundary layer at the polytube inlet.

The total velocity of the supply ($V_{t\text{supply}}$) is defined by the supply swirl angle and the continuity equation as (Fig. 1),

$$V_{t\text{supply}} = \frac{V_{\text{supply}}}{\cos(\phi_{\text{supply}})} \tag{7}$$

The general correlation for K_p from the data base is;

$$K_p = \left[0.5898 + 0.00355\,\frac{L}{D} - 1.7050\,\ln(AR) + 0.9473\,(\ln(AR))^2\right] + \left[3.0596 + 0.0125\,\frac{L}{D} - 0.6654\,(AR-1)\right] \times \phi_{\text{supply}}^3 \times 10^{-6} \tag{8}$$

The correlation does not include a pressure or supply velocity effect due to the large Reynolds numbers encountered. Hence, over the recommended supply pressure range of 20 Pa to 60 Pa, the correlation coefficient K_p varied by ± 0.15 percent or less, and typically was evaluated for a supply pressure of 30 Pa. Also, the K_p correlation provides agreement with all K_p values obtained from the computational procedure to within ± 0.65 percent.

The variation of K_p is influenced in decreasing order by; AR, L/D, and ϕ_{supply}. A convenient (and linear) correlation of K_p is obtained as a function of L/D that is the basis for equation (8) (Fig. 6). Values of $K_p \approx 0.5$ are often selected to limit the supply dynamic pressure to twice the typical supply static pressure of 30 Pa; so that excessive pressure rise will not occur at the end of short thin walled polytubes. It can be seen that $K_p = 0.5$ cannot be obtained for any polytube with $L/D > 210$, nor for any polytube if $AR = 1.0$ (Fig. 6).

Power Correlation. Again, assuming a nearly constant value of the velocity across the inlet to the polytube, the power of the fluid can be obtained from the average inlet total velocity $V_{t\text{supply}}$ to a sufficient accuracy for qualitative analysis of the trends. Hence, the power (ℙ) that must be supplied to fluid entering a polytube can be estimated as;

$$\mathbb{P} = \left(P_{\text{supply}} + \frac{\rho V_{t\text{supply}}^2}{2}\right) \times Q_{\text{supply}} \tag{9}$$

This power equation can be expressed more conveniently in terms of the axial component of the supply velocity and supply pressure correlation as,

$$\mathbb{P} = \frac{\rho V_{\text{supply}}^2}{2} + \left(K_p + \frac{1}{\cos(\phi_{\text{supply}})}\right) \times Q_{\text{supply}} \tag{10}$$

or as,

$$\mathbb{P} = \left[K_p + \frac{1}{\cos(\phi_{\text{supply}})}\right] \times \frac{\rho\ Q_{\text{supply}}^3}{2\ A_t^2} \tag{11}$$

Also, it is useful to examine the power density of the supply flow (ℙ) defined by,

$$\mathbb{P} = \frac{\mathbb{P}}{A_t} = \left[K_p + \frac{1}{\cos\ (\phi_{\text{supply}})}\right] \times \frac{\rho V_{\text{supply}}^3}{2} \tag{12}$$

ℙ is dominated by V_{supply} (Fig. 7) due to its cubic influence. Hence V_{supply} is often limited to 10 m/s or less. For many applications it is possible to increase D to reduce the velocity and to improve the discharge distribution (see below).

Discharge Correlations. Correlations for discharge are based upon the five segment computational procedure and resulting database. The analysis indicates that the first segment discharge (Q_1) is the most sensitive to the polytube and supply parameters, followed by the final segment discharge (Q_5) (Fig. 3). Hence, if the selection of appropriate polytube parameters is to be based upon some criterion of uniformity of the discharge profile, then Q_1 and Q_5 are the most appropriate indicators.

A correlation for the ratio of Q_1 to the averaged discharge for the five segments (Q_{ave}) to within ± 4 percent of the computed database for all parameter ranges is;

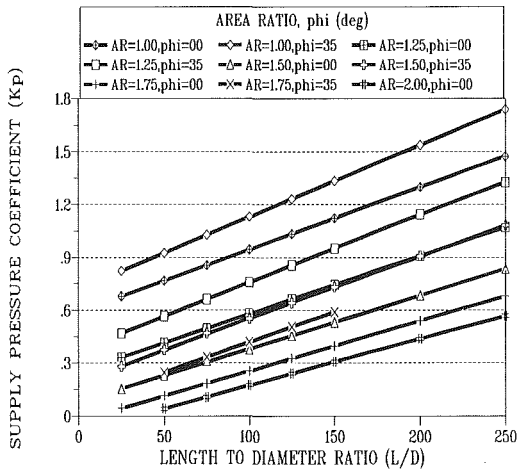

Fig. 6 Supply pressure coefficient (K_p) versus L/D for the parameter ranges $1.0 \le AR \le 2.0$ and for $\phi_{\text{supply}} = 0$, 35 deg

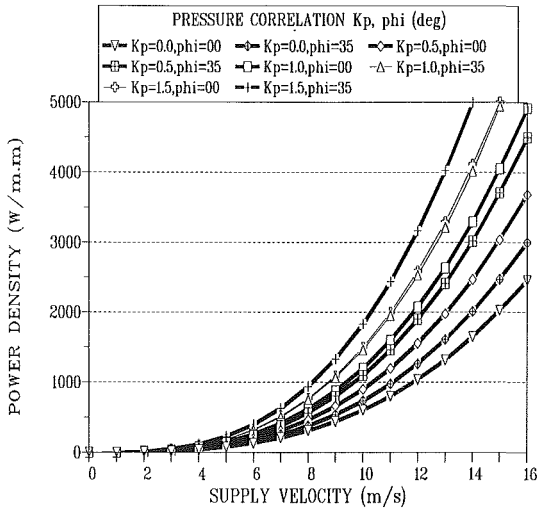

Fig. 7 Power density of the supply flow versus supply velocity for K_p = 0, 0.5, 1.0, 1.5, and for ϕ_{supply} = 0, 35 deg

$$\frac{Q_1}{Q_{ave}} = \left[1.228 - 0.3097\ AR + (0.002904\ AR - 0.001818)\frac{L}{D} \right] + \left[-.1631 + 1.7910\ (AR)^2 + (.002089 - .000689\ (AR)^4)\cdot\frac{L}{D} \right] \phi_{supply}^3 \times 10^{-6} \quad (13)$$

A similar correlation for the ratio of Q_5 to Q_{ave} to within ±4 percent of the computed database for all parameter ranges is;

$$\frac{Q_5}{Q_{ave}} = \left[0.7840 + 0.2760\ AR + (0.001433 - 0.002033\ AR)\frac{L}{D} \right] + \left[-.5016 - .5484\ (AR)^3 + (-.00083 + .00060\ (AR)^4)\frac{L}{D} \right] \phi_{supply}^3 \times 10^{-6} \quad (14)$$

These correlations indicate that the discharge profile adjusts most rapidly in the area ratio range of $1.0 \le AR \le 1.5$ and for $\phi_{supply} > 20$ deg. Examining equations (13) and (14), it can be seen that no selection of polytube and supply parameters will permit $Q_1/Q_{ave} = Q_5/Q_{ave} = 1.0$. However, if the discharge profile is permitted to vary by ±5 percent then restricted ranges of L/D can be chosen for specified polytube area ratios and supply swirl angles (Fig. 8). It is evident that $\phi_{supply} < 20$ deg permits selection of a reasonable range of L/D, particularly for $1.0 \le AR \le 1.25$, but that $\phi_{supply} = 35$ deg seriously reduces the range.

Polytube-Fan Matching

The selection of a suitable fan or blower for a polytube application requires the matching of the pressure-flow characteristics. Consider a fan or blower (fan) that has a maximum pressure for no flow of P_{max}, and a maximum flow of Q_{max} for no delivery pressure. For convenience, let the pressure-flow characteristics of the fan at constant shaft speed be approximated as a simple power relationship. Then, a given supply pressure and flow can be related to the fan maximum values as,

$$\frac{Q_{supply}}{Q_{max}} = 1 - \left(\frac{P_{supply}}{P_{max}}\right)^{Nf} \quad (15)$$

or more compactly as,

$$Q^* = 1 - (P^*)^{Nf} \quad (16)$$

Now the supply flow to the polytube can be obtained from the supply pressure correlation K_p (equations (6), (8)) and the continuity equation as,

$$Q_{supply} = A_t\ V_{supply} = A_t \left(\frac{2\ P_{supply}}{\rho\ K_p}\right)^{0.5} \quad (17)$$

or, in dimensionless form based upon P_{max} and Q_{max} of the selected fan as,

$$\frac{Q_{supply}}{Q_{max}} = \left(\frac{A_t}{Q_{max}}\left(\frac{2\ P_{max}}{\rho\ K_p}\right)^{0.5}\right)\left(\frac{P_{supply}}{P_{max}}\right)^{0.5} \quad (18)$$

or more compactly as,

$$Q^* = K_q (P^*)^{0.5} \quad (19)$$

Equations (16) and (19) can now be combined to yield a solution for P_{supply} in dimensionless form by eliminating Q^*, i.e.,

$$Q^* = K_q (P^*)^{0.5} = 1 - (P^*)^{Nf} \quad (20)$$

Values of P^* are given in Table 1. Values of $N_f < 1.0$ model many axial flow fans, while values of $N_f > 1.0$ model many blowers. A graphical solution of the dimensionless polytube and fan pressure-flow equations can be constructed (Fig. 9), with the dimensionless supply pressure and flow of the polytube being obtained as the intersection of the specified fan and polytube pressure curves. The graphical solution obtained by a standard spreadsheet curve plot is less accurate than the solution of equation (20) or Table 1, but is more intuitive, and can be applied readily to fans with complex flow-pressure curves (White (1986)).

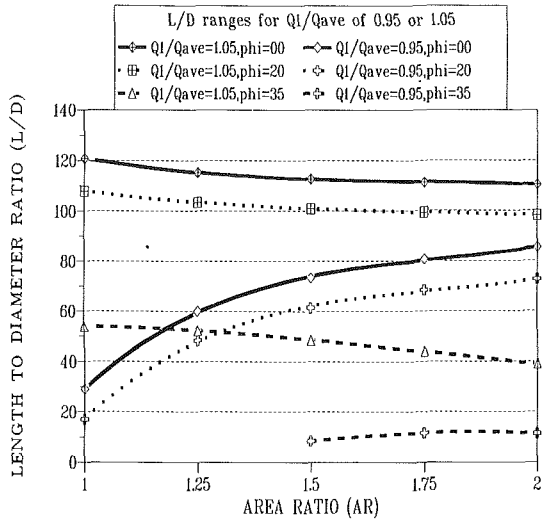

Fig. 8 Permissible ranges of L/D for $0.95 \le Q_1/Q_{ave} \le 1.05$ versus area ratio and supply swirl angle

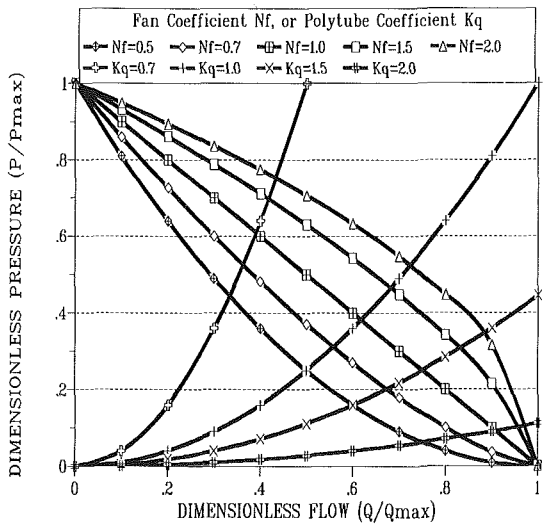

Fig. 9 Graphical matching of flow-pressure curves of polytubes ($0.5 \le N_f \le 2.0$) and fans ($0.5 \le K_q \le 2.0$). Intersection of polytube and fan curves provide Q_{supply} and P_{supply} (equation (20)).

Finally, the number of polytubes (N_{tube}) required to satisfy a demand flow Q_{demand} can be obtained as an integer by a slight adjustment of K_p and/or P_{supply} such that

$$N_{tube} \times Q_{supply} = Q_{demand} \quad (21)$$

Polytube and Supply Flow Error Analysis

Polytube Dimension Errors. The computational procedure was used to examine the effect of ±1 percent deviation of the polytube dimensions d, L, and D for combinations of AR and L/D. The orifice diameter (d) is the most sensitive; since a ±1 percent error will create typically ±2.5 percent error in ϕ_{supply}, but as much as ±9.47 percent for $AR = 2.0$ and $L/D = 50$. However, orifice dimension errors are less critical for large $L/$

Table 1 Values of the dimensionless fan supply pressure P^* obtained from equation (20) for extensive values of the polytube discharge parameter (K_q), and for typical values of the fan flow-pressure coefficient (N_f)

K_q	N_f=.25	N_f=.50	N_f=.75	N_f=1.0	N_f=1.5	N_f=2.0	N_f=3.0
			P^*	Values			
0.25	0.471	0.640	0.726	0.779	0.841	0.875	0.913
0.50	0.287	0.444	0.542	0.610	0.697	0.752	0.818
0.75	0.198	0.326	0.415	0.480	0.572	0.634	0.715
1.00	0.146	0.250	0.325	0.382	0.466	0.525	0.605
1.25	0.113	0.198	0.259	0.307	0.378	0.428	0.495
1.50	0.091	0.160	0.211	0.250	0.306	0.345	0.392

D ratios and for $AR \leq 1.5$. It is important to measure the orifice diameter when a prototype polytube has been inflated to the expected operating pressure since the diameter may adjust by 0.5 mm or more when a thin walled tube is inflated (Brundrett (1991)). Almost as important are errors of tube length and/or diameter which appear as errors of the L/D ratio in equations (8), (13), and (14), particularly for $AR \approx 2.0$. Again, it is recommended that the tube diameter be obtained when a prototype polytube has been inflated to the operational pressure, especially if the polytube is thin walled (a wall thickness of 0.075 mm or less).

Supply Flow Errors. The effect of supply pressure error on the supply flow can be obtained by an inspection of equation (17). A ±1 percent error in supply pressure will result in a ±0.5 percent error in the supply flow for a given supply swirl angle. Hence, an error in supply pressure of 1 Pa for a nominal value of 30 Pa will result in an error of approximately 1.5 percent. Measurement errors of the supply flow angle are more complex since ϕ^3_{supply} influences K_p (equations (6), (8) and Fig. 6). This is particularly true for $AR \geq 1.75$ and for $\phi_{supply} \geq 20$ deg. For most applications it would seem that the supply swirl angle should be known to; ±3 deg for $\phi_{supply} < 10$, to ±2 deg for 10 deg $< \phi_{supply} <$ 20 deg, and to ±1 deg for $\phi_{supply} > 20$ deg. The supply swirl angle can be conveniently obtained for a given fan and inlet geometry and fan loading by inserting a wool telltale near the start of the polytube (which is usually transparent), and by observing its direction with an external protractor (Brundrett and Vermes (1987)).

Conclusions

The agreement of the computational procedure of Brundrett (1991) with the available experimental data is placed conservatively at ±3 percent, and the agreement of the present correlations to the computational procedure is ±4 percent. Hence, an overall error band of ±7 percent should be placed upon the following 10 design recommendations for polytube selection.

1. To limit the power density ($\mathcal{P}$) of the supply flow, restrict the supply velocity to about 10 m/s and hence, limit the supply dynamic pressure to about 60 Pa. This limits the static pressure regain of short polytubes to about 50 Pa.
2. The supply static pressure must be 20 Pa or greater, and should be limited to 60 Pa maximum.
3. The supply swirl angle should be limited to the range 0 deg $\leq \phi_{supply} \leq$ 20 deg for stable and efficient operation. Usually, an antiswirl device will be required at the fan exit if the polytube is directly connected to a fan.
4. Examination of the K_p correlation (equation (8), Fig. 6) and recommendation 2 leads to the following permissible ranges for L/D versus the area ratio; $AR = 1.00$, $25 \leq L/D \leq 75$; $AR = 1.25$, $50 \leq L/D \leq 150$; $AR = 1.50$, $75 \leq L/D \leq 200$; $AR = 1.75$, $1.25 \leq L/D \leq 250$; $AR = 2.00$, $175 \leq L/D \leq 250$.
5. Examination of the polytube discharge profile (equations (13), (14)) and specifying a permissible variation in discharge of ±5 percent along the tube leads to the following recommendations for L/D versus the area ratio, (for 0 deg $\leq \phi_{supply} \leq$ 20 deg); $AR = 1.00$, $25 \leq L/D \leq 75$; $AR = 1.25$, $55 \leq L/D \leq 110$; $AR = 1.50$, $65 \leq L/D \leq 105$; $AR = 1.75$, $75 \leq L/D \leq 105$; $AR = 2.00$, $75 \leq L/D \leq 105$.
6. The K_p requirements of recommendation 4 and the discharge profile requirements of recommendation 5 create a restricted set of acceptable polytube parameters; $AR = 1.00$, $25 \leq L/D \leq 75$; $AR = 1.25$, $55 \leq L/D \leq 110$; $AR = 1.50$, $75 \leq L/D \leq 105$; $AR = 1.75$, not recommended; $AR = 2.00$, not recommended.
7. All polytube dimensions should be confirmed by inflating a prototype tube of the correct wall thickness to the specified supply pressure to determine the polytube diameter and particularly the orifice diameter. If the orifices are slightly elliptical an average diameter may be used provided that the orifice area is correctly computed to within ±0.1 percent.
8. The error analysis section should be consulted when predicting polytube flow based on the expected errors in measurement of the polytube dimensions, of the supply static pressure, and of the supply swirl angle.
9. Predicting flow from one or more polytubes requires matching the flow-pressure characteristics of the polytubes and fan (equations (15) to (20)). The polytube parameters must be adjusted to obtain an integer number of tubes (equation (21)) and to operate in the most efficient range of the fan (Fig. 9).
10. A polytube should be supported by simple clips attached to the top of the tube every 4D to 6D, and it should be in tension, to ensure wrinkle free inflation, and hence, to ensure smooth tube flow.

Acknowledgements

This research was supported by an operating grant from the Natural Sciences and Engineering Research Council of Canada, which the author gratefully acknowledges.

References

Bailey, B. J., 1975a, private communication based on the internal report, "Temperature Uniformity in Glasshouses Heated with Ducted Air," Nat. Inst. Agr. Eng. (UK), Dept. Note DN/G/562/2101.

Bailey, B. J., 1975b, "Fluid Flow in Perforated Pipes," *J. Mech. Eng. Sc.*, Vol. 17, pp. 338–347.

Brundrett, E., and Vermes, P. T., 1987, "Evaluation of Tube Diameter and Fan Induced Swirl in Polyethylene Ventilation Tubes," *Trans. ASAE*, Vol. 30, pp. 1131–1136.

Brundrett, E., 1991, "Prediction of Airflow with Swirl in Perforated Polyethylene Tubes," ASME JOURNAL OF FLUIDS ENGINEERING, Vol. 112, pp. 447–454.

Haaland, S. E., 1983, "Simple and Explicit Formulas for the Friction Factor in Turbulent Pipe Flow," ASME JOURNAL OF FLUIDS ENGINEERING, Vol. 105, p. 89.

Rogers, T., and Hersh, A. S., 1976, "Effect of Grazing Flow on Steady-State Resistance of Isolated Square-Edged Orifices," NASA CR-2681.

White, F. M., 1986, *Fluid Mechanics* (Second Edition), McGraw-Hill, New York, NY.

Finite-Element Analysis of Turbulent Flow in Annular Exhaust Diffusers of Gas Turbine Engines

E. A. Baskharone
Department of Mechanical Engineering,
Texas A&M University,
College Station, Texas 77843
Mem. ASME

A finite-element model of the turbulent flow field in the annular exhaust diffuser of a gas turbine engine is developed. The analysis is based on a modified version of the Petrov-Galerkin weighted residual method, coupled with a highly accurate bi-quadratic finite element of the Lagrangian type. The elemental weight functions in the finite-element formulation are so defined to ensure upwinding of the convection terms in the flow-governing equations while reverting to the conventional Galerkin's definition for all other terms. This approach is equivalent to altering the integration algorithm as the convection terms in the element equations are derived, with the exception that the latter technique is tailored for low-order elements of the linear and bilinear types. Numerical results of the current analysis indicate that spurious pressure modes associated with this type of inertia-dominated flow are alleviated while the false numerical diffusion in the finite-element equations is simultaneously minimized. Turbulence of the flow field is modeled using the two-layer algebraic turbulence closure of Baldwin and Lomax, and the eddy viscosity calculations are performed at variably spaced points which are different from those in the finite-element discretization model. This enhances the accuracy in computing the wall shear stress and the inner/outer layer interface location. The computational model is verified using a set of experimental data at design and off-design operation modes of the exhaust diffuser in a commercial gas turbine engine. Assessment of the results in this case is favorable and, as such, provides evidence of the model capability as an accurate predictive tool in the diffuser detailed design phase.

Introduction

Exhaust diffusers are critical components of gas turbine engines in both the propulsion and power system application fields. Perhaps the most common propulsion device that utilizes such a component is the small size turboprop engine, where the diffuser is of primary impact on the total-to-static efficiency of the turbine-exhaust system assembly (Fig. 1). Exit diffusing passages are also common in such power systems as auxiliary power units, which are frequently used in aircraft and various other applications. In all cases, the demand for maximum static pressure recovery and minimum total pressure loss across the diffuser is often a difficult design task. This is particularly true at the enigne off-design operation due to the excessive amount of turbine exit swirl that may lead to flow separation, normally over the diffuser inner wall, as a result of the high radial pressure gradient and long flow trajectory under such circumstances.

A literature survey reveals that a considerable amount of experimental research has been focused on annular diffuser flows (e.g., Sovran et al., 1967; Stevens et al., 1968; Takehira et al., 1977; and Japikse et al., 1979). Although several crucial design aspects have, in these and other publications, been addressed, most of this experimental work has predominantly been centered around straight-wall diffusers with modest area ratios. Nevertheless, the empirical relationships formulated in these studies and the charts produced in the process have long been appreciated and extensively utilized in the area of gas turbine industry.

In the area of diffuser flow analysis, emphasis has

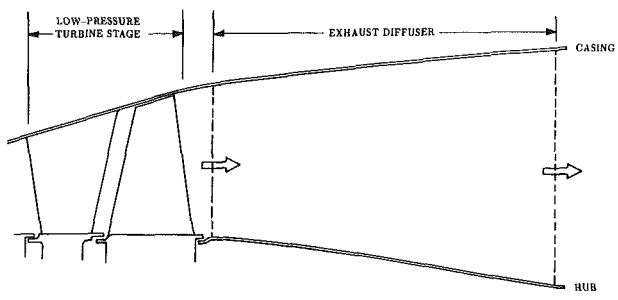

Fig. 1 Schematic of a gas turbine engine exhaust diffuser

Contributed by the Fluids Engineering Division for publication in the JOURNAL OF FLUIDS ENGINEERING. Manuscript received by the Fluids Engineering Division January 11, 1990.

historically been placed on the radial (e.g., Johnston et al., 1966), planar (e.g. Bardina et al., 1981) and conical (e.g., Hah, 1983; and Lai et al., 1989) diffuser configurations, with noticeably fewer models of the annular diffuser type (e.g., Japikse et al., 1979). These models have progressed from the simple one-dimensional approach to parabolic flows which are governed by the boundary layer integral equations (e.g., Japikse et al., 1979 and Bardina et al., 1981). To date, the most detailed models are those by Hah (1983) and Lai et al. (1989). While the accuracy of Hah's conical diffuser model is primarily a result of maintaining the flow ellipticity throughout the computational domain, the major contribution of the study by Lai et al. is in the area of the adverse pressure gradient effect on the flow structure in the near wall zone of planar and conical diffusers. Models with such level of accuracy have not yet been devised for annular diffuser flows. The finite element formulation of the current problem alleviates the long recognized drawbacks of using the conventional Galerkin's method in analyzing highly convective flow fields. These often appear in the form of "wiggles" in the pressure field and fictitious oscillations in the streamwise development of the through-flow velocity. Invalidity of the numerical solution, as a result, was reported by many authors (e.g., Heinrich et al., 1977 and Hughes, 1978). However, it was realized during an early phase of the current study that uniform upwinding of all terms in the flow equations of motion, in the manner devised by Heinrich and Zienkiewicz (1977), would have an adverse effect on the solution accuracy as a result of improperly modeling the equations diffusion terms. The numerical discrepancy in this case was conclusively eliminated by applying different weight functions to the different terms of these equations in the process of deriving the finite element equations. This, in fact, is consistent with the approach devised by Hughes (1978), with the exception that the latter is inapplicable to the biquadratic finite element configuration which is the discretization unit in the current analysis. Special attention in creating the finite element model of the current problem was paid to the findings of Gresho and Lee (1981), that unless the grid size in high-gradient subregions is sufficiently small, a smooth flow solution that results from the upwinding scheme may be grossly inaccurate.

Analysis

Flow-Governing Equations. Figure 1 shows the meridional view of a typical exhaust diffuser of the type often used in gas turbine engines. The flow in this passage is treated as generally swirling and turbulent. However, with the exception of far off-design operation modes, which are not under consideration here, the diffuser inlet Mach number is assumed to be sufficiently small (0.448 at the design point of the turbine stage shown in Fig. 1) to yield a practically incompressible flow at this station and, therefore, throughout the entire diffuser. Furthermore, the flow is assumed axisymmetric, adiabatic and steady. Under these conditions, the momentum and mass conversation equations can be cast in the cylindrical frame of reference as follows:

$$V_r \frac{\partial V_r}{\partial r} + V_z \frac{\partial V_r}{\partial z} - \frac{V_\theta^2}{r} = -\frac{1}{\rho}\frac{\partial p}{\partial r} + \nabla \cdot (\nu_{\text{eff}} \nabla V_r) + \frac{\partial \nu_t}{\partial r}\frac{\partial V_r}{\partial r} - \frac{\nu_{\text{eff}}}{r^2} V_r + \frac{\partial \nu_t}{\partial z}\frac{\partial V_z}{\partial r} \quad (1)$$

$$V_r \frac{\partial V_\theta}{\partial r} + V_z \frac{\partial V_\theta}{\partial z} + \frac{V_r V_\theta}{r} = \nabla \cdot (\nu_{\text{eff}} \nabla V_\theta) - \left[\frac{1}{r}\frac{\partial \nu_t}{\partial r} + \frac{\nu_{\text{eff}}}{r^2}\right] V_\theta \quad (2)$$

$$V_r \frac{\partial V_z}{\partial r} + V_z \frac{\partial V_z}{\partial z} = -\frac{1}{\rho}\frac{\partial p}{\partial z} + \nabla \cdot (\nu_{\text{eff}} \nabla V_z) + \frac{\partial \nu_t}{\partial z}\frac{\partial V_z}{\partial z} + \frac{\partial \nu_t}{\partial r}\frac{\partial V_r}{\partial z} \quad (3)$$

$$\frac{\partial V_r}{\partial r} + \frac{\partial V_z}{\partial z} + \frac{V_r}{r} = 0 \quad (4)$$

where:

V_r, V_θ, and V_z are the r, θ, and z velocity components
p is the static pressure,
ρ is the flow density,
ν_t and ν_{eff} are the eddy and effective kinematic viscosity coefficients, respectively (defined next).

Turbulence Closure. The algebraic eddy viscosity model by Baldwin and Lomax (1978) is extended to the current axisymmetric flow problem. In this case, the flow variables utilized by the model, including the vorticity and wall shear stress, are now based on the meridional as well as the tangential velocity components. According to this model, the effective kinematic viscosity, "ν_{eff}," in equations (1) through (3), is viewed as composed of two, molecular and eddy, components as follows:

$$\nu_{\text{eff}} = \nu_l + \nu_t \quad (5)$$

In calculating the eddy component, ν_t, the procedure assumes the presence of two, inner and outer, layers. In the inner layer, the Prandtl-Van Driest formulation yields the following expression:

Nomenclature

A = area
AR = diffuser exit/inlet crossflow area ratio
C_p = diffuser recovery coefficient $= (p_{\text{ex}} - p_{\text{in}})/(P_{\text{in}} - p_{\text{in}})$
l = mixing length
M_i = linear shape function associated with the ith node of a finite element
N_i = quadratic shape function associated with the ith node of a finite element
$\mathbf{n}$ = outward normal unit vector
P = total pressure
p = static pressure
q = dynamic pressure
r, θ, z = coordinates in the cylindrical frame of reference
V_r, V_θ, V_z = radial, tangential and axial velocity components
W_i = weight function in the Petrov-Galerkin weighted-residual analysis
y^+ = dimensionless wall coordinate
α_{in} = diffuser inlet swirl angle (positive in the direction opposite to the turbine rotation)
λ = near-wall grid refinement factor
ν = kinematic viscosity coefficient
ρ = density
τ_w = wall shear stress
ω = vorticity

Subscripts

ex = diffuser exit station
in = diffuser inlet station

$$\nu_{t,i} = l^2 |\omega| \tag{6}$$

where the subscript i refers to the inner layer. The mixing length, l, and the vorticity magnitude, $|\omega|$, in expression (6), are as follows:

$$l = ky\left[1 - \exp\left(\frac{-y^+}{A^+}\right)\right],\ y^+ = \frac{\sqrt{\rho_w \tau_w}}{\mu_w} y;\ \text{and} \tag{7}$$

$$\omega = \left\{\left(\frac{V_\theta}{r} + \frac{\partial V_\theta}{\partial r}\right)^2 + \left(\frac{\partial V_\theta}{\partial z}\right)^2 + \left(\frac{\partial V_r}{\partial z} - \frac{\partial V_z}{\partial r}\right)^2\right\}^{1/2} \tag{8}$$

where: y is the distance normal to the nearest wall,
A^+ is the sublayer thickness; and
τ_w is the wall shear stress

The model switches from Van Driest formulation to that of the outer region at the smallest value of y for which the inner and outer values of the eddy kinematic viscosity are equal. The formulation for the outer layer is given by:

$$\nu_{t,o} = KC_{cp} F_{\max} y_{\max} F_{KLEB} \tag{9}$$

where:

$$F_{\max} = y_{\max} |\omega| \left[1 - \exp\left(\frac{-y^+}{A^+}\right)\right];\ \text{and}$$

$$F_{KLEB} = \left[1 + 5.5\left(C_{KLEB} \frac{y}{y_{\max}}\right)^6\right]^{-1}$$

with $y_{\max}$ referring to the value of y at which $F_{\max}$ occurs. The various constants in Baldwin-Lomax model are as follows:

$A^+ = 26,\ k = 0.4,\ K = 0.0168,\ C_{cp} = 1.6;$ and $C_{KLEB} = 0.3$

Computation of the wall shear stress, τ_w, is based on the near-wall zone treatment proposed by Benim and Zinser (1985). The assumption here is that the universal law of the wall at any wall location is extendible to an interior computational node that is closest to the wall at this location. Referring to the distance of the interior node from the wall by $y_{\min}$, the following recursive expression for the wall shear stress is then obtained:

$$\tau_w = \begin{cases} \dfrac{\nu_l \rho V_{\min}}{y_{\min}} & \text{for } y^+_{\min} < 11.6 \\ \dfrac{\kappa C_D^{1/4} \rho V_{\min} k_{\min}^{1/2}}{\ln\left(E C_D^{1/4} y_{\min} \dfrac{k_{min}^{1/2}}{\nu_l}\right)} & \text{for } y^+_{\min} \geq 11.6 \end{cases} \tag{10}$$

where:

$$k_{\min} = \frac{\tau_w}{\rho C_D^{1/2}},\ C_D = 0.09,\ \kappa = 0.4,\ E = 9.0$$

with $V_{\min}$ referring to the magnitude of velocity, with the tangential component taken into account, at the interior node.

Remainder of the Benim and Zinser wall model was implemented in executing the test cases in the current study. This is pertinent to the use of the wall functions to calculate the slip velocity along the edge of the computational domain which, in this case, is located at a small pre-determined distance away from the wall. Along this distance, the dimensionless velocity, V^+, assumes the following form:

$$V^+ = \begin{cases} y^+ & \text{for } y^+ < 11.6 \\ \dfrac{1}{\kappa} \ln(Ey^+) & \text{for } y^+ \geq 11.6 \end{cases} \tag{11}$$

where:

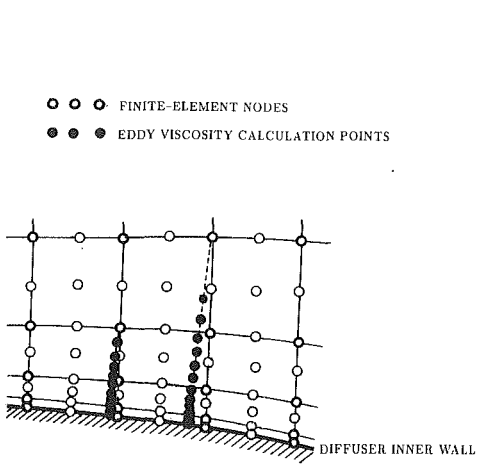

Fig. 2 Refinement of the near-wall region for accurate prediction of the eddy viscosity

$$V^+ = \frac{V}{\sqrt{\dfrac{\tau_w}{\rho}}} \tag{12}$$

Numerical implementation of the turbulence closure, including the near-wall zone analysis above, was achieved using an array of points that is different from the primary set of computational nodes. Figure 2 shows an enlarged segment of the computational domain near a solid wall, in which the primary nodes in the finite-element discretization model are identified by hollow circles, while the points used in the computations leading to the eddy viscosity at two selected nodes are solid circles. The objective here was twofold: to estimate the cut-off location between the inner and outer layer with sufficient accuracy, and to capture the steep gradients of the flow variables near the solid wall. A substantial enhancement of the solution was, as a result, observed during the phase of numerical experimentation. This, for the major part, was due to the excellent accuracy with which the wall shear stress was computed, for it was generally possible to compute the stress using an interior point where the dimensionless wall coordinate (y^+) was acceptably small. Worth noting is the fact that accurate evaluation of the wall shear stress would impact both the computed value of eddy viscosity and wall slip velocity, since the stress simultaneously appears in the turbulence closure as well as the universal law of the wall.

Boundary Conditions. Preserving the flow ellipticity throughout the computational domain requires the specification of appropriate boundary conditions over the entire boundary. Of these, the conditions imposed at the solid boundary segments, through the use of wall functions, are discussed above. At the flow inlet station, the entrance boundary-layer thickness was assumed to be 20 percent of the inlet annulus height. Outside the boundary layer, constant core values of the inlet velocity components were specified. As for the flow exit conditions, zero surface tractions were imposed as follows:

$$\frac{\partial V_z}{\partial_z} - \frac{p}{2\rho\nu_{\text{eff}}} = 0$$

$$\frac{\partial V_r}{\partial z} + \frac{\partial V_z}{\partial r} = 0$$

$$\frac{\partial V_\theta}{\partial z} = 0$$

Out of the various exit boundary conditions tested during the course of this study, the above conditions were found to be the least fictitious and most tolerant to nonuniform exit flow patterns. This observation was previously emphasized by Gresho and Lee (1981) in conjunction with their investigation of the confined and unconfined flow over a step, where the

flow recirculation downstream from the step extended to, and included, the exit station. This type of complication was to be anticipated in the current problem should the adverse pressure gradient and excessive swirl cause flow separation anywhere on the diffuser endwalls. In a situation such as this, the zero surface tractions boundary conditions, as reported by Gresho and Lee, would permit the flow to depart and re-enter the computational domain at different segments of the exit boundary. This, in principle, allows the flow recirculatory motion to prevail at exit, as would naturally be the case. It should be noted, at this point, that exit boundary conditions whereby the streamwise gradients of the flow variables are held constant, are hardly applicable to the current problem, even when accompanied by adjustments in the exit through-flow velocity between iterations in order to conserve the mass flow rate. Successful use of such simple exit conditions by Hah (1983), in his conical diffuser flow analysis, may have been a result of the relatively small divergence angle of the conical passage in Hah's study. The exit boundary conditions, in the present study, are finalized by fixing the static pressure magnitude at an arbitrary point on the exit station. This, in effect, defines a datum to which the static pressure throughout the computational domain is referenced.

Finite-Element Formulation. A special version of the Petrov-Galerkin weighted residual method is used to derive the finite-element form of the flow-governing equations. The current approach ensures upwinding of the convection terms in the momentum equations while preserving the elliptic nature of the diffusion terms. This, for a simple orthogonal grid, would be equivalent to backward-differencing the convection terms and central-differencing the diffusion terms in the conventional finite-difference analyses of inertia-dominated flows. Successful implementation of this strategy, within a finite-element context, was achieved by Hughes (1978) for only simple (linear and bilinear) finite-element configurations by modifying the integration algorithm in the process of deriving the element equations. This effectively eliminated the wiggles in the streamwise pressure variation which are typically associated with the conventional Galerkin's weighted residual approach when applied to high Reynolds number flows. Expansion of essentially the same concept to a highly accurate biquadratic element, by selecting the weight functions on a term-by-term basis, is described in this section. Note that an alternate, but impractical, means of obtaining a physically meaningful pressure field under the conventional, and recognizably accurate, Galerkin's method would require an unrealistically fine computational grid for the elemental Peclet numbers to be sufficiently small.

The characteristic features of the finite element discretization model in the current study are shown in Fig. 3. The discretization unit, which is a nine-noded curve-sided finite element of the Lagrangian type (Zienkiewicz, 1971) is separately shown in Fig. 3 in both the local and physical frames of reference. Within a typical element (e), let the spatial coordinates be interpolated as follows:

$$z^{(e)} = \sum_{i=1}^{9} N_i(\zeta, \eta) z_i, \quad r^{(e)} = \sum_{i=1}^{9} N_i(\zeta, \eta) r_i$$

where N_i are quadratic "shape" functions (Zienkiewicz, 1971) associated with the element corner, midside and interior nodes. Next, the flow variables are interpolated throughout the element in a similar fashion. Guided by the Ladyshenskaya-Babuska-Brezzi compatibility requirements (Carey and Oden, 1986) for the problem at hand, the velocity components and pressure are expressed as follows:

$$V_z^{(e)} = \sum_{i=1}^{9} N_i(\zeta, \eta) V_{z,i}, \quad V_r^{(e)} = \sum_{i=1}^{9} N_i(\zeta, \eta) V_{r,i},$$

$$V_\theta^{(e)} = \sum_{i=1}^{9} N_i(\zeta, \eta) V_{\theta,i}, \quad p^{(e)} = \sum_{k=1}^{4} M_k(\zeta, \eta) p_k$$

where M_k are the linear shape functions associated with the element corner nodes.

According to the weighted residual method, the error functions produced by equations (1) through (4) as a result of substituting the interpolation expressions, above, are then made orthogonal to a special set of weight functions over the finite element subdomain. In constructing the latter set of functions, the so-called error consistency criterion of Hood and Taylor (1974) was implemented, whereby the element shape functions, M_k were used in conjunction with the continuity equation. On the other hand, quadratic functions which include the element shape functions "N_i" and a set of derived functions "W_i" were used in conjunction with the momentum equations in such a way to ensure full upwinding of the convection terms. Of these, the functions "W_i" were previously defined by Heinrich and Zienkiewicz (1977) in terms of the shape functions and some upwinding constants which depend on the element geometry and local velocity direction.

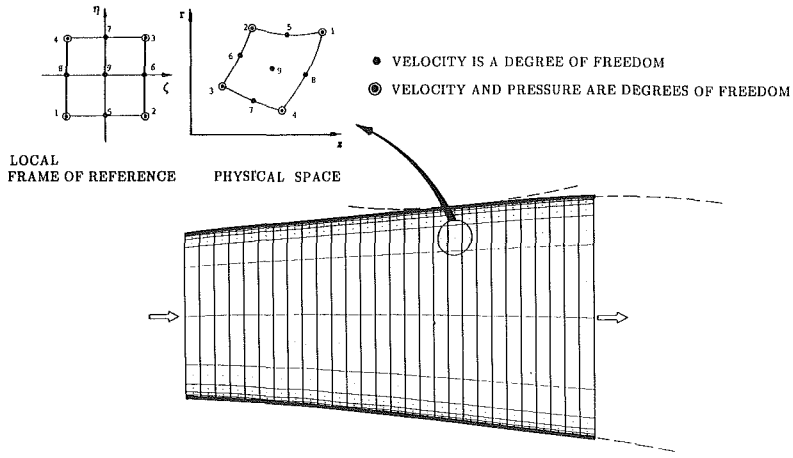

Fig. 3 Finite-element discretization model

Having defined the weight functions, derivation of the finite-element equivalent to equations (1) through (4) is straight forward. The process requires linearization of these equations, using known values for the velocity components and eddy viscosity, and use of Gauss divergence theorem. The final form of these equations for the typical element (e) is as follow:

$$\left[\iint_{A^{(e)}} \left\{\hat{\nu}_{\text{eff}}\left(\frac{\partial N_i}{\partial r}\frac{\partial N_j}{\partial r}+\frac{\partial N_i}{\partial z}\frac{\partial N_j}{\partial z}\right)+W_i\left(\hat{V}_r\frac{\partial N_j}{\partial r}+\hat{V}_z\frac{\partial N_j}{\partial z}\right)-N_i\frac{\partial \hat{\nu}_t}{\partial r}\frac{\partial N_j}{\partial r}+\frac{\hat{\nu}_{\text{eff}}}{r^2}N_iN_j\right\}rdA\right]V_{r,j}$$
$$-\left[\iint_{A^{(e)}}\frac{\hat{V}_\theta}{r}N_iN_jrdA\right]V_{\theta,j}-\left[\iint_{A^{(e)}}N_i\frac{\partial \hat{\nu}_t}{\partial z}\frac{\partial N_j}{\partial r}rdA\right]V_{z,j}$$
$$+\left[\iint_{A^{(e)}}\frac{1}{\rho}N_i\frac{\partial M_k}{\partial r}rdA\right]p_k=\oint_{L^{(e)}}\hat{\nu}_{\text{eff}}rN_i(\mathbf{n}\cdot\nabla V_r)dL \tag{13}$$

$$\left[\iint_{A^{(e)}}\left\{\hat{\nu}_{\text{eff}}\left(\frac{\partial N_i}{\partial r}\frac{\partial N_j}{\partial r}+\frac{\partial N_i}{\partial z}\frac{\partial N_j}{\partial z}\right)+W_i\left(\hat{V}_r\frac{\partial N_j}{\partial r}+\hat{V}_z\frac{\partial N_j}{\partial z}\right)+\left(\frac{1}{r}\frac{\partial \hat{\nu}_t}{\partial r}+\frac{\hat{\nu}_{\text{eff}}}{r^2}+\frac{\hat{V}_r}{r}\right)N_iN_j\right\}rdA\right]V_{\theta,j}$$
$$=\oint_{L^{(e)}}\nu_{\text{eff}}rN_i(\mathbf{n}\cdot\nabla V_\theta)dL \tag{14}$$

$$-\left[\iint_{A^{(e)}}N_i\frac{\partial \hat{\nu}_t}{\partial r}\frac{\partial N_j}{\partial z}rdA\right]V_{r,j}+\left[\iint_{A^{(e)}}\left\{\hat{\nu}_{\text{eff}}\left(\frac{\partial N_i}{\partial r}\frac{\partial N_j}{\partial r}+\frac{\partial N_i}{\partial z}\frac{\partial N_j}{\partial z}\right)+W_i\left(\hat{V}_r\frac{\partial N_j}{\partial r}+\hat{V}_z\frac{\partial N_j}{\partial z}\right)+N_i\frac{\partial \hat{\nu}_t}{\partial z}\frac{\partial N_j}{\partial z}\right\}rdA\right]V_{z,j}$$
$$+\left[\iint_{A^{(e)}}\frac{1}{\rho}N_i\frac{\partial M_k}{\partial r}rdA\right]p_k=\oint_{L^{(e)}}\nu_{\text{eff}}rN_i(\mathbf{n}\cdot\nabla V_z)dL \tag{15}$$

$$\left[\iint_{A^{(e)}}\left(M_k\frac{\partial N_j}{\partial r}+\frac{1}{r}M_kN_j\right)rdA\right]V_{r,j}+\left[\iint_{A^{(e)}}M_k\frac{\partial N_j}{\partial z}rdA\right]V_{z,j}=0 \tag{16}$$

In these equations, the subscripts "i" and "j" vary from 1 to 9, while "k" varies from 1 to 4. Also the symbol $\hat{(\ )}$ in these equations signifies a value that is known from a previous iteration or an initial guess. The global set of equations is achieved by assembling equations (13) through (16) among all elements, for the current iterative step, and the result is a system of linear algebraic equations in the flow nodal variables.

Method of Solution. In an attempt to reduce consumption of the computer resources, the θ-momentum equation (14) was uncoupled and separately solved as part of an iterative procedure that is basically similar to that by Baskharone and Hensel (1989). Note that the term containing "$V_{\theta,j}$" in equation (13) now belongs to the right hand side of the equation where it is treated as a "source" term, and is progressively updated during the iterative solution procedure. The set of finite-element equations in each computational step was assembled and simultaneously solved using the frontal method of Hood (1976).

In progressing from one iteration to the next, an underrelaxation factor is applied to the nodal values of flow variables to ensure monotonic convergence. The optimum value of this factor in the current study was found to be 0.7 for all cases considered.

Results and Discussion

The current computational model was applied to a representative exhaust diffuser of a commercial gas turbine engine (Fig. 3). This is one of the so-called "clean" diffusers in light of its low total pressure loss/static pressure recovery ratio. The diffuser is of the contoured-wall type, as shown in Fig. 3, with an area ratio of 1.61, a length-to-inlet height ratio of 3.70 and a design-point Reynolds number (based on the average inlet velocity and the diffuser length) of 5.4×10^5. Performance of this diffuser at design and off-design operation modes was simulated in a cold rig by varying the diffuser inlet swirl angle. The test established the diffuser recovery characteristics over a wide range of operation, part of which is investigated in this study.

Grid Dependency of the Flow Field. Sensitivity of the numerical solution to the size of the finite element model and the level of field resolution it provides was first investigated. In all cases considered, the number of cross-flow stations in the meridional view between the inlet and exit stations (Fig. 4) was fixed at 29, while the number of grid lines between the endwalls, referred to as N_r, was varied from 5 to 11. The latter family of grid lines was constructed with varying increments in the radial direction. To better quantify this variation, the growth of increments from either one of the diffuser walls to the mean line at any axial location was made to be that of the geometric sequence type with a common ratio "λ", where $1.5\le\lambda\le3.5$. Illustrated in Fig. 5 is the geometrical effects of varying "λ" from 1.75 to 2.25 for the case where N_r is fixed at 9. Note the drastic change in the width of the wall elements as a result.

Shown in Fig. 5 is the error, based on the experimental data, of the computed recovery coefficient "C_p" at the diffuser design point for a matrix of finite-element grids. The various

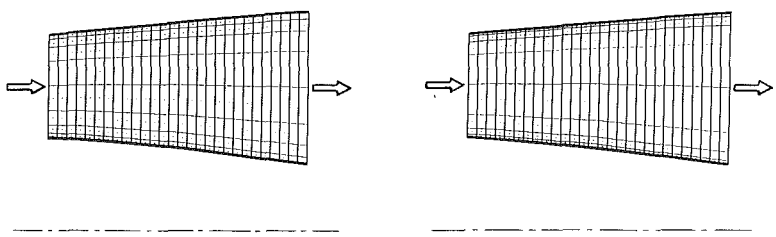

REFINEMENT FACTOR (λ) = 1.75 REFINEMENT FACTOR (λ) = 2.25

Fig. 4 Geometrical effects of varying the refinement factor (λ) in constructing the finite-element grid

combinations of "N_r" and "λ" in this figure represent viable finite-element model configurations which, to varied levels, ensure proper field resolution. Examination of the figure reveals that the error in the predicted recovery coefficient for $N_r = 9$ and $\lambda = 2.25$ is about 5.5 percent. This, plus the asymptotic nature of the error curve near this point, led to the choice of this "N_r" and "λ" combination for the remainder of the numerical investigation. The choice was, to a lesser degree, influenced by the desire to minimize the core and CPU time consumption that would naturally be associated with larger wall-to-wall station counts.

Diffuser Flow Field and Off-Design Performance. A primary objective in the current study was to apply the flow model to the diffuser off-design flow field. The intention here was to continue the process of verifying the computational model under some potentially challenging flow conditions, and to appraise the diffuser tolerance to off-design turbine operation as an important design criterion. Since the flow compressibility, as dictated by the turbine exit Mach number, was unchangingly negligible over the entire operation range, transition to off-design diffuser operation was simulated by incrementing the average inlet swirl angle while maintaining its characteristic profile, as well as that of the through-flow velocity. Figure 6 shows a comparison between the computed and measured recovery coefficient "C_p" over a range of off-design diffuser operation. The nonsymmetric shape of the experimental data in this figure is suspected to be primarily caused by such factors as distortions in the inlet velocity profiles and the presence of exhaust struts in the actual diffuser passage. In fact, it is perhaps more meaningful, yet not sufficiently rigorous, to compare the numerical results to an "adjusted" experimental curve whereby the actual curve is shifted in such a way to associate the point of maximum recovery with a diffuser inlet swirl angle of zero as shown in Fig. 6. Altering the experimental data in this manner is merely intended to establish common grounds for a qualitative comparison with the numerical results, since the latter are the outcome of a flow field in which the above-mentioned complications are neglected. With this in mind, it is apparent that the overall agreement between the two sets of data in Fig. 6 is clearly good and, to a sufficient extent of certainty, validates the various details of the computational model. Worth noting in Fig. 6 is also the fact that boundary layer separation over the hub surface begins to exist at an inlet swirl angle of 18 degrees (point "S" in Fig. 6). This flow recirculation zone is, at first, confined to the region just upstream from the exit station, but continues to grow in size as the inlet swirl angle is elevated.

It is apparent that the fairly wide range of decent pressure recovery by the diffuser (Fig. 6) is caused by the manner in which the diffuser boundary is contoured, particularly in the near-exit casing segment (Fig. 3). The concave shape of this segment is believed to retard the flow separation over the casing and, perhaps appreciably, over the hub as the exit station is approached. This favorable effect becomes more valuable at off-design operation where excessive swirl angles create the

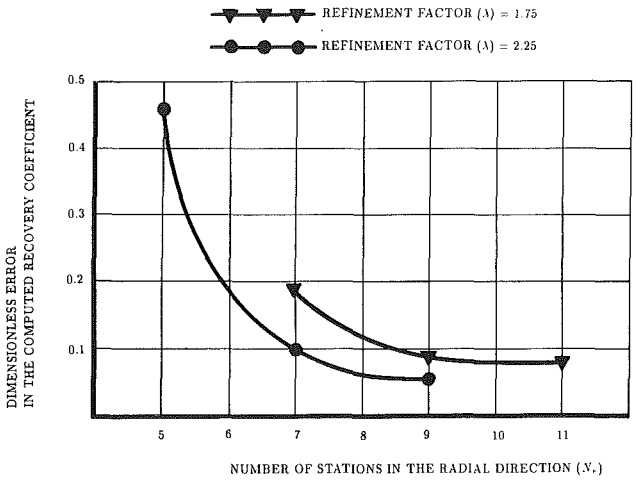

Fig. 5 Deviation of the computed recovery coefficient from the experimental value under design-point diffuser operation

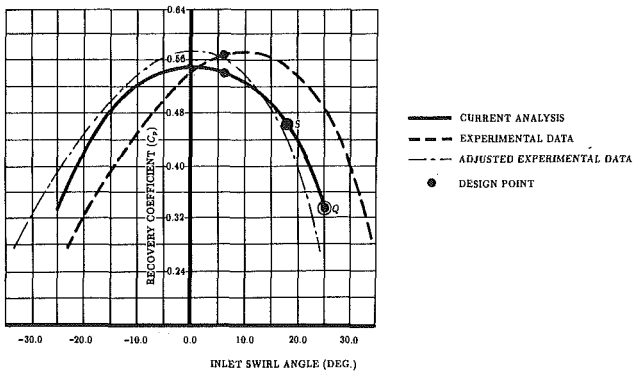

Fig. 6 Variation of the diffuser recovery coefficient with the inlet swirl angle at off-design operation

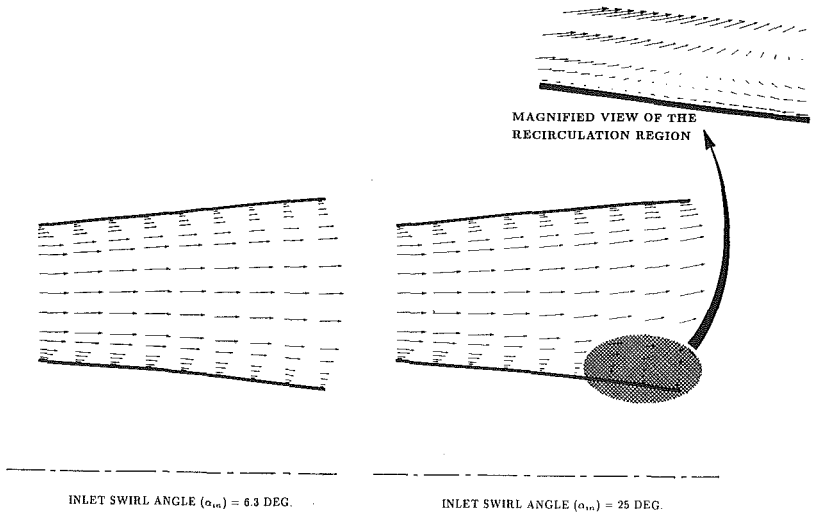

Fig. 7 Vector plots of the meridional velocity at design and off-design operating conditions

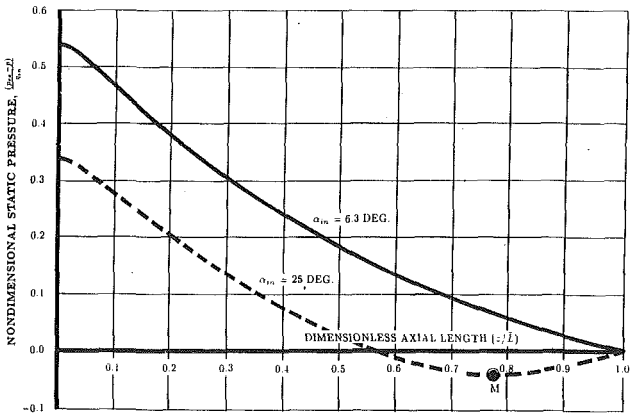

Fig. 8 Axial distribution of the radially-averaged static pressure at design and off-design operating conditions

tendency for boundary layer separation with which reattachment is, in view of the adverse pressure gradient, unlikely.

Figures 7 and 8 reveal significant details of the diffuser flow field at design and off-design operation. These correspond to inlet swirl angles of 6.3 degrees and 25 degrees, respectively. First, the radial profiles of the through-flow velocity are shown in Fig. 7, where it is evident that the design-point flow field is separation-free. The figure also shows that boundary-layer separation indeed prevails over the hub surface at $\alpha_{in} = 25$ degrees (point Q in Fig. 6) as a result of the substantial elongation of the flow trajectory across the diffuser in this case. Note that the large centrifugal force acting on the flow particle, as a result of the large tangential velocity component in this case, provides an additional source for flow separation since it creates a radially outward shifting of the flow particles. The impact of this flow pattern on the radially-averaged static pressure variation in the axial direction is illustrated in Fig. 8. Examination of this figure reveals that the blockage associated with the flow recirculation subdomain at $\alpha_{in} = 25$ degrees is, in an average sense, causing a local through-flow acceleration in the diffuser segment between point "M" (Fig. 8), where the local average pressure is higher than the exit pressure, and the exit station. The decline in static pressure across this segment is also a result of a significant total pressure loss in the recirculation zone.

Concluding Remarks

The swirling flow field in exhaust diffusers of the type used in gas turbine engines was analyzed with emphasis on the diffuser off-design operation. The analysis is based on the weighted-residual finite-element method, and employs the concept of upwinding in deriving the finite-element equations. Successful simulation of the flow turbulence within the flow model through an algebraic closure is believed to be a result of the accuracy with which the wall shear stress was computed. The model is provenly applicable to moderately separating flows which are typically associated with off-design performance of diffusing passages in gas turbines. A representative case involving the exhaust diffuser of a commercial gas turbine engine was used to both verify the model, as well as examine the pressure recovery characteristics which, in turn, dictate the total-to-static efficiency of the turbine/diffuser system. The good agreement between the numerical and experimental results in this case may be a sufficiently good basis for advocating the use of this, and perhaps more sophisticated, finite elment-based models in analyzing the flow fields in complex gas turbine components where domination of the inertia forces has traditionally been a discouraging feature.

Acknowledgment

This study was funded by NASA-Marshall Space Flight Center (Huntsville, Alabama), contract no. NAS8-37821, and the Houston Advanced Research Center (The Woodlands, Texas), grant no. 88-025. The experimental data in Fig. 6 were provided courtesy of a gas turbine manufacturing company as privileged information for the purpose of verifying the computational model.

References

Benim, A. C., and Zinser, W., 1985, "Investigation into the Finite Element Analysis of Confined Turbulent Flows Using a $k-\epsilon$ Model of Turbulence," *Computer Methods in Applied Mechanics and Engineering*, Vol. 51, pp. 507–523.

Baldwin, B. S., and Lomax, H., 1978, "Thin Layer Approximation and Algebraic Model for Separated Turbulent Flows," AIAA Paper No. 78-257.

Bardina, J., Lyrio, A., Kline, S. J., 1981, Ferziger, J. H., and Johnston, J. P., "A Prediction Method for Planar Diffuses Flows," ASME JOURNAL OF FLUIDS ENGINEERING, Vol. 103, pp. 315–321.

Baskharone, E. A., and Hensel, S. J., 1989, "A New Model for Leakage Prediction in Shrouded-Impeller Turbopumps," ASME JOURNAL OF FLUIDS ENGINEERING, Vol. 111, pp. 118–123.

Carey, G. F., and Oden, J. T., 1986, "Finite Elements: Fluid Mechanics," *The Texas Finite Element Series*, Vol. IV, Prentice-Hall Inc.

Gresho, P. M., and Lee, R. L., 1981, "Don't Suppress the Wiggles-They're Telling You Something!" *Computers & Fluids*, Vol. 9, No. 2, pp. 223–253.

Hah, C., 1983, "Calculation of Various Diffuser Flows with Inlet Swirl and Inlet Distortion Effects," *AIAA Journal*, Vol. 21, No. 8, pp. 1127–1133.

Heinrich, J. C., and Zienkiewicz, O. C., 1977, "Quadratic Finite Element Schemes for Two-Dimensional Convective-Transport Problems," *Int. J. Num. Meth. Engrg.*, Vol. 11, pp. 1831–1844.

Hood, P., 1976, "Frontal Solution Program for Unsymmetric Matrices," *Int. J. Num. Meth. Engrg.*, Vol. 10, No. 2, pp. 379–399.

Hood, P., and Taylor, C., 1974, "Navier-Stokes Equations Using Mixed Interpolation," *Proceedings of the International Symposium on Finite Element Methods in Flow Problems*, University of Wales, Swansea, United Kingdom.

Hughes, T. J. R., 1978, "A Simple Scheme for Developing 'Upwind' Finite Elements," *Int. J. Num. Meth. Engrg.*, Vol. 12, pp. 1359–1365.

Japikse, D., and Pampreen, R., 1979, "Annular Diffuser Performance for an Automotive Gas Turbine," ASME *Journal of Engineering for Power*, Vol. 101, pp. 358–372.

Johnston, J. P., and Dean, R. C., 1966, 'Losses in Vaneless Diffusers of Centrifugal Compressors and Pumps," ASME *Journal of Engineering for Power*, Vol. 99, pp. 49–62.

Lai, Y. G., and So, R. M. C., 1989, "Calculation of Planar and Conical Diffuser Flows," *AIAA Journal*, Vol. 27, No. 5, pp. 542–548.

Sovran, G., and Klomp, E. D., 1967, "Experimentally Determined Optimum Geometries for Rectilinear Diffusers with Rectangular, Conical, or Annular Cross Section," *Fluid Mechanics of Internal Flow*, Elsevier Publication.

Stevens, S. J., and Markland, E., 1968, "The Effect of the Inlet Conditions on the Performance of Two Annular Diffusers," ASME Paper No. 68-WA/FE-38.

Takehira, A., Tanaka, M., Kawashima, T., and Hanabusa, H., 1977, "An Experimental Study of the Annular Diffuser in Axial Flow Compressors and Turbines," *Proceedings of the Tokyo Joint Gas Turbine Congress*, pp. 319–328.

Zienkiewicz, O. C., 1971, *The Finite Element Method in Engineering Science*, McGraw-Hill.

Wall Pressure and Shear Stress Variations in a 90-Deg Bifurcation During Pulsatile Laminar Flow

J. M. Khodadadi
Assistant Professor,
Department of Mechanical Engineering,
Auburn University,
Auburn, AL 36849-5341,
Mem. ASME

Wall pressure distribution and shear stress fields for pulsatile laminar flow in a 90-degree bifurcation with rectangular cross sections are evaluated using the results of the numerical solution of the Navier-Stokes equation. The extent of the adverse pressure gradient on the bottom wall of the main duct and the upstream wall of the branch closely correlate to the behavior of the two dynamic recirculation zones which are formed on these two walls. Multiple zones of high and low shear stresses at various sites in the bifurcation are observed. The extent of the fluctuations of the maximum and minimum shear stress is identified. Next-to-the-wall laser Doppler anemometer velocity measurements are used to estimate the shear stress distribution on the walls. In general, qualitaitve agreement between the experimental and computed wall shear stress values is observed. The variation of the wall shear stress in the vicinity of the branch is discussed in light of the highly perturbed flow field.

1 Introduction

The hemodynamics of the human circulatory system have been identified as a contributing factor to atherogenesis and cardiovascular diseases by a number of researchers (see Pedley, 1980; Rodkiewicz, 1983; and Fung, 1984). Well-established clinical evidence clearly indicate that atheromatous lesions first form in specific regions of arteries, namely near bends and branches. Due to evidence of damage to arterial walls and blood components, shear stress has been cited as a parameter responsible for atherogenesis. Specifically, two shear stress dependent mechanisms for atheromatous plaque formation have been presented. Fry (1969) showed that the endothelium of arteries may be damaged due to presence of high shear stresses, and thus the plaques form in these regions. Caro et al. (1971) suggested that regions of low mass transfer, i.e., low shear stress, allow for areas of lipid accumulation and thus atherosclerosis. Accordingly, many researchers have investigated the role of arterial wall shear stress in the localization and/or initiation/development of lipid and cholesterol accumulation. A number of important papers in this area has already been referred to in the earlier publications of Liepsch et al. (1982) and Khodadadi et al. (1988), who investigated steady and pulsatile laminar flow in a plane 90-degree bifurcation, both experimentally and numerically. Thus, only those papers which directly relate to the present geometry and the focus of this study are reviewed here. Kawaguti and Hamano (1980) performed a numerical study of two-dimensional pulsatile flow in a 90-degree bifurcation. They concluded that for the case similar to blood flow in an artery, the amplitude of shearing stress variation is higher in the neighborhood of the trailing edge corner and downstream of the leading edge corner in the branch. A numerical investigation of steady laminar forced convective heat transfer in a two-dimensional 90-degree bifurcation was recently reported by Khodadadi et al. (1986). The locations and sizes of the three recirculation zones in the main duct and the branch were quantified for a wide range of the Reynolds number and dividing flow rate.

The present work is an extension of the recent paper of Khodadadi et al. (1988) and is concerned with evaluating the wall pressure and shear stress variations using the results of the numerical prediction of pulsatile laminar flow in a two-dimensional 90-degree bifurcation with solid walls. The schematic diagram of the bifurcation model is shown in Fig. 1. Although the bifurcation geometry has been simplified in order to study the basic flow phenomena while avoiding secondary flow effects, the successful application of the present computational method will guide its extension to three-dimensional geometries, which are encountered in human arterial tree.

2 Experimental Estimation of Wall Shear Stress

Extensive experimental studies in the bifurcation model of Fig. 1 have been reported by Liepsch et al. (1982) and Khodadadi et al. (1988), who obtained detailed velocity measurements in the symmetry plane ($z = W/2$) using a laser Doppler anemometer (LDA). The bifurcation test-section shown in Fig. 1 was fabricated from plexiglas with a 10 mm × 80 mm rectangular cross section. This aspect ratio of 8:1 was chosen in order to eliminate the effects of side wall boundary layer interactions, and to ensure two-dimensionality at the measurement plane. A glycerine-water solution with a dynamic viscosity of $\mu = 0.0084 - 0.0120$ Pa sec was pumped through the bifurcation model. The flow rate ratio, β, was adjusted by

Contributed by the Fluids Engineering Division for publication in the JOURNAL OF FLUIDS ENGINEERING. Manuscript received by the Fluids Engineering Division February 21, 1990.

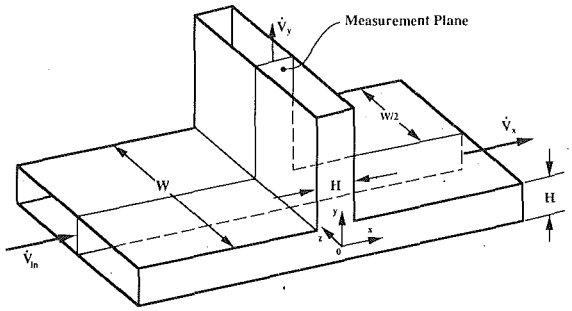

Fig. 1 Ninety degree bifurcation model

small regulator tanks and was determined by weighing the fluid collected over a time interval in both branches of the bifurcation. A sinusoidal oscillating flow produced by a piston pump was superimposed on the steady flow. Detailed description of the experimental apparatus and the LDA system can be found in the two papers referenced above. In both of these papers, the measured velocity profiles were compared to the numerical solution of the Navier-Stokes equation. The flow was predicted very well in regions away from the separation zones. The observed discrepancies in the separation regions were attributed to numerical inaccuracies which are inherent in the calculations. The flow conditions of the experimental and numerical study of Khodadadi et al. (1988) were:

(*a*) Re = 38, α = 4.1 and β = 0.7,

(*b*) Re = 102, α = 4.9 and β = 0.7.

The time-dependent characteristics of the computed wall pressure variation and shear stress fields corresponding to these operating conditions are presented in this paper. Limited temporally resolved wall pressure measurements were reported in the work of Khodadadi et al. (1988) at the inlet plane (x/H = − 3.5). Direct wall shear stress measurements were not performed. However, accurate next-to-the-wall LDA velocity measurements were obtained at a location 0.15 mm (1.5 percent of channel height) from the wall of the channel. The estimated accuracy of these velocity measurements was five percent of the local velocity. By assuming that a linear velocity profile exists very close to the wall, estimated wall shear stress values have been deduced from velocity measurements and are presented in this paper for the first time.

3 Mathematical Approach

The present calculations were based on the SIMPLE procedure of Patankar (1980). This prediction procedure uses primitive variables, i.e., velocity components and pressure.

3.1 Governing Equations and Boundary Conditions. The continuity and momentum transport equations governing the present flow are:

$$\nabla \cdot \bar{\mathbf{V}} = 0 \tag{1}$$

$$\frac{\partial \bar{\mathbf{V}}}{\partial t} + (\bar{\mathbf{V}} \cdot \nabla)\bar{\mathbf{V}} = -\frac{1}{\rho}\nabla p + \nu \nabla^2 \bar{\mathbf{V}} \tag{2}$$

The computational domain extended for ten channel heights in both directions (x/H from −3.5 to 6.5 and y/H from −0.5 to 9.5). The dependent variables or their normal gradients should be specified along all the boundaries of the bifurcation model. The inlet plane was located 3.5 channel heights upstream of the origin of the coordinate system identified in Fig. 1. The measured fluctuating velocity profiles at the inlet station compared very well to the analytic solution for fully developed oscillatory flow (see Khodadadi et al., 1988). The measured velocity profiles at 22.5 deg phase angle intervals were used as inlet boundary conditions for the numerical computations, whereas linear interpolation was utilized to obtain the inlet velocity profiles at phase angles other than increments of 22.5 deg. The v velocity component at the inlet plane was set to zero and no-slip condition was imposed along the walls. It was also guaranteed that the velocity profiles at both outlets were fully developed (oscillatory) by choosing the outlet boundaries at reasonable distances from the bifurcation.

3.2 Computational Details. An unevenly spaced grid of 36 × 35 was used, with dense grid lines placed in regions of steep spatial gradients. The grid independence test of Khodadadi et al. (1986), which involved computation of the flow with coarser and finer grids, has shown the adequacy of the present grid. Twenty-six time steps in a cycle were utilized. The number of iterations for each time step ranged from 60 to 100. Once the velocity field was obtained, the shear stress variation was found by evaluating:

$$\tau_{xy} = \mu\left(\frac{\partial u}{\partial y} + \frac{\partial v}{\partial x}\right) \tag{3}$$

The wall shear stress variations were obtained by assuming a linear velocity profile very close to the wall. The shear stress field was nondimensionalized by $\tau_w^* = 6\mu U_m/H$, the wall shear stress for steady, laminar fully developed channel flow.

4 Results and Discussion

A summary of previous findings relating to the locations of the two separation zones in the branch model is presented first. This will be followed by the discussion of the wall pressure distribution and shear stress field.

4.1 Recirculation Zones. The study of Khodadadi et al. (1988) showed that two dynamic separation regions are established in the bifurcation. One is located on the bottom wall of the main duct opposite of the downstream side of the branch and the other along the upstream side wall of the branch. The steady flow results of Khodadadi et al. (1986) indicated that for Re = 102, the separation and reattachment points in the main duct were located at x/H = − 0.11 and x/H = 1.46, respectively. For Re = 38, no recirculation pattern was observed in the main duct. The separation point in the T-branch

Nomenclature

f = frequency of pulsation
H = duct height, Fig. 1
p = pressure
p_{ref} = reference pressure near the inlet plane
Re = Reynolds number, HU_m/ν
t = time
u = velocity component in the x-direction
U_m = space-time averaged inlet velocity
v = velocity component in the y-direction
$\dot{v}$ = volumetric flowrate
$\bar{\mathbf{V}}$ = velocity vector
W = duct width, Fig. 1
x, y = Cartesian coordinates
α = Stokes number, $0.5H(2\pi f/\nu)^{1/2}$
β = dividing flow rate ratio, $\dot{v}_y/\dot{v}_{in}$, Fig. 1
μ = dynamic viscosity
ν = kinematic viscosity
ρ = density
τ_{max} = maximum nondimensional shear stress
τ_{min} = minimum nondimensional shear stress
τ_w = wall shear stress
τ_w^* = wall shear stress (fully developed steady flow)
τ_{xy} = shear stress, equation (3)
ω = angular frequency, $2\pi f$

was located around $y/H = 0.57$, while the reattachment points for Re = 38 and Re = 102 were found at $y/H = 1.17$ and 2.10, respectively.

The estimated location of the separation and reattachment points in the main and branching ducts are plotted as a function of phase angle in Figs. 2(*a*) and 2(*b*), respectively. The results indicate a substantial variation of the size of the recirculation zone during the cycle when compared to the steady flow case which was discussed above. An increase of the Reynolds number results in an increase of the size of the separation zones. There is a phase-lag of about 220 deg between the pressure gradient wave and the separated bubble size. Around zero phase angle, there is no recirculation region in the main duct for the two Reynolds numbers studied. Similarly, there is no separation in the branch for the lower Reynolds number around zero phase angle.

4.2 Wall Pressure Variation. The distribution of the wall pressure is closely related to the location of the separated zones which was presented in section 4.1. The variation of the nondimensional pressure along the lower wall of the main duct at 45 deg phase angle intervals is shown in Fig. 3. The case of Re = 102 is chosen since it clearly demonstrates the representative wall pressure behavior. Adverse pressure gradients $(\frac{\partial p}{\partial x} > 0)$ are present throughout the cycle in the range $-1 < x/H < 2$, which correlate closely to the location of the recirculation zone discussed in Fig. 2(*a*). The adverse pressure gradient is responsible for retarding the flow, thus causing it to separate. Farther downstream of the bifurcation, the pressure gradient assumes uniform values along the duct wall throughout the cycle as the fully developed (oscillatory) state is reached. In general, similar trends were observed for the case of Re = 38.

To further reinforce the conclusions drawn from Fig. 3, we turn our attention to the distribution of the pressure on the upstream wall of the T-branch, which shelters a recirculation zone as seen in Fig. 2(*b*). This variation is shown in Fig. 4 for Re = 102. The separation point on this wall is located at $y/H = 0.57$, while the reattachment point varies between $y/H = 1.5$ and 2.8 during the cycle. Between $y/H = 0.57$ and 1.5, the pressure gradient is always positive, while it might assume negative values in the range $1.5 < y/H < 2.8$, depending on the size of the separated region at that instant in the cycle.

4.3 Shear Stress Field. The perturbed flow field in the vicinity of the bifurcation can cause marked effects on the shear stress field. The contours of nondimensional shear stress field are presented in Fig. 5(*a–d*) for Re = 102, $\alpha = 4.9$ and $\beta = 0.7$, at 90 deg phase angle intervals. It is seen that similar to the findings of the numerical work of Kawaguti and Hamano (1980), two regions of high (absolute value) shear stress are permanently featured in the vicinity of the leading ($x/H = -0.5$, $y/H = 0.5$) and trailing ($x/H = y/H = 0.5$) edges of the bifurcation. Within the high stress zone of the trailing edge, τ_{min} fluctuates between the values of -2.10 and -5.18 in the cycle. Opposite to the trailing edge of the bifurcation and on the bottom wall of the main duct, a zone of low (absolute value) shear stress (nearly zero) is formed. A similar pattern of low shear stress is observed on the upstream side wall of the bifurcation. The shear stress field behaved similarly for the second case with Re = 38, however with reduced strength of the high shear stresses. The values of the maximum and minimum shear stresses during a cycle are summarized in Table 1. The maximum shear stresses for the two cases are very similar. On the other hand, the absolute values of the minimum shear stress for Re = 102 are generally twice those observed

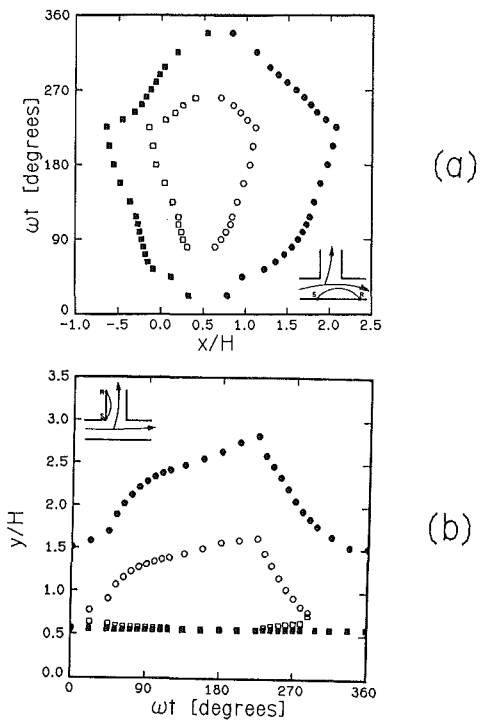

Re	α	β	Separation Point	Reattachment Point
38	4.1	0.7	□	○
102	4.9	0.7	■	●

Fig. 2 Temporal variation of the size of the recirculation zones in (*a*) main duct and (*b*) T-branch

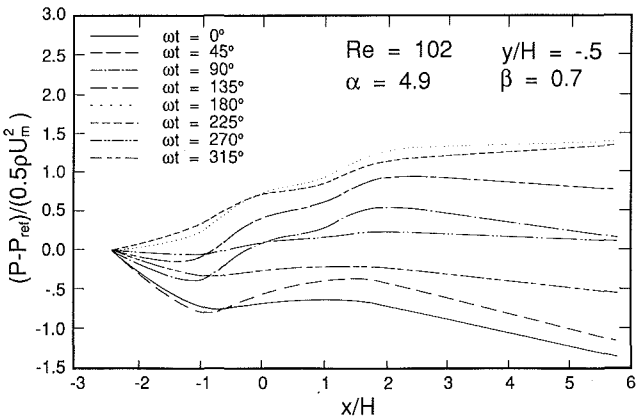

Fig. 3 Pressure variation on the bottom wall of the main duct for Re = 102

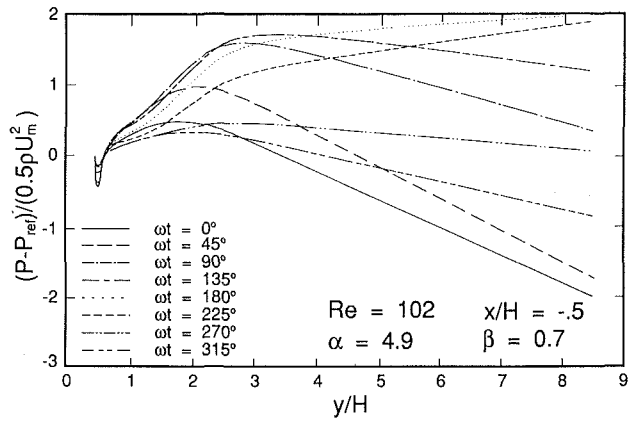

Fig. 4 Pressure variation on the upstream wall of the T-branch for Re = 102

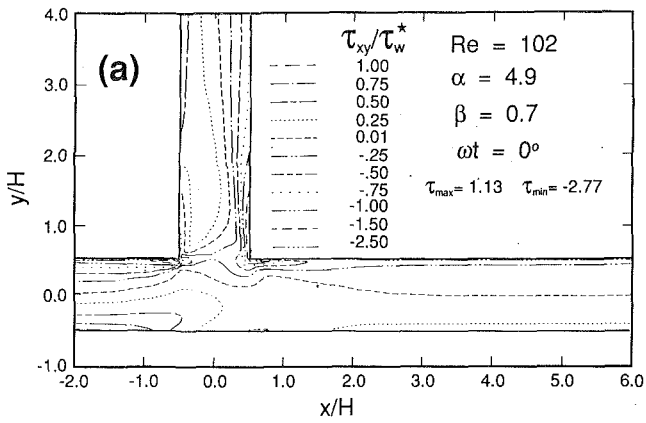

Fig. 5(a)

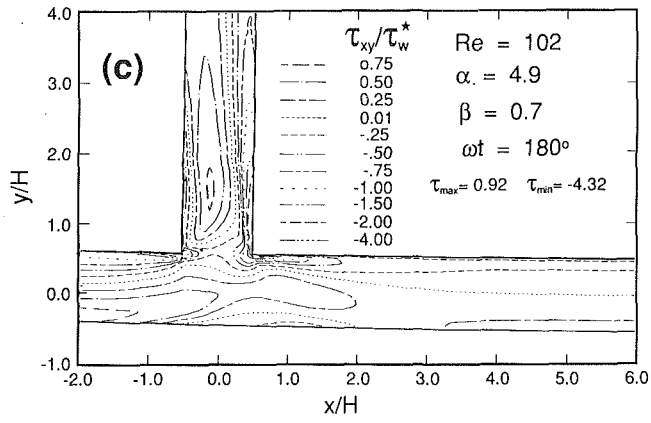

Fig. 5(c)

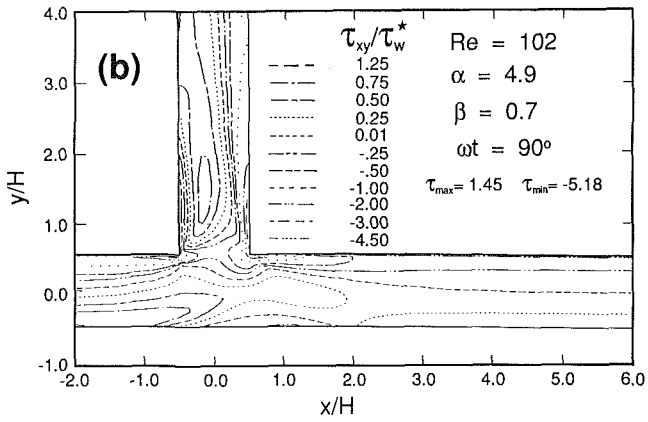

Fig. 5(b)

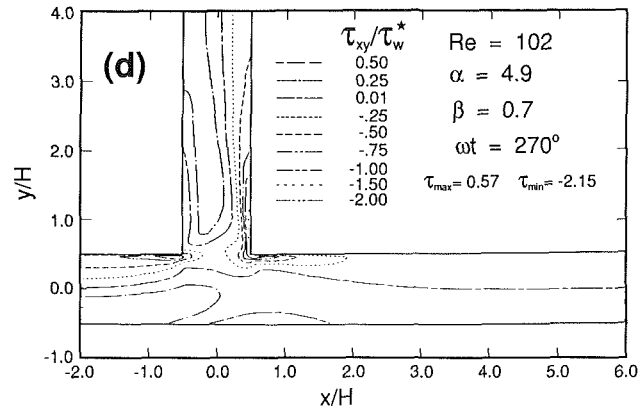

Fig. 5(d)

Fig. 5(*a–d*) Contours of nondimensional shear stress for Re = 102, α = 4.9, and β = 0.7

Table 1 Variation of the computed τ_{max} and τ_{min} in a cycle

Re	α	β	ωt =	0°	45°	90°	135°	180°	225°	270°	315°
38	4.1	0.7	τ_{max}	1.12	1.45	1.46	1.21	0.81	0.56	0.51	0.73
			τ_{min}	−1.58	−2.21	−2.91	−2.78	−2.19	−1.52	−0.94	−1.05
102	4.9	0.7	τ_{max}	1.13	1.45	1.45	1.22	0.92	0.71	0.57	0.74
			τ_{min}	−2.77	−3.94	−5.18	−5.12	−4.32	−3.23	−2.15	−2.10

Uncertainty in Re = ±2. Uncertainty in α = ±0.2.
Uncertainty in β = ±0.03. Uncertainty in τ_{max} and τ_{min} = ±0.05.
For all the uncertainty estimates, the assumed odds were 20:1

for Re = 38. Identifying these high and low shear stress zones are of great interest, since it is known that hemolysis may occur in zones of high shear stress with the undesirable release of hemoglobin in the blood stream. At the same time, coagulations may form in the low stress regions by the entrained platelets, red cells and lipoids which result in the establishment of atherotic plaques and thrombi. In making these general statements, it should be noted that the shear stress patterns are greatly influenced by the geometry of the arterial branch (radius of curvature of the branch) and flow conditions (Re and β).

The wall shear stress variations on the top and bottom walls of the main duct are presented next. The case of Re = 102 is only discussed due to its similarity to the case of Re = 38. The distribution of the computed and measured shear stresses (which are nondimensionalized by τ_w^*) on the two walls of the main duct are shown in Fig. 6. The symbols represent the estimated experimental values, whereas different types of lines are used for numerical predictions. Close to the inlet plane ($x/H < -2$), the absolute values of the computed shear stresses on the two walls at a given phase angle are nearly equal. However, as the fluid approaches the upstream edge of the bifurcation ($x/H = -0.5$), the absolute value of the shear stress on the top wall of the main duct monotonically increases, while the opposite behavior is observed on the bottom wall. This is due to the high value of the dividing flow rate ratio (β) which causes the boundary layer on the top wall to be much thinner than the one which has developed on the bottom wall. This trend is also exhibited by the measured stresses at the upstream edge. The flow separates on the bottom wall of the main duct and the values of computed wall shear stress in the separated zone vary between −0.4 and +0.4 in a cycle. The mismatch between the experimental and computed values in the range $0 < x/H < 1$ is mainly due to the poor performance of the computational technique in the separated zones (as high as 20 percent when compared to LDA measured values). High values of shear stress are observed at the trailing edge of the bifurcation which behaves very similar to a stagnation point.

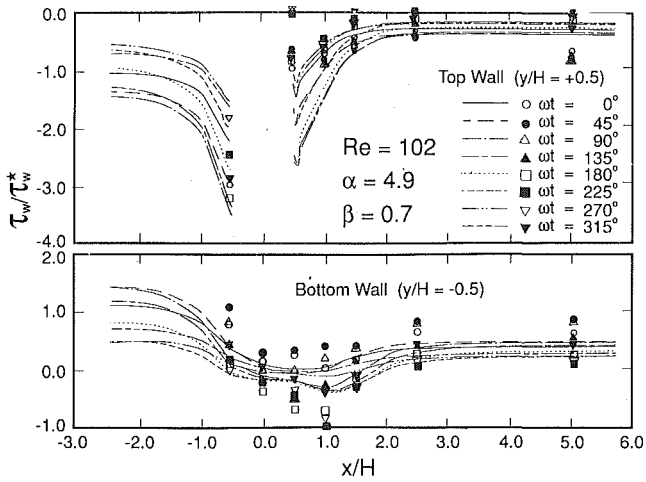

Fig. 6 Comparison of computed and measured wall shear stress distribution in the main duct for Re = 102 (uncertainty in measured wall shear stresses is ±0.03, in x/H = ±0.015 at 20:1 odds)

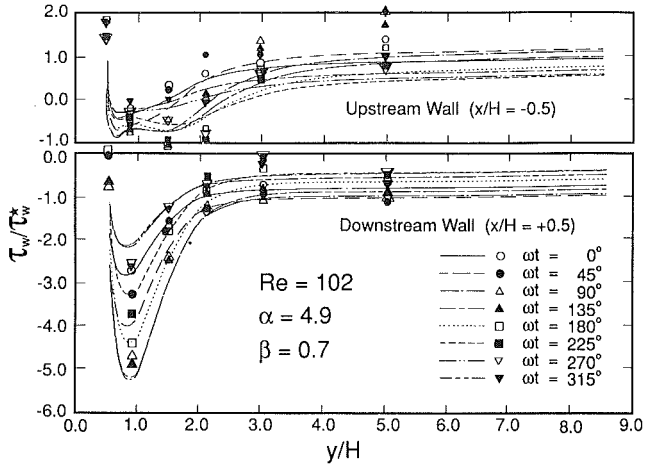

Fig. 7 Comparison of computed and measured wall shear stress distribution in the T-branch for Re = 102 (uncertainty in measured wall shear stresses is ±0.03, in y/H = ±0.015 at 20:1 odds)

Downstream of the $x/H = 2$ station, the shear stresses on both walls assume constant and nearly equal values (absolute value) as the flow approaches the fully developed oscillatory state. Finally, it should be noted that steady-state wall shear stress distribution is such that it is equal to -1 and $+1$ on the top and bottom walls at the inlet plane, respectively. Far downstream in the main duct, it is equal to $\pm(1-\beta)$ on the walls.

The comparison of the computed and experimental shear stresses on the two walls of the T-branch is presented in Fig. 7. The values of nondimensional shear stress within the separated zone which is formed on the upstream wall vary between -1 and $+1$ in a cycle. Very high values of shear stress are seen on the downstream wall of the branch in the range $0.5 < y/H < 1.5$. The minimum wall shear stress values shown in Table 1 were observed in this range. Specifically, they are located at $y/H = 0.8$. This phenomenon ensues from the presence of the dynamic recirculation zone on the upstream wall, which causes the velocity near the downstream wall to increase dramatically, thus resulting in the marked values of the wall shear stress. A similar less-pronounced behavior takes place on the top wall of the main duct at $x/H = 0.55$ (Fig. 6). Farther downstream of the $y/H = 3$ station, the shear stresses on both walls assume uniform values as the fully developed oscillatory state is reached.

Conclusions

From the results presented above, the following conclusions are drawn:

- The behavior of the two recirculation zones, which are formed on the bottom wall of the main duct and the upstream wall of the branch, is closely tied to the presence of adverse pressure gradients on the same two walls.
- Two zones of high shear stress are observed around the leading and trailing edges of the bifurcation. Regions of low shear stress occur in the same locations where the two dynamic recirculation zones are formed.
- The high dividing flow rate ratio and the presence of the two recirculation zones are directly responsible for the high wall shear stress values which are observed in the vicinity of the branch. In general, the computed and measured wall shear stresses exhibit qualitative agreement. The numerical technique performs poorly at the leading and trailing edges (zones of high shear stress), and inside the separation regions (zones of low shear stress). At other positions, poor correlation between the experimental and numerical results were also observed.

Acknowledgment

This research was supported by the CRAY Research, Inc., Mendota Heights, MN through a 1989 University Research & Development Grant Program. The financial support of the Department of Mechanical Engineering at Auburn University is also acknowledged.

References

Caro, C. G., Fitz-Gerald, J. M., and Schroter, R. C., 1971, "Atheroma and Arterial Wall Shear: Observation, Correlation and Proposal of a Shear Dependent Mass Transfer Mechanism for Atherogenesis," *Proceedings of the Royal Society of London*, Series B, Vol. 177, pp. 109–159.

Fry, D. L., 1969, "Certain Histological and Chemical Responses of the Vascular Interface to Acutely Induced Mechanical Stress in the Aorta of the Dog," *Circulation Research*, Vol. 24, pp. 93–108.

Fung, Y. C., 1984, *Biodynamics: Circulation*, Springer-Verlag, New York.

Kawaguti, M., and Hamano, A., 1980, "Numerical Study on Bifurcating Flow of a Viscous Fluid. II. Pulsatile Flow," *J. Physical Society of Japan*, Vol. 49, pp. 817–824.

Khodadadi, J. M., Nguyen, T. M., and Vlachos, N. S., 1986, "Laminar Forced Convective Heat Transfer in a Two-Dimensional 90° Bifurcation," *Numerical Heat Transfer*, Vol. 9, pp. 677–695.

Khodadadi, J. M., Vlachos, N. S., Liepsch, D., and Moravec, S., 1988, "LDA Measurements and Numerical Prediction of Pulsatile Laminar Flow in a Plane 90-Degree Bifurcation," ASME *Journal of Biomechanical Engineering*, Vol. 110, pp. 129–136.

Liepsch, D., Moravec, S., Rastogi, A. K., and Vlachos, N. S., 1982, "Measurement and Calculations of Laminar Flow in a Ninety Degree Bifurcation," *J. Biomechanics*, Vol. 15, pp. 473–485.

Patankar, S. V., 1980, *Numerical Heat Transfer and Fluid Flow*, Hemisphere Publishing Co., Washington, DC.

Pedley, T. J., 1980, *The Fluid Mechanics of Large Blood Vessels*, Cambridge Univ. Press, UK.

Rodkiewicz, C. M., 1983, "Flow in Large Arteries," in *Arteries and Arterial Blood Flow*, ed. by Rodkiewicz, C. M., Springer-Verlag, Wien, pp. 327–411.

Y. Keren

G. A. Bemporad

H. Rubin

CAMERI-Coastal and Marine Engineering Research Institute,
Department of Civil Engineering,
Technion-Israel Institute of Technology,
Haifa 32000, Israel

Basic Experiments Related to the Advanced Solar Pond (ASP) Performance

This paper concerns an experimental evaluation of the basic aspects of operation of the advanced solar pond (ASP). Experiments were carried out in a laboratory test section in order to assess the feasibility of the density gradient maintenance in stratified flowing layers. The density stratification was caused by a non uniform distribution of temperatures in the flow field. Results of the experiments are reported and analyzed in the paper. Experimental data were used in order to calibrate the numerical model able to simulate heat and momentum transfer in the ASP. The numerical results confirmed the validity of the numerical model adopted, and proved the latter applicability for the simulation of the ASP performance.

1 Introduction

The conventional solar pond (CSP) is schematically shown in Fig. 1(*a*). It is a shallow water body which virtually provides a trap for solar radiation. The solar radiation is converted into thermal energy, which is accumulated in the bottom layers of the water body.

In the CSP we identify three major fluid layers as shown in Fig. 1(*a*):

—*surface layer*, which is completely mixed due to atmospheric effects, and subject to a washflow,

—*barring layer*, which is comprised of a stagnant fluid, and subject to a large stabilizing salinity gradient. It separates the thermal layer from the surface layer,

—*thermal layer*, which is fully mixed and subject to horizontal flow needed for the exploitation of the thermal energy accumulated in this layer.

It should be noted that there is no definite terminology referrring to the various fluids layers of the CSP. Some studies utilize the term upper convective zone (UCZ) or surface convective zone (SCZ) for the surface layer of the CSP. Some studies apply the term gradient zone (GZ), other apply the term nonconvective zone (NCZ) to the barring layer. Some studies apply the term storage zone (SZ), other apply the term lower convective zone (LCZ) for the thermal layer of the CSP. In our present study as well as the previous ones (Rubin and Bemporad, 1989a; 1989b; Rubin et al., 1988) we prefer to apply the terminology represented in the previous paragraph and Fig. 1(*a*) due to the concise names of the fluid layers which do not need to be abbreviated. We also could find some difficulties in applying the abbreviated terminology for different types of improved solar ponds.

In the advanced solar pond (ASP) (Osdor, 1984; Rubin and Bemporad, 1989a; 1989b), there is an additional stratified thermal layer as shown in Fig. 1(*b*). This layer is comprised of several sublayers. Each sublayer is equipped with injection and withdrawal ports. Therefore a multiselective injection and withdrawal procedure characterizes the ASP.

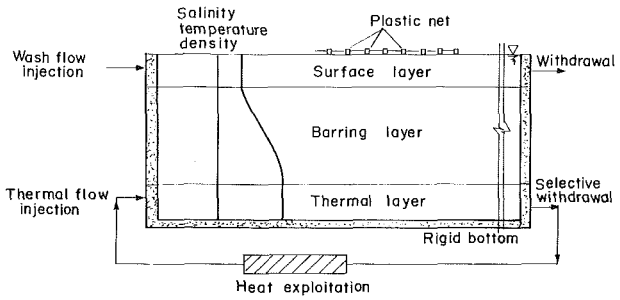

Fig. 1(*a*) The conventional solar pond (CSP)

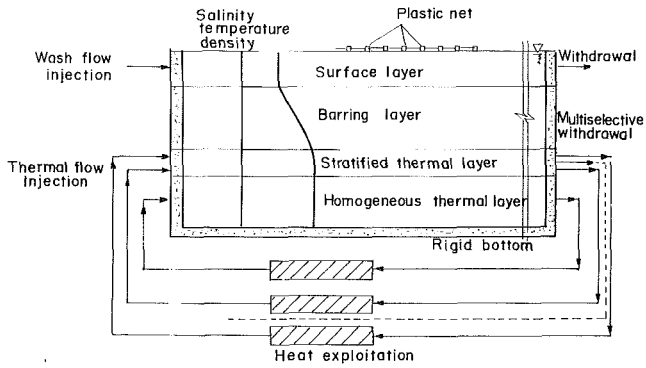

Fig. 1(*b*) The advanced solar pond (ASP)

Fig. 1 Basic configuration of major fluid layers in the solar pond

Contributed by the Fluids Engineering Division for publication in the JOURNAL OF ENGINEERING. Manuscript received by the Fluids Engineering Division October 4, 1980.

The idea of the ASP stems from the need to increase the efficiency of the CSP. The multiselective withdrawal system of the ASP should prevent any heat transfer from the thermal layer towards the solar pond surface. It should also enable catchment of some thermal energy accumulated in the barring layer by reducing the temperature existing at the top of the flowing thermal layer. Minimization of heat losses by diffusion from the thermal layer towards the surface of the CSP can be achieved by operating the CSP with a temperature gradient close to zero at the boundary between the thermal layer and the barring layer. However such a procedure means variable seasonal operating temperature. It also leads to comparatively large depths of the solar pond and thereby large quantities of thermal energy are caught in the barring layer of the CSP. It should also be noted that the zone of zero temperature gradient has a limited horizontal size. Catchment of some heat quantities from the barring layer of the CSP usually means a significant reduction of the operating temperature of the CSP thermal layer. Other advantages of the ASP include flexibility in operation as exemplified by our previous studies (Rubin and Bemporad, 1989a; 1989b)

Proper operation of the CSP depends on the ability to inject comparatively cold water at the solar pond entrance and to withdraw hot water at the pond exit, while preserving the stable density profile of the stagnant barring layer, which prevents thermohaline convection in the water body. Several studies (Hull, 1980; Joshi and Kishore, 1986; etc.) considered the basic theoretical aspects of the CSP performance. Beside all those aspects, in the ASP all issues associated with the stable nonuniform density distribution in the flowing stratified thermal layer should be studied. The major issue refers to the ability to generate and preserve the structure of such a flowing layer. In the present study we report on the first stage of the evaluation of such a capability. We utilize an experimental setup in which the density stratification in the flowing layer is induced by a stabilizing nonuniform distribution of temperature. In order to minimize mixing effects in the flowing layer it is designed to be subject to smooth laminar flow. In the following sections we describe the experimental setup and the performance of the experiments. Later we analyze the experimental results and utilize them for the calibration and verification of the applicability of the numerical model developed in our previous studies (Rubin and Bemporad, 1989a; 1989b) for the simulation of the ASP performance.

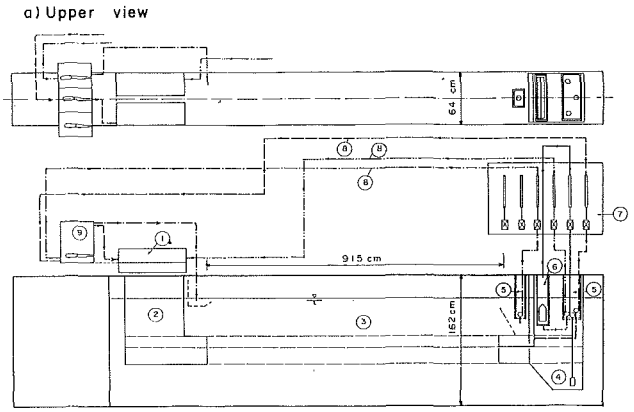

Fig. 2 Scheme and description of the experimental setup

2 Description of the Experimental Setup

The experiments were performed in the laboratory setup shown in Fig. 2. The major components of the experimental setup are described as follows:

1. *Mixing Unit.* Water of different temperature is introduced into this Unit where the multiselective injection is prepared. Each port sets the selected temperature to provide the profile in which density decreases upwards.

2. *Entrance Unit.* From the Mixing Unit the flowing thermal sublayers are injected to the Entrance Unit. This device provides a mechanism creating the most appropriate velocity distribution in the water body. In order to avoid turbulent mixing and instabilities of the Kelvin-Helmoltz type in the flow field, a laminar profile with no inflexion points was selected for all experiments. The Unit has 17 entrance ports to regulate the entrance of each sublayer into the channel test section. The upper and lower ports are 5 cm wide, other ports are 2 cm wide.

Nomenclature

C_p = specific heat, $JKg^{-1}\,°C^{-1}$
d = thickness of the stratified thermal layer, m
D = thickness of the test channel, m
g = gravitational acceleration, ms^{-2}
h = distance between the channel bottom and the surface layer, m
H = depth of the surface layer, m
K = coefficient, *dimensionless*
L = characteristic buoyancy length of the stratified layer, m
Q = flow-rate of the stratified layer, m^3s^{-1}
$Q^{(T)}$ = flow-rate of the surface layer, m^3s^{-1}
T = temperature, °C
$T^{(T)}$ = temperature of the surface layer, °C
T_{atm} = atmospheric temperature, °C
u = flow velocity, ms^{-1}
u_L = flow velocity at the left side of the test section, ms^{-1}
u_R = flow velocity at the right side of the test section, ms^{-1}
U_{max} = flow velocity at the centre of the stratified layer, ms^{-1}
x = horizontal coordinate, m
y = vertical coordinate, m
Y = local vertical coordinate, m
Z = lateral coordinate, m
w = width of the test section, m
α = ratio between shear stresses, *dimensionless*
ϵ = portion of heat lost in the test section, *dimensionless*
κ = heat diffusivity, m^2s^{-1}
μ = viscosity, Pas
ρ = density, Kgm^{-3}
$\rho_{(av)}$ = average density of the stratified layer, Kgm^{-3}
τ = shear stress, Pa
T_w = shear stress expected at a rigid boundary, Pa
τ_B = shear stress at the bottom of the stratified flowing layer, Pa
τ_L = shear stress at the left side of the test section, Pa
τ_R = shear stress at the right side of the test section, Pa
τ_T = shear stress at the top of the stratified flowing layer, Pa

Subscripts and Superscripts

$(\,)_{av}$ = average value
$(\,)_{en}$ = entrance value
$(\,)_{ex}$ = exit value
$(\,)^T$ = relative to surface layer

3. *Test Section.* The velocity and temperature field are set when the flowing sublayers enter the Test Section. The Test Section reproduces the flow conditions simulating a real size pond. Along the length of the Test Section temperatures and velocities are constantly monitored. The length, depth and width of the Test Section are 915 cm, 162 cm, and 64 cm, respectively. The walls of the Test Section are insulated.

4. *Exit Unit.* This unit is designed to perform the multi-withdrawal from the Test Section. It avoids the development of disturbances in the water body which can lead to destruction of the velocity and temperature profiles.

5. *Pumping Unit.* This device pumps water from the Test Section and diverts it to several flowmeters.

6. *Cooling Unit.* Excess heat is removed from the fluid in the Cooling Unit.

7. *Flowmeters.* They give on-line measurements of the discharge in the various sublayers of the stratified flowing layer.

8. *Pipelines.* They return the cooled fluid to the Entrance Unit.

9. *Heating Unit.* This Unit provides the required thermal energy to the fluid as needed for the creation of the temperature gradient in the Mixing Unit.

Several preliminary operations were performed in the laboratory to test and calibrate the apparatus. Finally, experiments were carried out to investigate the actual feasibility of the multiselective injection and withdrawal, and density gradient maintenance in the ASP.

3 Description of the Numerical Model

The theoretical assumptions regarding the ASP and the derived numerical model are fully described in previous papers (Rubin and Bemporad, 1989a; 1989b). In this contest only the basic aspect will be recalled. Some modifications of the model are introduced, as here we refer to a single component generating the density gradient. We also note that the boundary conditions of the system are different from those typical to the ASP.

In the previous studies (Rubin and Bemporad, 1989a, 1989b) we considered the ASP as an infinitely wide water body. In such a manner side wall effects were neglected, and transport phenomena were simulated by making use of a two-dimensional model. In this study the test section is modeled as a finite rectangular duct. The wall effects are considered in the simulation of heat and momentum transfer by using a three-dimensional model.

The numerical model of the experiments is based on the following scheme: four major fluid layers are identified in the water body, as shown in Fig. 3: a *flowing surface layer*, *a barring layer*, a *stratified flowing thermal layer*, and a *stagnant bottom*. The latter is adjacent to the stratified layer, and completes the test section scheme.

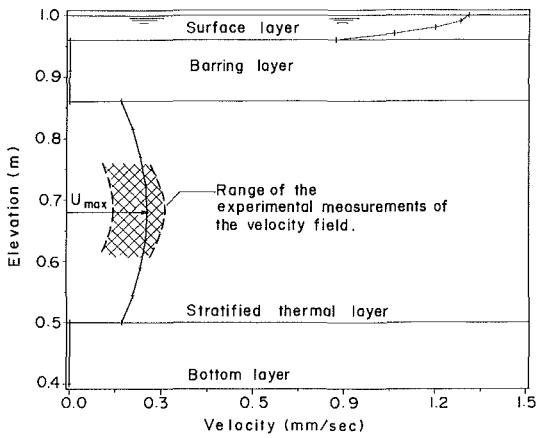

Fig. 3 Configuration of the experimental flow field (thermal layer discharge 195.2 l/hr/m; surface layer discharge 111.8 l/hr/m)

The surface thermal layer. This layer is subject to atmospheric effects and the wash flow; $Q^{(T)}$ is the surface flow-rate. Some studies (Hull, 1989; Atkinson and Harleman, 1983) refer to mixing effects generated by the atmosphere. Such effects cause the surface flow velocity to be assumed as being almost uniformly distributed. In the particular laboratory conditions such effects can be neglected, and velocity is assumed to have a laminar flow distribution. Evaporation is ruled out in this study because of the limited length and no direct exposure to the atmosphere of the test section. Therefore $Q^{(T)}$ is constant.

The barring layer. This layer is stagnant. The density gradient existing in this layer insulates the adjacent stratified thermal layer from the mixing effects existing in the ASP surface layer.

The stratified thermal layer. This layer is subject to horizontal flow, and its stable density gradient avoids the formation of circulating currents of thermal convection. The flow in this layer is carried out by the injection and withdrawal ports of the Entrance and Exit Units. The thickness of the stratified thermal layer d should probably be determined by the density gradient and flow conditions.

The bottom layer. This layer is stagnant and subject to constant temperature. The spatial transition from a flowing fluid layer to a stagnant one in a stratified flow field is associated with the formation of circulating flow. Therefore, such a flow is extended between the vertical walls representing the entrance and exit of the test section. However, as a first order approximation of the flowing layer description, the circulating currents can be ignored as such currents are smaller in an order of magnitude than the major flow of the fluid layer. The present study applies such an approximation. However, we consider that at the top and bottom of the stratified thermal layer a certain slip velocity takes place, namely the flow velocity of the stratified thermal layer does not vanish at the top and bottom of that layer.

The shear stress distribution in the stratified thermal layer is assumed to be as follows

$$\tau_{xy}=\tau_B - Y(\tau_B-\tau_T)/d; \quad \tau_{xz}=\tau_R-Z(\tau_R-\tau_L)/w \qquad (1)$$

where τ_B and τ_T are shear stresses at the bottom and top of the stratified layer, respectively; Y is a local vertical coordinate, namely $Y = 0$ at the bottom of the layer, and $Y = d$ at the top of the layer; τ_R and τ_L are shear stresses at the right and left sides of the stratified layer, respectively; Z is a lateral coordinate, namely $Z = 0$ at the extreme right of the layer, and $Z = w$ at the extreme left of the layer, w is the width of the test section.

According to some studies (Ippen and Harlemann, [1951]) we may assume that if the stratified thermal layer is subject to a continuous laminar velocity profile then the following condition is satisfied

$$\tau_B=\alpha\tau_w; \quad \tau_T= - \alpha\tau_w; \quad \alpha\simeq 0.62 \qquad (2)$$

where τ_w is the shear stress expected at the bottom of the thermal layer provided that it is a rigid boundary; α is a coefficient. Expressions (2) imply that a certain slip velocity takes place at the top and bottom of the stratified thermal layer, as stated in the preceding paragraphs.

In the lateral direction the no-slip condition at the rigid boundaries implies that the velocity vanishes at these locations, namely

$$u_R=u_L=0 \qquad (3)$$

where u_L and u_R are velocities at the left and right sides of the test section.

Considering laminar flow of the thermal layers, an integration of (1), after introducing the conditions (2) and (3), yields the following velocity profile

$$u(Y, Z) = U_{\max}\left[\frac{2}{3} + \frac{4}{3d}\left(Y - \frac{Y^2}{d}\right)\right]\left[\frac{4}{w}\left(Z - \frac{Z^2}{w}\right)\right] \quad (4)$$

where

$$U_{\max} = \frac{27}{16}\frac{Q}{dw} \quad (5)$$

In expression (5) $U_{\max}$ is the velocity existing at the center of the stratified layer; Q is the layer discharge defined as follows

$$Q = \int_0^w \int_0^d u(Y, Z)\,dY\,dZ \quad (6)$$

In the surface layer condition (2) is substituted by

$$\tau_B^{(T)} = \alpha\tau_w^{(T)}; \quad \tau_T^{(T)} = 0; \quad \alpha \simeq 0.62 \quad (7)$$

where the superscript $^{(T)}$ refers to the surface layer.

The resulting velocity profile is obtained as follows

$$u^{(T)}(Y, Z) = U_{\max}^{(T)}\left[\frac{2}{3} + \frac{2}{3H}\left(Y - \frac{Y^2}{2H}\right)\right]\left[\frac{4}{w}\left(Z - \frac{Z^2}{w}\right)\right] \quad (8)$$

where

$$U_{\max}^{(T)} = \frac{27}{16}\frac{Q^{(T)}}{Hw} \quad (9)$$

In expression (8) $U_{\max}^{(T)}$ is the velocity existing at the top center of the surface thermal layer, $Q^{(T)}$ is the surface layer discharge defined as follows

$$Q^{(T)} = \int_0^w \int_0^H u^{(T)}(Y, Z)\,dY\,dZ \quad (10)$$

Figure 4 reproduces the velocity distribution adopted in the numerical simulation of the laboratory experiments. The velocity profile of the stratified thermal layer stems from equation (4). Velocity profile of the surface layer stems from equation (8).

A three-dimensional modeling approach is employed to simulate the heat transport phenomenon in the test section. It is analyzed by assuming that, in each elementary fluid volume, heat convection is the dominant transport mechanism in the longitudinal direction, and molecular heat diffusion is the dominant transport mechanism in the vertical and lateral direction. As the barring layer is stagnant, in this layer only molecular diffusion of heat takes place. Mixing effects in the surface layer and intimate contact with the atmosphere cause its temperature to be uniformly distributed in the vertical direction. Some losses into the atmosphere are to be considered.

Formulating the assumptions represented in the preceding paragraph we obtain the following expression for the surface, barring, stratified thermal and bottom layers, respectively

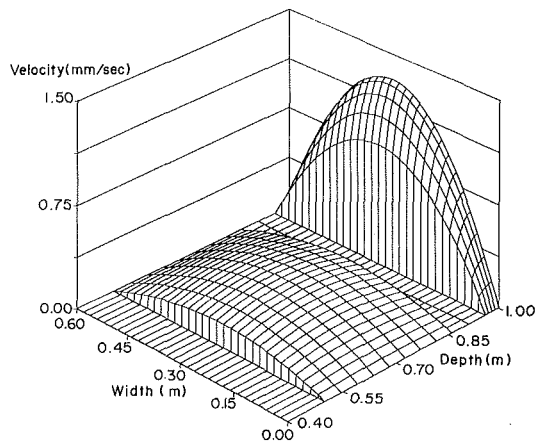

Fig. 4 Velocity distribution in the test section (thermal layer discharge 121.0 l/hr; surface layer discharge 69.3 l/hr)

$$\rho C_p H u^{(T)}\frac{\partial T^{(T)}}{\partial x} = \kappa\rho C_p H\frac{\partial^2 T^{(T)}}{\partial z^2} - \left(\kappa\rho C_p\frac{\partial T}{\partial y}\right)_{(y=h)} - a(T^{(T)} - T_{\text{atm}}) \quad (11)$$

$$\frac{\partial^2 T}{\partial y^2} + \frac{\partial^2 T}{\partial z^2} = 0 \quad (12)$$

$$\frac{u}{\kappa}\frac{\partial T}{\partial x} = \frac{\partial^2 T}{\partial y^2} + \frac{\partial^2 T}{\partial z^2} \quad (13)$$

$$\frac{\partial^2 T}{\partial y^2} + \frac{\partial^2 T}{\partial z^2} = 0 \quad (14)$$

where x is the longitudinal coordinate, z is the transverse coordinate, y is the vertical coordinate, h is the elevation of the surface layer bottom, H is the depth of the surface layer, $u^{(T)}$ is the velocity of the surface layer averaged in the vertical direction, $T^{(T)}$ is the surface layer temperature, C_p is the specific heat, T_{atm} is the atmospheric temperature, κ is the heat diffusivity, a is a constant representing losses into the atmosphere. The temperature $T^{(T)}$ of the surface layer is assumed to be uniformly distributed in the vertical direction. Some studies (Atkinson and Harleman, 1983 et al.) give some analytical expressions for the computation of heat exchanges in the surface layer due to evaporation, conduction and radiation. In this study the parameter a stems from calibration of the experimental data.

Due to the thermal capacity of test section body when compared with the heat transfer phenomena in the experiments, the bottom of the test section is assumed to be at constant temperature. There was almost no need to control this temperature. The boundary conditions at the side walls are assumed to be of the radiative type, in order to consider some losses into the atmosphere. These assumptions are represented as follows

$$\left[b\frac{\partial T}{\partial z} + c\right]_{(z=0;\ z=w)} = 0; \quad T_{(y=0)} = \text{const} \quad (15)$$

where b and c are constant. Expressions (11)–(15) are employed hereafter in order to develop a three-dimensional numerical model of heat transfer in the ASP simulator. Expressions (12)–(14), represent a set of parabolic partial differential equations which should be subject to boundary conditions with regard to the y and z directions, and initial conditions with regard to the x coordinate. The boundary conditions of the system are represented by expressions (11) and (15). The initial conditions of the system are represented by the imposed temperature profile at the entrance of the test section. We applied a finite difference numerical model with a variable mesh size in the y direction in order to approximate the set (12)–(14). Then we applied the ADI method in two successive schemes in order to obtain the numerical simulations. The first scheme yields the temperature distribution at the intermediate coordinate x^* by applying an implicit scheme in the y-direction. In the next step we calculate the temperature at $x + Dx$ by applying an implicit scheme in the z-direction. The variable mesh size was chosen after several attempts in order to compromise between accuracy of the solution and computation time. The size assumed in this study, for the two and three-dimensional models, is sufficient for the proper integration of the differential equations. Further refinement of the mesh had no effect on the accuracy and stability of the solution.

4 Description of the Experiments

Several tests and calibration procedures were carried out in the laboratory to calibrate the experimental setup. Finally, some experiments were performed to investigate the feasibility of an adverse temperature gradient maintenance in the thermal

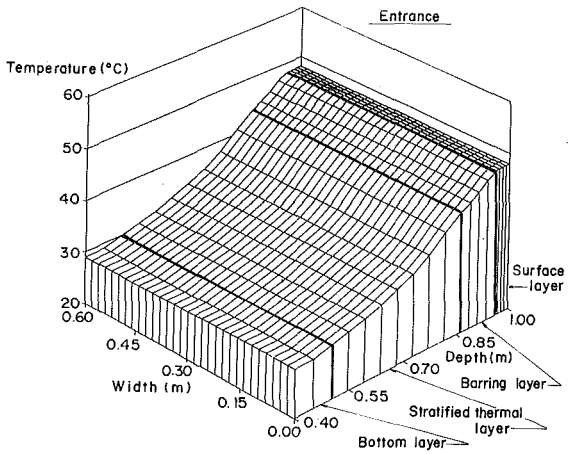

Fig. 5(*a*) Thermal layer discharge 121.0 l/hr; surface layer discharge 69.3 l/hr

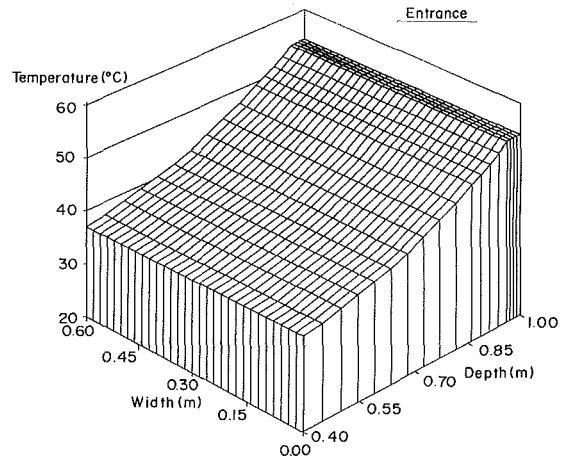

Fig. 5(*b*) Thermal layer discharge 143.6 l/hr; surface layer discharge 63.0 l/hr

Fig. 5 Temperature distribution in the test section

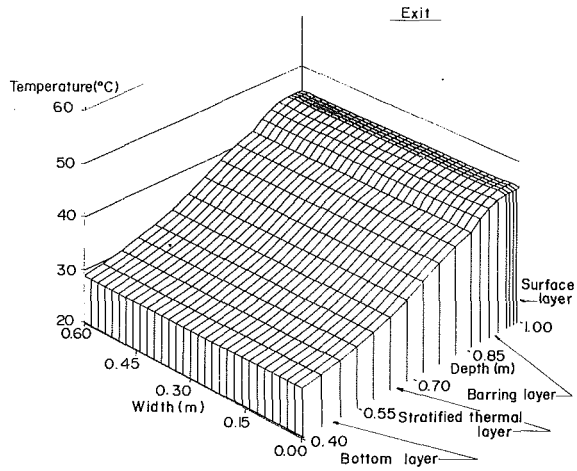

Fig. 6(*a*) Thermal layer discharge 121.0 l/hr; surface layer discharge 69.3 l/hr

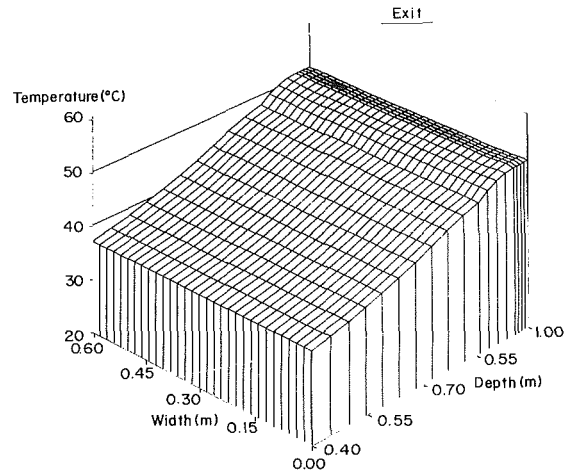

Fig. 6(*b*) Thermal layer discharge 143.6 l/hr; surface layer discharge 63.0 l/hr

Fig. 6 Temperature distribution in the test section

layers. The set of experiments analyzed herein is comprised of three runs. For each run different discharges in the surface and stratified thermal layer were assumed, and different initial temperature gradients were created.

In all the experiments, temperatures were measured at intervals of 5 cm along the vertical coordinate y. Four cross-sections were positioned at $x = 0, x = 1.63, x = 3.03$ and $x = 5.25$ respectively.

The experimental uncertainty in the temperature measurements was $\pm 0.25°$ C; uncertainty in the longitudinal and vertical displacements was ± 1 mm.

The velocity distribution was measured by following the movement of dye injected at a representative cross-section. Photographs were taken at different time intervals to assess the dye dispersion and displacement. Photographs 1–3 visualize that technique. These photos indicate that some circulating flows take place at the bottom and top of the stratified thermal layer. However, as stated in section 3, such flows were ignored in our theoretical calculations.

5 Results and Discussion

Numerical integration of expressions (11)–(15) was performed. In each numerical simulation the initial conditions, namely the temperature profile at the test section entrance, were set according to the appropriate values corresponding to the experimental run. Figure 5(*a*) and Fig. 5(*b*) represent such profiles related to two different sets of flow-rates of the surface layer and the thermal layer. Figure 6(*a*) represents the exit temperature profile associated with a set of flow-rates identical to that of Fig. 5(*a*). Figure 6(*b*) represents the exit temperature profile associated with a set of flow-rates identical to that of Fig. 5(*b*). According to Fig. 5 the entrance temperature profile is uniformly distributed in the lateral direction. Due to the three-dimensional nature of the velocity profile and the insulation of the side walls the numerical model predicts a certain temperature change at the side walls along the test section as indicated by Fig. 6. There is also a certain decrease in the temperature between the entrance and exit of the test section due to heat losses and some changes in the temperature distribution.

We performed measurements of the temperature profile at the plane $z = 0.30$ m representing the center of the test section. The experimental results referring to different flow-rates and locations along the test section are shown in Figs. 7 and 8. In Fig. 7 we compare the experimental measurements with the temperature profiles predicted by the three-dimensional model of the present study and the two-dimensional model presented in our previous studies (Rubin and Bemporad, 1989a; 1989b) which considered transport phenomena in the ASP subject to field conditions.

In the two-dimensional model we considered that the velocity profile is that typical to the plane Poiseuille flow, which is

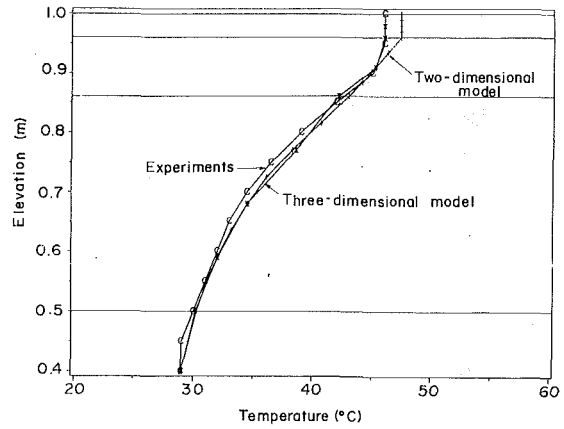

Fig. 7(*a*) $x = 1.63$ (thermal layer discharge 195.2 l/hr/m; surface layer discharge 111.8 l/hr/m)

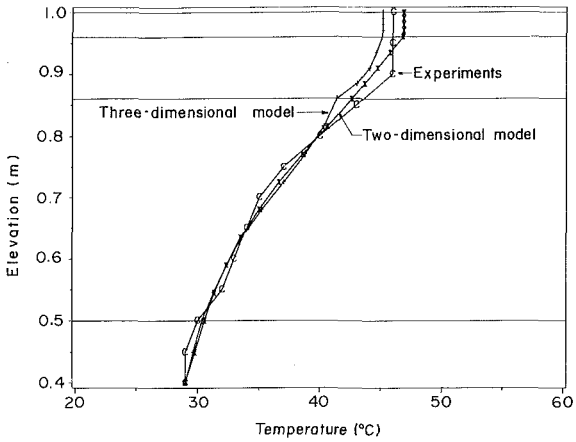

Fig. 7(*b*) Exit (thermal layer discharge 195.2 l/hr/m; surface layer discharge 111.8 l/hr/m)

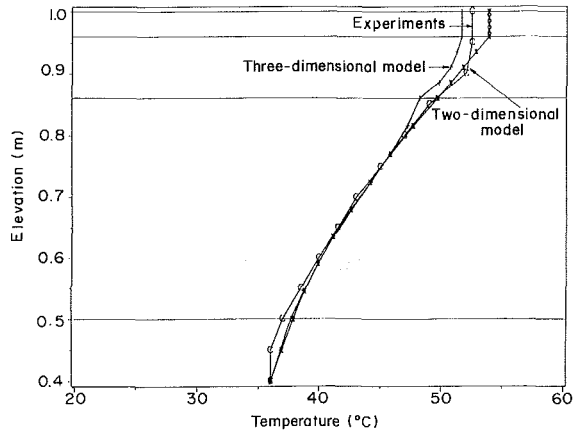

Fig. 7(*c*) Exit (thermal layer discharge 182.2 l/hr/m; surface layer discharge 101.6 l/hr/m)

Fig. 7 Comparison of the temperature distribution in the test section for the two and three-dimensional models (Uncertainty in temperature = ±0.25°C; in elevation = ± 1 mm)

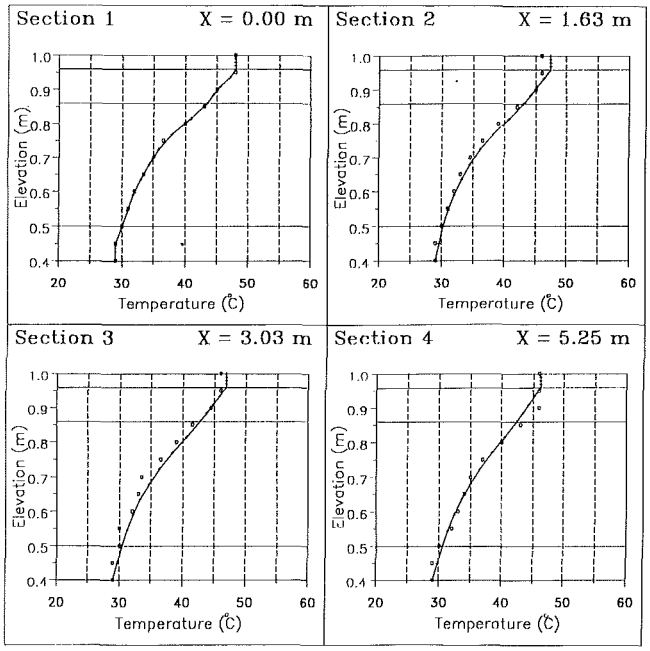

Fig. 8(*a*) Two-dimensional model (thermal layer discharge 195.2 l/hr/m; surface layer discharge 111.8 l/hr/m)

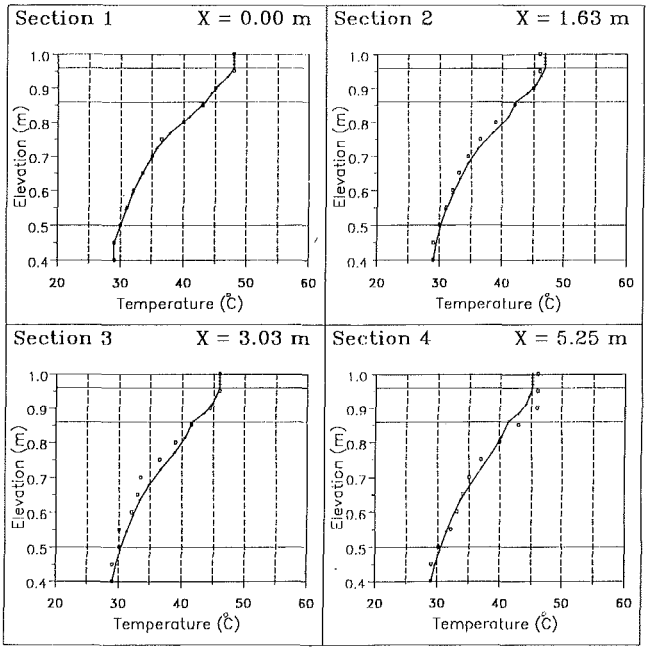

Fig. 8(*b*) Three-dimensional model (thermal layer discharge 195.2 l/hr/m; surface layer discharge 111.8 l/hr/m)

Fig. 8 Temperature distribution along the test section for the experiments and numerical models (Uncertainty in temperature = ± 0.25°C; in elevation = ± 1 mm)

conceptually not appropriate for the experimental set-up of the present study. However, at the center of the set-up this model provides temperature profiles which are very similar to those of the three dimensional model as well as the experimental results.

Differences between the predictions of the three-dimensional model and the two-dimensional model increase at the surface layer and the upper part of the barring layer. As indicated by Fig. 7(*a*) the three-dimensional model predictions are in better agreement with the experimental results. However, in Figs. 7(*b*) and 7(*c*) the experimental results agreement with both model predictions are almost identical. More precisely, Figs. 7(*b*) and 7(*c*) show that an application of the three dimensional model is superior than that of the two dimensional model at the bottom of the test section, whereas an application of the two dimensional model is superior at the top of the test section. The phenomenon that, in some locations of the experimental

setup, the apparently less sophisticated model provides better information probably stems from some lack of our knowledge with regard to surface and boundary effects which were not introduced into our calculations. Anyhow, it seems that, generally, both theoretical models may provide adequate predictions of the temperature distribution in the experimental setup. Figure 8 shows the variation of the temperature profile along the center plane of the test-section. In Fig. 8(*a*) the experimental measurements are compared with the two-dimensional model predictions. In Fig. 8(*b*) the experimental measurements are compared with the predictions of the three dimensional model. When utilizing the numerical models in order to obtain the theoretical predictions represented in Fig. 8 we considered negligible heat losses into the atmosphere and the side walls of the experimental setup. The velocity field stemming from the multiselective injection and withdrawal system was analyzed by tracing the variation of the injected dye pattern as shown in photographs 1–3. These photographs show the location of the dye front at different consecutive time periods. By calculating the velocity profile from such measurements the velocity distribution in a range of ± 10 percent was determined. Beside comparing experimental measurements of velocity and temperature distributions with those predicted by the theoretical models subject to best fitting of the temperature profiles. The part of heat lost in the experimental system is defined as follows

$$\epsilon = \int_0^w \int_0^D uC_p[\rho_{en}T_{en} - \rho_{ex}T_{ex}]dydz \Big/ \int_0^w \int_0^D uC_p\rho_{en}T_{en}dydz \quad (16)$$

where the subscripts $_{ex}$ and $_{en}$ refer to exit values and entrance values, respectively; D is the total depth of the test section. Calculations based on the experimental results showed that heat losses were between 4 and 6 percent. Best curve fitting of the three and two dimensional model predictions were obtained by assuming no heat loss into the atmosphere and about 2–3 percent loss of heat through the bottom of the test section. The two-dimensional model eventually does not allow heat losses through the side walls. We may summarize that the three dimensional model as well as the two dimensional model applied in this study and in our previous studies (Rubin and Bemporad, 1989a; 1989b), respectively, may be useful for the prediction of flow and density distributions in a stratified flowing layer generated by a multiselective and withdrawal system. However, it should be taken into account that the ASP is a double diffusive system in which two components, temperature and salinity, determine the density distribution in the flow field. We have also to consider that the two and three dimensional models referred in this study assume flow only in the horizontal direction, molecular heat diffusion only in directions perpendicular to the flow velocity, and heat convection only in a direction parallel to the flow velocity.

It should be noted that in the present study we made all efforts to create continuous velocity profiles which also fit the linear and continuous shear stress distribution represented by (1). However, some more studies considering more complicated velocity profiles are planned for the future, in order to provide good basis for the possible practical implications relevant to the ASP functioning.

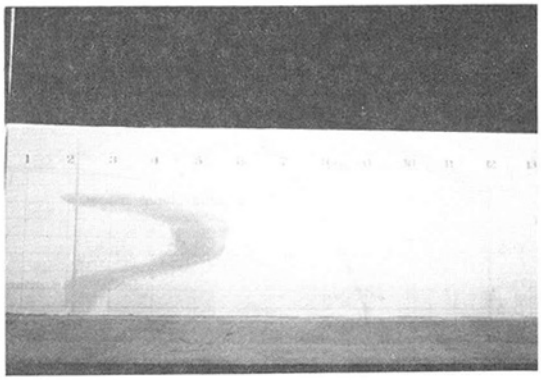

Photo n.1: Dye pattern 10 minutes after injection (thermal layer discharge 195.2 l/hr/m)

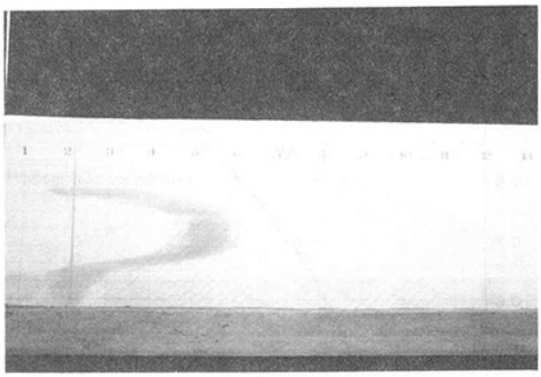

Photo n.2: Dye pattern 15 minutes after injection (thermal layer discharge 195.2 l/hr/m)

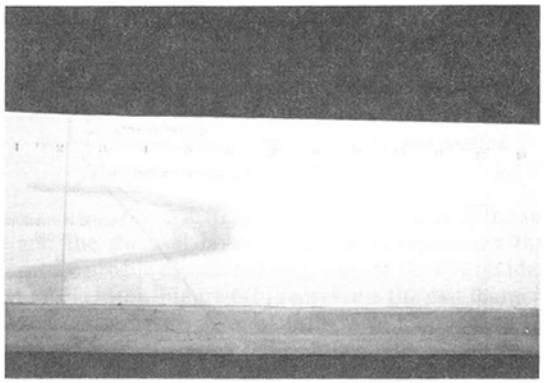

Photo n.3 Dye pattern 20 minutes after injection (thermal layer discharge 195.2 l/hr/m)

6 Summary and Conclusions

The experiments performed in the framework of the present study indicated that it is possible to generate and control a horizontal flow in a density stratified fluid layer. Density stratification was created in this study by non-uniform distribution of the temperature in the flow field.

The experimental results were utilized in order to calibrate and verify the applicability of the ASP modelling procedure developed in previous studies (Rubin and Bemporad, 1989a; 1989b). According to that procedure the flow in the water body is performed only in the horizontal direction, molecular heat diffusion is carried out only in the direction perpendicular to the horizontal flow velocity, heat convection is carried out only in direction parallel to the horizontal flow velocity. It is assumed that in the ASP the flow field is two dimensional. In the test section utilized in the present study the flow field was three dimensional. The boundary conditions of the test section were also different from those typical to the ASP. Therefore some modifications and changes were introduced into the two-dimensional original model developed in the previous studies. However it was found that the two-dimensional model as well as three-dimensional one could be utilized in order to predict transport phenomena in our experimental setup. Such phenomena in the ASP concern double diffusion of salinity and temperature. Therefore the present study should be extended

to double diffusive systems in order to provide more adequate information relevant to the ASP performance.

Acknowledgments

This study was supported by the Ministry of Energy and Infrastructure, Israel.

References

Atkinson, J. F., and Harleman, D. R. F., 1983, "A Wind Mixed Layer Model for Solar Ponds," *Solar Energy*, Vol. 31, p. 243.

Gariel, P., 1949, "Recherches Expérimentales sur l'écoulement de couches superposées de fluides de densités différentes," *La Houille Blanche*, Vol. 4, p. 56.

Hull, J. R., 1989, "Computer Simulation of Solar Pond Thermal Behavior," *Solar Energy*, Vol. 25, p. 33.

Ippen, A. T., and Harleman, D. R. F., 1951, "Steady State Characteristics of Subsurfae Flow," U.S. Nat. Bur. of Standards, Circ. 521, *Symp. on Gravity Waves*, p. 79.

Joshi, V., and Kishore, V. V. N., 1986, "Applicability of Steady State Equations for Solar Pond Thermal Performance Predictions," *Solar Energy*, Vol. II, p. 821.

Levin, O., and Elata, C., "Selective Flow of Density Stratified Fluid," Tech. Rept. No. 5/133/62, Dept. of Civil Eng., Technion, Haifa, Israel.

Osdor, A., 1984, "Method of Trapping and Utilizing Solar Heat," U.S. Patent No. 4,462,389.

Raymond, J. P., 1951 "Etude des courants d'eau boueuse dans les retenues," 4th Congress on Large Dams, *New Delhi, Trans.*, Vol. 4, p. R48.

Rubin, H., and Bemporad, G. A., 1989a, "The Advanced Solar Pond—Basic Theoretical Aspects," *Solar Energy*, Vol. 43, pp. 35–44.

Rubin, H., and Bemporad, G. A., 1989b, "Analysis of Turbulent Flow in Thermal Layers of the Advanced Solar Ponds (ASP)," *Solar Energy*, Vol. 43, pp. 25–33.

Rubin, H., Merchrez, Y., Keren, Y., and Bemporad, G. A., 1988, "Analysis of Transport Phenomena in the Advanced Solar Pond," *Proceedings of the Annual Meeting of the American Solar Energy Society*, M.I.T., Cambridge, Mass.

to double diffusive systems in order to provide more adequate information relevant to the ASP performance.

Acknowledgments

This study was supported by the Ministry of Energy and Infrastructure, Israel.

References

Atkinson, J. F., and Harleman, D. R. F., 1983, "A Wind Mixed Layer Model for Solar Ponds," *Solar Energy*, Vol. 31, p. 243.

Gariel, P., 1949, "Recherches Expérimentales sur l'écoulement de couches superposées de fluides de densités différentes," *La Houille Blanche*, Vol. 4, p. 56.

Hull, J. R., 1989, "Computer Simulation of Solar Pond Thermal Behavior," *Solar Energy*, Vol. 25, p. 33.

Ippen, A. T., and Harleman, D. R. F., 1951, "Steady State Characteristics of Subsurfae Flow," U.S. Nat. Bur. of Standards, Circ. 521, *Symp. on Gravity Waves*, p. 79.

Joshi, V., and Kishore, V. V. N., 1986, "Applicability of Steady State Equations for Solar Pond Thermal Performance Predictions," *Solar Energy*, Vol. II, p. 821.

Levin, O., and Elata, C., "Selective Flow of Density Stratified Fluid," Tech. Rept. No. 5/133/62, Dept. of Civil Eng., Technion, Haifa, Israel.

Osdor, A., 1984, "Method of Trapping and Utilizing Solar Heat," U.S. Patent No. 4,462,389.

Raymond, J. P., 1951 "Etude des courants d'eau boueuse dans les retenues," 4th Congress on Large Dams, *New Delhi, Trans.*, Vol. 4, p. R48.

Rubin, H., and Bemporad, G. A., 1989a, "The Advanced Solar Pond—Basic Theoretical Aspects," *Solar Energy*, Vol. 43, pp. 35-44.

Rubin, H., and Bemporad, G. A., 1989b, "Analysis of Turbulent Flow in Thermal Layers of the Advanced Solar Ponds (ASP)," *Solar Energy*, Vol. 43, pp. 25-33.

Rubin, H., Merchrez, Y., Keren, Y., and Bemporad, G. A., 1988, "Analysis of Transport Phenomena in the Advanced Solar Pond," *Proceedings of the Annual Meeting of the American Solar Energy Society*, M.I.T., Cambridge, Mass.

DISCUSSION

C. E. Nielsen.[1] The experiments reported in this paper were carried out, as the authors state, "to calibrate and verify the applicability of the ASP modeling procedure developed in previous studies (Rubin and Bemporad 1989a, 1989b)." That modeling procedure, as presented in the 1989a paper, involves calculations (*a*) relating to the flow in the "stratified thermal layer," (*b*) relating to the temperature distribution, (*c*) relating to the salinity distribution, and (*d*) relating to the pond performance, specifically the heat collected and temperature reached with a specified solar input. The 1989b paper is concerned with the effects of turbulence in the flow.

(*a*) For exploring the nature of the flow in the stratified thermal layer the present experiments have a serious limitation. They use a one component fluid stabilized by a temperature gradient, while the stratified flowing thermal layer in the proposed new type of solar pond is a two component system, stabilized by a salinity gradient strong enough to counterbalance the destabilizing temperature gradient. It is well known that the behavior of such double diffusive systems is very different from the behavior of one component systems. This discusser most heartily agrees with the authors' concluding statement that experiments should be extended to double-diffusive systems.

In a double-diffusive system it seems very likely, on the basis of a variety of observations relating to development of instabilities and growth of homogeneous internal zones in solar ponds, that separate flowing streams will remain separate and homogeneous and never merge into a smooth gradient. It should be noted that the stream stability criterion mentioned in the earlier theory paper (1989a, equation (2)) concerns only internal stability within a gradient region. It is well verified that at the boundary of a gradient region a much greater salinity gradient is required (Hull et al. 1989). What may happen if one establishes flows in a double diffusive system is that the separate flowing layers will remain homogeneous, separated by thin transition layers with strong gradients through which there is rapid conduction of heat and rapid diffusion of salt.

Incidently the flow rates used in the experiment are less than 0.3 mm/s (Fig. 3) whereas the earlier modeling paper (1989a, Fig. 2) assumed 1.5 mm/s. The authors do not discuss these magnitudes, and it may be asked whether there are scaling arguments by which 0.3 mm/sec flow demonstrates the feasibility of the assumed 1.5 mm/s.

(*b*) The important energy input for a solar pond is the solar input. Since there is no corresponding input in the experiment, it is not clear that the experiment verifies the applicability of the thermal modeling procedure in a very useful way, despite the verification that heat conduction and convection calculations yield a reasonable prediction of observed temperatures.

Since the motivation for this paper is to provide experimental support for modeling done previously, it is essential to relate it to that previous work. Unfortunately, a careful study of 1989a indicates that the modeling with solar input included is done incorrectly there. This is not the place to discuss that paper in detail, but we observe simply that in 1989a, Fig. 3, a straight line temperature profile in the gradient region is postulated as an "initial condition." A straight line is impossible, because this is a calculation of steady-state conditions with $200 W/m^2$ average solar input at the surface. The region in question is not flowing, and in steady state it necessarily must have a curved temperature profile as required for dissipating by heat conduction the energy deposited by absorbed radiation. This is not a trivial question; the effect of the curvature on energy loss from the pond is substantial.

(*c*) and (*d*) This experiment was not designed to give any new information about salinity distribution or pond thermal performance. However, in view of the difficulty discussed under (*b*), even the theoretical conclusions about pond performance and the comparative output of "conventional" and "advanced" solar ponds obtained in 1989a cannot be viewed as demonstrated, and new work is needed.

It may be useful for reference to compare another calculation of pond output with the results of 1989a, even though performance was not directly involved in the experiments under discussion. Pond output depends critically upon the radiation transmission of the water, and the authors do not state in 1989a what transmission function was used. In 1989b, Fig. 3 shows 47 percent transmission to 0.67m depth, which is exceptionally high but may be almost possible with very clean water. A steady-state calculation of temperature profiles and pond efficiency for ponds using clean sea water (having a lower value of transmission than shown in 1989b, Fig. 3) was published in 1980. Conveniently, these calculations were made for $200 W/m^2$ input and a surface layer of 0.2m exactly as used by Rubin and Bemporad in 1989a. They give, for a temperature difference of 45 C° between the surface layer and the thermal layer, as used in 1989a, Fig. 3, a net gain of $46 W/m^2$, which is 23 percent efficiency (see reference 2, p. 368). This is to be compared with the 8 percent efficiency given in 1989a for a conventional pond under similar conditions. The disagreement is about a factor of two larger than can be accounted for by the incorrect use of linear gradient in 1989a.

Additional References

Hull, J. R., and Nielsen, C. E., and Golding, P., 1989, *Salinity-Gradient Solar Ponds*, CRC Press, Boca Raton, FL. 1989.

Solar Energy Technology Handbook, 1980, eds., W. C. Dickinson and P. N. Cheremisinoff, Marcel Dekker, See Part A, Chapter 11.

[1]Professor, Department of Physics, The Ohio State University, Columbus, Ohio 43210-1106.

Authors' Closure

The experiments reported in this paper represent the first stage of an evaluation concerning the ability to create a flowing stratified layer and to control its performance. The paper does not claim to provide all the information needed to prove the feasibility of the ASP. It was mentioned several times in the paper, which was also concluded with a comment, that the study should be extended to double-diffusive systems in order to provide more information relevant to the ASP performance.

Considering the differences between single and double diffusive system as mentioned by Prof. Nielsen; they do not avoid the operation of the CSP and did not prevent us from carrying out recently the first successful set of double-diffusive experiments, which are now being analyzed. We found that the behavior of the double-diffusive system depends on various parameters, and the description of different immiscible streams is not so conclusive as stated by Prof. Nielsen. This issue is still being studied by us, and it is beyond the scope of the present paper.

Flow velocity considered in our 1989 paper was taken as a preliminary assumption of the ASP operation. At that time we also considered operating our experimental setup in other flow conditions. Only later was it decided to operate it as described in the present paper. At any rate, the slower flow velocity does not stem from any problem associated with the performance of the ASP subject to field conditions. The slower flow velocity used in the experimental setup provided better injection and withdrawal conditions as well as smaller side wall effects in our experimental setup, which is much shorter and narrower than a solar pond. The flow conditions described in the present paper created a comparatively long region of uniform flow without the entrance and outlet influence.

Section (*b*) of Prof. Nielsen's discussion also refers to the performance of solar ponds and is not concerned with the present paper. However, in the ASP procedure boundary conditions of the system are controlled by several injection and withdrawal ports. Therefore the ASP procedure allows much more flexibility in the operation of the ASP than the CSP, as was considered in our 1989 paper.

Sections (*c*) and (*d*) again refer to differences between the solar pond operation and the experiments reported in the present paper. As far as the numerical computations are concerned we checked the computer code, used in our 1989 paper, for the computation of the solar transmission factor in the water body. The formula which we used was the one proposed by Rabl and Nielsen in their 1975 paper. Unfortunately, we found a disagreement in the code where cos(r) (r is the angle of incidence) divides the exponentials instead of the coefficients of the exponentials. We could not recall at which level of our calculations that error was introduced, since in the final version of our paper we did not describe such a formulation. If that error was really introduced into our calculations then the 47 percent transmission is high. However, this error is very minor for small angle of incidence where most applications take place.

As correctly implied by Prof. Nielsen, the initial temperature profile and the ability to preserve the temperature and salinity profiles in the solar pond are major factors determining the solar pond efficiency. With regard to this issue we expect the advantage of the ASP in which the multiport injection and withdrawal procedures should control and provide adequate temperature and salinity profiles leading to high efficiency of the solar pond.

It should be noted that in different studies concerning solar ponds performance different assumptions and definitions of the efficiency have been introduced. Such differences may in some cases lead to completely different conclusions regarding the solar pond performance.

In the conclusions of our reply we have to admit that our motivation in studying the feasibility of the ASP stems from our belief that the future of solar pond usage very much depends on the ability to improve its efficiency and performance. It seems that the ASP represents a step in that direction. The present paper eventually refers to some general thermohydrodynamic aspects. It does not claim to contribute much to the understanding and the possible improvement of solar ponds. It was submitted to the JOURNAL OF FLUIDS ENGINEERING and not to a more specialized journal in order to reach a broader audience.

Correlating Single Phase Flow Measurements With Observations of Trailing Vortex Cavitation

S. I. Green
California Institute of Technology;
Presently,
Department of Mechanical Engineering,
University of British Columbia,
Vancouver, B.C. V6T 1W5

The single phase and cavitating tip vortex shed by a NACA 66-209 rectangular planform, rounded tip hydrofoil has been studied. Single-phase measurements of instantaneous flow velocity were made by taking double-pulsed holograms of microbubbles moving in and around the vortex core. The tailored air bubble technique of Ooi and Acosta (1983) was employed to measure both the mean and fluctuating single phase vortex core static pressure. Cavitation inception was determined visually. The flow in the vortex core is highly unsteady; the r.m.s. axial velocity fluctuation can be as high as $0.2U_\infty$. Core pressure fluctuations greater than the freestream dynamic pressure have been observed. These fluctuations are commensurate with the axial velocity unsteadiness. Cavitation inception in saturated water occurs at mean core pressures above the vapor pressure. However, the pressure fluctuations are certainly substantial enough to account for these elevated inception indices. The rapid establishment of fully developed trailing vortex cavitation when the cavitation number is reduced below inception is attributable to the small variation in mean core pressure with downstream distance. The inception index increases substantially with dissolved air content. The cause of this dependence is not presently known.

1 Introduction

Tip vortices are an important feature of a number of engineering flows. For example, strong tip vortices generated by one airplane may roll a following plane which inadvertently enters the leading airplane wing wake. Tip clearance flows in turbomachinery cause significant inefficiencies. Blade-vortex interaction (BVI) is an active topic in helicopter research; Poling et al. (1989) has 20 references to BVI literature published just since 1983. Finally, propellor tip vortex cavitation has its attendant problems of noise, vibration, and wear.

A rectangular NACA 66-209 hydrofoil with no twist was used to generate tip vortices. The tip of the foil consisted of a smooth cap with an approximately semicircular cross-section. The foil chord length was 0.152m and the distance from the reflection plane mount to the tip cap base was 0.175m, which implies an effective aspect ratio of about 2.3. Experiments were carried out in the $0.305\text{m} \times 0.305\text{m} \times 2.5\text{m}$ test section of the Low Turbulence Water Tunnel (LTWT) at the California Institute of Technology. The velocity data presented herein were obtained using double-pulsed holography of injected microbubbles. The "tailored air bubble" technique of Ooi and Acosta (1983) yielded core pressure data. Cavitation inception was observed under stroboscopic illumination.

One of the outstanding cavitation research problems is relating the single phase and cavitating behavior of flows. Prediction of the cavitation inception index using single phase flow measurements is particularly salient. The essence of this prediction capability is division of the cavitation inception problem into two simpler problems—measurement of the single phase flow, which need only be done once, and measurement of the nuclei content of the cavitating water, which would be necessary for each operating environment. This tip vortex flow is amenable to such study because its single phase flow has now been well characterized (see for example Green, 1988b; Green, 1989). The task of actually predicting the single phase flow in tip vortices is highly complex (Phillips, 1981 is a recent effort), so prediction of tip vortex cavitation must be doubly so. Rather, it is the primary purpose of this paper to relate the single phase and cavitating flow measurements of the tip vortex studied.

2 The Experimental Techniques

2.1 Holographic Velocimetry. Trailing vortices generated in a water or wind tunnel are known to flutter about in a seemingly random manner. This "vortex meandering" is believed to be due to freestream turbulence in the test facility (Corsiglia et al., 1973). As a consequence of this meandering, any conventional velocimetry technique, such as LDV or hot wire anemometry, is subject to considerable error because temporal averaging of a fixed probe velocity signal is equivalent to spatial averaging over the meandering amplitude. Corsiglia et al. (1973) have measured meandering amplitudes of one chord and greater. In contrast, important features of the trailing vortex, such as the core radius, are as small as a few hundredths of one wind chord (Higuchi et al., 1989); the error due to meandering can clearly be quite significant. It is largely possible to avoid difficulties due to meandering by taking

Contributed by the Fluids Engineering Division for publication in the JOURNAL OF FLUIDS ENGINEERING. Manuscript received by the Fluids Engineering Division October 2, 1989.

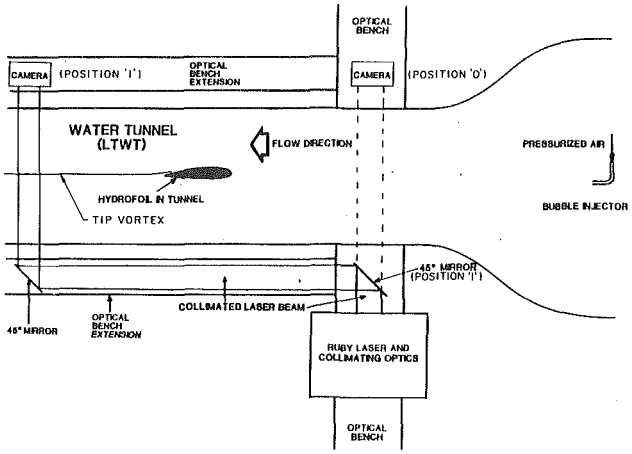

Fig. 1 Schematic of LTWT with holographic system. Only position "1" is used for double pulsed holography velocimetry. Positions "0" and "1" are used in the two phases of tailored air bubble pressure measurement.

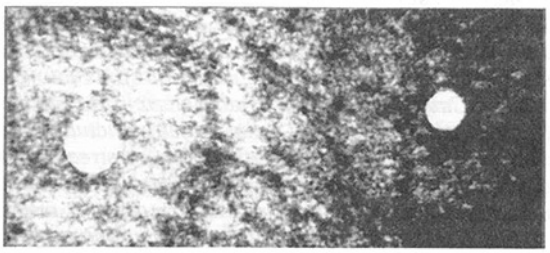

Fig. 2 Two injected bubbles in the trailing vortex core. $x/c = 4$, $\alpha = 5$ deg, $Re = 7.9 \times 10^5$. The bubble on the left is 265μm in the diameter ($p_C^* = 6.0$), and that on the right is 195μm in diameter ($p_C^* = 1.1$). These are pressure excursions of almost $2(p_C^*)'$ from p_C^*.

measurements only immediately downstream of the wing tip, where the meandering amplitude is small (e.g., Higuchi et al., 1989), or by sampling across the trailing vortex very rapidly, and discarding those scans which do not pass through the vortex centerline (e.g., Corsiglia et al., 1973).

The double-pulsed holographic technique for instantaneous velocity field measurement, which was used in this study, has been documented previously (Green, 1988a). Consider Fig. 1 in which microbubbles (20μm – 200μm in radius for this study) are injected into the flow upstream of the hydrofoil. A centripetal force drives some of the bubbles into the vortex core, where they very accurately define the centerline position. The majority of bubbles travel around the core and serve as nearly Lagrangian flow markers.[1] Double-pulsed in-line holograms (two holograms of a specific volume taken in succession) were recorded on holographic film. Holographic reconstruction was done by shining collimated He-Ne laser light through the developed holographic film, and recording the resultant real image using a video camera. Figure 2 is a portion of a typical reconstructed double-pulsed hologram. On holographic reconstruction, the displacement of each bubble between the two instants in time was measured. Because the vortex core location was marked precisely by numerous bubbles along its length, it was possible to measure these bubble displacements relative to the instantaneous location of the vortex core, thus eliminating the effects of vortex meandering on the measurements. Instantaneous tangential and axial velocities as a function of radial distance from the core were then calculated.

2.2 Tailored Air Bubble Pressure Measurement. The tailored air bubble technique for instantaneous static pressure measurement has also been described previously (Ooi and Acosta, 1983); again, only a brief overview is presented here. Microbubbles are injected into the flow upstream of the hydrofoil, where they respond to the imposed external pressure by varying their radii, R. Dynamically, the bubbles obey the Rayleigh-Plesset equation:

$$\rho R\ddot{R} + \frac{3}{2}\rho\dot{R}^2 = p_g - p_\infty + p_v - \frac{2S}{R} - \frac{4\mu\dot{R}}{R} \qquad (1)$$

where a superior dot represents differentiation with respect to time. S is the liquid surface tension, p_v is the vapor pressure, and p_g is the partial pressure of gas within the bubble.

Dry air bubbles were used in this study, and the evaporation rate into the bubble is slow relative to the bubble transit time (see below), so p_v can be neglected in equation (1). The natural frequency of the bubbles used in this study was $\approx$150kHz. This frequency is much higher than the highest velocity fluctuation frequencies observed in the trailing vortex (Green and Acosta, 1990), whence the bubbles should behave quasistatically. Furthermore, the water surrounding each bubble is isothermal, and because a summary heat transfer calculation shows the thermal response time of the injected bubbles was a few milliseconds, one may reasonably employ the assumption of isothermal bubble behavior. Equation (1) may therefore be considerably simplified to show that the pressure external to the bubble at some time "1," p_1, is related to the radius at that time, R_1, and the pressure, p_0, and radius, R_0, at some different time ("0," say) by:

$$p_1 = \left(p_0 + \frac{2S}{R_0}\right)\left(\frac{R_0}{R_1}\right)^3 - \frac{2S}{R_1} \qquad (2)$$

Thus, by measuring R_0 at a location where the static pressure is known, it is possible to infer the static pressure at a different location by measuring the bubble radius there.

In practice, it was extremely difficult to follow a single bubble as it travelled from a location of known pressure to a second location in the vortex core. Consequently, it was necessary to inject a flow of uniform bubbles upstream of the hydrofoil, thus avoiding the need to track individual bubbles. The task of producing monodisperse bubbles in the water tunnel was complex. A forced air-jet bubble injector, which consisted of a glass capillary tube (1.8mm in diameter) heated and pulled to form a nozzle 20μm in diameter, was produced and connected to a pressurized, filtered dry air supply. Numerous attempts were made to use this injector in the LTWT test section. Forced vibration of the injector, modification of the injector nozzle geometry, and angling the injector relative to the freestream were all tried, but none of these procedures yielded uniform bubbles. It was ultimately discovered that monodisperse bubbles could be obtained by injecting the bubbles in the LTWT settling tank, where the freestream velocity is fifteen times slower than in the test section (and hence the bubble detachment from the nozzle tip is more likely to be uniform).

The bubbles produced in the settling tank were convected downstream through the test section. Their radii, R_0, were measured at the start of the test section (3 chords upstream of the foil) by taking single-pulsed holograms of many bubbles. 95 percent of 48 measured, injected bubbles had radii within 3 percent of 92μm. The local static pressure at this location, p_0, was measured manometrically. The trailing vortex radial pressure gradient drives the bubbles onto the vortex centerline. Bubbles which had migrated to the vortex centerline at the time each hologram was taken were readily identifiable by their colinearity (Fig. 2). R_1, the bubble radius at some downstream position on the vortex centerline, was measured directly from reconstructed holograms taken of the downstream core. The bubble transit time from location '0' to location '1' was less than half a second.

[1] The extent to which radial bubble slip into the core affects these results is discussed in Green (1988b). Excluding data acquired in regions where the radial slip is significant ensures the error in the tangential velocity is slight. Radial slip causes no axial velocity error. Vortex meandering causes only a negligible inaccuracy in these velocity measurements.

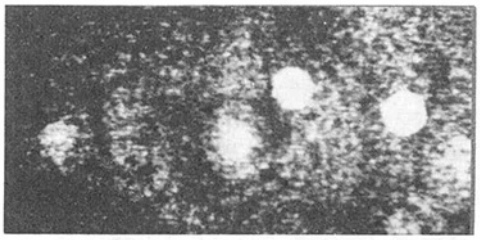

Fig. 3 A reconstructed portion of a double pulsed hologram. The in-focus bubble pair, outside the core, represents a bubble moving at 3.3 m/s. The out-of-focus bubble pair to the right, in the core, reveals a velocity of 5.1 m/s. Re = 5.2×10^5, $x/c = 2$, $\alpha = 10$ deg.

Scale: _____ = 1mm in flow.

The cubic dependence of p_1 on (R_0/R_1) in equation (2) causes fairly small errors in the measurement of R_0 and R_1 to be magnified into substantial errors in $p_c^* = (p_\infty - p_c)/0.5\rho U_\infty^2$. Specifically, the radii R_0 and R_1 have an uncertainty of 5μm (roughly the resolution of the holographic system). This radius error results in an error of ± 0.6 in each measurement of p_c^*.

2.3 Cavitation Observation. The occurrence of cavitation was detected by observation of the flow with stroboscopic lighting. Cavitation inception was defined as the appearance of approximately one bright flash of light—which was indicative of a cavitating nucleus—in the vortex core per second. Cavitation inception noise was also heard, though the volume of this noise was strongly dissolved air content (DAC) dependent. Photographs of cavitation were taken using the light of a high-speed flash directed in the spanwise direction.

3 Summary of Results and Discussion

This paper documents only the leading results of this research. A more extensive treatment is provided by Green (1988b). Green and Acosta (1990) describe substantially more details of the vortex velocity results.

3.1 Trailing Vortex Velocity Distribution. Figures 4(*a*,*b*) show plots of the vortex axial and tangential velocities two chords downstream of the hydrofoil leading edge. The angle of attack is 10 deg. U_θ/U_∞ is the tangential velocity around the core normalized by the freestream velocity. U_x/U_∞ is the normalized axial velocity. R/c is the radial distance from the core (R) normalized by the foil chord (c). The most important feature of these plots is the highly unsteady character of flow in the trailing vortex core. The r.m.s. axial velocity fluctuation in the core is $0.2U_\infty$ (the experimental error is $\pm 0.005U_\infty$ in the axial direction). The tangential velocity field around the vortex is also significantly unsteady (the experimental error is $\pm 0.01U_\infty$, much smaller than the typical $\pm 0.08U_\infty$ data spread at any radius).

3.2 Trailing Vortex Core Pressure. The tailored air bubble pressure results are summarized in Table 1. The leading result of these measurements is $\overline{p_c^*}$, the mean nondimensional freestream-to-core pressure drop, is 3.3 ± 0.5 for $\alpha = 10$ deg, and is approximately invariant with downstream distance. The final column of Table 1 lists the expected error in the mean core pressure drop results. The tabulated error is based on both the measured $\overline{(p_c^*)'}$ and the number of bubbles, and assumes Gaussian probability statistics. The measured value of $\overline{(p_c^*)'}$, the r.m.s. variation of p_c^*, is approximately 0.6 too large because of the experimental uncertainties described earlier. This result implies $\overline{(p_c^*)'} = 1.2 \pm 0.3$. Any dependence of $\overline{(p_c^*)'}$ on downstream distance is small and largely masked by experimental error.

It is possible to infer the pressure in the vortex core from the tangential velocity field by assuming steady, axisymmetric flow, and integrating the radial momentum equation from the

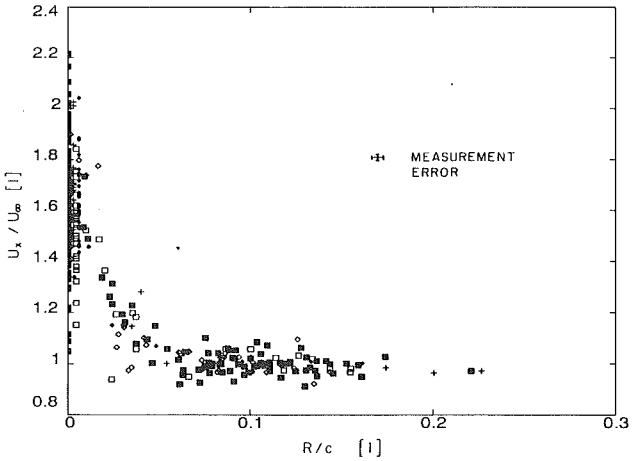

Fig. 4(*a*) Vortex axial velocity distribution. $x/c = 2$, $\alpha = 10$ deg, Re = 6.83×10^5. Results from 8 holograms. The data on the core have been distributed over the region $x/c \leq 0.006$. The set of solid square symbols represents the results of 4 different holograms. Each of the other 4 symbols displays the results from one hologram.

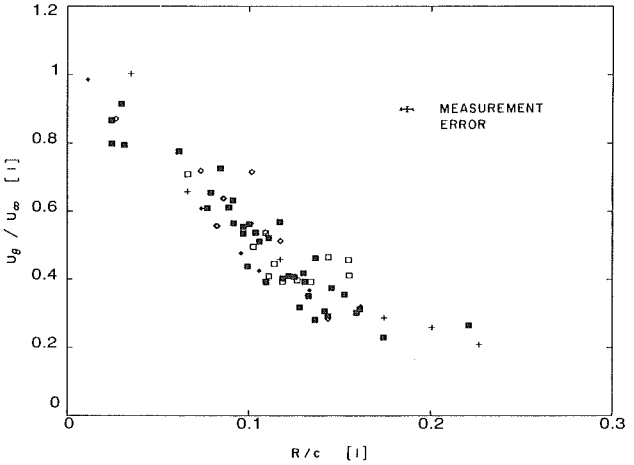

Fig. 4(*b*) Vortex tangential velocity distribution. $x/c = 2$, $\alpha = 10$ deg, Re = 6.83×10^5. The set of solid square symbols represent the results of 4 different holograms. Each of the other 4 symbols displays the results from one hologram.

Table 1 Tailored air bubble pressure results ($\alpha = 10$ deg)

x/c	Re	$\overline{p_c^*}$	$\overline{(p_c^*)'}$	# of bubbles	Expected error in $\overline{p_c^*}$
2	7.9×10^5	2.8	2.1	12	0.6
4	7.9×10^5	4.5	1.5	3	0.9
10	7.9×10^5	3.3	1.8	21	0.4

far field to the vortex center. The nondimensional core pressure is:

$$p_c^* = \frac{p_\infty - p_c}{0.5\rho U_\infty^2} = \frac{1}{0.5\rho U_\infty^2}\int_0^\infty \frac{\rho U_\theta^2 dR}{R}$$

$$= 2\int_0^\infty \frac{(U_\theta/U_\infty)^2 dR}{R} \tag{3}$$

The tangential velocity distribution was fairly well fit by a $1/R$ distribution for $R/c > 0.16$. A linear variation of U_θ was assumed for $R/c < 0.01$. Both these portions of the plot were integrated analytically. For $0.01 < R/c < 0.16$ sufficient data exist for a reasonably reliable numerical integration of the $U_\theta(R)$ curve. Combining the three contributions gives a mean core pressure $\overline{p_c^*} = 0.80 + 3.50 + 0.08 = 4.38$. The error in this value is quite large owing to the uncertainty in the predomi-

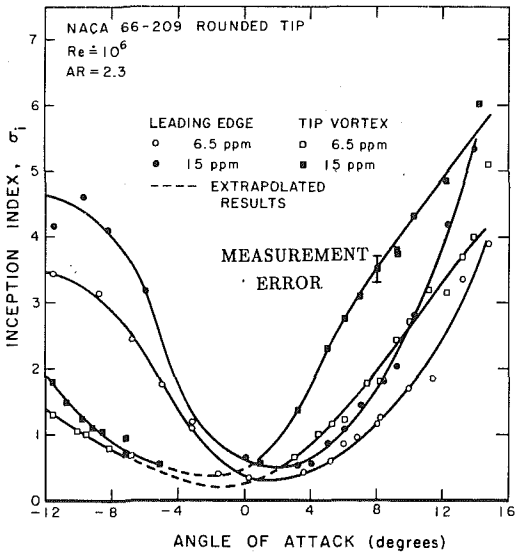

Fig. 5 Inception index versus angle of attack

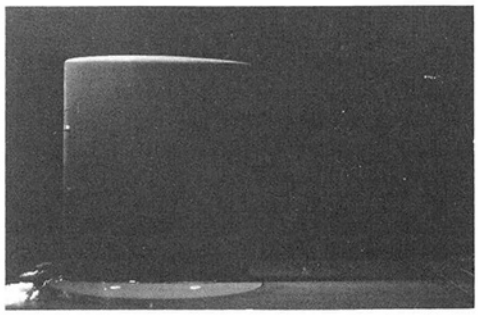

Fig. 6 Cavitation inception in the trailing vortex ($\alpha = 3$ deg, $\sigma = 0.63$, DAC = 6.5ppm). Flow is left to right. Some leading edge cavitation-due to a leading edge roughness-is visible.

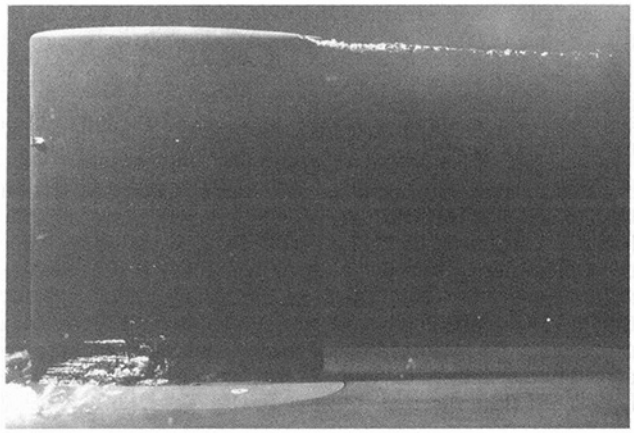

Fig. 7 Developed trailing vortex cavitation ($\alpha = 3$ deg, $\sigma = 0.53$, DAC = 6.5ppm). Flow is left to right. The trailing vortex cavity is contiguous for more than ten chords downstream of the wing. The cavity surface is very rough.

nant contribution to the integral—that from the region $R/c < 0.05$. A reasonable estimate of the error in $\overline{p_c^*}$ is ± 0.4. The discrepancy between $\overline{p_c^*}$ determined using the tailored air bubble technique (approximately 3.3 ± 0.5, invariant with downstream distance), and that based on integration of the tangential velocity data, is not statistically significant at the 95 percent confidence level.

Dunham (1979) has proposed a semitheoretical correlation for the pressure inside a trailing vortex core based in part on intrusive pressure probe measurements made by Mason and Marchman (1972). Those measurements are themselves somewhat suspect due to the sensitivity of trailing vortices to intrusive probes. Dunham's correlation is:

$$p_c^* = 3.44\left[\frac{(U_\theta)_{\max}}{U_\infty}\right]^2 \tag{4}$$

where $(U_\infty)_{\max}$ is the maximum tangential velocity in the flow around the trailing vortex. Referring to Fig. 4(*b*), $(U_\theta)_{\max}/U_\infty \approx 0.93$ for this hydrofoil at $\alpha = 10$ deg, whence the Dunham correlation predicts $p_c^* \approx 3.0$. This is in good agreement with the tailored air bubble measured value of 3.3. In view of all three aforementioned results, the best estimate of the mean core pressure drop is $\overline{p_c^*} = 3.8 \pm 0.6$ at $\alpha = 10$ deg; inferring the mean core pressure from measurements of tangential velocity seems to be viable.

One may attempt to relate the unsteadiness in core pressure to the core axial velocity unsteadiness. Consider core fluid being convected from a region where the axial velocity on the vortex centerline is $U_{xc} = \overline{U_{xc}}$ and the centerline pressure is $p_c = \overline{p_c}$, through a locally high axial velocity part of the core (where the velocity and pressure are respectively U_{xc}^+ and p_c^+). If the dynamics of the process are neglected, then the nondimensional pressure fluctuation, $(p_c^+)^*$ may be expressed as:

$$(p_c^+)^* = \frac{\overline{p_c} - p_c^+}{0.5\rho U_\infty^2} = \left(\frac{U_{xc}^+}{U_\infty}\right)^2 - \left(\frac{\overline{U_{xc}}}{U_\infty}\right)^2 \tag{5}$$

Typical values are $U_{xc}^+/U_\infty = 1.9$ and $\overline{U_{xc}}/U_\infty = 1.62$, for which $(p_c^+)^* = 1.0$. This value is in fairly good agreement with the best estimate of $\overline{(p_c^*)'}$, which suggests that axial velocity unsteadiness is a good predictor of core pressure unsteadiness.

3.3 Cavitation Observations Related to Single Phase Flow Phenomena. The inception index, σ_i, is plotted versus the angle of attack in Fig. 5. It is interesting to observe that the tip vortex inception index is larger than the leading edge surface inception index at the design angle of attack (7 deg). The tip vortex inception index at 10 deg is 4.2 for air saturated water, and much less—2.6—for deaerated water. Figure 6 is a photograph of inception in the trailing vortex. The instantaneous location of inception is 1.3 to 3 chords downstream of the hydrofoil leading edge, and fluctuates wildly in time.

Green and Acosta (1990) have shown the fluctuating axial velocity in the vortex core to be greater near the foil than farther from it. This implies that the fluctuations in core pressure are greatest in the region immediately downstream of the hydrofoil,[2] which in turn may explain why inception occurs there. The nearly uniform mean core pressure as a function of downstream distance is explication of the rapid development of a vapor-filled core when the cavitation number is reduced below σ_i (Fig. 7).

It is instructive to attempt to explain the measured cavitation inception numbers in terms of nuclei availability and core pressures. From Fig. 3(*b*) one may reasonably estimate the radius at which 95 percent of the pressure reduction from the freestream to the core has occurred. This radius is roughly 0.1cm. In one second, the volume of fluid swept through the area within this radius is $V = \pi(0.1\text{cm})^2 (\overline{U_{xc}} \times 1\text{s}) \approx 3 \times 10^{-5}\text{m}^3$ at inception conditions. Thus, if the lowest core pressure is reached at just one axial location in the core (a conservative assumption), $3 \times 10^{-5}\text{m}^3$ of fluid will pass through the minimum pressure location per second. Gates (1977) measured the nuclei content of near-saturated LTWT water. He found there to be $\approx 10^5$ bubbles/m^3, in the radius range from 150μm to 250μm (N(200μm) $\approx 10^9$/m^4). Thus, on the order of three of these large bubbles per second pass through the lowest pressure region of the core (this is a conser-

[2] It seems likely that this postulated decrease in pressure fluctuations with downstream distance was not observed using tailored air bubbles because of the poor statistics of the measurements. The error in $\overline{(p_c^*)'}$ resulting solely from statistical fluctuations is approximately ± 0.5.

vative estimate because centripetal forces drive additional bubbles into the vortex core). In summary, then, the bubbles which are on the order of 200μm in radius exist in sufficient numbers in saturated LTWT water to explain the cavitation event rate observed at inception.

One may relate the inception index to the core pressure as:

$$\sigma_i = \frac{p_\infty - p_v}{0.5\rho U_\infty^2} = p_c^* + \frac{p_c - p_v}{0.5\rho U_\infty^2} \tag{6}$$

If the core pressure at inception is approximately p_v (a 200μm bubble grows explosively at an external pressure only 500 Pa less than p_v (Knapp et al., 1970)), then $\sigma_i = p_c^*$. In fact, at $\alpha = 10$ deg $\sigma_i > p_c^*$. This implies the bubbles cavitate in regions of the core in which the flow unsteadiness has caused the local pressure to fall below p_v though the mean core pressure is above p_v. The large value $(p_c^*)' = 1.2$ is more than sufficient to account for the 0.4 difference between $\sigma_i = 4.2$ and our best estimate of $p_c^* = 3.8$.

For a dissolved air content (DAC) of 6.5ppm σ_i is only 2.6 at $\alpha = 10$ deg. Corroboration of the large dissolved air content effect on rectangular wing tip vortex cavitation may be found in studies done by Green (1988b) on different rectangular planform wings. This value of σ_i implies $(p_c - p_v)/(0.5\rho U_\infty^2) \approx -1.2 \pm 0.6$ or $p_c \approx -36 \pm 19$kPa ($U_\infty \approx 8$m/s). Fluctuations in core pressure tend to elevate σ_i, and therefore it is reasonable to posit that greater than a 20kPa core tension exists at inception. However, Katz and O'Hern (1983), Ooi (1981), and Gates (1977) have all measured $\approx 10^5$ bubbles/m^3 in the radius range from 25μm to 35μm for a low (3–6ppm) DAC in the LTWT. Bubbles of this size will cavitate when exposed to less than 1kPa tension; by way of contrast, only bubbles smaller than 2μm in radius will not cavitate with 20kPa of applied tension. In summary, then, there seems to be a paradox—at low DAC other researchers have measured plenty of microbubbles which should cavitate with low applied tensions, and yet the data presented herein imply that a considerable tension exists in the trailing vortex core before cavitation inception occurs. The reason for this is not presently known.

Arakeri et al. (1986) have previously related their tip vortex inception behavior to the flow Reynolds number and dissolved gas content. That analysis is predicated on the laminar separation which is observed to occur on their elliptical planform hydrofoil. Green (1988b) has demonstrated that the boundary layer flow on the hydrofoil studied herein is attached for $\alpha < 13$ deg. Consequently, Arakeri's analysis is not applicable to this geometry.

4 Conclusions

The instantaneous trailing vortex core pressure of a small aspect ratio rectangular planform hydrofoil has been determined using tailored air bubble injection. At a 10 deg angle of attack the best estimate of the mean pressure drop from the freestream to the core is 3.8 ± 0.6 freestream dynamic pressures. The core pressure fluctuates dramatically. The r.m.s. fluctuating component of the core pressure is more than one freestream dynamic pressure. The tangential and axial velocity distributions around the vortex have been measured using a double-pulsed holographic technique. An integrated form of the steady radial momentum equation and the Dunham (1979) correlation both use the tangential velocity data to predict the mean vortex core pressure. Both approaches give estimates of the core pressure which match the tailored air bubble measurement to within experimental error. Measurements of axial velocity unsteadiness on the vortex centerline, when combined with the Bernoulli equation, yield good estimates of core pressure fluctuations. Thus, accurate velocity measurements in the trailing vortex can be used to infer the vortex core pressure.

For water near saturation the inception index at $\alpha = 10$ deg is 4.2, which is greater than the mean pressure drop from the freestream to the core. The elevated inception index implies that inception occurs in regions of instantaneous low pressure in a core with mean pressure above the vapor pressure. Cavitation inception occurs in the region 1.3 to 3 chords downstream of the hydrofoil leading edge, in the most unsteady portion of the vortex core. Both of the above observations are consistent with the hypothesis that core pressure fluctuations contribute to the large values of σ_i of tip vortices. The observation of rapid vapor filling of many chords of the trailing vortex core when the cavitation number is reduced below σ_i is congruent with the small measured variation of core pressure with downstream distance. The inception index falls sharply when the dissolved air content is reduced. Although the reason for the strong dependence of σ_i on dissolved air content is not presently understood, it may have significant implications related to the cavitation behavior of nuclei in dynamic conditions.

Acknowledgments

The Office of Naval Research provided support under contract number N000167-85-K-0165. This research was largely carried out when the author was a graduate student, and subsequently a postdoctoral fellow, under the guidance of Professor Allan Acosta at Caltech.

References

Arakeri, V. H., Higuchi, H., and Arndt, R. E. A., 1986, "Analysis of Recent Tip Vortex Cavitation Inception Data," 21st ATTC, Washington.

Corsiglia, V. R., Schwind, R. G., and Chigier, N. A., 1973, "Rapid Scanning, Three-Dimensional Hot-Wire Anemometer Surveys of Wing-Tip Vortices," *J. Aircraft*, Vol. 10, pp. 752–757.

Dunham, J., 1979, "The Static Pressure in a Vortex Core," *Aeronautical J.*, Vol. 83, No. 8, pp. 402–406.

Gates, E. M., 1977, "The Influence of Freestream Turbulence, Freestream Nuclei Populations and a Drag-Reducing Polymer on Cavitation Inception on Two Axisymmetric Bodies," Ph.D. thesis, California Institute of Technology.

Green, S. I., 1988a, "Trailing Vortex Core Unsteadiness—An Exploratory Study of Reynolds Number Effects," AIAA/ASME 1st National Fluid Dynamics Congress, pp. 1064–1068.

Green, S. I., 1988b, "Tip Vortices—Single Phase and Cavitating Flow Phenomena," Ph.D. thesis, California Institute of Technology.

Green, S. I., 1989, "Tailored Air Bubble Determination of Trailing Vortex Core Pressure," ASME Cavitation and Multiphase Flow Forum, San Diego.

Green, S. I., and Acosta, A. J., 1990, "Unsteady Flow in Trailing Vortices," to appear in the *Journal of Fluid Mechanics*.

Higuchi, H., Arndt, R. E. A., Arakeri, V. H., and Killen, J. M., 1989, "The Structure of Tip Vortices Over a Range of Cavitation Number," 22nd ATTC, St. John's.

Katz, J., and O'Hern, T. J., 1983, "Holographic Observations of Cavitating Flows Within Regions of Flow Separation," Eighth Symposium on Turbulence, University of Missouri-Rolla.

Knapp, R. T., Daily, J. W., and Hammitt, F. G., 1970, Cavitation, McGraw-Hill, New York.

Mason, W. H., and Marchman, J. F., 1972, "Far Field Structure of an Aircraft Trailing Vortex Including Effects of Mass Injection," NASA CR-62078.

Ooi, K. K., "Scale Effects on Cavitation Inception in Submerged Jets," 1981, Ph.D. thesis, California Institute of Technology.

Ooi, K. K., and Acosta, A. J., 1983, "The Utilization of Specially Tailored Air Bubbles as Static Pressure Sensors in a Jet," ASME JOURNAL OF FLUIDS ENGINEERING, Vol. 106, No. 4, pp. 459–465.

Phillips, W. R. C., 1981, "The Turbulent Trailing Vortex During Roll-up," *J. Fluid Mechanics*, Vol. 105, pp. 451–467.

Poling, D. R., Dadone, L., and Telionis, D. P., 1989, "Blade-Vortex Interaction," *AIAA J.*, Vol. 27, No. 6, pp. 694–699.

Application of Lumley's Drag Reduction Model to Two-Phase Gas-Particle Flow in a Pipe

Kee Soo Han
Graduate Student.

Myung Kyoon Chung
Professor.

Hyung Jin Sung
Associate Professor.

Department of Mechanical Engineering,
Korea Advanced Institute of Science and Technology,
Cheongryang, Seoul, Korea

A "two-fluid model" has been incorporated with Lumley's drag reduction model to analyze the mechanism of momentum transfer in the turbulent dilute gas-particle flow in a vertical pipe. The change of the effective viscous sublayer thickness by the presence of particles is modeled by Lumley's theoretical model. The numerical computations of the friction factor and the pressure drop in a fully developed pipe flow are in good agreement with the corresponding experimental data for an average particle size of 15 μm. It is proved that Lumley's model is successful in predicting the correct reduction behavior of the drag in the gas-particle flows. It has been confirmed that the effective viscous sublayer thickness for two-phase gas-particle flow is dependent on the particle relaxation time, Kolmogoroff time scale and the solids-gas loading ratio.

1 Introduction

It is well known that the addition of solid particles to a flowing gas stream may increase or decrease the frictional resistance in turbulent flows. The frictional pressure drop increases in most of particle flow experimental studies (Boothroyd, 1966; Shimizu et al., 1978). On the contrary, Boothroyd (1966), Kane and Pfeffer (1973) and Tardos et al. (1983) found that the addition of small diameter solid particles to a gas flow in a pipe results in drag reduction depending on the particle size and its loading. Despite the large amount of work on this subject, however, the mechanism by which the drag reduction occurs is not well understood. This is mainly because of the complicated behavior of the gas-solid suspension flows. Many mechanisms have been proposed to explain this phenomenon; for examples, general turbulence suppression (Boothroyd, 1966; Soo, 1967), electrostatic charge effects (Richardson and McLeman, 1960), or thickening of the viscous sublayer (Kane and Pfeffer, 1973).

Tardos et al. (1983) found experimentally that the pressure drop in a vertical pipe flow is not significantly influenced by the charge build-up on the flowing particles at the loading ratios in the range 0.1 to 0.4. Boothroyd (1966) found that since spherical particles of a certain size were unable to follow the rapidly moving eddies near the wall in a pipe flow experiment, the turbulence was damped by these lagging particles, which resulted in reduction of the drag. Kane and Pfeffer (1973) asserted that the thickening of the viscous sublayer by the presence of the solid particles is the predominant factor of the drag reduction. Important observation in both these experimental studies is that the ratio of the friction factor of the suspension flow with small particles to that of the clean fluid flow at the same Reynolds number, first decreases and then increases as the particle loading ratio increases to have an optimum loading ratio for the maximum drag reduction; the maximum being as much as 75 percent. Such drag reduction has generally been observed in turbulent flows with fine spherical particles ($d_p < 75$ μm) in small pipes ($D < 3$ in.) under relatively low loading ratios ($Z < 4$).

In addition to the experimental studies, there have been a number of theoretical investigations to analyse the drag reduction phenomenon. Saffman (1962) tried to explain this phenomenon based on linear stability theory and found that under certain conditions the addition of particles stabilizes a gas-particle suspension flow. Jotaki and Tomita (1973) suggested that the viscous sublayer in suspension flow is dependent on the kinematic viscosity of the gas, the friction velocity, the relaxation time of particle and the solids-gas loading ratio, based on the generation and dissipation processes of turbulent kinetic energy. According to their theory, drag reduction increases always with increasing solids-gas loading ratio, which is in contradiction to the experimental data in pipe flow. Lumley (1976) suggested that because the particles have inertia, they cannot follow the smallest scale motions of the turbulence, and that such relative motion between the particles and the fluid causes increased loss in the fluid phase, effectively damping the small-scale turbulence and increasing the thickness of the viscous sublayer, which is the main reason of the drag reduction. However, there is a counter-balancing effect. The increased effective density of the bulk fluid resulting from the addition of particles decreases the effective kinematic viscosity of the bulk fluid and tends to increase the viscous cutoff wave number in the suspension shear flow, and as a result there is a relatively narrow range of loading, for particles of a given type, over which the net drag reduction is achieved. Based on this reasoning, he developed a drag reduction viscous sublayer model.

Contributed by the Fluids Engineering Division for publication in the JOURNAL OF FLUIDS ENGINEERING. Manuscript received by the Fluids Engineering Division, June 8, 1989.

Numerical studies have also been carried out to simulate the gas-particle suspension flow in a pipe. Abou-Arab and Abou-Ellail (1987) applied a recently developed two-phase k-ϵ model to analyze the momentum transfer in turbulent suspension flows. The two-phase k-ϵ model showed slight reduction in momentum transfer, but did not identify the reduction mechanism. Lee and Chung (1987) clearly showed that the application of a mixing length model based on an approximated balance equation for the turbulent kinetic energy can yield the correct reduction trend of momentum transfer. However, they did not treat the drag reduction mechanism separately in their model. They only obtained the correct numerical results by adjusting a few model constants and the wall boundary conditions.

The objective of the present study is to test Lumley's theoretical drag reduction model and to investigate the flow characteristics of the suspension flows at various loading conditions.

2 Governing Equations and Eddy Viscosity Models

(a) Governing Equations. The two-fluid approach is to regard the conveying gas phase and particulate phase as two interactive fluids in much the same way as one would regard the two species of a flowing binary mixture. The volume-averaged governing equations in differential form for cylindrical coordinates are given as follows.

Governing equations of gaseous phase:

$$\frac{\partial}{\partial x}\left[\rho_f(1-\alpha)U_f\right]+\frac{1}{r}\frac{\partial}{\partial r}\left[r\rho_f(1-\alpha)V_f\right]=\frac{1}{r}\frac{\partial}{\partial r}\left[r\rho_f\overline{\alpha' v_f'}\right] \quad (1)$$

$$\rho_f(1-\alpha)\left[U_f\frac{\partial U_f}{\partial x}+V_f\frac{\partial U_f}{\partial r}\right]=-(1-\alpha)\frac{\partial P}{\partial x}-\rho_f(1-\alpha)g+\frac{1}{r}\frac{\partial}{\partial r}\left[r\rho_f(1-\alpha)(\nu_{f\ell}\frac{\partial U_f}{\partial r}-\overline{u_f' v_f'})\right]+F_{px}+\rho_f\overline{\alpha' v_f'}\frac{\partial U_f}{\partial r}+\frac{\partial}{r\partial r}\left[r\rho_f\overline{\alpha' u_f'}\,V_f\right] \quad (2)$$

$$\rho_f(1-\alpha)\left[U_f\frac{\partial V_f}{\partial x}+V_f\frac{\partial V_f}{\partial r}\right]=-(1-\alpha)\frac{\partial P}{\partial r}+\frac{1}{r}\frac{\partial}{\partial r}\left[r\rho_f(1-\alpha)(\nu_{f\ell}\frac{\partial V_f}{\partial r}-\overline{v_f'^2})\right]-\frac{1}{r}\rho_f(1-\alpha)(\nu_{f\ell}\frac{V_f}{r}-\overline{w_f'^2})+F_{pr}+\rho_f\overline{\alpha' V_f'}\frac{\partial V_f}{\partial r}+\frac{\partial}{\partial x}\left[\rho_f\overline{\alpha' v_f'}\,U_f\right]+\frac{\partial}{r\partial r}\left[r\rho_f\overline{\alpha' v_f'}\,V_f\right] \quad (3)$$

Governing equations of particulate phase:

$$\frac{\partial}{\partial x}\left[\rho_s\alpha U_p\right]+\frac{1}{r}\frac{\partial}{\partial r}\left[r\rho_s\alpha V_p\right]=-\frac{1}{r}\frac{\partial}{\partial r}\left[r\rho_s\overline{\alpha' v_p'}\right] \quad (4)$$

$$\rho_s\alpha\left[U_p\frac{\partial U_p}{\partial x}+V_p\frac{\partial U_p}{\partial r}\right]=-\alpha\frac{\partial P}{\partial x}-(\rho_s-\rho_f)\alpha g+\frac{1}{r}\frac{\partial}{\partial r}\left[r\rho_s\,\alpha(\nu_{p\ell}\frac{\partial U_p}{\partial r}-\overline{u_p' v_p'})\right]-F_{px}-\rho_s\overline{\alpha' v_p'}\frac{\partial U_p}{\partial r}-\frac{\partial}{r\partial r}\left[r\rho_s\overline{\alpha' u_p'}\,V_p\right] \quad (5)$$

$$\rho_s\alpha\left[U_p\frac{\partial V_p}{\partial x}+V_p\frac{\partial V_p}{\partial r}\right]=-\alpha\frac{\partial P}{\partial r}+\frac{1}{r}\frac{\partial}{\partial r}\left[r\rho_s\alpha\,(\nu_{p\ell}\frac{\partial V_p}{\partial r}-\overline{v_p'^2})\right]-\frac{1}{r}\rho_s\,\alpha\,(\nu_{p\ell}\frac{V_p}{r}-\overline{w_p'^2})-F_{pr}-\rho_s\overline{\alpha' v_p'}\frac{\partial V_p}{\partial r}-\frac{\partial}{\partial x}\left[\rho_s\overline{\alpha' v_p'}\,U_p\right]-\frac{\partial}{r\partial r}\left[r\rho_s\overline{\alpha' v_p'}\,V_p\right] \quad (6)$$

In the above governing equations, we assumed that the particulate phase consists of spherical solid particles of uniform size, that, since the volume fraction α is small, the interparticle collision is negligible and that the lift force is also negligibly small. In the derivation procedure of the governing equations, the third-order correlation terms, for example, $\rho_s\,\alpha' u_p' v_p'$ and $\rho_s\,\overline{\alpha' v_p'^2}$ etc., have been omitted, simply due to lack of information.

F_{px} and F_{pr} are the axial and radial forces per unit volume due to interaction between the two phases, respectively. For the particle Reynolds number less than 700, these interaction forces were approximated by Rizk and Elghobashi (1985) as

$$F_{px}=C_1\frac{\rho_s}{t^*}\alpha(U_p-U_f) \quad (7)$$

$$F_{pr}=C_2\frac{\rho_s}{t^*}\alpha(V_p-V_f) \quad (8)$$

where t^* is the particle relaxation time given by $t^* = \rho_s d_p^2/18\mu(1+0.15\,\mathrm{Re}_p^{0.687})$.

The coefficients C_1 and C_2 in equations (7) and (8) are drag correction factors, which account for the effect of the wall on the Stokesian drag. Near the wall the fluid decelerates in order

Nomenclature

A = cross-sectional area of pipe
A^+ = van Driest damping constant
A_{DR}^+ = drag reduction viscous sublayer thickness
C_1, C_2 = drag correction factors
$C_{p\epsilon}'$, C_ϵ' = model constants
D = pipe diameter or van Driest damping function
d_p = particle diameter
f = friction factor
F_{px}, F_{pr} = Stokesian drag forces in axial and radial directions
g = gravitational acceleration
k = turbulent kinetic energy
$\hat{k}_d$ = ratio of viscous cutoff wave number under particle loading to that in the clean fluid
ℓ_f = characteristic length scale for gaseous phase flow
P = static pressure
R = pipe radius
Re = Reynolds number based on pipe diameter
Re_p = particle Reynolds number
r = radial distance from the pipe axis
s = viscous cutoff frequency
$\hat{s}$ = ratio of viscous cutoff frequency under particle loading to that in the clean fluid
t_ℓ = Lagrangian integral time scale
t^* = particle relaxation time scale
U, V = average mean velocity components in axial and radial directions
u', v' = fluctuating velocity

to satisfy the no-slip condition at the wall while the particle slip by. Accordingly, the relative velocity between the particles and the fluid increases, thus augmenting the drag force of the particle. C_1 and C_2 have the following form (Rizk and Elghobashi, 1985).

$$C_1 = \left[1 - \frac{9}{16}\left(\frac{d_p}{2y}\right) + \frac{1}{8}\left(\frac{d_p}{2y}\right)^3 - \frac{45}{256}\left(\frac{d_p}{2y}\right)^4 - \frac{1}{16}\left(\frac{d_p}{2y}\right)^5\right]^{-1} \tag{9}$$

$$C_2 = 1 + \frac{9}{8}\left(\frac{d_p}{2y}\right) + \left[\frac{9}{8}\left(\frac{d_p}{2y}\right)\right]^2 \tag{10}$$

Equations (9) and (10) indicate that the interaction drag forces F_{px} and F_{pr} are increased, for example, by about 20 and 30 percent, respectively, at $d_p/y = 0.5$ due to the wall presence.

(b) Eddy Viscosity Models. Under the assumption of turbulence in a state of local equilibrium between the production and dissipation of the turbulent kinetic energy for both the conveying gas and particulate phases, several turbulence models of the scalar eddy viscosities were developed (Lee and Chung, 1987; Choi and Chung, 1983; Chung et al., 1986). One of the well-proven models for the ratio of the scalar eddy viscosity in the particle laden flow to that in the clean fluid flow adopted in this study, has the form (Lee and Chung, 1987).

$$\frac{\epsilon_f}{\epsilon_{f0}} = \left[\frac{1}{1 + C_{p\epsilon}' \dfrac{\overline{\rho_p}}{\rho_f}\dfrac{t_\ell}{t^*}\left(1 - \dfrac{\epsilon_p}{\epsilon_f}\right)}\right]^{1/2} \tag{11}$$

where t_ℓ is the turbulent time scale and $C_{p\epsilon}'$ is a model constant of about 3.5.

The eddy viscosity of the clean pipe flow, ϵ_{f0}, is estimated from the mixing length model using the van Driest damping function, D, as

$$\epsilon_{f0} = \kappa^2 (R-r)^2 D^2 \frac{dU_f}{dr} \quad \text{for } (R-r) < \frac{\zeta\delta_{.99}}{\kappa} \tag{12}$$

$$= a\,\mathrm{Re}^b \nu_{f\ell} \quad \text{for } (R-r) > \frac{\zeta\delta_{.99}}{\kappa} \tag{13}$$

$$D = (1 - \exp(-y^+/A^+)) \tag{14}$$

where ζ is selected such that the numerical value of ϵ_{f0} matches smoothly between equations (12) and (13) at their interface and the values of a and b for pipe flow are 0.005 and 0.9, respectively (Crawford and Kays, 1975).

The effective nondimensional thickness of the viscous sublayer, A^+, in equation (14) plays an important role in the mixing-length model (Crawford and Kays, 1975). Experimental evidence in single phase flows is that the empirical value A^+ varies significantly with varying pressure gradient, transpiration or suction and surface roughness, etc.

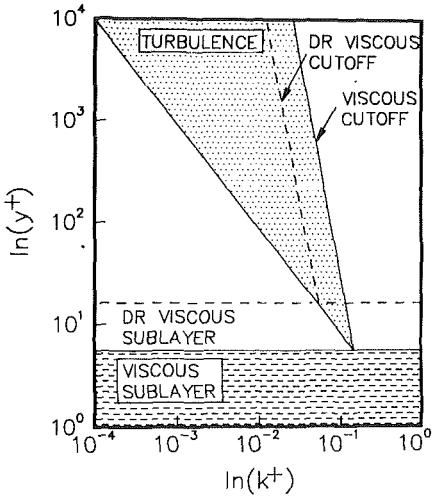

Fig. 1 Scaling relations in the viscous and inertial sublayers with and without particles, cited from Lumley (1976). DR refers to drag reduction.

Likewise, when the particulate phase is suspended in the conveying fluid, A^+ must depend upon the suspension conditions, particularly upon the loading ratio and the particle size. Turbulence structure of the dilute suspension flow is complicated by the fact that most particles of engineering interest are much larger than the Kolmogoroff length scale of the primary fluid near the wall region.

Lumley's drag reduction viscous sublayer model (Lumley, 1976) is derived as follows. For a relatively low Reynolds number flow, there is a fluctuating relative velocity between the fluid and the particles due to the particle inertia. In the wall region of a particle-free turbulent shear flow, the occurrence of turbulence may be plotted as in Fig. 1. The abscissa is a wave number and the ordinate is the distance from the wall, which are both scaled with the friction velocity. The shaded region represents the occurrence of turbulence, and further the peak of the spectrum of the energy-containing eddies corresponds to the left boundary of the shaded region. The peak of the dissipation spectrum corresponds to the right boundary scaled with the viscous cutoff wave number, k_d. Near the viscous sublayer, the two scales become the same order which is independent of the Reynolds number.

Lumley (1976) states that most of the particle phenomena

Nomenclature (cont.)

components in axial and radial directions
W = mass flux
x = axial distance
Z = solids-gas loading ratio (W_p/W_f)
α = volume fraction
ΔP = pressure drop
$\delta_{.99}$ = boundary layer thickness
$\hat{\delta}$ = ratio of sublayer thickness under particle loading to that in the clean fluid
ϵ = dissipation rate
ϵ_f, ϵ_p = kinematic eddy viscosities
κ = von Karman constant
μ = absolute laminar viscosity of gas
$\nu_{f\ell}$, $\nu_{p\ell}$ = kinematic laminar viscosities of the gaseous and particulate phases
ρ_f = density of gas
ρ_s = density of particle
$\overline{\rho_f}$ = bulk density of gaseous phase ($=\rho_f(1-\alpha)$)
$\overline{\rho_p}$ = bulk density of particulate phase ($=\rho_s\alpha$)
τ_w = wall shear stress

Subscripts

c = pipe center
DR = drag reduction
f = gas or gaseous phase
ℓ = laminar
0 = clean fluid
p = particle or particulate phase
s = solid
w = wall

Superscripts

$+$ = nondimensionalized wall coordinate
$\hat{}$ = ratio of relevant physical quantities of suspension fluid to clean fluid
$'$ = fluctuating quantity

with inertia happen when $1/t^*$ is smaller than the viscous cutoff frequency, s. For this case, the rate of energy dissipation at high frequencies due to the fluctuating relative velocities per unit total mass is modelled as follows:

$$1.8C_\epsilon'\epsilon(\pi/2-1/0.74st^*)\frac{Z}{1+Z} \tag{15}$$

where $C\epsilon'$ is a model constant of about 1.2 (Elghobashi and Abou-Arab, 1983) and Z is a solids-gas loading ratio. He also considers the viscous dissipation by the presence of the particles as $\nu_{f\ell}s^2/(1+Z)$. Since the viscous dissipation plus the dissipation associated with the particles should dissipate all of ϵ, we have

$$\frac{\nu_{f\ell}}{1+Z}s^2+1.8\ C_\epsilon'\epsilon(\pi/2-1/0.74st^*)\frac{Z}{1+Z}=\epsilon \tag{16}$$

In addition, Lumley shows that the viscous cutoff wave number, k_d, is proportional to $[(s/\nu_{f\ell})\ (1+Z)]^{1/2}$. Then, the ratio of k_d under particle loading to that in the clean fluid is given by

$$\hat{k}_d=[\hat{s}(1+Z)]^{1/2} \tag{17}$$

where $\hat{s}=s(\nu_{f\ell}/\epsilon)^{1/2}$.

Substitution of the solution for $\hat{s}$ from the equation (16) into the equation (17) dictates that the presence of particles reduces the value of $\hat{k}_d$. That is, just outside the viscous sublayer, this reduction in $\hat{k}_d$ will cause the apex of the shaded region to move farther from the wall and create the corresponding drag reduction viscous sublayer of the particle conveying suspension flow as can be seen in Fig. 1. By Lumley, the drag reduction viscous sublayer thickness, A_{DR}^+, is given by

$$\hat{\delta}=\hat{k}_d^{-4/3}=[\hat{s}(1+Z)]^{-2/3} \tag{18}$$

and

$$A_{DR}^+=\delta_0^+\hat{\delta} \tag{19}$$

where $\hat{\delta}$ is the ratio of sublayer thickness under particle loading to that in clean fluid and δ_0^+ is the viscous sublayer thickness for clean fluid. The drag reduction viscous sublayer thickness, A_{DR}^+, corresponds to the intersection of the right and left edges of the diagram in Fig. 1.

Accordingly, estimation of the damping constant A^+ of the particle conveying fluid, can be done by the following.

$$A^+=A_0^+ \qquad \text{for } A_0^+>A_{DR}^+ \tag{20}$$

$$A^+=A_{DR}^+ \qquad \text{otherwise} \tag{21}$$

where A_0^+ is an effective viscous sublayer thickness of clean fluid. It is found that the above model equation (20) and (21) yields the best agreement with the experimental data (Boothroyd, 1966). Thus, A^+ is strongly dependent on the particle relaxation time, Kolmogoroff time scale and loading ratio. All physical quantities in equations (15)–(21) are evaluated at the distance from the wall corresponding to the viscous sublayer thickness in clean fluid.

For estimating the eddy viscosity and the virtual laminar kinematic viscosity of the particulate phase, the models proposed by Choi and Chung (1983) are employed here.

$$\frac{\epsilon_p}{\epsilon_f}=\frac{1}{1+\left(\frac{t^*}{t_\ell}\right)^2} \tag{22}$$

$$\frac{\nu_{p\ell}}{\nu_{f\ell}}=\frac{\epsilon_p}{\epsilon_f} \tag{23}$$

For details of these models, refer to the original presentation in Choi and Chung (1983).

(c) Eddy Diffusivity Models. The turbulence closures for the time averaged products $\overline{\alpha' v_p'}$, $\overline{\alpha' u_p'}$, $\overline{\alpha' v_f'}$ and $\overline{\alpha' u_f'}$ in equations (1)–(6) are made by assuming scalar eddy diffusivities. The turbulent mass transfer may be represented by the scalar transport hypothesis with the turbulent Schmidt number ($\sigma_\phi = 0.7$); for example,

$$\rho_s\overline{\alpha' v_p'}=-\frac{\epsilon_p}{\sigma_\phi}\frac{\partial\overline{\rho_p}}{\partial r},\ \rho_s\overline{\alpha' u_p'}=-\frac{\epsilon_p}{\sigma_\phi}\frac{\partial\overline{\rho_p}}{\partial x},$$

$$\rho_f\overline{\alpha' v_f'}=\frac{\epsilon_f}{\sigma_\phi}\frac{\partial\overline{\rho_f}}{\partial r} \text{ and } \rho_f\overline{\alpha' u_f'}=\frac{\epsilon_f}{\sigma_\phi}\frac{\partial\overline{\rho_f}}{\partial x}.$$

3 Computational Procedure

Since the two-fluid momentum equations are parabolic differential equations, the forward marching technique (Patankar and Spalding, 1970) is applied in this study. The Patankar-Spalding (1970) coordinate system is appropriate for solving the boundary layer flows using the von Mises transformation. Pressure gradient in the momentum equation is calculated with a modified form of the formulae proposed by Patankar and Spalding (1970).

$$\frac{dP}{dx}=-\frac{2\tau_{wf}}{R}-\frac{W_fU_f}{A^2}\frac{dA}{dx}+\left[\frac{\overline{\rho_p}(U_p-U_f)}{(1-\alpha)t^*}\right]_{AA}+\left[\frac{\rho_f\overline{\alpha' v_f'}}{(1-\alpha)}\frac{\partial U_f}{\partial r}\right]_{AA} \tag{24}$$

where AA means area average and τ_{wf} is wall shear stress.

The initial mean velocity profiles of both phases are assumed to be fully developed ones. The inlet mean concentration of the particulate phase is assumed to be uniform across the section with the given particle loading, $\overline{\rho_p} = Z\overline{\rho_f}$. All the radial gradients are set to zero on the axis of symmetry.

The particles are known to slip over the wall surface, while the fluid satisfies the no-slip condition. A slip condition for the particulate phase at the wall is imposed on the streamwise velocity component. The mass center of the particles can not exist in very near the wall region, $y < 0.5d_p$, since the distance from the wall is smaller than the particle radius. Then the slip velocity for the particulate phase at the wall may be approximated as follows:

$$U_p=U_{f_{y=d_p/2}} \tag{25}$$

In our earlier study (Lee and Chung, 1987), the boundary condition of U_p at the wall was given by an empirical relation $\frac{dU_p}{dr}\simeq 0.8\frac{dU_f}{dr}$ based on experimental data of Lee and Durst (1982) and Tsuji et al. (1984). Since previous boundary condition can not be considered as a universal, applicability of such empirical boundary condition is not guaranteed to be valid in other flow conditions; for example, different particle size, Reynolds number and loading ratio.

The boundary conditions at the wall for other variables are $U_f = V_f = V_p = 0$ and $d\overline{\rho_p}/dr = 0$.

By combining equations (11) and (22), and using a relation $t_\ell = \ell_f^2/\epsilon_f$, the Lagrangian time scale, t_ℓ, can be obtained by solving the following equation by the Newton-Rhapson technique.

$$\epsilon_{f0}^2t_\ell^4+(\epsilon_{f0}^2t^{*2}-\ell_f^4)t_\ell^2-(C_{p\epsilon}'\frac{\overline{\rho_p}}{\rho_f}t^*\ell_f^4)t_\ell-\ell_f^4t^{*2}=0 \tag{26}$$

4 Computational Results and Discussion

Boothroyd's experiments (1966) with fine particles in vertical tubes are selected to test the present models for turbulent gas-particle flows. We have reviewed his experiments in some detail (Lee and Chung, 1987; Choi and Chung, 1983) and a brief description is as follows. The measurements were carried out

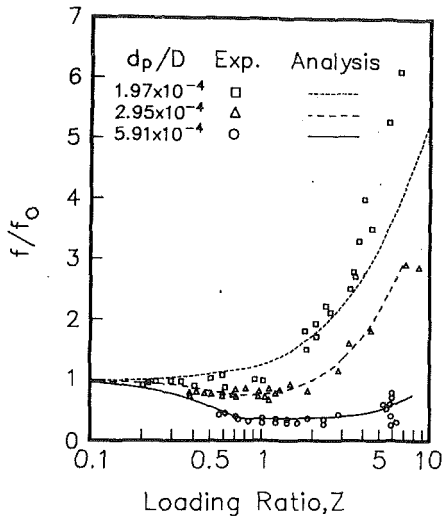

Fig. 2 Comparison of predicted friction factors with the experiments of Boothroyd (1966)

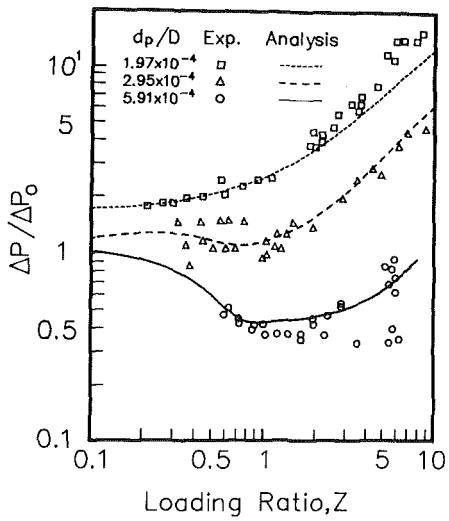

Fig. 3 Comparison of predicted pressure drops with the experiments of Boothroyd (1966)

with spherical zinc powders. The particle size was distributed over 0-40 μm with an average size of 15μm. Pipe diameters were 0.0254m ($d_p/D = 5.91\times10^{-4}$), 0.0508m ($d_p/D=2.95\times10^{-4}$), and 0.0762m ($d_p/D=1.97\times10^{-4}$) and the loading ratios varied between 0.5 to 5.

Comparisons of the present results with Boothroyd's data (Boothroyd, 1966) for the friction factor ratios are presented in Fig. 2. The Reynolds number based on the pipe diameter and average velocity of the clean flow was 53,000. This figure shows that as the relative particle size d_p/D increases, drag is significantly reduced. It can be seen that the results by the present model are in excellent agreement with the experimental data. Especially, predictions of the minimum friction factor ratios are satisfactory.

Figure 3 shows the ratio of the pressure drop of the suspension flow to that of clean gas flow under the same conditions as Fig. 2. The pressure drop in the vertical pneumatic conveying line can be broken down into the hydrostatic pressure drop, pressure drop due to acceleration, and frictional pressure drop for the conveying gas phase and the particulate phase (Boothroyd, 1971). In $d_p/D = 5.91\times10^{-4}$, the pressure drop and the frictional pressure drop are always less than those of clean fluid. For the case of $d_p/D = 1.97\times10^{-4}$, the pressure drop and the frictional pressure drop are always larger than those of clean fluid. From Fig. 2 and Fig. 3, it is found that as the relative particle size decreases and loading ratio increases, the hydrostatic pressure drop is a predominant factor of the pressure drop of gas-particle suspension flow.

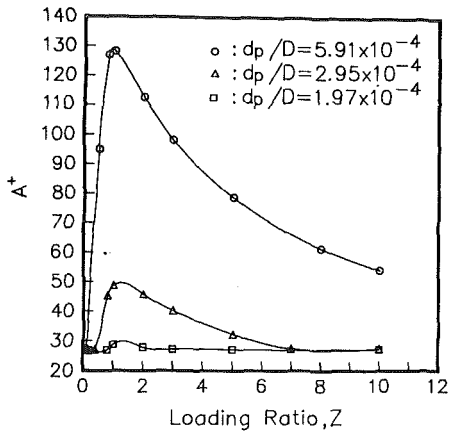

Fig. 4 Estimation of effective non-dimensional sublayer thickness using equations (20) and (21)

Figure 4 represents the effective non-dimensional sublayer thickness, A^+, calculated from equations (20) and (21). It shows that as the relative particle size, d_p/D, increases, the effective viscous sublayer thickness of the suspension flow increases notably. In the case of the largest relative particle size, the solid particles substantially reduce the level of near-wall turbulence at relatively low loading, which means that the effective viscous sublayer, A^+, is thickened from a value of $A^+ = 26$ to a value of the order of 100. The dramatic change of A^+ near $Z = 1$ is, however, not yet understood. When the pipe size becomes smaller, the velocity gradient becomes larger in the wall region under the same Reynolds number condition. In such a case, the lift force is not negligible. High lift force near the wall causes less particles to exist in that region, which reduces the viscous sublayer thickness. Since our model equation does not contain the lift force term, the suppression of the viscous sublayer thickness in smaller pipe due to such lift force can not be taken account of, and thus, our model may overpredict A^+ for low loading ratio in smaller pipe flow. However, for $d_p/D = 1.97\times10^{-4}$, it remains more or less the same at about 26. Therefore, for $d_p/D = 1.97\times10^{-4}$, drag reduction does not occur.

From the results of Figs. 2, 3, and 4, it is concluded that the effective viscous sublayer thickness for two-phase flow is dependent on the particle relaxation time, Kolmogoroff time scale and the solids-gas loading ratio.

Figure 5 shows the mean axial velocity profiles of gaseous phase normalized by the centerline mean velocity of the clean fluid in $d_p/D = 1.97\times10^{-4}$ and 5.91×10^{-4} with the solids-gas loading ratio as a parameter. The profile for $d_p/D = 1.97\times10^{-4}$ becomes more rounded for all non-zero loading ratios. For the case of $d_p/D = 1.97\times10^{-4}$, the trend of velocity profile with loading ratio is in agreement with experimental observation by Boothroyd (1967) (see Fig. 18 in Boothroyd (1967)). However, for loading ratio of unity in $d_p/D = 5.91\times10^{-4}$, the mean velocity profile in the turbulent core flattens and the center velocity is slower than that of the pure gas. The profile becomes more rounded and the center velocity becomes faster with increasing loading ratio.

Figure 6 shows the normalized spatial distribution of particles in $d_p/D=1.97\times10^{-4}$ and 5.91×10^{-4} with the loading ratio as a parameter. In $d_p/D=1.97\times10^{-4}$, as the loading ratio increases, the particles near the wall region are more concentrated than those in the turbulent core. This trend is in agree-

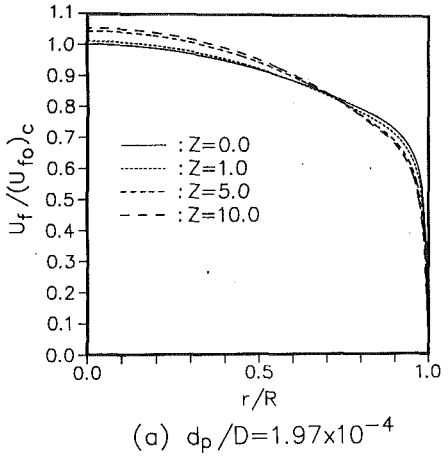

Fig. 5(*a*)

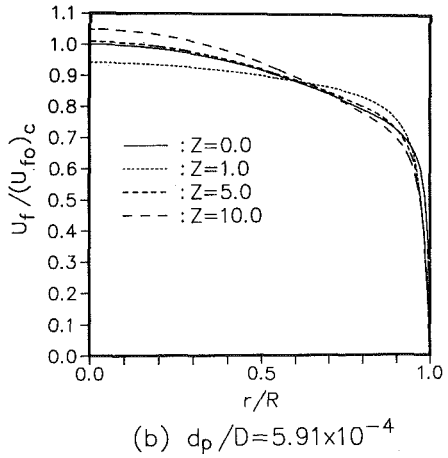

Fig. 5(*b*)

Fig. 5 Normalized mean axial velocity profiles of gaseous phase for various relative particle sizes and loading ratios: (*a*)$d_p/D = 1.97\times10^{-4}$; (*b*)$d_p/D = 5.91\times10^{-4}$

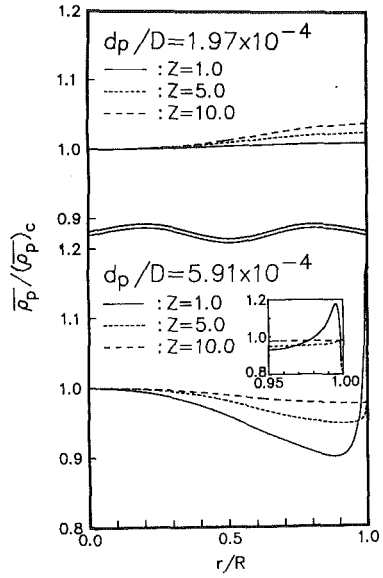

Fig. 6 Normalized spatial distribution of particulate phase density for various relative particle sizes and loading ratios

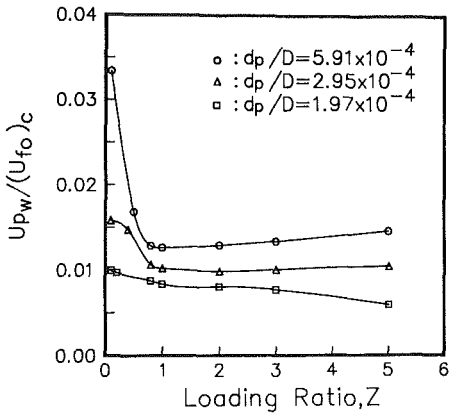

Fig. 7 Estimation of normalized particle wall slip velocity using equation (25)

ment with experimental observation by Boothroyd (1971) (see Fig. 9.1 in Boothroyd (1971)). However, because our models do not include the electrostatic charging effect, the concentration of the particles near the wall at higher loading ratio is underestimated more than that of Boothroyd's experimental data (Boothroyd, 1971). At the loading ratio of 1 in $d_p/D=5.91\times10^{-4}$ with the effective viscous sublayer thickness of the order of 100, the particle concentration first decreases and then rapidly increases approaching to the wall. The sharp variation of the particulate phase density near the wall region as shown in details in the inset of Fig. 6 is qualitatively consistent with a Lagrangian simulation of Kallio and Reeks (1989) (see Fig. 5 in Kallio and Reeks (1989)). Because the particle concentration near the wall region is directly related to the effective viscous sublayer thickness, it is thought that an optimum combination between the loading ratio and the relative particle size can be selected in order to maximize drag reduction.

Figure 7 shows the normalized particle slip velocity calculated from equation (25). In $d_p/D = 2.95\times10^{-4}$ and 5.91×10^{-4}, the normalized particle slip velocities first decrease and then slightly increase as the loading ratio increases. This phenomenon occurs due to the change of the effective viscous sublayer thickness as can be seen in Fig. 4. However, in $d_p/D = 1.97\times10^{-4}$, it decreases with increasing the loading ratio.

5 Conclusions

A "two-fluid model" using Lumley's drag reduction viscous sublayer model has been employed to investigate the two-phase vertical pipe flows using an extended mixing length theory. The following conclusions may be drawn from the predicted results, which are in agreement with experimental observations. The major cause of decrease in the friction factor at low loading ratios is the increase of viscous sublayer thickness caused by the suppression of turbulence near the wall by solid particles. The effective viscous sublayer thickness for two-phase flow is dependent on the particle relaxation time, Kolmogoroff time scale, and solids-gas loading ratio. An optimum combination between the loading ratio and the relative particle size can be selected in order to maximize drag reduction. As the relative particle size, d_p/D, increases, drag is reduced significantly. When drag reduction occurs at low loadings, the gas velocity in the central region of the pipe is slower than that of pure gas, and its profile flattens. However, the gas velocity is faster than that of pure gas and its profile becomes more rounded in the central region of the pipe for higher loading ratios or when drag reduction does not occur. For small relative particle sizes, the particles are more concentrated near the wall region with increasing loading ratio. As the relative particle size decreases and loading ratio increases, the pressure drop due to

gravity is a predominant factor of the suspension pressure drop.

References

Abou-Arab, T. W., and Abou-Ellail, M. M. M., 1987, "Computation of Heat and Momentum Transfer in Turbulent Gas/Solid Flows," *Proc. Int. Symposium of Multiphase Flows*, Hangzhou, China, pp. 374–379.

Boothroyd, R. G., 1966, "Pressure Drop in Duct Flow of Gaseous Suspensions of Fine Particles," *Trans. Instn. Chem. Engrs.*, Vol. 44, pp. 306–313.

Boothroyd, R. G., 1967, "Turbulence Characteristics of the Gaseous Phase in Duct Flow of a Suspension of Fine Particles," *Trans. Instn. Chem. Engrs.*, pp. 96–109.

Boothroyd, R. G., 1971, *Flowing Gas-Solids Suspensions*, Chapman and Hall, London.

Choi, Y. D., and Chung, M. K., 1983, "Analysis of Turbulent Gas-Solid Suspension Flow in a Pipe," ASME JOURNAL OF FLUIDS ENGINEERING, Vol. 105, pp. 329–334.

Chung, M. K., Sung, H. J., and Lee, K. B., 1986, "Computational Study of Turbulent Gas-Particle Flow in a Venturi," ASME JOURNAL OF FLUIDS ENGINEERING, Vol. 108, pp. 248–253.

Crawford, M. E., and Kays, W. M., 1975, "A Program for Numerical Computation of Two Dimensional Internal/External Boundary Layer Flows," Rept. HMT-23, Stanford University, California.

Elghobashi, S. E., and Abou-Arab, T. W., 1983, "A Two-Equation Turbulence Model for Two-Phase Flows," *Phys. Fluids*, Vol. 26, pp. 931–938.

Jotaki, T., and Tomita, Y., 1973, "Turbulent Friction Drag of a Dusty Gas," *Bulletin of the JSME*, pp. 93–99.

Kallio, G. A., and Reeks, M. W., 1989, "A Numerical Simulation of Particle Deposition in Turbulent Boundary Layers," *Int. J. Multiphase Flow*, Vol. 15, pp. 433–446.

Kane, R. S., and Pfeffer, R., 1973, "Characteristics of Dilute Gas-Solids Suspensions in Drag Reducing Flow," NASA CR-2267, cited from Rudinger, G., 1980, *Fundamentals of Gas-Particle Flow*, Elsevier Scientific Publishing Company.

Lee, K. B., and Chung, M. K., 1987, "Refinement of the Mixing-Length Model for Prediction of Gas-Particle Flow in a Pipe," *Int. J. Multiphase Flow*, Vol. 13, pp. 275–282.

Lee, S. L., and Durst, F., 1982, "On the Motion of Particles in Turbulent Duct Flows," *Int. J. Multiphase Flow*, Vol. 8, pp. 125–146.

Lumley, J. L., 1976, *Topics in Applied Physics*, Vol. 12, *Turbulence*, Edited by Bradshaw, P., Springer-Verlag, Berlin, Heidelberg, and New York, pp. 289–324.

Patankar, S. V., and Spalding, D. B., 1970, *Heat and Mass Transfer in Boundary Layers*, 2nd Edn., Intertext Books, London.

Richardson, J. F., and McLeman, M., 1960, "Pneumatic Conveying—Part II: Solids Velocities and Pressure Gradients in a One-Inch Horizontal Pipe," *Trans. Instn. Chem. Engrs.*, Vol. 38, pp. 257–266.

Rizk, M. A., and Elghobashi, S. E., 1985, "The Motion of a Spherical Particle Suspended in a Turbulent Flow near a Plane Wall," *Phys. Fluids*, Vol. 28, pp. 806–817.

Saffman, P. G., 1962, "On the Stability of Laminar Flow of a Dusty Gas," *J. Fluid Mech.*, Vol. 13, pp. 120–128.

Shimizu, A., Echigo, R., and Hasegawa, S., 1978, "Experimental Study on the Pressure Drop and the Entry Length of the Gas-Solid Suspension Flow in a Circular Tube," *Int. J. Multiphase Flow*, Vol. 4, pp. 53–64.

Soo, S. L., 1967, *Fluid Dynamics of Multiphase Systems*, Blaisdell, New York.

Tardos, G., Yen, B., and Pfeffer, R., 1983, "The Effect of Static Charges on Drag Reduction in Dilute Gas-Particle Suspension Flow," *Chemical Engineering, Communications*, Vol. 19, pp. 205–219.

Tsuji, Y., Morikawa, Y., and Shiomi, H., 1984, "LDV Measurements of an Air-Solid Two-Phase Flow in a Vertical Pipe," *Journal of Fluid Mechanics*, Vol. 139, pp. 417–434.

A Singular Perturbation Solution for Couette Flow Over a Semi-Infinite Porous Bed

C. T. Hsu
Fluid Mechanics Department,
TRW Space and Technology Group,
Redondo Beach, CA 90278

P. Cheng
Department of Mechanical Engineering,
University of Hawaii at Manoa,
Honolulu, HI 96822,
Fellow ASME

An analysis has been performed to study conjugate Couette flows in a channel over a packed-spheres bed of semi-infinite extent. The Brinkman model is used as the momentum equation in the porous bed with the variation of porosity approximated by an exponential function. An approximate expression for the permeability of the bed, applicable for a wide range of porosity, is constructed. A singular perturbation solution is obtained for the velocity distribution in the packed-spheres bed. The streamwise velocity and the shearing stress of the conjugate flows in the channel and in the packed-spheres bed are matched at the fluid/porous bed interface. An explicit analytical expression for the slip coefficient is obtained by comparing the results based on the present formulation with those based on Beavers and Joseph's formulation. It is shown that the value of the slip coefficient decreases as a result of the variable porosity effect.

I. Introduction

In recent years the problem of conjugate flows in superposed fluid and porous layers has attracted considerable attention because of its applications to groundwater flow in fractured reservoirs, and the contamination of pollutants in rivers and lakes. Traditionally, the analyses of flow in underground media have been based on Darcy's law where shearing stresses are neglected (Bear, 1972; Cheng, 1978). For flow in superposed layers, there is experimental evidence that the effect of the viscous shear in the fluid layer may penetrate into the permeable layer (Beavers and Joseph, 1967; Beavers et al. 1970). To account for this effect while retaining the Darcy-law formulation; Beavers and Joseph (1967) have proposed a slip velocity boundary condition at the interface given by:

$$\left.\frac{du^*}{dy^*}\right|_{y^*=0} = \frac{\alpha}{\sqrt{K^*}}(u_i^* - Q^*) \tag{1}$$

where u^* is the velocity in the fluid layer; u_i^* is the slip velocity at the interface at $y^* = 0$; K^* is the permeability of the porous bed which is assumed to be constant; Q^* is the velocity in the bulk of the porous bed; and α is the dimensionless slip coefficient which depends on the variation of the porosity. In an experiment of Poiseuille flow over a porous bed, Beavers and Joseph (1967) found that their predicted mass flow rate in the fluid layer would match with their experimental results if the value of $\alpha = 0.1$ is used for the aloxite porous specimens, and the value of $\alpha = 0.78 \sim 4.0$ is used for the foametal porous specimens. The smaller value of the slip coefficient α for the aloxite porous specimens is attributed to the fact that aloxite is a granular material which has a greater porosity near the edge of the material, while the foametal specimen is a "lattice-type" material which has a uniform porosity. In another experiment of coupled Poiseuille flow in a fluid layer and a porous layer consisting of metallic fibers, Beavers, et al. (1970) confirm that the value of $\alpha = 0.1$ should be used in the slip flow formulation in order to match their theoretical results with their experiments. On the other hand, Taylor (1971) found that $\alpha = 1$ should be used in the slip flow formulation in order to match their theoretical results with their experiments on Couette flow over a porous bed consisting of parallel plates.

Recently, a number of studies (Neale and Nader, 1974; Rudraiah, 1985; Somerton and Catton, 1982; Nield, 1977) have used the Brinkman model (Brinkman, 1947) with constant porosity for the study of flow in superposed fluid and porous layers. Based on this model, the artificial slip boundary condition given by equation (1) is not needed since the Brinkman model contains a shearing stress term which allows the matching of the shearing stress across the fluid/porous bed interface. For the problem of Poiseuille flow over a semi-infinite porous bed, Neale and Nader (1974) have shown that the Brinkman model with constant porosity is identical to the Beavers and Joseph's formulation if the slip coefficient α is identified as

$$\alpha = \sqrt{\frac{\mu^*}{\mu}} \tag{2}$$

where μ^* is the viscosity of the fluid in the porous medium which is assumed to be different from the viscosity of the fluid layer given by μ.

The purpose of this paper is to investigate the effect of porosity variation on fully-developed conjugate flows in a channel bounded by a semi-infinite porous bed where the motion of the fluid is induced by the movement of the upper

Contributed by the Fluids Engineering Division for publication in the JOURNAL OF FLUIDS ENGINEERING. Manuscript received by the Fluids Engineering Division December 20, 1987.

boundary of the fluid layer, i.e., a conjugate Couette flow. The Brinkman model, with the porosity variation approximated by an exponential function, is used as the momentum equation in the porous bed. This formulation is, admittably, an oversimplification of a complex physical phenomenon. However, a comparison of the theoretical results based on this model with a number of natural convection experimental data has shown that this is the most accurate model available for the study of transport phenomena in porous media with a finite ratio of particle diameter to the characteristic length of the problem (David et al. 1990).

In this paper, an approximate expression for the permeability, applicable for a wide range of the porosity from 0.4 to 1.0, is constructed. An analytical expression is obtained for the velocity distribution in the semi-infinite porous bed. The velocity and shearing stress of the conjugate flows in the porous bed and in the channel are matched at the interface. An explicit expression for the slip coefficient is obtained in terms of the parameters in the porosity variation. It is shown that the value of the slip coefficient decreases as a result of porosity variation near the porous bed/fluid interface, as postulated by Beavers and Joseph (1967).

II Wall Effects on Porosity and Permeability

Measurements on the porosity of a packed-sphere bed show that the porosity changes drastically near a bounding wall because of the point contact between the spheres and the wall. It has been found that the porosity changes from a value of $0.36 \sim 0.4$ in the core to almost unity near the bounding surface (Roblee et al. 1958; Benenati and Brosilow, 1962). Chandrasekhara and Vortmeyer (1979) have proposed that the porosity variation near a wall can be approximated by an exponential function. In this paper, the porosity variation in the packed-spheres bed at $y^* \geq 0$ (see Fig. 1) will be approximated by

$$\phi^* = \phi^*_\infty + (\phi^*_0 - \phi^*_\infty)e^{-N_1 y^*/d_p} \tag{3}$$

where y^* is the distance from the porous medium/fluid interface located at $y^* = 0$; d_p is the particle diameter; ϕ^*_0 and ϕ^*_∞ are the porosities at the interface and far away from the interface. In most of the previous studies (Chandrasekhara and Vortmeyer, 1979; Vortmeyer and Schuster, 1983; Vafai, 1984), the values of $\phi^*_0 = 0.8$, $\phi^*_\infty = 0.4$ and $N_1 = 2$ have been used in connection with equation (3). However, recent studies (Hunt and Tien, 1987; Cheng et al. 1990) have shown that the value of $N_1 = 5 \sim 6$ should be used in equation (3) instead.

For a packed-sphere bed with uniform porosity ($\phi^* = \phi^*_0 = \phi^*_\infty = 0.4$), the permeability and the porosity are related by

$$K^* = \frac{d_p^2 \phi^{*3}}{A(1-\phi^*)^2} \tag{4}$$

where $A = 180$ is the Ergun constant (Ergun, 1952). For a dilute array of spheres the drag on each sphere follows the Stokes law, and the permeability of such an array of spheres is given by

$$K^* = \frac{d_p^2 \phi^{*2}}{18(1-\phi^*)}, \text{ as } \phi^* \to 1 \tag{5}$$

Recently, Zick and Homsy (1982) have shown numerically that the permeability of a periodic array of spheres is in good agreement with equations (4) and (5) at the limits of $\phi^* = 0.4$ and $\phi^* \to 1$, respectively. Thus, for a variable porosity medium where the value of ϕ^* may vary from 0.4 to 1.0, the expression for the permeability valid for $0.4 \leq \phi^* \leq 1.0$ can be constructed from equations (4) and (5) to give

$$K^* = \frac{d_p^2 \phi^{*3} F(\phi^*)}{A(1-\phi^*)^2} \tag{6a}$$

with

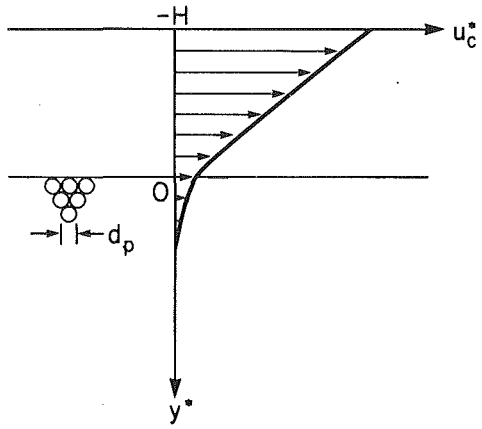

Fig. 1 Coordinate system

$$F(\phi^*) = 1 - \exp\left[-10\left(\frac{1-\phi^*}{\phi^*}\right)\right] \tag{6b}$$

where equation (6) reduces to equation (4) and (5) as $\phi^* \to 0.4$ and $\phi^* \to 1$ respectively. Equation (3) and (6) will be used as the expressions for the porosity and permeability in a variable porosity bed in this paper.

III Solutions for the Conjugate Flows

We now consider the problem of fully-developed conjugate flows in a channel bounded by a semi-infinite variable porosity bed at $y^* \geq 0$ (Fig. 1). The motion of the shear-driven flow is induced by the movement of the upper boundary of the channel located at $y^* = -H$. We shall now obtain the solutions for the channel flow and the porous media flow separately, and the solutions will be matched at the fluid and porous bed interface based on the continuity of velocity and shearing stress.

A. Solution for the Channel Flow. The governing dimensionless equation for the Couette flow in the channel is

$$\frac{d^2u^-}{dy^2} = 0, \quad -1 \leq y \leq 0 \tag{7}$$

where $y = y^*/H$ and $u^- = u^*/u_c^*$ with u_c^* denoting the velocity of the upper boundary. The boundary conditions are given by

$$y = -1, \quad u^- = 1 \tag{8}$$

$$y = 0^-, \quad u^- = u_i \tag{9}$$

where $u_i = u_i^*/u_c^*$ is the dimensionless velocity at the interface. The solution of equation (7) subject to boundary conditions (8) and (9) is

$$u^- = (y+1)u_i - y. \tag{10}$$

where the dimensionless interface velocity u_i remains to be determined.

B. Solutions for the Porous Media Flow. The governing dimensionless equations for the shear-driven flow in a variable porosity medium based on the Brinkman model with porosity and permeability given by equations (3) and (6) are

$$\sigma^2 \frac{d^2u^+}{dy^2} = \frac{\phi u^+}{K}, \quad y \geq 0 \tag{11}$$

$$\phi = 1 + (\phi_0 - 1)e^{-N_1 y/\gamma}, \quad y \geq 0 \tag{12}$$

$$K = \frac{\phi^3 F(\phi)}{[1 + c_\infty(1-\phi)]^2} \tag{13}$$

$$F = 1 - \exp\left\{-10\left[\frac{1-\phi^*_\infty \phi}{\phi^*_\infty \phi}\right]\right\} \tag{14}$$

where $u^+ = u^*/u_c^*$, $\phi = \phi^*/\phi_\infty^*$, $\phi_0 = \phi_0^*/\phi_\infty^*$, $K = K^*/K_\infty^*$, $c_\infty = \phi_\infty^*/(1 - \phi_\infty^*) = 2/3$ (if $\phi_\infty^* = 0.4$), and $\sigma = [\sqrt{K_\infty^*/\phi_\infty^*}]/H = \epsilon\gamma$ with $\epsilon = \phi_\infty^*/\sqrt{A(1-\phi_\infty^*)} = 0.005465$ (if $A = 180$ and $\phi_\infty^* = 0.4$) and $\gamma = d_p/H$ being the dimensionless particle diameter.

Equations (11)–(14) are to be solved subject to the following boundary condition at infinity

$$y \to \infty,\ u^+ = 0 \tag{15}$$

and the interface conditions

$$u^+(0^+) = u^-(0^-) \tag{16}$$

$$\frac{\mu}{\phi^*(0^+)}\frac{du^+}{dy}(0^+) = \mu\frac{du^-}{dy}(0^-) \tag{17a}$$

Note that for the special case of $\phi_0^* = \phi^*(0^+) = 1$, equation (17*a*) implies the continuity of slope across the interface. With the aid of equations (10) and (16), equation (17*a*) can be simplified as

$$\frac{1}{\phi_0^*}\frac{du^+}{dy}(0^+) = u^+(0^+) - 1 \tag{17b}$$

Equations (11)–(14) and (15)–(17) are the governing dimensionless equations and boundary conditions for flow in the semi-infinite porous bed. Numerical solutions to the two-point boundary value problem could have been obtained by the Runge-Kutta method, or by the finite difference method. However, an analytical solution is preferred here for the purpose of obtaining an analytic expression for Beavers and Joseph's slip coefficient (see Section IIIC below). To this end, we shall now obtain approximate analytical solutions for the cases of $\phi_0^* = 1$ and $\phi_0^* \neq 1$ separately.

Analytical Solution for the Case of $\phi_0^* = 1$. For this case we introduce the following new independent variable

$$\hat{Y} = Y/\epsilon^{2/3} = y/\Lambda \tag{18}$$

where $\epsilon = \sigma/\gamma$ and $\Lambda = \gamma\epsilon^{2/3}$. Substituting equation (18) into equations (11)–(14) gives the following equations for the first approximation:

$$\phi = \phi_0 - N_1(\phi_0 - 1)\epsilon^{2/3}\hat{Y} \tag{19a}$$

$$F = 10N_1(1 - \phi_\infty^*)\epsilon^{2/3}\hat{Y} \tag{19b}$$

$$K = \frac{10(1-\phi_\infty^*)}{\phi_\infty^*\epsilon^{2/3}\hat{Y}N_1} \tag{19c}$$

and

$$\frac{d^2u^+}{d\hat{Y}^2} - \hat{\lambda}^2\hat{Y}u^+ = 0 \tag{20}$$

where $\hat{\lambda} = \sqrt{\dfrac{\phi_\infty^{*2}N_1}{10(1-\phi_\infty^*)}} = 0.3651$ (if $\phi_0^* = 0.4$ and $N_1 = 5$).

Equation (20) is to be solved subject to the boundary conditions

$$\hat{Y} = 0:\ \frac{1}{\Lambda}\frac{du^+}{d\hat{Y}} = u^+ - 1 \tag{21a}$$

$$\hat{Y} \to \infty,\ u^+ = 0 \tag{21b}$$

The solution of equation (20) subject to the boundary condition (21*b*) is (Abramowitz and Stegun 1965)

$$u^+ = \frac{\hat{A}\,\hat{Y}^{1/2}K_{1/3}\left[\frac{2}{3}\hat{\lambda}\,\hat{Y}^{3/2}\right]}{\left[\hat{Y}^{1/2}K_{1/3}\left(\frac{2}{3}\hat{\lambda}\,\hat{Y}^{3/2}\right)\right]_{\hat{Y}=0}} = \frac{\hat{A}\Gamma\left(\frac{2}{3}\right)}{\pi}\left(\frac{\hat{\lambda}}{3}\right)^{1/3}\hat{Y}^{1/2}K_{1/3}\left(\frac{2}{3}\hat{\lambda}\,\hat{Y}^{3/2}\right) \tag{22}$$

where $K_{1/3}(z)$ is the Bessel function of the second kind, Γ is the Gamma function, and $\hat{A}$ is a constant to be determined. Substituting equation (22) into equation (17*b*) gives

$$\hat{A} = \frac{1}{1 + \dfrac{\hat{D}}{\Lambda}} \tag{23a}$$

where

$$\hat{D} = \frac{\Gamma\left(\frac{2}{3}\right)}{\Gamma\left(\frac{4}{3}\right)}\left(\frac{\hat{\lambda}}{3}\right)^{2/3} = 0.7290\hat{\lambda}^{2/3} \tag{23b}$$

Thus, for the case of $\phi_0^* = 1$, the velocity in the channel is

$$u^- = \frac{\Lambda(1+y)}{[\Lambda + 0.7290\hat{\lambda}^{2/3}]} - y,\ -1 \le y \le 0 \tag{24}$$

while the velocity in the semi-infinite porous bed is

$$u^+ = \frac{\Lambda(\hat{\lambda}/3)^{1/3}\Gamma(2/3)}{\pi(\Lambda + 0.7290\hat{\lambda}^{2/3})}(y/\Lambda)^{1/2}K_{1/3}\left[\frac{2}{3}\hat{\lambda}(y/\Lambda)^{3/2}\right],\ y \ge 0 \tag{25}$$

It follows that the velocity at the interface ($y = 0$) is

$$u_i = u^+(0^+) = u^-(0^-) = \frac{1}{1 + \dfrac{0.7290\,\hat{\lambda}^{2/3}}{\lambda}} \tag{26}$$

Analytical Solution for the Case $\phi_0^* \neq 1$. For $0.42 \le \phi_0^* \le 0.98$, we introduce the following new independent variable:

$$\tilde{Y} = y/\sigma \tag{27}$$

Substituting equation (27) into equations (11)–(14) yields the following equations:

$$\phi = \phi_0 + \epsilon\phi_1\tilde{Y} + 0(\epsilon^2)$$

$$F = F_0 + \epsilon F_1\tilde{Y} + 0(\epsilon^2) \tag{28}$$

$$\frac{1}{K} = \alpha_0 + \epsilon\alpha_1\tilde{Y} + 0(\epsilon^2)$$

and

$$\frac{d^2u^+}{d\tilde{Y}^2} = \tilde{\lambda}^2(z_0 + \tilde{Y})u^+ + 0(\epsilon^2) \tag{29}$$

where

$$\tilde{\lambda}^2 = \epsilon f_1,\quad z_0 = f_0/\tilde{\lambda}^2$$

$$f_0 = \phi_0\alpha_0,\quad f_1 = \phi_1\alpha_0 + \phi_0\alpha_1,\quad \phi_0 = \phi_0^*/\phi_\infty^* \tag{30}$$

$$\phi_1 = (\phi_0 - 1)N_1,\quad \alpha_0 = \frac{(1-\phi_0^*)^2}{\phi_0^3F_0(1-\phi_\infty^*)^2},$$

$$\alpha_1 = -\left(\frac{3\phi_1}{\phi_0} + \frac{2\phi_\infty^*\phi_1}{(1-\phi_\infty^*\phi_0)} + \frac{F_1}{F_0}\right)\alpha_0$$

with

$$F_0 = 1 - \exp\left[-10\left(\frac{1-\phi_0^*}{\phi_0^*}\right)\right] \text{ and}$$

$$F_1 = -\frac{10\phi_1}{\phi_\infty^*\phi_0^2}\exp\left[-10\left(\frac{1-\phi_0^*}{\phi_0^*}\right)\right].$$

Equation (29) is to be solved subject to the boundary conditions

$$\tilde{Y} = 0:\quad \frac{1}{\sigma\phi_0^*}\frac{du^+}{d\tilde{Y}} = u^+ - 1 \tag{31a}$$

$$\tilde{Y} \to \infty:\quad u^+ = 0 \tag{31b}$$

Here, the solution for u^+ is carried out directly to $O(\epsilon)$ to be in the same accuracy consistent with the solution for the case of $\phi_0^* = 1$ obtained in the preceding paragraph.

The solution to equations (29) and (31*b*) is (Abramowitz and Stegun, 1965)

$$u^+ = \tilde{A}\,\frac{(z_0+\tilde{Y})^{1/2}K_{1/3}\left[\frac{2}{3}\tilde{\lambda}(z_0+\tilde{Y})^{3/2}\right]}{z_0^{1/2}K_{1/3}\left[\frac{2}{3}\tilde{\lambda}z_0^{3/2}\right]},\quad 0\le\tilde{Y}\le\infty \tag{32}$$

Substituting equation (32) into equation (31*a*) yields

$$\tilde{A} = \frac{1}{1+\dfrac{\tilde{D}}{\sigma\phi_0^*}} \tag{33a}$$

where

$$\tilde{D} = \frac{Z_0^{1/2}\tilde{\lambda}K_{-2/3}\left[\frac{2\tilde{\lambda}}{3}Z_0^{3/2}\right]}{K_{1/3}\left[\frac{2}{3}\tilde{\lambda}\tilde{Z}_0^{3/2}\right]} = \frac{f_0^{1/2}K_{-2/3}\left[\frac{2}{3}f_0^{3/2}/\tilde{\lambda}^2\right]}{K_{1/3}\left[\frac{2}{3}f_0^{3/2}/\tilde{\lambda}^2\right]} \tag{33b}$$

and the interface velocity is given by

$$u_i = u^+(0) = \tilde{A} = \frac{1}{1+\dfrac{\tilde{D}}{\sigma\phi_0^*}} \tag{33c}$$

We now consider equations (32) and (33) at the limits of $\phi_0^* \to \phi_\infty^*$ and $\phi_0^* \to 1$, respectively. At the limit of $\phi_0^* \to \phi_\infty^*$ (which is the case of a constant porosity medium), we note that $F_1 = \phi_1 = \alpha_1 = f_1 = 0$, $F_0 = f_0 = \phi_0 = 1$, and consequently $z_0 \to \infty$. At this asymptotic limit, $\tilde{D} = 1$ and equations (32) and (33) give

$$u^+ = \tilde{A}\exp[-\tilde{Y}],\quad 0\le\tilde{Y}\le\infty \tag{34}$$

where

$$\tilde{A} = u^+(0) = \frac{1}{1+\dfrac{1}{\sigma\phi_0^*}} \tag{35}$$

Consider next the case of $\phi_0^* \to 1$. At this limit, we note that $f_0 \to 0$, $f_1 \to \phi_\infty^{*2}/10\,(1-\phi_\infty^*)$ and consequently $z_0 = 0$ and $\tilde{\lambda} = \epsilon^{1/2}\lambda$. At this asymptotic limit, equation (32) reduces to equation (25) since $\tilde{\lambda}\tilde{Y}^{3/2} = \lambda\tilde{Y}^{3/2}$.

C. Comparison With Beavers and Joseph's Formulation. We now obtain the solution of the present problem based on Beavers and Joseph's formulation. Their approach is based on the following assumptions: (1) Darcy's law is applicable in the porous bed, (2) the porosity is constant throughout the porous bed, i.e., $\phi^* = \phi_\infty^* = 0.4$, $K^* = K_\infty^*$, and (3) the interface condition is given by equation (1).

The solution for the channel flow is again given by equation (10). Imposing boundary condition (1) on equation (10) and noting $Q^* = 0$ in the porous bed for the present problem with no externally imposed pressure gradient, we obtain the following expression for the slip velocity at the interface

$$u_i = \frac{1}{1+\dfrac{\alpha H}{\sqrt{K_\infty^*}}} \tag{36}$$

Comparing equation (36) with equations (26), (32), and (35) gives the following expressions for the slip coefficient:

(*i*) For $\phi_0^* = 1$, $\alpha = \dfrac{0.729\phi_\infty^{*3/2}N_1^{1/3}}{180^{1/6}10^{1/3}(1-\phi_\infty^*)^{2/3}} = 0.08659$ (if $\phi_\infty^* = 0.4$ and $N_1 = 5$) (37*a*)

(*ii*) For $0.42 < \phi_0^* < 0.98$,

$$\alpha = \frac{\tilde{D}\sqrt{\phi_\infty^*}}{\phi_0^*} = f_0^{1/2}\,\frac{K_{-2/3}\left[\frac{2}{3}f_0^{3/2}/\tilde{\lambda}^2\right]}{K_{1/3}\left[\frac{2}{3}f_0^{3/2}/\tilde{\lambda}^2\right]}\,\frac{\sqrt{\phi_\infty^*}}{\phi_0^*} \tag{37b}$$

(*iii*) For $\phi_0^* = \phi_\infty^* = 0.4$, $= \dfrac{1}{\sqrt{\phi_0^*}} = \dfrac{1}{\sqrt{0.4}} = 1.58.$ (37*c*)

It is relevant to note that the analytic expression for the slip coefficient α given by equation (37) is possible because the interface slip velocity has been obtained in closed form as given by equations (26), (32), and (33*c*). Had we obtained a numerical solution to the problem, an explicit expression for the slip coefficient α cannot be obtained since a comparison with equation (36) is not possible. It can be concluded from equation (37) that the value of the slip coefficient α depends only on the porosity variations (i.e., the values of ϕ_0^*, ϕ_∞^* and N_1). The fact that the slip coefficient α is independent of the dimensionless particle diameter γ is unexpected and can only be shown when an analytical solution is obtained. Note that equation (37*c*) is in agreement with equation (2) since $\mu/\mu^* = \phi_\infty^*$ for a constant porosity medium according to the present formulation.

IV Results and Discussion

The velocity distributions of the conjugate flows given by equations (24)–(26) for $\phi_0^* = 1$, equations (32) and (33) for $0.42 \le \phi_0^* \le 0.98$, and equations (34)–(35) for $\phi_0^* = 0.4$ are computed with $\phi_\infty^* = 0.4$, $N_1 = 5$ and $A = 180$ at selected values of the dimensionless particle diameter γ. The computed velocity are presented in Figs. 2 and 3. Since no measurements are available for Couette flow over a packed-spheres bed, a comparison of theoretical and experimental results cannot be made.

Figure 2(*a*) shows the effect of the dimensionless particle diameter γ on the velocity distributions for the case of $\phi_0^* = 1$. It is shown that viscous shear effect penetrates into the porous bed. The depth of penetration increases with increasing value of the dimensionless particle diameter γ; the magnitude and slope of the tangential velocity are continuous across the interface.

Figure 2(*b*) shows the effect of the interfacial porosity ϕ_0^* on the velocity distributions at a given value of the dimensionless particle diameter γ ($\gamma = 0.3$). As the interfacial porosity increases from 0.4, the tangential velocity increases everywhere in the channel and in the porous bed. For the case of $\phi_0^* \ne 1$, although the magnitude of the tangential velocity is continuous across the interface, the slope of the tangential velocity is discontinuous. This is because although the shearing stress of the channel flow and the porous media flow are matched at the interface, the effective viscosity in the porous medium differs from that in the fluid layer, resulting in a discontinuity of slope at the interface (see equation (17*a*)). This effect becomes more pronounced as the interfacial porosity ϕ_∞^* decreases from unity.

The interfacial velocity as a function of the interfacial porosity ϕ_0^* and dimensionless particle diameter γ is presented in Fig. 3. It is shown that the interfacial velocity increases with increasing value of the interfacial porosity ϕ_0^* or the dimensionless particle diameter γ. For the case of uniform porosity ($\phi_0^* = \phi_\infty^* = 0.4$), the interfacial velocity increases almost linearly with the dimensionless particle diameter γ. For other values of interfacial porosity ϕ_0^*, the interfacial velocity is also linearly proportional to the dimensionless particle diameter γ for small value of γ ($\gamma < 0.2$). At higher value of the dimensionless particle diameter γ, the variation of the interfacial velocity begins to deviate from that of a straight line.

The slip coefficient α given by equation (44) is presented in

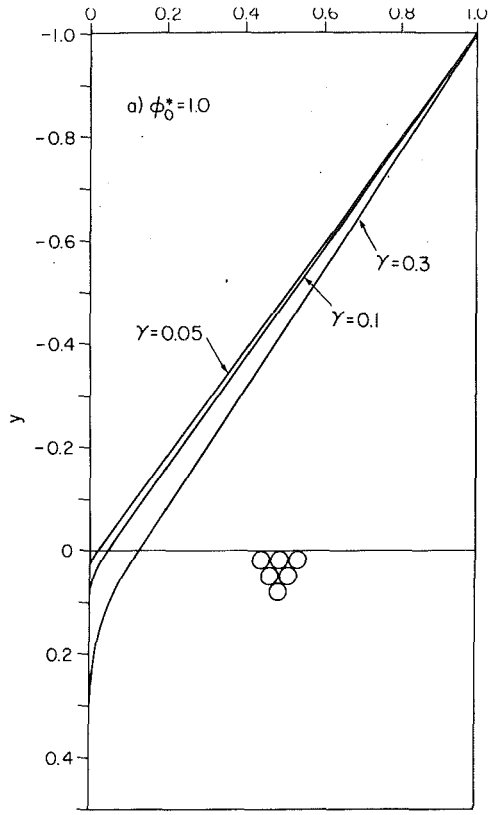

Fig. 2(*a*) Effects of dimensionless particle diameter γ on the velocity profile of the conjugate shear-driven flow

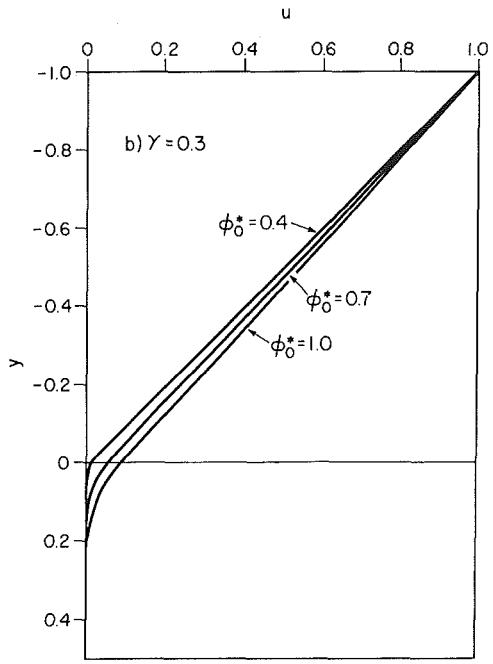

Fig. 2(*b*) Effects of interfacial porosity ϕ_0^* on the velocity profiles of the conjugate shear-driven flow

Fig. 4 as a function of the interfacial porosity ϕ_0^*. It is shown that the slip coefficient α decreases from a value of 1.58 at $\phi_0^* = 0.4$ (uniform porosity medium) to a value of 0.08659 at $\phi_0^* = 1$. This confirms with Beavers and Joseph's postulation that the value of the slip coefficient would decrease as a result of the variable porosity effect.

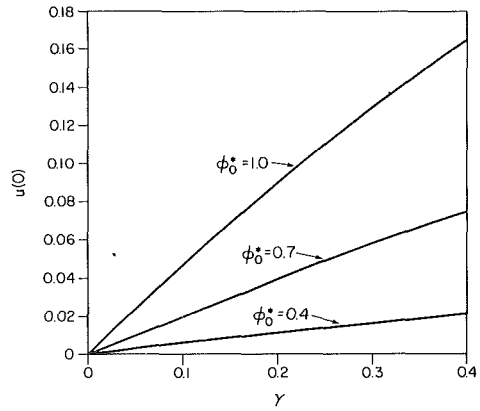

Fig. 3 The interfacial velocity u_i as a function of dimensionless particle diameter γ at selected values of interfacial porosity ϕ_0^*

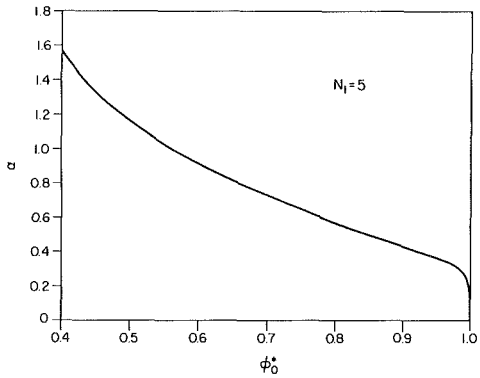

Fig. 4 The variation of the slip coefficient α as a function of the interfacial porosity ϕ_0^*

V Concluding Remarks

An approximate analytical solution based on a perturbation method has been obtained for the conjugate Couette flow in a channel over a semi-infinite medium with variable porosity. It is shown that the dimensionless velocity profiles in the channel and in the porous bed depend not only on the porosity variation (i.e., the values of ϕ_0^*, ϕ_∞^*, and N_1), but also on the dimensionless particle diameter γ. However, the slip coefficient α for the present problem is found to be independent of the dimensionless particle diameter γ. The value of the slip coefficient α is shown to decrease because of the variable porosity effect, which is in agreement with experimental observations.

Acknowledgment

The authors would like to thank Professor D. P. Telionis of the Virginia Polytechnic Institute and State University for helpful suggestions. The senior author (P. Cheng) would also like to acknowledge the support of the U. H. Foundation on this work through the 1989-90 Fujio Matsuda Fellow Award.

References

Abramowitz, N., and Stegun, I. A., 1965, *Handbook of Mathematical Functions*, Dover, New York.

Bear, J., 1972, *Dynamics of Fluids in Porous Media*, American Elsevier Publishing Inc., New York.

Beavers, G.S., and Joseph, D. D., 1967, "Boundary Conditions at a Naturally Permeable Wall," *Journal of Fluid Mechanics*, Vol. 30, pp. 197-207.

Beavers, G. S., Sparrow, E. M., and Magnuson, R. A., 1970, "Experiments on Coupled Parallel Flows in a Channel and a Bounding Porous Medium," *Basic Engg.*, Vol. , pp. 843-848.

Benenati, R. F., and Brosilow, C. B., 1962, "Void Fraction Distribution in Beds of Spheres," *A.I.Ch.E.J.*, Vol. 8, pp. 359-361.

Brinkman, H. C., 1947, "A Calculation of the Viscous Force Exerted by a Flowing Fluid on a Dense Swarm of Particles," *Applied Sci. Res.*, Vol. A1, pp. 27–34.

Chandrasekhara, B. C., and Vortmeyer, D., 1979, "Flow Model for Velocity Distribution in Fixed Porous Beds Under Isothermal Conditions," *Warm-und Stoffubertragung*, Vol. 12, pp. 105–111.

Cheng, P., 1978, "Heat Transfer in Geothermal Systems," *Advances in Heat Transfer*, Vol. 14, pp. 1–105.

Cheng, P., Chowdhury, A., and Hsu, C. T., 1990, "Forced Convection in Packed Tubes and Channels with Variable Porosity and Thermal Dispersion Effects," paper presented at the 1990 NATO Advanced Study Institute on Convective Heat and Mass Transfer in Porous Media, Izmir, Turkey.

Cheng, P., Hsu, C. T., and Chowdhury, A., 1988, "Forced Convection in Entrance Region of a Packed Channel with Asymmetric Heating," ASME *Journal of Heat Transfer*, Vol. 110, pp. 946–954.

Davis, E., Lauriat, G., and Cheng, P., 1990, "A Numerical Solution of Variable Porosity Effects on Natural Convection in a Packed-Sphere Cavity," ASME *Journal of Heat Transfer* (in press).

Ergun, E., 1952, "Fluid Flow Through Packed Columns," *Chem. Engg. Prog.*, Vol. 48, pp. 89–94.

Hunt, M. L., and Tien, C. L., 1987, "Non-Darcy Convection in Cylindrical Packed Beds," *Proc. of the 2nd ASME/JSME Thermal Engineering Joint Conference*, Vol. 2, pp. 433–438.

Neale, G., and Nader, W., 1974, "Practical Significance of Brinkman's Extension of Darcy's Law: Coupled Parallel Flows within a Channel and a Bounding Porous Medium," *Can. J. Chem. Eng.*, Vol. 52, pp. 475–478.

Nield, D. A., 1977, "Onset of Convection in a Fluid Layer Overlying a Layer of a Porous Medium," *Journal of Fluids Mechanics*, Vol. 81, pp. 513–522.

Rudraiah, N., 1985, "Coupled Parallel Flows in a Channel and a Bounding Porous Medium of Finite Thickness," Vol. 107, pp. 322–329.

Roblee, L. H. S., Baird, R. M., and Tiern, J. W., 1958, "Radial Porosity Variation in Packed Beds," *A.I.C.h.E.J.*, Vol. 4, pp. 460–464.

Somerton, C. W., and Catton, I., 1982, ASME *Journal of Heat Transfer*, Vol. 104, pp. 160–165.

Taylor, G. I., 1971, "A Model for the Boundary Condition of a Porous Material. Part I," *Journal of Fluid Mechanics*, Vol. 49, pp. 319–326.

Vafai, K., 1984, "Convective Flow and Heat Transfer in Variable Porosity Media," *Journal of Fluid Mechanics*, Vol. 147, pp. 233–259.

Vortemeyer, D., and Schuster, J., 1983, "Evaluation of Steady Flow Profiles in Rectangular and Circular Packed Beds by a Variational Method," *Chem. Engg. Sci.*, Vol. 38, pp. 1691–1699.

Zick, A. A, and Homsy, G. M., 1982, "Stokes Flow Through Periodic Arrays of Spheres," *Journal of Fluid Mechanics*, Vol. 115, pp. 13–26.

Journal of Fluids Engineering

Technical Briefs

Visualization of High Blockage Flow Behind a Flat Plate in a Rectangular Channel

C. O. Popiel[1] and J. T. Turner[2]

Nomenclature

a = length of plate ($a = 350$ mm) or cylinder
A = aspect ratio of plate or cylinder, a/b
b = width of plate or diameter of cylinder
B = area blockage ratio, b/h
h = height of channel having rectangular cross section, axh
R = length of recirculating wake
Re = Reynolds number, $U_1 h/\nu$
ΔT = camera exposure time
U_1 = mean gap velocity
x, y = coordinates (Fig. 2)
ν = kinematic viscosity of fluid

Introduction

Flow configurations involving a baffle or other bluff body located in a flow channel occur in many devices. Recently, interest in the influence of high blockage on cross flow has grown due to the need to verify computational solutions for the flow and temperature distributions in engineering situations, such as occur in nuclear reactor subchannels (e. g., Kottowski, 1981) and combustion systems (e. g., Gosman, 1987). Flow past a normal flat plate placed centrally in a confined two-dimensional channel is geometrically one of the simplest high blockage flow arrangements which can be envisaged. The details of the flow are characterised by a recirculating wake surrounded by two separated shear layers springing from the edges of the plate. The situation may be further complicated by the appearance of regular vortex shedding. When the frontal area of the bluff body relative to the channel cross section (the blockage ratio) becomes sufficiently high, significant changes in the mean flow distribution occur and vortex shedding may be suppressed. It is believed that the strong reverse flow in the wake on its axis can be an important factor in the mechanism that suppresses the vortex shedding (McKillop and Turner, 1986).

The mechanism by which coherent flow structures are formed in the near-wake region behind a flat plate, held normal to the nominally two-dimensional channel flow, is not fully understood and few papers on this subject appear to have been published. The effect of low levels of blockage (from 2 to 16 percent) and aspect ratio (from 4 to 10) on the flow past a circular cylinder was studied by West and Apelt (1982). They concluded that blockage ratios beyond 6 percent can produce considerable distortion of the flow. For high blockage two-dimensional flow over circular cylinders, the critical value of blockage ratio at which vortex shedding ceases, according to Sanei (1984) and Mabuchi and Hiwada (1982), is between 0.58 and 0.60. Other details concerning the near wake created by flow past a normal flat plate at a blockage ratio of 10 percent and aspect ratio of 15 were published by Bradbury (1976). His results, obtained with the pulsed-wire anemometer, showed that the wake extends to approximately two plate widths downstream and is characterized by a very high reverse flow in which the mean velocity level attains 50 percent of the freestream velocity in the gap. The purpose of the present visualization study was to obtain a direct insight into the nature of the high blockage flow and to recognize its general features.

Experimental Setup and Flow-Visualization Techniques

The experiments were performed in an open return recirculating water loop (Fig. 1) with a test section constructed from high quality 10 mm thick glass. The mean velocity profiles across the test section (without the blockage plate in position) measured with a laser Doppler anemometer revealed the presence of boundary layers on the top and bottom walls of the channel, with a thickness of about 18 percent of the channel height. The turbulence intensity at the center of the channel

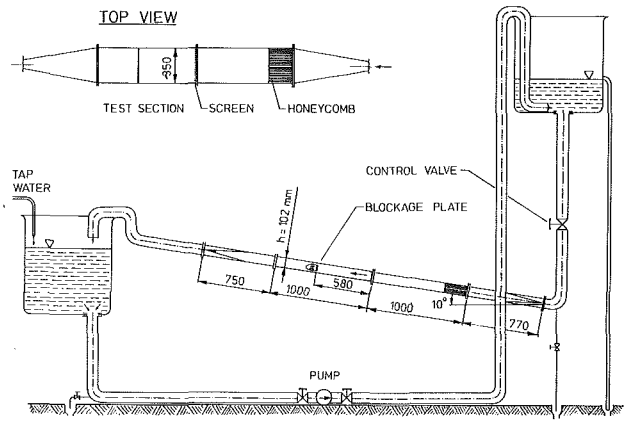

Fig. 1 Layout of water rig used for visualization of high blockage flow

[1]Technical University, 60965 Poznan, Piotrowo 3, Poland. Presently, Energy Laboratory, Rand Afikaans University, Johannesburg 2000, South Africa. Mem. ASME.
[2]University of Manchester, Manchester M13 9PL, England.
Contributed by the Fluids Engineering Division of THE AMERICAN SOCIETY OF MECHANICAL ENGINEERS. Manuscript received by the Fluids Engineering Division June 12, 1989

did not exceed the value of 4 percent. Two flat plates, 71 by 350 mm and 50.8 by 350 mm, respectively, and each 6 mm thick, were mounted symmetrically in turn in the test section with their planes normal to the incident flow. This produced corresponding values for the area blockage and plate aspect ratios of $B=0.7$ and $A=4.9$, or $B=0.5$ and $A=6.9$, respectively. The sharp edges of the plates were bevelled at 45°.

Particle Streak Photography. The flow was made visible by creating a suspension of small polystyrene beads (below 0.2 mm in diameter). Illumination was provided by a 15 mm wide sheet of intense light, which was generated by a 250W lamp using a cylindrical collimating lens attached to the optics of a standard slide projector. The light sheet was directed across the horizontal and vertical directions at the center of the channel and at right angles to the flow direction. The pictures were taken with the camera located to the side or above the test section (referred to subsequently as the side or top views).

Dye Flow Visualization. Red and blue dye were injected into the two boundary layers on the front surface of the plate through two small holes (1 mm in diameter) located symmetrically at the mid-span plane in the vicinity of the stagnation line ($y=\pm 6$mm). By this means, the evolution of the free shear layers after separation from the sharp edges of the plate could be made visible. It was found that reliable flow patterns could only be obtained at gap velocities higher than approximately 14 mm/s. At lower velocity levels, the inevitable slight differences in density between the food coloring dye solution and the bulk water caused significant deformation of the dye filaments. This typically appeared, after boundary-layer separation, as fine feathering on the edges of the dye streak.

Results and Discussion

No large-scale (of order b) regular vortex shedding could be found for either plate or Reynolds number, although a well-established large recirculating wake was observed in both cases. Three regions of distinct flow behavior, which evolved in the wake as the Reynolds number was increased, could be distinguished. This changing behavior of the wake flow produced the peculiar variation of the recirculating wake length with the Reynolds number which is shown as Fig. 2.

Laminar Region. At low Reynolds numbers (below about 300), the flow in the wake was characterized by the presence of two large elongated and essentially steady laminar "twin vortices" — see Fig. 3(*a*). Here, the wake length R could be precisely determined and was given by $R=1.3h$ for $B=0.7$ and $R=1.2h$ for $B=0.5$.

Transient Region. At Reynolds numbers between 300 and 8000, the flow in the near-wake was characterized by a growing instability of the initially laminar free shear layers that develop from the sharp edges of the plate. The development of turbulence was also observed in the central portion of the wake. The departure from symmetry of the instantaneous flow pattern was very clearly demonstrated both in and behind the wake. At first, the "twin vortices" were seen to become unstable, unsymmetrical, smaller, and shifted toward the end of the wake (Fig. 3(*b*)). At this stage the sharp increase of the wake length was observed. This length reached its local maximum, given by $R/h=1.6$ to 2.4, at the first critical Reynolds number of about $\mathrm{Re}_I=1600$, as shown in Fig. 2. At higher Reynolds numbers large-scale vortex structures developing in the free shear layers surrounding the (by now) highly disturbed interior of the wake were observed. Development of these structures on both sides of the wake caused stronger entrainment of the fluid from the interior of the wake to the shear layers. This, in turn, produced stronger flow reversal on the wake axis and a very strong decrease in the wake length. The

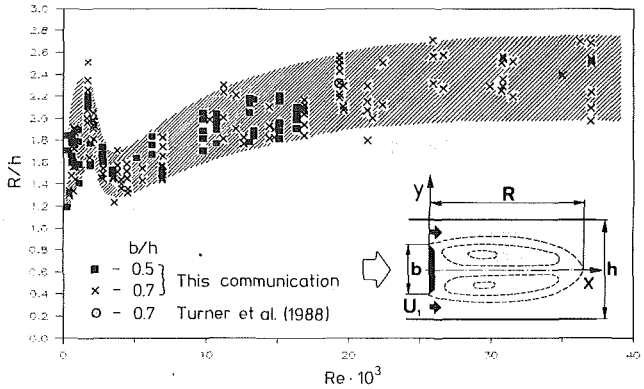

Fig. 2 Length of recirculating wake in a nominally 2-D high blockage flow. (Uncertainty in Re: less than ±5 percent and in R/h: less than ±3 percent.)

three-dimensional fluctuations of fluid in the wake prevailed and, occasionally, some strong reversed jet-like flows were observed close to the wake axis (Fig. 3(*c*)). This complicated situation persisted until a second critical Reynolds number of about $\mathrm{Re}_{II}=3{,}600$ was achieved where the wake length was at its minimum.

As the Reynolds number was further increased, the recirculating flow in the wake became strongly turbulent without any traces of a regular vortex pattern and the jet-like backward flow on the wake axis occurred more frequently. Flow downstream of each gap between the plate edges and the channel side walls then resembled a wall jet. At the downstream end of the wake, the flow emanating from the gaps separated from the side walls of the channel in a motion which was usually out-of-phase. Ultimately, these bypass flows were observed to spread and unite beyond the recirculating wake. Just behind the separation points on the side walls, large-scale "side wall eddies" appeared which rolled downstream along the walls, forcing the flow downstream of the wake to wave in a flag-like manner.

Turbulent Region ($Re>8{,}000$). In this region, the flow in the wake is characterized by a high level of turbulence, a mixture of small and large eddy scales, and a very strong reverse flow along the axis (Fig. 3(*d*)). The turbulence appears to be generated in the free shear layers behind the separation points and then develops further due to strong interactions between the side wall jet-like flow and the reversed flow in the wake. Besides this, at the plate rear surface and also at the end of the wake, strong large scale transverse fluctuations were observed (Fig. 4). Moreover, just downstream of the plate, in the corners between the channel end walls and the plate, two large standing "end wall vortices" with their axes parallel to the end walls and plate were observed. These vortices are clearly driven by the strong reversed flow zone. Presumably, they are necessary to close the loop of the vorticity line of the main vortex motions in the recirculation wake. The practical relevance of these vortices is that at low aspect ratios the flow in the wake cannot be treated as two-dimensional. Observe also that the coincidence point at the downstream end of the wake was now hardly discernible because of the turbulent fluctuations. Beyond the wake, one of the wall jets was occasionally seen to separate from the side wall to produce a typical "side wall eddy."

Length of Recirculating Wake. The variation of the normalized wake length with Reynolds number was deduced from a large number of streak photographs. The results of this analysis are presented in Fig. 2. The data points represent the instantaneous length of the wake, defined as the distance between the front plane of the plate and the coincidence point.

(*a*) Laminar twin vortices at $B = 0.7$, Re = 377, and $\Delta T = 5$ s

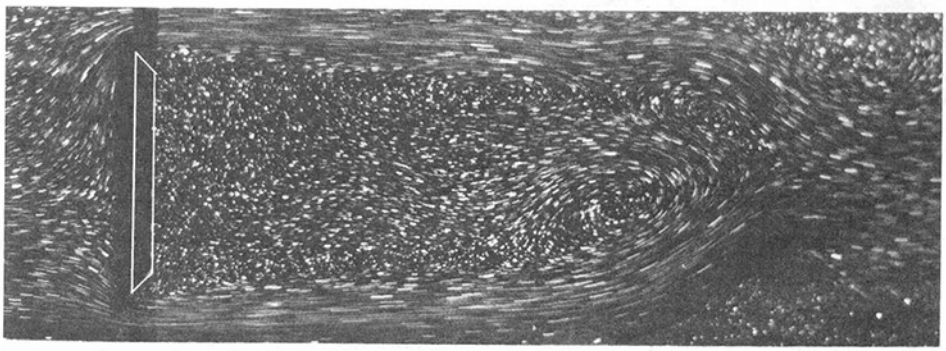

b) In transient region at $B = 0.7$, Re = 660, and $\Delta T = 1$s

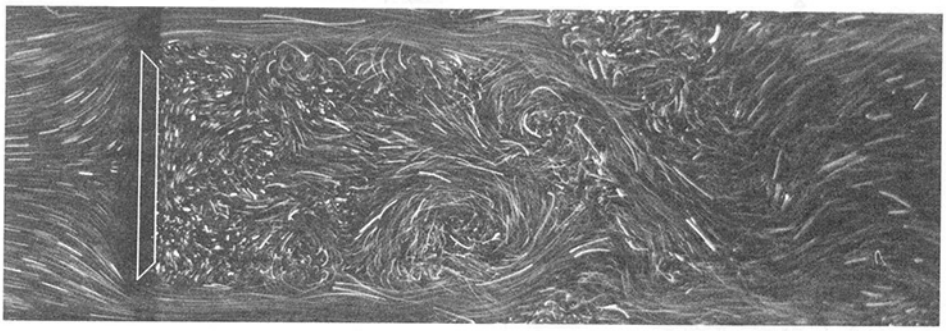

(*c*) In transient region at $B = 0.7$, Re = 4,500, and $\Delta T = 1/2$ s

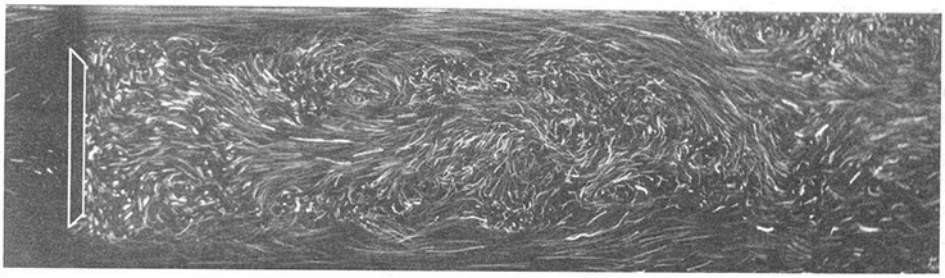

(*d*) In turbulent region at $B = 0.7$, Re = 35,000, and $\Delta T = 1/15$ s

Fig. 3 Particle path patterns (side view)

For the purpose of this investigation the coincidence point has been defined as the central point of the zone over which the fluid does not exhibit any preferred flow direction. The obviously wide spread of the experimental points (approximately ±20 percent, reflects the high level of large-scale fluctuation in the wake. The behavior of the flow behind the plate at the blockage of 50 percent was very similar to the flow at 70 percent blockage. Moreover, the data are similar when scaled by the height of the confining channel (h) and the gap velocity (U_1).

Finally, it is observed that the aspect ratio for the plate was changed from $A = 4.9$ to 6.9 when the blockage ratio was reduced from 0.7 to 0.5. Fail et al. (1957) have shown that the length of the wake generated by a rectangular flat plate (without end walls) depends strongly on the aspect ratio (Fig. 5). They recorded the highest wake length $R/b = 7.15$ at an aspect ratio of A = 10. In contrast, our results for corresponding aspect ratios are about 30 percent lower, which can be explained by allowing for the effects of the high blockage and the end

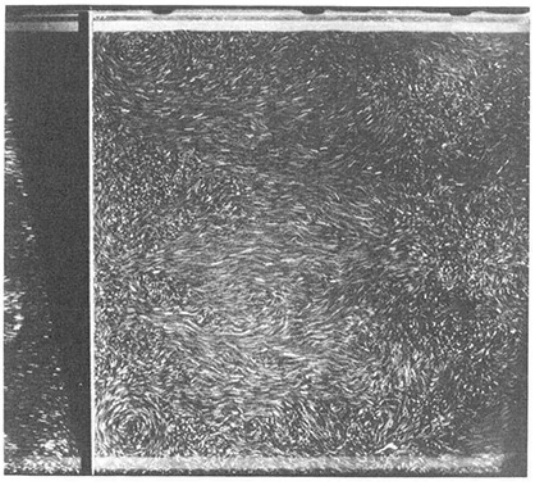

Fig. 4 Particle path patterns (top view) at B = 0.7, Re = 36,900 and ΔT = 1/30 s

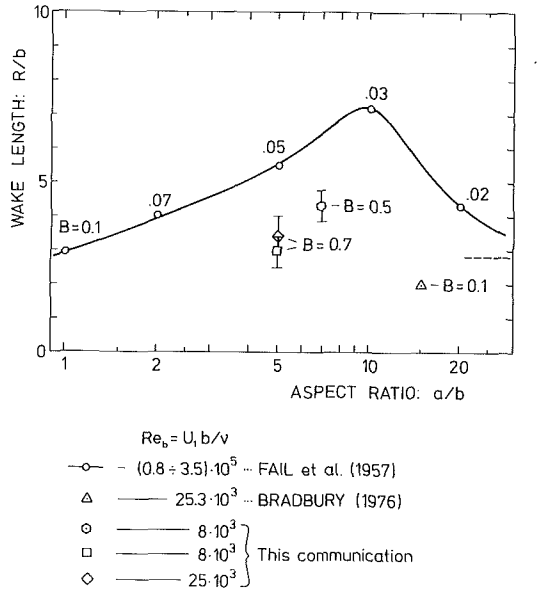

Fig. 5 Effect of aspect ratio on the length of recirculating wake

walls producing a different flow organization. In particular, the significantly lower result of Bradbury (1976) suggests that the effect of the end walls can be very important.

Dye Flow Visualization of the Shear Layers. The striking feature of the pattern of the vortex flow in the free shear layers is the perfect symmetry of the dye filament (see Fig. 6). The two boundary layers, separating from the edges of the plate, produce two shear layers which continued for some distance downstream (dependent on the Reynolds number) in a laminar state. These shear layers eventually become periodic and "roll-up" into discrete vortices, which are distributed as symmetrical pairs on the two sides of the wake. Every photographic record and visual observation show that these events occurred precisely at the same time and distance from the separation point, i. e., these vortex structures in the upper and lower free shear layers were formed and developed in precisely the same way as if one were a mirror image of the second. This suggests the existence of a common triggering mechanism which controls the Kelvin-Helmholtz instability of the initially steady laminar free shear layers. The origins of this mechanism are not yet fully understood, although there are some similarities to the observations made on a free jet by Bradshaw (1966). The most likely explanation is that the induced velocity field associated

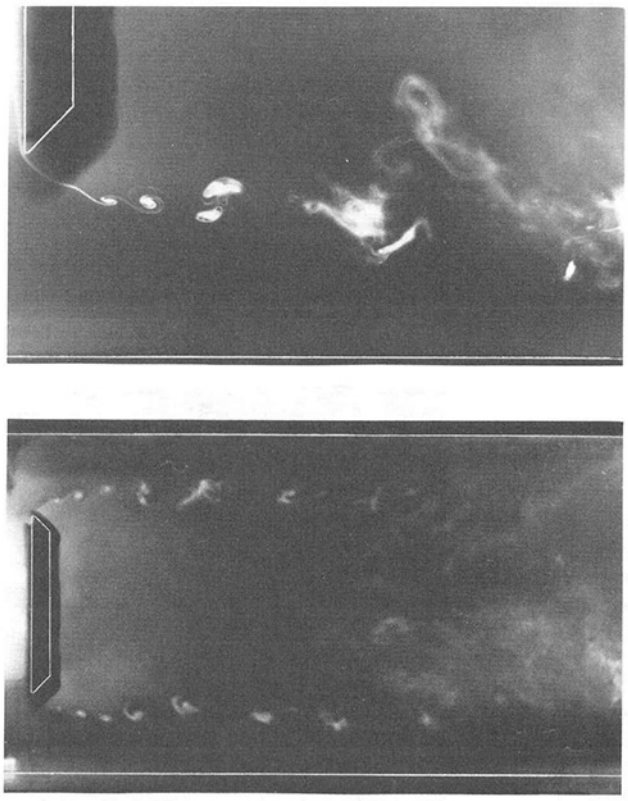

Fig. 6 Dye filament patterns of the free shear layers near the separation line behind plate at B = 0.5 and Re = 16,300

with the developing vortices produces small pressure pulsations across the rear surface of the blockage plate, thus synchronizing disturbances along the plate edges.

Acknowledgment

The authors are pleased to acknowledge the financial support of Thorn EMI Flow Measurement Ldt. during part of this investigation.

References

Bradbury, L. J. S., 1976, "Measurements with Pulsed-wire and Hot-wire Anemometer in the Highly Turbulent Wake of a Normal Flat Plate," *J. F. M.*, Vol. 77/3, pp. 473-497.

Bradshaw, P., 1966, "The Effect of Initial Conditions on the Development of a Free Shear Layer," *J. F. M.*, Vol. 26/2, pp. 225-236.

Fail, R., Lawford, J. A., and Eyre, R. C. W., 1957, "Low-speed Experiments on the Wake Characteristics of Flat Plates Normal to an Air Stream," Reports and Memoranda (R.A.E. Report Aero. 2516, 1958), No. 3120, June, pp. 1-23.

Gosman, A. D., 1987, "Application of LDA Measurements to Computational Fluid Mechanics," *Proc. 2nd Int. Conf. on "Laser Anemometry-Advances and Application."* Strathclyde, ed. J. T. Turner and S. M. Fraser, Springer-Verlag, pp. 23-29.

Kottowski, H. M., 1981, "Blockages in LMFBR Subassemblies," Chapter 22 "*Nuclear Reactor Safety Heat Transfer*," ed., O. C. Jones, Jr., Hemisphere, pp. 571-811.

Mabuchi, I., and Hiwada, M., 1987, "Flow Behaviour and Heat Transfer Around a Circular Cylinder at High Blockage Ratios," Heat Transfer, Japanese Research 11, Scripta Publ. Corp., Washington.

McKillop, A. A., and Turner, J. T., 1988, "The Effect of Vortex Shedding Suppression on Wake Flow Properties Behind Flat Plates," Selected papers from the 3rd Int. Symposium, Lisbon 1986, *Laser Anemometry in Fluid Mechanics*," ed. R. J. Adrian et al., pp. 213-225.

Sanei, N., 1984, "Effect of High Blockage on Flow Over Cylinders in a Duct with High Aspect Ratio," M. S. thesis, University of California, Davis.

Turner, J. T., Christodoulou, M., and McKillop, A. A., 1988, "Confined Turbulent Flow Around a Normal Flat Plate." 8th Symposium on Turbulence, University of Missouri-Rolla.

West, G. S., and Apelt, C. J., 1982, "The Effect of Tunnel Blockage and Aspect Ratio on the Mean Flows Past a Circular Cylinder with Reynolds Numbers Between 10^4 and 10^5," J. F. M., Vol. 114, pp. 361-377.

The Role of Residual Nonturbulent Disturbances on Transition Onset in Two-Dimensional Boundary Layers

Rama Govindarajan[1] and R. Narasimha[1,2]

An analysis of procedures in current use for prediction of transition onset location shows that they are generally in poor agreement with data obtained in test facilities at low freestream turbulence levels. It has been shown elsewhere that under such conditions transition is driven by residual nonturbulent disturbances in the facility. A method is developed for taking such disturbances into account by defining an equivalent freestream turbulence intensity; values for this parameter are derived for each facility from which onset data are available. A new correlation incorporating this effect is shown to be in good agreement with all available data on two-dimensional flows with pressure gradient. The correlation suggests that the onset Reynolds number (based on boundary-layer thickness) depends inversely on the total disturbance level when the latter is low.

Introduction

The boundary layer on a surface is laminar for some distance from the leading edge and undergoes transition to turbulence downstream as the Reynolds number increases. The streamwise position at which turbulent spots first appear is here called the transition onset location. The prediction of this onset location, and of the flow in the transition "zone" (see e.g., Narasimha, 1985) before the flow becomes fully turbulent are important engineering problems that are encountered in a variety of applications such as turbomachinery, the space shuttle, the aerospace plane etc.

The Reynolds number at onset, $R_t = U\theta_t/\nu$, (where U is the freestream velocity, θ_t is the momentum thickness at transition onset and ν is the kinematic viscosity) depends on several factors like pressure gradient, freestream turbulence, facility-dependent disturbances like vibration and noise in the case of test data, surface roughness, Mach number etc. Of these the first three are considered in this report. In the absence of any rational theory yet of the transition process, engineering estimates have often had to be based on empirical or semi-empirical procedures. Some of these procedures (e.g., Granville, 1953, and the e^n method of Smith and Gamberoni, 1956) take account of the influence of pressure gradient on the stability of the boundary layer. However, it has been known since the classical work of Schubauer and Skramstad (1948) that transition onset depends strongly on environmental disturbance levels. In low-speed wind tunnel experiments, such disturbances have usually been considered to arise solely from freestream turbulence, and some account of its effect has been sought to be taken either by modifications of earlier procedures (Arnal et al., 1984; Mack, 1977) or by empirical correlations. It is significant, however, that the proposal of Mack for n as a function of the intensity of freestream turbulence q does not agree with experimental data at low q. The empirical correlations consider the values at transition of q [in percent, defined as $100 \times (2K/3)^{1/2}/U$, where K, equal to half the sum of the mean squared fluctuating velocity components, is the turbulent kinetic energy per unit mass of fluid] and the Thwaites (1949) pressure gradient parameter λ [$= (dU/dx)\theta^2/\nu$ where dU/dx is the streamwise gradient of the freestream velocity U]. The predictions of three such correlations are compared with experimental data in Fig. 1. It is seen that both the correlation of Singh (1974) (which is a modified version of that of Seyb (1967) and of Dunham (1972) consistently predict onset at a higher Reynolds number than that observed experimentally. Abu-Ghannam and Shaw's (1980) correlation provides a good fit except at low q (see e.g., the appreciable difference from the data of Wells, 1967).

Present Correlation in Zero Pressure Gradient Flows

An analysis of the available experimental data shows, however, that the value of the Reynolds number R_{xt} (based on the steamwise distance x) observed in different facilities as q becomes very low is not the same. For example, while Schubauer and Klebanoff (1955) report $R_{xt} \sim 3 \times 10^6$ for $q < 0.03$ percent, Wells (1967) reports values as high as 5×10^6 for the same q. On the other hand, at somewhat higher values of q there is broad agreement among all available data. On the basis of such observations, the effect of freestream turbulence in constant-pressure boundary layers is best considered under three different regimes (Narasimha, 1985):

1. High freestream turbulence, where the onset Reynolds number is nearly independent of the turbulence level, and levels off around the instability-critical value.
2. Moderate turbulence, where the onset is chiefly dependent on the intensity of turbulence, although the scale and the spectrum must be expected to have some influence.
3. Very low turbulence level. Here, the dominant factor in the onset of transition is no longer the freestream turbulence. Since experiments in different facilities give widely different onset Reynolds numbers in this regime, it is reasonable to assume that transition is caused by residual disturbances specific to the facility in which the experiments are conducted.

The onset Reynolds number R_t' reported most often is the value at which a surface parameter (Pitot pressure, skin friction, etc.) shows a minimum. However, the onset Reynolds number R_t at which turbulent spots first appear is upstream of R_t' and may be derived from relations given by Narasimha and Dey (1986). These require knowledge of the extent of the transition zone, and we shall find it sufficient to use here the simpler conversion factor implicit in the correlations of Narasimha and Dey (1984), and tentatively take R_t as

$$R_t \sim 0.9\, R_t'. \tag{1}$$

In this report, experimental data are used to find an expression for R_t', and R_t is then calculated from the above equation.

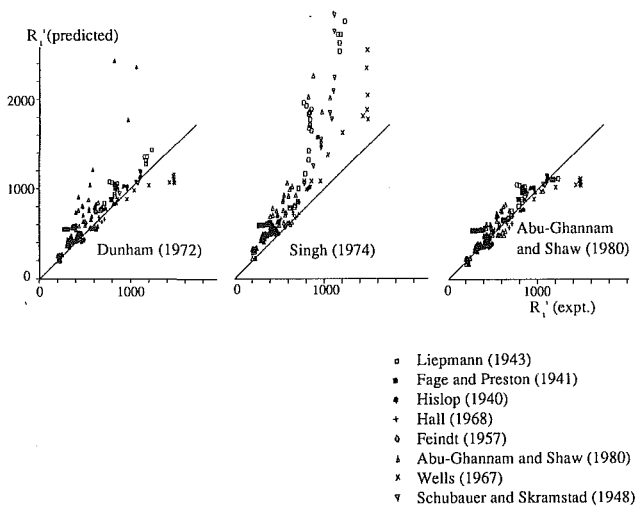

Fig. 1 Comparison of existing onset prediction correlations with experiment

[1]National Aeronautical Laboratory, Bangalore 560017, India.
[2]Dr. Narasimha's current address is University Engineering Department, Cambridge CB2 1PZ, UK.

Contributed by the Fluids Engineering Division of THE AMERICAN SOCIETY OF MECHANICAL ENGINEERS. Manuscript received by the Fluids Engineering Division December 14, 1989.

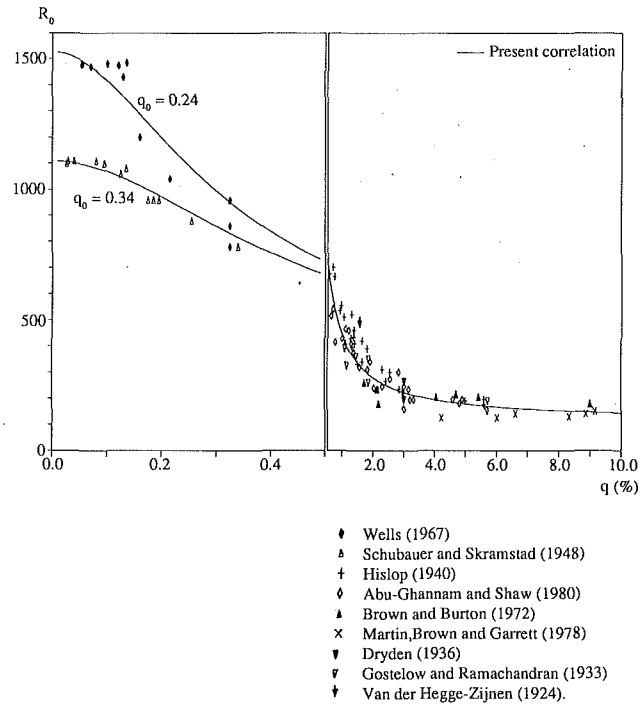

Fig. 2 Comparison of present correlation for zero pressure gradient with experiment. (Note expanded scale at low *q*.)

Earlier analysis (Narasimha and Dey, 1984) has shown that the onset Reynolds number at zero pressure gradient, R_0 has an approximate power law dependence on the freestream turbulence level q when it is in the "moderate" range. At moderate and high q, R_0 may therefore be expressed in the following form:

$$R_0 = a + b/q^p. \tag{2}$$

The experimental results for R_0 (compiled by Narasimha and Dey, 1984) at moderate to high values of q are best fitted by $a = 110$, $b = 340$ and $p = 1$ (see Fig. 2). We may argue that the residual facility-dependent disturbances may be represented by an equivalent turbulence intensity q_0; as this is in general uncorrelated with the freestream turbulence, the mean squares will add, and the total equivalent disturbances in the facility is just the quantity $(q^2 + q_0^2)^{1/2}$. In practice q_0 will in general depend on the operating conditions of the facility, but this is a factor that at the present stage has to be neglected. Equation (2) may now be written as

$$R_0 = 110 + \frac{340}{(q^2 + q_0^2)^{1/2}} \tag{3}$$

Values of q_0 providing the best fit are derived for each facility (using the data in Abu-Ghannam and Shaw, 1980), and are listed in Table 1; these must be seen as tentative and illustrative, as they have been derived assuming that all workers have used the same criterion for the location of transition onset, which is unlikely. If more precise information on how onset is defined is available, better values of q_0 can be derived.

Present Correlation in Flows Subjected to Pressure Gradients

The qualitative dependence of onset Reynolds number on the pressure gradient, as inferred from the experimental data in Abu-Ghannam and Shaw (1980), is shown in Fig. 3 (the data themselves are not shown as they are at many different values of q and q_0 and so would clutter the diagram). When the gradient is favorable, i.e., when $\lambda > 0$, the onset for a given q occurs, as expected, at a larger Reynolds number than at zero pressure gradient. However, although R_t' increases

Table 1 Inferred residual disturbance level of some facilities

	q_0 (%)
Abu-Ghannam and Shaw (1980)	0.33
Fage and Preston (1941)	0.70
Feindt (1957)	0.30
Hall (1968)	0.16
Hislop (1940)	0.30
Liepmann (1943)	0.36
Schubauer and Skramstad (1948)	0.34
Wells (1967)	0.24

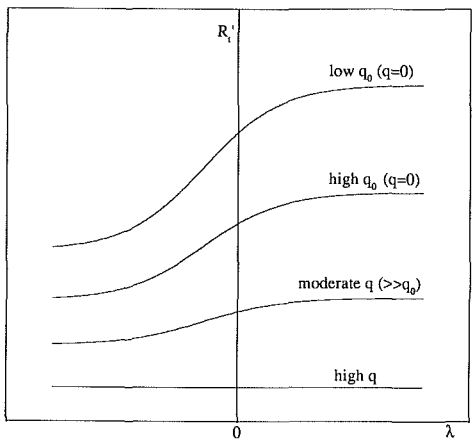

Fig. 3 Qualitative dependence of onset location on pressure gradient and freestream turbulence

rapidly at first as λ increases, it appears to level off toward an asymptotic value $R_t'(q, \lambda \to \infty)$ for a given q. Further, as q increases, the difference $R_t'(q, \lambda \to \infty) - R_0$ decreases; so at high turbulence levels the onset Reynolds number does not depend strongly on the pressure gradient. In adverse pressure gradients, the onset occurs earlier but otherwise the pattern is similar. With these features in mind, a pressure gradient factor can be imposed on (3), and the following empirical form is proposed:

$$R_t' = R_0\left\{1 + 0.17 \exp\left[-(q^2 + q_0^2)\right] \times \frac{1 - \exp(-60\lambda)}{1 + 0.4 \exp(-60\lambda)}\right\}. \tag{4}$$

The transition onset Reynolds numbers given by equations (3) and (4) are plotted against experimental data (from Abu-Ghannam and Shaw, 1980) in Fig. 4. It is seen that the present proposal fits all the data reasonably well.

Conclusion

The present proposal offers an improvement over existing onset prediction correlations since facility dependence is accounted for. The improvement is significant in facilities with low freestream turbulence. However, one comment is in order. It has recently been shown (Meier et al., 1987) that the onset of transition correlates better with the spectral density of the freestream turbulence in the frequency range of the Tollmien-Schlichting waves rather than with the total intensity. Unfortunately, such spectral information is not available in most experimental data published so far; it is for this reason that we have used the total turbulence intensity in the present work. As appropriate experimental data become available, however, it will be easy to implement the basic idea of the present proposal using the spectral density of the disturbances in the Tollmien-Schlichting band. Furthermore, we wish to emphasize that the present proposal of parametrizing facility-dependent disturbances can be used with other transition prediction tech-

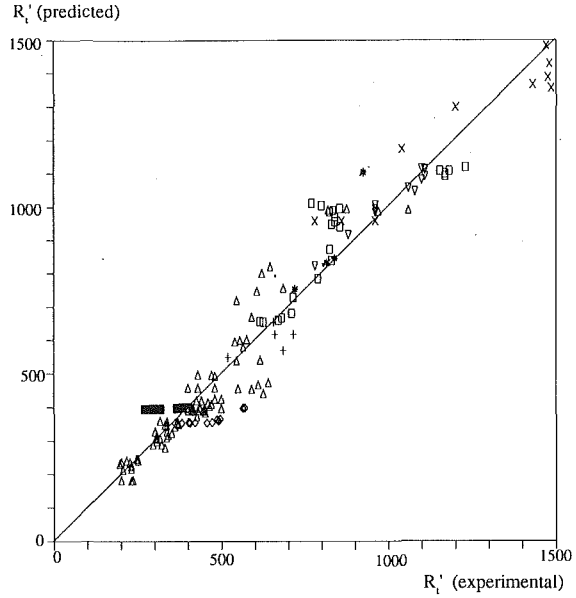

Fig. 4 Comparison of present correlation with experimental data (legend same as in Fig. 1)

niques as well, e.g., Granville (1953), Smith and Gamberoni (1956).

The fact that the onset Reynolds number is inversely proportional to the disturbance intensity when it is low may be of wider significance.

Acknowledgment

We thank Mr. R. Guruprasad and Mr. A. S. Rajasekar for their help with computer graphics.

References

Abu-Ghannam, B. J., and Shaw, R., 1980, "Natural Transition of Boundary Layers-the Effects of Turbulence, Pressure Gradient and Flow History," *J. Mech. Engg. Sci.*, Vol. 22, No. 5, pp. 213–228.

Arnal, D., Habiballah, M., and Coustols, E., 1984, "Theorie de l'Instabilite Laminaire et Criteres de Transition en Ecoulement Bi et Tridimensionnel," *La Recherche Aerospatiale*, No. 2, p. 125.

Dunham, J., 1972, "Prediction of Boundary Layer Transition on Turbomachinery Blades," AGARD AG 164, No. 3.

Granville, P. S., 1953, "The Calculation of the Viscous Drag on Bodies of Revolution, " David Taylor Model Basin Rep. 849.

Liepmann, H. W., 1943, "Investigations of Laminar Boundary Layer Stability and Transition on Curved Boundaries," NACA ACR 3H30.

Mack, L. M., 1977, "Transition and Laminar Instability," JPL Publ. 77-15.

Meier, H. U., Michel, U., Kreplin, H.-P., 1987, "The Influence of Wind Tunnel Turbulence on Boundary Layer Transition," *Perspectives in Turbulence Studies*, eds., H. U. Meier and P. Bradshaw, Springer-Verlag, pp. 26–46.

Narasimha, R., 1985, "The Laminar Turbulent Transition Zone in the Boundary Layer," *Prog. Aerospace Sci.*, Vol. 22, pp. 29–80.

Narasimha, R., and Dey, J., 1984, "Spot Formation Rate in Incompressible Constant-Pressure Boundary Layer," Rep. 84 FM 11, Aero. Engg. Dept., Indian Inst. of Sci., Bangalore.

Narasimha, R., and Dey, J., 1986, "Transitional Spot Formation Rate in Two-dimensional Boundary Layers," *Numerical and Physical Aspects of Aerodynamic Flows, III.*, ed., T. Cebeci, Springer-Verlag, pp. 57–74.

Schubauer, G. B., and Klebanoff, P. S., 1955, "Contributions on the Mechanics of Boundary Layer Transition," NACA TN 3489.

Schubauer, G. B., and Skramstad, H. K., 1948, "Laminar Boundary-Layer Oscillations and Transition on a Flat Plate," NACA Report 909.

Seyb, N. J., 1967, "A Simplified and Practical Method of Determining the External Heat-transfer Coefficient Round a Turbine Blade," ARC Report 29398.

Singh, U. K., 1974, "The Effect of Viscosity on the Flow Past Aerofoils in Cascade," PhD thesis, Liverpool University.

Smith, A. M. O., and Gamberoni, N., 1956, "Transition, Pressure Gradient and Stability Theory," Douglas Aircraft Co., Rep. ES26388.

Thwaites, B., 1949, "Approximate Calculation of the Laminar Boundary Layer," *Aero. Quart.*, Vol. 1, Part 3.

Wells, C. S., Jr., 1967, "Effects of Free-stream Turbulence on Boundary Layer Transition," *AIAA J.*, Vol. 5, No. 1, pp. 172–174.

An Erosion Resistant Pipe Bend

K.Horii,[1] Y. Matsumae,[2] X. M. Cheng,[2] M. Takei,[2] E. Yasukawa,[2] and B. Hashimoto[2]

A new 90-deg bend shape has been developed for erosion resistance. The design consists of a gradually expanding inlet, a large-diameter curved section, and a gradually contracting outlet. Tests were conducted using alumina particles in air at an average velocity of 27 m/s, passing through a carbon steel bend. The new bend design had an erosion life exceeding 4000 hr, compared to 38 hr for a conventional bend design.

Introduction

In pneumatic transportation of powders, the erosive action depends primarily on the particle speed (Mills and Mason, 1981), the impact angle (Tilly, 1969), and the physical properties of the powders. Many techniques have been employed to reduce erosion, but none is completely satisfactory.

Erosion can be reduced by decreasing the gas flow rate. However, plugging then occurs, as the gas flow rate drops below the blockage limit. Our earlier work (Horii et al., 1988) has shown that the critical blockage velocity depends upon the flow pattern. One may reduce erosion by deforming the flow pattern so as to reduce the blockage limit. In the case of a 90 deg bend, this change in flow pattern can be achieved by altering the shape of the bend.

Tilly (1969) has shown that the impact angle is crucial to erosion. For a bend made of cast iron, the erosion rate is greatest when the impact angle is between 30 and 60 deg. To minimize erosion, this critical range of impact angles has to be avoided. The present design alters the flow pattern with the goal of avoiding erosive impact.

A schematic of the new design is given in Fig. 1. All dimensions are in mm. The bend begins with a gradual expansion which increases the pipe diameter fivefold, followed by a 90

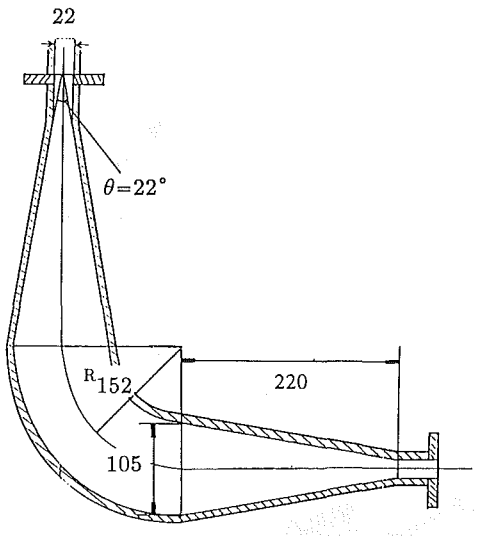

Fig. 1 Schematic of the new bend design

[1]Shirayuri Women's College, 1-25 Midorigaoka, Chofu-shi, Tokyo 182, Japan. Mem. ASME

[2]Waseda University, 3-4-1 Ohkubo, Shinjuku-ku, Tokyo 169, Japan.

Contributed by the Fluids Engineering Division of THE AMERICAN SOCIETY OF MECHANICAL ENGINEERS. Manuscript received by the Fluids Engineering Division March 20, 1988.

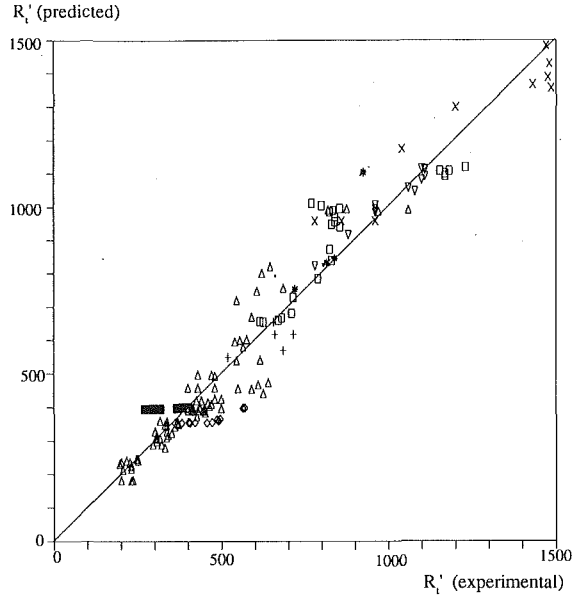

Fig. 4 Comparison of present correlation with experimental data (legend same as in Fig. 1)

niques as well, e.g., Granville (1953), Smith and Gamberoni (1956).

The fact that the onset Reynolds number is inversely proportional to the disturbance intensity when it is low may be of wider significance.

Acknowledgment

We thank Mr. R. Guruprasad and Mr. A. S. Rajasekar for their help with computer graphics.

References

Abu-Ghannam, B. J., and Shaw, R., 1980, "Natural Transition of Boundary Layers-the Effects of Turbulence, Pressure Gradient and Flow History," *J. Mech. Engg. Sci.*, Vol. 22, No. 5, pp. 213–228.

Arnal, D., Habiballah, M., and Coustols, E., 1984, "Theorie de l'Instabilite Laminaire et Criteres de Transition en Ecoulement Bi et Tridimensionnel," *La Recherche Aerospatiale*, No. 2, p. 125.

Dunham, J., 1972, "Prediction of Boundary Layer Transition on Turbomachinery Blades," AGARD AG 164, No. 3.

Granville, P. S., 1953, "The Calculation of the Viscous Drag on Bodies of Revolution, " David Taylor Model Basin Rep. 849.

Liepmann, H. W., 1943, "Investigations of Laminar Boundary Layer Stability and Transition on Curved Boundaries," NACA ACR 3H30.

Mack, L. M., 1977, "Transition and Laminar Instability," JPL Publ. 77-15.

Meier, H. U., Michel, U., Kreplin, H.-P., 1987, "The Influence of Wind Tunnel Turbulence on Boundary Layer Transition," *Perspectives in Turbulence Studies*, eds., H. U. Meier and P. Bradshaw, Springer-Verlag, pp. 26–46.

Narasimha, R., 1985, "The Laminar Turbulent Transition Zone in the Boundary Layer," *Prog. Aerospace Sci.*, Vol. 22, pp. 29–80.

Narasimha, R., and Dey, J., 1984, "Spot Formation Rate in Incompressible Constant-Pressure Boundary Layer," Rep. 84 FM 11, Aero. Engg. Dept., Indian Inst. of Sci., Bangalore.

Narasimha, R., and Dey, J., 1986, "Transitional Spot Formation Rate in Two-dimensional Boundary Layers," *Numerical and Physical Aspects of Aerodynamic Flows, III.*, ed., T. Cebeci, Springer-Verlag, pp. 57–74.

Schubauer, G. B., and Klebanoff, P. S., 1955, "Contributions on the Mechanics of Boundary Layer Transition," NACA TN 3489.

Schubauer, G. B., and Skramstad, H. K., 1948, "Laminar Boundary-Layer Oscillations and Transition on a Flat Plate," NACA Report 909.

Seyb, N. J., 1967, "A Simplified and Practical Method of Determining the External Heat-transfer Coefficient Round a Turbine Blade," ARC Report 29398.

Singh, U. K., 1974, "The Effect of Viscosity on the Flow Past Aerofoils in Cascade," PhD thesis, Liverpool University.

Smith, A. M. O., and Gamberoni, N., 1956, "Transition, Pressure Gradient and Stability Theory," Douglas Aircraft Co., Rep. ES26388.

Thwaites, B., 1949, "Approximate Calculation of the Laminar Boundary Layer," *Aero. Quart.*, Vol. 1, Part 3.

Wells, C. S., Jr., 1967, "Effects of Free-stream Turbulence on Boundary Layer Transition," *AIAA J.*, Vol. 5, No. 1, pp. 172–174.

An Erosion Resistant Pipe Bend

K.Horii,[1] Y. Matsumae,[2] X. M. Cheng,[2] M. Takei,[2] E. Yasukawa,[2] and B. Hashimoto[2]

A new 90-deg bend shape has been developed for erosion resistance. The design consists of a gradually expanding inlet, a large-diameter curved section, and a gradually contracting outlet. Tests were conducted using alumina particles in air at an average velocity of 27 m/s, passing through a carbon steel bend. The new bend design had an erosion life exceeding 4000 hr, compared to 38 hr for a conventional bend design.

Introduction

In pneumatic transportation of powders, the erosive action depends primarily on the particle speed (Mills and Mason, 1981), the impact angle (Tilly, 1969), and the physical properties of the powders. Many techniques have been employed to reduce erosion, but none is completely satisfactory.

Erosion can be reduced by decreasing the gas flow rate. However, plugging then occurs, as the gas flow rate drops below the blockage limit. Our earlier work (Horii et al., 1988) has shown that the critical blockage velocity depends upon the flow pattern. One may reduce erosion by deforming the flow pattern so as to reduce the blockage limit. In the case of a 90 deg bend, this change in flow pattern can be achieved by altering the shape of the bend.

Tilly (1969) has shown that the impact angle is crucial to erosion. For a bend made of cast iron, the erosion rate is greatest when the impact angle is between 30 and 60 deg. To minimize erosion, this critical range of impact angles has to be avoided. The present design alters the flow pattern with the goal of avoiding erosive impact.

A schematic of the new design is given in Fig. 1. All dimensions are in mm. The bend begins with a gradual expansion which increases the pipe diameter fivefold, followed by a 90

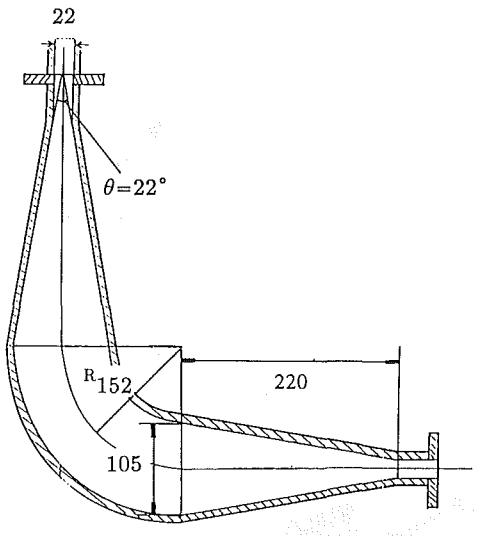

Fig. 1 Schematic of the new bend design

[1]Shirayuri Women's College, 1-25 Midorigaoka, Chofu-shi, Tokyo 182, Japan. Mem. ASME

[2]Waseda University, 3-4-1 Ohkubo, Shinjuku-ku, Tokyo 169, Japan.

Contributed by the Fluids Engineering Division of THE AMERICAN SOCIETY OF MECHANICAL ENGINEERS. Manuscript received by the Fluids Engineering Division March 20, 1988.

deg section and, finally, a gradual contraction back to the diameter of the transporting pipe. For erosion testing, the bends were made of carbon steel (JIS G3452 SGP, Shore hardness 21). For flow visualization, alternate bends were made of transparent acrylic.

Test Procedure

Experiments were carried out to study erosion in the new bend design and also in conventional bends. The bends were placed in various positions, including rising, falling, and horizontal sections. The total length of pipeline was 37 m (rise 4.8 m, fall 2.9 m, horizontal 29.3 m).

The test powder was alumina (160-200 mesh), which was fed into the pipe, using a rotary shelf-type bulk feeder, at a rate of 60 kg/hr.

The rate of airflow was 36 m^3/hr, corresponding to a mean velocity of 27 m/s in the 21.6-mm diameter pipe. The weight ratio of air to alumina was thus approximately 7 to 1.

Overall erosion rate was measured in terms of the time required to wear away a given thickness of pipe bend or, in some cases, the time to perforate a hole in the bend.

Flow Measurements and Visualization

Visualization of particle motion in the new bend design is shown in Fig. 2. In the expansion region, alumina was attracted to the internal wall and the flow formed an expanding vortex. In the contraction region, the particles moved toward the pipe axis and most of the alumina concentrated along the centerline, forming a central vortex.

Some representative velocity profile measurements by a fiber-optic laser anemometer are shown in Fig. 3 and verify the differing behavior of the particles in the inlet versus the exit. The inlet-cone profiles have a central valley, showing that flow is primarily near the wall. The exit contraction profiles show high velocity in the central region and less flow near the walls.

The outlet flow pattern shown in Figs. 2 and 3 does not seem to occur in a conventional bend. Outlet flow from a bend was visualized in Fig. 4 by a laser light sheet (Argon 4W) placed in the exit plane. Water vapor, produced by an ultrasonic vapor generator, provided the visualization. Exit flow from a conventional bend flows out along the outer wall due to centrifugal effects. Flow from the new bend design seems to concentrate near the pipe axis. Thus the flow pattern in the new bend appears, kinematically at least, to meet the desired goal of avoiding erosion.

This measured and observed behavior in the new band is in agreement with the theoretical studies of Batchelor (1967), who predicted that contraction of a swirling flow will tend to concentrate flow along the tube axis. Conversely, expanding a swirling flow will spread the flow out along the walls. It is believed that this changed flow pattern in the new design tends to avoid the critical erosion angles of 30-60 deg.

Erosion Results

Three different bends were tested: 1) a standard 21.6-mm or 20-A bend; 2) a standard bend five times larger, with diameter 105.3 mm or 100-A; and 3) the new bend design of Fig. 1. All were made of carbon steel. All bends were subjected to air at 36 m^3/hr and alumina at 60 kg/hr.

The 20-A conventional bend was perforated through its 2.8 mm thickness in 37.8 hr, for an erosion rate of 13.5 hr/mm at its mean air velocity of 27 m/s.

The fivefold-larger 100-A conventional bend had 25 times less air velocity, or 1.1 m/s. The bend suffered perforation of its 4.5 mm thickness in 144 hr, for an erosion rate of 32.0 hr/mm. Thus, although the air velocity was 25 times less, the

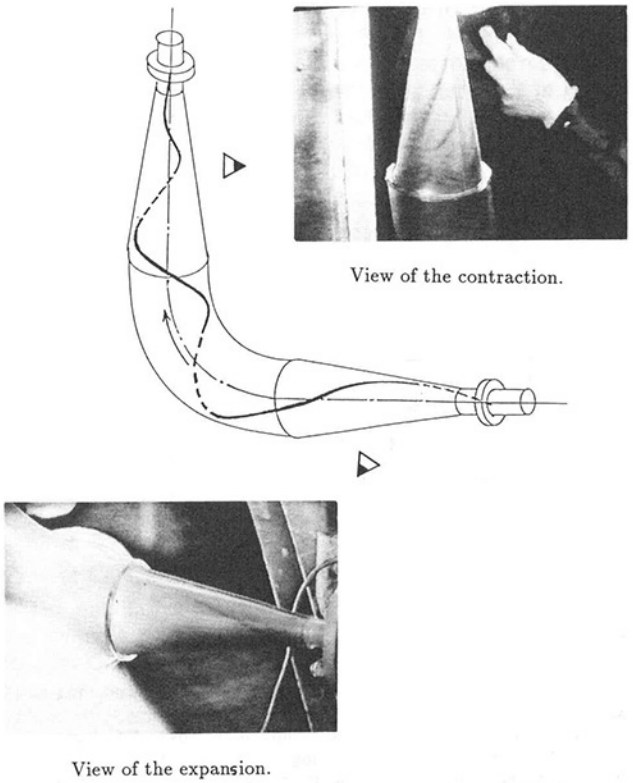

Fig. 2 Visualization of particle motion in the new bend

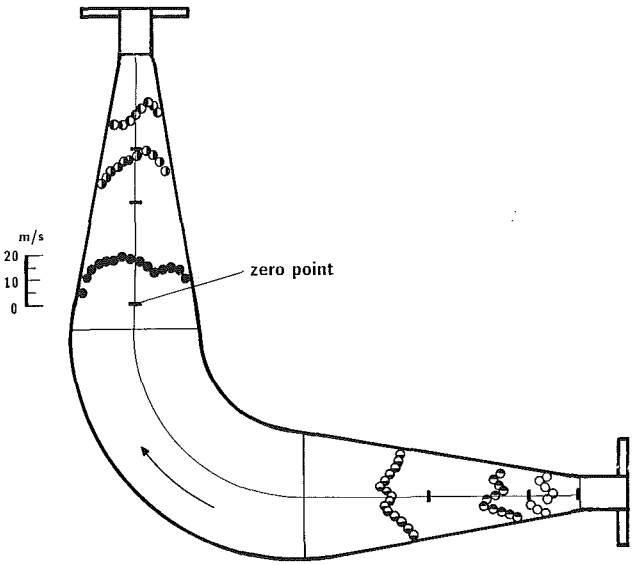

Fig. 3 Axial velocity distribution in the new bend

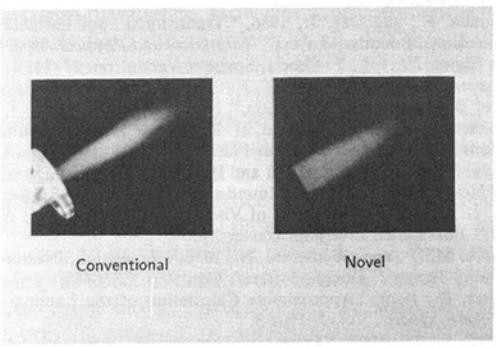

Fig. 4 Visualization of the flow pattern at a bend outlet

Table 1 Summary of the erosion test results

Bend shape	Conventional 20 A	Conventional 100 A	New Bend
Curvature, mm	200.0	152.4	152.4
Inside diameter, mm	21.6	105.3	105.3
Mean velocity, m/s	27.3	1.1	1.1
Mean bend life, hr	37.8 (holes form)	144 (holes form)	4000 (no holes)
Bend thickness, mm	2.8	4.5	4.5
Erosion depth, mm	2.8	4.5	3.0
Erosion rate, hr/mm	13.5	32.0	1330

erosion rate was only 2.4 times less. Total bend life was only increased by a factor of 3.8. Also, the flow velocity in this larger bend is below the blockage limit, and particle plugging occurred.

The new bend design, with the same maximum diameter of 105.3 mm and mean air velocity of 1.1 m/s as the larger conventional bend, did not perforate even after 4000 hours of continuous operation. The estimated erosion rate of the new bend was 1330 hr/mm: 42 times more than the large standard bend and 99 times more than the small standard bend. The new bend did not stagnate particles, and no plugging was observed. The alumina exited the bend in rotating string-like aggregations along the pipe axis.

Conclusions

The new bend design transported alumina particles continuously for 4000 hours, almost never plugging and beginning to form holes only at the end of the operation. The novel bend lasts one hundred times longer than a conventional bend of the same inlet diameter. It is believed that the new design changes the behavior of vortices in the entrance and exit cones so as to avoid the critical erosion angles of particles which might strike the bend surface. The new bend also avoids plugging and stagnation of the particles, even though its average air velocity is below the expected blockage limit.

References

Batchelor, G. K., 1967, *An Introduction to Fluid Dynamics*, Cambridge University Press, pp. 546–550.

Horii, K., Matsumae, Y., and Takei, M., *1988*, "An Erosion Resistant Bend-Theory and Development," ASME Forum on Industrial Applications of Fluid Mechanics, FED Vol. 70, pp. 13–17.

Mills, D., and Mason, J. S., 1981, "Conveying Velocity Effects in Bend Erosion," *J. Pipelines*, Vol. 1, No. 1, pp. 69–82.

Tilly, G. P., 1969, "Erosion Caused by Airborne Particles," *Wear*, Vol. 14, pp. 63–70.

Effect of Crossflow on Oscillatory Flow in a Porous Medium Between Two Parallel Plates in Relative Motion

V. Kumaran[1] and G. Ramanaiah[2]

This paper deals with the incompressible flow through a porous medium bounded by two parallel permeable plates, one of which is stationary and the other slides and oscillates in its own plane. Also uniform crossflow is superimposed through the plates. Analytical solutions for flow parameters are obtained. The effect of crossflow, permeability, and the frequency of the moving plate on the velocity, skin friction has been investigated. It is shown that skin friction can be reduced considerably by injection at the lower plate.

[1]Senior Research Fellow, Department of Mathematics, Anna University.

[2]Dean of Science and Humanities, Anna University, Madras, 600 025, India.

Contributed by the Fluids Engineering Division of THE AMERICAN SOCIETY OF MECHANICAL ENGINEERS. Manuscript received by the Fluids Engineering Division September 22, 1989.

Introduction

The effect of free-stream oscillation on the flow of an incompressible viscous fluid was studied by Lighthill (1954) and Stuart (1955). The unsteady flow between two infinite horizontal parallel plates with one plate oscillating about a nonzero mean velocity has been considered by Ishigaki (1971). Berman (1958) and Wang (1971) analyzed the unsteady flow between stationary permeable parallel plates under the influence of an oscillatory pressure gradient with a non-zero mean value. Soundalgekar et al, (1985) extended the study of velocity field obtained by Ishigaki (1971) to porous medium.

In this paper, in view of industrial applications (Longwell, 1966), (Esmond and Clark, 1966), we propose to analyze the influence of uniform cross-flow upon the unsteady flow through a porous medium bounded by two infinite horizontal permeable parallel plates when one plate oscillates with time about a nonzero velocity using Brinkman model (Sacheti, 1983).

Basic Equations

Consider a fluid flow through the porous medium of thickness h bounded by two infinite horizontal parallel permeable plates, the lower one is stationary and upper one slides in its own plane with velocity $U'(t') = U_0(1+p(w't'))$ where U_0 is a constant, t' is the time coordinate, w' is a constant having dimensions of frequency, and p is a dimensionless function of $w't'$. Origin is chosen on the lower plate and x'-axis is taken along the lower plate in the direction of the flow. Let the velocity $q = (u'(y', t'), V', 0)$ where y' is the normal coordinate, u' is the velocity along the x' direction, and V' is the magnitude of uniform cross-flow.

According to the Brinkman model the governing equations of the flow (Soundalgekar, 1985) are given by

$$\rho\left(\frac{\partial u'}{\partial t'} + V'\frac{\partial u'}{\partial y'}\right) = \rho\frac{dU'}{dt'} + \mu\frac{\partial^2 u'}{\partial y'^2} + \frac{\mu}{K}(U'-u') \tag{1a}$$

$$0 = -\frac{\partial p'}{\partial y'} - \frac{\mu}{K}V' \tag{1b}$$

where ρ, μ, ν, p' are the density, viscosity, kinematic viscosity, and pressure of the fluid, respectively, and K the permeability of the medium, with the boundary conditions

$$u' = 0 \text{ at } y' = 0,\ u' = U'(t') = U_0(1+p(w't')) \text{ at } y' = h \tag{2}$$

Introducting the following nondimensional quantities,

$$(u, U, y, t, w, R, \sigma) =$$

$$(u'/U_0,\ U'/U_0,\ y'/h,\ t'\,\nu/h^2,\ w'h^2/\nu,\ V'h/\nu,\ h/\sqrt{K})$$

where R is the suction Reynolds number and σ the permeability parameter, equations (1a) and (2) become

$$\frac{\partial u}{\partial t} + R\frac{\partial u}{\partial y} = \frac{\partial U}{\partial t} + \frac{\partial^2 u}{\partial y^2} + \sigma^2(U-u) \tag{3}$$

$$u(0) = 0,\ u(1) = U(t) = 1 + p(wt) \tag{4a,b}$$

Table 1 Summary of the erosion test results

Bend shape	Conventional 20 A	Conventional 100 A	New Bend
Curvature, mm	200.0	152.4	152.4
Inside diameter, mm	21.6	105.3	105.3
Mean velocity, m/s	27.3	1.1	1.1
Mean bend life, hr	37.8 (holes form)	144 (holes form)	4000 (no holes)
Bend thickness, mm	2.8	4.5	4.5
Erosion depth, mm	2.8	4.5	3.0
Erosion rate, hr/mm	13.5	32.0	1330

erosion rate was only 2.4 times less. Total bend life was only increased by a factor of 3.8. Also, the flow velocity in this larger bend is below the blockage limit, and particle plugging occurred.

The new bend design, with the same maximum diameter of 105.3 mm and mean air velocity of 1.1 m/s as the larger conventional bend, did not perforate even after 4000 hours of continuous operation. The estimated erosion rate of the new bend was 1330 hr/mm: 42 times more than the large standard bend and 99 times more than the small standard bend. The new bend did not stagnate particles, and no plugging was observed. The alumina exited the bend in rotating string-like aggregations along the pipe axis.

Conclusions

The new bend design transported alumina particles continuously for 4000 hours, almost never plugging and beginning to form holes only at the end of the operation. The novel bend lasts one hundred times longer than a conventional bend of the same inlet diameter. It is believed that the new design changes the behavior of vortices in the entrance and exit cones so as to avoid the critical erosion angles of particles which might strike the bend surface. The new bend also avoids plugging and stagnation of the particles, even though its average air velocity is below the expected blockage limit.

References

Batchelor, G. K., 1967, *An Introduction to Fluid Dynamics*, Cambridge University Press, pp. 546–550.

Horii, K., Matsumae, Y., and Takei, M., *1988*, "An Erosion Resistant Bend-Theory and Development," ASME Forum on Industrial Applications of Fluid Mechanics, FED Vol. 70, pp. 13–17.

Mills, D., and Mason, J. S., 1981, "Conveying Velocity Effects in Bend Erosion," *J. Pipelines*, Vol. 1, No. 1, pp. 69–82.

Tilly, G. P., 1969, "Erosion Caused by Airborne Particles," *Wear*, Vol. 14, pp. 63–70.

Effect of Crossflow on Oscillatory Flow in a Porous Medium Between Two Parallel Plates in Relative Motion

V. Kumaran[1] and G. Ramanaiah[2]

This paper deals with the incompressible flow through a porous medium bounded by two parallel permeable plates, one of which is stationary and the other slides and oscillates in its own plane. Also uniform crossflow is superimposed through the plates. Analytical solutions for flow parameters are obtained. The effect of crossflow, permeability, and the frequency of the moving plate on the velocity, skin friction has been investigated. It is shown that skin friction can be reduced considerably by injection at the lower plate.

[1]Senior Research Fellow, Department of Mathematics, Anna University.

[2]Dean of Science and Humanities, Anna University, Madras, 600 025, India.

Contributed by the Fluids Engineering Division of THE AMERICAN SOCIETY OF MECHANICAL ENGINEERS. Manuscript received by the Fluids Engineering Division September 22, 1989.

Introduction

The effect of free-stream oscillation on the flow of an incompressible viscous fluid was studied by Lighthill (1954) and Stuart (1955). The unsteady flow between two infinite horizontal parallel plates with one plate oscillating about a nonzero mean velocity has been considered by Ishigaki (1971). Berman (1958) and Wang (1971) analyzed the unsteady flow between stationary permeable parallel plates under the influence of an oscillatory pressure gradient with a non-zero mean value. Soundalgekar et al, (1985) extended the study of velocity field obtained by Ishigaki (1971) to porous medium.

In this paper, in view of industrial applications (Longwell, 1966), (Esmond and Clark, 1966), we propose to analyze the influence of uniform cross-flow upon the unsteady flow through a porous medium bounded by two infinite horizontal permeable parallel plates when one plate oscillates with time about a nonzero velocity using Brinkman model (Sacheti, 1983).

Basic Equations

Consider a fluid flow through the porous medium of thickness h bounded by two infinite horizontal parallel permeable plates, the lower one is stationary and upper one slides in its own plane with velocity $U'(t') = U_0(1+p(w't'))$ where U_0 is a constant, t' is the time coordinate, w' is a constant having dimensions of frequency, and p is a dimensionless function of $w't'$. Origin is chosen on the lower plate and x'-axis is taken along the lower plate in the direction of the flow. Let the velocity $q = (u'(y', t'), V', 0)$ where y' is the normal coordinate, u' is the velocity along the x' direction, and V' is the magnitude of uniform cross-flow.

According to the Brinkman model the governing equations of the flow (Soundalgekar, 1985) are given by

$$\rho\left(\frac{\partial u'}{\partial t'} + V'\frac{\partial u'}{\partial y'}\right) = \rho\frac{dU'}{dt'} + \mu\frac{\partial^2 u'}{\partial y'^2} + \frac{\mu}{K}(U'-u') \tag{1a}$$

$$0 = -\frac{\partial p'}{\partial y'} - \frac{\mu}{K}V' \tag{1b}$$

where ρ, μ, ν, p' are the density, viscosity, kinematic viscosity, and pressure of the fluid, respectively, and K the permeability of the medium, with the boundary conditions

$$u' = 0 \text{ at } y' = 0,\ u' = U'(t') = U_0(1+p(w't')) \text{ at } y' = h \tag{2}$$

Introducting the following nondimensional quantities,

$$(u, U, y, t, w, R, \sigma) =$$

$$(u'/U_0,\ U'/U_0,\ y'/h,\ t'\,\nu/h^2,\ w'h^2/\nu,\ V'h/\nu,\ h/\sqrt{K})$$

where R is the suction Reynolds number and σ the permeability parameter, equations (1a) and (2) become

$$\frac{\partial u}{\partial t} + R\frac{\partial u}{\partial y} = \frac{\partial U}{\partial t} + \frac{\partial^2 u}{\partial y^2} + \sigma^2(U-u) \tag{3}$$

$$u(0) = 0,\ u(1) = U(t) = 1 + p(wt) \tag{4a,b}$$

In view of the form of (4*b*) we assume,

$$u(y,t) = f_0(y) + p(wt) f_1(y) \tag{5}$$

in equations (3) and (4) and equate the steady, unsteady terms. Thus we get

$$f_0'' - R f_0' - \sigma^2 f_0 = -\sigma^2 \tag{6}$$

$$\frac{f_1'' - R f_1'}{f_1 - 1} - \sigma^2 = \frac{1}{p}\frac{dp}{dt} \tag{7}$$

and

$$f_0(0) = f_1(0) = 0, f_0(1) = f_1(1) = 1 \tag{8}$$

where primes denote differentiation with respect to y.

Since the left member of equation (7) is a function of y and that of the right member is a function of t, each must be a constant, C say. Hence the function p is exponential or periodic in time according as C is real or pure imaginary respectively. Choosing $C = iw$ (pure imaginary) so that $p(wt) = \epsilon\, e^{iwt}$ (ϵ is the amplitude of oscillation and w is the frequency) and equation (7) becomes

$$f_1'' - R f_1' - \sigma_1^2 f_1 = -\sigma_1^2 \tag{9}$$

where $\sigma_1^2 = \sigma^2 + iw$.

Solving equations (6), (8), and (9) we get from equation (5),

$$u(y,t) = 1 + e^{Ry/2}\,(\coth\sigma_3 \sinh\sigma_3 y - \cosh\sigma_3 y) + \epsilon\, e^{iwt}[1 + e^{Ry/2}\,(\coth\sigma_2 \sinh\sigma_2 y - \cosh\sigma_2 y)] \tag{10}$$

where $\sigma_3^2 = (R^2 + 4\sigma^2)/4$ and $\sigma_2^2 = (R^2 + 4\sigma_1^2)/4$.

The real part of equation (10) now gives the transient velocity corresponding to the upper plate velocity $U(t) = 1 + \epsilon \cos wt$ as

$$u = 1 + e^{Ry/2}\,(\coth\sigma_3 \sinh\sigma_3 y - \cosh\sigma_3 y) + \epsilon(M_r \cos wt - M_i \sin wt) \tag{11}$$

where $M_r + iM_i = f_1(y)$.

The skin friction at the stationary plate is given by,

$$T' = \mu \left.\frac{\partial u'}{\partial y'}\right|_{y'=0}, \text{ which takes the dimensionless form}$$

$$T = \frac{T'h}{\mu U_0} = \left.\frac{\partial u}{\partial y}\right|_{y=0} \tag{12}$$

(Another form of nondimensional skin friction is

$$\frac{T'}{\rho U_0^2} = T/\mathrm{Re}$$

where Re ($= \rho U_0 h/\mu$) is the flow Reynolds number.) Using equation (10) in (12), we get the skin friction as

$$T = T_0 + \epsilon\, e^{iwt}\left(\sigma_2 \coth\sigma_2 - \frac{R}{2}\right) \tag{13}$$

where $T_0 (= \sigma_3 \coth\sigma_3 - R/2)$ is the mean skin friction, or, in terms of amplitude Q and phase β,

$$T = T_0 + \epsilon\, Q \cos(wt + \beta) \tag{14}$$

where $Be^{i\alpha} = \sigma_2 \coth\sigma_2$,

$$Q = \left(B^2 + \frac{R^2}{4} - BR\cos\alpha\right)^{1/2}$$

$$\text{and } \tan\beta = \frac{\tan\alpha}{1 - R/(2B\cos\alpha)}$$

In the absence of crossflow i.e., $R = 0$, the velocity field given by equation (11) reduces to that of obtained by Soundalgekar et al. (1985) and equation (14) becomes

$$T = \sigma \coth\sigma + \epsilon\, B \cos(wt + \alpha) \tag{15}$$

where $Be^{i\alpha} = \sigma_1 \coth\sigma_1$,

which is the corrected version of their expression for T. Further for free flow ($\sigma = 0$), in the absence of crossflow, the velocity field and skin friction expressions reduce to that of Ishigaki (1971).

Discussion and Conclusions

For numerical computation we considered the case $\epsilon = 0.2$. It is seen from Fig. 1, the mean velocity $f_0(y)$ increases with decreasing R. Also the mean velocity increases with σ and it is more pronounced with increasing R. From Fig. 2, we found that the mean skin friction increases with σ, where as it decreases with increasing R. Note that the rate at which the mean friction decreases is more for decrease in suction ($R < 0$) than for increase in injection at the lower plate. The transient velocity profiles are shown in Figs. 3–5. From Fig. 3, it is clear that the transient velocity increases with increasing σ, i.e., with decreasing the permeability K. In Fig. 4, the transient velocity profiles for $w = 10$, $\sigma = .2$ is shown. As already noted for large injection (Fig. 2) the mean skin friction is small and the unsteady skin friction becomes negative for certain values of

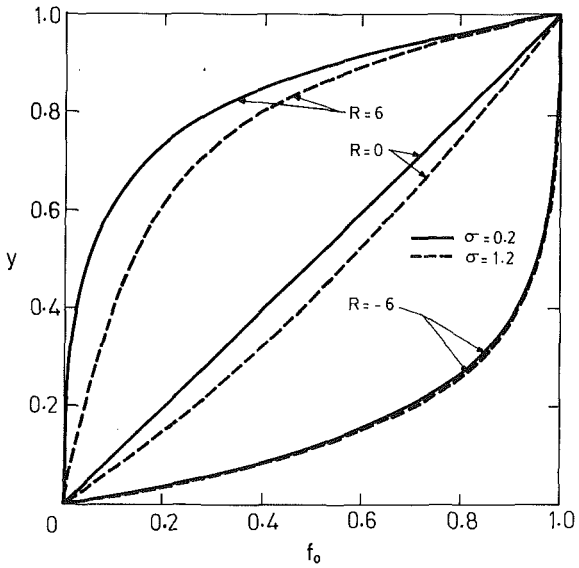

Fig. 1 Mean velocity profiles for different R and σ

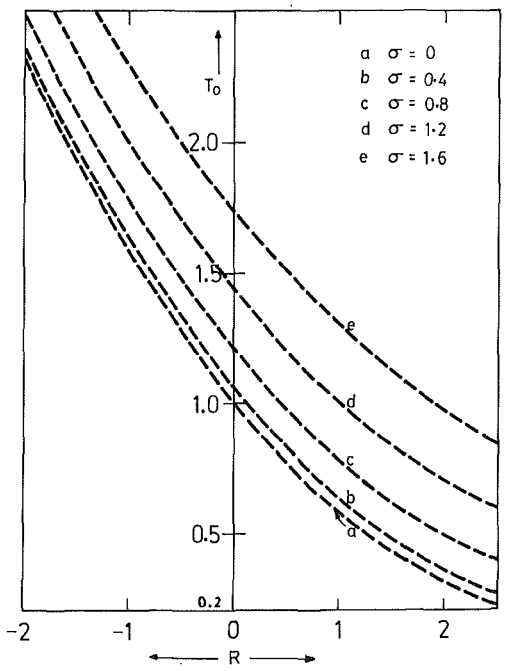

Fig. 2 Mean skinfriction versus R for various σ

wt (for $\pi/4$, $\pi/2$, π in Fig. 4) with large magnitude than the mean skin friction. Thus the overall skin friction at the lower plate becomes negative. Hence this causes back flow near the lower plate, which is seen from Fig. 4 for $R=6$. Where as for small frequencies (Fig. 5) back flow is not prevailed. In this case we see boundary layer character near the upper plate for large positive R (Injection) and near the lower plate for large negative R (suction at the lower plate).

The numerical values of skin friction at the lower plate for $w=10$ is given in Table 1. As pointed out by Mario Latelier (1986) the skin friction decreases with decreasing σ i.e., with increasing permeability K. The values of the amplitude of skin friction Q and the phase lead β of skin friction with respect to the oscillating plate have been shown in Table 2. The following results are set out from the above investigation.

(i) Increase in injection velocity ($R>0$) or decrease in suction velocity at lower plate leads to decrease in T, i.e., the skin friction can be reduced by injection at lower plate.

(ii) The amplitude of skin friction Q increases with frequency w.

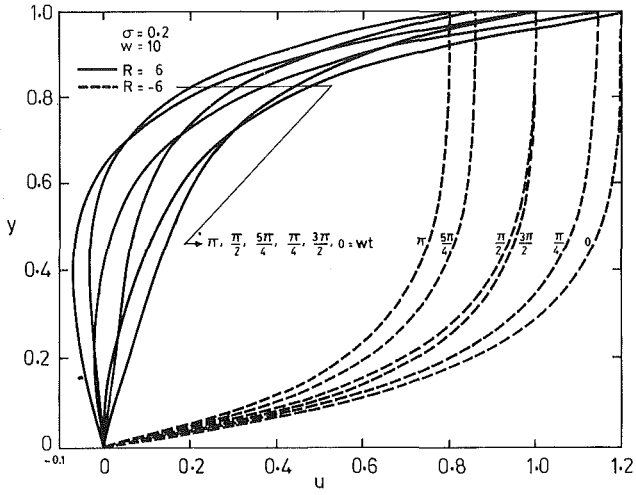

Fig. 4 Transient velocity profiles for $\sigma=0.2$, $w=10$

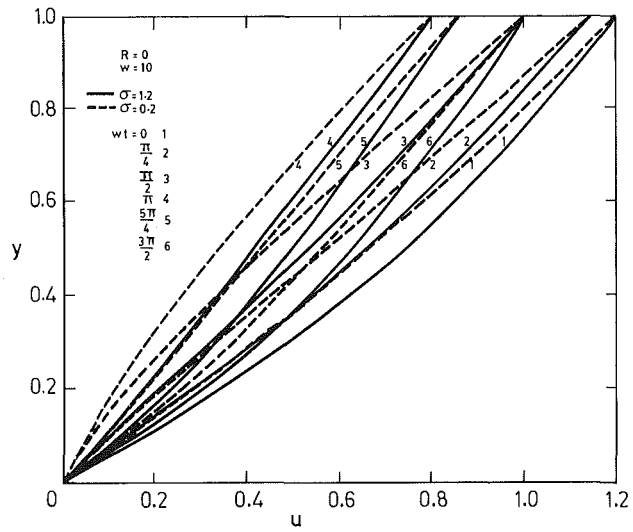

Fig. 3 Transient velocity profiles for $R=0$, $w=10$

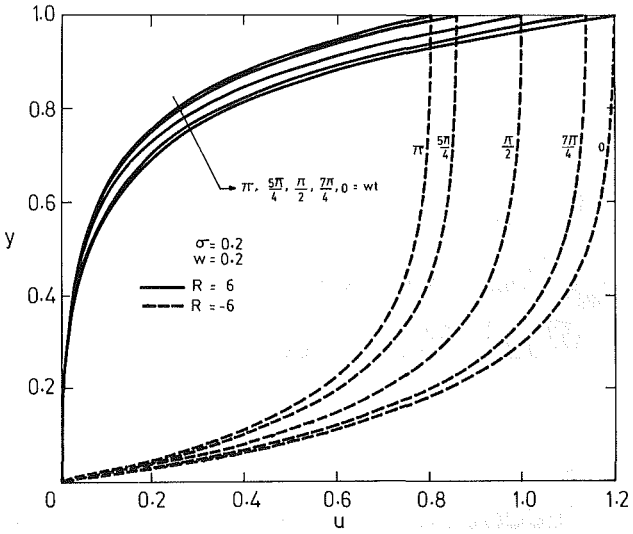

Fig. 5 Transient velocity profiles for $\sigma=0.2$, $w=0.2$

Table 1 Values of the skin friction T for $w=10$

R		-1.5		0		1.5	
σ		0.2	1.2	0.2	1.2	0.2	1.2
wt	0	2.7646	2.8002	1.4491	1.6701	0.9646	1.0002
	$\pi/2$	1.5004	1.7583	0.5598	0.7802	0.0036	0.2583
	π	1.3437	1.5300	0.5775	0.7290	0.1437	0.3300
	$3\pi/2$	2.3824	2.5719	1.4668	1.6189	0.8824	1.0719

Table 2 Values of the amplitude Q and $\tan\beta$

R		-1.5			0			1.5	
w	10	15	20	10	15	20	10	15	20
σ					$\tan\beta$				
0.2	0.7327	0.7662	0.7873	1.0407	1.0094	1.0078	1.4666	1.3293	1.2654
1.2	0.6405	0.7039	0.7396	0.8911	0.9188	0.9315	1.2140	1.1904	1.1694
4.2	0.2192	0.3084	0.3819	0.2635	0.3677	0.4516	0.3089	0.4294	0.5250
σ					Q				
0.2	3.7158	4.4608	5.0529	3.1447	3.8951	4.4881	2.6580	3.3950	3.9839
1.2	3.7711	4.4883	5.0753	3.1515	3.8940	4.4905	2.6353	3.3740	3.9708
4.2	5.2862	5.5692	5.8936	4.5020	4.8190	5.1637	3.8345	4.1594	4.5242

(iii) The phase lead β of the skin friction with respect to the oscillating plate decreases with increase in σ.

(iv) Decrease in injection velocity ($R > 0$) or increase in suction velocity at the lower plate leads to decrease in β but increase in Q.

Acknowledgment

One of the authors (V.K.) is thankful to the Council of Scientific and Industrial Research, New Delhi, India for the financial assistance. The authors are grateful to the referees for their valuable suggestions to improve the text.

References

Berman, A. S., 1958, "Laminar Flow in an Annulus with Porous Walls," *J. App. Physics*, Vol. 29, pp. 71–75.

Esmond, W. G., and Clark, H., 1966, "Mathematical Analysis and Mass Transfer Optimization of a Compact Low Cost, Pumpless System For Hemodialysis (Dialung)," *Proceedings, Biomedical Fluid Mechanics Symposium*, ASME.

Ishigaki, H., 1971, "An Exact Periodic Solution of the Energy Equation," *J. Fluid Mech.*, Vol. 50, pp. 657–668.

Lighthill, M. J., 1954, "The Response of Laminar Skin Friction and Heat Transfer to Fluctuations in the Stream Velocity," *Proc. Roy. Soc.* (London), Vol. A224, pp. 1–23.

Longwell, P. A., 1966, *Mechanics of Fluid Flow*, McGraw-Hill, New York.

Latelier, Mario, 1986, Discussion on "Unsteady Flow in a Porous Medium Between Two Infinite Parallel Plates in Relative Motion," ASME JOURNAL OF FLUIDS ENGINEERING, Vol. 108, p. 489.

Sacheti, N. C., 1983, "Application of Brinkman Model in Viscous Incompressible Flow Through a Porous Channel," *Jour. Math. Phy. Sci.*, Vol. 17, pp. 567–578.

Soundalgekar, V. M., Takhar, H. S., and Singh, M., 1985, "Unsteady Flow in a Porous Medium Between Two Infinite Parallel Plates in Relative Motion," ASME JOURNAL OF FLUIDS ENGINEERING, Vol. 107, pp. 534–535.

Stuart, I. T., 1955, "A Solution of Navier-Stokes and Energy Equations Illustrating the Response of Skin Friction and Temperature of an Infinite Plate Thermometer to Fluctuations in the Stream Velocity," *Proc. Roy. Soc.* (London), Vol. A231, pp. 116–130.

Wang, C. Y., 1971, "Pulsatile Flow in a Porous Channel," ASME *Journal of Applied Mechanics*, Vol. 38, pp. 553–555.